Evaluation of Microstructure, Mechanical and Biological Properties of Mg-Zn-RE Alloys for Biocompatible and Biodegradable Implant Applications

By

ARUNKUMAR S

Registration No: 20EE20J39023

A thesis submitted to the
Academy of Scientific and Innovative Research
for the award of the degree of

DOCTOR OF PHILOSOPHY
in
ENGINEERING

Under the Supervision of

Dr. A. Srinivasan
Senior Principal Scientist
&
Dr. K. G. Raghu
Chief Scientist
(Co-Supervisor)

CSIR-National Institute for Interdisciplinary Science and Technology

(CSIR-NIIST), Thiruvananthapuram- 695 019, Kerala, India

Academy of Scientific and Innovative Research
AcSIR Headquarters, CSIR-HRDC campus, Sector 19, Kamla Nehru Nagar,
Ghaziabad, U.P.- 201002, India

February 2025

राष्ट्रीय अंतर्विषयी विज्ञान तथा प्रौद्योगिकी संस्थान
वैज्ञानिक तथा औद्योगिक अनुसंधान परिषद् | विज्ञान तथा प्रौद्योगिकी मंत्रालय, भारत सरकार
इंडस्ट्रियल इस्टेट पी.ओ., पाप्पनंकोड, तिरुवनंतपुरम, भारत-695 019
CSIR-NATIONAL INSTITUTE FOR INTERDISCIPLINARY SCIENCE AND TECHNOLOGY (CSIR-NIIST)
Council of Scientific & Industrial Research | Ministry of Science and Technology, Govt. of India
Industrial Estate P.O., Pappanamcode, Thiruvananthapuram, India-695 019

CERTIFICATE

This is to certify that the work incorporated in this Ph.D. thesis entitled, "***Evaluation of Microstructure, Mechanical and Biological properties of Mg-Zn-RE alloys for Biocompatible and Biodegradable Implant Applications***", submitted by Mr. Arunkumar S, to the Academy of Scientific and Innovative Research (AcSIR) in fulfilment of the requirements for the award of the Degree of Doctor of Philosophy in Engineering, embodies original research work carried out by the student. We further certify that this work has not been submitted to any other University or Institution in part or full for the award of any degree or diploma. Research materials obtained from other sources and used in this research work have been duly acknowledged in the thesis. Images, illustrations, figures, tables etc., used in the thesis from other sources, have also been duly cited and acknowledged.

24/2/25
Mr. Arunkumar S
(Student)

24/02/2025
Dr. A Srinivasan
(Research Supervisor)

24/02/2025
Dr. K. G. Raghu
(Research Co-Supervisor)

STATEMENTS OF ACADEMIC INTEGRITY

I, Arun Kumar S., a PhD student of the Academy of Scientific and Innovative Research (AcSIR) with Registration No. 20EE20J39023 hereby undertake that, the thesis entitled "***Evaluation of Microstructure, Mechanical and Biological properties of Mg-Zn-RE alloys for Biocompatible and Biodegradable Implant Applications***" has been prepared by me and that the document reports original work carried out by me and is free of any plagiarism in compliance with the UGC regulations on "Promotion of Academic Integrity and Prevention of Plagiarism in Higher Educational Institutions (2018)" and the CSIR Guidelines for "Ethics in Research and in Governance (2020)".

24/2/25

Mr. Arunkumar S

Thiruvananthapuram
24-02-2025

It is hereby certified that the work done by the student, under our supervision, is plagiarism free in accordance with the UGC Regulations on "Promotion of Academic Integrity and Prevention of Plagiarism in Higher Educational Institutions (2018)" and the CSIR Guidelines for "Ethics in Research and in Governance (2020)".

24/02/2025

Dr. A Srinivasan
(Research Supervisor)

24/02/2025

Dr. K. G. Raghu
(Research Co-Supervisor)

Thiruvananthapuram
24-02-2025

ACKNOWLEDGEMENT

I would like to take this opportunity to extend my sincere gratitude and appreciation to all those who have been helped me for doing the work and made this Ph.D. thesis possible.

With deep regards and respect, I would like to express my profound gratitude to my research supervisors Dr. A. Srinivasan, Senior Principal Scientist of Materials Science and Technology Division and Dr. K.G. Raghu, Chief Scientist of Agroprocessing and Technology Division, CSIR-National Institute for Interdisciplinary Science and Technology (CSIR-NIIST), Thiruvananthapuram, for suggesting this exciting area, their sustained enthusiasm, creative suggestions, dedicated help, encouragement, advice, and useful corrections of this research work.

I thank Dr. C Anandharamakrishnan Director and Dr. A. Ajayagosh, former director of the NIIST for providing the necessary facilities for carrying out this work. Thanks, are also due to Dr. S. Savithri, Dr. M. Ravi and Dr. S. Ananthakumar the heads of Materials Science and Technology Division during my tenure at CSIR-NIIST, for their valuable help in various academic and official matters.

I would like to acknowledge the former and present AcSIR coordinators, Dr. C. H. Suresh, Dr. Karunakaran Venugopal and Dr. Jayamurthy P, for the help rendered during my admission and all other academic activities.

I wish to acknowledge Dr. T.P.D. Rajan, Dr. Sreeja Kumari S.S. and Dr. P. Jayamurthy my doctoral advisory committee members and Dr. U. T.S. Pillai, Dr. Parijat Pallab Jana and Mr. Venkatesan for their insightful comments and discussions which helped me to widen my research from various perspectives.

I gratefully acknowledge all the scientists and staffs in CSIR-NIIST, Thiruvananthapuram, for their help, support and encouragement.

My wholehearted thanks to Mr. Kiran Mohan, Mr. Harish Raj V., and Mr. Peer Mohamed for their technical support by extending different instrumental facilities. I also thank Mr. Arun and Mr. Giri for their invaluable help in sample preparations. I thank all the members of the MSTD of CSIR-NIIST for their help and cooperation.

I convey my sincere thanks to Dr. Jithu Jayaraj, Dr. Rajesh K.R., Dr. Simi, Mr. Pranav K.J., Mr. Chithu and Mr. Vineeth for the technical support. Your expertise and mentoring brought out the quality in my research work.

I extend my thanks to Dr. Abhilash Vishwanath, Mr. Akhil M.G, Mr. Ananthu, Ms. Anju P., Mr. Arun V. S, Dr. Arsha A. G., Mr. Hari Sanil, Mr. Hari Krishnan, Ms. Haritha, Dr. Jerin Pancreacious, Mr. Justin Robert, Mr. Karthik, Mr. Muhammad M. N., Mr. Muhammad Riyas, Dr. Rajesh Kumar, Dr. Rajimol P.R, Ms. Ragi T.M, Ms. Revathy Sreekumar, Mr. Sibi, Mr. Siva, Ms. Suja P., Mr. Vasudevan, Mr. Vishakh Manoj, Mr. Vishnu R.L, Mr. Vineeth K.P, and for all the help and support.

Also, I would like to extend heartfelt gratitude to Dr. Anaga Nair, Mr. Ashin, Dr Anupama Nair, Dr. Anusha, Ms. Amala, Mr Billu Abraham, Dr Genu George, Dr Poornima M S, Dr Soumya R S, Dr Preetha Rani, Dr Salin Raj, Dr Shyni G L, Dr Sindhu, Dr. Nidhina, Dr. Roopasree, Dr Swapna, Dr Sruthi C R, Mrs. Shini,

Words are inadequate to express my gratitude to my parents Mr. C. Surendran and Mrs. V. Laila Kumari., sister Mrs. Meera Ratheesh, brother Mr. Ratheesh Kumar. I extend my heartfelt gratitude to my niece Rithika and nephew Rithvik for their absolute love and support.

I thank Council of Scientific and Industrial Research (CSIR), Government of India for financial assistance.

Arunkumar S

CONTENTS

Chapter 3: Experimental Methodology

List of Tables

List of Figures

List of Abbreviation

A	Ampere
at.%	Atomic percentage
BE	Binding energy
C	Capacitance
cm	Centimeter
CPE	Constant phase element
d	Diameter
°C	Degree Celsius
DAPI	4′,6-diamidino-2-phenylindole
E_{break}	Breakdown potential
E_{corr}	Corrosion potential
EDS	Energy-dispersive X-ray spectroscopy
EIS	Electrochemical impedance spectroscopy
eV	Electron volt
f	Frequency
g	Gram
GOS	Grain orientation spread
h	Hour
Hz	Hertz
i	Current density
i_{corr}	Corrosion current density
IPF	Inverse pole figures
ICP-MS	Inductively coupled plasma spectrometer
KAM	Kernel average misorientation
L	Inductance
L	Liter

Mg	Magnesium
MEM	Minimum essential medium
min	Minute
mm	Millimeter
mM	Millimolar
mL	Milliliter
MTT	3-[4,5-Dimethylthiazol-2-Yl] −2,5 Diphenyltetrazolium Bromide
n	CPE constant
nm	Nanometer
OCP	Open circuit potential
OES	Optical emission spectroscopy
R_{ct}	Charge transfer resistance
R_p	Polarization resistance
R_s	Solution resistance
s	Second
SCE	Standard calomel electrode
SEM	Scanning electron microscopy
t	Time
V	Voltage
V	Volume
Vs.	Versus
Wt.%	Weight percentage
XPS	X-ray photoelectron spectroscopy
XRD	X-ray diffraction
y	Year
Z	Impedance
μm	Micrometer
Ω	ohm

Chapter 1

Introduction

1.1 Overview of the Problem

Magnesium (Mg) and its alloys have gained significant attention as potential biodegradable implant materials in recent decades. Mg is an essential for the human body, with adults requiring a daily intake of 240-420 mg. Mg alloys as orthopaedic implants are advantageous as they can prevent the stress shielding effect often associated with permanent metallic implants. This is due to magnesium's Young's modulus (E = 45 GPa) and density (ρ = 1.7 g/cc), which closely resemble those of human bone (E = 15-25 GPa and ρ = 1.8-2.1 g/cc) (1–3). Additionally, Mg has demonstrated the ability to promote bone formation when utilized as a bone-regenerative material. Its biodegradable nature in the body makes it a suitable alternative to permanent implants, eliminating the need for a secondary surgery to remove the implant. The degradation products of Mg alloys are generally bio-absorbable and can be excreted through the kidneys. However, due to its highly active nature (-2.37 V vs SHE), Mg tends to degrade rapidly in the presence of chloride ions in bodily fluids, which can lead to the alloy dissolving before bone healing is completed. Rapid degradation may also result in gas pockets forming in surrounding tissues, potentially delaying bone healing. Consequently, research is focused on developing Mg alloys with enhanced degradation resistance and mechanical strength, ensuring they maintain their integrity until bone healing is achieved (4–7).

Although different methods like alloying, secondary processing or providing a surface coating can enhance the degradation resistance of Mg, alloying is always given the priority as the choice of alloying elements can also influence the biocompatibility. In this regard, Mg alloys containing rare earth (RE) elements offer several benefits, including improved melt purification and enhanced properties. Rare earth elements (REEs) act as nucleation sites for non-metallic inclusions such as oxides, sulfides, and nitrides. These elements form compounds with the inclusions, which are denser than the surrounding Mg matrix, causing them to settle and be removed more effectively from the melt by

gravitational forces. This purification process obviously increases the degradation resistance. Furthermore, REEs refine the microstructure of Mg alloys, leading to improved mechanical strength, ductility and overall performance of Mg alloys (8,9). Although certain rare earth elements like cerium, praseodymium, and holmium have been reported to exhibit toxicity, elements such as gadolinium (Gd) and neodymium (Nd) are considered safe within specific limits (8–10).

1.2 Origin of the problem

Mg based alloys have been extensively studied over the past few decades for their potential use in biodegradable implants. For instance, a biodegradable product called "Resomet" (Mg-Zn-Ca alloy screws) was introduced in South Korea, where case studies involving 53 patients with hand fractures showed that the screws were completely replaced by newly formed bone (3,5). High purity Mg based screws are by Eontech company in China and were already clinically approved (11). Also, WE43 (Mg-4Y-3Nd) screws (MAGNEZIX) developed by Syntellix AG, and PLLA-coated WE43 stents (Magmaris) by Biotronik Germany, were designed for bone fixation and cardiovascular applications, respectively (12–14). Although, WE43 alloy, garnered attention due to their superior mechanical properties and biocompatibility, concerns surrounding the long-term safety of certain rare-earth elements (e.g., yttrium, with an LD50 of 88 mg/kg) prompted the search for alternative systems with reduced toxicity risks (15–17).

The Mg-Gd/Nd-Zn alloy systems offer a promising solution. These alloys have shown potential for improved mechanical strength, elongation, and controlled degradation rates, essential for supporting bone regeneration while gradually degrading in physiological environments. Unlike WE43, these systems aim to utilize Gd and Nd as the primary rare-earth elements, which may present lower toxicity concerns. Studies show that, Gd-based particles are commonly used as contrast agents in magnetic resonance imaging (18,19). Gd has also been shown to possess anti-inflammatory and immunomodulatory properties, which can help minimize adverse tissue reactions and support the healing process (20,21). Despite ongoing challenges, such as controlling the degradation rate and managing the release of alloy constituents, Gd-containing alloys show promise for developing safer and more effective biodegradable implants, though a thorough investigation into the toxicity and long-term effects of RE elements, released as ions into tissues, is still lacking (22,23).

Furthermore, the properties of Mg-Zn-Gd alloys can be tailored by varying the Zn/Gd ratio, leading to the formation of different ternary phases, such as the W phase ($Mg_3Zn_3Gd_2$) with a cubic structure, the I phase (Mg_3Zn_6Gd) with an icosahedral quasicrystalline structure, and the X phase ($Mg_{12}ZnGd$) with a long-period stacking order (LPSO) structure (24,25). Regarding medical applications, the daily allowable limits of Zn and RE in the human body are around 15 mg and 4.2 mg, respectively (5). Despite these advantages, only limited studies are reported on Gd/Nd containing Mg alloys for biomedical applications in comparison with conventional WE43 and Mg-Zn-Ca alloys. In view of this, the present research work systematically investigated the corrosion behavior, microstructural evolution, mechanical properties, and biocompatibility of Mg-Zn-RE (RE = Gd, Nd) alloys to assess their potential for biodegradable implant applications.

1.3 Structure of the Thesis

The thesis was structured into seven chapters. The Chapters 1 and 2 provided the introduction and an in-depth literature review, focusing on the biodegradation, mechanical performance, and biocompatibility of magnesium-rare earth alloy systems, respectively. Chapter 3 furnished the details of the experimental techniques applied to generate the results presented in subsequent chapters. The corrosion behaviour of Mg-Zn-RE (RE = Gd, Nd) alloys in 1 wt.% NaCl, highlighting the role of rare earth elements and the grain refiner Zr was discussed in Chapter 4. The alloys were designed such a way that they replicated the composition of ZE41 alloys (Mg-4Zn-1RE, wt.%), which have potential applications across industries such as aerospace and biomedical. Chapter 5 illustrated the influence of varying Zn/Gd ratios on the formation of secondary phases, along with their implications for mechanical properties, biodegradation, and biocompatibility. Chapter 6 focused on the extrusion process of Mg-Zn-Gd-Zr alloys to enhance their properties for biodegradable implant applications. The final chapter, Chapter 7, summarized the synthesis of the thesis findings, and suggestions for future research opportunities.

References

1. Bairagi D, Mandal S. A comprehensive review on biocompatible Mg-based alloys as temporary orthopaedic implants: Current status, challenges, and future prospects. J Magnes Alloys. 2022 Mar 1;10(3):627–69.

2. Greatbatch W, Holmes CF. History of implantable devices. IEEE Eng Med Biol Mag Q Mag Eng Med Biol Soc. 1991;10(3):38–41.

3. Jaganathan SK, Supriyanto E, Murugesan S, Balaji A, Asokan MK. Biomaterials in cardiovascular research: applications and clinical implications. BioMed Res Int. 2014;2014:459465.

4. Peron M, Torgersen J, Berto F. Mg and Its Alloys for Biomedical Applications: Exploring Corrosion and Its Interplay with Mechanical Failure. Metals. 2017 Jul;7(7):252.

5. Li N, Zheng Y. Novel Magnesium Alloys Developed for Biomedical Application: A Review. J Mater Sci Technol. 2013 Jun 1;29(6):489–502.

6. Chen XB, Zhou X, Abbott TB, Easton MA, Birbilis N. Double-layered manganese phosphate conversion coating on magnesium alloy AZ91D: Insights into coating formation, growth and corrosion resistance. Surf Coat Technol. 2013 Feb 25;217:147–55.

7. Pan F, Yang M, Chen X. A Review on Casting Magnesium Alloys: Modification of Commercial Alloys and Development of New Alloys. J Mater Sci Technol. 2016 Dec;32(12):1211–21.

8. Kumar A, Choudhari A, Gupta AK, Kumar A. Rare-Earth based magnesium alloys as a potential biomaterial for the future. J Magnes Alloys. 2024 Oct 1;12(10):3841–97.

9. Fernandes D, Resende C, Cavalcanti J, Liu D, Elias C. Biocompatibility of bioabsorbable Mg–Ca alloys with rare earth elements addition. J Mater Sci Mater Med. 2019 Dec 3;30(12):134.

10. Liu J, Bian D, Zheng Y, Chu X, Lin Y, Wang M, et al. Comparative in vitro study on binary Mg-RE (Sc, Y, La, Ce, Pr, Nd, Sm, Eu, Gd, Tb, Dy, Ho, Er, Tm, Yb and Lu) alloy systems. Acta Biomater. 2020 Jan 15;102:508–28.

11. Huang S, Wang B, Zhang X, Lu F, Wang Z, Tian S, et al. High-purity weight-bearing magnesium screw: Translational application in the healing of femoral neck fracture. Biomaterials. 2020 Apr;238:119829.

12. Bennett J, De Hemptinne Q, McCutcheon K. Magmaris resorbable magnesium scaffold for the treatment of coronary heart disease: overview of its safety and efficacy. Expert Rev Med Devices. 2019 Sep;16(9):757–69.

13. Cerrato E, Barbero U, Gil Romero JA, Quadri G, Mejia-Renteria H, Tomassini F, et al. Magmaris^{TM} Resorbable Magnesium Scaffold: state-of-art Review. Future Cardiol. 2019 Jul 1;15(4):267–79.

14. Biber R, Pauser J, Brem M, Bail HJ. Bioabsorbable metal screws in traumatology: A promising innovation. Trauma Case Rep. 2017 Apr 1;8:11–5.

15. Amukarimi S, Mozafari M. Biodegradable magnesium-based biomaterials: An overview of challenges and opportunities. MedComm. 2021;2(2):123–44.

16. Chandra G, Pandey A. Biodegradable bone implants in orthopedic applications: a review. Biocybern Biomed Eng. 2020 Apr;40(2):596–610.

17. Chandra G, Pandey A. Preparation Strategies for Mg-Alloys for Biodegradable Orthopaedic Implants and Other Biomedical Applications: A Review. IRBM. 2022 Jun 1;43(3):229–49.

18. Zhou Z, Lu ZR. Gadolinium-based contrast agents for magnetic resonance cancer imaging. WIREs Nanomedicine Nanobiotechnology. 2013;5(1):1–18.

19. Caravan P. Protein-Targeted Gadolinium-Based Magnetic Resonance Imaging (MRI) Contrast Agents: Design and Mechanism of Action. Acc Chem Res. 2009 Jul 21;42(7):851–62.

20. Huang Y, Zhai X, Ma T, Zhang M, Pan H, Weijia Lu W, et al. Rare earth-based materials for bone regeneration: Breakthroughs and advantages. Coord Chem Rev. 2022 Jan 1;450:214236.

21. Natarajan D, Ye Z, Wang L, Ge L, Pathak JL. Rare earth smart nanomaterials for bone tissue engineering and implantology: Advances, challenges, and prospects. Bioeng Transl Med. 2022;7(1):e10262.

22. Feyerabend F, Fischer J, Holtz J, Witte F, Willumeit R, Drücker H, et al. Evaluation of short-term effects of rare earth and other elements used in magnesium alloys on primary cells and cell lines. Acta Biomater. 2010 May;6(5):1834–42.

23. Zhang Y, Liu Y, Zheng R, Zheng Y, Chen L. Research progress on corrosion behaviors and biocompatibility of rare-earth magnesium alloys in vivo and in vitro. J Rare Earths [Internet]. 2023 Mar 11 [cited 2023 Oct 26]; Available from: https://www.sciencedirect.com/science/article/pii/S1002072123000753

24. Srinivasan A, Blawert C, Huang Y, Mendis CL, Kainer KU, Hort N. Corrosion behavior of Mg–Gd–Zn based alloys in aqueous NaCl solution. J Magnes Alloys. 2014 Sep 1;2(3):245–56.

25. Yin S, Duan W, Liu W, Wu L, Yu J, Zhao Z, et al. Influence of specific second phases on corrosion behaviors of Mg-Zn-Gd-Zr alloys. Corros Sci. 2020 Apr 15;166:108419.

Chapter 2
Literature Review

2.1 Magnesium as Biodegradable Implant

The conventionally used permanent metallic, non-degradable implants, such as Ti-6Al-4V, SS316L, and Co-20Cr-15Ni-7Mo alloys, often require surgical removal after fulfilling their purpose within the body. This additional procedure not only increases healthcare costs but also poses additional inconvenience as well as severe discomfort to the patient. In contrast, biodegradable implants naturally dissolve in the body over time [**Figure 2.1(a)**], eliminating the need for revision surgeries and reducing associated complications. In addition, permanent metallic implants come with inherent drawbacks. For instance, they can cause a stress shielding effect [**Figure 2.1(b)**], where the implant bears the load instead of the surrounding bone, leading to bone resorption and weakening. Additionally, they may trigger inflammatory responses, affecting long-term biocompatibility [1–4]. Also, non-metallic materials, such as bioceramics and polymers, have been used as implant materials. Bioceramics, like hydroxyapatite (HAP), are highly biocompatible, non-immunogenic, and non-toxic, making them suitable for specific applications. However, their extreme brittleness limits their use in load-bearing applications [5–7]. Similarly, polymers, though biodegradable, have inferior mechanical properties compared to metals and bioceramics, restricting their applications to low-load-bearing conditions [8–10].

Due to these challenges, metallic materials such as magnesium (Mg), zinc (Zn), iron (Fe), and their respective alloys have garnered significant attention for use as biodegradable implants. Among these:

- **Iron-based implants** degrade very slowly in physiological conditions, which may delay the healing process. To address this, manganese (Mn) is often alloyed with Fe to create micro-galvanic corrosion sites, enhancing the degradation rate [12–15].
- **Zinc-based implants** exhibit an ideal biodegradation rate due to their standard electrode potential (-0.763 V), which lies between the highly active Mg (-2.363 V) and Fe (-0.44 V). However, Zn is limited by its poor plasticity (strain, $\varepsilon < 0.25\%$) and high elastic modulus, which may cause stress shielding [16–19].

- **Magnesium and its alloys** stand out as exceptional candidates among degradable metallic implants. Mg offers an elastic modulus closely matching that of natural bone, minimizing stress shielding. Furthermore, its biodegradability aligns well with the body's healing process, providing temporary mechanical support while gradually resorbing into the body [20–23].

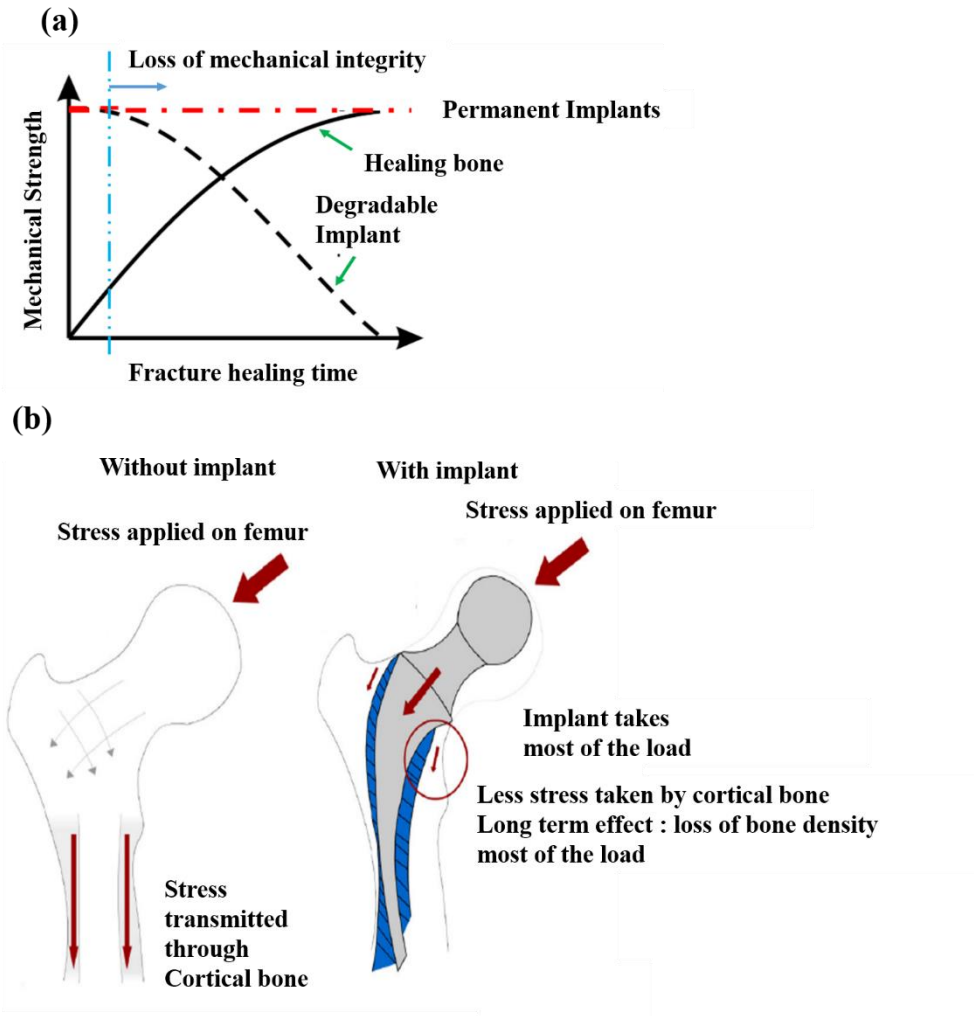

Figure 2.1. (a) Degradation behaviour of biodegradable implant vs permanent implant, (b) Stress shielding effect observed in permanent implants [11].

Table 2.1 highlights the mechanical and physical properties of various metallic and non-metallic materials relative to those of natural bone. Among the explored materials, magnesium exhibits properties most similar to bone, making it the preferred choice for developing next-generation biodegradable implants.

Table 2.1. Mechanical properties of various bio implants

		Non degradable metals			**Non degradable Ceramics**	**Degradable polyesters**		**Degradable Metals**		
Material	Cortical bone	Ti-6Al-4V	SS 316L	Co-20Cr-15Ni-7Mo	Synthetic hydroxy-apatite	PLA	PGA	Fe	Zn	Mg
Density (g/cm^3)	1.8-2.1	4.43	7.9	7.8	3.15	1.8	1.3-1.34	7.7	5.79	1.74
Elastic modulus (GPa)	15-25	113.8	200	195-230	70-120	3.7	1.69	207	90	41-45
Yield strength (MPa)	104-121	880	190	240-450	-	70	3.8-26.6	420	171	65-100
Ultimate tensile strength (MPa)	110-130	950	490	450-960	40-200	59	13.9-16.7	700	210	90-190
Elongation to break (%)	0.7-3	14	40	50	-	7	5.7	8	1	2-10
Reference	[24]	[25]	[26]	[27]	[28]	[29]	[30]	[31]	[32]	[22]

Mg is not only a promising material for biodegradable implants but also an essential nutrient vital for various physiological functions in the human body. It plays a critical role in enhancing bone growth, promoting the biomineralization of osteoblasts (bone-forming cells), and reducing the risks associated with conditions such as osteoporosis and coronary artery disease. Importantly, the biodegradation products of magnesium are typically non-toxic, causing no physical irritation or allergic reactions in vivo. This inherent biocompatibility makes Mg a highly favourable material for biomedical applications [11,33–35]. The average daily dietary intake of Mg for an adult is approximately 360 mg, of which around 120 mg is absorbed in the intestine. **Figure 2.2 (a)** illustrates this daily magnesium intake, emphasizing its significance in maintaining bodily functions. Within the body, Mg is distributed such that about 52% is stored in bones, 27% in muscles, and 20% in non-muscular soft tissues, as shown in **Figure 2.2 (b)**. These statistics underscore the natural compatibility of magnesium with bone and its role in skeletal health [36–38].

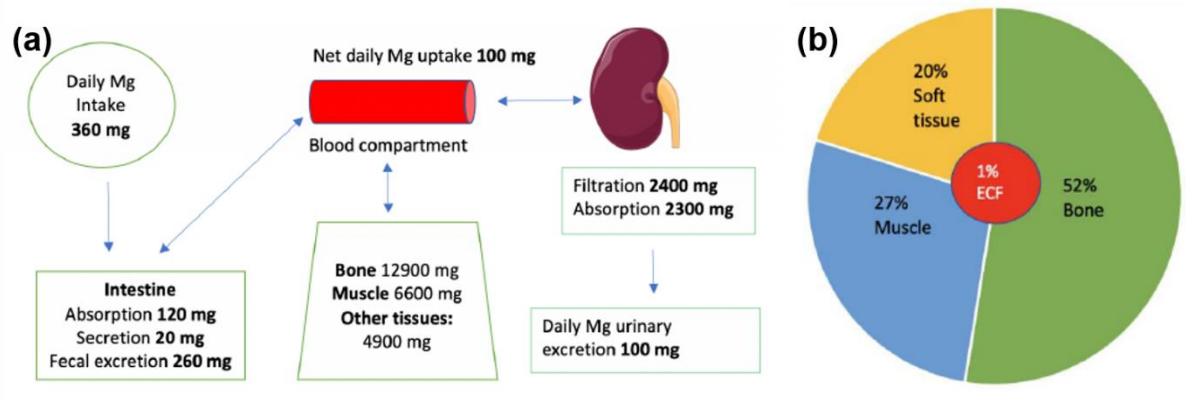

Figure 2.2. (a) Daily intake of Mg in humans, (b) Distribution of Mg in the human body [11].

Despite its benefits, magnesium and its alloys face significant challenges due to their high reactivity. In physiological conditions with a pH range of 7.2 to 7.4 and an environment rich in aggressive ions (e.g., chloride ions), Mg degrades rapidly. This accelerated biodegradation poses challenges for maintaining mechanical integrity during the required healing period [39].

2.2 Corrosion/Biodegradation mechanism of Mg alloys

The overall corrosion reaction in Mg and alloys in aqueous medium can be expressed as follows: [40–42].

$$Mg \rightarrow Mg^{2+} + 2e^{-} \text{ (Anodic reaction);} \quad (2.1)$$

$$2H_2O + 2e^{-} \rightarrow H_2 + 2OH^{-} \text{ (Cathodic reaction);} \quad (2.2)$$

$$Mg^{2+} + 2\,OH^{-} \rightarrow Mg(OH)_2 \text{ (Product formation);} \quad (2.3)$$

$$Mg + 2H_2O \rightarrow Mg(OH)_2 + H_2 \text{ (Overall corrosion reaction).} \quad (2.4)$$

[The biodegradation of a material within the human body or under laboratory conditions is commonly referred to as biodegradation. Therefore, throughout this thesis, the terms corrosion and biodegradation will be used interchangeably, depending on the context of the discussion]. However, the biodegradation behaviour of Mg based materials in the human body is significantly more complex than the simplified chemical reactions typically described. This complexity arises from the dynamic and multifaceted nature of the physiological environment, which includes water, ions, proteins, cells, and various biomolecules.

2.2.1 Role of Plasma Ions in Biodegradation:

Blood plasma, the medium in which implants are often exposed, contains a range of ions such as Na^+, K^+, Ca^{2+}, Cl^-, HCO^{3-}, HPO_4^{2-}, PO_4^{3-}, SO_4^{2-}, and Mg^{2+} ions. Among these ions:

- Chloride ions (Cl^-): These are particularly aggressive and compromise the protective oxide layer (MgO) that forms on Mg. Chloride ions react with this layer, leading to the formation of soluble magnesium chloride ($MgCl_2$), which accelerates the biodegradation process [43–45].
- Phosphates and carbonates: In contrast to chloride ions, these contribute to forming protective layers, such as magnesium phosphate or carbonate films, which improve the biodegradation resistance of Mg-based alloys [46].

2.2.2 Influence of Biological Components

Beyond ions, several biological factors influence the biodegradation of Mg alloys:

- Cells and Osteoblasts: The attachment and proliferation of cells, especially osteoblasts, on the Mg surface can slow the biodegradation rate. These cells form a biological barrier that reduces direct exposure to the surrounding environment [47,48].
- Proteins and Biomolecules: Proteins adhered to the Mg implant surface play a dual role. On one hand, they facilitate cell attachment and proliferation; on the other, they may interact with the surface, potentially altering the local chemical environment and influencing biodegradation behaviour [47,48].
- Bacteria: The presence of bacteria and their biofilms can either accelerate or retard the biodegradation rate, depending on the nature of their interaction with the Mg surface [47,48].

2.2.3 Hydrodynamic and Physical Factors

- Blood Flow Dynamics: The rate of blood flow varies across different implantation sites. Higher flow rates increase the transport of aggressive ions to the implant surface and accelerate the biodegradation process. For example, Mg-based stents in arterial blood flow corrode faster than Mg scaffolds implanted in areas with minimal blood flow [49].

- Temperature: Biodegradation typically accelerates with increasing temperature. At the human body temperature (37 °C), Mg corrodes faster than at room temperature, highlighting the importance of environmental control in laboratory experiments [50].
- pH of the Surrounding Medium: The pH value plays a critical role in Mg biodegradation. According to Pourbaix's diagrams: Mg degrades faster in acidic, neutral, and slightly alkaline conditions. As the pH becomes more alkaline, the biodegradation rate decreases due to the stabilization of the protective $Mg(OH)_2$ layer, which is more resilient at higher pH values [50,51].

2.2.4 Synergistic Effects

The biodegradation behaviour of Mg in the human body is not governed by a single factor but rather the synergistic interplay of these chemical, biological, and physical influences. The interaction of plasma ions, biological entities, hydrodynamic conditions, and pH variations dictates the overall biodegradation behaviour, making it essential to consider all these aspects in the design of Mg-based biodegradable implants. **Figure 2.3** provides a schematic representation of the interactions between Mg-based materials and the human body, illustrating the interplay of the various factors influencing biodegradation behaviour. This holistic understanding is crucial for optimizing Mg alloys for biomedical applications.

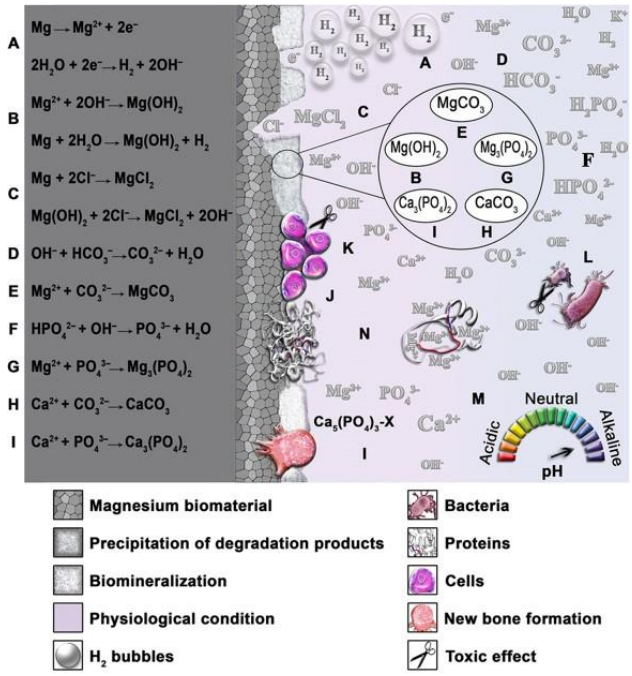

Figure 2.3. Schematic illustration of the biodegradation behaviour of biodegradable magnesium biomaterial in physiological conditions and several possible chemical reactions [49].

2.3 Adverse effect of severe biodegradation of Mg in the body

2.3.1 Hydrogen Gas Evolution

The biodegradation of Mg is accompanied by the production of hydrogen gas, with approximately 1 mL of H_2 generated for every 1 mg of Mg degraded (Equation 2.4). This rapid release of hydrogen can lead to the accumulation of hydrogen gas in surrounding tissues can form gas pockets, causing necrosis and potentially entering the bloodstream, where it may result in life-threatening conditions [52–54]. If the hydrogen release rate is maintained below 0.01 mL/cm²/day, the gas can diffuse away from the site, preventing the local accumulation of large bubbles and minimizing adverse effects. However, it is also reported that H_2 gas possess antioxidant and anti-inflammatory properties, which may aid in reducing reactive oxygen species (ROS) and promoting healing in conditions such as ischemia-reperfusion injuries [55–57]. However, the overall effects of continuous hydrogen evolution during Mg biodegradation remain a topic of debate [58–60].

2.3.2 Increase in the pH of the surrounding environment

Due to the release of OH^- ions, the pH of the surrounding environment of the implant will rise which can cause local alkalinity that may disrupt cell functions and lead to cell death. On the other hand, a $Mg(OH)_2$ layer will be stable in this alkaline environment with a pH greater than 10, which slows further biodegradation. Also, OH^- ions released during biodegradation have antibacterial properties. For instance, Robinson et al. [61] reported that increased OH^- concentrations inhibited the growth of bacteria such as Escherichia coli, Pseudomonas aeruginosa, and Staphylococcus aureus.

2.3.3 Release of Biodegradation Products

Rapid biodegradation releases Mg and alloying elements into the body at rates that may cause severe toxicity [62–64]. The biodegradation products must be biocompatible and safe for host tissues [65,66]. Released ions from alloying elements can affect the biocompatibility of Mg alloy biomaterials; some alloying elements may cause toxicity and adverse tissue reactions, while others are only harmful in excessive amounts [67,68].

2.4 Strategies to Mitigate Biodegradation in Magnesium Alloys

The rapid biodegradation of magnesium (Mg) alloys poses a significant challenge, but several strategies such as alloying, secondary processing and surface treatment can mitigate this issue.

- Alloying: Although pure magnesium demonstrates superior resistance to biodegradation compared to most Mg alloys, its application is restricted by poor mechanical strength. The severe biodegradation in Mg alloys arises primarily from the formation of micro-galvanic couples between secondary phases and the α-Mg matrix. However, the addition of specific elements has been shown to enhance corrosion resistance by facilitating the formation of stable surface oxide films and secondary phases that have lower Volta potential differences with the α-Mg matrix, thereby minimizing micro-galvanic corrosion [46,49]. The choice of alloying elements is particularly critical for biomedical applications, where biocompatibility is paramount. For instance, while aluminium can improve biodegradation resistance, its neurotoxic effects make it unsuitable for implants [69,70]. Instead, elements naturally present in the body, such as calcium (1100 g in the body), zinc (2 g in the body), manganese (12 mg in the body), strontium (0.3 g in the body), lithium (2–4 ng/g in blood serum), zirconium (<250 mg in the body) are preferable due to their compatibility and ability to improve biodegradation resistance [71,72].
- Secondary Processing: Another method to mitigate biodegradation is secondary processing, which includes heat treatments or deformation-based techniques. These processes modify the distribution, size, and morphology of precipitates, as well as the grain size and texture of the material. A uniform distribution of secondary phases can significantly improve biodegradation resistance, and grain refinement may enhance the formation of uniform protective surface films. However, the effect of grain refinement on biodegradation resistance is not always straightforward. Some studies suggest that finer grains may reduce biodegradation resistance, possibly due to increased dislocation density in deformed materials, which creates high-energy sites prone to biodegradation. Nevertheless, deformation processing can produce ultrafine-grained (UFG) materials with enhanced mechanical properties without requiring additional

alloying elements, providing an attractive alternative for controlling biodegradation. Different deformation processes widely used are extrusion, rolling, friction stir processing (FSP), equal channel angular processing (ECAP), multi axial deformation (MAD), rotary swaging (RS) and high pressure torsion (HPT) [73,74].

- Surface treatments/coatings: surface treatments and coatings play a vital role in influencing both the biodegradation behaviour and biocompatibility of Mg alloys [75]. The surface characteristics of degradable implants, such as roughness, wettability, and surface energy, significantly affect biodegradation rates and biological interactions. For instance, smooth, hydrophilic surfaces promote better cell adhesion compared to rough, hydrophobic ones [76,77]. Surface modification can be achieved by applying protective coatings, altering the surface microstructure or composition through treatments, or employing a combination of these methods. These modifications not only enhance biodegradation resistance but also optimize the biological response, making them particularly relevant for biomedical applications [78,79].

2.5 Magnesium Alloys Currently Being Explored for Bio-implant Applications

Among the various strategies employed to enhance biodegradation resistance, alloying stands out as a primary focus. This approach involves intentionally modifying the chemical composition of the base material, which fundamentally alters its intrinsic properties. By incorporating specific alloying elements, the material's microstructure can be tailored to achieve homogeneity, a critical factor in resisting biodegradation effectively. Furthermore, alloying offers the advantage of precise control over a wide range of material properties. These include not only enhanced biodegradation resistance but also improved mechanical strength and an optimized biological response. This versatility makes alloying a highly effective and adaptable method for developing advanced materials tailored to specific applications.

- **Mg-Al Alloys**

Aluminium (Al) serves as both a solid solution and a precipitate strengthening element in magnesium alloys. When the Al content increases, it lowers the temperatures at which the alloy transitions from liquid to solid, thus enhancing the castability of magnesium alloys [80]. However, the normal concentration of Al in the human body is very low, ranging between 2.1 and 4.8 µg/L [81]. Elevated levels of Al can have detrimental effects, particularly on neurons and osteoblasts. It has been associated with conditions such as dementia and Alzheimer's disease, as well as causing muscle fiber damage and reducing osteoblast viability [82–84].

In Al-containing Mg alloys, the biodegradation layer often includes both $Mg(OH)_2$ and Al_2O_3. $Mg(OH)_2$ is slightly soluble in water and can transform into soluble $MgCl_2$ through interaction with chloride ions. In contrast, Al_2O_3 is water-insoluble and resistant to chloride ion biodegradation, thus contributing to enhanced biodegradation resistance when Al is present in the alloy. Al_2O_3 naturally forms on the surface of the alloy and remains more stable than $Mg(OH)_2$ in environments containing chloride ions, further improving biodegradation resistance. However, higher Al concentrations can lead to the formation of the $Mg_{17}Al_{12}$ phase, which increases susceptibility to pitting corrosion [85]. Although the AZ-series alloys (AZ31, AZ91 etc.,) have been studied for their short-term use as implants, with no toxicity observed in the short term, concerns about long-term Al toxicity have prompted a shift towards Al-free magnesium alloys for medical applications [86,87].

- **Mg-Ca Alloys**

Calcium plays a critical role in magnesium alloys, contributing to solid solution and precipitate strengthening. It also acts as a grain refining agent, enhancing grain boundary strength in these alloys. However, larger amounts of calcium (>1 wt.%) can lead to issues such as hot tearing or sticking, which can compromise the material's performance during processing [88,89]. As the most abundant mineral in the human body, with approximately 1–1.1 kg stored primarily in bones and teeth, calcium is tightly regulated by the homeostatic mechanisms of

the skeleton, kidneys, and intestines. Normal serum levels of calcium range from 0.919 to 0.993 mg/L [90].

Li et al. [91] investigated the impact of calcium on the mechanical and biodegradation properties of binary Mg-xCa (x=1–3 wt.%) alloys. They found that the ultimate tensile strength and elongation of as-cast Mg-1Ca alloy were 71.4 MPa and 1.87%, respectively. During in-vivo implantation, the biodegradation of Mg-1 wt.% Ca alloy pins occurred gradually over 90 days, with a biodegradation rate of 1.27 mm/year. Erdmann et al. [92] studied the in-vivo degradation and biomechanical properties of Mg-0.8Ca alloy screws. They observed a significant reduction in the mechanical integrity of the screws after six weeks of implantation. Krause et al. [93] focused on the initial mechanical strength and biodegradation behaviour of Mg-0.8Ca, LAE442 Mg-4Li-4Al-2RE), and WE43 (Mg04Y-3Nd-0.5Zr) alloys used in osteosynthesis implants. It was found that Mg-0.8Ca implants exhibited the least initial strength and the highest loss in volume after six months.

- **Mg-Zn alloys**

Zinc (Zn) is nearly as effective as Al in enhancing the properties of magnesium alloy, particularly in terms of strengthening [94,95,95]. For example, Mg-6 wt.% Zn alloy shows a tensile strength of approximately 279.5 MPa and an elongation of 18.8% after solid solution treatment and hot working [96]. In addition, Zn is a vital trace element in the human body, with a normal blood serum concentration ranging from 12.4 to 17.4 µmol/L. It plays a crucial role in the immune system and serves as a co-factor for enzymes involved in bone and cartilage development. Nevertheless, excessive Zn levels can cause neurotoxicity [88]. Mg-6 wt.% Zn alloy was implanted into the femoral shaft of rabbits, where they degraded gradually over time at a rate of 2.32 mm/year. This biodegradation was accompanied by new bone formation around the implant, demonstrating good biological integration [96].

- **Mg-Li Alloys**

Lithium (Li) is unique among alloying elements for magnesium as it can alter the lattice structure of Mg from hexagonal close-packed (h.c.p) to body-

centered cubic (b.c.c), resulting in improved ductility and formability. However, this transformation does not contribute to enhanced strength [97]. Li is present in trace amounts in the human body, with normal blood serum levels ranging from 2 to 4 ng/g [88]. It is commonly used in compounds for treating psychiatric disorders, but excessive levels can lead to severe health issues such as kidney or lung dysfunction and potential birth defects [98]. Additionally, due to the high chemical reactivity of Li, the corrosion and biodegradation behaviour of Mg-Li alloys remains a subject of ongoing debate [99,100]. Lithium (Li) has been observed to stimulate the release of nitric oxide (NO) in brain vascular cells [101,102]. Alloys such as Mg-Li-Ca and Mg-Li-Al-RE have shown great potential as biodegradable materials, particularly for stent applications. In the case of Mg-9.29Li-0.88Ca alloy, its dual-phase structure has been linked to the formation of a multi-layered surface film. This unique surface film causes a distinct biodegradation behaviour in Hank's solution, where one phase is selectively attacked while the other remains protected [103]. Additionally, Mg-Li-based alloys containing rare earth elements (REE), designed for stent applications, have demonstrated excellent biodegradation resistance during static immersion tests along with promising cytocompatibility [104].

- **Mg-RE alloys**

Rare earth (RE) elements encompass a group of 17 elements in the periodic table, comprising the 15 lanthanides along with scandium and yttrium [105]. These elements are typically categorized into two groups: the heavy rare earth metals (e.g., Y, Gd, Tb, Dy, Ho, Er, Tm, Yb, and Lu) exhibits significant solid solubility in magnesium, while the light rare earth metals (e.g., Nd, La, Ce, Pr, Sm, and Eu) demonstrates limited solid solubility [99]. The inclusion of RE elements enhances both the mechanical and biodegradation resistance of magnesium alloys. Those with high solubility contribute to solution and precipitation strengthening, while RE elements with limited solubility often form intermetallic phases at grain boundaries during solidification. These intermetallics effectively stabilize grain boundaries at elevated temperatures, improving creep resistance and raising the service temperature of magnesium alloys [71]. For instance, yttrium, with its high solubility in magnesium, is frequently used alongside other RE elements to enhance creep

resistance and improve biodegradation properties at elevated temperatures. Notable RE-containing magnesium alloys such as WE43, Mg–8Y, Mg–10Gd, and LAE442 have been proposed for biomedical implants [106–108]. Research by Witte et al. demonstrated the in-vivo degradation and biocompatibility of LAE442 and WE43 alloys, with implanted rods degrading completely within 18 weeks [63,109]. Heublein et al. [110] reported linear biodegradation behaviour of AE21 (Mg-2Al-1RE) alloy in coronary arteries, suggesting that magnesium-based vascular implants could serve as viable alternatives to permanent implants. These findings highlight the potential of non-toxic Mg-RE alloys as biomaterials for medical applications. A significant milestone in the clinical use of Mg-RE alloys was reported by Peeters et al., [111] where absorbable magnesium stents were used to treat 20 patients undergoing suboptimal angioplasty. The procedure achieved a 100% limb salvage rate with no amputations required. However, in a six-month study involving 60 patients, the stents degraded rapidly, leading to restenosis within six months [111,112]. Mg stents were also used to treat recoarctation in a newborn, demonstrating biocompatibility as no pathological Mg levels were detected in the serum [112]. A larger multicenter non-randomized study by Erbel et al. [113] revealed that magnesium stents provided immediate angiographic results comparable to other metallic stents and safely degraded within four months [113].

2.6 Current status on the Mg based biodegradable implants

1. **Orthopaedic Implants**

- MAGNEZIX Compression Screws (Germany): Developed by Syntellix AG, MAGNEZIX screws were the first commercial Mg-based devices to receive CE mark approval in 2013 [114]. Made from Mg-Y-RE-Zr alloy, they have been used primarily for hallux valgus surgery. By 2021, MAGNEZIX screws had gained regulatory approval in 58 countries for treating various fractures [115].
- K-MET Screws (South Korea): These screws, made from Mg-Ca-Zn alloys by U&I, were approved in 2015 for distal radius fractures. Clinical studies have demonstrated successful healing with minimal inflammation and no adverse effects during the biodegradation process [116].

- HP Mg Screws (China): Produced by Eontech Ltd., these screws were approved for multicenter clinical trials in 2019. They have been used in vascularized bone flap fixation for treating femoral head necrosis. Patients demonstrated effective bone regeneration and complete implant biodegradation [117].
- JDBM (Mg-Nd-Zn-Zr) Screws with Ca-P Coating (China): A recent study on medial malleolus fractures showcased the successful use of JDBM screws coated with calcium-phosphate (Ca-P). All patients achieved proper alignment and complete fracture healing without screw breakage [118].

2. Cardiovascular Implants

- Lekton Magic AMS Stent (WE43): The stent was implanted in a preterm infant's pulmonary artery. The study demonstrated complete stent degradation within five months, with sustained lung reperfusion throughout the follow-up period. Serum magnesium levels briefly increased but normalized within 48 hours [113].
- DREAMS AMS (WE43) Stents: The PROGRESS-AMS clinical trial (2007), involving 63 patients, established the safety of these stents. No cases of myocardial infarction or thrombosis were reported after the implantation of 71 stents. Subsequent trials, such as BIOSOLVE-1 (2013), further validated their efficacy, with no cardiac deaths or scaffold thrombosis at the 12-month mark [119].
- DREAMS-2G (Magmaris) Stents: Magmaris stents represent the next generation of Mg-based cardiovascular devices, combining WE43 alloy with a PLLA drug carrier. This innovation enables extended biodegradation times (9-12 months) and controlled drug release, reducing restenosis rates [120–122]. **Figure 2.4** shows the various Mg alloys clinically approved in different countries.

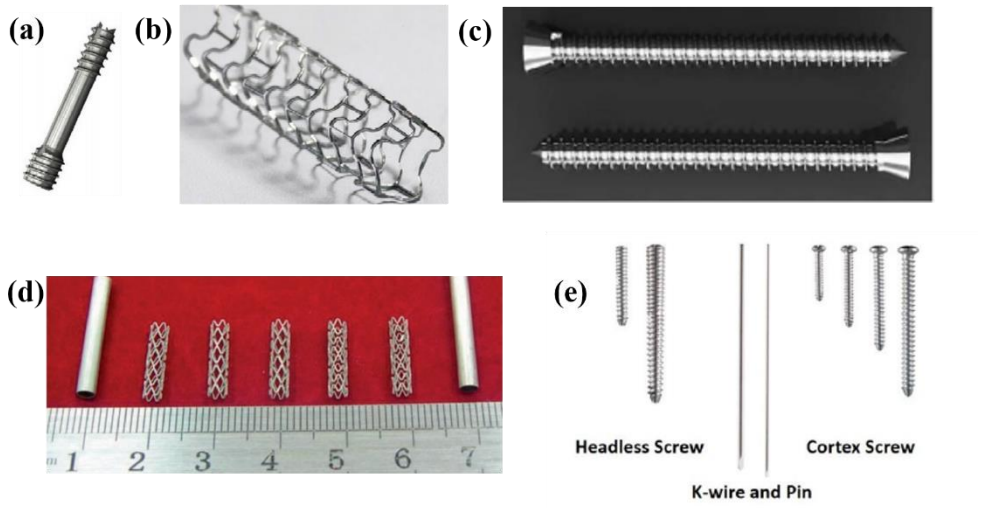

Figure 2.4. Mg alloy based degradable biomaterial products currently available in the market (a) MAGNEZIX tightening screw (b) AMS cardio vascular stent (c) High Purity Mg screws by Eontec, China (d) Cardiovascular stents of JDBM (e) K-wire pin and screws by U & I Corporation South Korea [114,115].

2.7 Potential Mg-RE based alloys for implant applications

Mg-RE alloys are promising candidates for biodegradable implant applications due to their biocompatibility, controlled degradation, and superior mechanical properties compared to other Mg-based systems. The clinical success and widespread adoption of Mg-RE systems, such as MAGNEZIX screws and DREAMS-2G stents, underscore their superiority over other Mg-based implants discussed. MAGNEZIX screws, made from Mg-Y-RE-Zr alloy, have achieved regulatory approval in 58 countries by 2021, far surpassing the reach of Mg-Ca-Zn-based K-MET screws, as well as high purity Mg screws. Similarly, the DREAMS-2G stents, combining WE43 alloy with a PLLA drug carrier, are now utilized in over 50 countries, showcasing a significant advantage in global clinical relevance compared to earlier-generation AMS stents. The key to Mg-RE systems' success lies in their superior mechanical properties, controlled biodegradation profiles, and broader application range.

2.7.1 Mechanical Properties

The mechanical properties of a biodegradable implant play a crucial role in ensuring structural stability, load-bearing capability, and compatibility with natural bone during the healing process. An ideal implant should possess sufficient strength and ductility to support physiological loads while gradually degrading at a rate that allows for tissue regeneration without premature failure. Therefore, tailoring mechanical properties is key to the successful performance of biodegradable implants.

2.7.1.1 Factors influencing mechanical properties

- **Grain refinement**: The reduction in grain size is accompanied by an increase in YS of the material. According to the Hall-Petch relation, yield strength (σ) is given by

$$\sigma = \sigma_0 + k * d^{-1/2} \quad (2.5)$$

where σ_0 is a material constant, d is the average grain diameter, and k is the strengthening coefficient [89,123,124]. Grain refinement can occur due to both alloying as well as secondary processing processes. In Mg-RE alloy system, during solidification RE atoms move to the solid-liquid interface due to the solute redistribution. This leads to constitutional undercooling and thus enhances the nucleation of α-Mg grains [125–129]. For example, 1 wt.% Nd addition in AZ80 alloy resulted in grain refinement from 448 μm to 125 μm [130], 2 wt% Er addition in Mg-9Zn-0.6Zr resulted in grain size reduction from 102 μm to 32 μm [131].

- **Solid solution strengthening**:

The factors that govern the solubility of elements are atomic size difference, crystal structure, electronegativity and valency, which are compiled in **Table 2.2**. The atomic size of most of the rare earth elements are with in ±15% range to form a solid solution in Mg except Eu. Also, the crystal structure of the rare earths is HCP (same as Mg) except Ce, Eu and Yb. The electronegativity values of the rare earth elements are much different compared to Mg and the valency of almost all of the rare earth elements are different except a few RE. Thus most of the REs have limited solubility in Mg thus promoting the formation of intermetallics. However, the addition of elements within the solubility limit allows for the formation of solid

solutions [132,133]. The dissolution of RE in α-Mg matrix results in lattice distortion which leads to RE-dislocation interactions. This interaction primarily impedes the dislocation movement and enhances the strength [134,135]. Solid solution strengthening is evaluated by the following equation:

$$\sigma = CX^{2/3}, \quad (2.6)$$

where, C is binary alloy strengthening rate and X is the atomic fraction of the solute [136,137]. Yang et al. [138] compared the effects of dysprosium (Dy) and gadolinium (Gd) on the properties of magnesium alloys and found that the solid solubility of Dy in magnesium (approximately 10 wt.%) is higher than that of Gd (approximately 3 wt.%) at 200 °C. It was determined that all of the Dy dissolved in the magnesium alloy, thereby improving the alloy's mechanical properties primarily through solid solution strengthening. Conversely, Gd mainly precipitated from the alloy, enhancing its strength through second-phase strengthening.

- **Precipitation strengthening**: The formation of intermetallic phases in an alloy depends on the solubility of the corresponding element in Mg. The addition of elements beyond the solubility limit results in the precipitation of intermetallics along the grain boundaries. The intermetallics are generally effective in pinning down the dislocations and thus enhances the strength [139–142]. The increase in strength due to the presence of precipitates is governed by the following equation [143]

$$\sigma = \frac{MGb}{2\Pi\sqrt{(1-\nu)}} * \frac{1}{\lambda} * \ln(\frac{D}{r}) \quad (2.7)$$

Where, σ is the increase in critically resolved shear stress due to dispersion strengthening, G is the shear modulus, b is the burgers vector, D is the planar diameter of point obstacles, ν is poisons ratio, λ is the inter obstacle spacing, r is the radius of dislocations. Age hardening is also usually done as a secondary processing in Mg alloys to improve mechanical properties. The age hardening involves three steps: (1) solutionizing the material at an elevated temperature to dissolve the intermetallics into α-Mg, (2) water quenching to produce a super saturated solid solution, (3) aging at relatively low temperature to form precipitates. These precipitates formed may be under aged, peak aged or over aged depending on the aging time and temperature, which decides whether the phase is metastable or equilibrium phase. The ability of different precipitates to pin down the

dislocations vary and the dislocation arrest leads to improvement in mechanical properties [144–146].

Table 2.2 Solubility limit, atomic radius, crystal structure, electronegativity and valency of rare earth elements [147,148].

Element	Solubility limit (wt.%)	Atomic radius (A)	Crystal Structure	Electronegativity	Valency
Mg	-	1.6	HCP	1.31	+2
Sc	24.5	1.64	HCP	1.36	+3
Y	12.5	1.8	HCP	1.22	+3
La	0.23	1.88	HCP	1.1	+3
Ce	0.5	1.84	FCC	1.12	+3, +4
Pr	0.6	1.82	HCP	1.13	+3
Nd	3.6	1.81	HCP	1.14	+3
Sm	6.4	1.8	HCP	1.17	+2, +3
Eu	0	2.04	BCC	1.2	+2, +3
Gd	23.49	1.8	HCP	1.2	+3
Tb	24	1.79	HCP	1.22	+3, +4
Dy	25.8	1.78	HCP	1.22	+3
Ho	28.08	1.77	HCP	1.23	+3
Er	33.8	1.76	HCP	1.24	+3
Tm	31.8	1.75	HCP	1.25	+2, +3
Yb	8	1.92	FCC	1.1	+2, +3
Lu	41	1.74	HCP	1.27	+3

The solubility of REEs in Mg decreases with temperature (**Figure 2.5**) and this is more prominent in heavy rare earth elements (HREs). Gadolinium (Gd) is one of the most used HRE in age hardening treatment as its solid solubility is 4.53 at.% at 548°C, which drops to just 0.35 at.% at 200°C [147,148].

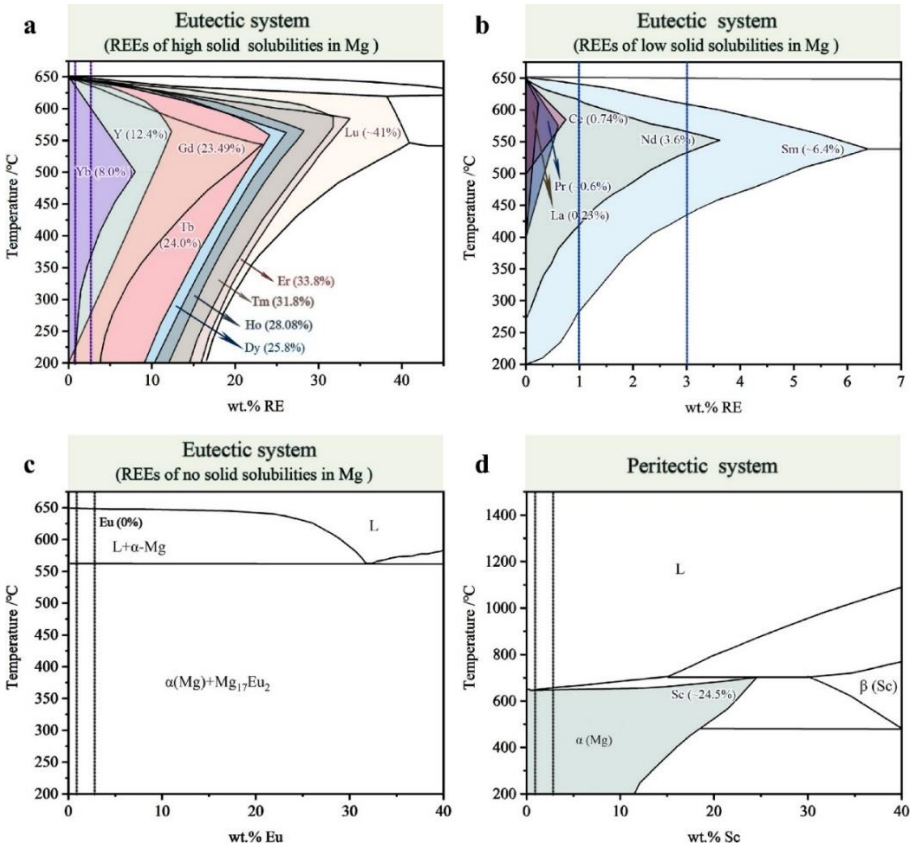

Figure 2.5. (a) REEs of high solid solubilities in Mg (b) REEs of low solid solubilities in Mg (c) REEs of no solid solubilities in Mg (d) Peritectic system [148].

- **Dislocation Strengthening**: Plastic deformation is accompanied with the generation of dislocation and as the deformation process progresses an increase in dislocation density occurs. This leads to dislocation interactions, cross overs and entanglements which leads to resistance in dislocation movement and thus enhancing the mechanical strength at the expense of ductility. The governing equation for dislocation strengthening is as follows [149]:

$$\sigma = \alpha M G b \sqrt{\rho} \tag{2.8}$$

Where $\boldsymbol{\alpha}$ is the Taylor constant, M is the Taylor factor, G is the shear modulus of magnesium, b is the Burgers vector, and ρ is the dislocation density **[150]**.

- **Texture Weakening**: Texture refers to the preferred orientation of crystals within the material, and a strong texture can significantly limit the material's ability to deform, leading to brittleness. Achieving good ductility in magnesium alloys is dependent upon weakening the crystallographic texture [150–152]. The most

effective strategy for weakening texture in magnesium alloys utilizes a combination of rare earth (RE) elements alongside non-rare earth elements such as zinc (Zn) and calcium (Ca). This approach has proven highly successful in reducing texture intensity, thereby enhancing the overall ductility of the magnesium alloy. Additionally, these alloying combinations promote alternative deformation mechanisms beyond deformation twinning, which can weaken the material. By encouraging these alternative mechanisms, the combination of RE and non-RE elements leads to a stronger and more ductile magnesium alloy [153–156].

2.7.1.2 The mechanical properties of Mg-RE alloys

- **Mg-RE binary alloys**

Liu et al. [148] compared the effects of different REEs on the mechanical properties of magnesium alloys. Increase in La from 1 to 3 wt.% improved its yield strength but due to the formation of brittle secondary phases ductility was reduced. Mg-1Er alloys exhibited higher yield strength compared to Mg-1Y alloys despite having a larger grain size (7.3 μm vs. 3.4 μm). The lower strength of Mg-1Y alloys was attributed to a weaker solid-solution strengthening effect of Y in comparison to Er [148]. The introduction of Ho into Mg-1Zr-2Sr alloy leads to the enhancement of mechanical strength owing to the precipitation of stable secondary phases such as $MgHo_3$, Mg_2Ho, and $Mg_{17}Sr_2$ [157].

- **Mg-Li/Al-RE alloys**

The suppression of brittle intermetallic β- $Mg_{17}Al_{12}$ phase in Mg-Al alloys with the addition of RE is reported by various researchers. For example, addition of RE (La, Ce/La mixed RE, Ce, Pr or Nd) in high pressure die cast Mg-4Al-4RE-0.4Mn alloy resulted in the suppression of $Mg_{17}Al_{12}$ phase and promoted the formation of strengthening phases like $Al_{11}RE_3$ and Al_2RE. The proportion, morphology, content and stability of Al-RE phase varied with the specific RE. The grain refinement and Al-RE phase precipitation followed by the RE addition resulted in the enhancement of mechanical properties in the alloys [145,146]. Rzychoń et al. [160] found out that it is effective to maintain a RE/Al ratio greater than 0.5 to suppress $Mg_{17}Al_{12}$. The suppression of $Mg_{17}Al_{12}$ also improves the thermal stability of the alloy as Al-RE phases have higher melting point compared to $Mg_{17}Al_{12}$ phase. Zhang et al. [161]

credited the high structural stability and strength of the Mg-3.0Al-1.8Ce-0.3Y-0.2Mn alloy to the presence of $Al_{11}(Ce,Y)_3$ intermetallic compounds at the dendrite boundaries.

- **Mg-Zn-RE alloys**

The incorporation of zinc (Zn) alongside specific rare earth elements (REEs), particularly yttrium (Y), gadolinium (Gd), erbium (Er), and holmium (Ho), leads to the formation of various ternary secondary phases. These phases significantly enhance the mechanical properties of magnesium (Mg) alloys. In both Mg-Gd-Zn and Mg-Y-Zn alloy systems, the type of secondary phases formed is dependent on the ratio of Zn to RE. When the Zn/RE ratio falls between 1 and 1.5, W phase ($Mg_3Zn_3RE_2$, Cubic structure) is formed, if the ratio is greater than 1.5 an I (Mg_3Zn_6RE, Icosahedral) phase forms and if it is less than 1 then X ($Mg_{12}REZn$, Long period stacking order phase, LPSO) phase forms. This trend is similar in both Mg-Gd-Zn and Mg-Y-Zn alloys [135,162,163]. Zhang et al. [164] reported that the varying Zn/Y ratio in Mg-Zn-Y alloys resulted in a change in mechanical properties according to the different secondary phases. The alloys containing, I phase showed superior strength compared to alloys having both I and W phase or only W phase. This is due to the fact that I phase is coherent with the Mg matrix and it is effective in hindering the dislocation movement. The addition of 1 wt.% Zn in Mg-8Er alloy showed an increase in YS (153 to 207 MPa) and UTS (260 to 318 MPa) while the ductility decreased (44 to 21%). The increase in the tensile strength of the alloy was attributed to the presence of stacking faults (SF) in Mg-8Er-1Zn alloy. The SFs acts as obstacles for dislocation movement and also accumulates dislocations leading to strain hardening. The SFs generated due to the addition of Zn to Mg-Er alloy is shown in **Figure 2.6** (marked in box A) [165]. Similarly, Srinivasan et al., [162] observed that alloys with LPSO phase containing alloy had superior mechanical strength and reduced ductility compared to alloys with I or W phase (**Figure 2.7**). Chen et al. [166] observed that the increase in Nd content from 0.5 to 2 wt.% in Mg-2Zn-xNd-0.5Zr alloy resulted in the grain refinement from 60 to 40 µm and the increase in volume fraction of T phase (Mg_7Zn_3Nd) along the grain boundaries. These two factors resulted in the better mechanical strength with increase in Nd content.

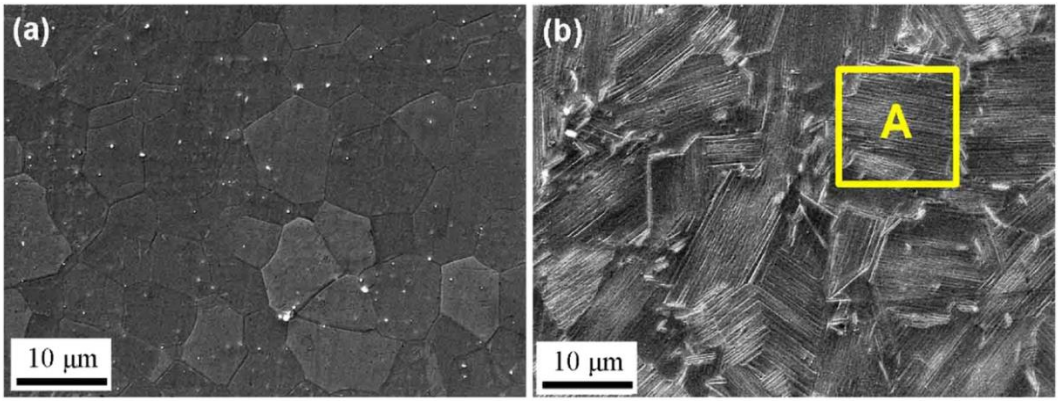

Figure 2.6. SEM micrographs of (a) Mg-8Er alloy, (b) Mg-8Er-1Zn alloy [165].

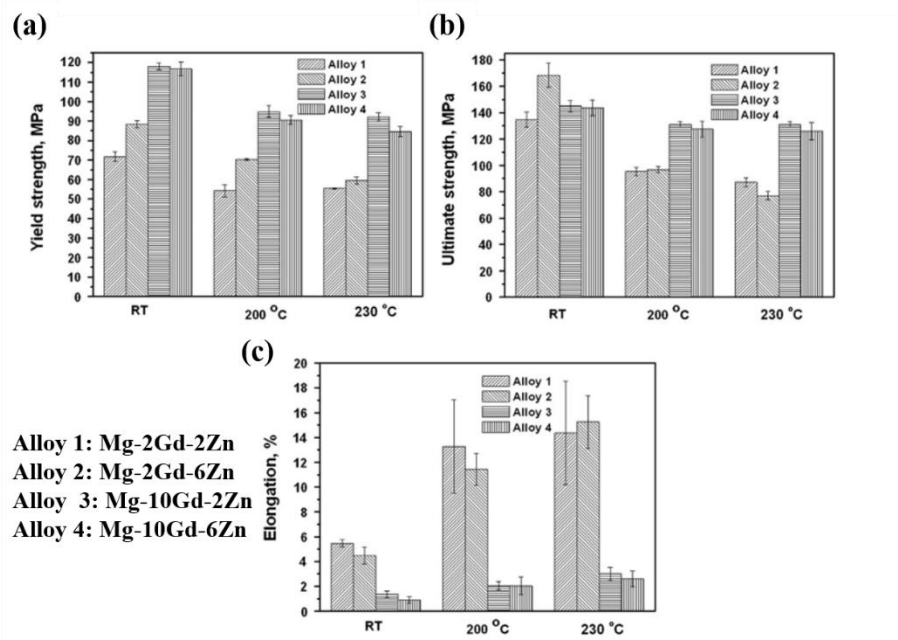

Figure 2.7. Tensile properties of Mg alloys tested at different temperatures (a) YS (b) UTS (c) % Elongation [162].

2.7.1.3 Mechanical properties of secondary processed Mg-RE alloys

The mechanical properties of the secondary processed alloys exhibit superior mechanical properties owing to the significant grain refinement, dislocation density and precipitation of new secondary phases during the processing. The Yield Strength (YS), Ultimate Tensile Strength (UTS), and Elongation (EL) of the FSPed Mg-1Zn-2Dy alloy showed enhancements of 60%, 55%, and 53%, respectively, compared to the as cast

specimen [167]. Mechanical properties of the Mg-10Gd alloy show significant improvement post-ECAP treatment, YS increasing from 123 MPa to 211 MPa, UTS from 185 MPa to 258 MPa, and elongation from 13.2% to 18.0% owing to the grain refinement from 70.8 μm to 1-2 μm. The combined effect of grain refinement and precipitation of intermetallic phases, such as Mg_5Gd, contributes to strengthening of the alloy [168]. Similarly, an increase in mechanical properties is observed in ECAP processed Mg-2.9Gd-1.5Nd-0.3Zn-0.3Zr alloy as UTS increased from 161.4 MPa to 267.8 MPa, YS increased from 85.8 MPa to 217.3 MPa and % elongation increased from 11.8 to 18 [169]. Martynenko et al. [170] reported that the WE43 alloy, processed through various deformation routes (ECAP, MAD, RS), exhibited nearly identical grain sizes, despite showing significant differences in mechanical properties. The superior mechanical strength (UTS = 416 MPa) observed in the RS processed alloy attributed to the existence of deformation twins. Conversely, the improved ductility (17.2%) observed in the alloy processed through the multiple axial deformation (MAD) route was attributed to the heightened activity of pyramidal slip mechanisms.

Chen et al. [171] reported that with an increase in the number of extrusion passes, the mechanical properties of Mg–2Zn–*x*Gd–0.5Zr (*x* = 0, 0.5, 1, 2 wt%) alloys exhibited noticeable enhancement primarily due to grain refinement. The grain refinement of the alloys is evident from the optical microstructure images as shown in **Figure 2.8**. In the case of the 1Gd alloy, compared to two-pass extrusion, the UTS, YS and % elongation after four passes of extrusion increased by approximately 17%, 30%, and 60%, respectively. However, when subjected to the same number of extrusion passes (four passes), there were no significant differences in mechanical properties among the 0.5Gd, 1Gd, and 2Gd alloys. This suggests that while both the Gd content and the number of extrusion passes influence the mechanical properties of the alloys, the extrusion pass plays the dominant role. Furthermore, it indicates that grain refinement strengthening is more effective than second-phase strengthening during severe plastic deformation [171].

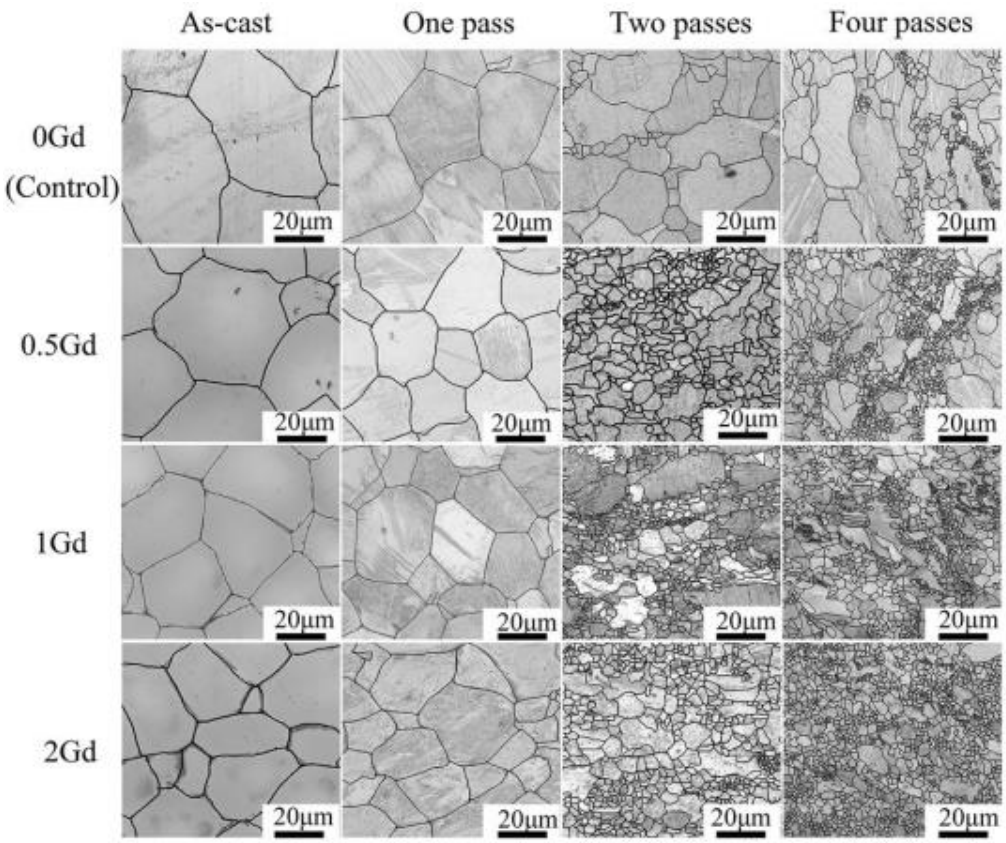

Figure 2.8. Optical microstructure of extruded Mg-xGd-2Zn-0.5Zr alloys [171].

Du et al. [172] reported that increasing the extrusion ratio from 7 to 14 results in larger grain size, weakening of the basal texture, and refinement of secondary phases in the Mg–4Zn-1.2Y-0.8Nd alloy, consequently reducing strength but enhancing ductility. On the other hand, raising the extrusion pass refines grains and secondary phases while strengthening the basal texture, thereby improving both strength and ductility [172]. With more no of secondary passes, the grains get refined resulting in the increase of mechanical strength at the expense of ductility owing to higher dislocation density. Certain processes adopted by researchers have the ability to increase both the mechanical strength as well as ductility. For example, Zhang et al. [173] observed that the microstructure of the Mg-Nd-Zn-Zr (Mg–2.25Nd–0.11Zn–0.43Zr and Mg–2.70Nd–0.20Zn–0.41Zr) alloys subjected to double extrusion is significantly finer and more uniform compared to those subjected to single extrusion. This is due to the fact that following double extrusion of the alloys, a sufficient amount of stored plastic energy is present to initiate Dynamic Recrystallization (DRX). Consequently, the elongated grains dissipate, and the matrix grains become finer and more uniform. Additionally, the precipitated grains in the alloys subjected to double

extrusion exhibit greater homogeneity compared to those in alloys subjected to single extrusion only. The yield strength, ultimate tensile strength, and elongation of the alloys subjected to double extrusion were superior compared to single pass extrusion and is credited to two main factors: the refinement of grain size and the formation of fine precipitated $Mg_{12}Nd$ during hot extrusion. Moreover, it has been noted that in double extruded fine-grain magnesium alloys, both basal and non-basal slip systems are activated due to the grain-boundary compatibility effect, resulting in the enhanced ductility [173]. Also, in comparison with one pass extruded and aged Mg–2Nd–0.1Zn–0.4Zr alloy, the double extrusion followed by aging resulted in a 27% increase in yield strength, 16% increase in ultimate tensile strength and 121% increase in elongation [174]. The tensile properties of different Mg-RE based alloys considered for biodegradable implant applications are summarised in the **Table 2.3** below.

Table 2.3. Mechanical properties of Mg-RE based alloys

Alloy	Processing Route	Y.S	UTS	% Elongation	Mechanism	Reference
Mg-0.6Zr-0.5Sr-3Sc	As cast	74	95	5.9	Sc inhibited the growth of Mg17Sr2 along the grain boundaries leading to thinner grain boundaries	[175]
Mg–2Dy–8Gd–0.2Zr	Heat treated (T6)	210	350	7.5	β' precipitates arrests dislocation movement	[138]
Mg-2Gd-2Zn-0.5Zr	As cast	43	107	6	Weak interface between secondary phase and matrix	[176]
Mg-2Dy-2Zn-0.5Zr	As cast	62	119	10	Low bonding strength between matrix and Mg_8ZnDy	
Mg-2Gd-2Zn-2Nd-0.5Zr	As cast	65	131	12	Eutectic phase along the grain boundaries arrests dislocation movement	
Mg-9Gd-1Zn-0.2Ca	As cast	88	165	6.2	Solution strengthening and the formation of divorced eutectic phase	[177]
ZE41 (Mg-4Zn-1RE)	FSP	83.5	187.6	8.3	Grain boundary strengthening	[178]

Mg-2.9Gd-1.5Nd-0.3Zn-0.3Zr	ECAP	217.3	267.8	18.5	Grain refinement strengthening	[169]
Mg-10Gd	ECAP	123	185	13.2	Grain refinement and precipitation of fine Mg_5Gd phases	[168]
Mg-15Gd	Aged	200	250	0.74	Precipitation hardening by Mg_5Gd phases	[108]
Mg-1Zn-2Y-0.17Zr	Extruded	150	280	25	Grain refinement due to dynamic recrystalisation and the alignment of LPSO phase along the extrusion direction	[179]
Mg-2Y-0.6Nd-0.6Zr	Rolled	216	246	3.75	Grain refinement and work hardening	[180]
Mg-2Y-0.6Nd-0.6Zr	Rolled + ECAP	-	225	10.5	Grain refinement and texture weakening	[180]
WE43	ECAP	260	300	13.2	Activation of prismatic slip enhanced ductility	[170]
WE43	MAD	210	300	17.2		[170]
WE43	RS	287	416	7.9	Grain refinement and large number of deformation twins	[170]
WE43	ECAP + Ex	340	390	10.9	Activation of prismatic slip and grain refinement	[181]
Mg–6Ho–1.5Zn	Extruded	210	322	31	Stacking faults accumulates dislocations and enhances strain hardening	[182]
ZK60-2Yb (Mg-6Zn-0.5Zr-2Yb)	Heat treated (T6)	146.4	297.5	8.9	Nanoscaled precipitates	[183]
Mg–2Zn–0.4Mn–0.1Sr–1Gd alloys	Extruded	-	248.5	22.4	grain refinement and second-phase strengthening.	[184]

ZE20 (Mg-2Zn-0.8RE)	Extruded	213	264	13.2	Grain refinement	[185]
GZ60K (Mg-6Gd-0.4Zn-0.5Zr)	Extruded	186	252	24.5	Formation of stacking faults and dynamically recrystallized precipitates	[186]
Mg-4Zn-1.2Y-0.8Nd	Extruded	297	320	17	Uniform grain formation	[172]
Mg-1Mn-2Zn-1.5Nd	Extruded	212	287	26.6	Solid solution strengthening and work hardening	[187]
Mg-9Gd-0.5Mn	Extruded	164	268	22.9	Mn and Gd addition results in improved recrystallization without grain growth	[188]
Mg-3Nd-0.5Zn	Extruded	250	270	2.6	Presence of very fine secondary phases resulted in the better mechanical properties in WE43	[189]
Mg-2Y-1Zn	Extruded	260	300	2.4		[189]
WE43	Extruded	250	300	4		[189]
Mg-2Zn-5.7Y	Extruded	364	430	4.6	Uniformly distributed LPSO phase and grain refinement	[190]
Mg-10Gd	Extrusion + ECAP	189	255	20.9	Combined effect of grain refinement and the increased probability of basal and pyramidal glides	[168]
WE43	Extruded + ECAP	260	380	10	Grain refinement	[191]
Mg-2Zn-2Gd-0.5Zr	ECAP	230	280	33	Disintegrated secondary phases along and within the grain boundaries inhibits dislocation movement	[171]
Mg-2Zn-1Gd	Extrusion	284	338	24	Grain refinement, fine secondary phases, and weakened texture	[192]

Mg-1Zn-2Dy	FSP	120	242	28	Combination of grain refinement and precipitation strengthening	[167]
WE43	FSP	250	280	19	Grain refinement and prismatic slip activation	[193]
Mg-2Zn-0.5Gd-0.5Zr	ECAP	250	280	19	Grain refinement and prismatic slip activation resulted in excellent combination of strength and ductility	[194]
Mg-2Zn-0.5Nd-0.5Zr		270	300	22		
Mg-2Zn-0.5Y-0.5Zr		295	315	17		
Mg-1.8Zn-0.2Gd	Rolling		300	14	Presence of twins acted as dislocation barriers	[195]
Mg–2.25Nd–0.11Zn–0.43Zr	Double extrusion	276	309	34.3	Uniformly refined grains and fine $Mg_{12}Nd$ secondary phases	[173]
WE43	ECAP + Extrusion	350	398	9.45	Grain refinement and increased dislocation density	[181]
Mg-2Zn-0.5Nd-0.5Zr	Extrusion	238	281	22.4	Refined grains uniformly distributed secondary phases	[196]
Mg–2Nd–0.1Zn–0.4Zr	Double extrusion + aging	304	320	27.4	Fine grains and homogenous microstructure	[174]
Mg-2Zn-0.5Nd	Extrusion	136	245	19.3	Fine grain size and uniformly distributed secondary phases	[197]

2.7.2 Biodegradation behaviour

The biodegradation behaviour of Mg alloys is primarily governed by their microstructure, secondary phases, and surface oxide formation. Achieving an optimized degradation rate is crucial for biomedical applications to ensure that the implant maintains structural integrity while gradually resorbing in sync with tissue healing.

2.7.2.1 Factors influencing corrosion/biodegradation behaviour of Mg based alloys

- **High reactivity of Magnesium:** Magnesium has a very low standard electrode potential (-2.37 V vs. Standard Hydrogen Electrode), making it highly reactive compared to many other metals. This high reactivity means magnesium readily participates in oxidation-reduction reactions, leading to rapid corrosion. The electrode potentials of REEs (For example: Y: −2.37 V, La: −2.37 V, Gd: −2.40 V, Nd: −2.44 V, Ce: −2.48 V) are similar to that of magnesium (-2.37 V), and their compounds have low electrode potentials. This similarity helps to lower the overall potentials of the cathode phase, reducing corrosion rates [198–200].
- **Effect of Secondary Phases:** The corrosion behaviour of Mg alloys is impacted by the formation and distribution of secondary phases. The secondary phases can influence the corrosion of Mg alloys in two contrasting ways. 1. Micro-galvanic corrosion: The volta potential difference between secondary phase and the surrounding α-Mg matrix leads to the formation of a micro galvanic couple. The anodic phase (usually the α-Mg matrix) will start to corrode and the intensity will depend on the difference in volta potential difference between secondary phase and α-Mg matrix. 2. Barrier effect: The uniformly distributed secondary phases can eventually prevent the spread of corrosion into the grain interior by acting as a barrier [201,202]. REEs are effective in forming secondary phases that are less cathodic and can thus minimize micro-galvanic corrosion. The **Table 2.4** shows the volta potential difference of different secondary phases and α-Mg matrix. The positive volta potential difference indicates that the secondary phases are cathodic and vice versa. It can be observed that very few secondary phases are anodic in nature. For example, Liu et al. [203] showed that the addition of RE (Ce, La) to AM60 (Mg-6%Al-0.6%Mn) alloy improved its corrosion resistance. The enhanced corrosion resistance was due to the reduction in volume fraction of β-$Mg_{17}Al_{12}$ and the formation of γ-AlRE. The γ-AlRE phase is more active thus reducing the galvanic corrosion effect. The corrosion barrier effect of continuously distributed secondary phases in ZK60-3.6Nd (Mg-6Zn-0.4Zr-3.6Nd) enhanced its corrosion resistance compared to ZK60 (Mg-6Zn-0.4Zr) and ZK60-1.8Nd (Mg-6Zn-0.4Zr-1.8Nd) [204].

Table 2.4. Volta potential difference of secondary phases with respect to Mg matrix in different Mg-RE alloys.

Alloy	Phase	Volta potential difference (mV)	Reference
Mg-6Zn-1Ce-0.5Zr	$MgZn_2Ce$	-90	[205]
Mg-5Nd	$Mg_{41}Nd_5$	35	[206]
ZE41 (Mg-4Zn-1Ce)	Mg_7Zn_3Ce	100	[207]
WE43	Mg_{12}(RE,Y)	25	[207]
WE43	Y rich	50	[207]
Mg-8.9Gd-2.8Y-1.8Zn-0.4Zr-0.2Ca	Block shaped LPSO	50	[208]
Mg-8.9Gd-2.8Y-1.8Zn-0.4Zr-0.2Ca	Lamellar LPSO	-100	[208]
Mg-8.9Gd-2.8Y-1.8Zn-0.4Zr-0.2Ca	RE rich phase	200	[208]
Mg-1.2Y-1.2Ho-0.6Zn-0.1Zr (at.%)	(As cast) LPSO	90	[209]
	(Heat treated) LPSO	37	
Mg-2Zn-0.6Zr-0.2Nd	T3 phase	-400	[210]
Mg-15Gd-2Zn-0.39Zr	$(Mg,Zn)_3Gd$ as cast	290	[211]
Mg-15Gd-2Zn-0.39Zr	LPSO (T4)	243	[211]
Mg–2Zn–0.4Mn–0.1Sr–1Gd	Gd rich phase	137	[184]
Mg-5.0Y-7.0Gd-1.3Nd-0.5Zr	RE phases	-35	[200]
Mg-4.23Zn-9.27Gd-0.44 Zr	W phase	120	[202]
Mg-6.87Zn-4.91Gd-0.42 Zr	I phase	25	
Mg-2.77Zn-11.40Gd-0.45 Zr	X phase	60	

- **Formation of Corrosion Product Films:** The corrosion product film or the oxide film forming on the surface of the alloy can inhibit the corrosion depending on their protective capability in corrosive environments [41,212]. The effectiveness in protective nature of the oxides can be evaluated using the Pilling-Bedworth ratio (PBR) [213]

  PBR = Molecular volume of the oxide layer/Molecular volume of the metallic substrate

According to PBR theory, oxide layers with PBR < 1 will be porous and will not offer protection, like wise oxide layers with PBR > 2 will be susceptible to breakage due to stress and also does not offer protection. Whereas, the oxide layers with PBR between 1 and 2 have the capability to protect the material from further corrosion [41]. For instance, the PBR of MgO is 0.81 which does not offer any protection to the surface. However, certain RE oxides like Sc_2O_3 (PBR = 1.1), Y_2O_3 (PBR = 1.19), Nd_2O_3 (PBR = 1.02) will offer protection to the otherwise porous MgO layer and thus enhancing the corrosion resistance [214–216] [217]. For example, Liu et al. [218] showed that the formation of Y_2O_3, Gd_2O_3, and Nd_2O_3 in the Mg–5Y–7Gd–1Nd–0.5Zr alloy enhanced the corrosion resistance [218]. Similarly, Zhang et al. [150] found that the formation of a stable and compact Nd_2O_3 film on the surface, along with $Mg(OH)_2$ resulted in its superior corrosion resistance. Also, elements such as La, Ce, Er, Y, and Gd have been reported to increase the compactness of corrosion films of oxides or hydroxides [203,218–222].

- **Role of impurities:** Common impurity elements like Fe, Ni and Cu are highly detrimental to corrosion resistance in Mg alloys. They have limited solubility in Mg which results in the formation of highly active cathodic phases which accelerates corrosion [223]**.** In addition, impurities react with major alloying elements thus reducing their effectiveness as alloying elements [224]. Thus, it is important to control the number of impurities in the alloy systems. The threshold limits for impurities Fe, Ni and Cu are 50 ppm, 5 ppm and 300 ppm respectively [212,225]. Alloying elements like RE have the ability to scavenge these impurities by forming stable intermetallic phases with them. Thus the micro-galvanic corrosion due to the impurities can be reduced to a great extent [219,226].
- **Grain size:** The reduction in grain size leads to an increase in the number of grain boundaries. The high density of grain boundaries facilitates the formation of a more uniform and protective surface oxide layer, thereby enhancing its corrosion resistance. In addition, the higher number of grain boundaries will lead to a reduction in the disorder and mismatch between the metal surface and oxide layer. This reduction ensures a better adherence of protective films. However, there are contradicting reports suggesting that grain refinement occurring during deformation processing has led to a decrease in corrosion resistance. However, this might be due to the fact that other microstructural parameters such as internal stress, texture and

secondary phase distribution also play a role in the corrosion behaviour of the material [227,228]. The collective impact of grain boundaries can be summarized as follows. Grain boundaries play a role in increasing the rate of diffusion and electron activity while decreasing atom coordination. This reduction in atom coordination results in a lower work function of the surface, facilitating the removal and adsorption of species and potentially increasing the rate of charge transfer. The heightened reactivity associated with grain boundaries supports the idea that they can have an adverse effect on corrosion resistance, serving as initiation sites for corrosion. However, magnesium presents a unique case due to the instability of its oxide layer in aqueous solutions. This instability arises from a significant geometrical mismatch between the oxide layer and substrate. Furthermore, in aqueous solutions, cubic magnesium oxide transforms into hexagonal magnesium hydroxide upon hydration, with a volume approximately double that of magnesium oxide. This transformation leads to disturbances in the film, causing compressive rupture and initiating a continual corrosion process. A fine-grained microstructure is likely a means of relieving this stress, primarily through a high fraction of grain boundaries, thereby reducing the degree of oxide cracking [229].

- **Texture:** The crystallographic texture has a significant influence on the corrosion behaviour of Mg based alloys. The basal plane {0001} in magnesium alloys exhibits lower surface energy in comparison to the prism planes {1010} and {1120}. Orientations closer to the basal planes have demonstrated lower corrosion rates compared to atomic planes with less packing density [230,231]. Grains with orientations near the basal planes, characterized by higher work function values than grains with non-highly packed planes, require more energy to remove atoms from their surfaces [232–234]. The closely packed nature of basal planes makes it challenging to remove atoms from them, hindering the perpendicular propagation of corrosion in the direction of the basal plane. Thus, the basal planes are more resistant to biodegradation in comparison with the prism planes. The theoretical corrosion rate of the prism planes is significantly higher than basal planes [235,236]. For example, Zhang et al. [169] observed that the presence of a dominant basal plane in Mg-2.9Gd-1.5Nd-0.3Zn-0.3Zr alloy contributed to its superior biodegradation resistance. Similarly, FSPed EZ33 (Mg-3Nd-3Zn-0.5Zr) showed better biodegradation resistance owing to a strong basal texture [237].

- **Dislocation density and twins:** The dislocation sites have higher energy and act as anodic sites compared to the matrix thus accelerating corrosion. Thus, a significant increment in dislocation density during deformation processing usually leads to an increase in corrosion rate. Also, the formation of twins during deformation process accelerates corrosion rate as atoms in twin planes are more active than those in normal crystallographic plane.

  Martyneko et al. [170] studied the influence of different processes such as ECAP, Multi axial deformation (MAD) and rotary swaging (RS) on the properties of a bioresorbable WE43 alloy. It was reported that although lowest grain size of 0.61 μm was observed for WE43 processed by RS technique, large number of deformation twins associated with the processing caused a deterioration in its biodegradation resistance. Koleini et al. [238] reported that despite the grain refinement induced by rolling, it was revealed that the corrosion resistance of Mg–1Ca decreased due to an escalation in the number of twinning planes. The heightened density of twinning and dislocation altered the anodic polarization behaviour, with untwinned samples exhibiting self-passivation characteristics, while twinned ones demonstrated active dissolution in the electrolyte.

2.7.2.2 Biodegradation behaviour of as cast Mg-RE based alloys

- **Mg-RE binary alloys**

Yang et al. [239] observed that the biodegradation layer of Mg-10Dy alloy was rich in Dy and this resulted in the suppression of pitting corrosion. Mao et al. [240] observed that the formation of Nd_2O_3 in the biodegradation layer of Mg–2.5Nd–0.2Zn–0.4Zr alloy inhibit the release of Mg^{2+}, thus hindering further biodegradation. Munir et al. [175] reported that Sc addition in Mg-Sr-Zr alloy resulted in an enhancement in biodegradation resistance owing to the suppression of the growth of $Mg_{17}Sr_{12}$ at grain boundaries and the formation of Sc_2O_3 on the biodegradation layer. Similarly, Brar et al. [241] demonstrated the effectiveness of Y and Sc in forming protective oxide films on the surface of Mg alloys. Further, Brar et al. [242] found that the surface film of Mg-Gd alloy consisted of MgO and Gd_2O_3, Mg-Y alloy had MgO and Y_2O_3 oxide layers, and Mg-Sc alloys had MgO and Sc_2O_3 oxide layers. However, the kinetic speed of formation of oxide in Mg-3Gd was the highest and that of Mg-3Sc was the lowest. But,

the formation of a rare earth oxide need not always protect the alloy from severe biodegradation. For example, Zhang et al. [206] observed that although Nd_2O_3 formed on the biodegradation layer of Mg-2Nd alloy, the presence of $Mg_{41}Nd_5$ phase accelerated the micro galvanic corrosion. The increment in the addition of Nd (5%) resulted in the uniform distribution of $Mg_{41}Nd_5$ phase and a more compact surface film ensured the better biodegradation resistance.

- **Mg-Li/Al-RE**

Geng et al. [243] reported that the addition of Gd to Mg-17Al-3Zn-7Cu shifted the corrosion potential to a more noble direction, thus enhancing its biodegradation resistance. Liu et al. [244] observed that Y incorporation into AZ61 alloy suppressed the formation of $Mg_{17}Al_{12}$ phase and enhanced the formation of Al_2Y phase. The Al_2Y phase has a higher corrosion potential, which inhibits the micro-galvanic corrosion.

- **Mg-Zn-RE**

As mentioned in section 2.7.1.2 the different Zn/RE ratios result in the formation of different ternary phases such as I, W and LPSO phases. These secondary phases have significant effect on the biodegradation behaviour of the alloys. Zhang et al. [245] observed that the enhanced biodegradation resistance in Mg-2Zn-0.2Mn-0.62Nd was due to reduced micro galvanic biodegradation and the formation of stable surface oxide. However, the presence of secondary phases such as Mg_3Zn_6Nd and Mg_2Zr in Mg-2Zn-0.8Nd-0.2Zr alloy accelerated the degradation rate [246]. There are also reports of anodic secondary phases in Mg-Zn-RE alloy systems that preferably corrodes rather than the matrix. For example, the addition of 0.2-1 wt.% Nd in Mg-2Zn-0.6Zr alloy resulted in the formation of $Mg_{60}Zn_{32}Nd_8$ (T2) and $Mg_{35}Zn_{40}Nd_{25}$ (T3) phases. T2 and T3 phases, with a relative Volta potential of approximately -400 mV, served as micro-anodes, leading to their preferential corrosion rather than the Mg matrix [210]. Although cathodic or anodic secondary phases accelerate the biodegradation process, the uniform distribution of secondary phases are effective in slowing down the biodegradation. For instance the LPSO structure in Mg-3Gd-1Zn-0.4Zr alloy acted as a corrosion barrier and enhanced the biodegradation resistance [247]. Similarly, Xie et al. [209] observed that the lamellar structure containing LPSO and stacking faults (SF) effectively impedes the biodegradation propagation. Also, the authors observed that severe micro galvanic corrosion is observed with the cathodic LPSO phase than the

anodic SF. This is evident from the **Figure 2.9** [209]. Similarly, the uniform corrosion observed in Mg–6Ho–0.5Zn was due to the presence of SF. SFs are parallel within a grain and are arranged in different orientations across the grains. Thus, due to the different orientations in the adjacent grains, the corrosion spreading can be impeded [182]

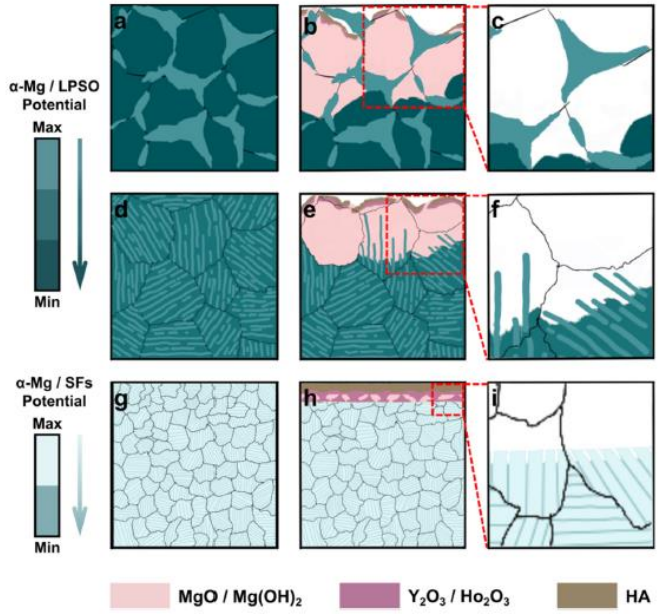

Figure 2.9. Schematic diagrams of the corrosion mechanism of (a-c) as-cast, (d-f) heat-treated, (g-i) as-extruded Mg96.9Y1.2Ho1.2Zn0.6Zr0.1 (at.%) alloy [209].

2.7.2.3 Biodegradation behaviour of secondary processed Mg-RE alloys

The secondary processing of the material refines the grains, distributes secondary phases, changes the texture as well as introduces internal stress and increases dislocation density. All these factors have a definite influence on the biodegradation behaviour of Mg alloys. However, during biodegradation of secondary processed alloys, all these factors come into play and that makes the biodegradation behaviour a bit unpredictable [167,248]. As it is well reported that the grain refinement usually leads to a better biodegradation resistance owing to the formation of a passivation film over the grain boundaries. For instance, Friction stir processing (FSP) of WE43 resulted in the grain size reduction from 53 to 2.7 µm and which led to biodegradation rate declining from 38.41 to 15.12 mm/y and the authors have attributed this to the improved passivation kinetics of the fine-grained microstructure [248]. Similarly grain refinement of ZE41 alloy subjected to 60 ECAP passes also resulted in a better biodegradation resistance [230,249]. However, there are

reports suggesting that although grain refinement occurred the biodegradation resistance deteriorated. This is due to the fact that other factors played a major role in the biodegradation behaviour. For example, the grain refinement enabled enhanced biodegradation resistance was observed for the 8 pass ECAP processed Mg-1Y-0.5Zn alloy. However, although the grains continued to get refined till 12 pass, the biodegradation resistance declined owing to the complete breaking up of LPSO phase accelerating the dissolution of Mg [250]. Similarly, after two ECAP passes, the Mg-2Zn-1Gd-0.5Zr alloy exhibited improved biodegradation resistance due to uniform fine grains and the transformation of bulk secondary phases into smaller particles. However, increasing the passes to four created a bimodal microstructure with high-energy grain boundaries, accelerating biodegradation. The change in the microstructure of the alloys is shown as a schematic in **Figure 2.10** [171]. Straumal et al. [168] reported that a significant reduction in grain size was observed with ECAP of Mg-10Gd alloy from 70.8 to 1-2 µm with the biodegradation rate increasing from 0.l5 to 2.19 mm/y owing to the accumulation of increase in dislocation density. Similarly, the dispersion of the secondary phase plays a more crucial role than grain size in biodegradation behaviour of ECAP processed WE43 alloys. The samples till 3 ECAP pass showed increased biodegradation resistance owing to the grain refinement as well as the uniform distribution of secondary phases. Conversely, a further decrease in grain size observed with 4 pass, but the coarse spherical phase grew which resulted in the decline of biodegradation resistance [251].

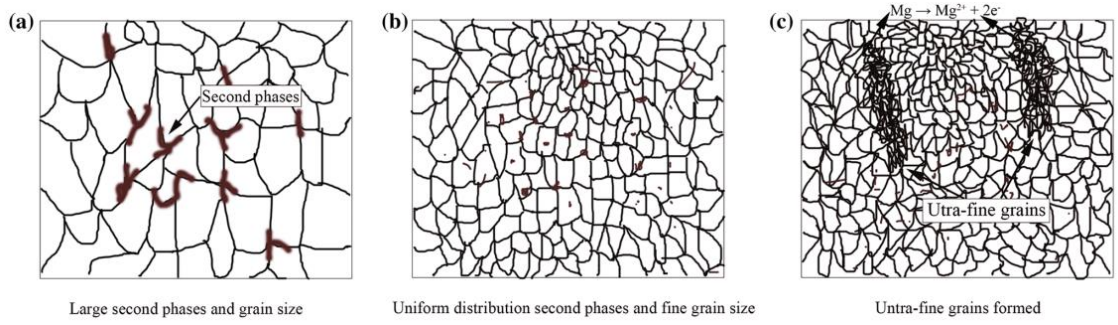

Figure 2.10. (a) The as-cast Mg-2Zn-1Gd-0.5Zr alloy features large grains and second phases, (b) two extrusion passes result in smaller grains and uniform distribution of second phases, (c) four passes produce finer grains and strip-shaped ultrafine grains [171].

However, these reports may not accurately convey the adverse impact of grain refinement on biodegradation resistance. Extrusion, as an example, leads to a wide range of grain size values due to non-homogeneous strain. To address this issue, alternative

processing routes such as cyclic extrusion and compression (CEC) [252] and double extrusion [173] have been explored by researchers. An increase in extrusion ratio from 7 to 14 in Mg-4Zn-1.2Y-.8Nd resulted in 100% dynamic recrystallization and the authors have reported that biodegradation rate was reduced owing to the distribution of uniform grains [172]. These modifications resulted in the formation of a homogeneous fine grain structure and demonstrated improved biodegradation resistance. Also, for designing a biodegradable implant, uniform biodegradation should be preferred rather than achieving lower biodegradation rate. Zhang et al. [186] reported that extruded GZ61K (Mg-6Gd-1Zn-0.5Zr) alloy had lower biodegradation rate compared to GZ60K (Mg-6Gd-0.6Zn-0.5Zr) alloy owing to the finer grain size. But the uniform biodegradation observed in GZ60K alloy attributed to its longer retention of mechanical integrity over GZ61K alloy.

Similar to the deformation processing, heat treatment alone or the combination of heat treatment along with deformation processing has also proved effective in reducing the biodegradation rate. The size, distribution, morphology, and volume fraction of the precipitates after the heat treatment play a key role in the biodegradation behaviour of these alloys. Maier et al. [253] observed that aging of Mg-2.78Y-1.43Nd-0.43Gd-0.41Dy (WE32) and Mg-3.05Y-1.81Nd-0.50Gd-0.43Dy (WE33) alloys at 200 °C for 45 hours lead to the formation of a passive layer leading to a reduction in biodegradation rate. The solution treatment of Mg-1.59Nd-2.91Zn-0.05Zr-0.35Mn (NZKM) alloy at 480 °C for 10 hours resulted in the alteration of continuously distributed β phase [$(MgNd)_4Zn_7$] to discontinuous necklace type distribution. This led to a decrease in the micro-galvanic couples and thus increasing the biodegradation resistance [254]. Similarly, solution treatment of Mg-2.7Nd-0.2Zn-0.4Zr alloy at 475 °C for 1 hour, resulted in the enhanced biodegradation resistance owing to the lower volume fraction of secondary phases [255]. However, there are reports of a decline in biodegradation rate owing to the heat treatment. For instance, solution treatment of Mg-2.5Nd-0.3Zn-0.1Sr-0.4Zr alloy led to a decrease in biodegradation resistance due to grain growth and the presence of a discontinuous intermetallic phase. The as cast alloy showed superior biodegradation resistance because of the barrier effect offered by the continuous distribution of secondary phase [256]. Also, solution treatment of as-cast Mg-5Y-1.5Nd alloys at 535 °C for 20 hours, followed by aging at 225 °C for different durations (6, 14, and 24 hours), deteriorated biodegradation resistance owing to the increase in micro-galvanic couples. The T6-24 h (overaged) alloy exhibited the highest amount of bulky secondary phases and the highest biodegradation

rate, while the T6-14 h (peak-aged) alloy showed a more uniform distribution of precipitates, forming a corrosion barrier and improving biodegradation resistance [257]. **Table 2.5** summarizes the biodegradation behaviour of as cast and secondary processed Mg-RE based alloys.

Table 2.5. Biodegradation rates of Mg-RE based alloys

Aloy code	Process Parameters	Solution	Biodegradation rate	Mechanism	reference
Mg-1.27Ce	As cast	SBF	9.6	Reduced volume fractions of $Mg_{12}Nd$ resulted in the smallest ratio of cathode-to-anode area	[258]
Mg-0.69La	As cast	SBF	14.7		[258]
Mg-2.13Nd	As cast	SBF	4.1		[258]
Mg-3Gd-1Zn	As cast	SBF	0.61	Presence of LPSO phase along the grain boundaries	[177]
Mg–6Ho–0.5Zn	Extruded	SBF	0.25	Presence of $Ho(OH)_3$ stabilises the corrosion film.	[182]
Mg-10Dy	Heat treated (T4)	DMEM + FBS	0.56	Dy_2O_3 and $Dy(OH)_3$ in the biodegradation layer offers protection	[239]
Mg-6.0Gd-1.2Cu-1.2Zr	Heat treated (T4)	SBF	60	Barrier effect of LPSO and reduced microgalvanic corrosion post heat treatment	[259]
Mg-10Gd-0.5Zr	Heat treated (T4)	DMEM + FBS	0.79	Dissolution of secondary phases and Gd enhances the passivation film	[260]
Mg-4Y-1Ag	Heat treated (T4)	DMEM + FBS	0.2	Homogenised microstructure and reduced microgalvanic corrosion owing to the dissolution of $Mg_{24}Y_5$ phase	[261]
Mg–2Dy–8Gd–0.2Zr	Heat treated (T6)	DMEM + FBS	0.3	Protective oxide layer	[138]
Mg-5Nd	Extruded + Solutionized + aged	DMEM + FBS	1.2	Uniformly distributed $Mg_{41}Nd_5$ acted as barriers for corrosion propagation	[262]
Mg-5.8Zn-2Yb-0.5Zr	Heat treated (T4)	SBF	1.49	Corrosion barrier effect induced by dispersed nanoscale precipitates	[183]
Mg–2Zn–0.4Mn–0.1Sr–1Gd	Extruded	Hanks	0.48	Gd_2O_3 in the corrosion layer	[184]

Mg-2Zn-0.72Ce	Extruded	MEM + 10% FBS	0.38	Refined grains	[185]
GZ60	Extruded	SBF	0.45	Presence of high density stacking faults	[186]
Mg-5Nd	Extruded	DMEM + FBS	0.15	The combination of uniformly distributed $Mg_{41}Nd_5$ phases and the protection offered by Nd_2O_3 and $Nd(OH)_2$	[206]
Mg-0.6Gd-0.3Dy-0.2Zr	Extruded	Hanks solution	0.36	Few secondary phases resulting in the reduction of galvanic couples	[263]
Mg-4Y-3Nd	Extruded	SBF	0.3	Formation Y_2O_3 and $Y(OH)_3$ enhances the stability of the corrosion layer	[189]
Mg-3Nd-0.5Zn	Extruded	SBF	1.25	Mg-Nd binary phases have very low potential difference with Mg matrix	
Mg-2Y-1Zn	Extruded	SBF	2.25	LPSO phases induce micro galvanic corrosion	
Mg-2Zn-5.7Y	Extruded	SBF	2.3	Bimodal microstructure and low induced strain	[190]
Mg-10Gd	Extruded + ECAP	DMEM	2.19	Increased dislocation density increased the biodegradation rate	[168]
Mg-2.9Gd-1.5Nd-0.3Zn-0.3Zr	ECAP	SBF	0.126	Grain refinement and strong basal structure	[169]
Mg-2Zn-1Gd-0.5Zr	ECAP	Hanks`	0.5	Grain refinement and uniform distribution of secondary phases	[171]
Mg-2Zn-1Gd	Extruded	Hanks	0.24	Uniformly distributed secondary phases leads to suppression of micro galvanic corrosion	[192]
LAE442	Extruded + ECAP	MEM + FBS	0.25	Formation of compact surface layer	[264]
Mg-Y-Zn	ECAP	SBF	2.35	Uniform grain refinement,	[250]

EZ33	FSP	HBSS	0.35	Uniform distributed secondary phases, grain refinement and basal texture	[237]
WE43	FSP	SBF	15.12	Uniformly fine grained microstructure	[248]
Mg-1Zn-2Dy	FSP	DMEM	0.72	grain refinement, uniform distribution of secondary precipitates and strong basal texture	[167]
Mg-2Zn-0.5Gd-0.5Zr	ECAP 4 pass	hanks	0.48	Presence of large secondary phases proved detrimental to corrosion	[194]
Mg-2Zn-0.5Nd-0.5Zr			0.35	Large amount of calcium phosphate deposition	
Mg-2Zn-0.5Y-0.5Zr			0.63	High volume fraction of secondary phases causes more micro galvanic corrosion	
Mg-1.8Zn-0.2Gd	Rolled	Hanks	0.16	Single α Mg phase was predominant thus eliminating the formation of galvanic couples	[195]
Mg-2Zn-0.2Mn-0.62Nd	Rolling	Kokubo	0.92	Presence of Nd_2O_3, Nd inhibits the Cl^- penetration into the oxide film,	[245]
Mg-2.73Nd-0.16Zn-0.45Zr	Cyclic extrusion and compression	Hanks solution	1.25	Uniformly distributed secondary phases and refined grains	[246]
Mg–2Nd–0.1Zn–0.4Zr	Double extrusion + aging	SBF	1.2	Fine grains and homogensou microstructure	[174]
Mg-1.84Zn-0.5Nd	FSP	Simulated intestinal fluid	1.5	Fine grain size, strong basal texture and	[265]

2.7.3. Biocompatibility of Mg-RE based alloys

Along with biodegradation as well as sufficient mechanical strength the implant must be non-toxic, non-genotoxic, and not irritating to the human body. Although Mg is a highly biocompatible element, the alloying element added to Mg to improve its biodegradation resistance as well as mechanical strength can influence the biological properties of the alloys. Therefore, it is important to know that that REEs are not typically involved in biochemical processes, and thus the body has limited mechanisms for their handling. However, the ionic radius of REEs are similar to that of Ca^{2+} which facilitates them to interact with various biological pathways [266–268]. Although, certain REEs find suitability to be used in the body, they are primarily added into Mg to enhance the mechanical as well biodegradation properties. Thus, the focus should be to use those REEs as alloying element in Mg having an excellent combination of biocompatibility, mechanical strength as well as biodegradation resistance. However, selection of REEs on the basis of biocompatibility should be given the utmost priority as the LD50 values of almost all of the REEs fall well short of the biocompatible elements like Mg and Ca [**Table 2.6**]. LD50, or Lethal Dose 50%, is a term used in toxicology to measure the acute toxicity of a substance. It represents the dose required to kill 50% of a test population (usually lab animals like rats or mice) within a specified period. The value is typically expressed in terms of milligrams of the substance per kilogram of body weight (mg/kg) [269].

Table 2.6. LD50 values of various elemental chlorides (given as oral dosage to rats)

Element	Sc	Y	La	Ce	Pr	Nd	Sm	Lu
LD50	755	88	372.4	353	358	600	585	315
Reference	[270]	[271]	[272]	[269]	[273]	[274]	[275]	[276]
Element	**Eu**	**Gd**	**Tb**	**Dy**	**Ho**	**Er**	**Tm**	**Yb**
LD50	550	550	550	585	560	535	485	395
Reference	[277]	[278]	[279]	[280]	[280]	[280]	[281]	[282]
Element	**Mg**	**Ca**	**Zn**					
LD50	3450	2000	1100					
Reference	[283]	[284]	[285]					

Also it should be noted that certain REEs do not necessarily show any toxicity at lower dosage, at higher dosage they may severely harm the biological functions [286]. For example, a study on the effect of different $RECl_3$ (RE = Y, Nd, Dy, Pr, Gd, La, Ce, and Eu)

on the cytocompatibility of MG63, human umbilical cord perivascular (HUCPV), and RAW 264.7 cell lines proved that La and Ce had the highest toxicity [287]. Similar observation was made by Grillo et al. [288], La exhibited a more detrimental effect on the cell lines in comparison to Gd and La even exhibited toxicity at lower concentrations (≥200 μM RE) when exposed to longer times (more than six days) [288]. However, there are also reports of $LaCl_3$ and $CeCl_3$ behaving as inhibitors of leukemic cells and resulting in apoptosis of cells which suggests they have anticancer capabilities [289]. Also, REEs shows antimicrobial properties and they are also used in burn treatments [277–279]. For instance, Wakabayashi et al. [293] showed that REEs have the potential to show antibacterial as well as antifungal properties similar to Cu, which is usually used as an antibacterial metal. In addition, unlike Cu which is toxic to lymphoblastoid cells, REEs does not affect the cells in an alarming manner. The antibacterial and antifungal properties of REEs can be seen from the **Figure 2.11**.

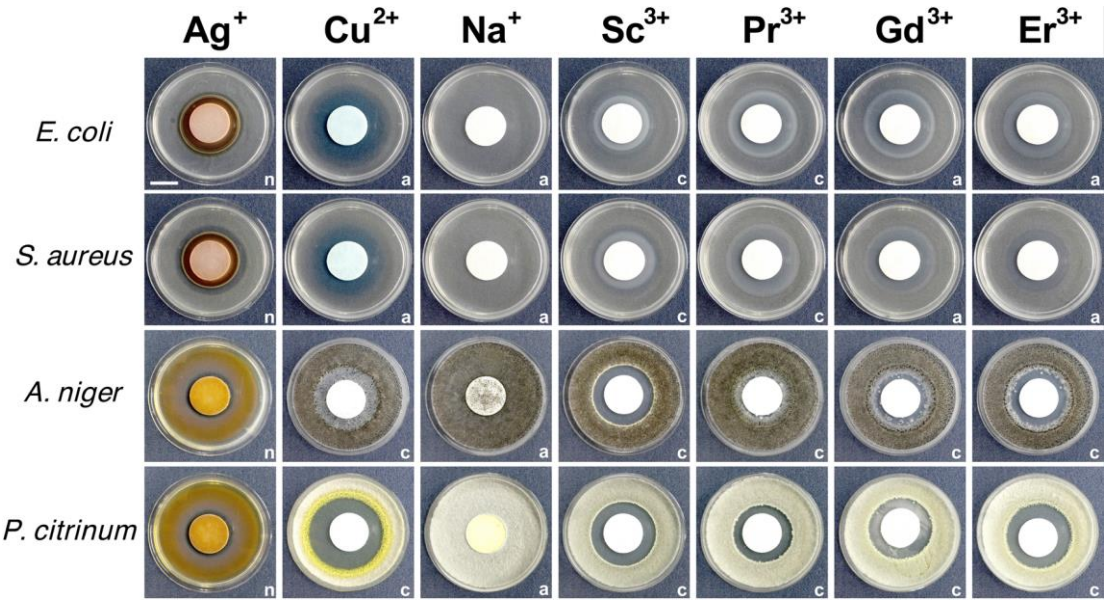

Figure 2.11. Antibacterial effects against E.coli and S. aureus and antifungal effects against A. niger and P. citrinum of RE ions (Sc, Pr, Gd and Er ions), Cu and Ag ions [293].

2.7.3.1 Influence of individual rare earth elements on the biocompatibility

Scandium (Sc)

In-vitro studies have highlighted the benign impact of Sc on cell viability, particularly in human osteosarcoma and vascular smooth muscle cells. Sintered scandium oxide (Sc_2O_3) has demonstrated non-toxicity and, notably, the ability to stimulate cell growth, suggesting its potential as a biocompatible biomaterial [294]. In-vivo investigations have shown similarly encouraging results. Acute toxicity assessments in mice have reported relatively high median lethal doses for scandium chloride, indicating low acute toxicity. Additionally, long-term studies in rats, involving dietary incorporation of Sc, revealed no signs of chronic toxicity over a 90-day period [270,273].

Yttrium (Y)

Y compounds, such as yttrium chloride (YCl_3), exhibit notable biological interactions and potential health implications. Intraperitoneal (I.P.) administration in murine models has shown similarities with iron and chromium chlorides ($FeCl_2$ and $CrCl_3$), while intravenous (I.V.) injections of YCl_3 demonstrate a strong affinity for the liver and spleen, causing significant calcium ion displacement [271]. Chronic oral exposure to yttrium raises concerns about potential hepatic injury, despite some reports of enhanced rodent longevity and improved in-vitro cell viability under specific conditions [295]. Additionally, yttrium oxide nanoparticles (Y_2O_3) have been identified as neuroprotective agents, offering protection to nerve cells against oxidative stress [296]. However, animal studies have linked YCl_3 to acute hepatic injury, highlighting the need for comprehensive research to fully understand its toxicity profile and therapeutic potential

Lanthanum (La)

La demonstrates severe toxicity, mostly when administered as a chloride salt via intraperitoneal (I.P.) or intravenous (I.V.) routes. Acute and chronic exposure to La has been associated with neurological impairments, including memory deficits, as well as adverse hepatic effects such as lipid accumulation, necrosis, and hemorrhage. In-vitro studies corroborate its cytotoxicity, with notable inhibition of cell viability. However, contrasting evidence suggests that La ions can stimulate the growth of human dermal fibroblastic cells, highlighting its complex biological interactions. Despite these concerns,

lanthanum carbonate [$La_2(CO_3)_3$] is clinically used to treat hyperphosphatemia in patients with renal failure undergoing dialysis. Nonetheless, reports of genotoxicity and its potential to induce cellular mutations and carcinogenesis emphasize the need for further investigation into its safety and therapeutic applications [272,297,298].

Cerium (Ce)

Ce exhibits a strong affinity for the liver, leading to significant uptake by liver cells and hepatotoxic effects such as lipid accumulation, hepatic necrosis, hemorrhage, and increased vascular permeabilization. Conflicting findings regarding the genotoxicity and mutagenicity of cerium compounds have been reported. While some studies found no mutagenic effects with cerium oxide or chloride, cerium nitrate [$Ce(NO_3)$] has been linked to chromosomal breaks in rat bone marrow cells. Further research on nanoparticulate ceria (CeO_2) revealed genotoxic and mutagenic effects following oral exposure in rats, emphasizing the need for more comprehensive investigations. Despite these concerns, cerium compounds also exhibit beneficial properties. Nanoparticles of CeO_2 have shown neuroprotective effects by shielding nerve cells from oxidative stress, and $Ce(NO_3)_3$ has demonstrated potential as an antiseptic treatment for burns. However, excessive doses of $Ce(NO_3)_3$ can lead to toxicity and methemoglobinemia, highlighting the importance of cautious administration. These findings underscore the dual nature of cerium's biological interactions, necessitating further research to balance its therapeutic potential against its toxicity [296,297,299].

Praseodymium (Pr)

Similar to other light rare earth elements (REEs), it has been associated with hepatotoxicity and demonstrates a notably slow clearance from the liver. Evidence of hepatic damage and potential long-term effects on liver function highlights the need for further investigation into its biological impact and safety profile. The biological role of praseodymium remains controversial. While some studies suggest that Pr may protect liver cells against phalloidin-induced toxicity in-vivo, others report hepatotoxic effects, raising questions about its potential suitability for biomedical applications. These contrasting findings emphasize the necessity for more detailed research to clarify the biological interactions and therapeutic potential of praseodymium salts [289,300].

Neodymium (Nd)

Nd demonstrates a relatively higher LD50 compared to other rare earth elements, suggesting a less severe biological impact. However, exposure to Nd salts has been linked to adverse effects such as fever, headaches, muscle pain, nausea, and vomiting, indicating potential hepatotoxicity. Typical application of neodymium chloride ($NdCl_3$) can irritate abraded skin and eyes, while its nitrate salt exhibits mild embryotoxicity. Studies have also highlighted genotoxic effects, including chromosomal aberrations in bone marrow cells, raising concerns about its safety. Nd demonstrates a relatively higher LD50 compared to other rare earth elements, suggesting a less severe biological impact. However, exposure to Nd salts has been linked to adverse effects such as fever, headaches, muscle pain, nausea, and vomiting, indicating potential hepatotoxicity. Topical application of neodymium chloride ($NdCl_3$) can irritate abraded skin and eyes, while its nitrate salt exhibits mild embryotoxicity. Studies have also highlighted genotoxic effects, including chromosomal aberrations in bone marrow cells, raising concerns about its safety [274,289,301].

Samarium (Sm)

The application of solid samarium chloride ($SmCl_3$) to abraded skin in rabbits caused severe adverse effects, including deep ulcers penetrating muscle tissue, with minimal healing observed over a two-week period. Intraperitoneal exposure to $SmCl_3$ also resulted in acute symptoms such as lethargy, cramping, diarrhoea, and muscle spasms. Additionally, the nitrate form of samarium [$Sm(NO_3)_3$]) has been associated with moderate liver effects, including alterations in RNA synthesis. Despite these toxicological concerns, radioactive samarium-153 (Sm-153) is effectively used in the treatment of cancers such as osteosarcoma. However, ingestion of $Sm(NO_3)_3$ has been linked to pathological changes in various organs, particularly the liver, highlighting the need for cautious use and further investigation into its safety profile [274,282,302]

Europium (Eu)

Eu has limited clinical applications, with its primary use as an MRI sensor in the form of an Eu DOTA-tetraamide complex. Toxicity studies suggest that europium exhibits mild biological effects, supporting its potential for biomedical applications. In animal studies, intraperitoneal administration of europium hydroxide nanorods at doses ranging from 1.25 to 125 mg/kg/day over seven days showed no significant changes in blood

hematology or serum clinical chemistry, aside from slight elevations in liver enzymes. At higher doses (1000 mg/kg), mice exhibited localized irritation, including hyperkeratosis in the forestomach and eosinocyte infiltration in the stomach submucosa. Europium accumulation was dose-dependent, with small amounts detected in the liver, kidneys, spleen, and femurs. Additionally, administration of $EuCl_3 \cdot 6H_2O$ to increased serum iron levels in males and altered total iron binding capacity in both sexes, while cholinesterase activity decreased in females at high doses. These findings highlight the need for further investigation into the safety and long-term effects of europium exposure in biomedical contexts [277,303–305]

Gadolinium (Gd)

Gd has no known natural biological role, and its biocompatibility remains a topic of debate [270,273]. Toxicity studies have reported an intraperitoneal median lethal dose (LD50) of 550 mg/kg for $GdCl_3$ in mice, while $Gd(NO_3)_3$ caused acute toxicity at doses of 300 mg/kg in mice and 230 mg/kg in rats [270,306]. High levels of Gd have been shown to compromise biocompatibility, as excessive release of Gd ions can induce toxic effects. For example, elevated Gd content in Mg-10Gd alloys disrupted bone remodeling and led to significant accumulation of gadolinium in major organs of SD rats [147,307]. However, despite the potential toxicity of free Gd ions, gadolinium-chelated compounds have been widely used as contrast agents in magnetic resonance imaging (MRI) [308,309]. Additionally, Gd compounds have shown promise in oncology, where they can generate reactive oxygen species to induce DNA damage and apoptosis in tumor cells [310]. Phase II clinical trials of motexafin gadolinium have suggested its potential as an adjuvant therapy for metastatic renal cell carcinoma [311]. Gd-loaded nanoparticles are also being investigated for targeted radiation therapy [312], while selective gadolinium-based agents are under exploration for photodynamic therapy in cancer treatment [313].

Terbium (Tb)

Tb is recognized for its moderate acute toxicity relative to other rare earth elements, yet it presents remarkable irritation potential to both eyes and abraded skin. Notably, it induces intense irritation even on intact skin, hinting at possible adverse effects upon contact. Furthermore, intravenous administration of terbium has been linked to pulmonary edema and heightened lipid peroxidation. Acute hepatic effects encompass perinuclear vacuolization, minor enlargement of cells, focal necrosis, and mild fibro genic potential.

Chronic oral exposure to terbium has resulted in growth suppression, implying potential long-term consequences. The document underscores the necessity of considering terbium's adverse effects in the development and application of biomedical magnesium alloys. Additionally, radioactive Tb could find utility in phantom studies and radiolabelling. Notably, Tb exhibits delayed acute toxicity, and specific doses of terbium chloride have been shown to suppress the growth of mice [273,279,314].

Dysprosium (Dy)

Dy has been studied for its acute in-vivo toxicity, which manifests as symptoms like writhing, ataxia, and excessive lacrimation at high doses. Typical application of dysprosium chloride has been associated with scar formation on abraded skin and ulcerative conjunctivitis upon eye exposure. Despite these findings, its chronic toxic effects appear minimal, with reports indicating moderate to low hepatotoxicity. Dysprosium chelate complexes have shown potential as contrast agents for magnetic resonance imaging. However, dysprosium-based shift reagents have demonstrated nephrotoxic effects at concentrations exceeding 5 mM, highlighting the need for careful dose management in biomedical applications [315,316].

Holmium (Ho)

Ho exhibits toxicity profiles similar to dysprosium, with both acute and chronic effects reported. Acute exposure has been linked to focal liver necrosis, though without the formation of fatty deposits. Additionally, studies suggest potential associations with nephrogenic systemic fibrosis (NSF) and genetic damage in mouse bone marrow cells, raising concerns about its hepatic and genotoxic effects. Despite these risks, holmium has been employed in biomedical applications, such as YAG surgical lasers for procedures like laparoscopic partial nephrectomy. Notably, delayed acute toxicity has been observed in cats, emphasizing the need for careful evaluation of holmium's safety in medical use [280,317–319].

Erbium (Er)

Er is considered moderately more toxic in-vivo compared to most other lanthanides. While it shows no notable impact on the proliferation of human vascular cells in-vitro, it shares acute toxic effects with dysprosium and holmium, including symptoms such as writhing, ataxia, and laboured breathing. However, studies have not indicated significant

chronic effects. Pharmacological and toxicological assessments reveal that erbium exhibits delayed acute toxicity, similar to dysprosium and holmium, aligning with its relatively higher toxicity profile observed in-vivo. However, erbium is effectively utilized in medical applications, such as YAG lasers for procedures like YAG lithotripsy, where it demonstrates efficacy in stone fragmentation [280,317–319].

Thulium (Tm)

Tm is recognized as one of the more toxic lanthanide ions in mice, although its toxicity is notably reduced in rat studies. In rats, chronic exposure to thulium chloride has been associated with growth inhibition and the development of perinuclear vacuolization in parenchymal liver cells. However, studies have not identified significant genotoxic effects or related concerns. In medical applications, Tm serves as an efficient laser medium for procedures such as nephrectomy and superficial tissue ablation. Additionally, it is employed as an X-ray source in brachytherapy for cancer treatment. Despite its therapeutic potential, Tm demonstrates delayed acute toxicity and growth suppression in animal models, emphasizing the importance of assessing its safety for biomedical use [281,320,321].

Ytterbium (Yb)

Yb exhibits both acute and chronic toxic effects that share similarities with those of Tm, though some distinctions are observed, particularly in its chronic effects when administered as the chloride salt. Compared to most other rare earth elements, Yb has lower LD50 values, indicating higher in-vivo toxicity. However, it is notable for having one of the lowest levels of hepatotoxicity among rare earth elements, with a stronger affinity for osseous tissue than its lighter counterparts. Although Yb remains relatively understudied, it is recognized for its fibro genic potential and possible teratogenic effects. The radioisotope 175Yb has been utilized in the palliative treatment of bone metastases as a tracer for polyaminophosphonates. Additionally, YbF_3 is employed as a non-toxic and inert material for dental fillings. Despite these applications, ytterbium exhibits delayed acute toxicity and has been associated with stomach haemorrhages, particularly in females, highlighting the need for further investigation into its safety and long-term effects [273,282,320,322].

Lutetium (Lu)

Lu, while not extensively researched, shows moderate toxicity similar to some other rare earth elements. Animal toxicity studies, particularly in rats, indicate that chronic exposure to lutetium leads to growth suppression and changes in liver cell structure, such as perinuclear vacuolization. Despite these adverse effects, Lu has promising applications in the medical field. The radionuclide 177Lu is used in radio immunotherapy and SPECT imaging, offering potential for cancer treatment. Furthermore, Lu has been explored as a photosensitizer in photodynamic therapy. However, it is important to note that lutetium chloride ($LuCl_3$) can have a depressant effect on organisms, highlighting the need for further safety evaluations in its biomedical uses [276,323,324].

However, rare earth elements (REEs), when incorporated as alloying elements into magnesium, tend to exhibit significantly reduced toxicity compared to their ionic forms, such as chlorides, oxides, or nitrates. This is because, in the alloyed state, REEs are bound within the metal matrix, limiting their direct interaction with biological systems and reducing their bioavailability. In contrast, ionic forms of REEs are more reactive and can readily interact with cells and tissues, potentially causing toxic effects. Therefore, it is crucial to evaluate the biocompatibility of Mg-RE alloy systems to better understand their actual biological behaviour and safety for biomedical applications.

2.7.3.2 In-vitro biocompatibility of Mg-RE alloy systems

In-vitro biocompatibility studies typically involve assessing key parameters such as cytotoxicity**,** hemocompatibility**,** cell adhesion**,** alkaline phosphatase (ALP) activity, and biomineralization to determine the toxicity and viability of a biodegradable material. These parameters provide comprehensive insights into how the material interacts with cells, tissues, and blood, serving as a foundation for evaluating its potential for biomedical applications.

- **Cytotoxicity** is a primary indicator of biocompatibility that evaluates whether a material releases substances harmful to cells. Cytotoxicity tests involve exposing cells to material extracts or culturing them directly on the material's surface to measure their viability and metabolic activity using assays like MTT or LDH. A

low cytotoxic response is crucial for ensuring that the material does not harm surrounding tissues when implanted.

- **Haemocompatibility**, or the compatibility of a material with blood, is vital for implants interacting with the circulatory system, such as vascular stents. This parameter evaluates platelet adhesion, aggregation, and activation, along with haemolysis (red blood cell destruction). Excessive platelet aggregation can lead to thrombosis (blood clot formation), posing significant risks, while high haemolysis rates indicate red blood cell damage. Materials with minimal platelet aggregation and haemolysis rates within acceptable limits (less than 5%) are considered haemocompatible.
- **Cell adhesion** is essential for tissue integration. A material that supports strong adhesion allows cells to attach, spread, and proliferate on its surface, facilitating tissue regeneration and implant stability. Poor adhesion can compromise integration and lead to implant failure. Microscopy techniques are often used to assess cell morphology and distribution on material surfaces.
- **Alkaline phosphatase (ALP) activity** is a marker of osteoblast differentiation and is particularly important for materials intended for bone applications. Osteoblasts are cells responsible for bone formation, and higher ALP activity indicates that the material can promote their differentiation and enhance bone regeneration. In-vitro ALP assays help determine whether a material actively supports bone tissue development [272].
- **Bio-mineralization** is another critical parameter for biodegradable materials, especially those used in orthopaedic applications. It refers to the material's ability to support the deposition of calcium-phosphate minerals, mimicking natural bone formation. Bio-mineralization tests typically involve immersing the material in simulated body fluid (SBF) and observing the formation of apatite layers on its surface. The presence of these layers indicates the material's potential to integrate with bone tissue and promote healing.

With these parameters, various in-vitro studies have been conducted on magnesium-rare earth (Mg-RE) alloy systems to evaluate their biocompatibility. For instance, Liu et al. [148] studied platelet adhesion on Mg-RE alloys using scanning electron microscopy (SEM) and observed significant platelet aggregation on alloys such as Mg-3Ce, Mg-0.5Pr, and Mg-1Pr, suggesting reduced haemocompatibility for these compositions due

to a higher risk of thrombosis (**Figure 2.12**). Wang et al. [325] investigated the biocompatibility of REEs in WE alloys (Y: 2.5, 5.0, 6.5, 7.5 wt.%, Nd: 1.0, 2.5, 2.6, 4.2 wt.%, Zr: 0.8 wt.%) and discovered that Nd addition resulted in the enhanced cell viability as well as hemocompatibility in comparison with pure Mg. Song et al. [286] investigated the cytotoxicity of Mg-Zn-Y-Nd alloys and found that they not only exhibited low cytotoxicity but also enhanced ALP activity, indicating their potential to promote osteoblast differentiation and bone regeneration. Zhou et al. [326] conducted haemolysis and cytotoxicity tests on Mg-Al-Li-RE alloys, showing acceptable haemolysis rates and encouraging results for endothelial cell activity, except for Mg-8.5Li-2Al-2RE, which slightly reduced cell viability. Yang et al. [239] examined Mg-10Dy alloy and observed that its Dy-rich oxide layer exhibited no cytotoxicity, supporting the biocompatibility of dysprosium-containing alloys. Sc added Mg-1.5Zn-xSc-0.6Zr alloys enhanced ALP activity and biomineralization but negatively impacted hemocompatibility at higher concentrations [327]. The biocompatibility study using endothelial assay on MgZnCaY-1RE (RE = Dy and Gd), MgZnCaY-2RE (RE = Nd and Gd), and MgYZr-1RE (RE = Gd and Dy) alloys showed that Nd and Gd significantly enhanced cell adhesion and proliferation [328]. These findings highlight that alloy composition and the specific rare earth elements used play a significant role in determining in-vitro biocompatibility. While in-vitro studies provide valuable insights, discrepancies between in-vitro and in-vivo results emphasize the need for comprehensive research. For example, Mg-1.27Ce alloy extracts exhibited cytotoxic effects on MC3T3-E1 cells in-vitro, but implantation in rabbits showed no adverse effects. Such inconsistencies highlight the complexity of biological systems and the importance of combining in-vitro and in-vivo studies to fully evaluate the biocompatibility of Mg-RE alloys [258]. The in-vitro cell viabilities of different Mg-RE based alloys are compiled in **Table 2.7.**

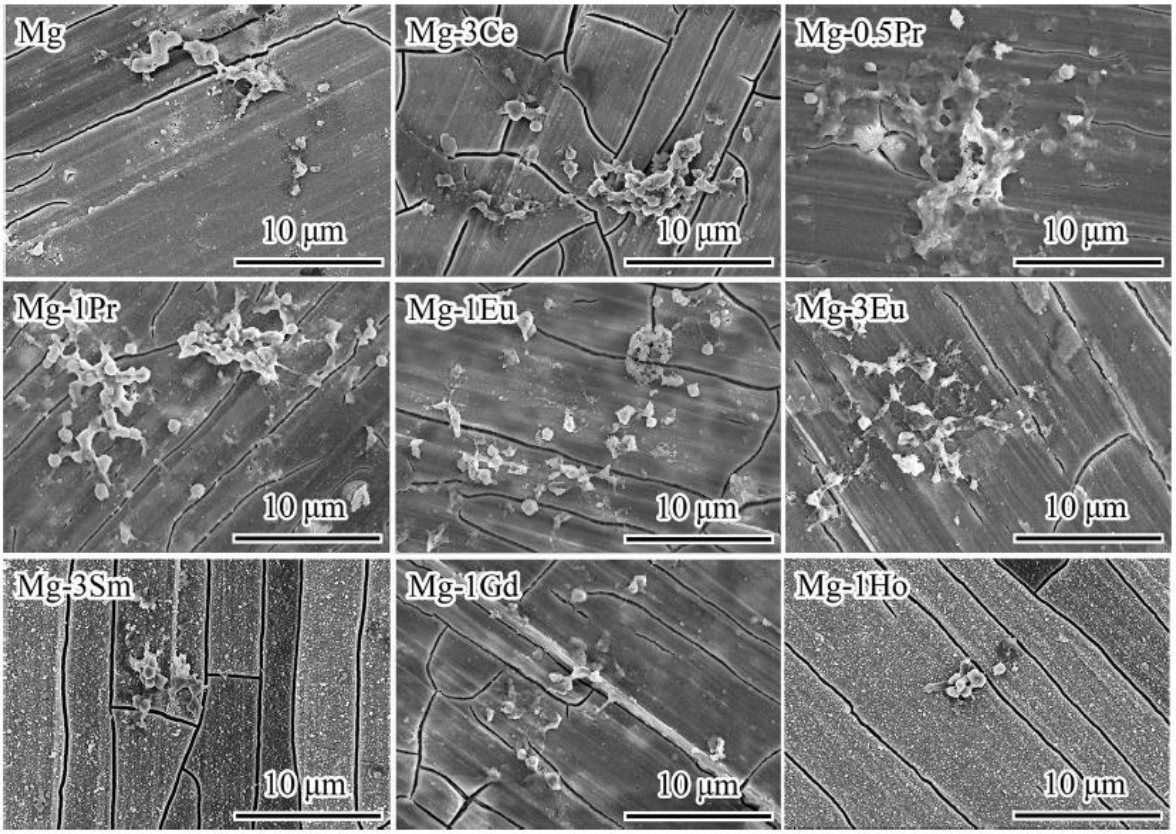

Figure 2.12. SEM micrograph showing typical platelet adhesion of Mg-RE model alloys and pure Mg [148].

Table 2.7. In-vitro cell viability of different Mg-RE alloys

Alloy code	**Processing conditions**	**Cell line**	**Remarks**	**reference**
Mg-1.27Ce	As cast	MC3T3E1	100% REE was toxic to cell line due to high pH and osmolality	[258]
Mg-1.8Zn-0.2Gd	Rolled	L929, MG63 and VSMC cells	No cytotoxicity	[195]
Mg-0.6Zr-0.5Sr-3Sc	As cast	SaOS2	No cytotoxicity	[175]
Mg-2Zn-1Gd	Extruded	MC3T3E1	100% extract was cytotoxic but 50 and 10% extracts were grade 0~1,	[192]

			good biocompatibility	
Mg-1Mn-2Zn-1Nd	Extruded	SaOS2	Good viability	[187]
WE43	Extruded	VSMC, HUVEC	No cytotoxicity, excellent platelet adhesion	[325]
Mg-10Gd	ECAP	PC-3	Suppressed the proliferation of PC-3 tumor cells	[329]
LAE442	Extrusion + ECAP	L929	No cytotoxicity	[264]
EZ33	FSP	NH3T3	Grade 0 cytotoxicity	[237]
Mg-1Zn-2Dy	FSP	MC3T3E1	80% viability	[167]
Mg-2Zn-0.5Gd-0.5Zr	ECAP	MC3T3E1	grade 1 cytotoxicity within the range of 75–99%. M	[194]
Mg-1.5Zn-1Sc-0.6Zr	As cast	L929, SP2/0	Greater than 90% viability	[327]
Mg-Y-Zr-1RE (RE= Dy and Gd)	As cast	HAEC	No significant cytotoxicity observed up to 7 days and non-haemolytic	[328]
Mg-Zn-Y-Zr-1RE (RE= Dy and Gd)				
MgZnCaY-1RE (RE= Dy and Gd)				
MgZnCaY-2RE (RE= Nd and Gd)				

2.7.3.3 In-vivo performance of Mg-RE based alloys

Although in-vitro studies provide valuable insights into the behaviour of magnesium-rare earth (Mg-RE) alloys, they cannot fully replicate the complex and dynamic biological interactions occurring in living organisms. In-vitro experiments typically involve controlled laboratory environments with simplified conditions, such as stable pH, temperature, and fluid composition. In contrast, in-vivo conditions are far more complex, involving a range of factors like immune responses, tissue interactions, varying

oxygen concentrations, fluid dynamics, and mechanical stresses. These elements can accelerate or inhibit the biodegradation of Mg-RE alloys in ways that cannot be predicted in-vitro. For instance, the buffering capacity of body fluids, the presence of proteins and cells, and the localized anatomy of implantation sites significantly influence how these materials behave once inside the body [64,330–332]. For example, Simulated Body Fluid (SBF), widely used as a biodegradation medium during in-vitro biodegradation analysis of Mg alloys, mimics physiological conditions with buffers such as HEPES, Tris-HCl, and HCO_3^-/CO_2. These systems profoundly impact the biodegradation of Mg and its alloys. HEPES and Tris-HCl actively buffer pH fluctuations by neutralizing hydroxide ions (OH^-), influencing the nature of biodegradation products formed and potentially accelerating Mg dissolution. The bicarbonate-carbon dioxide buffer (HCO_3^-/CO_2), which mirrors a natural physiological system, not only mitigates pH shifts by consuming OH^- ions but also promotes the formation of magnesium carbonate ($MgCO_3$). This carbonate layer acts as a protective barrier, reducing the rate of biodegradation. The impact of inorganic ions in physiological fluids adds another layer of complexity. For instance, chloride ions (Cl^-), present in high concentrations under physiological conditions, can aggressively attack the protective passivation layer on Mg, leading to pitting corrosion. Conversely, anions such as HPO_4^{2-}/PO_4^{2-} and HCO_3^-/CO_3^{2-}, together with calcium ions (Ca^{2+}), facilitate the deposition of calcium phosphate and carbonate salts. These deposits reinforce the protective passivation layer, reducing susceptibility to localized corrosion [341–343].

- **In-vivo Biodegradation Dynamics**

Studies comparing in-vitro and in-vivo biodegradation conditions have revealed notable differences. For example, research by Willbold et al. [258] highlighted the contrasting biodegradation susceptibilities of Mg-Ce and Mg-La alloys under laboratory and biological conditions, observing that while Mg-Ce alloys exhibited lower biodegradation rates in biological environments compared to Mg-La alloys, the trend was reversed under laboratory conditions, where Mg-La alloys showed better biodegradation resistance. A similar divergence was observed with LAE442, the alloy exhibited slower degradation in biological environments compared to its behaviour in controlled laboratory settings, emphasizing the complexity of predicting real-world performance solely based on laboratory data [109]. The Mg-2.0Zn-1.0Gd alloy exhibited a higher in-vivo biodegradation rate of 0.31 mm/year compared to its in-vitro rate of 0.24 mm/year. This

was attributed to extensive exposure to physiological fluids and proteins in cranial defect models [192]. Conversely, MAD-processed WE43 alloys demonstrated superior in-vivo biodegradation resistance compared to in-vitro findings [333]. Similarly, the in-vivo biodegradation rate of Mg-2Y-1Zn, as assessed through volume loss, was observed to be significantly slower (up to 49 times) when compared to its in-vitro biodegradation rate [334]. The anatomical placement of an implant also plays a crucial role in its biodegradation. Implants located within bone environments typically experience slower biodegradation rates due to limited fluid exposure and reduced oxygen levels. Conversely, implants placed in subcutaneous or intramuscular sites degrade more rapidly because of increased fluid dynamics and oxygen availability. For example, Willbold et al. [335] observed varying biodegradation rates for Mg-6Zn-1Y-0.6Ce-0.6Zr implants, with the highest rate occurring subcutaneously (5.29 mm/year), followed by intramuscular (4.18 mm/year) and bone environments (3.82 mm/year).A study on rabbits investigated the magnesium alloy WE43 for its suitability as an implant in anterior cruciate ligament reconstruction. The results showed no clinical cases of tendon rupture or loosening and the implant was intact till 24 weeks. Furthermore, a significant reduction in gas accumulation near the implant was observed within the first 24 weeks post-implantation (**Figure 2.13**) [336].

The type of implant and the implant design also plays a role in the biodegradation behaviour of an alloy. For instance, the interaction between WE43 in the plate-and-screw system significantly impacts the overall biodegradation process. The configuration promotes crevice corrosion, which intensifies material biodegradation in contact areas. Notably, biodegradation was most evident at the screw shafts beneath the head and around the borehole regions of the plates. This localized biodegradation in contact zones supports the hypothesis that crevice corrosion plays a crucial role in the observed material breakdown [337]. In contrast to plate-and-screw systems, intraosseous devices such as nails, pins, and compression screws have demonstrated more reliable performance. These implants are entirely embedded within the bone, which may contribute to their effectiveness by reducing the surface-to-volume ratio exposed to the surrounding environment, thereby mitigating biodegradation. Rössig et al. [297] explored the use of magnesium-based implants for load-bearing intramedullary interlocking nailing in sheep and compared their performance with traditional steel devices. Their findings highlighted that degradable magnesium implants could successfully handle the mechanical demands of load-bearing

applications. Also, the WZ42 alloy (Mg-4Y-2Zn-1-Zr-0.6Ca) was employed as cerclage wires and pins in rat femurs. These implants facilitated normal bone healing without adverse effects, demonstrating their potential for orthopaedic use [338].

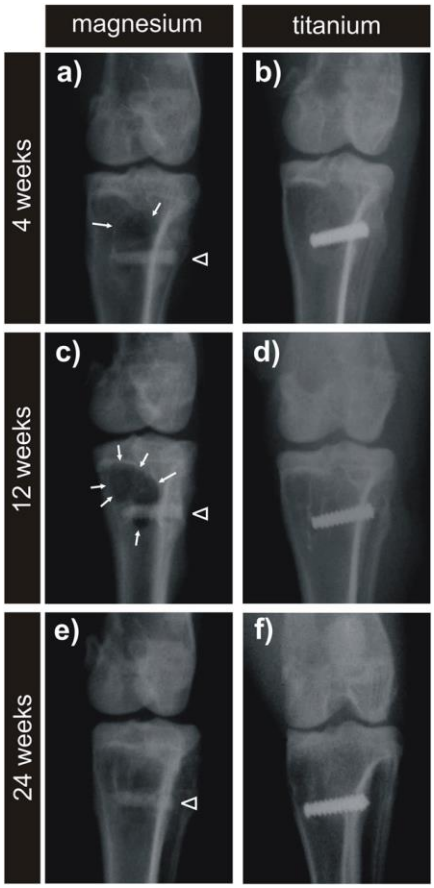

Figure 2.13. X-ray images at different time periods of Mg and Ti implanted into femoral bone of rabbits [336].

- **Biocompatibility and Osseo-integration**

The interaction between Mg implants and surrounding tissues is pivotal for ensuring their success in biomedical applications. Osseo-integration, the bonding of implants with bone, is a key factor in achieving implant stability and long-term functionality. Studies have consistently shown that Mg alloys not only integrate effectively with bone but also stimulate new bone formation. For instance, FSPed EZ33 alloys demonstrated enhanced bone formation in both cortical and medullary regions without hindering bone regeneration. This can be observed in **Figure 2.14** [237]. Similarly, Mg-1.8Zn-0.2Gd implants showed excellent osseo-integration in rat models, where strong bonding with cortical bone and new trabecular bone formation were observed within two months. The bone-implant interface

significantly influenced osseo-integration and bonding strength, varying across different implant segments. While the ends embedded in cortical bone showed strong integration after six months, the middle section, exposed to bone marrow, exhibited newly formed trabecular bones, some in direct contact and others at a distance. Localized biodegradation in both cortical and marrow regions occasionally caused non-bonding or delayed osseo-integration [**Figure 2.15**] [195]. A 36-week study on Mg10Gd pins in femoral bones showed gadolinium accumulation in various organs, with the spleen having the highest concentration (3240 μg Gd/kg), followed by the lung, liver, and kidney (up to 1040, 685, and 207 μg Gd/kg, respectively). In contrast, minimal accumulation was detected in the brain, muscle, and heart (<20 μg/kg), and no traces of magnesium or gadolinium were found in blood serum. This indicates that while gadolinium from the implant accumulates in specific organs, the systemic circulation remains unaffected [307,339]. Similarly, Huehnerschulte et al. [340] noted that ZEK100 (Mg-1Zn-0.1RE-0.1Zr) displayed biodegradation properties that are beneficial from an engineering perspective. However, its biodegradation in-vivo triggered adverse host responses, including increased osteoclast-driven bone resorption and rapid reactive periosteal bone formation in rabbits. Grunewald et al. [341] examined how bone structure responds to WZ21 (Mg-2Y-1Zn-0.25Ca-0.15Mn) implant placement and its subsequent resorption over time. Their findings revealed structural changes on both macroscopic and nanometer scales, including a reduction in mineral platelet size, decreased stacking order, and a significant alteration in the typical alignment of the collagen/mineral nanocomposite along the bone shaft. These changes may reflect delayed bone maturation or could result from increased local magnesium levels, potentially substituting calcium in hydroxyapatite (HAP) and hindering normal mineral crystal development. This suggests that magnesium release during implant biodegradation may influence bone remodeling processes. Zhang et al. [342] conducted a 20-month study to assess the performance of a bare JDBM stent (Mg-2.2Nd-0.1Zn-0.4Zr) implanted in the common carotid artery of New Zealand white rabbits. The results showed that the stent was both safe and effective, achieving full re-endothelialization within 28 days. Over four months, the stent struts were largely replaced by biodegradation byproducts, with a gradual reduction in their volume and calcium content over time, addressing concerns about vessel calcification. The magnesium and zinc components of the stent were metabolized without

accumulation in major organs, though neodymium and zirconium levels temporarily spiked in the spleen and liver one-month post-implantation.

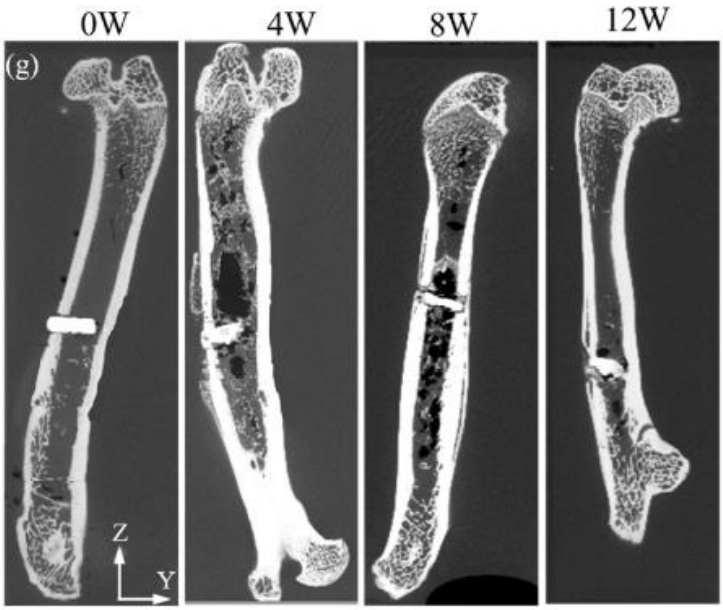

Figure 2.14. μCT figure showing biodegradation of FSPed EZ33 implants over the time [237].

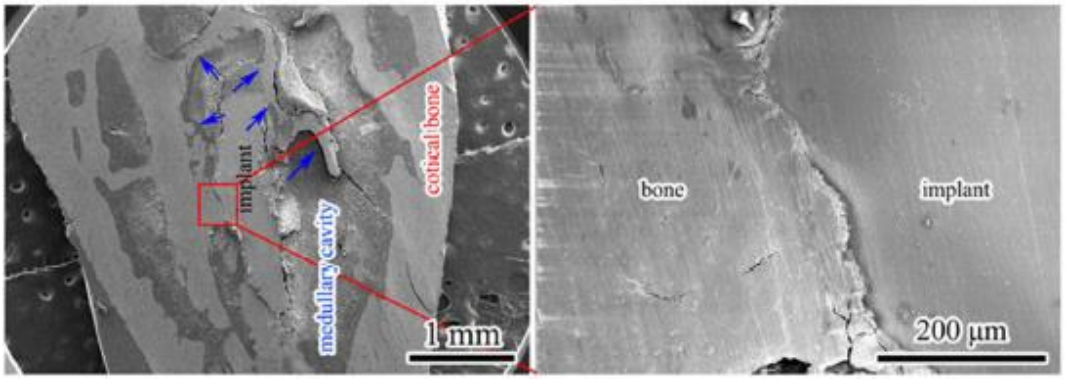

Figure 2.15. SEM images of cortical bone implanted with Mg-1.8Zn-0.2Gd reveal newly formed bone tissue around the implant [195].

Table 2.8. In-vivo behaviour of Mg-RE alloys

Alloy code	Processing Route	Animal model	Implantation period	Biodegradation rate (mm/y)	Remarks	Reference
Mg-1.27Ce	As cast	Rabbit, Knee joint	4 weeks	1.46	No sign of toxicity, inflammation and gas cavities	[258]
Mg-0.69La				1.35		
Mg-2.13Nd				0.91		
LAE442	As cast	Guinea pig, femoral	18 weeks	1.2×10^{-4}	Very low biodegradation compared to in-vitro results	[109]
Mg-1.8Zn-0.2Gd	Rolled	SD rat, tibia	6 months	-	rapid osseointegration with surrounding bones	[195]
LAE442	Extruded	Rabbit, medullar cavity of tibia	6 months	Volume loss 0.097 cm^3	Uniform biodegradation in LAE442 initiation of pitting in WE43 alloys.	[343]
WE43				Volume loss 0.081 cm^3		
LAE442	Double extruded	Rabbit tibia	27 weeks	0.0134	Uniform biodegradation	[344]
WE43	Ex + MAD	Mice, subcutaneous	6 weeks	N.A	Gas accumulation, swollen tissues	[333]
EZ33	FSP	SD rats, femur	8 weeks	0.7	No sign of inflammation	[237]
WE43	ECAP	Dog, Femur	12 weeks	-	Grade 2 inflammation	[181]
LAE442	Extruded	Rabbit, medullar cavity	3.5 years	-	Accumulation of alloying elements in the organs	[345]
WE43	As cast	Rabbit, anterior	24 weeks	0.17	No rupture of tendon, no inflammation or necrosis	[336]

		cruciate ligament				
Mg–6 Zn–1Y–0.6Ce–0.6Zr	Rapidly solidified + extruded	Rabbit, subcutaneous	8 weeks	5.29 mm/y	Normal foreign body reaction	[335]
		Rabbit, muscle		4.18 mm/y		
		Rabbit, femur condyle		3.82 mm/y		
Mg-2Y-1Zn	Porous samples	Rabbit, femoral condyle	24 weeks	0.06	Small gas bubble formation, No severe Toxicity	[334]
Mg4Y				0.08		
Mg-10Gd	Extruded	SD rat, femur	36 weeks	-	Gd accumulation in organs	[307]
ZEK100 (Mg-1Zn-1RE-1Zr)	Extruded	Rabbit, tibia	6 months	-	Adverse host reactions, huge number of osteoclasts were detected in the bone	[340]
WZ21	Extruded	SD rat, femur	52 weeks	-	Homogeneous biodegradation, low gas evolution	[346]
JDBM	Extruded microtubes	Rabbit, stents	20 months	-	Rapid re-endothelialization	[342]
WE43	Extruded	Pig, cranio-osteoplasty	30 weeks	-	Formation of lacunas in the bone implant interface	[337]
WZ21	Extruded	SD rats, femur	24 weeks	0.5% volume loss per day	Enhanced bone formation, uniform biodegradation and excellent osteoconductivity	[347]

ZEK100	Extruded	Rabbit, tibia	12 months	1.285	Mild toxicity	[348]
WE43	Extruded	Rabbit, tibia	16 weeks	55% reduction in volume	Excellent bone regeneration	[349]
LANd442	Extruded	Rabbit, tibia	26 weeks	13.7% weight loss	Severe pitting	[350]
ZEK100	Extruded	Rabbit, tibia	24 weeks	0.065	Uniform biodegradation	[351]
Mg-4Y-1Zr-06Ca	Extruded	Mouse, subcutaneous	1 month	3.4% weight loss	No accumulation observed in vital organs	[352]
ZEK100	Extruded	Rabbit, tibia	6 months	-	Adverse host reactions, high number of osteoclasts observed	[340]
WE43	Extruded	Dog, midfacial area	24 weeks	80.63% volume loss	Swelling, infraorbital fistula and inflammatory symptoms	[353]
WE43	Extruded	Sheep, Frontonasal region	6 weeks	-	Y content of 2125 ppb and other RE content of 0.183 – 0.713 ppb observed in the lymph node	[354]
ZEK100	As cast	Rabbit, tibia	6 weeks	Weight loss = 7.5%	Increase in inflammatory tissue response	[355]
JDBM	As cast	SD rat, femur	4 weeks	0.092	No adverse effects	[356]
WZ21	Extruded	Minipig, subcutaneous	12 weeks	-	Thin-walled granuloma with limited vascularization, and	[357]

					numerous eosinophils	
WX11 (Mg-1Y-0.6Ca)	Solutionized	Mice, subcutaneous	10 weeks	0.73	No adverse effects	[358]
WX41 (Mg-4Y-0.6Ca)				0.068	No adverse effects	

2.8 Summary

The literature review highlights the significance of magnesium rare-earth (Mg-RE) based alloys in the development of biodegradable implants, emphasizing their superior biodegradation rate, biocompatibility, and mechanical properties compared to other Mg alloy systems. These alloys, under both as-cast and secondary processed conditions, demonstrate promising attributes for medical applications. Secondary processing, in particular, plays a pivotal role in enhancing these properties by refining the microstructure, promoting the uniform distribution of secondary phases, improving grain refinement, and increasing dislocation density. These microstructural improvements contribute to better control over the biodegradation rate and mechanical performance, ensuring the alloy's reliability in biomedical environments.

However, the choice of rare-earth elements (RE) is crucial for achieving optimal biocompatibility and safety. The potential toxicity of certain elements, such as yttrium (Y), which has a low LD50 value, raises concerns despite the clinical approval of Y-containing Mg alloys like WE43. While such alloys have demonstrated short-term success, their long-term implications on human health warrant caution. Thus, to advance Mg-RE alloys for biodegradable implant applications, careful alloy design is essential. Selecting the appropriate rare-earth elements, balancing their concentrations, and optimizing secondary processing techniques are critical to producing materials with superior performance. This tailored approach ensures not only the functional success of the implants but also their safety and compatibility with human biology. By addressing these considerations, Mg-RE alloys can be further established as a reliable and innovative solution for next-generation biodegradable implants

2.9. Research Gap

Biodegradable materials are designed to provide temporary support during the healing of diseased or damaged tissues, gradually degrading over time and eliminating the need for surgical removal. For orthopaedic applications such as screws, pins, and needles, these materials must exhibit a carefully balanced combination of mechanical properties, controlled biodegradation rates, biocompatibility, and bioactivity. The design and selection of these materials must be tailored to meet specific clinical requirements. For instance, orthopaedic implants requiring mechanical integrity for 12–18 weeks demand a biodegradation rate below 0.5 mm/year in simulated body fluid at 37 °C, a tensile yield strength exceeding 200 MPa, and elongation above 10% [147]. These criteria, as established in the literature review, serve as a benchmark for identifying suitable alloy systems. Based on a detailed review of mechanical and in-vitro biodegradation properties of the Mg-RE alloys (**Table 2.3 and 2.5**), only a limited number of systems meet the required combination of mechanical and biodegradation properties. The shortlisted alloys include (Except the WE43 alloys which are currently clinically used): Mg-2.9Gd-1.5Nd-0.3Zn-0.3Zr (ECAP) [169], Mg-2Zn-1Gd (Extruded) [192], Mg-2Zn-0.5Gd-0.5Zr (ECAP) and Mg-2Zn-0.5Nd-0.5Zr (ECAP) [194]. Among these, it is evident that all alloys underwent secondary processing, predominantly through extrusion or equal channel angular pressing (ECAP), emphasizing the importance of post-casting treatments in achieving the desired mechanical and biodegradation properties. Additionally, all the shortlisted alloys were Mg-RE-Zn systems and show promise as viable alternatives to WE43 alloys. Notably, the clinically approved WE43 alloy contains yttrium (Y), which has an LD50 value of 88 mg/kg, a potential concern for long-term use. The Mg-RE-Zn alloys exhibit remarkable potential due to their ability to achieve high tensile strength, elongation, and optimal biodegradation rates. However, most existing studies on these alloys are confined to in-vitro conditions and only handful of Mg-RE-Zn alloys have been studied under in-vivo conditions (**Table 2.8**), which fail to fully simulate the complexities of physiological environments. This creates a significant knowledge gap regarding their performance in-vivo, where interactions with biological tissues, bodily fluids, and dynamic loading conditions critically affect biodegradation behaviour, biocompatibility, and mechanical integrity key factors for successful clinical application.

Furthermore, while systemic studies have investigated the effects of varying Zn /RE ratios in Mg-Zn-RE alloys on microstructure, mechanical properties, and corrosion in 1

wt.% NaCl solutions, there remains a lack of comprehensive research exploring the impact of these variations on biodegradation rates and biocompatibility under conditions that closely mimic the human body. Understanding the synergistic effects of Zn and RE ratios on key properties such as grain refinement, secondary phase distribution, and biodegradation kinetics is crucial for optimizing Mg-Zn-RE alloys for orthopaedic implant applications.

Thus, the present research work focused on the development of Mg-Zn-RE (RE = Gd and Nd) alloys for biodegradable implants, with a particular emphasis on systematically varying Zn and RE ratios to elucidate their effects on mechanical properties, biodegradation behaviour, and biocompatibility. Extrusion, a proven secondary processing technique, was utilized to refine microstructure and enhance alloy performance, with a focus on optimizing processing parameters to achieve the desired property balance. In addition, the study also involved a short term in-vivo evaluation to understand how these alloys behave in actual physiological environments.

2.10. Objectives

For orthopaedic implant applications, it is crucial for materials to have a yield strength greater than 200 MPa and a biodegradation rate of less than 0.5 mm/year in in-vitro conditions. While alloying Mg with REEs can enhance both its mechanical as well as biodegradation properties, these improvements alone are insufficient to meet the desired standards. Therefore, secondary processing is typically employed to achieve these necessary properties. Among various secondary processes, such as rolling, forging, extrusion, and severe plastic deformation, extrusion stands out due to its scalability and long-established industrial use. Thus, the thesis investigated the influence of different RE and extrusion on the microstructure, mechanical and biological properties of high strength (yield strength > 200 MPa) and low biodegradation rate (biodegradation rate < 0.5 mm/y) Mg-Zn-RE alloys. The detailed objectives of the thesis were as follows:

1. To study the effect of different rare earth elements (Gd/Nd) and grain refiner (Zr) on the microstructure, mechanical and corrosion properties of Mg-Zn-RE alloys.

2. To assess the influence of varying Zn/Gd ratio on the microstructure, mechanical and in-vitro behaviour of Mg-Zn-Gd-Zr alloys.

3. Evaluate the properties of extruded Mg-Zn-Gd-Zr alloys through in-vitro and in-vivo analysis for biodegradable implant applications.

References

[1] G. Chandra, A. Pandey, Biodegradable bone implants in orthopedic applications: a review, Biocybern. Biomed. Eng. 40 (2020) 596–610. https://doi.org/10.1016/j.bbe.2020.02.003.

[2] Significant improvement of corrosion resistance of biodegradable metallic implants processed by laser shock peening - ScienceDirect, (n.d.). https://www.sciencedirect.com/science/article/abs/pii/S0007850612001278 (accessed June 15, 2024).

[3] J. Nagels, M. Stokdijk, P.M. Rozing, Stress shielding and bone resorption in shoulder arthroplasty, J. Shoulder Elbow Surg. 12 (2003) 35–39. https://doi.org/10.1067/mse.2003.22.

[4] G. Chandra, A. Pandey, Design approaches and challenges for biodegradable bone implants: a review, Expert Rev. Med. Devices 18 (2021) 629–647. https://doi.org/10.1080/17434440.2021.1935875.

[5] P. Ducheyne, L.L. Hench, A. Kagan II, M. Martens, A. Bursens, J.C. Mulier, Effect of hydroxyapatite impregnation on skeletal bonding of porous coated implants, J. Biomed. Mater. Res. 14 (1980) 225–237. https://doi.org/10.1002/jbm.820140305.

[6] H. Yoshikawa, N. Tamai, T. Murase, A. Myoui, Interconnected porous hydroxyapatite ceramics for bone tissue engineering, J. R. Soc. Interface 6 (2008) S341–S348. https://doi.org/10.1098/rsif.2008.0425.focus.

[7] S. Itoh, M. Kikuchi, Y. Koyama, H.N. Matumoto, K. Takakuda, K. Shinomiya, J. Tanaka, Development of a novel biomaterial, hydroxyapatite/collagen (HAp/Col) composite for medical use, Biomed. Mater. Eng. 15 (2005) 29–41.

[8] D.S. Kohane, R. Langer, Polymeric Biomaterials in Tissue Engineering, Pediatr. Res. 63 (2008) 487–491. https://doi.org/10.1203/01.pdr.0000305937.26105.e7.

[9] CSIRO Molecular Science, Bag 10, Clayton South MDC, Vic 3169, Australia, P. Gunatillake, Biodegradable synthetic polymers for tissue engineering, Eur. Cell. Mater. 5 (2003) 1–16. https://doi.org/10.22203/eCM.v005a01.

[10] B. Guo, P.X. Ma, Synthetic biodegradable functional polymers for tissue engineering: a brief review, Sci. China Chem. 57 (2014) 490–500. https://doi.org/10.1007/s11426-014-5086-y.

[11] J.-L. Wang, J.-K. Xu, C. Hopkins, D.H.-K. Chow, L. Qin, Biodegradable Magnesium-Based Implants in Orthopedics—A General Review and Perspectives, Adv. Sci. 7 (2020) 1902443. https://doi.org/10.1002/advs.201902443.

[12] H. Ibrahim, S.N. Esfahani, B. Poorganji, D. Dean, M. Elahinia, Resorbable bone fixation alloys, forming, and post-fabrication treatments, Mater. Sci. Eng. C 70 (2017) 870–888. https://doi.org/10.1016/j.msec.2016.09.069.

[13] H. Li, Y. Zheng, L. Qin, Progress of biodegradable metals, Prog. Nat. Sci. Mater. Int. 24 (2014) 414–422. https://doi.org/10.1016/j.pnsc.2014.08.014.

[14] Additive manufacturing of biodegradable metals: Current research status and future perspectives - ScienceDirect, (n.d.). https://www.sciencedirect.com/science/article/pii/S1742706119302892 (accessed July 15, 2024).

[15] H. Hermawan, Updates on the research and development of absorbable metals for biomedical applications, Prog. Biomater. 7 (2018) 93–110. https://doi.org/10.1007/s40204-018-0091-4.

[16] G. Katarivas Levy, J. Goldman, E. Aghion, The Prospects of Zinc as a Structural Material for Biodegradable Implants—A Review Paper, Metals 7 (2017) 402. https://doi.org/10.3390/met7100402.

[17] A. Pola, M. Tocci, F.E. Goodwin, Review of Microstructures and Properties of Zinc Alloys, Metals 10 (2020) 253. https://doi.org/10.3390/met10020253.

[18] E. Mostaed, M. Sikora-Jasinska, J.W. Drelich, M. Vedani, Zinc-based alloys for degradable vascular stent applications, Acta Biomater. 71 (2018) 1–23. https://doi.org/10.1016/j.actbio.2018.03.005.

[19] B. Jia, H. Yang, Y. Han, Z. Zhang, X. Qu, Y. Zhuang, Q. Wu, Y. Zheng, K. Dai, *In vitro* and *in vivo* studies of Zn-Mn biodegradable metals designed for orthopedic applications, Acta Biomater. 108 (2020) 358–372. https://doi.org/10.1016/j.actbio.2020.03.009.

[20] W. Pachla, J. Skiba, M. Kulczyk, S. Przybysz, M. Przybysz, M. Wróblewska, R. Diduszko, R. Stępniak, J. Bajorek, M. Radomski, W. Fąfara, Nanostructurization of 316L type austenitic stainless steels by hydrostatic extrusion, Mater. Sci. Eng. A 615 (2014) 116–127. https://doi.org/10.1016/j.msea.2014.07.069.

[21] Y. Xin, C. Liu, K. Huo, G. Tang, X. Tian, P.K. Chu, Corrosion behavior of ZrN/Zr coated biomedical AZ91 magnesium alloy, Surf. Coat. Technol. 203 (2009) 2554–2557. https://doi.org/10.1016/j.surfcoat.2009.02.074.

[22] E. Poinern, S. Brundavanam, D. Fawcett, Biomedical Magnesium Alloys: A Review of Material Properties, Surface Modifications and Potential as a Biodegradable Orthopaedic Implant, Am. J. Biomed. Eng. 2 (2012) 218–240. https://doi.org/10.5923/j.ajbe.20120206.02.

[23] L. Xu, F. Pan, G. Yu, L. Yang, E. Zhang, K. Yang, *In vitro* and *in vivo* evaluation of the surface bioactivity of a calcium phosphate coated magnesium alloy, Biomaterials 30 (2009) 1512–1523. https://doi.org/10.1016/j.biomaterials.2008.12.001.

[24] J.-Y. Rho, L. Kuhn-Spearing, P. Zioupos, Mechanical properties and the hierarchical structure of bone, Med. Eng. Phys. 20 (1998) 92–102. https://doi.org/10.1016/S1350-4533(98)00007-1.

[25] M. Niinomi, Mechanical properties of biomedical titanium alloys, Mater. Sci. Eng. A 243 (1998) 231–236. https://doi.org/10.1016/S0921-5093(97)00806-X.

[26] E. Menthe, A. Bulak, J. Olfe, A. Zimmermann, K.-T. Rie, Improvement of the mechanical properties of austenitic stainless steel after plasma nitriding, Surf. Coat. Technol. 133–134 (2000) 259–263. https://doi.org/10.1016/S0257-8972(00)00930-0.

[27] D.A. Bridgeport, W.A. Brantley, P.F. Herman, Cobalt-Chromium and Nickel-Chromium Alloys for Removable Prosthodontics, Part 1: Mechanical Properties, J. Prosthodont. 2 (1993) 144–150. https://doi.org/10.1111/j.1532-849X.1993.tb00398.x.

[28] D. Munz, T. Fett, Ceramics: Mechanical Properties, Failure Behaviour, Materials Selection, Springer Science & Business Media, 2013.

[29] G. Perego, G.D. Cella, C. Bastioli, Effect of molecular weight and crystallinity on poly(lactic acid) mechanical properties, (n.d.).

https://onlinelibrary.wiley.com/doi/10.1002/(SICI)1097-4628(19960103)59:1<37::AID-APP6>3.0.CO;2-N (accessed June 18, 2024).

[30] L. Leung, C. Chan, S. Baek, H. Naguib, Comparison of morphology and mechanical properties of PLGA bioscaffolds, Biomed. Mater. 3 (2008) 025006. https://doi.org/10.1088/1748-6041/3/2/025006.

[31] H. Hermawan, D. Dubé, D. Mantovani, Degradable metallic biomaterials: Design and development of Fe–Mn alloys for stents, J. Biomed. Mater. Res. A 93A (2010) 1–11. https://doi.org/10.1002/jbm.a.32224.

[32] R. Michalik, The Effect of Modification with Rare Earth Elements on ZnAl22Cu3 Alloy Structure And Mechanical Properties / Wpływ Modyfikacji Pierwiastkami Ziem Rzadkich Na Strukture I Własciwosci Mechaniczne Stopu ZnAl22Cu3, Arch. Metall. Mater. 58 (2013). https://doi.org/10.2478/v10172-012-0149-6.

[33] J. Blaine, M. Chonchol, M. Levi, Renal Control of Calcium, Phosphate, and Magnesium Homeostasis, Clin. J. Am. Soc. Nephrol. 10 (2015) 1257. https://doi.org/10.2215/CJN.09750913.

[34] J.J. DiNicolantonio, J.H. O'Keefe, W. Wilson, Subclinical magnesium deficiency: a principal driver of cardiovascular disease and a public health crisis, Open Heart 5 (2018) e000668. https://doi.org/10.1136/openhrt-2017-000668.

[35] G.K. Schwalfenberg, S.J. Genuis, The Importance of Magnesium in Clinical Healthcare, Scientifica 2017 (2017) 4179326. https://doi.org/10.1155/2017/4179326.

[36] N.-E.L. Saris, E. Mervaala, H. Karppanen, J.A. Khawaja, A. Lewenstam, Magnesium: An update on physiological, clinical and analytical aspects, Clin. Chim. Acta 294 (2000) 1–26. https://doi.org/10.1016/S0009-8981(99)00258-2.

[37] A. Hartwig, Role of magnesium in genomic stability, Mutat. Res. Mol. Mech. Mutagen. 475 (2001) 113–121. https://doi.org/10.1016/S0027-5107(01)00074-4.

[38] M. Tinawi, Disorders of Magnesium Metabolism: Hypomagnesemia and Hypermagnesemia, Arch. Clin. Biomed. Res. 4 (2020) 205–220.

[39] G. Song, B. Johannesson, S. Hapugoda, D. StJohn, Galvanic corrosion of magnesium alloy AZ91D in contact with an aluminium alloy, steel and zinc, Corros. Sci. 46 (2004) 955–977. https://doi.org/10.1016/S0010-938X(03)00190-2.

[40] G.L. Makar, J. Kruger, Corrosion of magnesium, Int. Mater. Rev. 38 (1993) 138–153. https://doi.org/10.1179/imr.1993.38.3.138.

[41] G.L. Song, A. Atrens, Corrosion Mechanisms of Magnesium Alloys, Adv. Eng. Mater. 1 (1999) 11–33. https://doi.org/10.1002/(SICI)1527-2648(199909)1:1<11::AID-ADEM11>3.0.CO;2-N.

[42] G. Song, Recent Progress in Corrosion and Protection of Magnesium Alloys, Adv. Eng. Mater. 7 (2005) 563–586. https://doi.org/10.1002/adem.200500013.

[43] N.T. Kirkland, J. Lespagnol, N. Birbilis, M.P. Staiger, A survey of bio-corrosion rates of magnesium alloys, Corros. Sci. 52 (2010) 287–291. https://doi.org/10.1016/j.corsci.2009.09.033.

[44] S.S. Gropper, J.L. Smith, Advanced nutrition and human metabolism, Cengage Learning, 2013. https://thuvienso.hoasen.edu.vn/handle/123456789/9488 (accessed June 18, 2024).

[45] A. Oyane, H.-M. Kim, T. Furuya, T. Kokubo, T. Miyazaki, T. Nakamura, Preparation and assessment of revised simulated body fluids, J. Biomed. Mater. Res. A 65A (2003) 188–195. https://doi.org/10.1002/jbm.a.10482.

[46] A. Atrens, S. Johnston, Z. Shi, M.S. Dargusch, Viewpoint - Understanding Mg corrosion in the body for biodegradable medical implants, Scr. Mater. 154 (2018) 92–100. https://doi.org/10.1016/j.scriptamat.2018.05.021.

[47] S. Höhn, S. Virtanen, A.R. Boccaccini, Protein adsorption on magnesium and its alloys: A review, Appl. Surf. Sci. 464 (2019) 212–219. https://doi.org/10.1016/j.apsusc.2018.08.173.

[48] S. Virtanen, Biodegradable Mg and Mg alloys: Corrosion and biocompatibility, Mater. Sci. Eng. B 176 (2011) 1600–1608. https://doi.org/10.1016/j.mseb.2011.05.028.

[49] S. Amukarimi, M. Mozafari, Biodegradable magnesium-based biomaterials: An overview of challenges and opportunities, MedComm 2 (2021) 123–144. https://doi.org/10.1002/mco2.59.

[50] P. M, Atlas of Electrochemical Equilibria in Aqueous Solutions, NACE (1966). https://cir.nii.ac.jp/crid/1572543024422924800 (accessed June 18, 2024).

[51] M. Esmaily, J.E. Svensson, S. Fajardo, N. Birbilis, G.S. Frankel, S. Virtanen, R. Arrabal, S. Thomas, L.G. Johansson, Fundamentals and advances in magnesium alloy corrosion, Prog. Mater. Sci. 89 (2017) 92–193. https://doi.org/10.1016/j.pmatsci.2017.04.011.

[52] S. Remennik, I. Bartsch, E. Willbold, F. Witte, D. Shechtman, New, fast corroding high ductility Mg–Bi–Ca and Mg–Bi–Si alloys, with no clinically observable gas formation in bone implants, Mater. Sci. Eng. B 176 (2011) 1653–1659. https://doi.org/10.1016/j.mseb.2011.07.011.

[53] M. Razavi, Y. Huang, Assessment of magnesium-based biomaterials: from bench to clinic, Biomater. Sci. 7 (2019) 2241–2263. https://doi.org/10.1039/C9BM00289H.

[54] D. Noviana, D. Paramitha, M.F. Ulum, H. Hermawan, The effect of hydrogen gas evolution of magnesium implant on the postimplantation mortality of rats, J. Orthop. Transl. 5 (2016) 9–15. https://doi.org/10.1016/j.jot.2015.08.003.

[55] The Effects of Hydrogen Gas Inhalation on Adverse Left Ventricular Remodeling After Percutaneous Coronary Intervention for ST-Elevated Myocardial Infarction ― First Pilot Study in Humans ―, (n.d.). https://www.jstage.jst.go.jp/article/circj/81/7/81_CJ-17-0105/_article/-char/ja/ (accessed July 15, 2024).

[56] K. Hayashida, M. Sano, N. Kamimura, T. Yokota, M. Suzuki, S. Ohta, K. Fukuda, S. Hori, Hydrogen Inhalation During Normoxic Resuscitation Improves Neurological Outcome in a Rat Model of Cardiac Arrest Independently of Targeted Temperature Management, Circulation 130 (2014) 2173–2180. https://doi.org/10.1161/CIRCULATIONAHA.114.011848.

[57] T. Matsuoka, M. Suzuki, M. Sano, K. Hayashida, T. Tamura, K. Homma, K. Fukuda, J. Sasaki, Hydrogen gas inhalation inhibits progression to the “irreversible” stage of shock after severe hemorrhage in rats, J. Trauma Acute Care Surg. 83 (2017) 469. https://doi.org/10.1097/TA.0000000000001620.

[58] R. Yamamoto, K. Homma, S. Suzuki, M. Sano, J. Sasaki, Hydrogen gas distribution in organs after inhalation: Real-time monitoring of tissue hydrogen concentration in rat, Sci. Rep. 9 (2019) 1255. https://doi.org/10.1038/s41598-018-38180-4.

[59] I. Ohsawa, M. Ishikawa, K. Takahashi, M. Watanabe, K. Nishimaki, K. Yamagata, K. Katsura, Y. Katayama, S. Asoh, S. Ohta, Hydrogen acts as a therapeutic antioxidant by selectively reducing cytotoxic oxygen radicals, Nat. Med. 13 (2007) 688–694. https://doi.org/10.1038/nm1577.

[60] A. Yoshida, H. Asanuma, H. Sasaki, S. Sanada, S. Yamazaki, Y. Asano, Y. Shinozaki, H. Mori, A. Shimouchi, M. Sano, M. Asakura, T. Minamino, S. Takashima, M. Sugimachi, N. Mochizuki, M. Kitakaze, H2 Mediates Cardioprotection Via Involvements of KATP Channels and Permeability Transition Pores of Mitochondria in Dogs, Cardiovasc. Drugs Ther. 26 (2012) 217–226. https://doi.org/10.1007/s10557-012-6381-5.

[61] D.A. Robinson, R.W. Griffith, D. Shechtman, R.B. Evans, M.G. Conzemius, *In vitro* antibacterial properties of magnesium metal against *Escherichia coli*, *Pseudomonas aeruginosa* and *Staphylococcus aureus*, Acta Biomater. 6 (2010) 1869–1877. https://doi.org/10.1016/j.actbio.2009.10.007.

[62] E. Ghali, Corrosion Resistance of Aluminum and Magnesium Alloys: Understanding, Performance, and Testing, John Wiley & Sons, 2010.

[63] F. Witte, V. Kaese, H. Haferkamp, E. Switzer, A. Meyer-Lindenberg, C.J. Wirth, H. Windhagen, In vivo corrosion of four magnesium alloys and the associated bone response, Biomaterials 26 (2005) 3557–3563. https://doi.org/10.1016/j.biomaterials.2004.09.049.

[64] S. Agarwal, J. Curtin, B. Duffy, S. Jaiswal, Biodegradable magnesium alloys for orthopaedic applications: A review on corrosion, biocompatibility and surface modifications, Mater. Sci. Eng. C 68 (2016) 948–963. https://doi.org/10.1016/j.msec.2016.06.020.

[65] I. Slutsky, N. Abumaria, L.-J. Wu, C. Huang, L. Zhang, B. Li, X. Zhao, A. Govindarajan, M.-G. Zhao, M. Zhuo, S. Tonegawa, G. Liu, Enhancement of Learning and Memory by Elevating Brain Magnesium, Neuron 65 (2010) 165–177. https://doi.org/10.1016/j.neuron.2009.12.026.

[66] U. Gröber, J. Schmidt, K. Kisters, Magnesium in Prevention and Therapy, Nutrients 7 (2015) 8199–8226. https://doi.org/10.3390/nu7095388.

[67] Q. Chen, G.A. Thouas, Metallic implant biomaterials, Mater. Sci. Eng. R Rep. 87 (2015) 1–57. https://doi.org/10.1016/j.mser.2014.10.001.

[68] Z. Zhai, X. Qu, H. Li, K. Yang, P. Wan, L. Tan, Z. Ouyang, X. Liu, B. Tian, F. Xiao, W. Wang, C. Jiang, T. Tang, Q. Fan, A. Qin, K. Dai, The effect of metallic magnesium degradation products on osteoclast-induced osteolysis and attenuation of NF-κB and NFATc1 signaling, Biomaterials 35 (2014) 6299–6310. https://doi.org/10.1016/j.biomaterials.2014.04.044.

[69] X. Li, X. Liu, S. Wu, K.W.K. Yeung, Y. Zheng, P.K. Chu, Design of magnesium alloys with controllable degradation for biomedical implants: From bulk to surface, Acta Biomater. 45 (2016) 2–30. https://doi.org/10.1016/j.actbio.2016.09.005.

[70] Aluminium in brain tissue in familial Alzheimer's disease - ScienceDirect, (n.d.). https://www.sciencedirect.com/science/article/pii/S0946672X16303777 (accessed July 16, 2024).

[71] H. Hermawan, Biodegradable Metals: State of the Art, in: H. Hermawan (Ed.), Biodegrad. Met. Concept Appl., Springer, Berlin, Heidelberg, 2012: pp. 13–22. https://doi.org/10.1007/978-3-642-31170-3_2.

[72] Y. Ding, C. Wen, P. Hodgson, Y. Li, Effects of alloying elements on the corrosion behavior and biocompatibility of biodegradable magnesium alloys: a review, J. Mater. Chem. B 2 (2014) 1912–1933. https://doi.org/10.1039/C3TB21746A.

[73] M. Kasaeian-Naeini, M. Sedighi, R. Hashemi, Severe plastic deformation (SPD) of biodegradable magnesium alloys and composites: A review of developments and prospects, J. Magnes. Alloys 10 (2022) 938–955. https://doi.org/10.1016/j.jma.2021.11.006.

[74] M. Mohammadi Zerankeshi, R. Alizadeh, E. Gerashi, M. Asadollahi, T.G. Langdon, Effects of heat treatment on the corrosion behavior and mechanical properties of biodegradable Mg alloys, J. Magnes. Alloys 10 (2022) 1737–1785. https://doi.org/10.1016/j.jma.2022.04.010.

[75] S. Cometa, M.A. Bonifacio, A.M. Ferreira, P. Gentile, E. De Giglio, Surface Characterization of Electro-Assisted Titanium Implants: A Multi-Technique Approach, Materials 13 (2020) 705. https://doi.org/10.3390/ma13030705.

[76] M. Rahmati, E. A. Silva, J. E. Reseland, C.A. Heyward, H. J. Haugen, Biological responses to physicochemical properties of biomaterial surface, Chem. Soc. Rev. 49 (2020) 5178–5224. https://doi.org/10.1039/D0CS00103A.

[77] Y. Su, I. Cockerill, Y. Zheng, L. Tang, Y.-X. Qin, D. Zhu, Biofunctionalization of metallic implants by calcium phosphate coatings, Bioact. Mater. 4 (2019) 196–206. https://doi.org/10.1016/j.bioactmat.2019.05.001.

[78] F. Witte, F. Feyerabend, P. Maier, J. Fischer, M. Störmer, C. Blawert, W. Dietzel, N. Hort, Biodegradable magnesium–hydroxyapatite metal matrix composites, Biomaterials 28 (2007) 2163–2174. https://doi.org/10.1016/j.biomaterials.2006.12.027.

[79] J. Yang, F. Cui, I.Seop. Lee, Surface Modifications of Magnesium Alloys for Biomedical Applications, Ann. Biomed. Eng. 39 (2011) 1857–1871. https://doi.org/10.1007/s10439-011-0300-y.

[80] C.H. Cáceres, D.M. Rovera, Solid solution strengthening in concentrated Mg–Al alloys, J. Light Met. 1 (2001) 151–156. https://doi.org/10.1016/S1471-5317(01)00008-6.

[81] J.E. Tahán, V.A. Granadillo, R.A. Romero, Electrothermal atomic absorption spectrometric determination of Al, Cu, Fe, Pb, V and Zn in clinical samples and in certified environmental reference materials, Anal. Chim. Acta 295 (1994) 187–197. https://doi.org/10.1016/0003-2670(94)80350-1.

[82] P.C. Ferreira, K. de A. Piai, A.M.M. Takayanagui, S.I. Segura-Muñoz, Aluminum as a risk factor for Alzheimer's disease, Rev. Lat. Am. Enfermagem 16 (2008) 151–157. https://doi.org/10.1590/s0104-11692008000100023.

[83] A.V. Rousselle, D. Heymann, V. Demais, C. Charrier, N. Passuti, M.F. Baslé, Influence of metal ion solutions on rabbit osteoclast activities in vitro, Histol. Histopathol. 17 (2002) 1025–1032. https://doi.org/10.14670/HH-17.1025.

[84] M. Shingde, J. Hughes, R. Boadle, E.J. Wills, R. Pamphlett, Macrophagic myofasciitis associated with vaccine-derived aluminium, Med. J. Aust. 183 (2005) 145–146. https://doi.org/10.5694/j.1326-5377.2005.tb06963.x.

[85] Y. Xin, T. Hu, P.K. Chu, *In vitro* studies of biomedical magnesium alloys in a simulated physiological environment: A review, Acta Biomater. 7 (2011) 1452–1459. https://doi.org/10.1016/j.actbio.2010.12.004.

[86] F. Witte, N. Hort, C. Vogt, S. Cohen, K.U. Kainer, R. Willumeit, F. Feyerabend, Degradable biomaterials based on magnesium corrosion, Curr. Opin. Solid State Mater. Sci. 12 (2008) 63–72. https://doi.org/10.1016/j.cossms.2009.04.001.

[87] X.N. Gu, Y.F. Zheng, L.J. Chen, Influence of artificial biological fluid composition on the biocorrosion of potential orthopedic Mg-Ca, AZ31, AZ91 alloys, Biomed. Mater. Bristol Engl. 4 (2009) 065011. https://doi.org/10.1088/1748-6041/4/6/065011.

[88] F. Witte, N. Hort, C. Vogt, S. Cohen, K.U. Kainer, R. Willumeit, F. Feyerabend, Degradable biomaterials based on magnesium corrosion, Curr. Opin. Solid State Mater. Sci. 12 (2008) 63–72. https://doi.org/10.1016/j.cossms.2009.04.001.

[89] Y.C. Lee, A.K. Dahle, D.H. StJohn, The role of solute in grain refinement of magnesium, Metall. Mater. Trans. A 31 (2000) 2895–2906. https://doi.org/10.1007/BF02830349.

[90] K.Y. Renkema, R.T. Alexander, R.J. Bindels, J.G. Hoenderop, Calcium and phosphate homeostasis: concerted interplay of new regulators, Ann. Med. 40 (2008) 82–91. https://doi.org/10.1080/07853890701689645.

[91] Z. Li, X. Gu, S. Lou, Y. Zheng, The development of binary Mg–Ca alloys for use as biodegradable materials within bone, Biomaterials 29 (2008) 1329–1344. https://doi.org/10.1016/j.biomaterials.2007.12.021.

[92] N. Erdmann, N. Angrisani, J. Reifenrath, A. Lucas, F. Thorey, D. Bormann, A. Meyer-Lindenberg, Biomechanical testing and degradation analysis of MgCa0.8 alloy screws: a comparative in vivo study in rabbits, Acta Biomater. 7 (2011) 1421–1428. https://doi.org/10.1016/j.actbio.2010.10.031.

[93] A. Krause, N. von der Höh, D. Bormann, C. Krause, F.-W. Bach, H. Windhagen, A. Meyer-Lindenberg, Degradation behaviour and mechanical properties of magnesium implants in rabbit tibiae, J. Mater. Sci. 45 (2010) 624–632. https://doi.org/10.1007/s10853-009-3936-3.

[94] D. Yin, E. Zhang, S. Zeng, Effect of Zn content on microstructure, mechanical properties and fracture behavior of Mg-Mn alloy, in: 2009. https://www.semanticscholar.org/paper/Effect-of-Zn-content-on-microstructure%2C-

mechanical-Yin-Zhang/d3b2173e44d4d367801bef6866260e966e1e21ae (accessed December 13, 2024).

[95] E. Zhang, D. Yin, L. Xu, L. Yang, K. Yang, Microstructure, mechanical and corrosion properties and biocompatibility of Mg–Zn–Mn alloys for biomedical application, Mater. Sci. Eng. C 29 (2009) 987–993. https://doi.org/10.1016/j.msec.2008.08.024.

[96] C. Lhotka, T. Szekeres, I. Steffan, K. Zhuber, K. Zweymüller, Four-year study of cobalt and chromium blood levels in patients managed with two different metal-on-metal total hip replacements, J. Orthop. Res. Off. Publ. Orthop. Res. Soc. 21 (2003) 189–195. https://doi.org/10.1016/S0736-0266(02)00152-3.

[97] M. Zohrevand, R. Alizadeh, R. Mahmudi, Using different strategies to improve properties of the biodegradable Mg–4Li–4Zn alloy, J. Mater. Res. Technol. 27 (2023) 2066–2079. https://doi.org/10.1016/j.jmrt.2023.10.059.

[98] Y. Song, D. Shan, R. Chen, E.-H. Han, Corrosion characterization of Mg–8Li alloy in NaCl solution, Corros. Sci. 51 (2009) 1087–1094. https://doi.org/10.1016/j.corsci.2009.03.011.

[99] M. Pogorielov, E. Husak, A. Solodivnik, S. Zhdanov, Magnesium-based biodegradable alloys: Degradation, application, and alloying elements, Interv. Med. Appl. Sci. 9 (n.d.) 27–38. https://doi.org/10.1556/1646.9.2017.1.04.

[100] C. Liu, Z. Ren, Y. Xu, S. Pang, X. Zhao, Y. Zhao, Biodegradable Magnesium Alloys Developed as Bone Repair Materials: A Review, Scanning 2018 (2018) 9216314. https://doi.org/10.1155/2018/9216314.

[101] M. Ghasemi, A.R. Dehpour, The NMDA receptor/nitric oxide pathway: a target for the therapeutic and toxic effects of lithium, Trends Pharmacol. Sci. 32 (2011) 420–434. https://doi.org/10.1016/j.tips.2011.03.006.

[102] S. Guo, K. Arai, M.F. Stins, D.-M. Chuang, E.H. Lo, Lithium upregulates vascular endothelial growth factor in brain endothelial cells and astrocytes, Stroke 40 (2009) 652–655. https://doi.org/10.1161/STROKEAHA.108.524504.

[103] R.-C. Zeng, L. Sun, Y.-F. Zheng, H.-Z. Cui, E.-H. Han, Corrosion and characterisation of dual phase Mg–Li–Ca alloy in Hank's solution: The influence of

microstructural features, Corros. Sci. 79 (2014) 69–82. https://doi.org/10.1016/j.corsci.2013.10.028.

[104] W.R. Zhou, Y.F. Zheng, M.A. Leeflang, J. Zhou, Mechanical property, biocorrosion and in vitro biocompatibility evaluations of Mg–Li–(Al)–(RE) alloys for future cardiovascular stent application, Acta Biomater. 9 (2013) 8488–8498. https://doi.org/10.1016/j.actbio.2013.01.032.

[105] Nomenclature of Inorganic Chemistry – IUPAC Recommendations 2005, Chem. Int. -- Newsmag. IUPAC 27 (2005). https://doi.org/10.1515/ci.2005.27.6.25.

[106] Q. Peng, Y. Huang, L. Zhou, N. Hort, K.U. Kainer, Preparation and properties of high purity Mg-Y biomaterials, Biomaterials 31 (2010) 398–403. https://doi.org/10.1016/j.biomaterials.2009.09.065.

[107] F. Witte, J. Fischer, J. Nellesen, C. Vogt, J. Vogt, T. Donath, F. Beckmann, In vivo corrosion and corrosion protection of magnesium alloy LAE442, Acta Biomater. 6 (2010) 1792–1799. https://doi.org/10.1016/j.actbio.2009.10.012.

[108] N. Hort, Y. Huang, D. Fechner, M. Störmer, C. Blawert, F. Witte, C. Vogt, H. Drücker, R. Willumeit, K.U. Kainer, F. Feyerabend, Magnesium alloys as implant materials – Principles of property design for Mg–RE alloys, Acta Biomater. 6 (2010) 1714–1725. https://doi.org/10.1016/j.actbio.2009.09.010.

[109] F. Witte, J. Fischer, J. Nellesen, H.-A. Crostack, V. Kaese, A. Pisch, F. Beckmann, H. Windhagen, In vitro and in vivo corrosion measurements of magnesium alloys, Biomaterials 27 (2006) 1013–1018. https://doi.org/10.1016/j.biomaterials.2005.07.037.

[110] B. Heublein, R. Rohde, V. Kaese, M. Niemeyer, W. Hartung, A. Haverich, Biocorrosion of magnesium alloys: a new principle in cardiovascular implant technology?, Heart Br. Card. Soc. 89 (2003) 651–656. https://doi.org/10.1136/heart.89.6.651.

[111] P. Peeters, M. Bosiers, J. Verbist, K. Deloose, B. Heublein, Preliminary results after application of absorbable metal stents in patients with critical limb ischemia, J. Endovasc. Ther. Off. J. Int. Soc. Endovasc. Spec. 12 (2005) 1–5. https://doi.org/10.1583/04-1349R.1.

[112] H. Hermawan, D. Dubé, D. Mantovani, Developments in metallic biodegradable stents, Acta Biomater. 6 (2010) 1693–1697. https://doi.org/10.1016/j.actbio.2009.10.006.

[113] R. Erbel, C.D. Mario, J. Bartunek, J. Bonnier, B. de Bruyne, F.R. Eberli, P. Erne, M. Haude, B. Heublein, M. Horrigan, C. Ilsley, D. Böse, J. Koolen, T.F. Lüscher, N. Weissman, R. Waksman, Temporary scaffolding of coronary arteries with bioabsorbable magnesium stents: a prospective, non-randomised multicentre trial, The Lancet 369 (2007) 1869–1875. https://doi.org/10.1016/S0140-6736(07)60853-8.

[114] Y. Luo, J. Wang, M.T.Y. Ong, P.S. Yung, J. Wang, L. Qin, Update on the research and development of magnesium-based biodegradable implants and their clinical translation in orthopaedics, Biomater. Transl. 2 (2021) 188–196. https://doi.org/10.12336/biomatertransl.2021.03.003.

[115] V. Tsakiris, C. Tardei, F.M. Clicinschi, Biodegradable Mg alloys for orthopedic implants – A review, J. Magnes. Alloys 9 (2021) 1884–1905. https://doi.org/10.1016/j.jma.2021.06.024.

[116] B.J. Park, K.Y. An, Y.S. Choi, Arthroscopic Assisted Bioabsorbable Screw Fixation for Radial Head Fractures: A Report of Two Cases, J. Korean Fract. Soc. 30 (2017) 35–39. https://doi.org/10.12671/jkfs.2017.30.1.35.

[117] Y. Sun, H. Wu, W. Wang, R. Zan, H. Peng, S. Zhang, X. Zhang, Translational status of biomedical Mg devices in China, Bioact. Mater. 4 (2019) 358–365. https://doi.org/10.1016/j.bioactmat.2019.11.001.

[118] K. Xie, L. Wang, Y. Guo, S. Zhao, Y. Yang, D. Dong, W. Ding, K. Dai, W. Gong, G. Yuan, Y. Hao, Effectiveness and safety of biodegradable Mg-Nd-Zn-Zr alloy screws for the treatment of medial malleolar fractures, J. Orthop. Transl. 27 (2021) 96–100. https://doi.org/10.1016/j.jot.2020.11.007.

[119] M. Haude, R. Erbel, P. Erne, S. Verheye, H. Degen, D. Böse, P. Vermeersch, I. Wijnbergen, N. Weissman, F. Prati, R. Waksman, J. Koolen, Safety and performance of the drug-eluting absorbable metal scaffold (DREAMS) in patients with de-novo coronary lesions: 12 month results of the prospective, multicentre, first-in-man BIOSOLVE-I trial, The Lancet 381 (2013) 836–844. https://doi.org/10.1016/S0140-6736(12)61765-6.

[120] Y. Onuma, J. Ormiston, P.W. Serruys, Bioresorbable Scaffold Technologies, Circ. J. 75 (2011) 509–520. https://doi.org/10.1253/circj.CJ-10-1135.

[121] Serruys Patrick W., Kutryk Michael J.B., Ong Andrew T.L., Coronary-Artery Stents, N. Engl. J. Med. 354 (2006) 483–495. https://doi.org/10.1056/NEJMra051091.

[122] J. Bennett, Q. De Hemptinne, K. McCutcheon, Magmaris resorbable magnesium scaffold for the treatment of coronary heart disease: overview of its safety and efficacy, Expert Rev. Med. Devices 16 (2019) 757–769. https://doi.org/10.1080/17434440.2019.1649133.

[123] D.H. StJohn, M. Qian, M.A. Easton, P. Cao, Z. Hildebrand, Grain refinement of magnesium alloys, Metall. Mater. Trans. A 36 (2005) 1669–1679. https://doi.org/10.1007/s11661-005-0030-6.

[124] H. Yu, Y. Xin, M. Wang, Q. Liu, Hall-Petch relationship in Mg alloys: A review, J. Mater. Sci. Technol. 34 (2018) 248–256. https://doi.org/10.1016/j.jmst.2017.07.022.

[125] H. Lin, M. Yang, H. Tang, F. Pan, Effect of minor Sc on the microstructure and mechanical properties of AZ91 Magnesium Alloy, Prog. Nat. Sci. Mater. Int. 28 (2018) 66–73. https://doi.org/10.1016/j.pnsc.2018.01.006.

[126] F. Zhong, H. Wu, Y. Jiao, R. Wu, J. Zhang, L. Hou, M. Zhang, Effect of Y and Ce on the microstructure, mechanical properties and anisotropy of as-rolled Mg-8Li-1Al alloy, J. Mater. Sci. Technol. 39 (2020) 124–134. https://doi.org/10.1016/j.jmst.2019.04.045.

[127] G. Tong, H. Liu, Y. Liu, Effect of rare earth additions on microstructure and mechanical properties of AZ91 magnesium alloys, Trans. Nonferrous Met. Soc. China 20 (2010) s336–s340. https://doi.org/10.1016/S1003-6326(10)60493-1.

[128] M. Zhang, Y. Feng, J. Zhang, S. Liu, Q. Yang, Z. Liu, R. Li, J. Meng, R. Wu, Development of extruded Mg-6Er-3Y-1.5Zn-0.4Mn (wt.%) alloy with high strength at elevated temperature, J. Mater. Sci. Technol. 35 (2019) 2365–2374. https://doi.org/10.1016/j.jmst.2019.05.053.

[129] C. Xu, B. Lu, Z. Lü, W. Liang, Grain refinement of AZ31 magnesium alloy by Al-Ti-C-Y master alloy, J. Rare Earths 26 (2008) 604–608. https://doi.org/10.1016/S1002-0721(08)60146-5.

[130] Y. Wang, J. Fu, Y. Yang, Effect of Nd addition on microstructures and mechanical properties of AZ80 magnesium alloys, Trans. Nonferrous Met. Soc. China 22 (2012) 1322–1328. https://doi.org/10.1016/S1003-6326(11)61321-6.

[131] J. Zhang, Q. Ma, F.S. Pan, R.L. Zuo, Microstructures and Mechanical Properties of Mg-9Zn-Zr Magnesium Alloys, Mater. Sci. Forum 654–656 (2010) 643–646. https://doi.org/10.4028/www.scientific.net/MSF.654-656.643.

[132] Y. Liu, H. Ren, W.-C. Hu, D.-J. Li, X.-Q. Zeng, K.-G. Wang, J. Lu, First-principles Calculations of Strengthening Compounds in Magnesium Alloy: A General Review, J. Mater. Sci. Technol. 32 (2016) 1222–1231. https://doi.org/10.1016/j.jmst.2016.04.003.

[133] K. Chen, K.P. Boyle, Alloy solid solution strengthening of Mg alloys: Valence effect, Phys. Status Solidi B 249 (2012) 2089–2095. https://doi.org/10.1002/pssb.201248195.

[134] Understanding solid solution strengthening at elevated temperatures in a creep-resistant Mg–Gd–Ca alloy - ScienceDirect, (n.d.). https://www.sciencedirect.com/science/article/pii/S1359645419306512 (accessed June 19, 2024).

[135] J. Xie, J. Zhang, Z. You, S. Liu, K. Guan, R. Wu, J. Wang, J. Feng, Towards developing Mg alloys with simultaneously improved strength and corrosion resistance via RE alloying, J. Magnes. Alloys 9 (2021) 41–56. https://doi.org/10.1016/j.jma.2020.08.016.

[136] C.R. Hutchinson, J.F. Nie, S. Gorsse, Modeling the precipitation processes and strengthening mechanisms in a Mg-Al-(Zn) AZ91 alloy, Metall. Mater. Trans. A 36 (2005) 2093–2105. https://doi.org/10.1007/s11661-005-0330-x.

[137] Progress in Research on Biodegradable Magnesium Alloys: A Review - Li - 2020 - Advanced Engineering Materials - Wiley Online Library, (n.d.). https://onlinelibrary.wiley.com/doi/full/10.1002/adem.202000213 (accessed June 24, 2024).

[138] L. Yang, Y. Huang, F. Feyerabend, R. Willumeit, C. Mendis, K.U. Kainer, N. Hort, Microstructure, mechanical and corrosion properties of Mg–Dy–Gd–Zr alloys for medical applications, Acta Biomater. 9 (2013) 8499–8508. https://doi.org/10.1016/j.actbio.2013.03.017.

[139] S. Wang, H. Pan, D. Xie, D. Zhang, J. Li, H. Xie, Y. Ren, G. Qin, Grain refinement and strength enhancement in Mg wrought alloys: A review, J. Magnes. Alloys 11 (2023) 4128–4145. https://doi.org/10.1016/j.jma.2023.11.002.

[140] A. Luo, M.O. Pekguleryuz, Cast magnesium alloys for elevated temperature applications, J. Mater. Sci. 29 (1994) 5259–5271. https://doi.org/10.1007/BF01171534.

[141] Y. Yang, X. Xiong, J. Chen, X. Peng, D. Chen, F. Pan, Research advances in magnesium and magnesium alloys worldwide in 2020, J. Magnes. Alloys 9 (2021) 705–747. https://doi.org/10.1016/j.jma.2021.04.001.

[142] H. Pan, Y. Ren, H. Fu, H. Zhao, L. Wang, X. Meng, G. Qin, Recent developments in rare-earth free wrought magnesium alloys having high strength: A review, J. Alloys Compd. 663 (2016) 321–331. https://doi.org/10.1016/j.jallcom.2015.12.057.

[143] J.F. Nie, Effects of precipitate shape and orientation on dispersion strengthening in magnesium alloys, Scr. Mater. 48 (2003) 1009–1015. https://doi.org/10.1016/S1359-6462(02)00497-9.

[144] J.-F. Nie, Precipitation and Hardening in Magnesium Alloys, Metall. Mater. Trans. A 43 (2012) 3891–3939. https://doi.org/10.1007/s11661-012-1217-2.

[145] J. Song, J. She, D. Chen, F. Pan, Latest research advances on magnesium and magnesium alloys worldwide, J. Magnes. Alloys 8 (2020) 1–41. https://doi.org/10.1016/j.jma.2020.02.003.

[146] Q. Wang, Z. Li, S. Pang, X. Li, C. Dong, P.K. Liaw, Coherent Precipitation and Strengthening in Compositionally Complex Alloys: A Review, Entropy 20 (2018) 878. https://doi.org/10.3390/e20110878.

[147] Y. Chen, Z. Xu, C. Smith, J. Sankar, Recent advances on the development of magnesium alloys for biodegradable implants, Acta Biomater. 10 (2014) 4561–4573. https://doi.org/10.1016/j.actbio.2014.07.005.

[148] J. Liu, D. Bian, Y. Zheng, X. Chu, Y. Lin, M. Wang, Z. Lin, M. Li, Y. Zhang, S. Guan, Comparative in vitro study on binary Mg-RE (Sc, Y, La, Ce, Pr, Nd, Sm, Eu, Gd, Tb, Dy, Ho, Er, Tm, Yb and Lu) alloy systems, Acta Biomater. 102 (2020) 508–528. https://doi.org/10.1016/j.actbio.2019.11.013.

[149] H.S. Jiang, X.G. Qiao, C. Xu, M.Y. Zheng, K. Wu, S. Kamado, Ultrahigh strength as-extruded Mg–10.3Zn–6.4Y–0.4Zr–0.5Ca alloy containing W phase, Mater. Des. 108 (2016) 391–399. https://doi.org/10.1016/j.matdes.2016.06.116.

[150] X. Zhang, G. Yuan, L. Mao, J. Niu, P. Fu, W. Ding, Effects of extrusion and heat treatment on the mechanical properties and biocorrosion behaviors of a Mg–Nd–Zn–Zr alloy, J. Mech. Behav. Biomed. Mater. 7 (2012) 77–86. https://doi.org/10.1016/j.jmbbm.2011.05.026.

[151] M.R. Barnett, M.D. Nave, C.J. Bettles, Deformation microstructures and textures of some cold rolled Mg alloys, Mater. Sci. Eng. A 386 (2004) 205–211. https://doi.org/10.1016/j.msea.2004.07.030.

[152] A. Imandoust, C.D. Barrett, T. Al-Samman, M.A. Tschopp, E. Essadiqi, N. Hort, H. El Kadiri, Unraveling Recrystallization Mechanisms Governing Texture Development from Rare-Earth Element Additions to Magnesium, Metall. Mater. Trans. A 49 (2018) 1809–1829. https://doi.org/10.1007/s11661-018-4520-8.

[153] J.P. Hadorn, K. Hantzsche, S. Yi, J. Bohlen, D. Letzig, S.R. Agnew, Effects of Solute and Second-Phase Particles on the Texture of Nd-Containing Mg Alloys, Metall. Mater. Trans. A 43 (2012) 1363–1375. https://doi.org/10.1007/s11661-011-1018-z.

[154] N. Stanford, Micro-alloying Mg with Y, Ce, Gd and La for texture modification—A comparative study, Mater. Sci. Eng. A 527 (2010) 2669–2677. https://doi.org/10.1016/j.msea.2009.12.036.

[155] K. Hantzsche, J. Bohlen, J. Wendt, K.U. Kainer, S.B. Yi, D. Letzig, Effect of rare earth additions on microstructure and texture development of magnesium alloy sheets, Scr. Mater. 63 (2010) 725–730. https://doi.org/10.1016/j.scriptamat.2009.12.033.

[156] G.G. Yapici, I. Karaman, Common trends in texture evolution of ultra-fine-grained hcp materials during equal channel angular extrusion, Mater. Sci. Eng. A 503 (2009) 78–81. https://doi.org/10.1016/j.msea.2008.01.098.

[157] Mechanical properties, in vitro corrosion and biocompatibility of newly developed biodegradable Mg-Zr-Sr-Ho alloys for biomedical applications | Scientific Reports, (n.d.). https://www.nature.com/articles/srep31990 (accessed July 1, 2024).

[158] J. Zhang, J. Wang, X. Qiu, D. Zhang, Z. Tian, X. Niu, D. Tang, J. Meng, Effect of Nd on the microstructure, mechanical properties and corrosion behavior of die-cast Mg–4Al-based alloy, J. Alloys Compd. 464 (2008) 556–564. https://doi.org/10.1016/j.jallcom.2007.10.056.

[159] J. Zhang, D. Zhang, Z. Tian, J. Wang, K. Liu, H. Lu, D. Tang, J. Meng, Microstructures, tensile properties and corrosion behavior of die-cast Mg–4Al-based alloys containing La and/or Ce, Mater. Sci. Eng. A 489 (2008) 113–119. https://doi.org/10.1016/j.msea.2007.12.024.

[160] T. Rzychoń, A. Kiełbus, J. Cwajna, J. Mizera, Microstructural stability and creep properties of die casting Mg–4Al–4RE magnesium alloy, Mater. Charact. 60 (2009) 1107–1113. https://doi.org/10.1016/j.matchar.2009.05.014.

[161] J. Zhang, S. Liu, Z. Leng, X. Liu, Z. Niu, M. Zhang, R. Wu, Structure stability and mechanical properties of high-pressure die-cast Mg–Al–La–Y-based alloy, Mater. Sci. Eng. A 531 (2012) 70–75. https://doi.org/10.1016/j.msea.2011.10.025.

[162] A. Srinivasan, Y. Huang, C.L. Mendis, C. Blawert, K.U. Kainer, N. Hort, Investigations on microstructures, mechanical and corrosion properties of Mg–Gd–Zn alloys, Mater. Sci. Eng. A 595 (2014) 224–234. https://doi.org/10.1016/j.msea.2013.12.016.

[163] P. Trivedi, K.C. Nune, R.D.K. Misra, Degradation behaviour of magnesium-rare earth biomedical alloys, Mater. Technol. 31 (2016) 726–731. https://doi.org/10.1080/10667857.2016.1213550.

[164] E. Zhang, W. He, H. Du, K. Yang, Microstructure, mechanical properties and corrosion properties of Mg–Zn–Y alloys with low Zn content, Mater. Sci. Eng. A 488 (2008) 102–111. https://doi.org/10.1016/j.msea.2007.10.056.

[165] New horizon for high performance Mg-based biomaterial with uniform degradation behavior: Formation of stacking faults | Scientific Reports, (n.d.). https://www.nature.com/articles/srep13933 (accessed June 30, 2024).

[166] J. Chen, L. Tan, I.P. Etim, K. Yang, Comparative study of the effect of Nd and Y content on the mechanical and biodegradable properties of Mg-Zn-Zr-xNd/Y (x=0.5, 1, 2) alloys, Mater. Technol. 33 (2018) 659–671. https://doi.org/10.1080/10667857.2018.1492227.

[167] U. Rokkala, S. Bontha, M.R. Ramesh, V.K. Balla, Influence of friction stir processing on microstructure, mechanical properties and corrosion behaviour of Mg-Zn-

Dy alloy, J. Mater. Sci. 58 (2023) 2893–2914. https://doi.org/10.1007/s10853-023-08208-w.

[168] B. Straumal, N. Martynenko, D. Temralieva, V. Serebryany, N. Tabachkova, I. Shchetinin, N. Anisimova, M. Kiselevskiy, A. Kolyanova, G. Raab, R. Willumeit-Römer, S. Dobatkin, Y. Estrin, The Effect of Equal-Channel Angular Pressing on Microstructure, Mechanical Properties, and Biodegradation Behavior of Magnesium Alloyed with Silver and Gadolinium, Crystals 10 (2020) 918. https://doi.org/10.3390/cryst10100918.

[169] J. Zhang, Z. Kang, F. Wang, Mechanical properties and biocorrosion resistance of the Mg-Gd-Nd-Zn-Zr alloy processed by equal channel angular pressing, Mater. Sci. Eng. C 68 (2016) 194–197. https://doi.org/10.1016/j.msec.2016.05.118.

[170] N. Martynenko, E. Lukyanova, N. Anisimova, M. Kiselevskiy, V. Serebryany, N. Yurchenko, G. Raab, N. Birbilis, G. Salishchev, S. Dobatkin, Y. Estrin, Improving the property profile of a bioresorbable Mg-Y-Nd-Zr alloy by deformation treatments, Materialia 13 (2020) 100841. https://doi.org/10.1016/j.mtla.2020.100841.

[171] J.-X. Chen, X.-Y. Zhu, L.-L. Tan, K. Yang, X.-P. Su, Effects of ECAP Extrusion on the Microstructure, Mechanical Properties and Biodegradability of Mg–2Zn–xGd–0.5Zr Alloys, Acta Metall. Sin. Engl. Lett. 34 (2021) 205–216. https://doi.org/10.1007/s40195-020-01136-7.

[172] B. Du, Z. Hu, J. Wang, L. Sheng, H. Zhao, Y. Zheng, T. Xi, Effect of extrusion process on the mechanical and in vitro degradation performance of a biomedical Mg-Zn-Y-Nd alloy, Bioact. Mater. 5 (2020) 219–227. https://doi.org/10.1016/j.bioactmat.2020.02.002.

[173] X. Zhang, Z. Wang, G. Yuan, Y. Xue, Improvement of mechanical properties and corrosion resistance of biodegradable Mg–Nd–Zn–Zr alloys by double extrusion, Mater. Sci. Eng. B 177 (2012) 1113–1119. https://doi.org/10.1016/j.mseb.2012.05.020.

[174] K. Chen, X.B. Zhang, J.W. Dai, Y. Fei, Z.Z. Wang, Enhanced mechanical and corrosion properties of NZ20K alloy by double extrusion and aging processes for biomedical applications, Mater. Technol. 31 (2016) 210–215. https://doi.org/10.1179/1753555715Y.0000000043.

[175] K. Munir, J. Lin, C. Wen, P.F.A. Wright, Y. Li, Mechanical, corrosion, and biocompatibility properties of Mg-Zr-Sr-Sc alloys for biodegradable implant applications, Acta Biomater. 102 (2020) 493–507. https://doi.org/10.1016/j.actbio.2019.12.001.

[176] R.R. Kottuparambil, S. Bontha, R.M. Rangarasaiah, S.B. Arya, A. Jana, M. Das, V.K. Balla, S. Amrithalingam, T.R. Prabhu, Effect of zinc and rare-earth element addition on mechanical, corrosion, and biological properties of magnesium, J. Mater. Res. 33 (2018) 3466–3478. https://doi.org/10.1557/jmr.2018.311.

[177] X. Zhang, J. Dai, H. Yang, S. Liu, X. He, Z. Wang, Influence of Gd and Ca on microstructure, mechanical and corrosion properties of Mg–Gd–Zn(–Ca) alloys, Mater. Technol. 32 (2017) 399–408. https://doi.org/10.1080/10667857.2016.1262310.

[178] B. Kiran Babu, A. Jawahar Babu, G. Ranga Janardhana, Tailoring ZE41 Mg Alloy by Friction Stir Processing for Biomedical Applications: Role of Microstructure on the Degradation and Mechanical Behavior in Simulated Body Fluids, Trans. Indian Inst. Met. 73 (2020) 2889–2899. https://doi.org/10.1007/s12666-020-02090-9.

[179] X. Zhao, L. Shi, J. Xu, Biodegradable Mg-Zn-Y alloys with long-period stacking ordered structure: optimization for mechanical properties, J. Mech. Behav. Biomed. Mater. 18 (2013) 181–190. https://doi.org/10.1016/j.jmbbm.2012.11.016.

[180] Y. Tan, W. Li, W. Hu, X. Shi, L. Tian, The Effect of ECAP Temperature on the Microstructure and Properties of a Rolled Rare Earth Magnesium Alloy, Materials 12 (2019) 1554. https://doi.org/10.3390/ma12091554.

[181] A. Torkian, G. Faraji, M.S. Pedram, Mechanical properties and in vivo biodegradability of Mg–Zr–Y–Nd–La magnesium alloy produced by a combined severe plastic deformation, Rare Met. 40 (2021) 651–662. https://doi.org/10.1007/s12598-019-01353-9.

[182] Y. Jiao, J. Zhang, P. Kong, Z. Zhang, Y. Jing, J. Zhuang, W. Wang, L. Zhang, C. Xu, R. Wu, M. Zhang, Enhancing the performance of Mg-based implant materials by introducing basal plane stacking faults, J. Mater. Chem. B 3 (2015) 7386–7400. https://doi.org/10.1039/C5TB01060H.

[183] L. Li, T. Wang, Y. Wang, C. Zhang, H. Lv, H. Lin, W. Yu, C. Huang, Effects of ytterbium addition and heat treatment on the mechanical properties and biocorrosion

behaviors of Mg–Zn–Zr alloy, J. Magnes. Alloys 8 (2020) 499–509. https://doi.org/10.1016/j.jma.2019.11.013.

[184] Y. Xu, J. Li, M. Qi, J. Gu, The influence of Gd content on the microstructure, mechanical properties, corrosion behavior and corrosion film deposition mechanisms of as-extruded Mg–Zn–Mn–Sr–Gd alloys for biomedical applications, J. Mater. Sci. 57 (2022) 2053–2072. https://doi.org/10.1007/s10853-021-06622-6.

[185] J. Bohlen, S. Meyer, B. Wiese, B.J.C. Luthringer-Feyerabend, R. Willumeit-Römer, D. Letzig, Alloying and Processing Effects on the Microstructure, Mechanical Properties, and Degradation Behavior of Extruded Magnesium Alloys Containing Calcium, Cerium, or Silver, Materials 13 (2020) 391. https://doi.org/10.3390/ma13020391.

[186] X. Zhang, J. Dai, Q. Dong, Z. Ba, Y. Wu, Corrosion behavior and mechanical degradation of as-extruded Mg–Gd–Zn–Zr alloys for orthopedic application, J. Biomed. Mater. Res. B Appl. Biomater. 108 (2020) 698–708. https://doi.org/10.1002/jbm.b.34424.

[187] Y.-L. Zhou, Y. Li, D.-M. Luo, Y. Ding, P. Hodgson, Microstructures, mechanical and corrosion properties and biocompatibility of as extruded Mg–Mn–Zn–Nd alloys for biomedical applications, Mater. Sci. Eng. C 49 (2015) 93–100. https://doi.org/10.1016/j.msec.2014.12.057.

[188] B. Wiese, J. Harmuth, R. Willumeit-Römer, J. Bohlen, Property Variation of Extruded Mg-Gd Alloys by Mn Addition and Processing, Crystals 12 (2022) 1036. https://doi.org/10.3390/cryst12081036.

[189] D. Dvorský, J. Kubásek, I. Voňavková, D. Vojtěch, Structure, mechanical and corrosion properties of extruded Mg-Nd-Zn, Mg-Y-Zn and Mg-Y-Nd alloys, Mater. Sci. Technol. 35 (2019) 520–529. https://doi.org/10.1080/02670836.2019.1570680.

[190] D. Merson, A. Brilevsky, P. Myagkikh, A. Tarkova, A. Prokhorikhin, E. Kretov, T. Frolova, A. Vinogradov, The Functional Properties of Mg–Zn–X Biodegradable Magnesium Alloys, Materials 13 (2020) 544. https://doi.org/10.3390/ma13030544.

[191] Y. Zhang, M. Gao, I.P. Etim, L. Tan, K. Yang, Optimising the torsional properties and corrosion resistance of biodegradable WE43 Mg alloy by ECAP and subsequent ageing, Mater. Technol. 35 (2020) 402–410. https://doi.org/10.1080/10667857.2019.1688539.

[192] H. Miao, D. Zhang, C. Chen, L. Zhang, J. Pei, Y. Su, H. Huang, Z. Wang, B. Kang, W. Ding, H. Zeng, G. Yuan, Research on Biodegradable Mg–Zn–Gd Alloys for Potential Orthopedic Implants: In Vitro and in Vivo Evaluations, ACS Biomater. Sci. Eng. 5 (2019) 1623–1634. https://doi.org/10.1021/acsbiomaterials.8b01563.

[193] B. Wu, F. Yusof, F. Li, B.B. Abdul Razak, M.R. Bin Muhamad, I.A. Badruddin, M. Hussien, S. Kamangar, M.Z. Ibrahim, Influence of Friction Stir Processing Parameters on Microstructure, Hardness and Corrosion Resistance of Biocompatible Mg Alloy WE43, Arab. J. Sci. Eng. (2023). https://doi.org/10.1007/s13369-023-08037-8.

[194] J. Chen, J. Zhan, S.K. Kolawole, L. Tan, K. Yang, J. Wang, X. Su, Effects of Different Rare Earth Elements on the Degradation and Mechanical Properties of the ECAP Extruded Mg Alloys, Materials 15 (2022) 627. https://doi.org/10.3390/ma15020627.

[195] D. Bian, J. Deng, N. Li, X. Chu, Y. Liu, W. Li, H. Cai, P. Xiu, Y. Zhang, Z. Guan, Y. Zheng, Y. Kou, B. Jiang, R. Chen, In Vitro and in Vivo Studies on Biomedical Magnesium Low-Alloying with Elements Gadolinium and Zinc for Orthopedic Implant Applications, ACS Appl. Mater. Interfaces 10 (2018) 4394–4408. https://doi.org/10.1021/acsami.7b15498.

[196] J. Chen, S. Wei, L. Tan, K. Yang, Effects of solution treatment on mechanical properties and degradation of Mg-2Zn-0.5Nd-0.5Zr alloy, Mater. Technol. 34 (2019) 592–601. https://doi.org/10.1080/10667857.2019.1603657.

[197] Y. Luan, P. Mao, L. Tan, J. Sun, M. Gao, Z. Ma, Optimising the mechanical properties and corrosion resistance of biodegradable Mg-2Zn-0.5Nd alloy by solution treatment, Mater. Technol. 37 (2022) 663–672. https://doi.org/10.1080/10667857.2020.1868747.

[198] R. Pinto, M.G.S. Ferreira, M.J. Carmezim, M.F. Montemor, The corrosion behaviour of rare-earth containing magnesium alloys in borate buffer solution, Electrochimica Acta 56 (2011) 1535–1545. https://doi.org/10.1016/j.electacta.2010.09.081.

[199] Y. Song, D. Shan, E.-H. Han, Pitting corrosion of a Rare Earth Mg alloy GW93, J. Mater. Sci. Technol. 33 (2017) 954–960. https://doi.org/10.1016/j.jmst.2017.01.014.

[200] J. Liu, Y. Song, J. Chen, P. Chen, D. Shan, E.-H. Han, The Special Role of Anodic Second Phases in the Micro-galvanic Corrosion of EW75 Mg Alloy, Electrochimica Acta 189 (2016) 190–195. https://doi.org/10.1016/j.electacta.2015.12.075.

[201] G. Song, A. Atrens, Understanding Magnesium Corrosion—A Framework for Improved Alloy Performance, Adv. Eng. Mater. 5 (2003) 837–858. https://doi.org/10.1002/adem.200310405.

[202] S. Yin, W. Duan, W. Liu, L. Wu, J. Yu, Z. Zhao, M. Liu, P. Wang, J. Cui, Z. Zhang, Influence of specific second phases on corrosion behaviors of Mg-Zn-Gd-Zr alloys, Corros. Sci. 166 (2020) 108419. https://doi.org/10.1016/j.corsci.2019.108419.

[203] W. Liu, F. Cao, L. Chang, Z. Zhang, J. Zhang, Effect of rare earth element Ce and La on corrosion behavior of AM60 magnesium alloy, Corros. Sci. 51 (2009) 1334–1343. https://doi.org/10.1016/j.corsci.2009.03.018.

[204] C. Shuai, Y. Yang, S. Peng, C. Gao, P. Feng, J. Chen, Y. Liu, X. Lin, S. Yang, F. Yuan, Nd-induced honeycomb structure of intermetallic phase enhances the corrosion resistance of Mg alloys for bone implants, J. Mater. Sci. Mater. Med. 28 (2017) 130. https://doi.org/10.1007/s10856-017-5945-0.

[205] V.B. Oliveira, L.R. Viera, B. de A. Lima, P.R.T. Avila, G.C. Rêgo, H.C. Pinto, I.N. Bastos, E.P. da Silva, Corrosion behavior of as-cast ZK60 alloy modified with rare earth addition in sodium sulfate medium, Corros. Sci. 158 (2019) 108092. https://doi.org/10.1016/j.corsci.2019.108092.

[206] Y. Zhang, Y. Huang, F. Feyerabend, C. Blawert, W. Gan, E. Maawad, S. You, S. Gavras, N. Scharnagl, J. Bode, C. Vogt, D. Zander, R. Willumeit-Römer, K.U. Kainer, N. Hort, Influence of the amount of intermetallics on the degradation of Mg-Nd alloys under physiological conditions, Acta Biomater. 121 (2021) 695–712. https://doi.org/10.1016/j.actbio.2020.11.050.

[207] A.E. Coy, F. Viejo, P. Skeldon, G.E. Thompson, Susceptibility of rare-earth-magnesium alloys to micro-galvanic corrosion, Corros. Sci. 52 (2010) 3896–3906. https://doi.org/10.1016/j.corsci.2010.08.006.

[208] X. Yuan, Y. Du, D. Dong, D. Liu, B. Jiang, Corrosion Resistance Improvement of an Extruded Mg-Gd-Y-Zn-Zr-Ca via Aging Treatment, J. Mater. Eng. Perform. 31 (2022) 2909–2917. https://doi.org/10.1007/s11665-021-06455-z.

[209] J. Xie, L. Wang, J. Zhang, L. Lu, Z. Zhang, Y. He, R. Wu, Developing new Mg alloy as potential bone repair material via constructing weak anode nano-lamellar structure, J. Magnes. Alloys 11 (2023) 154–175. https://doi.org/10.1016/j.jma.2022.08.011.

[210] C. Cai, R. Song, L. Wang, J. Li, Effect of anodic T phase on surface micro-galvanic corrosion of biodegradable Mg-Zn-Zr-Nd alloys, Appl. Surf. Sci. 462 (2018) 243–254. https://doi.org/10.1016/j.apsusc.2018.08.107.

[211] J. Liu, L. Yang, C. Zhang, B. Zhang, T. Zhang, Y. Li, K. Wu, F. Wang, Role of the LPSO structure in the improvement of corrosion resistance of Mg-Gd-Zn-Zr alloys, J. Alloys Compd. 782 (2019) 648–658. https://doi.org/10.1016/j.jallcom.2018.12.233.

[212] A. Atrens, M. Liu, N.I. Zainal Abidin, Corrosion mechanism applicable to biodegradable magnesium implants, Mater. Sci. Eng. B 176 (2011) 1609–1636. https://doi.org/10.1016/j.mseb.2010.12.017.

[213] Pilling-Bedworth ratio for oxidation of alloys: Materials Research Innovations: Vol 3, No 4, (n.d.). https://www.tandfonline.com/doi/abs/10.1007/s100190050008 (accessed April 21, 2024).

[214] J. Liu, Y. Lin, D. Bian, M. Wang, Z. Lin, X. Chu, W. Li, Y. Liu, Z. Shen, Y. Liu, Y. Tong, Z. Xu, Y. Zhang, Y. Zheng, In vitro and in vivo studies of Mg-30Sc alloys with different phase structure for potential usage within bone, Acta Biomater. 98 (2019) 50–66. https://doi.org/10.1016/j.actbio.2019.03.009.

[215] Y.M. Kim, C.D. Yim, H.S. Kim, B.S. You, Key factor influencing the ignition resistance of magnesium alloys at elevated temperatures, Scr. Mater. 65 (2011) 958–961. https://doi.org/10.1016/j.scriptamat.2011.08.019.

[216] Q. Jiang, D. Lu, C. Liu, N. Liu, B. Hou, The Pilling-Bedworth Ratio of Oxides Formed From the Precipitated Phases in Magnesium Alloys, Front. Mater. 8 (2021). https://doi.org/10.3389/fmats.2021.761052.

[217] R.-C. Zeng, L. Sun, Y.-F. Zheng, H.-Z. Cui, E.-H. Han, Corrosion and characterisation of dual phase Mg–Li–Ca alloy in Hank's solution: The influence of

microstructural features, Corros. Sci. 79 (2014) 69–82. https://doi.org/10.1016/j.corsci.2013.10.028.

[218] J. Liu, E. Han, Y. Song, D. Shan, Effect of twins on the corrosion behavior of Mg–5Y–7Gd–1Nd–0.5Zr Mg alloy, J. Alloys Compd. 757 (2018) 356–363. https://doi.org/10.1016/j.jallcom.2018.05.105.

[219] F. Rosalbino, E. Angelini, S. De Negri, A. Saccone, S. Delfino, Electrochemical behaviour assessment of novel Mg-rich Mg–Al–RE alloys (RE=Ce, Er), Intermetallics 14 (2006) 1487–1492. https://doi.org/10.1016/j.intermet.2006.01.056.

[220] T. Takenaka, T. Ono, Y. Narazaki, Y. Naka, M. Kawakami, Improvement of corrosion resistance of magnesium metal by rare earth elements, Electrochimica Acta 53 (2007) 117–121. https://doi.org/10.1016/j.electacta.2007.03.027.

[221] O.I. Velikokhatnyi, P.N. Kumta, First-principles studies on alloying and simplified thermodynamic aqueous chemical stability of calcium-, zinc-, aluminum-, yttrium- and iron-doped magnesium alloys, Acta Biomater. 6 (2010) 1698–1704. https://doi.org/10.1016/j.actbio.2009.08.016.

[222] J. Zhang, M. Xu, X. Teng, M. Zuo, Effect of Gd addition on microstructure and corrosion behaviors of Mg–Zn–Y alloy, J. Magnes. Alloys 4 (2016) 319–325. https://doi.org/10.1016/j.jma.2016.09.003.

[223] D. Persaud-Sharma, A. McGoron, Biodegradable Magnesium Alloys: A Review of Material Development and Applications, J. Biomim. Biomater. Tissue Eng. 12 (2011) 25–39. https://doi.org/10.4028/www.scientific.net/JBBTE.12.25.

[224] Q. Peng, Y. Huang, L. Zhou, N. Hort, K.U. Kainer, Preparation and properties of high purity Mg–Y biomaterials, Biomaterials 31 (2010) 398–403. https://doi.org/10.1016/j.biomaterials.2009.09.065.

[225] Z. Xu, C. Smith, S. Chen, J. Sankar, Development and microstructural characterizations of Mg–Zn–Ca alloys for biomedical applications, Mater. Sci. Eng. B 176 (2011) 1660–1665. https://doi.org/10.1016/j.mseb.2011.06.008.

[226] A. Boby, A. Srinivasan, U.T.S. Pillai, B.C. Pai, Mechanical characterization and corrosion behavior of newly designed Sn and Y added AZ91 alloy, Mater. Des. 88 (2015) 871–879. https://doi.org/10.1016/j.matdes.2015.09.010.

[227] D. Ahmadkhaniha, M. Fedel, M. Heydarzadeh Sohi, F. Deflorian, Corrosion behavior of severely plastic deformed magnesium based alloys: A review, Surf. Eng. Appl. Electrochem. 53 (2017) 439–448. https://doi.org/10.3103/S1068375517050039.

[228] A. Bahmani, M. Lotfpour, M. Taghizadeh, W.-J. Kim, Corrosion behavior of severely plastically deformed Mg and Mg alloys, J. Magnes. Alloys 10 (2022) 2607–2648. https://doi.org/10.1016/j.jma.2022.09.007.

[229] C. op't Hoog, N. Birbilis, Y. Estrin, Corrosion of Pure Mg as a Function of Grain Size and Processing Route, Adv. Eng. Mater. 10 (2008) 579–582. https://doi.org/10.1002/adem.200800046.

[230] J. Jiang, F. Zhang, A. Ma, D. Song, J. Chen, H. Liu, M. Qiang, Biodegradable Behaviors of Ultrafine-Grained ZE41A Magnesium Alloy in DMEM Solution, Metals 6 (2016) 3. https://doi.org/10.3390/met6010003.

[231] B.J. Wang, D.K. Xu, Y.C. Xin, L.Y. Sheng, E.H. Han, High corrosion resistance and weak corrosion anisotropy of an as-rolled Mg-3Al-1Zn (in wt.%) alloy with strong crystallographic texture, Sci. Rep. 7 (2017) 16014. https://doi.org/10.1038/s41598-017-16351-z.

[232] R.S. Lillard, G.F. Wang, M.I. Baskes, The Role of Metallic Bonding in the Crystallographic Pitting of Magnesium, J. Electrochem. Soc. 153 (2006) B358. https://doi.org/10.1149/1.2218108.

[233] Effects of Deformation Texture and Grain Size on Corrosion Behavior of Mg–3Al–1Zn Alloy Sheets | ACS Omega, (n.d.). https://pubs.acs.org/doi/full/10.1021/acsomega.9b03009 (accessed January 31, 2024).

[234] G. Han, J.-Y. Lee, Y.-C. Kim, J.H. Park, D.-I. Kim, H.-S. Han, S.-J. Yang, H.-K. Seok, Preferred crystallographic pitting corrosion of pure magnesium in Hanks' solution, Corros. Sci. 63 (2012) 316–322. https://doi.org/10.1016/j.corsci.2012.06.011.

[235] X. Liu, G. Chen, X. Zhong, T. Wang, X. He, W. Yuan, P. Zhang, Y. Liu, D. Cao, S. Chen, K. Manabe, Z. Jiang, T. Furushima, D. Kent, Y. Chen, G. Ni, M. Gao, H. Li, Degradation of differently processed Mg-based implants leads to distinct foreign body reactions (FBRs) through dissimilar signaling pathways, J. Magnes. Alloys (2022). https://doi.org/10.1016/j.jma.2022.03.017.

[236] Y. Liu, J. Wen, H. Li, J. He, Effects of extrusion parameters on the microstructure, corrosion resistance, and mechanical properties of biodegradable Mg–Zn–Gd–Y–Zr alloy, J. Alloys Compd. 891 (2022) 161964. https://doi.org/10.1016/j.jallcom.2021.161964.

[237] V.C. Shunmugasamy, M. AbdelGawad, M.U. Sohail, T. Ibrahim, T. Khan, T.D. Seers, B. Mansoor, In vitro and in vivo study on fine-grained Mg–Zn–RE–Zr alloy as a biodegradeable orthopedic implant produced by friction stir processing, Bioact. Mater. 28 (2023) 448–466. https://doi.org/10.1016/j.bioactmat.2023.06.010.

[238] S. Koleini, M.H. Idris, H. Jafari, Influence of hot rolling parameters on microstructure and biodegradability of Mg–1Ca alloy in simulated body fluid, Mater. Des. 33 (2012) 20–25. https://doi.org/10.1016/j.matdes.2011.06.063.

[239] L. Yang, N. Hort, D. Laipple, D. Höche, Y. Huang, K.U. Kainer, R. Willumeit, F. Feyerabend, Element distribution in the corrosion layer and cytotoxicity of alloy Mg-10Dy during in vitro biodegradation, Acta Biomater. 9 (2013) 8475–8487. https://doi.org/10.1016/j.actbio.2012.10.001.

[240] L. Mao, L. Shen, J. Niu, J. Zhang, W. Ding, Y. Wu, R. Fan, G. Yuan, Nanophasic biodegradation enhances the durability and biocompatibility of magnesium alloys for the next-generation vascular stents, Nanoscale 5 (2013) 9517–9522. https://doi.org/10.1039/C3NR02912C.

[241] A study of a biodegradable Mg–3Sc–3Y alloy and the effect of self-passivation on the in vitro degradation - ScienceDirect, (n.d.). https://www.sciencedirect.com/science/article/pii/S1742706112003716?via%3Dihub (accessed January 22, 2024).

[242] H.S. Brar, I.S. Berglund, J.B. Allen, M.V. Manuel, The role of surface oxidation on the degradation behavior of biodegradable Mg–RE (Gd, Y, Sc) alloys for resorbable implants, Mater. Sci. Eng. C 40 (2014) 407–417. https://doi.org/10.1016/j.msec.2014.03.055.

[243] Z. Geng, D. Xiao, L. Chen, Microstructure, mechanical properties, and corrosion behavior of degradable Mg-Al-Cu-Zn-Gd alloys, J. Alloys Compd. 686 (2016). https://doi.org/10.1016/j.jallcom.2016.05.288.

[244] L. Liu, F. Yuan, M. Zhao, C. Gao, P. Feng, Y. Yang, S. Yang, C. Shuai, Rare Earth Element Yttrium Modified Mg-Al-Zn Alloy: Microstructure, Degradation Properties and Hardness, Materials 10 (2017) 477. https://doi.org/10.3390/ma10050477.

[245] Y. Zhang, J.-Y. Li, Y. Liu, L.-S. Chen, Microstructure characteristics, film layer rupture mechanism and corrosion behavior of hot-rolled Mg-2Zn-0.2Mn-*x*Nd, Mater. Charact. 165 (2020) 110368. https://doi.org/10.1016/j.matchar.2020.110368.

[246] X. Zhang, G. Yuan, Z. Wang, Mechanical properties and biocorrosion resistance of Mg-Nd-Zn-Zr alloy improved by cyclic extrusion and compression, Mater. Lett. 74 (2012) 128–131. https://doi.org/10.1016/j.matlet.2012.01.086.

[247] Corrosion behavior of Mg–3Gd–1Zn–0.4Zr alloy with and without stacking faults - ScienceDirect, (n.d.). https://www.sciencedirect.com/science/article/pii/S2213956719300313 (accessed July 16, 2024).

[248] G. Cao, D. Zhang, W. Zhang, W. Zhang, In Vitro Corrosion Study of Friction Stir Processed WE43 Magnesium Alloy in a Simulated Body Fluid, Materials 9 (2016) 542. https://doi.org/10.3390/ma9070542.

[249] F. Zhang, A. Ma, J. Jiang, H. Xu, D. Song, F. Lu, Y. Nishida, Enhanced biodegradation behavior of ultrafine-grained ZE41A magnesium alloy in Hank's solution, Prog. Nat. Sci. Mater. Int. 23 (2013) 420–424. https://doi.org/10.1016/j.pnsc.2013.06.003.

[250] L.-S. Wang, J.-H. Jiang, B. Saleh, Q.-Y. Xie, Q. Xu, H. Liu, A.-B. Ma, Controlling Corrosion Resistance of a Biodegradable Mg–Y–Zn Alloy with LPSO Phases via Multi-pass ECAP Process, Acta Metall. Sin. Engl. Lett. 33 (2020) 1180–1190. https://doi.org/10.1007/s40195-020-01042-y.

[251] E. Naderi, A. Davoodi, H.R. Jafarian, Investigating Effect of ECAP Process on Corrosion Behavior of WE43 Magnesium Alloy in Simulated Body Fluid, Met. Mater. Int. 29 (2023) 3161–3177. https://doi.org/10.1007/s12540-023-01453-3.

[252] Q. Wu, S. Zhu, L. Wang, Q. Liu, G. Yue, J. Wang, S. Guan, The microstructure and properties of cyclic extrusion compression treated Mg–Zn–Y–Nd alloy for vascular stent application, J. Mech. Behav. Biomed. Mater. 8 (2012) 1–7. https://doi.org/10.1016/j.jmbbm.2011.12.011.

[253] P. Maier, N. Lauth, C.L. Mendis, M. Bechly, N. Hort, Mechanical and Corrosion Properties of Two Precipitation-Hardened Mg-Y-Nd-Gd-Dy Alloys with Small Changes in Chemical Composition, JOM 71 (2019) 1426–1435. https://doi.org/10.1007/s11837-019-03359-1.

[254] Z. Gui, Z. Kang, Y. Zhou, J. Zhang, Effect of the Content and Morphology of β-Compounds and Precipitation on the Corrosion Behavior of Biodegradable Magnesium Alloys, Adv. Eng. Mater. 23 (2021) 2000752. https://doi.org/10.1002/adem.202000752.

[255] X.B. Zhang, G.Y. Yuan, X.X. Fang, Z.Z. Wang, T. Zhang, Effects of solution treatment on yield ratio and biocorrosion behaviour of as-extruded Mg–2·7Nd–0·2Zn–0·4Zr alloy for cardiovascular stent application, Mater. Technol. 28 (2013) 155–158. https://doi.org/10.1179/1753555712Y.0000000048.

[256] X.B. Zhang, Y. Zhang, K. Chen, Z.X. Ba, Z.Z. Wang, Q. Wang, Microstructure, mechanical and corrosion properties of Mg–Nd–Zn–Sr–Zr alloy as a biodegradable material, Mater. Sci. Technol. 31 (2015) 866–873. https://doi.org/10.1179/1743284714Y.0000000661.

[257] X. Ma, Q. Jiang, Y. Li, B. Hou, Effect of Heat Treatment on Corrosion Behaviors of Mg-5Y-1.5Nd Alloys, Int. J. Electrochem. 2016 (2016) 7097589. https://doi.org/10.1155/2016/7097589.

[258] E. Willbold, X. Gu, D. Albert, K. Kalla, K. Bobe, M. Brauneis, C. Janning, J. Nellesen, W. Czayka, W. Tillmann, Y. Zheng, F. Witte, Effect of the addition of low rare earth elements (lanthanum, neodymium, cerium) on the biodegradation and biocompatibility of magnesium, Acta Biomater. 11 (2015) 554–562. https://doi.org/10.1016/j.actbio.2014.09.041.

[259] J. Dai, X. Zhang, Z. Wang, Microstructure and enhanced corrosion resistance of biodegradable Mg–Gd–Cu–Zr alloy by solution treatment, Mater. Technol. 33 (2018) 301–310. https://doi.org/10.1080/10667857.2018.1438154.

[260] L. Shi, Y. Huang, L. Yang, F. Feyerabend, C. Mendis, R. Willumeit, K. Ulrich Kainer, N. Hort, Mechanical properties and corrosion behavior of Mg–Gd–Ca–Zr alloys for medical applications, J. Mech. Behav. Biomed. Mater. 47 (2015) 38–48. https://doi.org/10.1016/j.jmbbm.2015.03.003.

[261] M. Vlček, F. Lukáč, H. Kudrnová, B. Smola, I. Stulíková, M. Luczak, G. Szakács, N. Hort, R. Willumeit-Römer, Microhardness and In Vitro Corrosion of Heat-Treated Mg–Y–Ag Biodegradable Alloy, Materials 10 (2017) 55. https://doi.org/10.3390/ma10010055.

[262] Y. Zhang, Y. Huang, F. Feyerabend, S. Gavras, Y. Xu, R. Willumeit-Römer, K.U. Kainer, N. Hort, Effects of Intermetallic Microstructure on Degradation of Mg-5Nd Alloy, Metall. Mater. Trans. A 51 (2020) 5498–5515. https://doi.org/10.1007/s11661-020-05926-7.

[263] C. Liu, J. Wang, Y. Xu, Y. Fu, J. Han, Z. Cao, X. Chen, S. Zhao, X. Zhu, In Vitro Corrosion Performance of As-Extruded Mg–Gd–Dy–Zr Alloys for Potential Orthopedic Applications, Metals 12 (2022) 604. https://doi.org/10.3390/met12040604.

[264] P. Minárik, E. Jablonská, R. Král, J. Lipov, T. Ruml, C. Blawert, B. Hadzima, F. Chmelík, Effect of equal channel angular pressing on in vitro degradation of LAE442 magnesium alloy, Mater. Sci. Eng. C 73 (2017) 736–742. https://doi.org/10.1016/j.msec.2016.12.120.

[265] M. Gao, C. Jia, D. Ni, Y. Luan, I.P. Etim, K. Yang, R.D.K. Misra, L. Tan, Z. Ma, Influence of microstructure modification on corrosion resistance of friction stir processing biodegradable Mg-Zn-Nd alloy, Mater. Technol. 37 (2022) 57–62. https://doi.org/10.1080/10667857.2020.1807788.

[266] JCI - THE ANTICOAGULANT EFFECTS IN RABBITS AND MAN OF THE INTRAVENOUS INJECTION OF SALTS OF THE RARE EARTHS, (n.d.). https://www.jci.org/articles/view/101321 (accessed January 22, 2024).

[267] Exposure, metabolism, and toxicity of rare earths and related compounds. - PMC, (n.d.). https://www.ncbi.nlm.nih.gov/pmc/articles/PMC1469566/ (accessed January 22, 2024).

[268] C.H. Evans, Biochemistry of the Lanthanides, in: Springer US, Boston, MA, 1990. https://doi.org/10.1007/978-1-4684-8748-0.

[269] G. Pagano, F. Tommasi, M. Guida, Comparative toxicity of cerium and of other rare earth elements (REEs) in plant and invertebrate test systems, Cerium Mol. Struct. Technol. Appl. Health Eff. (2012) 107–124.

[270] T.J. Haley, N. Komesu, L. Mavis, J. Cawthorne, H.C. Upham, Pharmacology and Toxicology of Scandium Chloride, J. Pharm. Sci. 51 (1962) 1043–1045. https://doi.org/10.1002/jps.2600511107.

[271] S. Hirano, N. Kodama, K. Shibata, K.T. Suzuki, Metabolism and Toxicity of Intravenously Injected Yttrium Chloride in Rats, Toxicol. Appl. Pharmacol. 121 (1993) 224–232. https://doi.org/10.1006/taap.1993.1149.

[272] J. Yang, Q. Liu, L. Zhang, S. Wu, M. Qi, S. Lu, Q. Xi, Y. Cai, Lanthanum chloride impairs memory, decreases pCaMK IV, pMAPK and pCREB expression of hippocampus in rats, Toxicol. Lett. 190 (2009) 208–214. https://doi.org/10.1016/j.toxlet.2009.07.016.

[273] T.J. Haley, Pharmacology and Toxicology of the Rare Earth Elements, J. Pharm. Sci. 54 (1965) 663–670. https://doi.org/10.1002/jps.2600540502.

[274] R.J. Palmer, J.L. Butenhoff, J.B. Stevens, Cytotoxicity of the rare earth metals cerium, lanthanum, and neodymium *in vitro:* Comparisons with cadmium in a pulmonary macrophage primary culture system, Environ. Res. 43 (1987) 142–156. https://doi.org/10.1016/S0013-9351(87)80066-X.

[275] S. Weilin, S. Xiuying, M. Xiying, Effects of Samarium on Liver and Kidney of Rats, J. Rare Earths 24 (2006) 415–418. https://doi.org/10.1016/S1002-0721(07)60416-5.

[276] Pharmacology and Toxicology of Lutetium Chloride - ScienceDirect, (n.d.). https://www.sciencedirect.com/science/article/abs/pii/S0022354915346128 (accessed April 24, 2024).

[277] T.J. Haley, N. Komesu, G. Colvin, L. Koste, H.C. Upham, Pharmacology and Toxicology of Europium Chloride, J. Pharm. Sci. 54 (1965) 643–645. https://doi.org/10.1002/jps.2600540435.

[278] E.J. Bernstein, C. Schmidt-Lauber, J. Kay, Nephrogenic systemic fibrosis: A systemic fibrosing disease resulting from gadolinium exposure, Best Pract. Res. Clin. Rheumatol. 26 (2012) 489–503. https://doi.org/10.1016/j.berh.2012.07.008.

[279] A. Shinohara, M. Chiba, M. Kikuchi, Determination of Terbium in Organs of Mice Administered Terbium Chloride: Comparative Study of Fluorometry and Atomic Absorption Spectrometry, J. Anal. Toxicol. 13 (1989) 135–140. https://doi.org/10.1093/jat/13.3.135.

[280] T.J. Haley, L. Koste, N. Komesu, M. Efros, H.C. Upham, Pharmacology and toxicology of dysprosium, holmium, and erbium chlorides, Toxicol. Appl. Pharmacol. 8 (1966) 37–43. https://doi.org/10.1016/0041-008X(66)90098-6.

[281] A.Z. Thomas, L. Smyth, D. Hennessey, F. O'Kelly, D. Moran, T.H. Lynch, Zero Ischemia Laparoscopic Partial Thulium Laser Nephrectomy, J. Endourol. 27 (2013) 1366–1370. https://doi.org/10.1089/end.2012.0527.

[282] F. Li, Y. Wang, Z. Zhang, J. Sun, H. Xiao, Z. Chai, Distribution of samarium and ytterbium in rats measured by enriched stable isotope tracer technique and INAA, J. Radioanal. Nucl. Chem. 251 (2002) 437–441. https://doi.org/10.1023/A:1014886226165.

[283] S.A. Mirmalek, E. Jangholi, M. Jafari, S. Yadollah-Damavandi, M.A. Javidi, Y. Parsa, T. Parsa, S.A. Salimi-Tabatabaee, H.G. Kolagar, S.K. Jalil, R. Alizadeh-Navaei, Comparison of in Vitro Cytotoxicity and Apoptogenic Activity of Magnesium Chloride and Cisplatin as Conventional Chemotherapeutic Agents in the MCF-7 Cell Line, Asian Pac. J. Cancer Prev. 17 (2016) 131–134. https://doi.org/10.7314/APJCP.2016.17.S3.131.

[284] object Object, CALCIUM CHLORIDE, (n.d.). https://core.ac.uk/reader/24061280 (accessed December 26, 2024).

[285] T. Gupta, G. Talukder, A. Sharma, Cytotoxicity of zinc chloride in mice in vivo, Biol. Trace Elem. Res. 30 (1991) 95–101. https://doi.org/10.1007/BF02990346.

[286] X. Song, L. Chang, J. Wang, S. Zhu, L. Wang, K. Feng, Y. Luo, S. Guan, Investigation on the in vitro cytocompatibility of Mg-Zn-Y-Nd-Zr alloys as degradable orthopaedic implant materials, J. Mater. Sci. Mater. Med. 29 (2018) 44. https://doi.org/10.1007/s10856-018-6050-8.

[287] F. Feyerabend, J. Fischer, J. Holtz, F. Witte, R. Willumeit, H. Drücker, C. Vogt, N. Hort, Evaluation of short-term effects of rare earth and other elements used in magnesium alloys on primary cells and cell lines, Acta Biomater. 6 (2010) 1834–1842. https://doi.org/10.1016/j.actbio.2009.09.024.

[288] C.A. Grillo, F. Alvarez, M.A.F.L. de Mele, Cellular response to rare earth mixtures (La and Gd) as components of degradable Mg alloys for medical applications, Colloids Surf. B Biointerfaces 117 (2014) 312–321. https://doi.org/10.1016/j.colsurfb.2014.02.030.

[289] K.T. Rim, K.H. Koo, J.S. Park, Toxicological Evaluations of Rare Earths and Their Health Impacts to Workers: A Literature Review, Saf. Health Work 4 (2013) 12–26. https://doi.org/10.5491/SHAW.2013.4.1.12.

[290] Aylward and Findlay's SI Chemical Data, 7th Edition | Wiley, Wiley.Com (n.d.). https://www.wiley.com/en-gb/Aylward+and+Findlay%27s+SI+Chemical+Data%2C+7th+Edition-p-9780730302469 (accessed January 22, 2024).

[291] Antibacterial property of Ce-bearing stainless steels | Journal of Materials Science, (n.d.). https://link.springer.com/article/10.1007/s10853-006-0603-9 (accessed January 22, 2024).

[292] J.P. Yuan, W. Li, C. Wang, Effect of the La alloying addition on the antibacterial capability of 316L stainless steel, Mater. Sci. Eng. C Mater. Biol. Appl. 33 (2013) 446–452. https://doi.org/10.1016/j.msec.2012.09.012.

[293] T. Wakabayashi, A. Ymamoto, A. Kazaana, Y. Nakano, Y. Nojiri, M. Kashiwazaki, Antibacterial, Antifungal and Nematicidal Activities of Rare Earth Ions, Biol. Trace Elem. Res. 174 (2016) 464–470. https://doi.org/10.1007/s12011-016-0727-y.

[294] H.M.T.U. Herath, L.D. Silvio, J.R.G. Evans, Scandia—A potential biomaterial?, J. Mater. Sci. Mater. Med. 16 (2005) 1061–1065. https://doi.org/10.1007/s10856-005-4760-1.

[295] S. Hirano, K.T. Suzuki, Exposure, metabolism, and toxicity of rare earths and related compounds., Environ. Health Perspect. 104 (1996) 85–95. https://doi.org/10.1289/ehp.96104s185.

[296] D. Schubert, R. Dargusch, J. Raitano, S.-W. Chan, Cerium and yttrium oxide nanoparticles are neuroprotective, Biochem. Biophys. Res. Commun. 342 (2006) 86–91. https://doi.org/10.1016/j.bbrc.2006.01.129.

[297] C. Rössig, N. Angrisani, P. Helmecke, S. Besdo, J.-M. Seitz, B. Welke, N. Fedchenko, H. Kock, J. Reifenrath, In vivo evaluation of a magnesium-based degradable intramedullary nailing system in a sheep model, Acta Biomater. 25 (2015) 369–383. https://doi.org/10.1016/j.actbio.2015.07.025.

[298] F. Albaaj, A.J. Hutchison, Lanthanum carbonate (Fosrenol®): a novel agent for the treatment of hyperphosphataemia in renal failure and dialysis patients, Int. J. Clin. Pract. 59 (2005) 1091–1096. https://doi.org/10.1111/j.1368-5031.2005.00592.x.

[299] A. Rachid, M. Christophe, B.-M. Marc, O. Laure, T. Sylvie, P. Paul, Methemoglobinemia by cerium nitrate poisoning, Burns 32 (2006) 1060–1061. https://doi.org/10.1016/j.burns.2006.04.005.

[300] Y. Dai, J. Li, J. Li, L. Yu, G. Dai, A. Hu, L. Yuan, Z. Wen, Effects of rare earth compounds on growth and apoptosis of leukemic cell lines, Vitro Cell. Dev. Biol. - Anim. 38 (2002) 373–375. https://doi.org/10.1290/1071-2690(2002)038<0373:EORECO>2.0.CO;2.

[301] C. Yüksel, The Use of Neodymium Magnets in Healthcare and Their Effects on Health, North. Clin. Istanb. (2017). https://doi.org/10.14744/nci.2017.00483.

[302] P.M. Anderson, G.A. Wiseman, A. Dispenzieri, C.A.S. Arndt, L.C. Hartmann, W.A. Smithson, B.P. Mullan, O.S. Bruland, High-Dose Samarium-153 Ethylene Diamine Tetramethylene Phosphonate: Low Toxicity of Skeletal Irradiation in Patients With Osteosarcoma and Bone Metastases, J. Clin. Oncol. 20 (2002) 189–196. https://doi.org/10.1200/JCO.2002.20.1.189.

[303] B. Song, Y. Wu, M. Yu, P. Zhao, C. Zhou, G. E. Kiefer, A. Dean Sherry, A europium(iii)-based PARACEST agent for sensing singlet oxygen by MRI, Dalton Trans. 42 (2013) 8066–8069. https://doi.org/10.1039/C3DT50194A.

[304] Y. Ogawa, S. Suzuki, K. Naito, M. Saito, E. Kamata, A. Hirose, A. Ono, T. Kaneko, M. Chiba, Y. Inaba, Toxicity study of europium chloride in rats, J. Environ. Pathol. Toxicol. Oncol. 14 (1995) 1–9.

[305] C.R. Patra, S.S. Abdel Moneim, E. Wang, S. Dutta, S. Patra, M. Eshed, P. Mukherjee, A. Gedanken, V.H. Shah, D. Mukhopadhyay, *In vivo* toxicity studies of europium hydroxide nanorods in mice, Toxicol. Appl. Pharmacol. 240 (2009) 88–98. https://doi.org/10.1016/j.taap.2009.07.009.

[306] D.W. Bruce, B.E. Hietbrink, K.P. DuBois, The acute mammalian toxicity of rare earth nitrates and oxides, Toxicol. Appl. Pharmacol. 5 (1963) 750–759. https://doi.org/10.1016/0041-008X(63)90067-X.

[307] A. Myrissa, S. Braeuer, E. Martinelli, R. Willumeit-Römer, W. Goessler, A.M. Weinberg, Gadolinium accumulation in organs of Sprague–Dawley® rats after implantation of a biodegradable magnesium-gadolinium alloy, Acta Biomater. 48 (2017) 521–529. https://doi.org/10.1016/j.actbio.2016.11.024.

[308] A. deRoos, J. Doornbos, H.L. Bloem, T.H.M. Falke, D. Baleriaux, Clinical applications of gadolinium-DTPA in MRI, Raven Press, United States, 1988.

[309] G. Ratzinger, P. Agrawal, W. Körner, J. Lonkai, H.M.H.F. Sanders, E. Terreno, M. Wirth, G.J. Strijkers, K. Nicolay, F. Gabor, Surface modification of PLGA nanospheres with Gd-DTPA and Gd-DOTA for high-relaxivity MRI contrast agents, Biomaterials 31 (2010) 8716–8723. https://doi.org/10.1016/j.biomaterials.2010.07.095.

[310] Motexafin gadolinium generates reactive oxygen species and induces apoptosis in sensitive and highly resistant multiple myeloma cells | Blood | American Society of Hematology, (n.d.). https://ashpublications.org/blood/article/105/3/1265/19629/Motexafin-gadolinium-generates-reactive-oxygen (accessed April 27, 2024).

[311] R.J. Amato, J. Jac, J. Hernandez-McClain, Motexafin gadolinium for the treatment of metastatic renal cell carcinoma: phase II study results, Clin. Genitourin. Cancer 6 (2008) 73–78. https://doi.org/10.3816/CGC.2008.n.011.

[312] K. Matsumoto, H. Saitoh, T.L.H. Doan, A. Shiro, K. Nakai, A. Komatsu, M. Tsujimoto, R. Yasuda, T. Kawachi, T. Tajima, F. Tamanoi, Destruction of tumor mass by gadolinium-loaded nanoparticles irradiated with monochromatic X-rays: Implications for the Auger therapy, Sci. Rep. 9 (2019) 13275. https://doi.org/10.1038/s41598-019-49978-1.

[313] T. Zhang, R. Lan, C.-F. Chan, G.-L. Law, W.-K. Wong, K.-L. Wong, In vivo selective cancer-tracking gadolinium eradicator as new-generation photodynamic therapy agent, Proc. Natl. Acad. Sci. 111 (2014) E5492–E5497. https://doi.org/10.1073/pnas.1414499111.

[314] R. P. Baum, A. Singh, M. Benešová, C. Vermeulen, S. Gnesin, U. Köster, K. Johnston, D. Müller, S. Senftleben, H. R. Kulkarni, A. Türler, R. Schibli, J. O. Prior, N.P. van der Meulen, C. Müller, Clinical evaluation of the radiolanthanide terbium-152: first-in-human PET/CT with 152 Tb-DOTATOC, Dalton Trans. 46 (2017) 14638–14646. https://doi.org/10.1039/C7DT01936J.

[315] A.D. Watson, The use of gadolinium and dysprosium chelate complexes as contrast agents for magnetic resonance imaging, J. Alloys Compd. 207–208 (1994) 14–19. https://doi.org/10.1016/0925-8388(94)90168-6.

[316] Z.H. Endre, J.L. Allis, G.K. Radda, Toxicity of dysprosium shift reagents in the isolated perfused rat kidney, Magn. Reson. Med. 11 (1989) 267–274. https://doi.org/10.1002/mrm.1910110215.

[317] J.M.H. Teichman, K.F. Chan, P.P. Cecconi, N.S. Corbin, A.D. Kamerer, R.D. Glickman, A.J. Welch, ERBIUM:YAG VERSUS HOLMIUM:YAG LITHOTRIPSY, J. Urol. 165 (2001) 876–879. https://doi.org/10.1016/S0022-5347(05)66548-2.

[318] Y. Lotan, M.T. Gettman, K. Ogan, L.A. Baker, J.A. Cadeddu, Clinical Use of the Holmium:YAG Laser in Laparoscopic Partial Nephrectomy, J. Endourol. 16 (2002) 289–292. https://doi.org/10.1089/089277902760102767.

[319] P.W. Durbin, Distribution of the Transuranic Elements in Mammals, Health Phys. 8 (1962) 665.

[320] J. Taylor, J. Kieser, Forensic Odontology: Principles and Practice, John Wiley & Sons, 2016.

[321] A.F. El-Sherif, T.A. King, Soft and hard tissue ablation with short-pulse high peak power and continuous thulium-silica fibre lasers, Lasers Med. Sci. 18 (2003) 139–147. https://doi.org/10.1007/s10103-003-0267-5.

[322] P. Chellan, P.J. Sadler, The elements of life and medicines, Philos. Trans. R. Soc. Math. Phys. Eng. Sci. 373 (2015) 20140182. https://doi.org/10.1098/rsta.2014.0182.

[323] Z. Liu, T. Ma, H. Liu, Z. Jin, X. Sun, H. Zhao, J. Shi, B. Jia, F. Li, F. Wang, 177Lu-Labeled Antibodies for EGFR-Targeted SPECT/CT Imaging and Radioimmunotherapy in a Preclinical Head and Neck Carcinoma Model, Mol. Pharm. 11 (2014) 800–807. https://doi.org/10.1021/mp4005047.

[324] J.L. Sessler, W.C. Dow, D. O'Connor, A. Harriman, G. Hemmi, T.D. Mody, R.A. Miller, F. Qing, S. Springs, K. Woodburn, S.W. Young, Biomedical applications of lanthanide (III) texaphyrins Lutetium(III) texaphyrins as potential photodynamic therapy photosensitizers, J. Alloys Compd. 249 (1997) 146–152. https://doi.org/10.1016/S0925-8388(96)02517-0.

[325] G. Wang, S. Ge, Y. Shen, H. Wang, Q. Dong, Q. Zhang, J. Gao, Y. Wang, Study on the biodegradability and biocompatibility of WE magnesium alloys, Mater. Sci. Eng. C 32 (2012) 2190–2198. https://doi.org/10.1016/j.msec.2012.05.050.

[326] W.R. Zhou, Y.F. Zheng, M.A. Leeflang, J. Zhou, Mechanical property, biocorrosion and in vitro biocompatibility evaluations of Mg–Li–(Al)–(RE) alloys for future cardiovascular stent application, Acta Biomater. 9 (2013) 8488–8498. https://doi.org/10.1016/j.actbio.2013.01.032.

[327] T. Li, Y. He, J. Zhou, S. Tang, Y. Yang, X. Wang, Effects of scandium addition on biocompatibility of biodegradable Mg–1.5Zn–0.6Zr alloy, Mater. Lett. 215 (2018) 200–202. https://doi.org/10.1016/j.matlet.2017.12.097.

[328] N. Zhao, N. Watson, Z. Xu, Y. Chen, J. Waterman, J. Sankar, D. Zhu, In Vitro Biocompatibility and Endothelialization of Novel Magnesium-Rare Earth Alloys for Improved Stent Applications, PLOS ONE 9 (2014) e98674. https://doi.org/10.1371/journal.pone.0098674.

[329] N. Anisimova, M. Kiselevskiy, N. Martynenko, R. Willumeit-Römer, E. Kornyushenkov, M. Rodionov, S. Dobatkin, Y. Estrin, Anti-tumour activity of Mg-6%Ag and Mg-10%Gd alloys in mice with inoculated melanoma, Mater. Sci. Eng. C 130 (2021) 112464. https://doi.org/10.1016/j.msec.2021.112464.

[330] Y. Xin, K. Huo, H. Tao, G. Tang, P.K. Chu, Influence of aggressive ions on the degradation behavior of biomedical magnesium alloy in physiological environment, Acta Biomater. 4 (2008) 2008–2015. https://doi.org/10.1016/j.actbio.2008.05.014.

[331] Progress and Challenge for Magnesium Alloys as Biomaterials - Zeng - 2008 - Advanced Engineering Materials - Wiley Online Library, (n.d.). https://onlinelibrary.wiley.com/doi/abs/10.1002/adem.200800035?casa_token=myOMbY3-GkYAAAAA%3A3JrgHITh_WCLZK1Nww-DgXrXnGQW5q4Fl2oMQ6Yu6f9useVj_MOFs5HRxrEsd-gcMvYdIuxHOz7s0nAa (accessed July 14, 2024).

[332] M. Bobby Kannan, R. k. Singh Raman, F. Witte, C. Blawert, W. Dietzel, Influence of circumferential notch and fatigue crack on the mechanical integrity of biodegradable magnesium-based alloy in simulated body fluid, J. Biomed. Mater. Res. B Appl. Biomater. 96B (2011) 303–309. https://doi.org/10.1002/jbm.b.31766.

[333] S. Dobatkin, N. Martynenko, N. Anisimova, M. Kiselevskiy, D. Prosvirnin, V. Terentiev, N. Yurchenko, G. Salishchev, Y. Estrin, Mechanical Properties, Biodegradation, and Biocompatibility of Ultrafine Grained Magnesium Alloy WE43, Materials 12 (2019) 3627. https://doi.org/10.3390/ma12213627.

[334] K. Bobe, E. Willbold, M. Haupt, M. Reebmann, I. Morgenthal, O. Andersen, T. Studnitzky, J. Nellesen, W. Tillmann, C. Vogt, K. Vano-Herrera, F. Witte, Biodegradable open-porous scaffolds made of sintered magnesium W4 and WZ21 short fibres show biocompatibility *in vitro* and in long-term *in vivo* evaluation, Acta Biomater. 148 (2022) 389–404. https://doi.org/10.1016/j.actbio.2022.06.005.

[335] E. Willbold, K. Kalla, I. Bartsch, K. Bobe, M. Brauneis, S. Remennik, D. Shechtman, J. Nellesen, W. Tillmann, C. Vogt, F. Witte, Biocompatibility of rapidly solidified magnesium alloy RS66 as a temporary biodegradable metal, Acta Biomater. 9 (2013) 8509–8517. https://doi.org/10.1016/j.actbio.2013.02.015.

[336] J. Diekmann, S. Bauer, A. Weizbauer, E. Willbold, H. Windhagen, P. Helmecke, A. Lucas, J. Reifenrath, I. Nolte, M. Ezechieli, Examination of a biodegradable magnesium screw for the reconstruction of the anterior cruciate ligament: A pilot *in vivo* study in rabbits, Mater. Sci. Eng. C 59 (2016) 1100–1109. https://doi.org/10.1016/j.msec.2015.11.037.

[337] H. Naujokat, J.-M. Seitz, Y. Açil, T. Damm, I. Möller, A. Gülses, J. Wiltfang, Osteosynthesis of a cranio-osteoplasty with a biodegradable magnesium plate system in miniature pigs, Acta Biomater. 62 (2017) 434–445. https://doi.org/10.1016/j.actbio.2017.08.031.

[338] D.-T. Chou, D. Hong, S. Oksuz, R. Schweizer, A. Roy, B. Lee, P. Shridhar, V. Gorantla, P.N. Kumta, Corrosion and bone healing of Mg-Y-Zn-Zr-Ca alloy implants: Comparative in vivo study in a non-immobilized rat femoral fracture model, J. Biomater. Appl. 33 (2019) 1178–1194. https://doi.org/10.1177/0885328219825568.

[339] A. Myrissa, N.A. Agha, Y. Lu, E. Martinelli, J. Eichler, G. Szakács, C. Kleinhans, R. Willumeit-Römer, U. Schäfer, A.-M. Weinberg, *In vitro* and *in vivo* comparison of binary Mg alloys and pure Mg, Mater. Sci. Eng. C 61 (2016) 865–874. https://doi.org/10.1016/j.msec.2015.12.064.

[340] T.A. Huehnerschulte, J. Reifenrath, B. von Rechenberg, D. Dziuba, J.M. Seitz, D. Bormann, H. Windhagen, A. Meyer-Lindenberg, In vivo assessment of the host reactions to the biodegradation of the two novel magnesium alloys ZEK100 and AX30 in an animal model, Biomed. Eng. OnLine 11 (2012) 14. https://doi.org/10.1186/1475-925X-11-14.

[341] T.A. Grünewald, A. Ogier, J. Akbarzadeh, M. Meischel, H. Peterlik, S. Stanzl-Tschegg, J.F. Löffler, A.M. Weinberg, H.C. Lichtenegger, Reaction of bone nanostructure to a biodegrading Magnesium WZ21 implant – A scanning small-angle X-ray scattering time study, Acta Biomater. 31 (2016) 448–457. https://doi.org/10.1016/j.actbio.2015.11.049.

[342] J. Zhang, H. Li, W. Wang, H. Huang, J. Pei, H. Qu, G. Yuan, Y. Li, The degradation and transport mechanism of a Mg-Nd-Zn-Zr stent in rabbit common carotid artery: A 20-month study, Acta Biomater. 69 (2018) 372–384. https://doi.org/10.1016/j.actbio.2018.01.018.

[343] A. Krause, N. von der Höh, D. Bormann, C. Krause, F.-W. Bach, H. Windhagen, A. Meyer-Lindenberg, Degradation behaviour and mechanical properties of magnesium implants in rabbit tibiae, J. Mater. Sci. 45 (2010) 624–632. https://doi.org/10.1007/s10853-009-3936-3.

[344] B. Ullmann, J. Reifenrath, J.-M. Seitz, D. Bormann, A. Meyer-Lindenberg, Influence of the grain size on the in vivo degradation behaviour of the magnesium alloy LAE442, Proc. Inst. Mech. Eng. [H] 227 (2013) 317–326. https://doi.org/10.1177/0954411912471495.

[345] N. Angrisani, J. Reifenrath, F. Zimmermann, R. Eifler, A. Meyer-Lindenberg, K. Vano-Herrera, C. Vogt, Biocompatibility and degradation of LAE442-based magnesium alloys after implantation of up to 3.5 years in a rabbit model, Acta Biomater. 44 (2016) 355–365. https://doi.org/10.1016/j.actbio.2016.08.002.

[346] T. Kraus, S. Fischerauer, S. Treichler, E. Martinelli, J. Eichler, A. Myrissa, S. Zötsch, P.J. Uggowitzer, J.F. Löffler, A.M. Weinberg, The influence of biodegradable magnesium implants on the growth plate, Acta Biomater. 66 (2018) 109–117. https://doi.org/10.1016/j.actbio.2017.11.031.

[347] T. Kraus, S.F. Fischerauer, A.C. Hänzi, P.J. Uggowitzer, J.F. Löffler, A.M. Weinberg, Magnesium alloys for temporary implants in osteosynthesis: In vivo studies of

their degradation and interaction with bone, Acta Biomater. 8 (2012) 1230–1238. https://doi.org/10.1016/j.actbio.2011.11.008.

[348] D. Dziuba, A. Meyer-Lindenberg, J.M. Seitz, H. Waizy, N. Angrisani, J. Reifenrath, Long-term in vivo degradation behaviour and biocompatibility of the magnesium alloy ZEK100 for use as a biodegradable bone implant, Acta Biomater. 9 (2013) 8548–8560. https://doi.org/10.1016/j.actbio.2012.08.028.

[349] J. Levorova, J. Duskova, M. Drahos, R. Vrbova, D. Vojtech, J. Kubasek, M. Bartos, L. Dugova, D. Ulmann, R. Foltan, In vivo study on biodegradable magnesium alloys: Bone healing around WE43 screws, J. Biomater. Appl. 32 (2018) 886–895. https://doi.org/10.1177/0885328217743321.

[350] B. Ullmann, J. Reifenrath, D. Dziuba, J.-M. Seitz, D. Bormann, A. Meyer-Lindenberg, In Vivo Degradation Behavior of the Magnesium Alloy LANd442 in Rabbit Tibiae, Materials 4 (2011) 2197–2218. https://doi.org/10.3390/ma4122197.

[351] Materials | Free Full-Text | In Vivo Corrosion of Two Novel Magnesium Alloys ZEK100 and AX30 and Their Mechanical Suitability as Biodegradable Implants, (n.d.). https://www.mdpi.com/1996-1944/4/6/1144 (accessed April 18, 2024).

[352] D. Zhao, T. Wang, K. Nahan, X. Guo, Z. Zhang, Z. Dong, S. Chen, D.-T. Chou, D. Hong, P.N. Kumta, W.R. Heineman, *In vivo* characterization of magnesium alloy biodegradation using electrochemical H2 monitoring, ICP-MS, and XPS, Acta Biomater. 50 (2017) 556–565. https://doi.org/10.1016/j.actbio.2017.01.024.

[353] Biodegradable magnesium alloy (WE43) in bone-fixation plate and screw - Byun - 2020 - Journal of Biomedical Materials Research Part B: Applied Biomaterials - Wiley Online Library, (n.d.). https://onlinelibrary.wiley.com/doi/full/10.1002/jbm.b.34582 (accessed June 13, 2024).

[354] A. Torroni, C. Xiang, L. Witek, E.D. Rodriguez, R.L. Flores, N. Gupta, P.G. Coelho, Histo-morphologic characteristics of intra-osseous implants of WE43 Mg alloys with and without heat treatment in an in vivo cranial bone sheep model, J. Cranio-Maxillofac. Surg. 46 (2018) 473–478. https://doi.org/10.1016/j.jcms.2017.12.028.

[355] J. Reifenrath, A. Krause, D. Bormann, B. von Rechenberg, H. Windhagen, A. Meyer-Lindenberg, Profound differences in the in-vivo-degradation and biocompatibility

of two very similar rare-earth containing Mg-alloys in a rabbit model, Mater. Werkst. 41 (2010) 1054–1061. https://doi.org/10.1002/mawe.201000709.

[356] H. Qin, Y. Zhao, Z. An, M. Cheng, Q. Wang, T. Cheng, Q. Wang, J. Wang, Y. Jiang, X. Zhang, G. Yuan, Enhanced antibacterial properties, biocompatibility, and corrosion resistance of degradable Mg-Nd-Zn-Zr alloy, Biomaterials 53 (2015) 211–220. https://doi.org/10.1016/j.biomaterials.2015.02.096.

[357] A.C. Hänzi, I. Gerber, M. Schinhammer, J.F. Löffler, P.J. Uggowitzer, On the in vitro and in vivo degradation performance and biological response of new biodegradable Mg–Y–Zn alloys, Acta Biomater. 6 (2010) 1824–1833. https://doi.org/10.1016/j.actbio.2009.10.008.

[358] D.-T. Chou, D. Hong, P. Saha, J. Ferrero, B. Lee, Z. Tan, Z. Dong, P.N. Kumta, In vitro and in vivo corrosion, cytocompatibility and mechanical properties of biodegradable Mg–Y–Ca–Zr alloys as implant materials, Acta Biomater. 9 (2013) 8518–8533. https://doi.org/10.1016/j.actbio.2013.06.025.

Chapter 3
Experimental Methodology

The experimental techniques and methods used for the present research work is briefly presented in this chapter.

3.1 Casting Procedure

The alloys were prepared in a resistance furnace under a protective gas mixture of argon and 0.1% sulphur hexafluoride (SF_6) (**Figure 3.1**). Pure magnesium, gadolinium, Mg-30 wt.% Neodymium master alloy, zinc granules, and Mg-30 wt.% Zirconium master alloy were used for the preparation of Mg-RE-Zn-Zr alloys. Magnesium was melted and superheated to 740˚C, and then the corresponding REE was added to the melt. After 20 min., zinc granules were added, followed by the Mg-30 wt.% Zr master alloy. The melt was hand-stirred for 2 min. to obtain a homogenous composition throughout the melt. The melt was poured into a preheated (350 ˚C) rectangular-shaped cast iron mold [**Figure 3.2 (a)**]. The size of the casting block was 200 mm x 250 mm x 20 mm [**Figure 3.2 (b)**]. The chemical composition the alloys were determined using ICP OES (Make: SPECTRO Analytical Instruments GmbH, Germany, Model: ARCOS).

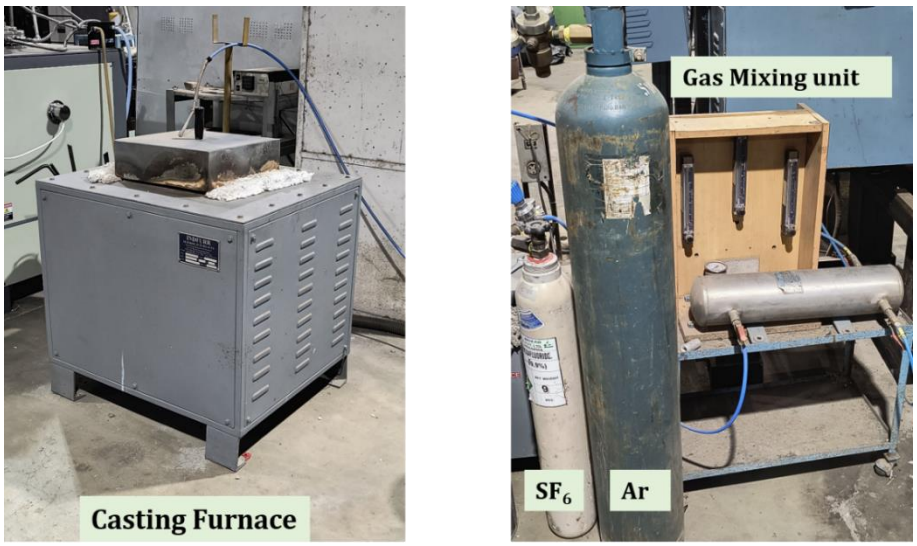

Figure 3.1. Casting setup used for alloy making.

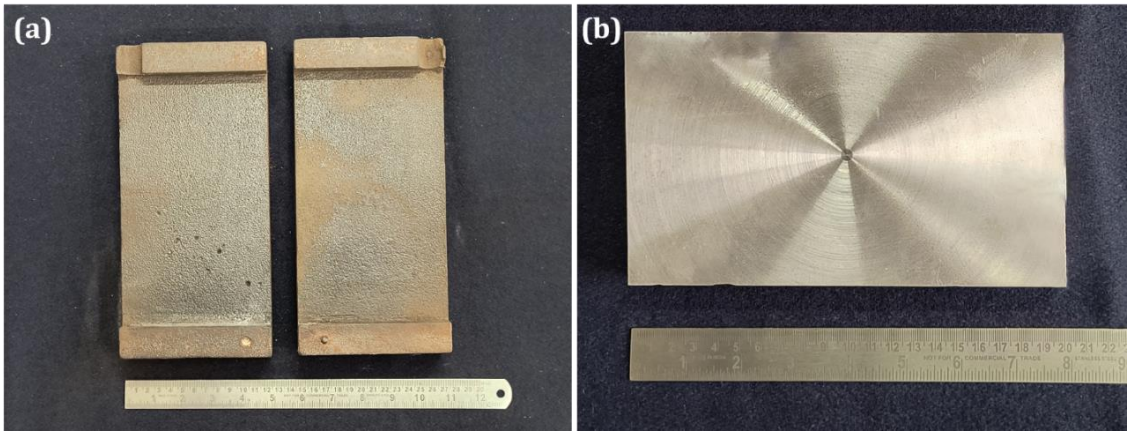

Figure 3.2. Photograph of (a) Cast iron mold used for casting (b) Machined Mg alloy cast block.

3.2 Microstructure characterization

The morphology and composition analysis of different phases were carried out with a scanning electron microscope (SEM, Carl Zeiss EVO18) with energy-dispersive X-ray spectroscopy (EDS). The samples for microstructural characterization was subjected to grinding using different grades of SiC papers and by cloth polishing using 1 µm size alumina suspension. The samples were then etched using a solution containing 10 mL distilled water, 100 mL ethanol, 6 g picric acid, and 5 mL glacial acetic acid. The TEM analysis was done in JEOL JEM F 200 with STEM EDA EELS HRTEM. The specimens for TEM observations were initially ground to a thickness of 100 µm, then 3 mm discs were punched out and thinned down using ion milling (Gatan precision ion-polishing system). Electron backscatter diffraction (EBSD) analysis was carried out using a Nova Nano SEM 450 with velocity pro EBSD detector at a scan step size of 0.08 microns. The specimens for EBSD analysis was electro polished using a solution having 10% perchloric acid in methanol at 20 V and -15 °C. The EBSD data was analyzed using TSL OIM software.

3.3 Corrosion studies

3.3.1 Electrochemical measurements

The electrochemical tests were performed using AMETEK VersaStat 4, with reference electrode of saturated calomel electrode (SCE), counter electrode of platinum mesh, and the working electrode as sample (**Figure 3.3**). The tests were performed under ambient conditions (room temperature 25±1 °C) and in electrolyte of 1 wt.% NaCl. A sample surface area of 1 cm^2 was exposed to 200 mL electrolyte solution throughout the

testing period. The samples were immersed in the electrolyte for 30 – 40 min. prior to open circuit potential (OCP) measurement. The samples were scanned at a rate of 1 mV/s from - 250 mV to +350 mV with respect to their OCP values. The corrosion potential (E_{corr} *vs.* SCE) and corrosion current density (i_{corr}) were obtained from the Tafel plot. The impedance of the alloys was measured at their OCP with a peak-to-peak amplitude of 10mV in the frequency range from 10^5 to 10^{-1} Hz. The impedance values of all the alloys were fitted using equivalent circuit and the corresponding circuit element values were obtained from ZSimpWin 3.21 software. The electrochemical tests were performed three times for repeatability. Electrochemical experiments were done according to ASTM G3-89 (1).

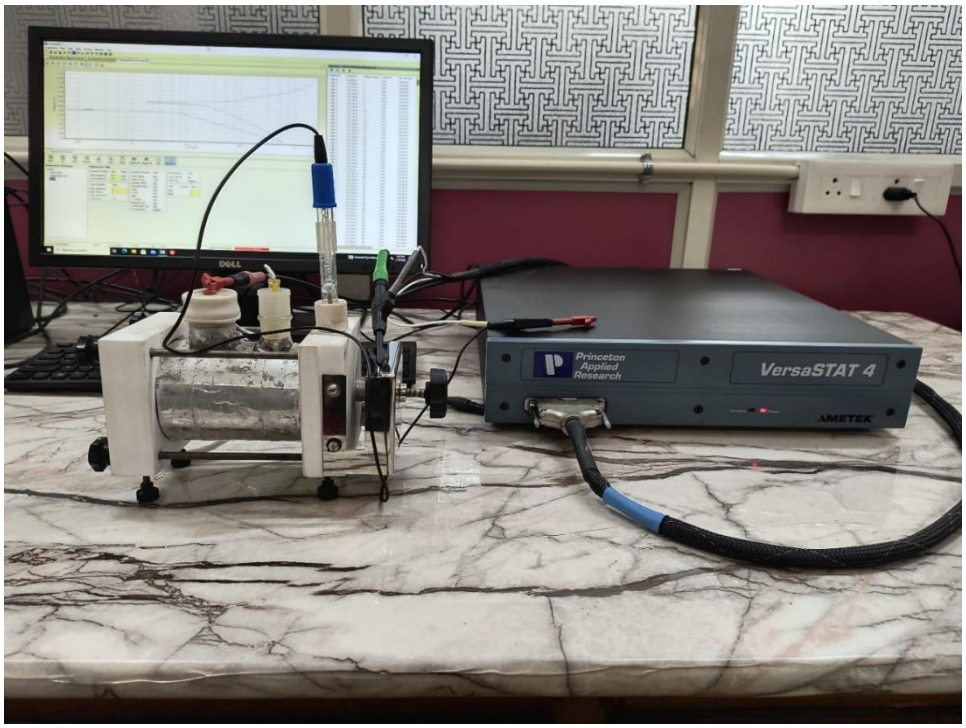

Figure 3.3. Electrochemical workstation (AMETEK VersaStat 4) used for electrochemical studies.

3.3.2 Weight loss measurement

Weight loss measurement was performed on samples by maintaining solution volume to surface area as 50 mL/cm^2. Each cleaned and weighed samples were immersed separately in 1 wt.% NaCl solution for a period of 14 days at room temperature (25±1 °C). Distilled water followed by ethanol was used to clean the samples after weight loss measurement. The corrosion products were removed using chromic acid (180 g/L) at room temperature for 15 min according to ASM handbook on Magnesium and Magnesium alloys

(2). The following formula was used for calculating the corrosion rate of samples in millimeter per year (mm/y):

$$\text{Corrosion rate} = \frac{8.76 \text{ X } 10^4 \text{ X } \Delta}{\rho \text{ X } A \text{ X } t} \quad (3.1)$$

where Δ is weight loss in g, A is total surface area in cm^2, ρ is density of the alloy in g/cm^3, t is immersion time in h. The weight loss measurements were done in accordance with ASTM G31-72 (3).

3.3.3 Hydrogen evolution test

The overall corrosion reaction in Mg and alloys in aqueous medium can be expressed as follows: (4–6).

$Mg \rightarrow Mg^{2+} + 2e^-$ (Anodic reaction); (3.2)

$2H_2O + 2e^- \rightarrow H_2 + 2OH^-$ (Cathodic reaction); (3.3)

$Mg^{2+} + 2\ OH^- \rightarrow Mg(OH)_2$ (Product formation); (3.4)

$Mg + 2H_2O \rightarrow Mg(OH)_2 + H_2$ (Overall corrosion reaction). (3.5)

When magnesium dissolves, it theoretically produces an equal amount of hydrogen gas, meaning that 1 mole of Mg corresponds to 1 mole of H_2 evolution [5]. This principle allows the volume of hydrogen released during corrosion [refer to equation (3.5)] to be directly linked to the amount of magnesium dissolved. By expressing both in the same units, the hydrogen evolution rate can be used to determine corrosion rates. Unlike the immersion test, which provides a single corrosion rate value after a fixed duration, hydrogen evolution measurements offer a continuous monitoring of corrosion behavior over a period of time, allowing a deeper understanding of the material's degradation over the course of the experiment. To measure hydrogen gas evolution, a eudiometer-based experimental setup was employed, as illustrated in **Figure 3.4**. The setup included a double-wall tube system, where the inner tube was connected to an air-tight glass chamber containing the test sample immersed in 1 wt.% NaCl solution. The exposure ratio of the sample surface area to the solution volume was set at 1 cm^2: 50 mL. The outer tube was linked to a water reservoir, and a hand vacuum pump was used to adjust the water level, which was then stabilized with a stopper. As corrosion progressed, the hydrogen gas released from the sample moved from the inner tube to the outer tube, displacing an

equivalent volume of water to the reservoir. The collected hydrogen volume in the outer tube was recorded over time to evaluate the corrosion rate and behavior of the test material (7).

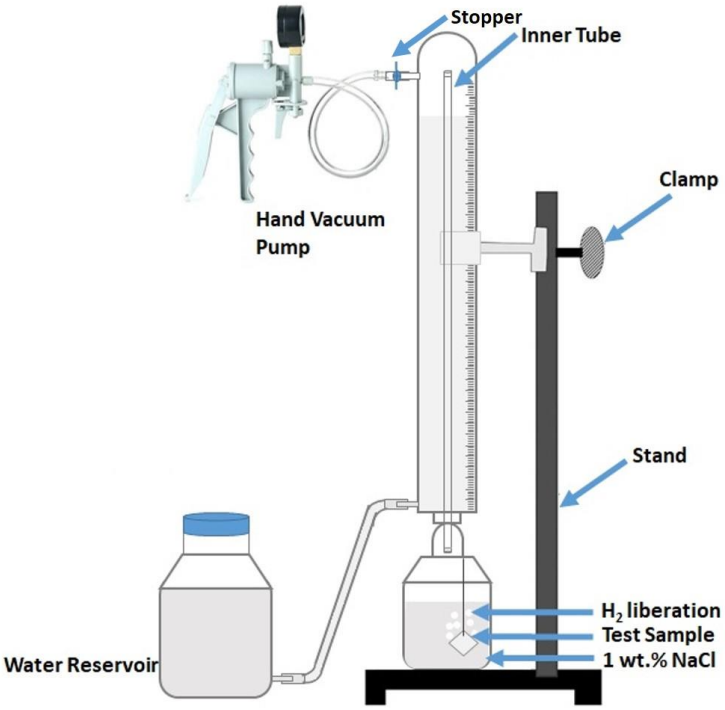

Figure 3.4. Schematic diagram of hydrogen evolution measuring setup (eudiometer) (8).

3.3.4 X-ray Photoelectron Spectroscopy (XPS)

The composition of the oxide layers formed on the surface of the alloys immersed in 1 wt.% NaCl solution for a short time were studied using XPS (PHI 5000 VersaProbe II, ULVAC-PHI Inc., USA) equipped with micro-focused (200 μm, 15 KV) monochromatic Al-Kα X-Ray source (hν = 1486.6 eV). XPS data were analysed using multipak software in the instrument.

3.3.5 X-ray diffraction (XRD)

XRD studies were carried out on the corrosion product collected from the samples immersed in 1 wt.% NaCl for 14 days. Cu-Kα radiation (wavelength λ = 0.15406 nm, voltage = 40 kV and current = 40 mA) was used to carry out the analysis with a scanning range of 10° – 90° (step interval = 0.033°, scan rate = 0.05 /s). XRD data analysis was done using X'Pert highscore Plus 2.1 software. XRD analysis was also used to identify the

phases present in the prepared alloy, for which alloy 5 mg chips obtained from drilling was used.

3.4 Tensile test

Threaded tensile samples of 6 mm gauge diameter and a gauge length of 25 mm were made according to ASTM standard B557M-10 (9). The tensile testing was carried out at a crosshead speed of 2 mm/min (strain rate: 1.66 x 10^{-3}), and at room temperature. Minimum five samples from each alloys were tested and average values were reported.

3.5 In-vitro biodegradation behaviour

3.5.1 Biodegradation test

The samples were immersed in cell culture medium containing MEM supplemented with 10% fetal bovine serum (BSA) and 1% penicillin for 14 days, maintaining a medium volume to the surface area of sample ratio of 1.25 cm^2/mL according to ISO 10993 under cell culture conditions (37 °C, 5% CO_2, 20% O_2, 95% relative humidity) (10). The medium was changed every two days to maintain the pH and semi-static conditions. Schematic representation of the biodegradation test for Mg alloys in cell culture medium is shown in **Figure 3.5**. The left tube represents the initial state, where the medium had a neutral pH (7.4–7.8). Upon immersion of the Mg alloy sample, corrosion occurred, leading to hydroxide ion (OH^-) release, which increased the pH, making the solution more alkaline. Change in pH could be visually seen with a color change in the medium (right tube), signifying degradation of the Mg alloy. After 14 days of immersion, the specimens were cleaned using distilled water and 100% ethanol. After immersion, the degradation products of the samples were removed by immersing them in a chromic acid solution (180 g/L) for 15 min. at room temperature. The weight loss measurement was taken after the 14 days immersion in cell culture medium. Weight loss measurement was calculated according to equation 3.1.

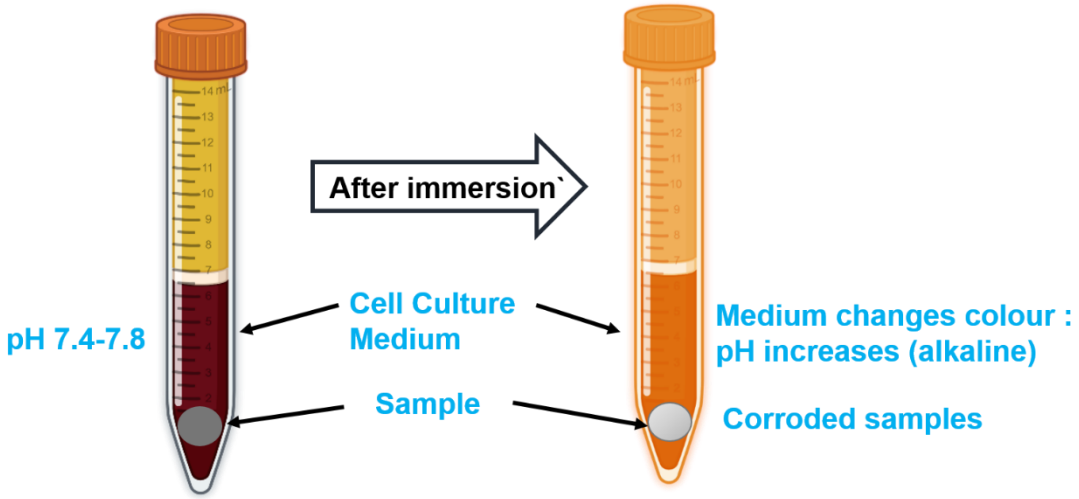

Figure 3.5. Schematic representation of the biodegradation test for Mg alloys in cell culture medium.

3.5.2 Electrochemical test

The electrochemical experiments were carried out using an AMETEK Versastat4 instrument (Refer Section 3.3.1). The electrochemical experiments were conducted at 37±1 °C with minimum essential medium (MEM) as the electrolyte. The experimental parameters used were the same as mentioned in section 3.3.1. The experiments were performed in triplicates.

3.5.3 X-ray Photoelectron Spectroscopy (XPS)

The composition of the degradation layer developed on the sample surface after being immersed in cell culture medium for 24 h was analyzed using XPS instrument with specifications as mentioned in section 3.3.4.

3.6 In-vitro cell culture tests

In-vitro culture tests are essential for assessing the biocompatibility and biological response of magnesium (Mg) alloys intended for implant applications. These tests simulate physiological conditions to evaluate how Mg alloys interact with cells and tissues. Among these, indirect and direct cell culture tests are commonly employed.

- **Indirect Cell Culture Tests:** These involve exposing cells to the degradation products of Mg alloys. A conditioned medium called as extract solution is obtained by immersing the alloy in a culture medium for a fixed time. The medium is then

used to culture cells, and assays such as MTT, Alamar Blue, or LDH are performed to assess cell viability, metabolic activity, and cytotoxicity. This approach helps to understand the effects of released ions, pH changes, and other degradation products on the cell viability without the physical presence of the alloy (10).

- **Direct Cell Culture Tests:** In these tests, cells are cultured directly on the surface of the Mg alloy. Schematic representation of the direct cell culture method used for cytocompatibility evaluation is shown in **Figure 3.6**. This method evaluates how the alloy's surface properties, such as roughness, corrosion behaviour, and surface chemistry, influence cell attachment, proliferation, and viability. The surrounding culture medium provides the necessary nutrients while also allowing any released metal ions or degradation products to influence cell behavior (10).

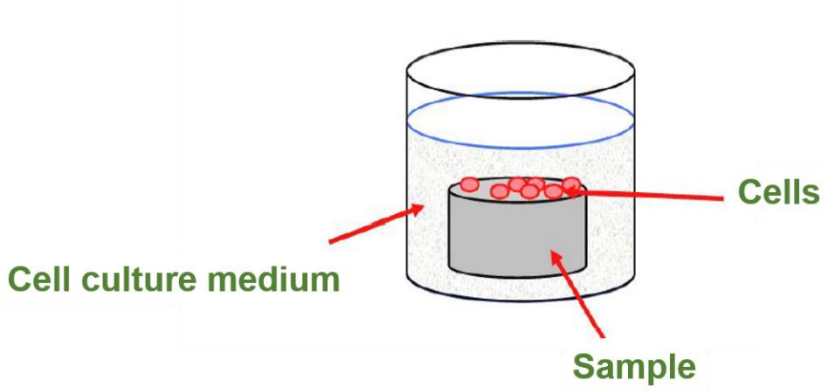

Figure 3.6. Schematic representation of the direct cell culture method.

These tests are vital for determining whether Mg alloys can support cell growth and function without inducing cytotoxicity, thereby guiding alloy optimization for safe and effective biomedical implant applications.

3.6.1 Indirect cell viability tests

3.6.1.1 Extract preparation

Figure 3.7 shows the schematic representation of the preparation of extract solutions for the MTT assay. The metallic samples (diameter: 10 mm, height: 2 mm) were immersed in cell culture medium (CCM) containing MEM, 10% FBS and 1% penicillin for 3 days by maintaining a medium volume to the surface area of sample ratio of 1.25 cm^2/mL. This results in the release of metal ions into the CCM. The supernatant solution was then

centrifuged at 3000 rpm for 15 min. and filtered using a 0.22 µm filter, to get 100% extract. The resulting extract solution was then diluted with fresh cell culture medium to obtain different concentrations (e.g., 50% of 100% extract + 50% cell culture medium and 25% extract + 75% cell culture medium), which were subsequently used for cell viability testing in the MTT assay.

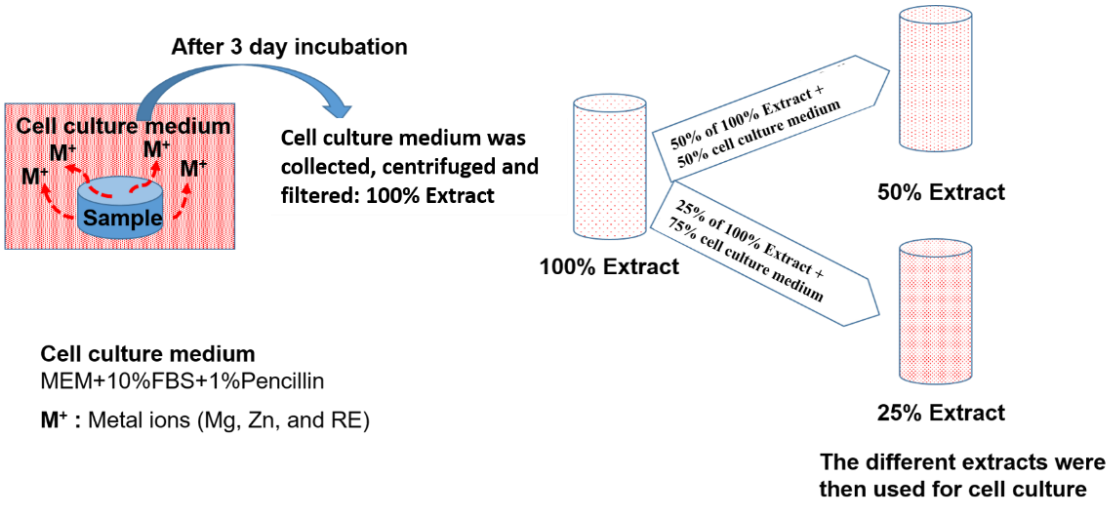

Figure 3.7. Schematic representation of the preparation of extract solutions for the MTT assay.

3.6.1.2 MTT (3-(4,5-Dimethylthiazol-2-Yl) −2,5 Diphenyltetrazolium Bromide) assay

MTT assays were performed according to ISO 10993:2009 to evaluate the toxicity of the alloys (10). MG-63 cells [from National Centre for Cell Science (NCCS) Pune] were cultured with CCM and incubated in a CO_2 incubator at 37 °C. A cell suspension (100 µL) with CCM containing 1 $\times 10^4$ cells was seeded in the 96-well cell culture plate. After 24 h, the culture medium was replaced with extracts (100%, 50%, or 25%) and was incubated for 1 and 3 days. After the specified incubation time, the extracts were discarded, and MTT was added to each well (1 µL MTT in 100 µL MEM) and was incubated for 2-4 h in the cell culture conditions. After incubation, 100 µL of dimethyl sulphoxide (DMSO) was added to each well. Viability of cells were determined by measuring the absorbance at 570 nm using a TECAN microplate reader (USA). The assay was performed in triplicates, and the percentage of cell viability was calculated as follows:

$$Cell\ viability = \frac{Absorbance\ of\ sample}{Absorbance\ of\ control}\ x\ 100 \qquad (3.6)$$

3.6.1.3 Elemental toxicity evaluation

The chlorides of Mg, Zn and Gd obtained from Sigma-Aldrich was used for elemental toxicity studies. The chlorides were dissolved in sterile water at a concentration of 50,000 μM. Cell culture medium was used to dilute the chloride solutions to different concentrations. The toxicity of elements was done using MTT assay as explained above.

3.6.1.4 Live / Dead staining

A cell suspension (100 μL) with MEM containing 1×10^4 cells was seeded in the 96 well black cell culture plate. After 24 h, the culture medium was replaced with extracts (100%, 50%, or 25%) and was incubated for 1 and 3 days. After the specified incubation time, the extracts were discarded, and wells were washed with 1x-phosphate buffer saline (PBS). The cells were stained using acridine orange and ethidium bromide solution for 10 min. Finally, wells were rinsed with PBS and observed under fluorescence microscope (Olympus IX –83). At least five images were taken and analyzed to quantify the fluorescence using free software ImageJ.

3.6.1.5 Inductively Coupled Plasma Mass Spectroscopy (ICP-MS) analysis

The extract solutions used for viability studies was analysed using ICP-MS to find out the concentration of different elements in the solution. Inductively coupled plasma spectrometer iCAP RQ (Make: Thermo Scientific) equipped with quadrupole mass analyser and an auto-sampler ASX-280 (Teledyne, CETAC Technologies, USA) was used for the multi-elemental analysis.

3.6.2 Direct Cell viability methods

3.6.2.1 DAPI staining

The metallic samples (diameter: 10 mm, height: 2 mm) were immersed in CCM for 3 days by maintaining a medium volume to the surface area of sample ratio of 1.25 cm^2/mL. After discarding the CCM, 50,000 cells were seeded on top of the samples and incubated for 1 h, followed by adding 3 mL of CCM to the wells containing metallic samples. After 1 and 3 days of culturing, the samples were washed using PBS, then stained using DAPI (1:1000 in MEM) for 15 min. Finally, samples were rinsed with PBS and observed using fluorescence microscope (Olympus IX –83). At least 6 images were taken and analyzed to quantify the cells using the free software ImageJ.

3.6.2.2 Cell observation using SEM

The cells were seeded on top of the metallic samples as in DAPI staining analysis. After the respective incubation, the cells were fixed in 2.5% glutaraldehyde for 30 min. Then the samples were washed with PBS and subjected to gradual ethanol dehydration with various concentrations of 10%, 20%, 40%, 60%, 80%, or 100% for 10 min. each. The samples were air-dried and images were taken using SEM Carl Zeiss EVO18.

3.7 In-vivo studies

3.7.1 Animal model and experimental design

The animal experiments conducted in this study were approved by the institutional animal ethical committee at KMCH College of Pharmacy, Coimbatore, India (Approval Number: KMCRET/ReRc/Ph.D/33/2021). Sprague dawley rats, aged four to eight weeks and weighing between 180-220 g, were obtained and housed in a controlled, pathogen-free environment throughout the duration of the experiment. The rats underwent anesthesia using Ketamine hydrochloride injection. Following anesthesia, the rats were shaved, and a subcutaneous injection of buprenorphine (0.6 mg/kg) was administered. Segments of cellular porcine pericardium, measuring 20 mm x 20 mm, were placed over the muscle beneath the skin. The samples (5 mm in diameter and 2 mm in height) were subcutaneously implanted without the need for suturing or fixation. The subcutaneous implantation sites were closed using Vicryl 4-0, and topical tetracycline was applied. The rats were then monitored for a period of 30 days post-implantation.

3.7.2 Histological evaluation after surgery

Subcutaneous tissues and vital organs (heart and liver) were harvested after 30 days. The subcutaneous tissues and vital organs were fixed in 10% formalin and embedded in paraffin. The tissue sections were deparaffined by xylol for 5 to 10 min., and xylol was removed by 100% ethanol. The tissue sections were stained using hematoxylin, counter-stained with 0.5% eosin, and observed under microscope for any ultrastructural changes.

3.8 Statistical analysis

The data are reported as mean ± standard deviation, and the statistical significance of difference between groups was evaluated using one-way analysis of variance (ANOVA). A significance level of $p < 0.05$ was considered significant. The statistical analyses were conducted using GraphPad Prism 8 software (GraphPad Software, Inc., San Diego, CA).

References

1. Standard Practice for Conventions Applicable to Electrochemical Measurements in Corrosion Testing [Internet]. [cited 2022 May 12]. Available from: https://www.astm.org/g0003-89r10.html

2. Avedesian MM, Baker H. ASM Specialty Handbook: Magnesium and Magnesium Alloys. ASM International; 1999. 336 p.

3. ASTM G31-72_Laboratory Immersion Corrosion Testing of Metals - Free Download PDF [Internet]. [cited 2022 May 12]. Available from: https://kupdf.net/download/astm-g31-72laboratory-immersion-corrosion-testing-of-metals_59966135dc0d607665300d1d_pdf

4. Makar GL, Kruger J. Corrosion of magnesium. Int Mater Rev. 1993 Jan 1;38(3):138–53.

5. Song GL, Atrens A. Corrosion Mechanisms of Magnesium Alloys. Adv Eng Mater. 1999;1(1):11–33.

6. Song G. Recent Progress in Corrosion and Protection of Magnesium Alloys. Adv Eng Mater. 2005;7(7):563–86.

7. Srinivasan A, Blawert C, Huang Y, Mendis CL, Kainer KU, Hort N. Corrosion behavior of Mg–Gd–Zn based alloys in aqueous NaCl solution. J Magnes Alloys. 2014 Sep 1;2(3):245–56.

8. Jayaraj J, Kumar SA, Srinivasan A, Raghu KG, Arunchandran C, Rajinikanth V. Corrosion and invitro characteristics of cerium phosphate based chemical conversion coating on AZ31 magnesium alloy. Appl Surf Sci. 2024 Jan 30;644:158797.

9. B07 Committee. Test Methods for Tension Testing Wrought and Cast Aluminum- and Magnesium-Alloy Products (Metric) [Internet]. ASTM International; [cited 2025 Jan 1]. Available from: http://www.astm.org/cgi-bin/resolver.cgi?B557M-10

10. Health C for D and R. Use of International Standard ISO 10993-1, "Biological evaluation of medical devices - Part 1: Evaluation and testing within a risk management process" [Internet]. FDA; 2023 [cited 2025 Jan 1]. Available from: https://www.fda.gov/regulatory-information/search-fda-guidance-documents/use-international-standard-iso-10993-1-biological-evaluation-medical-devices-part-1-evaluation-and

Chapter 4

Role of RE and Grain refiner in Mg-Zn-RE alloys

4.1 Introduction

The design of biodegradable implants requires a comprehensive understanding of how alloying elements influence key properties such as mechanical strength, biodegradation resistance, and biocompatibility. These attributes are interdependent and play a critical role in determining the overall performance and safety of the implant. Alloying elements can modify the microstructure, corrosion behaviour, and biological interactions of the material, making their selection and optimization pivotal in implant design [1,2].

A vital step in evaluating the biodegradation resistance of metallic alloys is to study their behavior in simulated physiological environments. Historically, researchers have employed a 1 wt.% NaCl solution as a test medium for initial screening of corrosion resistance. The choice of NaCl is particularly relevant because it provides a standardized and reproducible environment, allowing researchers to explore the fundamental electrochemical interactions between the alloy surface and a chloride-rich corrosive medium. Such studies are essential for understanding the underlying corrosion mechanisms before transitioning to more complex physiological conditions. Moreover, the osmolality of NaCl solution is close to that of human blood. Thus researchers can gain valuable insights into the alloy's performance under simplified conditions. This step is crucial in establishing a baseline understanding of corrosion behavior, which can then be compared and extended to in-vitro or in-vivo studies. Therefore, the initial investigation of the corrosion properties of Mg-based alloys in 1 wt.% NaCl solution forms the foundation for subsequent analyses under physiological conditions [3–5].

The influence of rare earth (RE) elements on the corrosion behavior of Mg-RE binary alloys has been the subject of significant research [6,7]. For example, Birbilis et al. [6] reported that Mg-Ce alloys exhibited the highest corrosion rate compared to Mg-Nd and Mg-La alloys. Their study also revealed that an increase in the volume fraction of secondary phases in these alloys directly correlated with a higher corrosion rates. Furthermore, microcapillary electrochemical testing demonstrated that the secondary phase $Mg_{12}Ce$ was

the most inert among the phases studied, whereas $Mg_{12}La$ exhibited the least inertness. Consequently, Mg-Ce alloys suffered from severe micro-galvanic corrosion due to the presence of secondary phases [6]. In contrast, Azzedine et al. [7] presented different observations, reporting that Mg-Ce binary alloys showed better corrosion resistance than Mg-La and Mg-Nd alloys. Their findings suggested that the corrosion rates of various alloys followed the order: Mg-0.41Dy < Mg-0.3Ce < Mg-0.63Gd < Mg-1.44Nd < Mg-1.43La (wt.%). The improved corrosion resistance of Mg-0.41Dy and Mg-0.3Ce was attributed to the formation of protective oxide films, either complete or partially protective, on their surfaces. Although the corrosion mechanism of Mg-0.3Ce, Mg-1.44Nd and Mg-0.63Gd were similar, the small grain size (70 μm) observed in Mg-0.3Ce alloy enhanced the corrosion resistance whereas the presence of diverse secondary phases ($Mg_{12}Nd$, $Mg_{41}Nd_5$ and $Mg_{24}Nd$) in Mg-1.44Nd resulted in its poor corrosion resistance compared to Mg-0.3Ce and Mg-0.63Gd. The poor corrosion resistance of Mg-1.43La alloy was attributed to the presence of $Mg_{12}La$ secondary phase along the grain boundaries. However, it is important to note that the weight percentages of RE elements were not uniform across these alloys, and the effect of the volume fraction of secondary phases on their corrosion behavior was not systematically evaluated. This variability highlights the need for a more controlled and systematic approach to studying the impact of alloying elements on the corrosion properties of Mg-RE alloys.

Also, combination of RE and Zn in Mg alloys draw a special attention due to the enhanced mechanical properties as well as corrosion resistance [8,9]. In addition, the extensive literature review (Chapter 2) suggested that among the different RE based Mg alloys, Mg-Zn-RE alloys showed the optimum combination of tensile properties as well as biodegradation resistance. Given this background, in the Part A of this chapter two different Mg-Zn-RE alloys (RE = Gd and Nd) were prepared with same wt.% of RE and Zn, to replicate ZE41 alloys, and the effects of these REEs on the microstructure and corrosion behavior of Mg-Zn-RE alloys were investigated. Moreover, ZE41 (Mg-4Zn-1RE, wt.%) alloy already find potential applications ranging from aerospace to biomedical industries [10,11]. In early stage of development, La based misch metal (MM) were added to Mg-Zn to prepare ZE alloys. Later MM was replaced by Nd for the better tensile properties.

Part B of this chapter extends the investigation to the influence of zirconium (Zr) as an additional element in the Mg-Zn-Gd and Mg-Zn-Nd alloy systems. Zr was

incorporated due to its well-documented role as a potent grain refiner in magnesium alloys. According to the Mg-Zr phase diagram (**Figure 4.1**), Zr exhibits a solubility limit of 0.565 wt.% in molten Mg at temperatures above 650 °C. Given that Mg-RE alloys are typically melted at temperatures exceeding 740 °C, a substantial amount of Zr remains dissolved during melting. As the melt is poured into a casting mold and cools, the solubility of Zr decreases, leading to the precipitation of finely dispersed α-Zr particles when the temperature drops to approximately 650 °C. These α-Zr particles act as potent nucleation sites for the α-Mg phase, which forms at around 646 °C, resulting in the development of a fine, equiaxed grain structure in Zr-containing Mg-RE alloys [12–14] . Both α-Zr and α-Mg share a similar hexagonal close-packed (HCP) structure with nearly identical c/a ratios (1.60 for α-Zr and 1.625 for α-Mg). This structural similarity enhances Zr's ability to act as an efficient nucleant for Mg solidification. Furthermore, a peritectic reaction at 653.5 °C in the Mg-Zr system further promotes α-Mg nucleation, reinforcing the grain refinement effect [10–12]. This refinement is critical in improving mechanical properties such as yield strength and ductility, as well as enhancing the corrosion resistance by reducing localized galvanic effects associated with coarse grains or intermetallic phases. By studying the combined effects of REEs and Zr, this work aims to achieve an optimized balance of mechanical and corrosion properties, tailored for biodegradable implant applications. The findings from this section will provide valuable insights into the synergistic effects of REEs and grain refiners on the microstructure and properties of magnesium alloys.

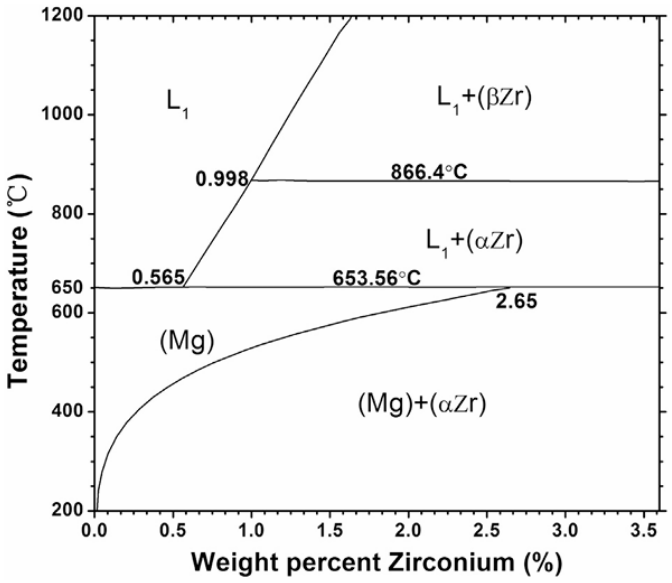

Figure 4.1. Mg-Zr phase diagram [14].

4.2. Materials and Methods

The magnesium alloys with compositions of Mg-4Zn-1Gd band Mg-4Zn-1Nd, Mg-4Zn-1Gd-0.5Zr, Mg-4Zn-1Nd-0.5Zr (wt.%, hereinafter referred to as GZ, NZ, GZK and NZK respectively) were prepared in a steel crucible protected by a gas mixture of Ar+0.02% SF_6 (As detailed in Chapter 3). The chemical composition the alloys were determined using ICP-AES (**Table 4.1**). The characterization techniques used to analyze the properties of the prepared alloys are already described in detail in Chapter 3. The microstructural characterization of the alloys was performed using optical microscopy (OM) and scanning electron microscopy (SEM, Zeiss EVO 18), equipped with energy-dispersive X-ray spectroscopy (EDS). Grain size and secondary phase volume fractions were measured using ImageJ software, while electron backscatter diffraction (EBSD) was conducted using a Nova NanoSEM 450 with a Velocity Pro EBSD detector at a scan step size of 0.08 μm. Electrochemical tests were performed using an AMETEK VersaStat 4 potentiostat in 1 wt.% NaCl solution at room temperature (25 ± 1°C). Weight loss measurements were conducted using 15 mm × 15 mm × 3 mm samples immersed in 1 wt.% NaCl for 1, 3, 7, and 14 days at room temperature, with a solution volume-to-sample surface area ratio of 50 mL/cm². Hydrogen evolution tests were performed under identical conditions as the weight loss tests for 14 days. Corrosion product analysis was carried out using X-ray Photoelectron Spectroscopy (XPS) and X-ray Diffraction (XRD). Tensile testing was carried out on alloys using threaded tensile specimens with a 6 mm gauge diameter and 25 mm gauge length, prepared according to ASTM B557M-10. In-vitro biodegradation behavior of Mg-Zn-RE-Zr alloys was evaluated using immersion tests in cell culture medium containing Minimum Essential Medium (MEM) supplemented with 10% fetal bovine serum (FBS) and 1% penicillin, maintaining a medium volume-to-sample surface area ratio of 1.25 cm²/mL according to ISO 10993. The samples were incubated at 37 °C, 5% CO_2, 20% O_2, and 95% relative humidity for 14 days, with medium replacement every two days to maintain pH stability. MTT (3-(4,5-Dimethylthiazol-2-Yl)-2,5 Diphenyltetrazolium Bromide) assays were performed according to ISO 10993:2009 to evaluate the cytotoxicity of Mg-Zn-RE-Zr alloys.

Table 4.1. Chemical composition of the developed alloys (wt.%)

Nominal composition	**Analysed chemical composition (wt.%)**						
	RE	**Zn**	**Fe**	**Cu**	**Ni**	**Zr**	**Mg**
Mg-4Zn-1Gd (GZ)	1.12	4.05	0.0168	0.0036	0.0012	-	Bal.
Mg-4Zn-1Nd (NZ)	0.98	3.95	0.0172	0.0046	0.0020	-	Bal.
Mg-4Zn-1Gd-0.5Zr (GZK)	1.27	3.90	0.0155	0.0039	0.0019	0.49	Bal.
Mg-4Zn-1Nd-0.5Zr (NZ)	0.95	4.36	0.0187	0.0041	0.0033	0.45	Bal.

4.3 Results and Discussion

Part A: Role of RE in Mg-Zn-RE (RE= Gd and Nd) alloys

4.3.1. Microstructure

The XRD patterns of the alloys showed (**Figure 4.2**) only α-Mg peaks, with no detectable peaks related to any secondary phases. This absence of secondary phase peaks in the XRD patterns could be attributed to the limited volume fraction of secondary phases, making them difficult to detect due to the restriction in detection limits of XRD. **Figure 4.3** shows the SEM micrographs of the developed alloys and **Table 4.2** shows EDS analysis of various phases observed in these alloys. The GZ alloys had discrete secondary particles distributed along the grain boundaries [**Figure 4.3 (a)**] whereas NZ alloy had network of secondary phases distributed more evenly throughout the grain boundaries [**Figure 4.3 (c)**]. GZ alloy consisted of secondary phases with different morphologies as seen in **Figure 4.3 (a)**. Elongated phases and large spherical particles [shown as A & B in **Figure 4.3 (b)**] had stoichiometric composition of Zn/Gd ratio equal to 3.21 and 5.22 respectively which are close to the ideal ratio 2 reported for W ($Mg_3Zn_3Gd_2$) phase and 6 reported for I (Mg_3Zn_6Gd) respectively [18]. The cuboid phase, marked as C in **Figure 4.3 (b)**, was

identified as Mg_5Gd. EDS analysis of small spherical particles, [marked as D in **Figure 4.3 (b)**], revealed that these were Mg-Zn binary phases.

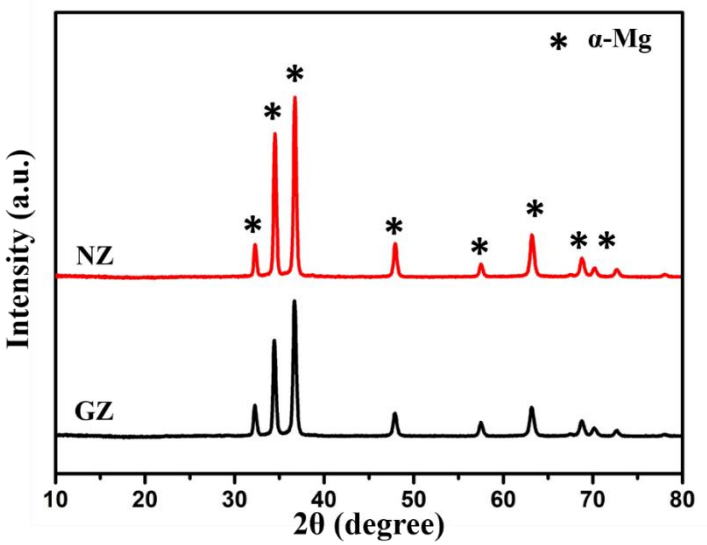

Figure 4.2. XRD patterns of the developed Mg-Zn-RE alloys.

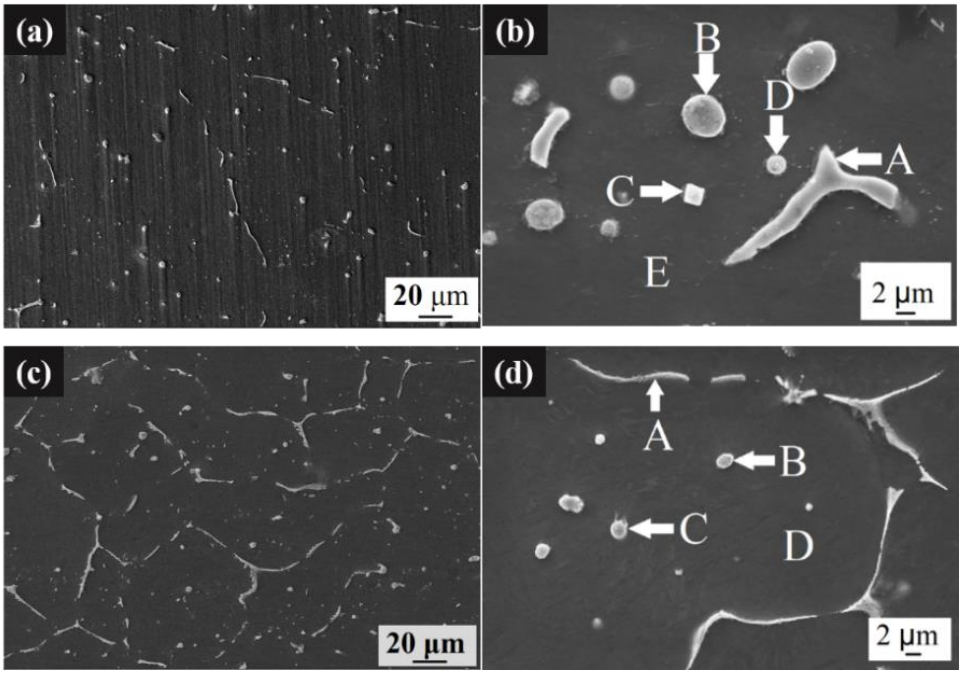

Figure 4.3. SEM micrographs of alloys (a&b) GZ, (c&d) NZ.

Unlike GZ alloys, a semi network of secondary phases along with small sized particles were observed in NZ alloy. From the EDS analysis, both phases, marked as A, B and C in **Figure 4.3 (d)**, were identified as T (Mg_7Zn_3Nd) phases as the measured

composition of Mg, Zn and RE were approximately 7:3:1 [19,20]. Though few binary phases were (Mg-Zn, Mg-RE) observed in both the alloys, ternary phases such as W phase in GZ, and T phases in NZ alloy were dominant. The grain boundary overlaid inverse pole figure (IPF) maps [**Figure 4.4**] of the alloys showed that the grain size of GZ and NZ alloys were 524 (±171) μm and 203 (±63) μm respectively. In as-cast conditions, grain size is predominantly controlled by solute solubility and the formation of secondary phases**.** Nd has a much lower solubility in Mg (~3.6 wt% at eutectic temperature) compared to Gd (23.49% at eutectic temperature), leading to earlier precipitation of Nd-containing intermetallics, which effectively pin grain boundaries and restrict grain growth [1,21]. In contrast, Gd remains more soluble in the matrix for a longer duration during solidification, resulting in fewer early precipitates and allowing grains to grow larger.

Table 4.2. EDS analysis of different secondary phases in the alloys.

Alloy	Position	Elements (at.%)			Phase
		Mg	Zn	RE	
GZ	Figure 4.2 (b) – A	61.9	28.83	8.97	W ($Mg_3Zn_3Gd_2$)
	Figure 4.2 (b) – B	69.35	25.73	4.92	I (Mg_3Zn_6Gd)
	Figure 4.2 (b) – C	76.53	1.37	22.09	Mg_5Gd
	Figure 4.2 (b) – D	87.34	10.94	1.73	Mg-Zn binary
	Figure 4.2 (b) – E	98.5	1.05	0.45	Matrix
NZ	Figure 4.2 (d) – A	71.9	22.11	6	T (Mg_7Zn_3Nd)
	Figure 4.2 (d) – B	72.03	22.58	5.38	T (Mg_7Zn_3Nd)
	Figure 4.2 (d) – C	69.52	24.17	6.31	T (Mg_7Zn_3Nd)
	Figure 4.2 (d) – D	98.82	1.11	0.07	Matrix

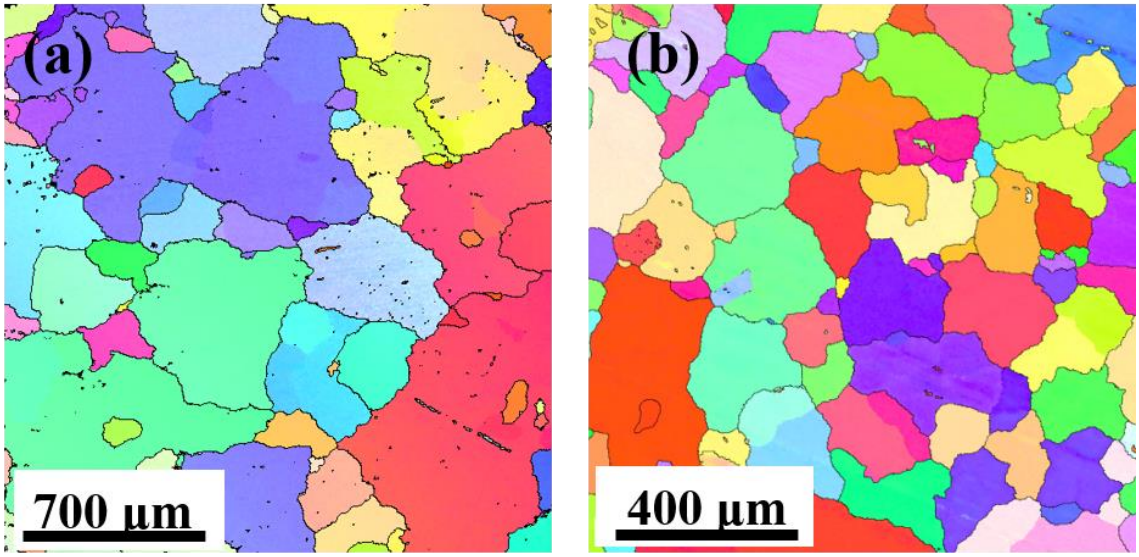

Figure 4.4. Grain boundary overlaid inverse pole figure maps (IPF) of (a) GZ (b) NZ alloy.

4.3.2 Electrochemical measurement

The cathodic and anodic branches of a polarization curve represents the hydrogen evolution and Mg matrix dissolution respectively during the polarization measurement. The polarization curves (**Figure 4.5**) and **Table 4.3** show that the NZ Alloy had a more negative E_{corr} compared to that of GZ alloy. Though NZ alloy showed slightly higher cathodic activity (relatively high cathodic current density at all cathodic potentials), it exhibited a more positive corrosion potential due to the lesser anodic dissolution behaviour. However, the i_{corr} of alloys NZ were the lowest.

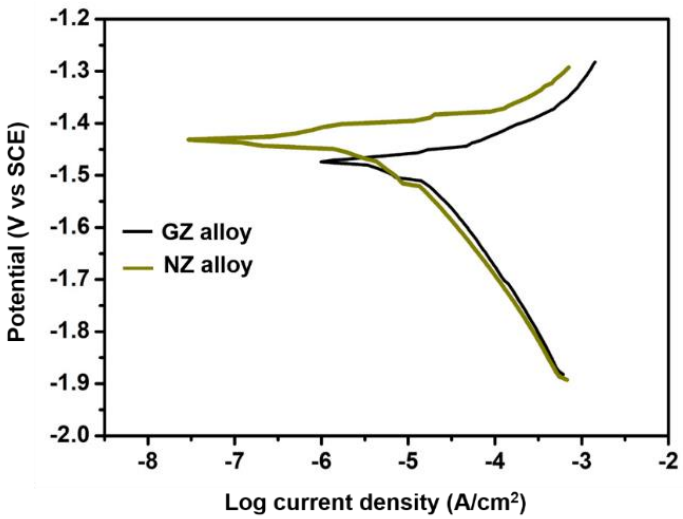

Figure 4.5. Polarization curves of alloys in 1 wt.% NaCl solution at 25˚C.

Table 4.3. OCP, E_{corr} and i_{corr} values of alloys obtained from polarization measurements in 1 wt.% NaCl.

Alloy	OCP (mV vs SCE)	E_{corr} (mV vs SCE)	i_{corr} (μA/cm^2)
GZ	-1571	-1486	12.58
NZ	-1423	-1430	5.16

Electrochemical Impedance behaviour of alloys after immersion in 1 wt.% NaCl for 30 min., and 1, 3, 7 and 14 days (**Figure 4.6**) show that initially all the alloys had a similar behaviour (although the dimensions of the loops seem to be different indicating marginal differences in corrosion rates). The nyquist plots of alloys measured after 30 min. immersion in electrolyte [**Figure 4.6 (a)**] showed two capacitive loops: well defined at high-medium frequencies and depressed at low frequencies. However, the alloys showed inductive loop [**Figure 4.6 (b)**] after 1-day immersion indicating the initiation of pits. Also the capacitive loops became single with reduced diameters suggesting that the dissolution of corrosion layers occurred. Similarly, the continuous decrease in size of the capacitive loops after 3, 7 and 14 days of immersion indicated that the corrosion layer was unstable and leading to continuous dissolution of alloys. However, initially the alloys showed strong inductive loops after 1-day immersion but as immersion time increased this behaviour was suppressed. It seems that the formation of pits during initial stage of corrosion leads to a strong inductive loop whereas spreading of corrosion further into the matrix leads to weakened inductive loops [18,22,23].

For more details on the corrosion characteristics of the alloys, the EIS spectra were fitted using the equivalent circuits as shown in the **Figure 4.7**. The data were fitted using ZSimpWin 3.20 software where, R_s refers to solution resistance, R_{ct} represents charge transfer resistance, CPE_{dl} represents electric double layer capacitance at the interface of substrate and solution, R_f represents film resistance, CPE_f represents film capacitance, and R_L and L represents resistance and inductance of the low frequency inductive loop respectively. The capacitive loop at high frequencies represents double layer capacitance and charge transfer resistance. The resistance offered by the corrosion film on the surface was indicated by the capacitive loop at medium or lower frequencies. Inductive loop is an indication of the failure of the surface film and initiation of pits [18,24]. The polarisation

resistance R_p (R_{ct} + R_f or R_{ct} + R_f + R_L) [25–27] calculated for the alloys (**Figure 4.8**) after 30 min. immersion indicated that NZ alloys had the highest, whereas GZ alloys had the lowest resistance which was in agreement with the i_{corr} values obtained from Tafel plots. After 1 day of immersion, due to inductive loops at lower frequencies the Rp values of all the alloys dropped. However, beyond 3 days the resistance of the alloys had only a marginal change till the 14-day immersion. GZ alloys exhibited lowest resistance at all immersion times indicating that it was most susceptible to corrosion.

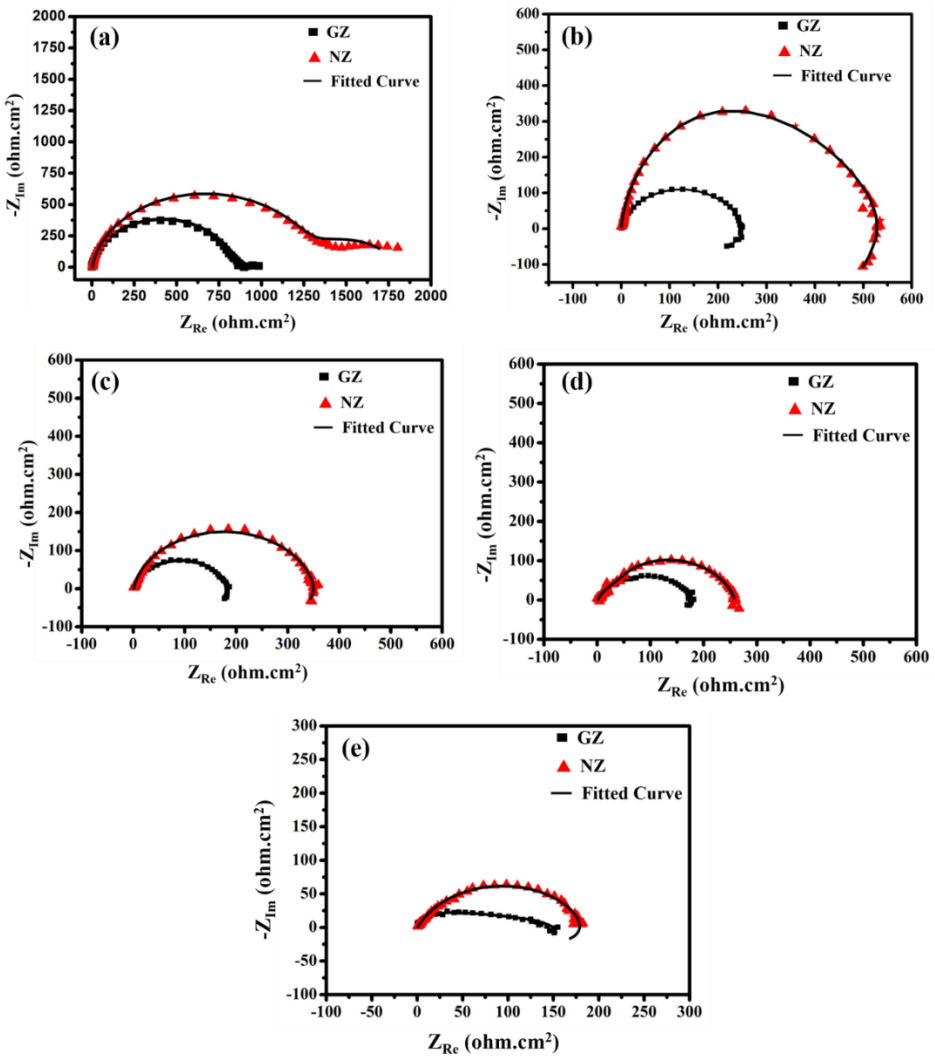

Figure 4.6. Nyquist plots of alloys measured in 1 wt.% NaCl at different times (a) 30 min. (b) 1 day (c) 3 days (d) 7 days (e) 14 days.

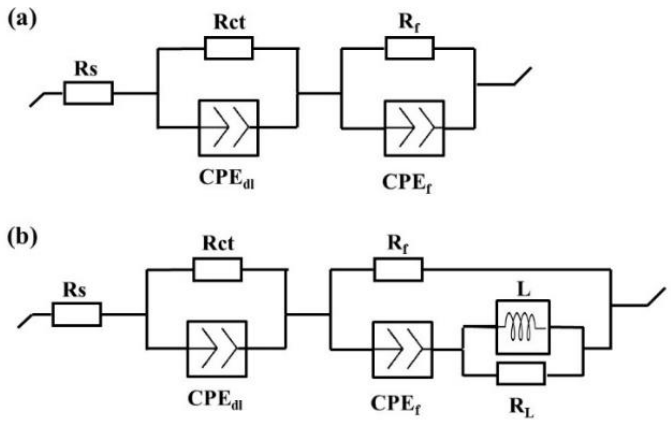

Figure 4.7. Equivalent electrochemical circuits of the alloys at different immersion times in 1 wt.% NaCl (a) 30 min. (b) 1-14 days.

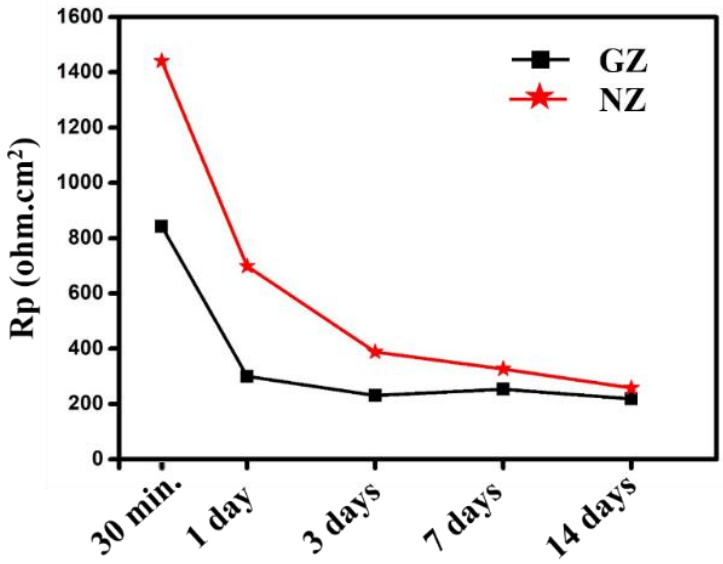

Figure 4.8. (a) Rp (R_{ct} + R_f or R_{ct} + R_f + R_L) of alloys obtained from impedance measurement in 1 wt.% NaCl at different immersion time.

4.3.3 Weight loss measurement

The results of weight loss measurement in 1 wt.% NaCl for 3, 7 and 14 days (**Figure 4.9**) show that GZ alloy exhibited highest corrosion rate at all immersion time intervals. However, corrosion rate of NZ was much lower than that of GZ alloy at all-time intervals. Slight increase in corrosion rate beyond 3 days of immersion was observed for both these alloys and the corrosion rate was more or less same till 14-days of immersion. This is in

agreement with the EIS results as the Rp value (**Figure 4.8**) decreases as immersion time increases but the changes in Rp values is marginal beyond 3 days immersion.

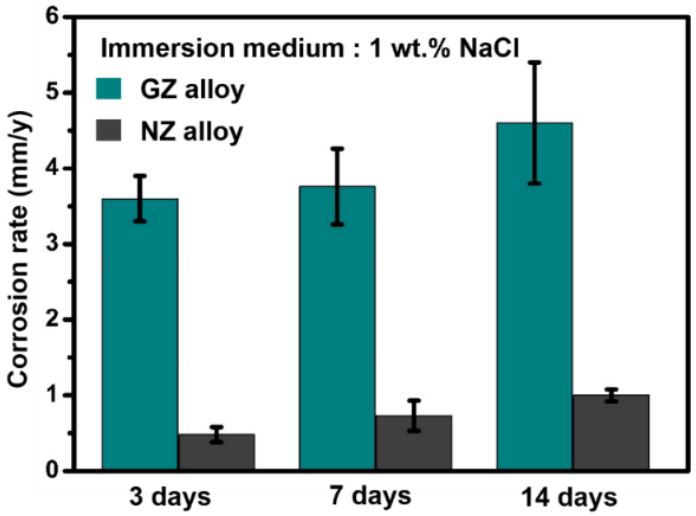

Figure 4.9. Corrosion rate of the alloys calculated from weight loss measurement of samples immersed in 1 wt.% NaCl at different immersion times.

4.3.4 Hydrogen evolution

Figure 4.10. shows the hydrogen volume measured during immersion of samples in 1 wt.% NaCl for 336 h (14 days). GZ alloy had the highest slope of hydrogen volume curve which indicated that it had undergone severe corrosion compared NZ. The measurement for GZ alloy was stopped at 120 h since the maximum measurable amount of H_2 was reached (the maximum limit of the apparatus was 330 mL). The result of hydrogen evolution of the alloys was in good agreement with the weight loss measurements as the total hydrogen evolution volume was lowest for alloy NZ.

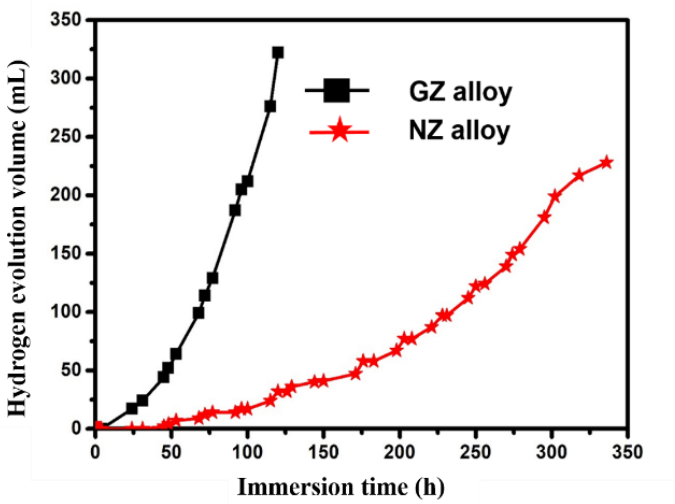

Figure 4.10. Volume of evolved hydrogen from the alloys immersed in 1 wt.% NaCl for 14 days.

4.3.5 XPS analysis of corrosion layer

To analyze the composition of corrosion layer, XPS measurements were done on the samples immersed in 1 wt.% NaCl for 30 min. Depth profiling measurement was carried out for 1800 seconds of sputtering and the sputtered depth was calculated from a related removal rate of 20 nm/min. for SiO_2 which was found to be approximately 600 nm (The sputtering was not carried out beyond 600 nm due to the limitations of the instrument and machine safety concerns). The depth profiles of the corrosion films on the samples (**Figure 4.11**) indicated that the atomic concentration of Mg at a depth of 600 nm was highest for GZ alloy. This indicates that that after 30 min. immersion, corrosion layer thickness was lowest for GZ. Moreover, both the alloys showed the presence of Zn. Relatively minimum or negligible atomic concentration of Gd was observed in the corrosion layers of GZ. In contrast, an appreciable amount of Nd was present in the oxide layer on NZ alloy from the surface to the end of sputter depth up to 600 nm.

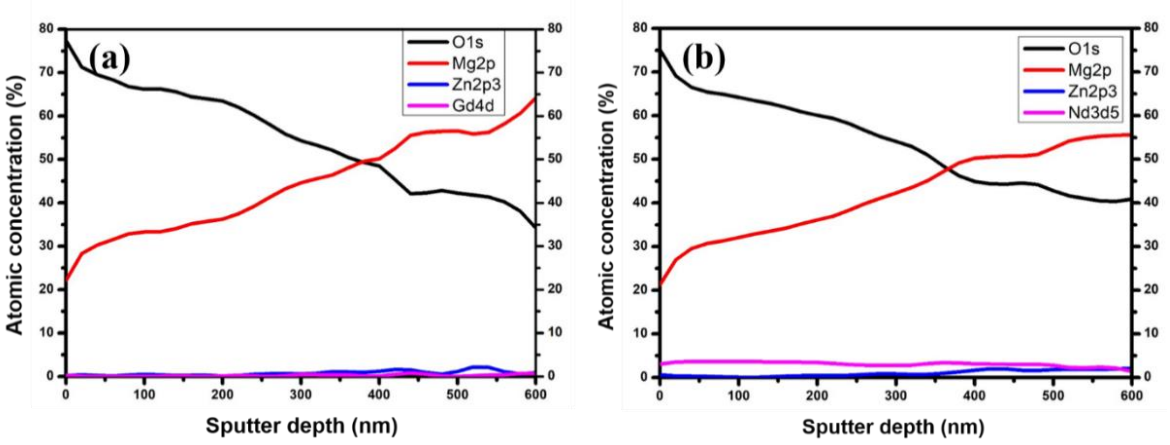

Figure 4.11. Depth profile analysis of the corrosion layers on the samples immersed in 1 wt.% NaCl for 30 min. (a) GZ, (b) NZ.

The DP-XPS spectra of O1s, Mg2p and Zn2p3 of the alloys were similar. Therefore, for analysis, XPS depth profiling (DP-XPS) spectra of O1s, Mg2p and Zn2p3 of the corrosion film on the GZ alloy is shown in **Figure 4.12**. The higher bond energy (BE) peak centred at 533.5 eV in O1s spectra [**Figure 4.12 (a)**] and the broader low BE peak at 300 nm depth centred at 531 eV confirmed the presence of hydroxide and oxide state of oxygen respectively [9]. Mg2p spectra [**Figure 4.12 (b)**] were in good agreement with the O1s spectra [**Figure 4.12 (a)**]. The Mg2p spectra of the surface of GZ alloy shows the BE peak was centred between 49.5 eV ($Mg(OH)_2$) and 50.25 eV (MgO). The energy peak at 49.6 eV and 51 eV at 400 nm corresponded to magnesium hydroxide and magnesium oxide [28].

Energy peak of Mg2p spectra at 600 nm showed the presence of Mg (at 49.4 eV) and MgO (at 50.8 eV). However, the area fraction of the $Mg(OH)_2$ decreased where as that of MgO and Mg increased as the sputtering depth increased. This also explains why the atomic percentage of oxygen decreased as the sputtering depth increased. Zn2p3 profile [**Figure 4.12 (c)**] showed a distinguishable peak after 400 nm at 1021.2 eV that corresponds to ZnO [29]. However, no such distinguishable peaks were seen in the DP-XPS spectra of [**Figure 4.13 (a)**], indicating that the presence of Gd was were minimal in the corrosion film till 600 nm of depth. However, in the NZ alloy presence of broader BE peaks at 983.2 eV [**Figure 4.13 (b)**] in Nd3d5 spectra indicating the presence of Nd_2O_3 in the corrosion layer.

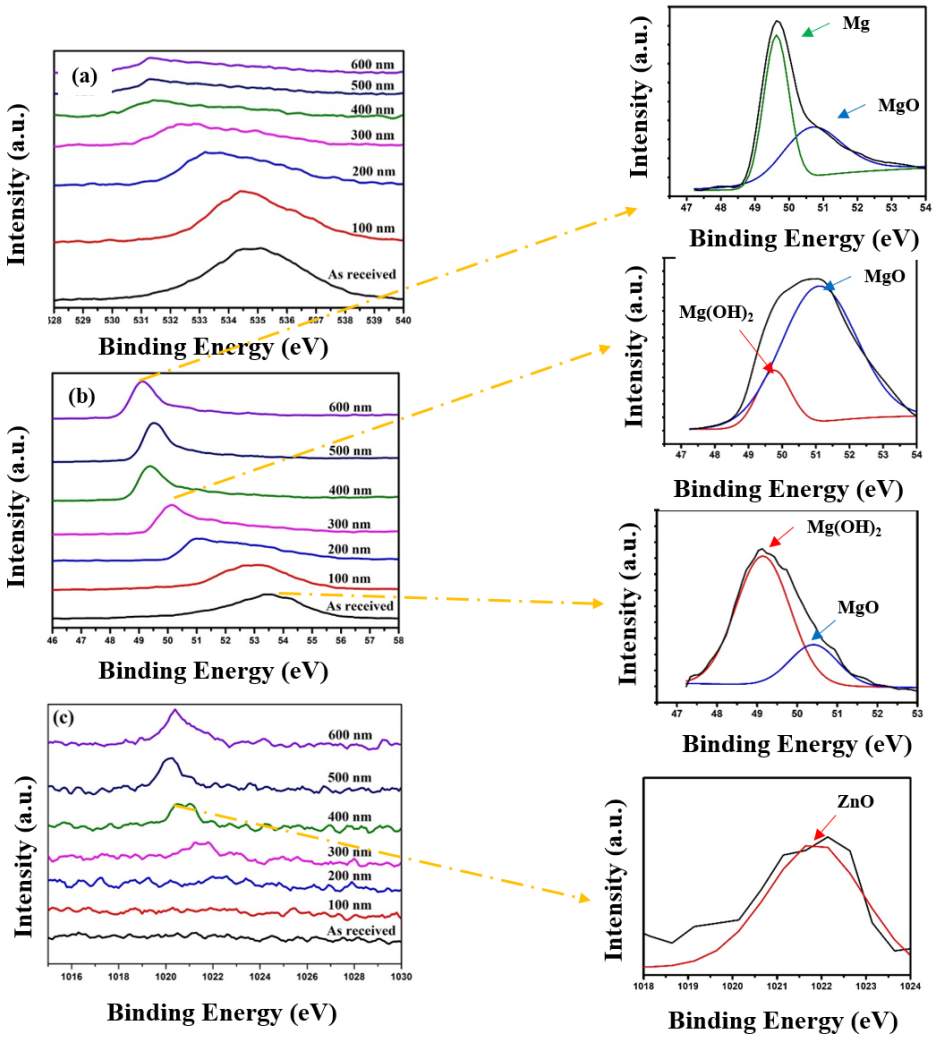

Figure 4.12. DP-XPS spectra of different elements on the corrosion layers on GZ alloy sample immersed in 1 wt.% NaCl for 30 min. (a) Mg2p (b) O1s (c) Zn2p3.

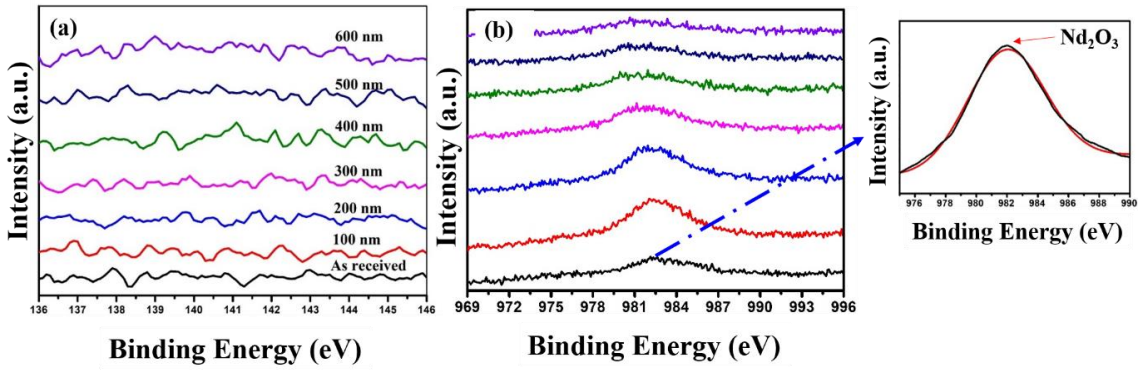

Figure 4.13. DP-XPS spectra of the rare earth elements on the corrosion layers on the alloys immersed in 1 wt.% NaCl for 30 min. (a) Gd4d (b) Nd3d5.

Thus, the XPS analysis of corrosion layer after 30 min. immersion revealed that both the alloys consisted of $Mg(OH)_2$ in the outer layer and MgO and ZnO in the inner layer. In addition, NZ alloy had the presence of Nd_2O_3 in the corrosion layer. Although the presence of rare earths in GZ was minimal in corrosion layer, the surface films were reasonably protective in nature initially as it was evident from EIS analysis of the alloys after 30 min. immersion [**Figure 4.6 (a)**] that there were no inductive loops in the alloy. The Rp values obtained using electrochemical impedance measurement (**Figure 4.8**) showed that NZ alloy had the highest resistance at 30 min. immersion owing to the presence of Nd_2O_3 on the surface.

4.3.6 Corrosion product analysis

The XRD analysis (**Figure 4.14**) of the corrosion product obtained by immersing the samples in 1 wt.% NaCl for 14 days suggested that they mainly composed of $Mg(OH)_2$ (JCPDS: 019-0771) and traces of ZnO (JCPDS: 001-1136). Other than these elements the diffraction patterns suggested the presence of Gd_2O_3 (JCPDS: 01-088-2165) in GZ alloy, and Nd_2O_3 (JCPDS: 040-1283) in NZ alloy. As expected, peaks corresponding to Gd_2O_3 in GZ alloy were weak, whereas and peaks for Nd_2O_3 in NZ alloy was relatively significant. However, no diffraction peaks corresponding to any of the second phases in the alloys were seen and might be due to the restriction in the detecting limit of XRD.

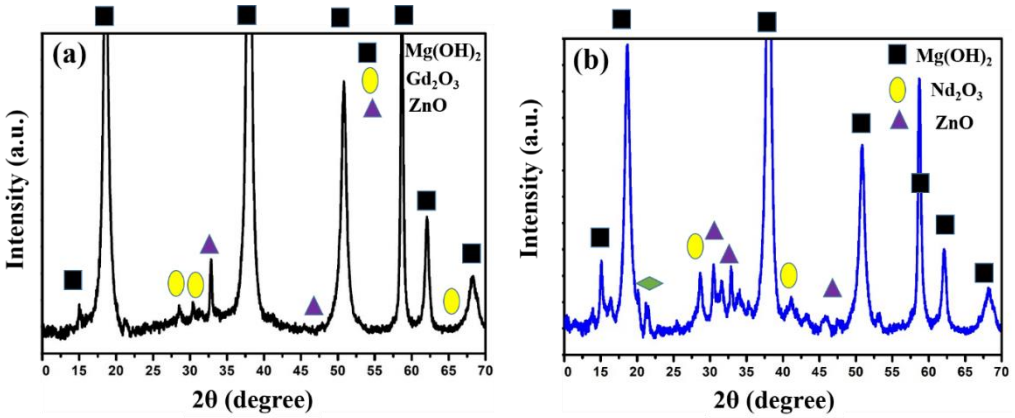

Figure 4.14. XRD analysis of the corrosion products obtained from samples immersed in 1 wt.% NaCl for 14 days (a) GZ (b) NZ alloys.

The effectiveness in protective nature of the oxides can be evaluated using the Pilling-Bedworth ratio (PBR) [30]. According to PBR theory, oxide layers with PBR < 1 will be porous and will not offer protection, like wise oxide layers with PBR > 2 will be susceptible to breakage due to stress and also does not offer protection. Whereas, the oxide layers with PBR between 1 and 2 have the capability to protect the material from further corrosion [31]. For instance, the PBR of MgO is 0.81 which does not offer any protection to the surface. However, certain RE oxides like Sc_2O_3 (PBR = 1.1), Y_2O_3 (PBR = 1.19), Nd_2O_3 (PBR = 1.02) will offer protection to the otherwise porous MgO layer and thus enhancing the corrosion resistance [32–34] [35]. Thus, the incorporation of alloying elements in the surface film influences the stability as well as dissolution kinetics of the film. For example, the presence of Al_2O_3 in the surface film of Mg-Al alloy offers better protection to the surface compared to $Mg(OH)_2$ or MgO [36,37]. Similarly, Zhang et al. [38] reported that the spontaneous formation of Nd_2O_3 on the corrosion layer enhanced the compactness of the surface film in Mg-2Zn-0.2Mn-xNd. Incorporation of the Nd_2O_3 on the corrosion film found to improve the corrosion resistance of AZ91 alloy [39] as well as in Mg-8Li-3Al-2Zn alloy containing Nd [40].

Although the surface film also consisted of $Mg(OH)_2$, it has a hexagonal crystalline structure and makes way for an easy basal cleavage. The hydrogen evolution accompanied with the cathodic reaction further weaken the surface film. The equilibrium pH of $Mg(OH)_2$ is around 11 which suggests that the film is non protective in normal aqueous environments where the pH is usually less than 11. Moreover, anions such as chloride,

sulphate, and nitrate tends to destroy the passivity of Mg as they are capable of breaking down the surface film on Mg [41].

In addition to the presence of Nd_2O_3 on the surface of the corrosion layer, which provided enhanced passivation and stability, the smaller grain size of the NZ alloy compared to the GZ alloy played a crucial role in improving its corrosion resistance. The grain size effect on corrosion behavior is primarily due to the higher density of grain boundaries in finer-grained materials. A smaller grain size results in a greater number of grain boundaries per unit area, which accelerates the formation of a more uniform and protective oxide layer across the alloy surface. These grain boundaries act as preferential sites for rapid oxide nucleation, allowing the development of a dense and continuous passive film that reduces localized attack and minimizes corrosion propagation. In contrast, coarser-grained alloys have fewer grain boundaries, leading to heterogeneous oxide formation, which is more susceptible to localized breakdown and pitting corrosion. The synergy between the protective Nd_2O_3 layer and the grain boundary-induced uniform oxide formation ultimately resulted in the superior corrosion resistance of the NZ alloy compared to the GZ alloy [42].

4.3.7 Corrosion Morphology

SEM analysis of the corroded samples at different immersion times were carried out to understand the corrosion initiation and propagation in the alloys. The second phases in Mg alloys are usually more inert than α-Mg matrix and they act as cathodic sites resulting in initiation of corrosion in the matrix next to the second phase [43]. The corrosion then spreads and gets accelerated as immersion time increases. The SEM micrograph of the alloys (**Figure 4.15**) immersed in 1 wt.% NaCl for 30 min. and without removing the corrosion products revealed that the corrosion was initiated next to the secondary phases as corrosion products (marked in white arrows) could be seen in the close proximity of secondary phases. More corrosion products were seen around the secondary phases in GZ alloy, suggesting that secondary phases found in GZ alloys were more cathodic in nature and susceptible to severe micro galvanic corrosion.

As the immersion time increased to 12 h, the SEM micrographs of all the alloys taken after cleaning the corrosion products exhibited a filament type propagation [**Figure 4.16**] of corrosion indicating the occurrence of filiform corrosion. Filiform corrosion occurs due to the movement of an active corrosion cell across the metal surface. Filament head

acts as the anode and the tail acts as cathode. It is usually observed in anodized or protective coated surfaces. However, the filiform corrosion in uncoated Mg alloys are also reported due to breakage of protective corrosion film on the alloy surfaces [31,44]. The filaments propagated through the matrix adjacent to the secondary phases. Pitting corrosion occurred in both the alloys but was least in NZ alloy. Few secondary phases still intact in the alloys are shown in **Figure 4.16 (c-d)** by white arrows.

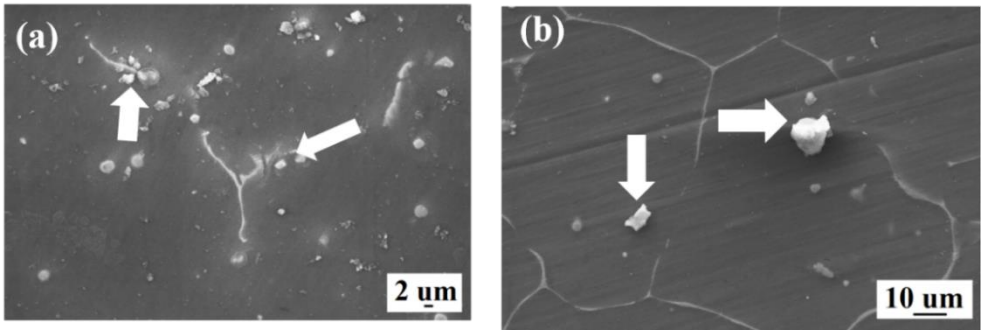

Figure 4.15. Corrosion morphology of alloys immersed in 1 wt.% NaCl for 30 min. without the removal of corrosion products (a) GZ (b) NZ alloy (corrosion products are marked in white arrows).

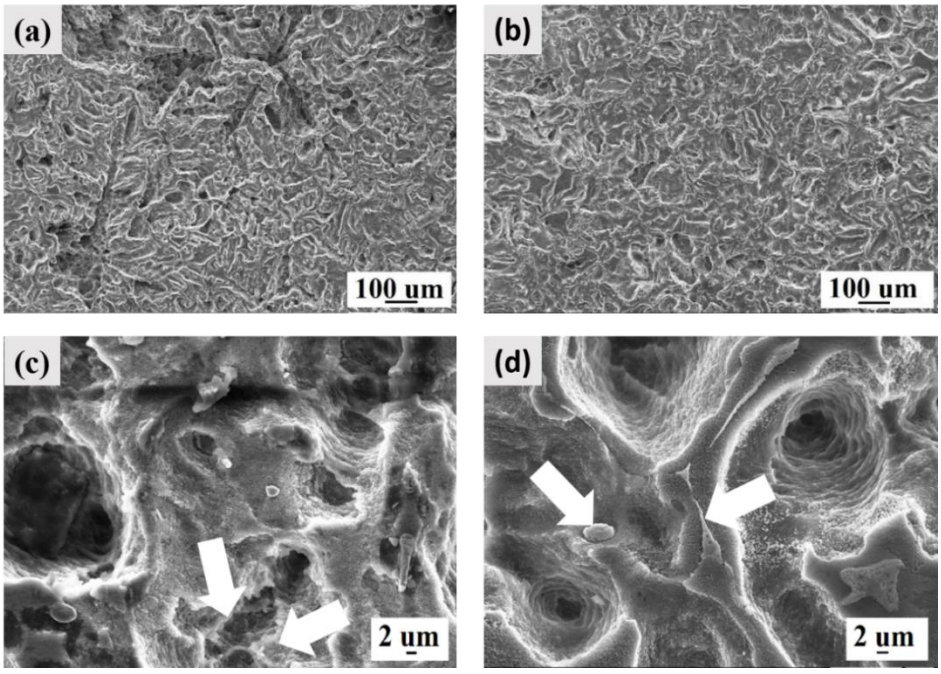

Figure 4.16. Corrosion morphology of samples immersed in 1 wt.% NaCl for 12 h after the removal of corrosion product (a& c) GZ, (b & d) NZ (secondary phases are marked in white arrows).

The cross section of the alloys after 12 h immersion shows that severe pitting has occurred in GZ alloy and that the secondary phases are in fact accelerating the corrosion [**Figure 4.17 (a)**]. Similar to GZ alloy, the cross section of the NZ alloy also showed small pits, however the propagation of pits further seemed to be impeded by the dendritic T phase [marked in blue arrows, **Figure 4.17 (b)**]. Similarly, the cross sectional SEM images of the alloys immersed for 3 days showed that GZ alloy showed severe pitting corrosion [**Figure 4.18 (a)**]. However, careful examination revealed that the elongated dendritic shaped W phase [marked in white arrows, **Figure 4.18 (b)**] was still intact, although the corrosion pits were spreading into the grain interior. This suggests that the dendritic W phase was not accelerating the corrosion unlike other discrete secondary phases found in GZ alloy and was able to retard it to an extent. The cross sectional morphology of the 3-day immersed NZ alloy showed that T phase [marked in white arrows, **Figure 4.18 (c)**] was able to impede the corrosion propagation.

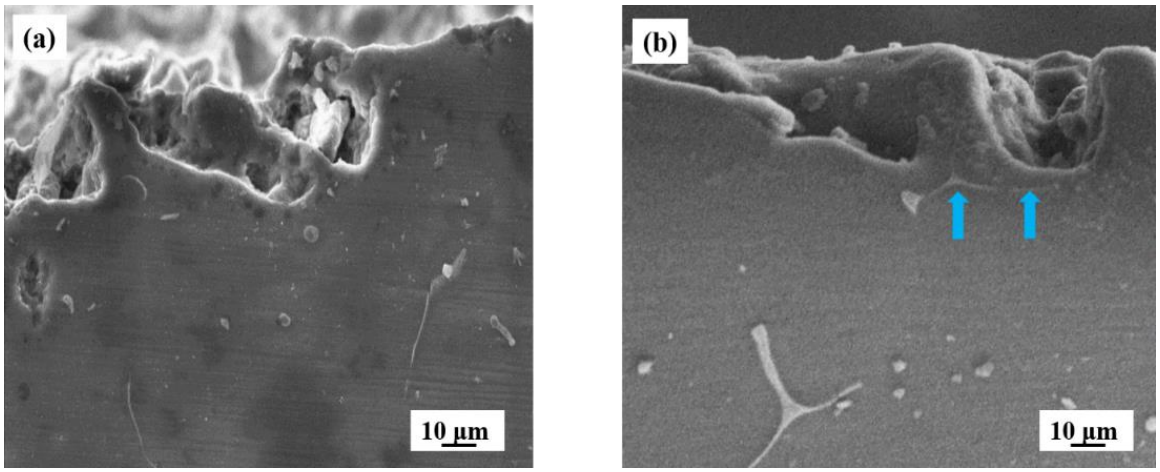

Figure 4.17. Corrosion morphology of the cross section of samples immersed in 1 wt.% NaCl for 12 hours after the removal of corrosion product (a) GZ, (b) NZ.

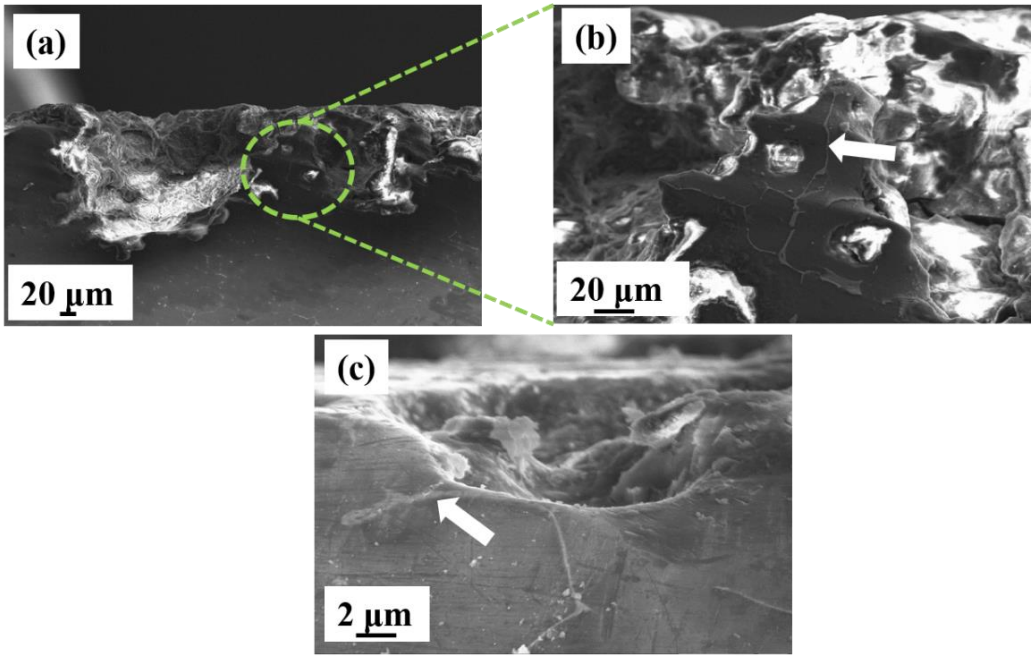

Figure 4.18. Corrosion morphology of the cross section of samples immersed in 1 wt.% NaCl for 3 days after the removal of corrosion product (a &b) GZ, (c) NZ.

The secondary phase in Mg alloys can either act as micro cathode to accelerate corrosion or to retard corrosion by acting as an effective barrier depending up on the volume fraction and distribution. This dual role of secondary phase is more obvious in AZ alloys where continuously distributed β phase (second phase) effectively retards the corrosion whereas corrosion is accelerated by the presence of discontinuously distributed β phase [9,45]. Although almost all secondary phases found in Mg alloys are cathodic in nature, the secondary phases in certain Mg alloys are reported to be relatively anodic, and are preferentially corrode [31,43]. In the present study, micro galvanic corrosion initiated around the secondary phases in all the alloys (**Figure 4.15**) and it gradually spread into grain interior (**Figure 4.16**), indicating that secondary phases present in these alloys were cathodes to α Mg matrix. The secondary phases in GZ alloys were more cathodic and more cluster of corrosion products near the phases in GZ alloy after 30 min. immersion [**Figure 4.15 (a)**]. In addition, severe pits in the corrosion morphology after 12 h immersion [**Figure 4.16 (a)**] suggesting that severe micro galvanic corrosion occurred in GZ alloy. Similarly, Tafel analysis (**Figure 4.5**) showed higher cathodic activity in NZ alloy due to second phase, and the corrosion pits evident from the SEM analysis of corrosion morphology after 12 h immersion [**Figure 4.16 (b)**] suggesting that the secondary phase in NZ acted as cathodic and accelerated micro galvanic corrosion. In spite of that, the uniformly

distributed network shaped secondary phases in NZ alloys inhibited the corrosion and improved the overall corrosion resistance of the alloy. The corrosion barrier effect of network secondary phases was also evident from the SEM analysis of corrosion morphology after 3 days immersion [**Figure 4.18 (c)**] that showed a severely corroded matrix was surrounded by a network of second phase. The distribution of secondary phases was different from alloy to alloy, and continuous network of phases retarded the corrosion spreading as evident from NZ alloy.

4.3.8 Conclusion

The corrosion behavior of Mg-Zn-RE alloys is strongly influenced by the morphology and distribution of secondary phases, along with the characteristics of the oxide layer formed during corrosion. The distinct effects of Gd and Nd on phase formation and corrosion resistance emphasize the importance of RE selection in optimizing alloy performance. The key findings are as follows:

- Secondary phases observed in Mg-4Zn-1Gd discrete whereas they were distributed as network shape in Mg-4Zn-01Nd alloys.
- The discontinuously distributed secondary phases accelerated corrosion in Mg-4Zn-1Gd alloy.
- In spite of higher cathodic activity of second phases, the network morphology as well as the presence of Nd_2O_3 in the corrosion layer significantly improve the corrosion resistance of Mg-4Zn-01Nd alloy.

Part B: Role of Zr in Mg-Zn-RE alloys

4.3.9 Microstructure

The XRD patterns of the Zr-added alloys are shown in the **Figure 4.19**. As observed in the GZ and NZ alloys, only Mg peaks were present, with no detectable peaks related to secondary phases. The SEM micrographs shown in the **Figure 4.20** revealed that the Zr addition to the alloys did not change the phase compositions and morphology. The EDS analysis (**Table 4.4**) of the alloys revealed that the network shaped secondary phases marked as A in **Figure 4.4 (b)** was found to be W phase, spherical phases marked as B in **Figure 4.4 (b)** was found to be Mg-Zn binary phase and very fine particle shaped secondary phase found in the grain interior [marked as C in **Figure 4.4 (b)**] was found to be Mg-Zr binary phase. Also, EDS analysis of NZK alloy revealed that the network shaped phase [marked as A in **Figure 4.4 (d)**] and spherical phases [marked as B in **Figure 4.4 (d)**] were

found to be T phase. Similar to GZK alloy, the particle shaped secondary phase [marked as C in **Figure 4.4 (d)**] in the grain interior was found to be Mg-Zr binary phase.

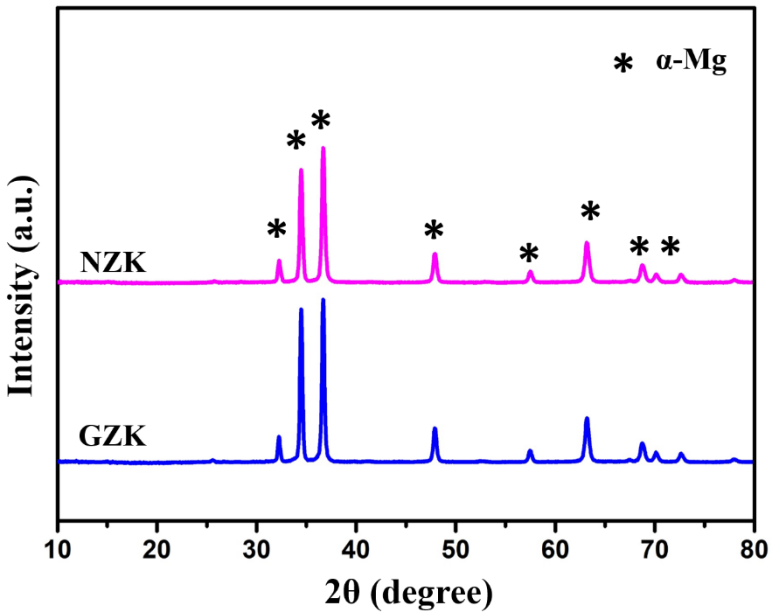

Figure 4.19. XRD patterns of GZK and NZK alloys.

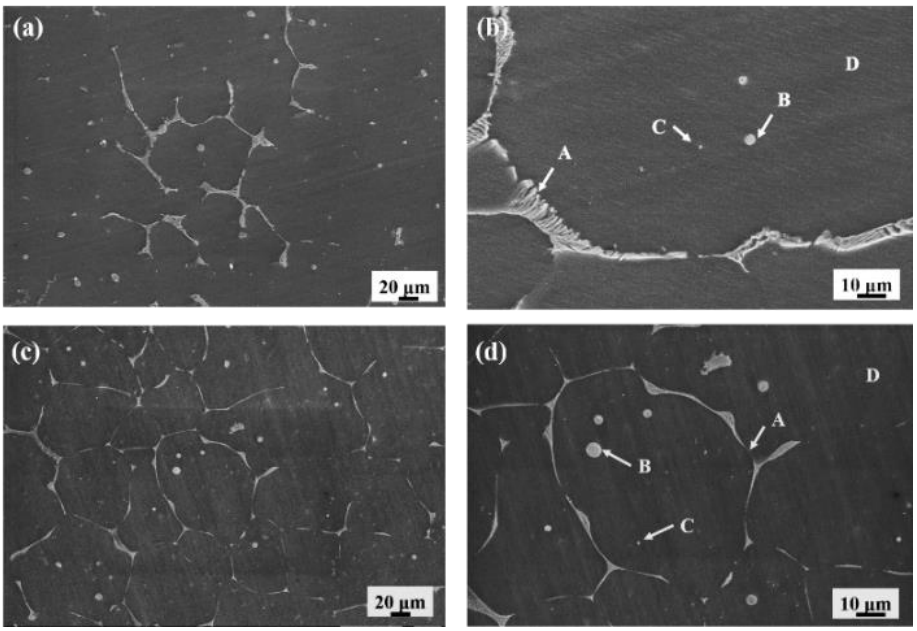

Figure 4.20. SEM micrographs of as-cast alloys (a&b) GZK, (c&d) NZK.

The EBSD micrograph of the alloys (**Figure 4.21**) shows that Zr addition resulted in the significant grain refinement in GZK alloys. A significant grain size reduction from 524 (±171) µm to 144 (±50) µm was observed in Gd containing alloy where as in Nd containing alloy the grain size was reduced from 203 (±63) µm to 166 (±42) µm. The significant reduction in grain size observed in the Mg-Gd-Zn-Zr alloy compared to the Mg-Nd-Zn-Zr alloy can be attributed to the combined effects of zirconium (Zr) as a grain refiner and the influence of rare earth elements (Gd and Nd) on solidification behavior. Zr is known to refine grains in magnesium alloys by forming fine Zr-rich particles that act as heterogeneous nucleation sites during solidification [10–12]. However, in the NZ alloy the grain size was already finer compared to GZ alloy. This might have hampered the grain refinement effectiveness of Zr in NZ alloys. Whereas, the scope for grain refinement was high in the coarse grained GZ alloy.

Table 4.4. EDS analysis of the different secondary phases in the alloys

Alloy	Position	Elements (at.%)			Phase
		Mg	Zn	RE	
GZK	Figure 4.16 (b) – A	79.35	14.18	6.47	$Mg_3Zn_3Gd_2$
	Figure 4.16 (b) – B	55.93	42.14	1.89	Mg-Zn binary
	Figure 4.16 (b) – C	80.32	2.05	17.61 (Zr)	Mg-Zr
	Figure 4.16 (b) – D	98.56	1.39	0.06	Matrix
NZK	Figure 4.16 (d) – A	79.27	16.38	4.35	Mg_7Zn_3Nd
	Figure 4.16 (d) – B	72.96	21.59	5.45	Mg_7Zn_3Nd
	Figure 4.16 (d) – C	80.34	1.05	18.61 (Zr)	Mg-Zr binary
	Figure 4.16 (d) – D	98.8	1.16	0.04	Matrix

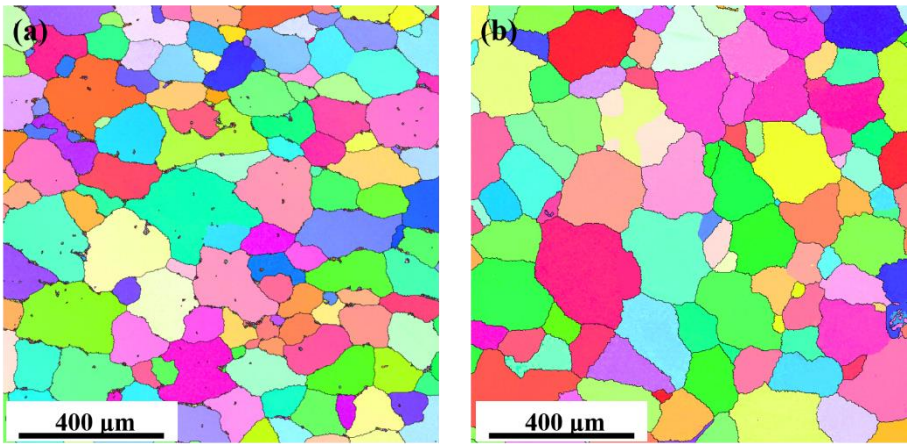

Figure 4.21. Grain boundary overlaid inverse pole figure maps (IPF) of (a) GZ, (b) NZ alloy.

4.3.10 Tensile Properties

The tensile properties of the Mg-Zn-RE alloys exhibit significant variations due to differences in grain size, secondary phases, and the specific roles of the rare-earth elements (Gd and Nd) in strengthening mechanisms. The tensile properties of the alloys (YS, UTS, and % elongation) are summarized in **Table 4.5**, and the corresponding stress-strain curves are shown in **Figure 4.22**. The GZ alloy, with largest grain size of 524 (±171) µm, unexpectedly exhibited a similar yield strength (YS) of 60 (±8.6) MPa. that might be primarily attributed to the strong solid-solution strengthening effect of Gd. The greater solubility of Gd in Mg (~23.5 wt%) compared to Nd (~3.7 wt%) allows for more extensive solid-solution strengthening, compensating for the lack of grain boundary strengthening in the coarse-grained GZ alloy. However, the ductility was lowest for GZ alloys (3.9% elongation) owing to its coarse grains. On the other hand, the NZ alloy, which had a finer grain size, exhibited a higher UTS [188 (±13.8) MPa] and similar YS [58 (±5.7) MPa] compared to GZ. The improved strength in NZ was attributed to grain boundary strengthening. The elongation of NZ [4.8 (±0.82) %] was higher than that of GZ, which suggested that the finer grain structure and uniformly distributed finer precipitates facilitated better plastic deformation, preventing premature crack formation. With the introduction of Zr, the grain sizes in both alloy systems were further refined, leading to significant improvements in strength and ductility. The GZK alloy, with a substantially refined grain size of 144 (±50) µm, exhibited the highest UTS of 215 (±10.16) MPa and a sharp increase in YS to 95 (±6.3) from 60 (±8.6) MPa. The combination of strong solid-

solution strengthening from Gd, and grain refinement due to Zr addition enhanced the tensile properties of GZK. The drastic increase in YS from 60 (±8.6) MPa (for GZ) to 95 MPa (±6.3) (for GZK) confirmed that grain boundary strengthening was a dominant factor in determining yield strength. In contrast, the NZK alloy, which also underwent grain refinement to 163 (±42) µm, exhibited a UTS of 196 (±7.82) MPa and maintained a YS of 60 (±8.2) MPa, but showed the highest elongation of 5.82 (±0.55) %.

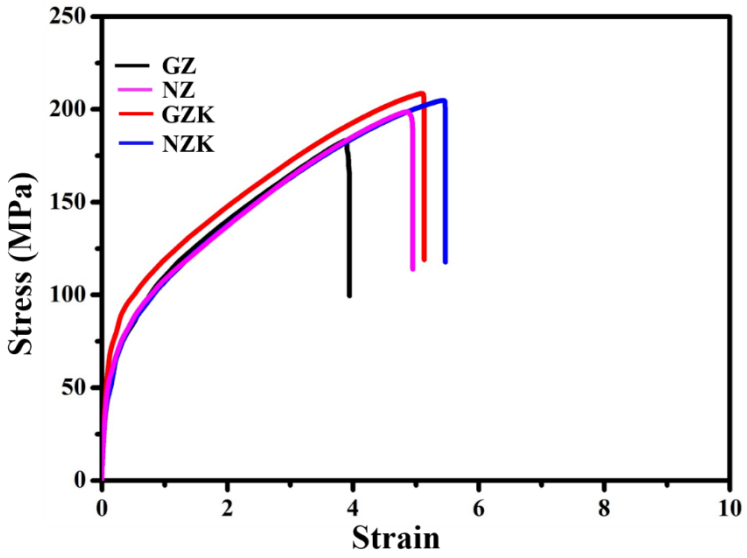

Figure 4.22. Tensile stress-strain curves of the alloys.

Table 4.5. Yield strength (YS), Ultimate tensile strength (UTS) and Elongation (%) of Alloys.

Alloy code	UTS	YS	% Elongation
GZ	175 (±24.4)	60 (±8.6)	3.9 (±0.94)
NZ	188 (±13.8)	58 (±5.7)	4.8 (±0.82)
GZK	215 (±10.16)	95 (±6.3)	5.09 (±0.76)
NZK	196 (±7.82)	60 (±8.2)	5.82 (±0.55)

4.3.11 Electrochemical corrosion measurement

The Tafel extrapolation data of the alloys before and after the Zr addition are summarised in **Table 4.6** (values for GZ and NZ alloys were reproduced from **Table 4.3**) and the Tafel plots of the Zr added alloys are shown in **Figure 4.23**. The OCP of GZ (-

1571 mV vs. SCE) and GZK (-1570 mV vs. SCE) were nearly identical, suggesting that Zr addition did not significantly alter the initial electrochemical stability of the passive film in the GZ system. A similar trend was observed for NZ (-1423 mV vs. SCE) and NZK (-1467 mV vs. SCE), although the more negative OCP of NZK suggests a slight shift toward a more active state. The corrosion potential (E_{corr}) showed a notable trend, with GZ exhibiting a value of -1486 mV, while GZK shifted to a more negative value of -1500 mV, indicating a slightly increased tendency for electrochemical dissolution. In contrast, NZ (-1430 mV) and NZK (-1425 mV) show minimal variation, suggesting that the influence of Zr on E_{corr} in the NZ system was less pronounced compared to the GZ system.

The corrosion current density (i_{corr}), which reflects the corrosion rate, revealed a significant improvement after Zr addition, particularly in the GZ system. The i_{corr} of GZ decreased from 12.58 μA/cm² to 7.94 μA/cm² in GZK, indicating that Zr effectively enhanced corrosion resistance by refining the microstructure and reducing localized galvanic corrosion effects. The observed reduction in i_{corr} was likely due to a more uniform grain structure and reduced segregation of Gd-containing intermetallic phases, which would otherwise have created cathodic sites that accelerated localized attack. However, Zr addition to Nd containing alloy increased i_{corr} marginally to 6.18 μA/cm² (NZK) from 5.16 μA/cm² (NZ) suggesting that effect of grain refinement was marginal in Nd alloys.

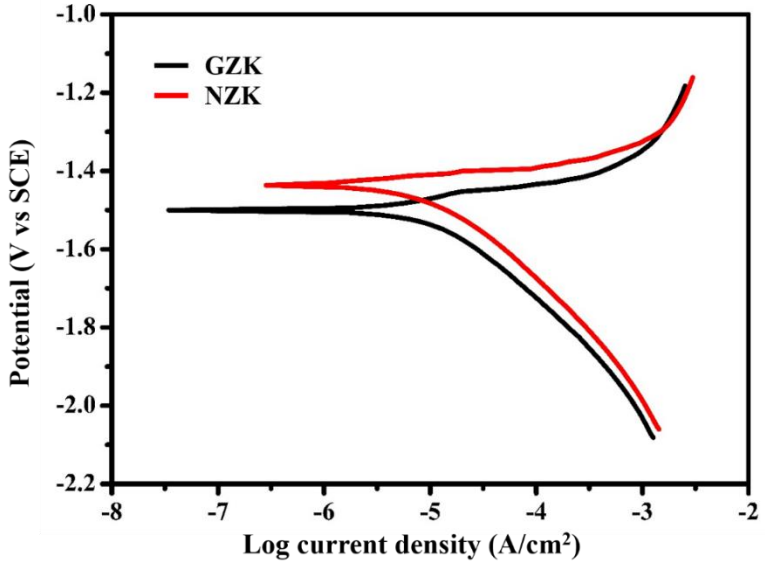

Figure 4.23. Polarization curves of GZK and NZK alloys in 1 wt.% NaCl.

Table 4.6. OCP, E_{corr} and i_{corr} values of alloys obtained from polarization measurements in 1 wt.% NaCl.

Alloy	OCP (mV vs SCE)	E_{corr} (mV vs SCE)	i_{corr} (μA/cm^2)
GZ	-1571	-1486	12.58
NZ	-1423	-1430	5.16
GZK	-1570	-1500	7.94
NZK	-1467	-1425	6.18

The EIS analysis of the alloys was performed using Nyquist and Bode plots (**Figure 4.24**). The Nyquist plots [**Figure 4.24 (a)**] and bode plots [**Figure 4.24 (b&c)**] of the GZK and NZK alloys were almost similar, suggesting that the corrosion rates and mechanisms were similar. In addition, the inductive loop was absent in both the alloys, suggesting that pitting corrosion was not initiated. The Bode plots also revealed that there were no sudden dips indicating no pitting corrosion associated with any of the alloys. The EIS spectra of the alloys were fitted using the ZSimpWin 3.20 software with the electrochemical circuit as shown in **Figure 4.24 (d)** for GZK and NZK alloys and the data is summarized in **Table 4.7**. The solution resistance (R_s), which represents the electrolyte resistance, is similar for both alloys, with GZK at 130.65 Ω·cm² and NZK at 122.7 Ω·cm², indicating minimal influence from the electrolyte conductivity. The charge transfer resistance (R_1), which reflects the resistance to charge transfer at the metal-electrolyte interface, is slightly higher for NZK (1222.3 Ω·cm²) compared to GZK (1147 Ω·cm²), suggesting that NZK forms a more stable passive layer that reduces corrosion initiation.

The constant phase element (CPE_1), which represents the capacitance of the passive film, was slightly higher for NZK (8.92×10^{-6} Sn/Ω·cm²) than GZK (8.28×10^{-6} Sn/Ω·cm²), with both alloys exhibited a similar exponent ($n_1 \approx 0.94$), indicating near-ideal capacitive behavior of the passive film. Also, the secondary charge transfer resistance (R_2), which corresponds to the resistance offered by the corrosion product layer and secondary interfacial reactions was similar. GZK exhibited a higher R_2 value (303.55 Ω·cm²) compared to NZK (238.43 Ω·cm²), indicating that the corrosion product layer in GZK

provided slightly better resistance to charge transfer. Conversely, the second constant phase element (CPE_2) values were higher in NZK (1753 × 10^{-6} Sn/Ω·cm²) than in GZK (1214 × 10^{-6} Sn/Ω·cm²), with the exponent n_2 values of 0.844 (GZK) and 0.841 (NZK). The significantly lower CPE_2 value in case of GZK suggested that the corrosion layer in GZK had a lower capacitance, implying a more compact corrosion product layer compared to GZK. The lower CPE_2 value in GZK could be attributed to its smaller grain size, which resulted in a higher density of grain boundaries. These grain boundaries acted as nucleation sites for corrosion products, promoting the formation of a more compact and adherent passive layer. As a result, the corrosion film in GZK was denser and less porous, leading to lower capacitance.

Additionally, the polarization resistance (R_p), a key indicator of overall corrosion resistance, is slightly higher for NZK (1460.73 Ω·cm²) compared to GZK (1450.55 Ω·cm²), reinforcing the trend observed in charge transfer resistance values. This aligns well with the Tafel analysis, where NZK exhibited a lower corrosion current density (i_{corr}), confirming a slower corrosion rate.

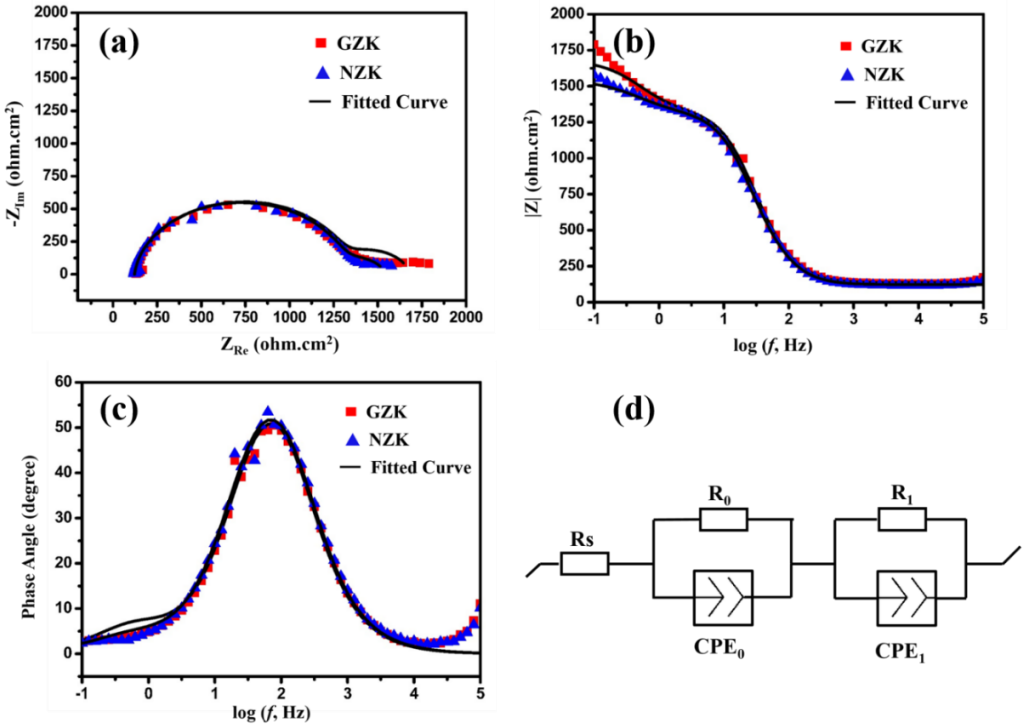

Figure 4.24. (a) Nyquist plots, (b) Bode plots of log *Z*mod *vs.* log *f*, (c) Bode plot of Phase angle *vs.* log *f*, of alloys measured in 1 wt.% NaCl, (d) Equivalent electrochemical circuits of GZK & NZK.

Table 4.7. The fitted values of EIS measurements of alloys using equivalent circuits shown in **Figure 4.24.**

Alloy	R_s ($\Omega.cm^2$)	R_1 ($\Omega.cm^2$)	CPE_1 x 10^{-6} ($S^n/\ \Omega.cm^2$)	n_1	R_2 ($\Omega.cm^2$)	CPE_2 x 10^{-6} ($S^n/\ \Omega.cm^2$)	n_2	R_p ($\Omega.cm^2$)
GZK	130.65 (±6.43)	1147 (±45.25)	8.28 (±0.084)	0.94 (±0.002)	303.55 (±53.36)	1214 (±255)	0.844 (±0.02)	1450.55
NZK	122.7 (±10.17)	1222.3 (±68.93)	8.92 (±0.304)	0.94 (±0.007)	238.433 (±27.205)	1753 (±317)	0.841 (±0.032)	1460.73

4.3.12 Weight loss measurement

The corrosion rate of alloys calculated using weight loss measurements in 1 wt.% NaCl of Mg-Zn-RE alloys are shown in **Figure 4.25**. The GZ alloy exhibited the highest corrosion rate at 4.6 (±0.85) mm/y, while the GZK alloy demonstrated a significant reduction in corrosion rate to 1.45 (±0.24) mm/y. The NZ alloy exhibited the lowest corrosion rate at 1.01 (±0.19) mm/y. However, after Zr addition, NZK showed a slightly increased corrosion rate [1.5 (±0.29) mm/y] compared to NZ. The increase in corrosion rate for NZK can be attributed to the formation of Zr-rich precipitates within the grain interiors, which might act as highly cathodic sites due to their large volta potential difference with the Mg matrix, thereby accelerating localized corrosion [20,41]. Although the NZ alloy already possessed a protective oxide layer due to the presence of Nd_2O_3 [**Figure 4.11. (b) & 4.13. (b)**], the detrimental effect of Zr might have been dominant in NZK alloy. In contrast, the significant grain refinement in GZK might have overshadowed the negative effects of Zr-rich particles due to the formation of a compact oxide layer, which was absent in GZ [**Figure 4.11. (a)**]. Also, the photograph of the corroded samples after 14 days [**Figure 4.25. (b)**] showed that although all the alloys exhibited signs of pitting corrosion, GZ alloy suffered the most.

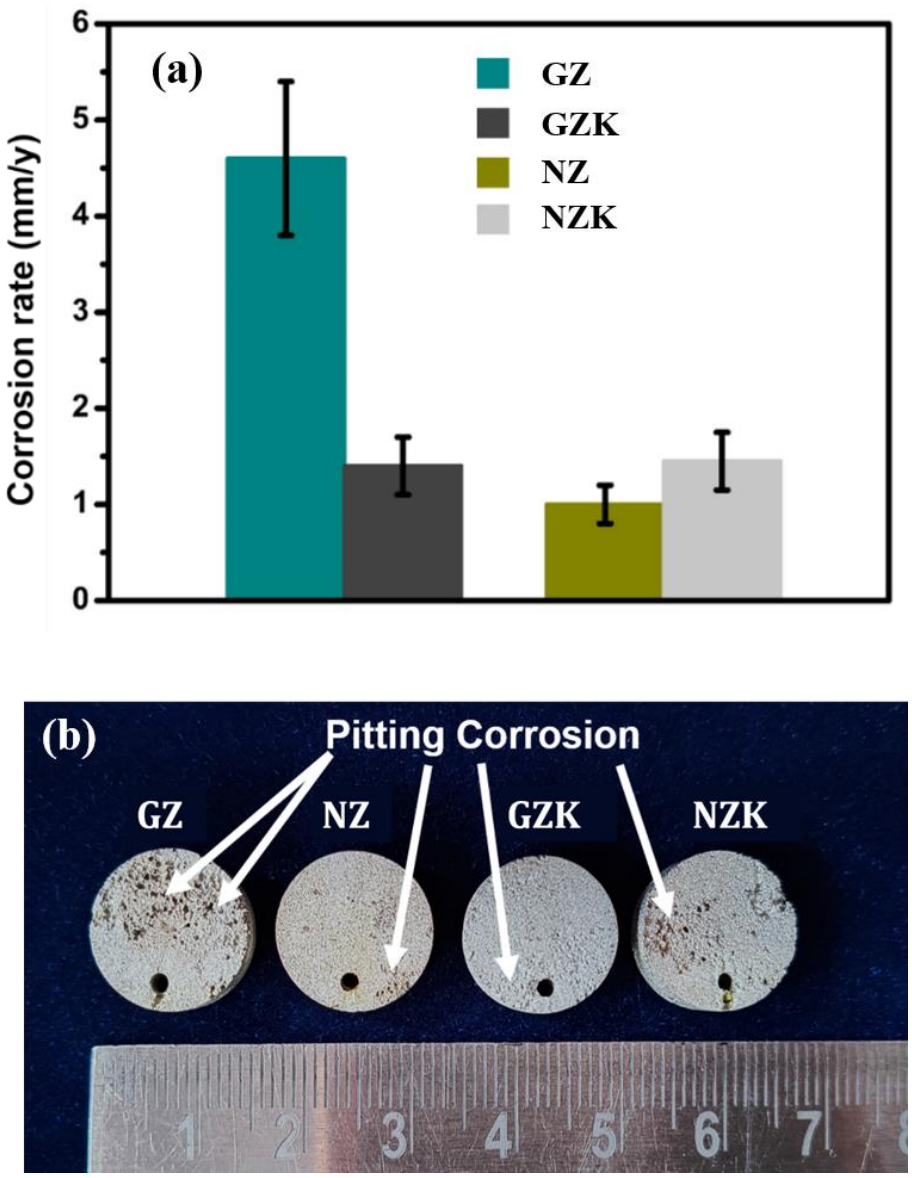

Figure 4.25. (a) Corrosion rate of alloys immersed in 1 wt.% NaCl for 14 days, (b) Photographs of corroded samples after immersed in 1 wt.% NaCl for 14 days.

The corrosion layer formed on the alloy surfaces was analyzed using XPS after immersion in 1 wt.% NaCl for 30 minutes. Depth profiling measurements were conducted up to 500 nm, with sputtering limited to this depth due to safety concerns and equipment constraints. Depth profile (DP) analysis (**Figure 4.26**) revealed that throughout the corrosion layer, the atomic concentrations of O and Mg remained nearly constant, indicating a uniform distribution of these oxides across the degradation layers in both alloys. Thus, the significant grain refinement achieved by Zr addition in the GZK alloy resulted in a compact corrosion layer comparable to that of the NZK alloy, leading to a similar corrosion rate. However, as seen in the Zr-free alloy, no presence of Gd was

detected in the GZK alloy either. Consequently, DP spectra for individual elements are not presented, as the addition of Zr does not alter the composition of the corrosion layer.

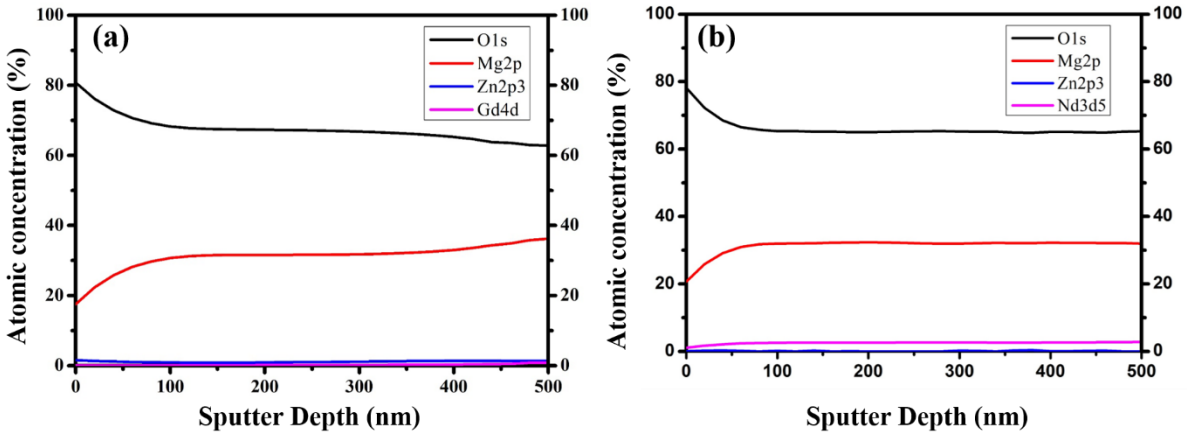

Figure 4.26. Depth profile analysis of the degradation layers on the sample immersed in 1 wt.% NaCl for 30 min. (a) GZK (b) NZK.

4.3.13 In-vitro studies

For biodegradable implant applications, achieving an optimal balance between tensile properties and corrosion resistance is crucial to ensure structural integrity during the initial healing phase while allowing controlled degradation over time. The tensile property evaluation of the Mg-Zn-RE alloys showed that Zr-added alloys (GZK and NZK) exhibited superior strength and ductility compared to their Zr-free counterparts, making them more suitable for load-bearing applications. Additionally, electrochemical analysis and weight loss measurements confirmed that GZK alloy had significantly improved corrosion resistance while NZK alloy had only a marginal change in corrosion rate in 1 wt.% NaCl solution. Since a controlled degradation rate is critical for biodegradable implants, and Zr-containing alloys demonstrated a better combination of tensile properties and corrosion resistance**,** only GZK and NZK were selected for in-vitro analysis to further evaluate their biocompatibility and degradation behavior under simulated physiological conditions.

4.3.13.1 Biodegradation test

The biodegradation rate of the alloys was done by immersing the samples in cell culture medium (MEM + 10% FBS + 1% Antibody) for 14 days (**Figure 4.27**). The biodegradation rate of the GZK and NZK alloys in Minimum Essential Medium (MEM) was 3.02 (±0.52) mm/y and 3.25 (±0.78) mm/y, respectively, which was significantly higher than their corrosion rates in 1 wt.% NaCl solution (1.45 mm/y and 1.5 mm/y,

respectively). This difference highlights the limitations of using isotonic NaCl solution for accurately predicting the in-vivo degradation behavior of biodegradable implants. While 1 wt.% NaCl solution is commonly used in corrosion studies, it does not fully replicate the complex physiological environment of the human body. NaCl solution primarily contains chloride ions, which are aggressive and promote pitting corrosion, but it lacks essential physiological components such as proteins, amino acids, organic molecules, and buffering agents, all of which influence biodegradation. In contrast, MEM provides a more physiologically relevant environment by simulating the ionic composition and organic content found in body fluids, leading to different electrochemical interactions at the alloy surface. The higher degradation rate in MEM can be attributed to the combined effects of proteins, amino acids, and bicarbonate ions, which can alter surface film stability, promote local pH fluctuations, and facilitate complexation reactions that accelerate Mg dissolution. Additionally, the biodegradation study was conducted at physiological temperature (37 °C), which further enhances reaction kinetics and ion mobility, leading to an increased corrosion rate compared to experiments in NaCl at room temperature. The results indicated that in-vitro studies in MEM provide a more realistic assessment of Mg alloy degradation behavior for biomedical applications**.** The image of the GZK and NZK alloys [**Figure 4.27 (b)**] after the biodegradation test clearly shows signs of pitting corrosion, indicating a localized rather than uniform degradation mechanism. Both the alloys were susceptible to non-uniform pitting corrosion. But the corrosion pits seem to be more uniform in NZK alloys.

To understand the degradation behaviour of these alloys in CCM, the degradation layer formed on their surface was analyzed. The XPS analysis of the degradation layer formed on the alloys immersed in cell culture medium for 24 h was done, and the depth profiling measurement was also carried out till 500 nm (Sputtering was limited to 500 nm due to the safety concerns and limitation of the machine) [**Figure 4.28**]. Depth profile (DP) analysis showed that throughout the thickness of the degradation layer, the elements such as O, Ca, and Mg did not have significant changes in the atomic concentrations indicating that the degradation layer was uniform in both the alloys till the analyzed sputter depth (**Figure 4.28**). Also, the presence of Zn, Gd and Nd was also confirmed through the depth profile analysis (**Figure 4.28**). Intensity of Zn and Gd was significantly low compared to Nd. The DP-XPS spectra of O1s, Mg2p and Ca2p of both the alloys were similar, and hence for representation, only DP-XPS spectra of GZK alloy is shown in **Figure 4.28**.

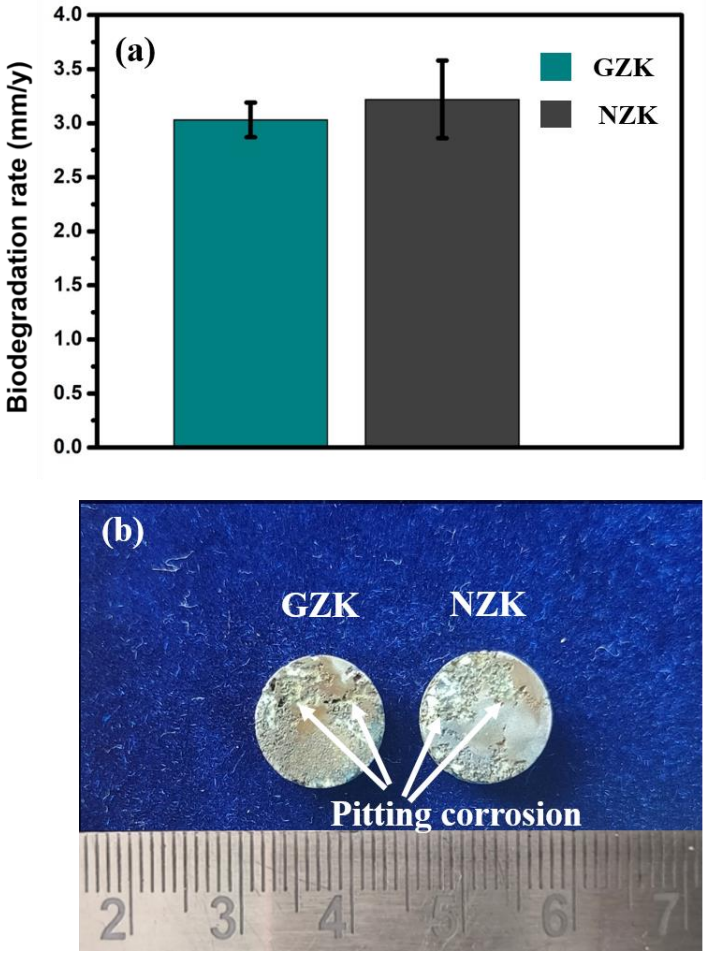

Figure 4.27. (a) Degradation rate of alloys immersed in cell culture medium for 14 days, (b) Photographs of degraded samples after immersed in cell culture medium for 14 days.

Also, the DP XPS spectra of O1s [**Figure 4.29 (a)**], Mg2p [**Figure 4.29 (b)**] and [**Figure 4.29 (c)**] was almost similar till 500 nm and thus only deconvoluted peak at 200 nm is shown for analysis. The binding energy (BE) peaks of O1s at 200 nm [**Figure 4.29 (d)**] centered at 530.1 eV, 532.4 eV, and 532.9 eV were attributed to the presence of oxygen in the form of oxide, phosphate, and hydroxides, respectively [9]. The Mg2p spectra [**Figure 4.29 (e)**] of the alloy at 200 nm depth showed the presence of $Mg(OH)_2$ (at 50.1 eV), $MgCO_3$ (at 50.95 eV) as well as MgO (at 51.5 eV) [28]. The Ca2p spectra of the alloy at 200 nm [**Figure 4.29 (f)**] confirmed the presence of CaO (at 351.5 eV) and hydroxyapatite [$Ca_{10}(PO_4)_6(OH)_2$ (at 347.9 eV)] in the degradation layer [46,47]. The DP-XPS spectra of Zn2p3, Gd4d of GZK and Nd3d5 of NZK alloys are shown in **Figure 4.30 (a-c)**. Zn2p3

spectra [**Figure 4.30 (d)**] at 400 nm (The presence of Zn was minimal up to 300 nm, making it challenging to extract meaningful data in this range. Therefore, the peaks at 400 nm were utilized for deconvolution, ensuring a more accurate analysis of the Zn distribution) from GZK alloy showed that the degradation layer comprised ZnO (at 1022.3 eV) [29] and the Gd4d spectra [**Figure 4.30 (e)**] from GZK alloy confirmed the presence of Gd_2O_3 (at 141.7 eV). Nd3d5 spectra [**Figure 4.30 (f)**] from NZK alloy showed that the degradation layer comprised Nd_2O_3 (at 1022.3 eV). Thus the degradation layer of GZK and NZK alloys consisted of $Mg(OH)_2$, MgO, $MgCO_3$, $Ca_{10}(PO_4)_6(OH)_2$, CaO, and ZnO, and the respective rare earth oxides (Gd_2O_3 in GZK and Nd_2O_3 in NZK). Thus the degradation layer was similar for both the alloys with both of the alloys having their respective rare earth oxides in the degradation film. The marginally better degradation resistance of GZK alloy could be attributed to the slightly finer grain size observed in GZK alloys compared to NZK [48,49].

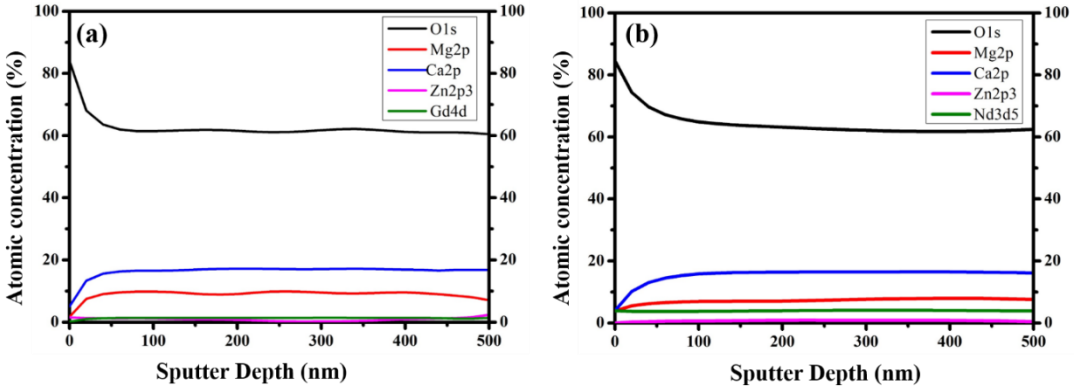

Figure 4.28. Depth profile analysis of the degradation layers on the sample immersed in cell culture medium for 24h (a) GZK (b) NZK.

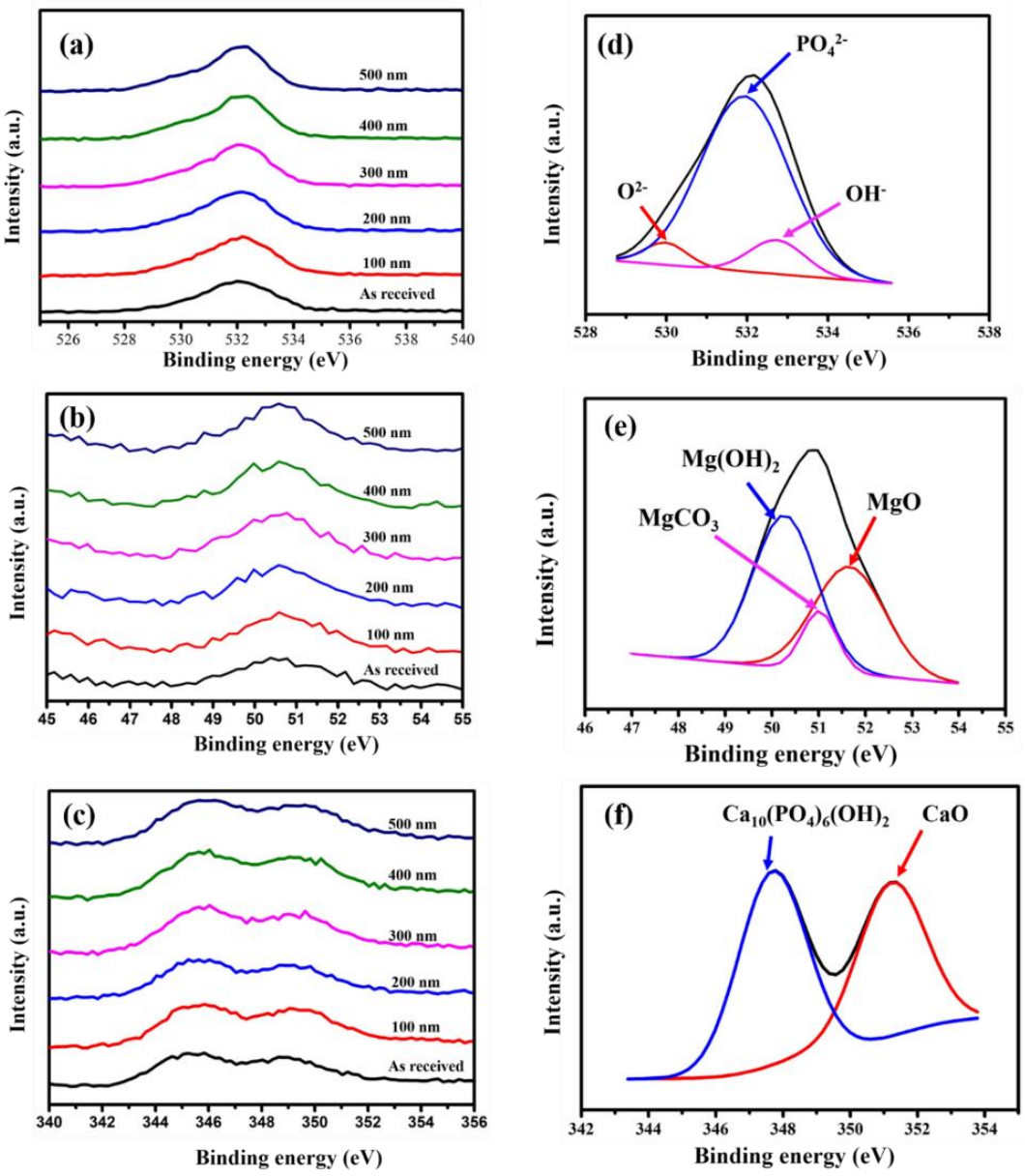

Figure 4.29. DP-XPS spectra of the corrosion layers on GZK alloy sample immersed in cell culture medium for 24h (a) O1s, (b) Mg2P (c) Ca2P and deconvoluted peaks (d) O1s peak at 200nm, (c) Mg2p, (d) deconvoluted Mg2p peak at 200 nm (e) Ca2p and (f) deconvoluted Ca2p peak at 200 nm.

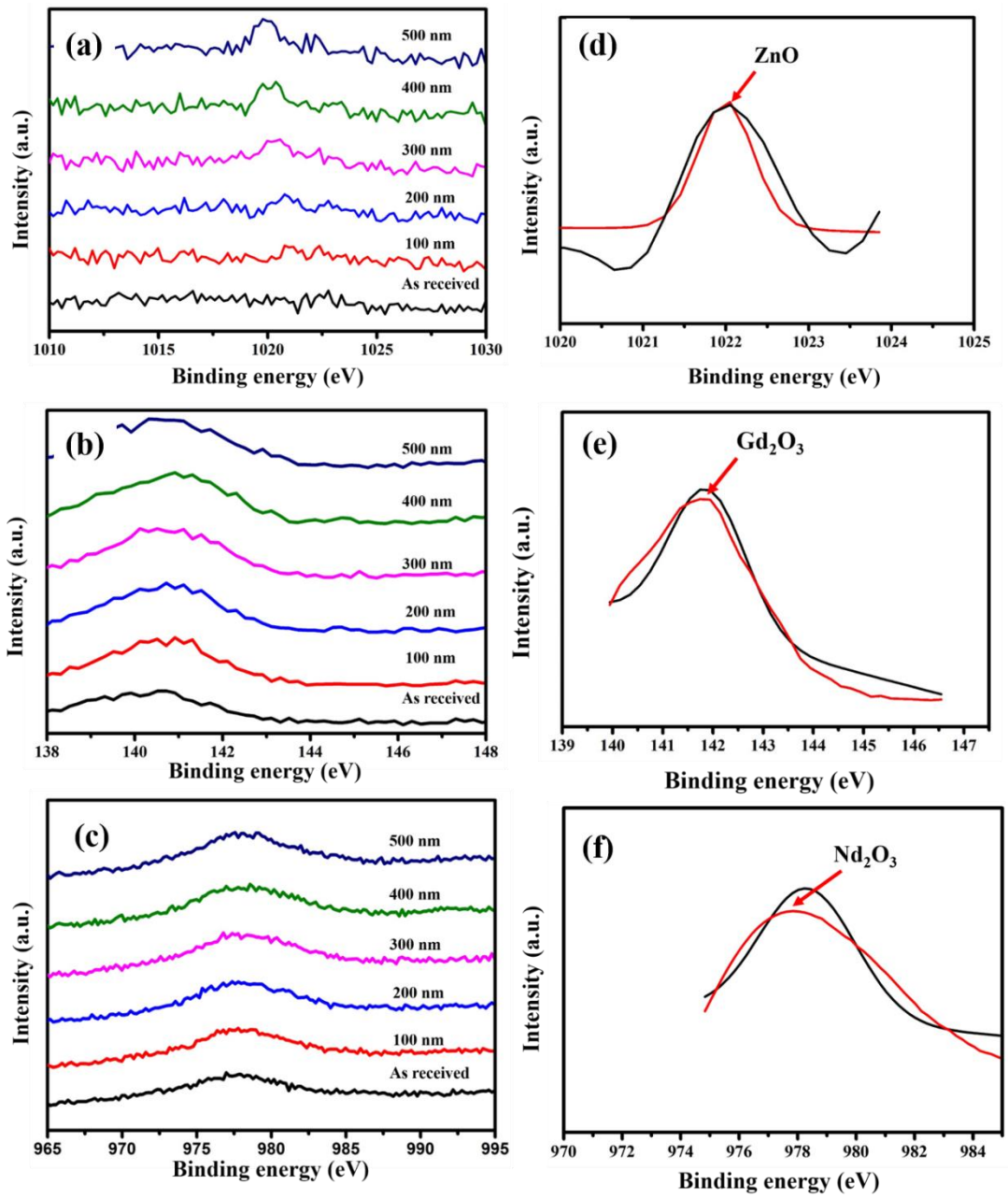

Figure 4.30. DP-XPS spectra of the corrosion layers on GZK & NZK alloy sample immersed in cell culture medium for 24 h (a) Zn2p3, (b) Gd4d, (c) Nd3d5, (d) deconvoluted Zn2p3 peak at 400 nm, (e) deconvoluted Gd4d peak at 200 nm, (f) deconvoluted Nd3d5 peak at 200 nm.

4.3.13.2 MTT Assay

According to ISO 10993-5:2009 standards, a minimum cell viability of 75% is required for implant materials. However, these standards are designed for permanent implants and not for biodegradable materials, which naturally degrade and interact with surrounding cells. Since biodegradable materials are foreign to the body, their degradation products influence the surrounding environment, often leading to temporarily reduced cell viability in static in-vitro conditions. In vivo, however, the dynamic nature of the body, including continuous blood flow and fluid exchange, helps to regulate the ionic concentration and pH, mitigating potential cytotoxic effects observed in static in-vitro tests. As a result, it is difficult to achieve 75% viability with 100% extract of a biodegradable material in vitro conditions. To better simulate the dynamic conditions of the body, the 100% extract is diluted with complete cell culture medium (CCM) to reduce the immediate ionic impact and allow for a more physiologically relevant response.

The MTT cell viability test results for GZK and NZK alloys at 1 day and 3 days are shown in **Figure 4.31**. At 1 day [**Figure 4.31 (a)**], both alloys exhibit moderate to high cell viability, with GZK showing slightly higher values than NZK. The viability of both alloys was close to or above 75%, which is generally considered the threshold for good biocompatibility. However, after 3 days, the MTT results showed a clear difference between the 100% extract and diluted extracts. The 100% extracts of NZK, showed a cell viability below 40%, suggesting that the high concentration of degradation products affected cellular metabolism. However, in the diluted conditions, both alloys exhibited significantly higher viabilities.

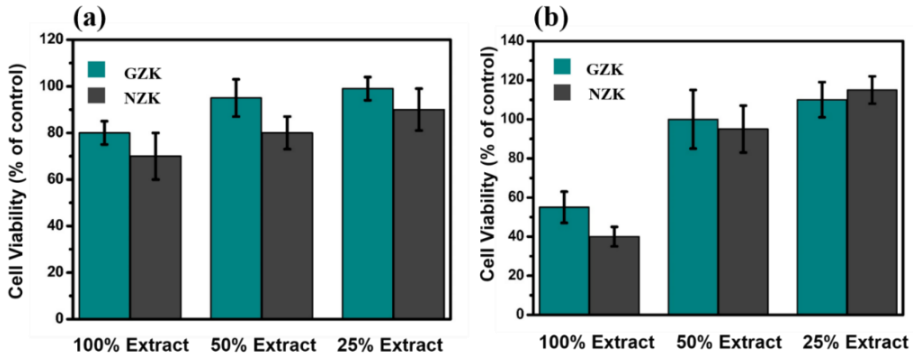

Figure 4.31. MTT assay results of MG63 cells cultured in sample extracts for (a) 1 day, (b) 3 days.

4.3.14. Conclusion

The addition of Zr to Mg-4Zn-1RE (RE = Gd, Nd) resulted in grain refinement, which led to change in corrosion, degradation as well as the tensile characteristics of the alloys. The Key findings are as follows:

- The addition of Zr led to a significant grain size reduction in the Mg-4Zn-1Gd alloy, decreasing from 524 (±171) μm to 144 (±50) μm, while the Mg-4Zn-1Nd alloy exhibited only a marginal reduction from 203 (±63) μm to 166 (±42) μm.
- Due to the substantial grain refinement and the formation of a compact corrosion layer, the corrosion rate of the Mg-4Zn-1Gd-0.5Zr alloy significantly decreased compared to that of Mg-4Zn-Gd alloy, reduced from 4.6 (±0.85) mm/y to 1.45 (±0.24) mm/y, making it slightly lower than that of the Mg-4Zn-1Nd-0.5Zr alloy.
- The Mg-4Zn-1Gd-0.5Zr alloy demonstrated superior yield strength and ultimate tensile strength compared to Mg-4Zn-1Nd-0.5Zr.
- While the biodegradation rate of Mg-4Zn-1Gd-0.5Zr was slightly lower than that of Mg-4Zn-1Nd-0.5Zr, the degradation layers in both alloys comprised $Mg(OH)_2$, MgO, $MgCO_3$, $Ca_{10}(PO_4)_6(OH)_2$, CaO, ZnO, and their respective rare-earth oxides.
- The Mg-4Zn-1Gd-0.5Zr alloy exhibited better cell viability than the Mg-4Zn-1Nd-0.5Zr alloy with all extract concentrations and time intervals.

References

[1] Y. Chen, Z. Xu, C. Smith, J. Sankar, Recent advances on the development of magnesium alloys for biodegradable implants, Acta Biomater. 10 (2014) 4561–4573. https://doi.org/10.1016/j.actbio.2014.07.005.

[2] S. Agarwal, J. Curtin, B. Duffy, S. Jaiswal, Biodegradable magnesium alloys for orthopaedic applications: A review on corrosion, biocompatibility and surface modifications, Mater. Sci. Eng. C 68 (2016) 948–963. https://doi.org/10.1016/j.msec.2016.06.020.

[3] D. Mei, S.V. Lamaka, X. Lu, M.L. Zheludkevich, Selecting medium for corrosion testing of bioabsorbable magnesium and other metals – A critical review, Corros. Sci. 171 (2020) 108722. https://doi.org/10.1016/j.corsci.2020.108722.

[4] B. Hadzima, M. Mhaede, F. Pastorek, Electrochemical characteristics of calcium-phosphatized AZ31 magnesium alloy in 0.9 % NaCl solution, J. Mater. Sci. Mater. Med. 25 (2014) 1227–1237. https://doi.org/10.1007/s10856-014-5161-0.

[5] A. Pardo, M.C. Merino, A.E. Coy, R. Arrabal, F. Viejo, E. Matykina, Corrosion behaviour of magnesium/aluminium alloys in 3.5 wt.% NaCl, Corros. Sci. 50 (2008) 823–834. https://doi.org/10.1016/j.corsci.2007.11.005.

[6] N. Birbilis, M.A. Easton, A.D. Sudholz, S.M. Zhu, M.A. Gibson, On the corrosion of binary magnesium-rare earth alloys, Corros. Sci. 51 (2009) 683–689. https://doi.org/10.1016/j.corsci.2008.12.012.

[7] H. Azzeddine, A. Hanna, A. Dakhouche, L. Rabahi, N. Scharnagl, M. Dopita, F. Brisset, A.-L. Helbert, T. Baudin, Impact of rare-earth elements on the corrosion performance of binary magnesium alloys, J. Alloys Compd. 829 (2020) 154569. https://doi.org/10.1016/j.jallcom.2020.154569.

[8] S. Tekumalla, S. Seetharaman, A. Almajid, M. Gupta, Mechanical Properties of Magnesium-Rare Earth Alloy Systems: A Review, Metals 5 (2015) 1–39. https://doi.org/10.3390/met5010001.

[9] G.-L. Song, 1 - Corrosion electrochemistry of magnesium (Mg) and its alloys, in: G. Song (Ed.), Corros. Magnes. Alloys, Woodhead Publishing, 2011: pp. 3–65. https://doi.org/10.1533/9780857091413.1.3.

[10] S. Verdier, N. van der Laak, S. Delalande, J. Metson, F. Dalard, The surface reactivity of a magnesium–aluminium alloy in acidic fluoride solutions studied by electrochemical techniques and XPS, Appl. Surf. Sci. 235 (2004) 513–524. https://doi.org/10.1016/j.apsusc.2004.03.250.

[11] I. Polmear, Light Alloys: From Traditional Alloys to Nanocrystals, Elsevier, 2005.

[12] M. Qian, D.H. Stjohn, Grain nucleation and formation in Mg–Zr alloys, Int. J. Cast Met. Res. 22 (2009) 256–259. https://doi.org/10.1179/136404609X367885.

[13] M. Qian, D.H. StJohn, M.T. Frost, Heterogeneous nuclei size in magnesium–zirconium alloys, Scr. Mater. 50 (2004) 1115–1119. https://doi.org/10.1016/j.scriptamat.2004.01.026.

[14] J. Li, R. Chen, Y. Ma, W. Ke, Effect of Zr modification on solidification behavior and mechanical properties of Mg–Y–RE (WE54) alloy, J. Magnes. Alloys 1 (2013) 346–351. https://doi.org/10.1016/j.jma.2013.12.001.

[15] M. Sun, D. Yang, Y. Zhang, L. Mao, X. Li, S. Pang, Recent Advances in the Grain Refinement Effects of Zr on Mg Alloys: A Review, Metals 12 (2022) 1388. https://doi.org/10.3390/met12081388.

[16] M. Qian, A. Das, Grain refinement of magnesium alloys by zirconium: Formation of equiaxed grains, Scr. Mater. 54 (2006) 881–886. https://doi.org/10.1016/j.scriptamat.2005.11.002.

[17] M. Qian, A. Das, Grain refinement of magnesium alloys by zirconium: Formation of equiaxed grains, Scr. Mater. 54 (2006) 881–886. https://doi.org/10.1016/j.scriptamat.2005.11.002.

[18] A. Srinivasan, C. Blawert, Y. Huang, C.L. Mendis, K.U. Kainer, N. Hort, Corrosion behavior of Mg–Gd–Zn based alloys in aqueous NaCl solution, J. Magnes. Alloys 2 (2014) 245–256. https://doi.org/10.1016/j.jma.2014.08.002.

[19] W.C. Neil, M. Forsyth, P.C. Howlett, C.R. Hutchinson, B.R.W. Hinton, Corrosion of magnesium alloy ZE41 – The role of microstructural features, Corros. Sci. 51 (2009) 387–394. https://doi.org/10.1016/j.corsci.2008.11.005.

[20] A.E. Coy, F. Viejo, P. Skeldon, G.E. Thompson, Susceptibility of rare-earth-magnesium alloys to micro-galvanic corrosion, Corros. Sci. 52 (2010) 3896–3906. https://doi.org/10.1016/j.corsci.2010.08.006.

[21] J. Liu, D. Bian, Y. Zheng, X. Chu, Y. Lin, M. Wang, Z. Lin, M. Li, Y. Zhang, S. Guan, Comparative in vitro study on binary Mg-RE (Sc, Y, La, Ce, Pr, Nd, Sm, Eu, Gd, Tb, Dy, Ho, Er, Tm, Yb and Lu) alloy systems, Acta Biomater. 102 (2020) 508–528. https://doi.org/10.1016/j.actbio.2019.11.013.

[22] R. Arrabal, A. Pardo, M.C. Merino, M. Mohedano, P. Casajús, K. Paucar, G. Garcés, Effect of Nd on the corrosion behaviour of AM50 and AZ91D magnesium alloys in 3.5wt.% NaCl solution, Corros. Sci. 55 (2012) 301–312. https://doi.org/10.1016/j.corsci.2011.10.033.

[23] R. Pinto, M.G.S. Ferreira, M.J. Carmezim, M.F. Montemor, The corrosion behaviour of rare-earth containing magnesium alloys in borate buffer solution, Electrochimica Acta 56 (2011) 1535–1545. https://doi.org/10.1016/j.electacta.2010.09.081.

[24] L. Bao, Z. Zhang, Q. Le, S. Zhang, J. Cui, Corrosion behavior and mechanism of Mg-Y-Zn-Zr alloys with various Y/Zn mole ratios, J. Alloys Compd. 712 (2017) 15–23. https://doi.org/10.1016/j.jallcom.2017.04.053.

[25] M. Jamesh, S. Kumar, T.S.N. Sankara Narayanan, Corrosion behavior of commercially pure Mg and ZM21 Mg alloy in Ringer's solution – Long term evaluation by EIS, Corros. Sci. 53 (2011) 645–654. https://doi.org/10.1016/j.corsci.2010.10.011.

[26] M.I. Jamesh, G. Wu, Y. Zhao, D.R. McKenzie, M.M.M. Bilek, P.K. Chu, Electrochemical corrosion behavior of biodegradable Mg–Y–RE and Mg–Zn–Zr alloys in Ringer's solution and simulated body fluid, Corros. Sci. 91 (2015) 160–184. https://doi.org/10.1016/j.corsci.2014.11.015.

[27] M.I. Jamesh, G. Wu, Y. Zhao, D.R. McKenzie, M.M.M. Bilek, P.K. Chu, Effects of zirconium and oxygen plasma ion implantation on the corrosion behavior of ZK60 Mg alloy in simulated body fluids, Corros. Sci. 82 (2014) 7–26. https://doi.org/10.1016/j.corsci.2013.11.044.

[28] J. Kim, K.C. Wong, P.C. Wong, S.A. Kulinich, J.B. Metson, K.A.R. Mitchell, Characterization of AZ91 magnesium alloy and organosilane adsorption on its surface, Appl. Surf. Sci. 253 (2007) 4197–4207. https://doi.org/10.1016/j.apsusc.2006.09.030.

[29] B.R. Strohmeier, D.M. Hercules, Surface spectroscopic characterization of the interaction between zinc ions and γ-alumina, J. Catal. 86 (1984) 266–279. https://doi.org/10.1016/0021-9517(84)90372-5.

[30] Pilling-Bedworth ratio for oxidation of alloys: Materials Research Innovations: Vol 3, No 4, (n.d.). https://www.tandfonline.com/doi/abs/10.1007/s100190050008 (accessed April 21, 2024).

[31] G.L. Song, A. Atrens, Corrosion Mechanisms of Magnesium Alloys, Adv. Eng. Mater. 1 (1999) 11–33. https://doi.org/10.1002/(SICI)1527-2648(199909)1:1<11::AID-ADEM11>3.0.CO;2-N.

[32] J. Liu, Y. Lin, D. Bian, M. Wang, Z. Lin, X. Chu, W. Li, Y. Liu, Z. Shen, Y. Liu, Y. Tong, Z. Xu, Y. Zhang, Y. Zheng, In vitro and in vivo studies of Mg-30Sc alloys with different phase structure for potential usage within bone, Acta Biomater. 98 (2019) 50–66. https://doi.org/10.1016/j.actbio.2019.03.009.

[33] Y.M. Kim, C.D. Yim, H.S. Kim, B.S. You, Key factor influencing the ignition resistance of magnesium alloys at elevated temperatures, Scr. Mater. 65 (2011) 958–961. https://doi.org/10.1016/j.scriptamat.2011.08.019.

[34] Q. Jiang, D. Lu, C. Liu, N. Liu, B. Hou, The Pilling-Bedworth Ratio of Oxides Formed From the Precipitated Phases in Magnesium Alloys, Front. Mater. 8 (2021). https://doi.org/10.3389/fmats.2021.761052.

[35] R.-C. Zeng, L. Sun, Y.-F. Zheng, H.-Z. Cui, E.-H. Han, Corrosion and characterisation of dual phase Mg–Li–Ca alloy in Hank's solution: The influence of microstructural features, Corros. Sci. 79 (2014) 69–82. https://doi.org/10.1016/j.corsci.2013.10.028.

[36] J.H. Nordlien, S. Ono, N. Masuko, K. Nisancioglu, A TEM investigation of naturally formed oxide films on pure magnesium, Corros. Sci. 39 (1997) 1397–1414. https://doi.org/10.1016/S0010-938X(97)00037-1.

[37] J.H. Nordlien, K. NişancioĞu, S. Ono, N. Masuko, Morphology and Structure of Oxide Films Formed on MgAl Alloys by Exposure to Air and Water, J. Electrochem. Soc. 143 (1996) 2564. https://doi.org/10.1149/1.1837048.

[38] Y. Zhang, J. Li, P. Liaw, Y. Xu, H. Lai, Effects of composition modification on the mechanical properties and corrosion behaviour of the heat-treated Mg-2Zn-0.2Mn-xNd alloys, J. Alloys Compd. 769 (2018). https://doi.org/10.1016/j.jallcom.2018.07.359.

[39] Y.L. Song, Y.H. Liu, S.R. Yu, X.Y. Zhu, S.H. Wang, Effect of neodymium on microstructure and corrosion resistance of AZ91 magnesium alloy, J. Mater. Sci. 42 (2007) 4435–4440. https://doi.org/10.1007/s10853-006-0661-z.

[40] M.Y. Gu, G.L. Wei, W.C. Liu, G.H. Wu, Influence of neodymium on microstructure and corrosion behavior of Mg-8Li-3Al-2Zn alloy, Mater. Corros. 68 (2017) 436–443. https://doi.org/10.1002/maco.201609141.

[41] J.-W. Chang, X.-W. Guo, P.-H. Fu, L.-M. Peng, W.-J. Ding, Effect of heat treatment on corrosion and electrochemical behaviour of Mg–3Nd–0.2Zn–0.4Zr (wt.%) alloy, Electrochimica Acta 52 (2007) 3160–3167. https://doi.org/10.1016/j.electacta.2006.09.069.

[42] A. Bahmani, S. Arthanari, K.S. Shin, Formulation of corrosion rate of magnesium alloys using microstructural parameters, J. Magnes. Alloys 8 (2020) 134–149. https://doi.org/10.1016/j.jma.2019.12.001.

[43] G. Song, A. Atrens, Understanding Magnesium Corrosion—A Framework for Improved Alloy Performance, Adv. Eng. Mater. 5 (2003) 837–858. https://doi.org/10.1002/adem.200310405.

[44] O. Lunder, K. Nisancioglu, R.S. Hansen, Corrosion of Die Cast Magnesium-Aluminum Alloys, SAE International, Warrendale, PA, 1993. https://doi.org/10.4271/930755.

[45] Y.-C. Zhao, M.-C. Zhao, R. Xu, L. Liu, J.-X. Tao, C. Gao, C. Shuai, A. Atrens, Formation and characteristic corrosion behavior of alternately lamellar arranged α and β in as-cast AZ91 Mg alloy, J. Alloys Compd. 770 (2019) 549–558. https://doi.org/10.1016/j.jallcom.2018.08.103.

[46] M.I. Sosulnikov, Yu.A. Teterin, X-ray photoelectron studies of Ca, Sr and Ba and their oxides and carbonates, J. Electron Spectrosc. Relat. Phenom. 59 (1992) 111–126. https://doi.org/10.1016/0368-2048(92)85002-O.

[47] Y. Tanizawa, H. Tsuchikane, K. Sawamura, T. Suzuki, Reaction characteristics of hydroxyapatite with F– and PO3F2– ions. Chemical states of fluorine in hydroxyapatite, J. Chem. Soc. Faraday Trans. 87 (1991) 2235–2240. https://doi.org/10.1039/FT9918702235.

[48] Y. Xu, J. Li, M. Qi, W. Guo, Y. Deng, A newly developed Mg-Zn-Gd-Mn-Sr alloy for degradable implant applications: Influence of extrusion temperature on microstructure, mechanical properties and in vitro corrosion behavior, Mater. Charact. 188 (2022) 111867. https://doi.org/10.1016/j.matchar.2022.111867.

[49] W. Li, S. Guan, J. Chen, J. Hu, S. Chen, L. Wang, S. Zhu, Preparation and in vitro degradation of the composite coating with high adhesion strength on biodegradable Mg–Zn–Ca alloy, Mater. Charact. 62 (2011) 1158–1165. https://doi.org/10.1016/j.matchar.2011.07.005.

Chapter 5

Influence of Zn/Gd Ratio in Mg-Zn-Gd-Zr Alloys

5.1 Introduction

Chapter 4 established that the Mg-Zn-Gd-Zr alloy demonstrates superior properties compared to the Mg-Zn-Nd-Zr alloy, a lower biodegradation rate, better cell viability, and enhanced mechanical properties. These findings highlight the potential of Mg-Zn-Gd-Zr alloys for advanced biomedical applications. As discussed in Chapter 2 (literature review), the Zn/Gd ratio plays a pivotal role in influencing the microstructural, mechanical, and corrosion properties of Mg-Zn-Gd alloys. By tailoring this ratio, the alloy's phase constitution and overall performance can be optimized for specific applications. While Mg-Zn-Y alloys have been extensively studied, Mg-Zn-Gd-based alloys are gaining attention due to the unique properties of gadolinium (Gd). Based on the Zn/Gd ratio, the alloys' microstructure consists of W phase ($Mg_3Zn_3Gd_2$) with a cubic structure, I phase (Mg_3Zn_6Gd) characterized by an icosahedral quasicrystalline structure, and X phase ($Mg_{12}ZnGd$) with a long-period stacking order (LPSO) structure. Zhang et al. [1] systematically investigated the effect of Zn/Gd ratios on phase constitution in as-cast Mg-Zn-Gd alloys. Their findings revealed that, I phase and $(Mg,Zn)_3Gd$ form when $Zn/Gd \geq 1.5$ and $1.0 < Zn/Gd < 1.5$, respectively and LPSO structures dominate when $Zn/Gd \leq 1.0$. In high-Gd-containing Mg-Zn-Gd systems, LPSO phases play a dual role by improving mechanical strength and heat resistance. Yamasaki et al. [2] proposed a time–temperature-transformation diagram for Mg97Zn1Gd2 (at.%), detailing how low-temperature aging (<523 K) leads to coherent β'-phase precipitation, whereas medium and high-temperature aging (>623 K) produces stacking faults and 14H LPSO structures, significantly enhancing the alloy's strength. The role of LPSO phases in corrosion resistance, however, remains controversial [3]. While Liu et al. [4] reported improved corrosion resistance due to the lamellar LPSO phase, others, such as Zhang et al. [5], observed increased corrosion rates caused by galvanic coupling effects associated with bulk X phase containing LPSO structures at grain boundaries.

Additionally, gadolinium-based particles are used as contrast agents for magnetic resonance imaging. Also, Gd has been shown to possess anti-inflammatory and immunomodulatory properties, which can be beneficial in minimizing adverse tissue reactions and promoting the healing process. While challenges like controlling the degradation rate and managing the release of alloy constituents remain, Gd containing alloys hold potential in the development of safer and more effective biodegradable implants [6]. However, a comprehensive investigation into the toxicity and long-term effects of RE elements, released as ions into tissue, is still lacking. Studies show that the release of Gd from Mg-xGd alloys has been demonstrated to remain below toxicity thresholds in cell culture [7,8]. Furthermore, Mg-10Gd alloy has exhibited enhanced osteoblast-induced mineralization in cell culture conditions [9]. Cells cultured on Mg-10Gd alloy have demonstrated healthy cellular structures, promoting strong adhesion to the surface [10]. Kruger et al. [11] studied the degradation behavior of Mg-5Gd and Mg-10Gd screw implants. Mg-10Gd exhibited lower degradation rates, a more uniform microstructure degradation pattern, and a less pronounced texture compared to Mg-5Gd. This weaker texture, characterized by a more random orientation of crystallographic poles within grains, results in favourable mechanical properties [11].

Thus, despite their promising properties, Mg-Zn-Gd-based alloys have not been explored as extensively as conventional biomedical alloys like WE43 and Mg-Zn-Ca. Thus, the present research work focused on addressing this gap by preparing three Mg-Zn-Gd-Zr alloys with varying Zn/Gd ratios and their influence on their microstructure, mechanical and biological properties.

5.2. Materials and Methods

The alloys Mg-2Gd-2Zn-0.5Zr (GZ22), Mg-2Gd-6Zn-0.5Zr (GZ26) and Mg-10Gd-1Zn-0.5Zr (GZ101) were prepared as described in Chapter 3. The chemical composition the alloys were determined using ICP-AES (**Table 5.1**). The morphology and composition analysis of different phases were carried out with a scanning electron microscope (SEM, Carl Zeiss EVO18) with energy-dispersive X-ray spectroscopy (EDS) and the TEM analysis was done in JEOL JEM F 200 with STEM EDA EELS HRTEM. The various other characterization techniques used to analyze the properties of the prepared alloys are already described in detail in Chapter 3. Tensile testing was carried out on alloys using threaded tensile specimens with a 6 mm gauge diameter and 25 mm gauge length,

prepared according to ASTM B557M-10. In-vitro biodegradation behavior of alloys was evaluated using immersion tests in cell culture medium containing Minimum Essential Medium (MEM) supplemented with 10% fetal bovine serum (FBS) and 1% penicillin, maintaining a medium volume-to-sample surface area ratio of 1.25 cm^2/mL according to ISO 10993. The samples were incubated at 37°C, 5% CO_2, 20% O_2, and 95% relative humidity for 14 days, with medium replacement every two days to maintain pH stability. MTT (3-(4,5-Dimethylthiazol-2-Yl)-2,5 Diphenyltetrazolium Bromide) assays were performed according to ISO 10993:2009 to evaluate the cytotoxicity. Elemental toxicity evaluation was conducted using chloride salts of Mg, Zn, and Gd (Sigma-Aldrich), which were dissolved in sterile water at 50,000 μM and further diluted with cell culture medium to different concentrations. The toxicity study was performed using the MTT assay, as described earlier. To assess the elemental concentrations in the extract solutions used for viability studies, Inductively Coupled Plasma Mass Spectrometry (ICP-MS) analysis was performed using an iCAP RQ spectrometer (Thermo Scientific) equipped with a quadrupole mass analyzer and an auto-sampler (ASX-280, Teledyne, CETAC Technologies, USA). For DAPI staining, metallic samples (10 mm diameter, 2 mm height) were first incubated in cell culture medium for 3 days, followed by seeding 50,000 cells on their surface and incubating for 1 h, after which 3 mL of fresh medium was added. After 1 and 3 days of culturing, the samples were washed with PBS, stained using DAPI (1:1000 in MEM) for 15 min, and observed under a fluorescence microscope (Olympus IX-83). At least six images were captured and analyzed using ImageJ software to quantify cell attachment and distribution.

Table 5.1. Chemical composition of the developed alloys (wt.%)

Nominal composition	**Analysed chemical composition (wt.%)**						
	Gd	**Zn**	**Zr**	**Fe**	**Cu**	**Ni**	**Mg**
Mg-2Gd-2Zn-0.5Zr (GZ22)	1.92	2.05	0.42	0.0129	0.0045	0.0020	Bal.
Mg-2Gd-6Zn-0.5Zr (GZ26)	2.08	6.43	0.48	0.0115	0.0034	0.0032	Bal.
Mg-10Gd-1Zn-0.5Zr (GZ101)	10.24	1.40	0.45	0.0180	0.0051	0.0044	Bal.

5.3 Results and Discussion

5.3.1 Microstructure

The XRD diffraction patterns of all the alloys (**Figure 5.1**) were primarily characterized by α-Mg peaks, while the peaks corresponding to secondary phases were either masked by the dominant α-Mg peaks or exhibited low intensity. As a result, the XRD analysis was unable to clearly identify the secondary phases present in the alloys. The SEM micrographs and the EDS analysis of the as-cast alloys are shown in **Figure 5.2** and **Table 5.2** respectively. As the Zn/Gd ratio varied, the microstructures of alloys also showed significant changes. Network-like secondary phases were dominant in GZ22 alloy (Zn/Gd ratio of 1) whereas, skeleton-shaped secondary phases and discrete particles were uniformly distributed in GZ26 alloy (Zn/Gd ratio of 3). GZ101 alloy (Zn/Gd ratio of 0.1) exhibited mainly flake-like secondary phases. The EDS analysis revealed that the network-shaped phase [marked as A in **Figure 5.2 (b)**] and discrete particle [marked as B in **Figure 5.2 (b)**] in GZ22 had a Zn to Gd atomic ratio of 1.92 and 1.79 respectively, which is close to the ideal atomic ratio of 1.5 for $Mg_3Zn_3Gd_2$ phase (W phase). Similarly, the skeleton-shaped phase [marked as A in **Figure 5.2 (d)**] in GZ26 had a Zn/Gd atom ratio of 2.23 which is similar to the W phase, and small discrete particles [marked as B in **Figure 5.2 (d)**] had a Zn/Gd atom ratio of 7.08 which is close to the ideal Zn/Gd ratio of 6 for Mg_3Zn_6Gd phase (I phase). The flake-like phases [marked as A in **Figure 5.2 (f)**] and other discrete phases [marked as B and C in **Figure 5.2 (f)**] in GZ101 had a Zn/Gd ratio close to 0.6. However, the stoichiometric composition of this particular phase was not similar to the well-reported $(Mg,Zn)_3Gd$ phase found in high Gd containing Mg-Gd-Zn alloys in the literature [12,13]. Hence TEM analysis was carried out to identify the phase [**Figure 5.3 (a)**] and confirmed that the phase was $(Mg,Zn)_3Gd$ phase with face-center-cubic structure with a lattice constant of 0.73 nm [14,15]. Also, the TEM micrograph showed the presence of LPSO phase in α-Mg matrix of GZ101 [**Figure 5.3 (b)**].

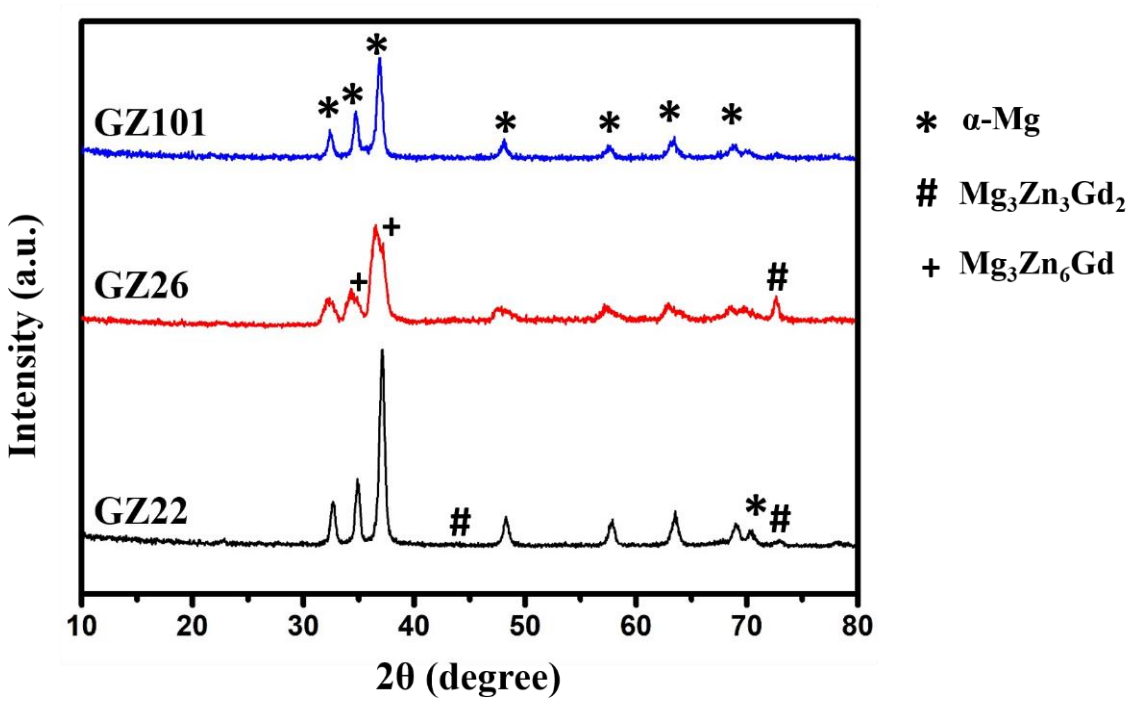

Figure 5.1. XRD patterns of the developed Mg-Zn-Gd-Zr alloys.

The number of different secondary phases in the alloys was analyzed using SEM analysis by considering at least 800 particles in each alloy and results are presented as **Figure 5.4**. For making the analysis simple, Zn/Gd ratio between 0 to 0.5 was considered as the Mg-Gd binary phase, 0.5 to 1 as $(Mg,Zn)_3Gd$, 1 to 3.5 was considered as the W phase, 3.5 to 8.5 was I phase and greater than 8.5 was considered as Mg-Zn binary phase. The analysis revealed that GZ22 had 75% of the W phase, GZ26 had 43.7% I phase and 29.5% W phase, and GZ101 had 72.7% $(Mg,Zn)_3Gd$ phase. Thus the major ternary phases were found to be the W phase in GZ22, a mixture of W and I phase in GZ26, and $(Mg,Zn)_3Gd$ phase in GZ101 alloy.

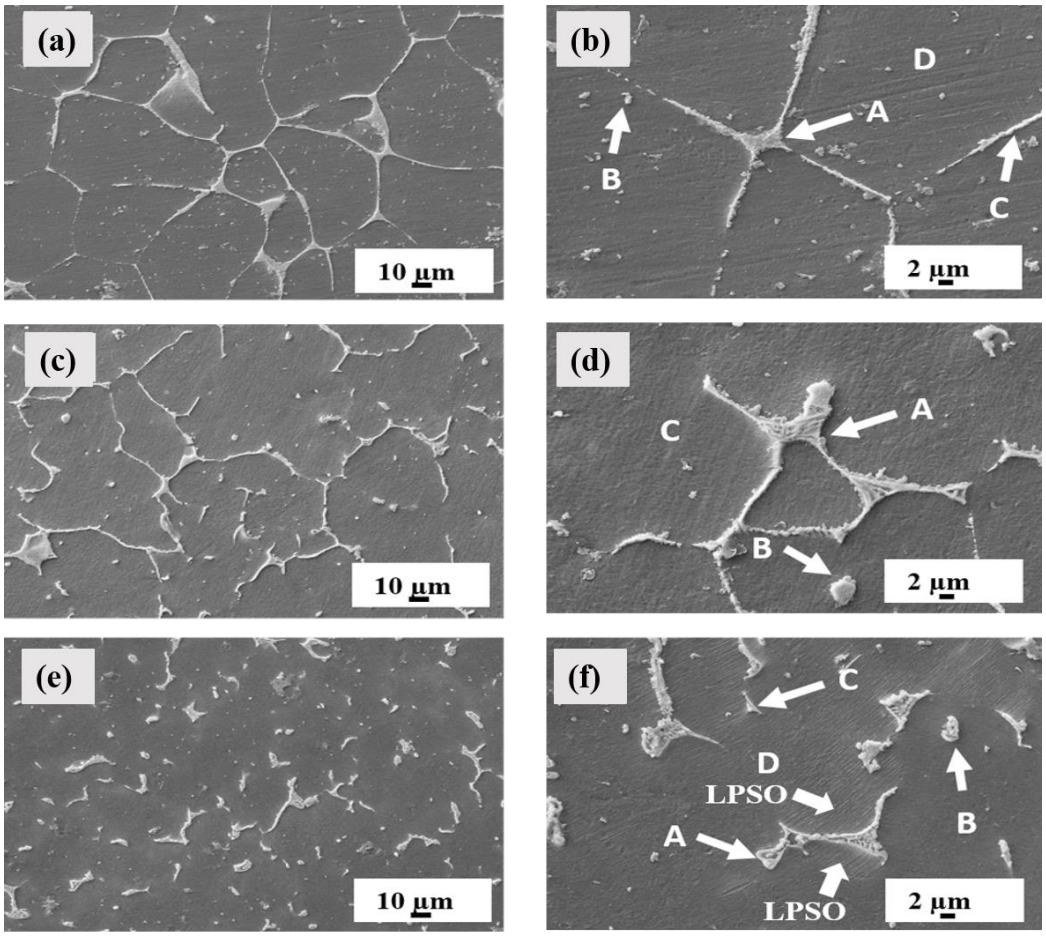

Figure 5.2. SEM micrographs of as-cast alloys (a&b) GZ22, (c&d) GZ26, (e&f) GZ101.

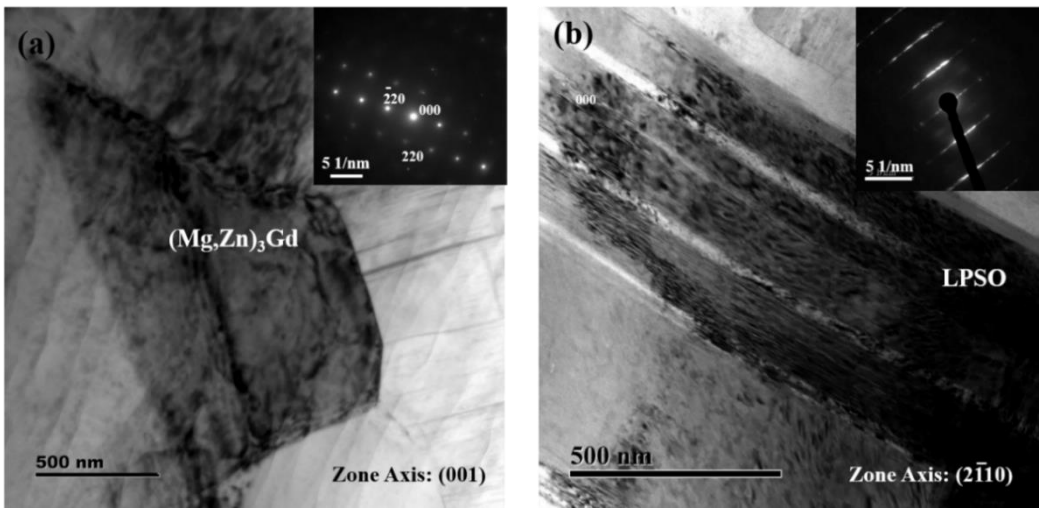

Figure 5.3. Bright-field TEM micrographs and corresponding diffraction patterns of (a) $(Mg,Zn)_3Gd$ phase (b) LPSO phase in GZ101 alloy.

Table 5.2. EDS analysis of different secondary phases in the alloys.

Position	Elements (at.%)			Zn/Gd	Phase
	Mg	Zn	Gd		
Figure 5.2.b(A)	85.108	9.22	4.80	1.92	W phase
Figure 5.2.b(B)	94.16	3.75	2.09	1.79	W phase
Figure 5.2.b(C)	84.36	10.48	5.16	2.03	W phase
Figure 5.2.b(D)	99.02	0.7	0.28	-	Matrix
Figure 5.2.d(A)	67.93	22.15	9.92	2.23	W phase
Figure 5.2.d(B)	62.83	32.57	4.60	7.08	I phase
Figure 5.2.d(C)	98.67	1.08	0.25	-	Matrix
Figure 5.2.f(A)	89.88	4	6.12	0.65	Mg-Zn-Gd phase
Figure 5.2.f(B)	91.53	3.27	5.30	0.62	Mg-Zn-Gd phase
Figure 5.2.f(C)	91.68	3.19	5.14	0.62	Mg-Zn-Gd phase
Figure 5.2.f(D)	98.52	0.10	1.38	-	Matrix

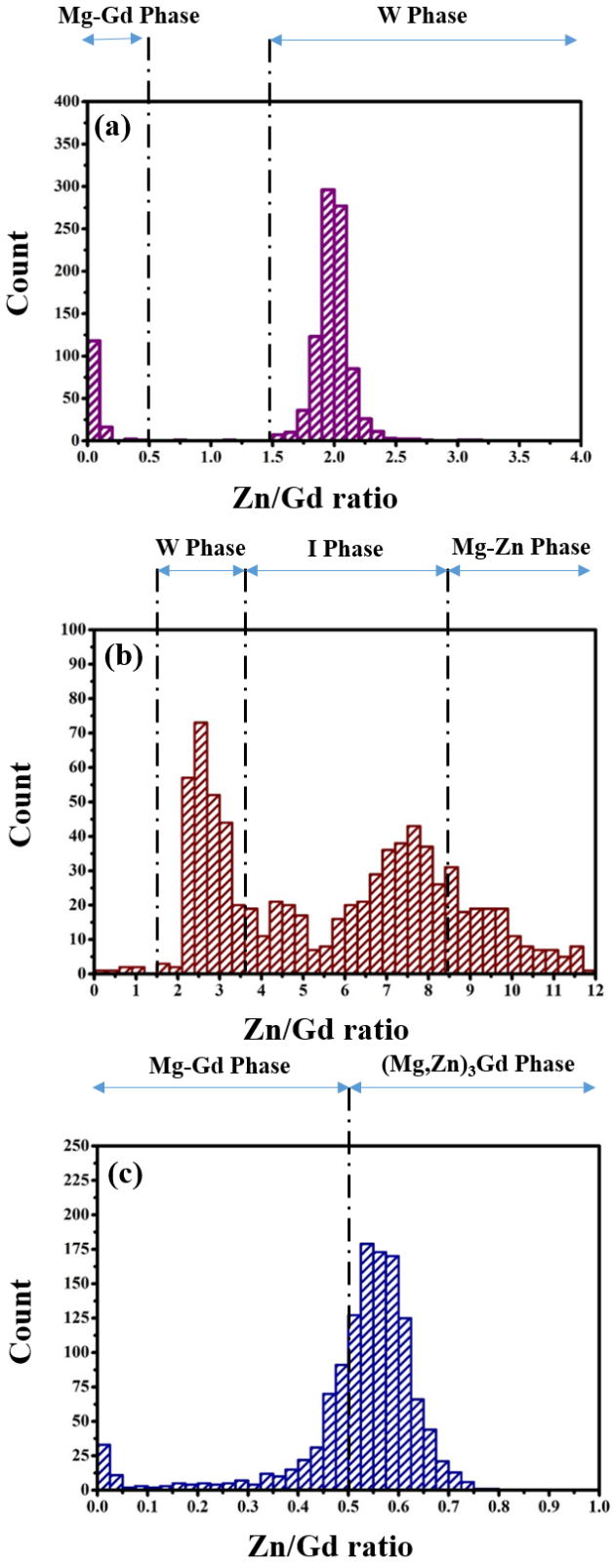

Figure 5.4. The number of different ternary phases in as-cast alloys (a) GZ22, (b) GZ26 (c) GZ101.

5.3.2 Tensile Properties

The tensile properties of the alloys (YS, UTS, and % elongation) are summarized in **Table 5.3**, and the corresponding stress-strain curves are shown in **Figure 5.5**. The GZ22 alloy had lowest YS of 95 (±10.5) MPa, but it had highest elongation of 12.1 (±2.52) %. On the other hand, the GZ101 alloy showed the highest YS of 145 (±15.4) MPa and lowest elongation of 6.9 (±1.83) %. The GZ26 alloy provides a balanced combination, offering moderate strength [119 (±12.5) MPa YS, 234 (±12.01) MPa UTS] while maintaining reasonable elongation [11.3 (±1.46) %]. To comprehensively analyse the tensile properties of the alloys, the influence of secondary phases needs to be understood as the second phases present in the alloys were different. It is evident from the microstructural analysis that the GZ22 alloys contained predominantly of W phase, GZ26 contained I phase and GZ101 alloy had the presence of LPSO phase. The significant difference in crystal structures and lattice parameters between the α-Mg matrix (hcp structure with a = 0.3209 nm and c = 0.5210 nm) and the W phase (FCC structure with a ≈ 0.6927 nm) leads to their incoherency [16,17]. The incoherent interfaces create weak bonding between the phase and the matrix, which can act as potential sites for crack initiation under tensile loading. This reduces the load transfer efficiency between the matrix and the secondary phase, thereby lowering the alloy's tensile strength. Thus W phase containing alloys (GZ22) have lower tensile strength [18,19]. Whereas, the I phase having icosahedral lattice structure is coherent with the α-Mg matrix because its atomic arrangement closely matches those of the α-Mg matrix at the interface. This coherence ensures strong interfacial bonding, facilitating efficient load transfer between the I phase and the matrix during tensile testing. As a result, the I phase can effectively pin dislocations and impede their motion, contributing to enhanced tensile strength. The presence of W phase as well as I phase in GZ26 alloy thus contributed in its optimum combination of tensile strength as well as reasonable ductility [20,21]. In contrast, the LPSO phase is a hard, thermally stable structure that resists deformation, providing strong barriers to dislocation motion and effectively pinning dislocations [22,23].

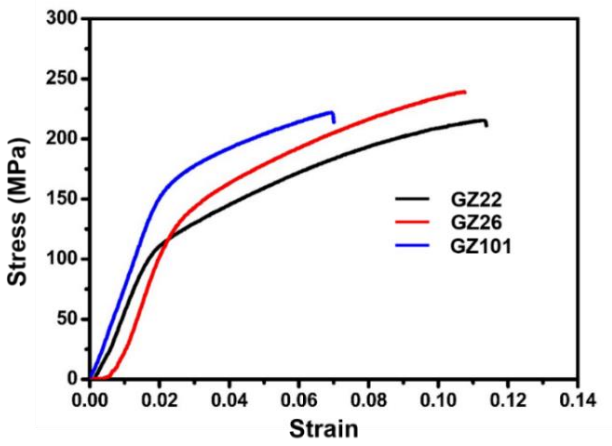

Figure 5.5. Tensile stress-strain curves of the alloys.

Table 5.3. Yield strength (YS), Ultimate tensile strength (UTS) and Elongation (%) of Alloys.

Alloy	Y.S (MPa)	UTS (MPa)	% Elongation
GZ22	95 (±10.5)	201 (±7.31)	12.1 (±2.52)
GZ26	119 (±12.5)	234 (±12.01)	11.3 (±1.46)
GZ101	145 (±15.4)	218 (±5.99)	6.9 (±1.83)

5.3.3. Biodegradation test

For the analysis of the degradation behaviour, the alloys were immersed in cell culture medium (CCM) for 14 days by maintaining the pH between 7.4 to 8. The results [**Figure 5.6 (a)**] showed that the degradation rate was lowest for the GZ101 alloy [1.25 (±0.30) mm/y] and the degradation rate of the GZ26 alloy [3.14 (±0.22) mm/y] was the highest. The degradation surface of the alloys after 14 days of immersion [**Figure 5.6 (b)**] showed that the GZ22 and GZ26 alloy suffered severe pitting corrosion while the GZ101 alloy showed few signs of pits indicating its superior resistance to degradation in cell culture medium.

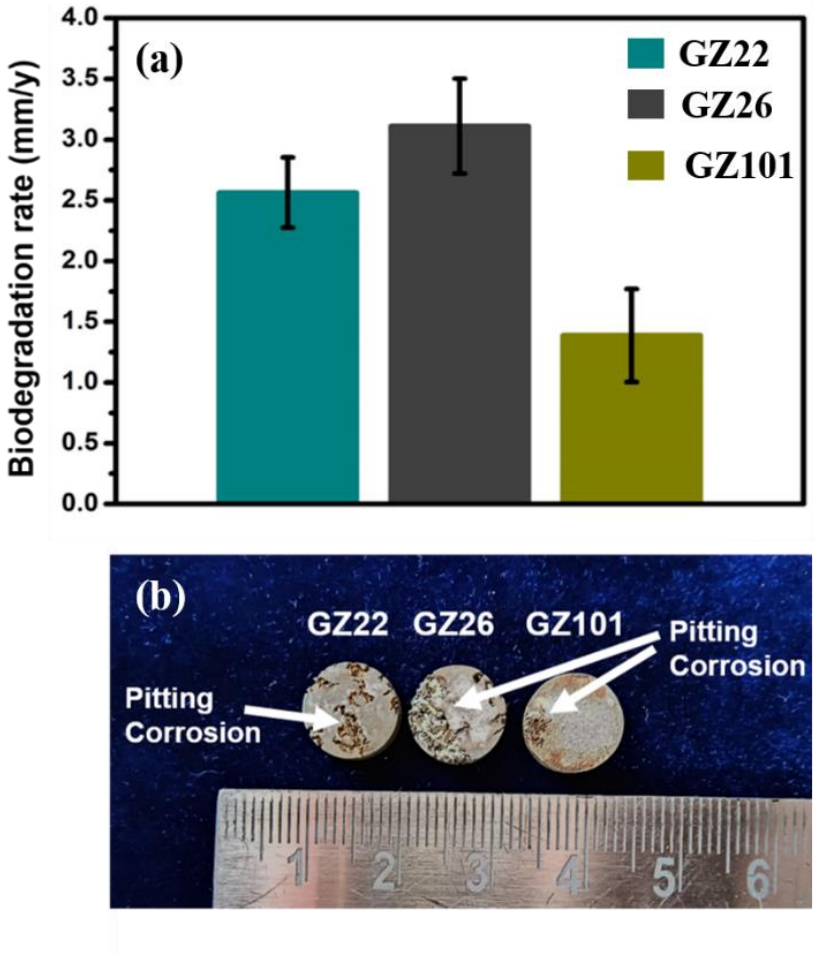

Figure 5.6. (a) Degradation rate of alloys immersed in cell culture medium for 14 days, (b) Photographs of degraded samples after immersed in cell culture medium for 14 days.

To understand the degradation behaviour of these alloys in CCM, the degradation layer formed on their surface was analyzed. The XPS analysis of the degradation layer formed on the alloys immersed in cell culture medium for 24 h was done, and the depth profiling measurement was also carried out till 400 nm (Sputtering was limited to 400 nm due to the safety concerns and limitation of the machine). Depth profile (DP) analysis showed that throughout the thickness of the degradation layer, the elements such as O, Ca, and Mg did not have significant changes in the atomic concentrations indicating that the distribution of these elements was almost uniform throughout the degradation layers in all the alloys (**Figure 5.7**). Moreover, the presence of Gd was not detected in GZ22, and GZ26 alloys, and Zn was absent in the degradation layer of GZ101 alloy. The DP-XPS spectra of O1s and Mg2p of all the alloys were almost similar, and hence for representation, only DP-XPS spectra of GZ101 alloy are shown in **Figure 5.8**. The binding energy (BE) peaks

of O1s [**Figure 5.8 (a)**] centered at 530.5 eV, 532.3 eV, and 533.5 eV were attributed to the presence of oxygen in the form of oxide, phosphate, and hydroxides , respectively [24]. The Mg2p spectra [**Figure 5.8 (b)**] of the surface of the alloy showed the presence of $MgCO_3$ (at 50.81 eV) as well as $Mg(OH)_2$ (at 49.7 eV). At 200 nm depth, the presence of MgO (at 51.1 eV) along with $MgCO_3$ and $Mg(OH)_2$ was observed [25]. The Ca2p spectra of GZ101 [**Figure 5.8 (c)**] confirmed the presence of CaO (at 350.5 eV) and hydroxyapatite [$Ca_{10}(PO_4)_6(OH)_2$ (at 347.7 eV)] in the degradation layer [26,27]. Though the presence of CaO (at 350.5 eV) and hydroxyapatite [$Ca_{10}(PO_4)_6(OH)_2$ (at 347.7 eV)] was observed from the Ca2P spectra of GZ26 [**Figure 5.9 (a)**], unlike in case of GZ101, intensity of $Ca_{10}(PO_4)_6(OH)_2$ was lower compared to that of CaO suggesting that more hydroxyapatite deposition occured on the surface of GZ101 alloy. The Gd4d spectra [**Figure 5.9 (b)**] from GZ101 alloy confirmed the presence of Gd_2O_3 (at 143.5 eV and at 141.4 eV), and Zn2p3 spectra [**Figure 5.9 (c)**] from GZ26 alloy showed that the degradation layer comprised ZnO (at 1021.9 eV) [28].

Thus the degradation layer of GZ22 and GZ26 alloys consisted of $Mg(OH)_2$, MgO, $MgCO_3$, $Ca_{10}(PO_4)_6(OH)_2$, CaO, and ZnO, whereas GZ101 alloy had Gd_2O_3 in the layer in addition to other said compounds above. The presence of Gd_2O_3 along with $MgCO_3$, $Ca_{10}(PO_4)_6(OH)_2$, and CaO made the otherwise porous oxide layer of $Mg(OH)_2$ and MgO more compact in GZ101 alloy, and contributed greatly to the observed superior resistance of GZ101 alloys [29,30].

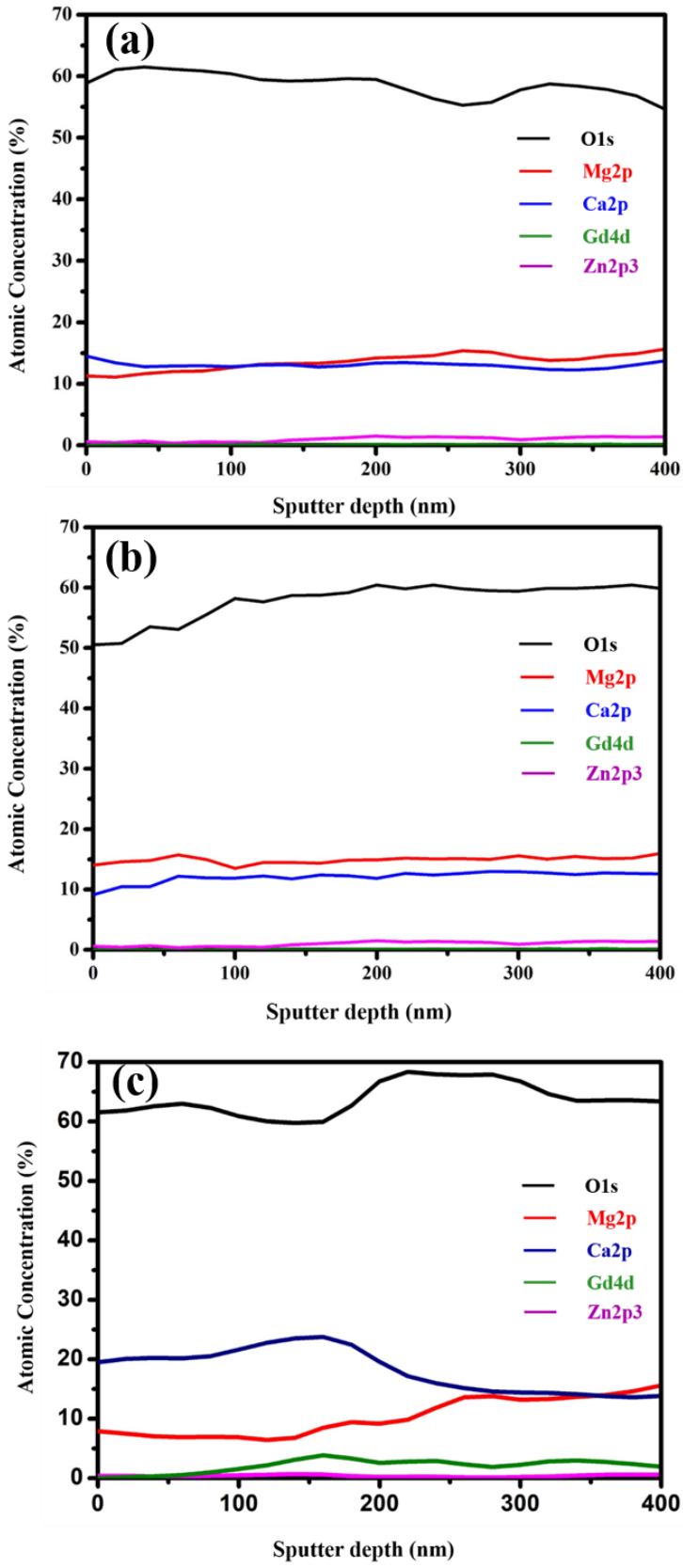

Figure 5.7. Depth profile analysis of the degradation layers on the sample immersed in cell culture medium for 24h (a) GZ22 (b) GZ26 (c) GZ101.

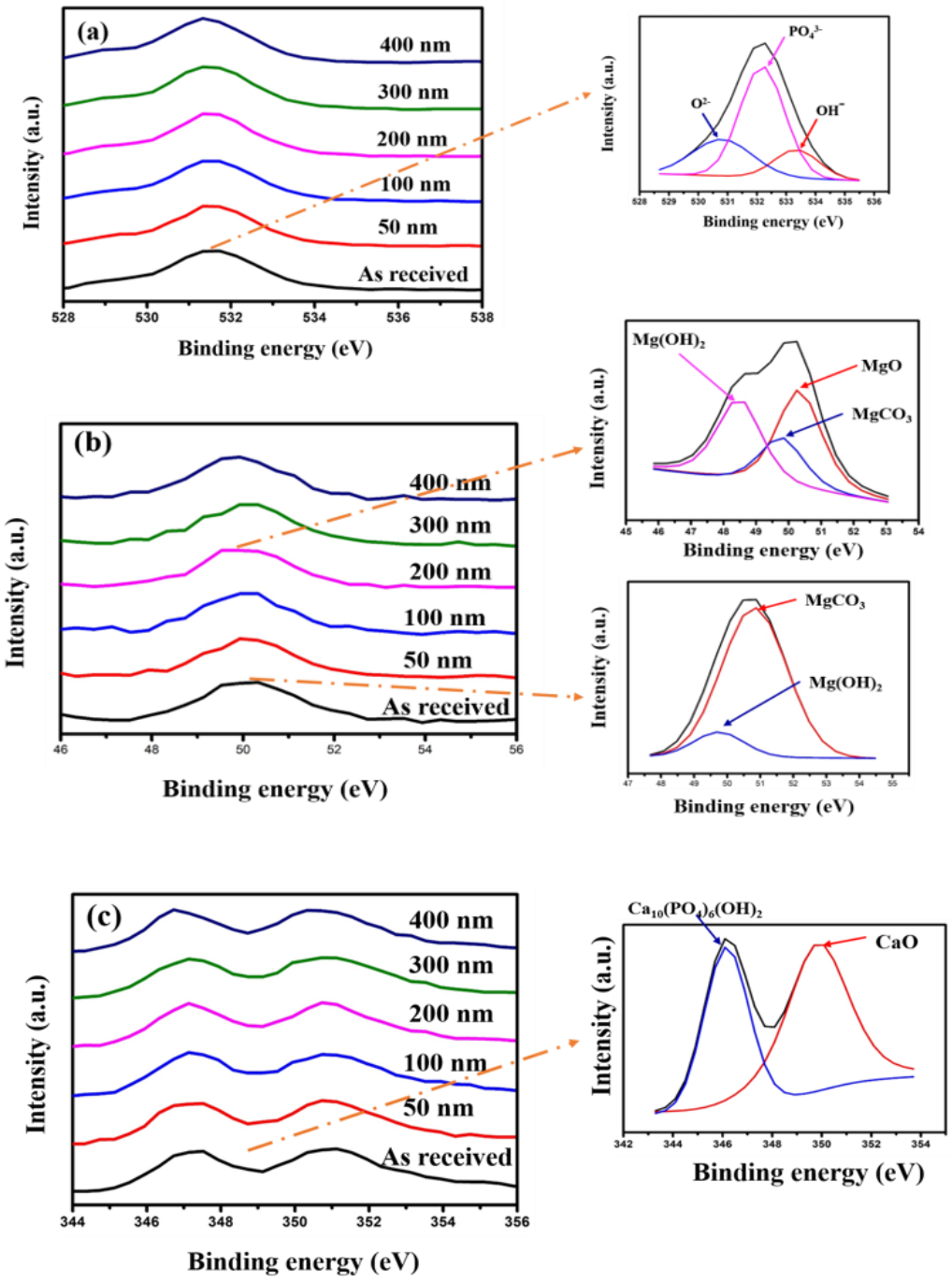

Figure 5.8. DP-XPS spectra of different elements on the corrosion layers on GZ101 alloy sample immersed in cell culture medium for 24h (a) O1s (b) Mg2p (c) Ca2p.

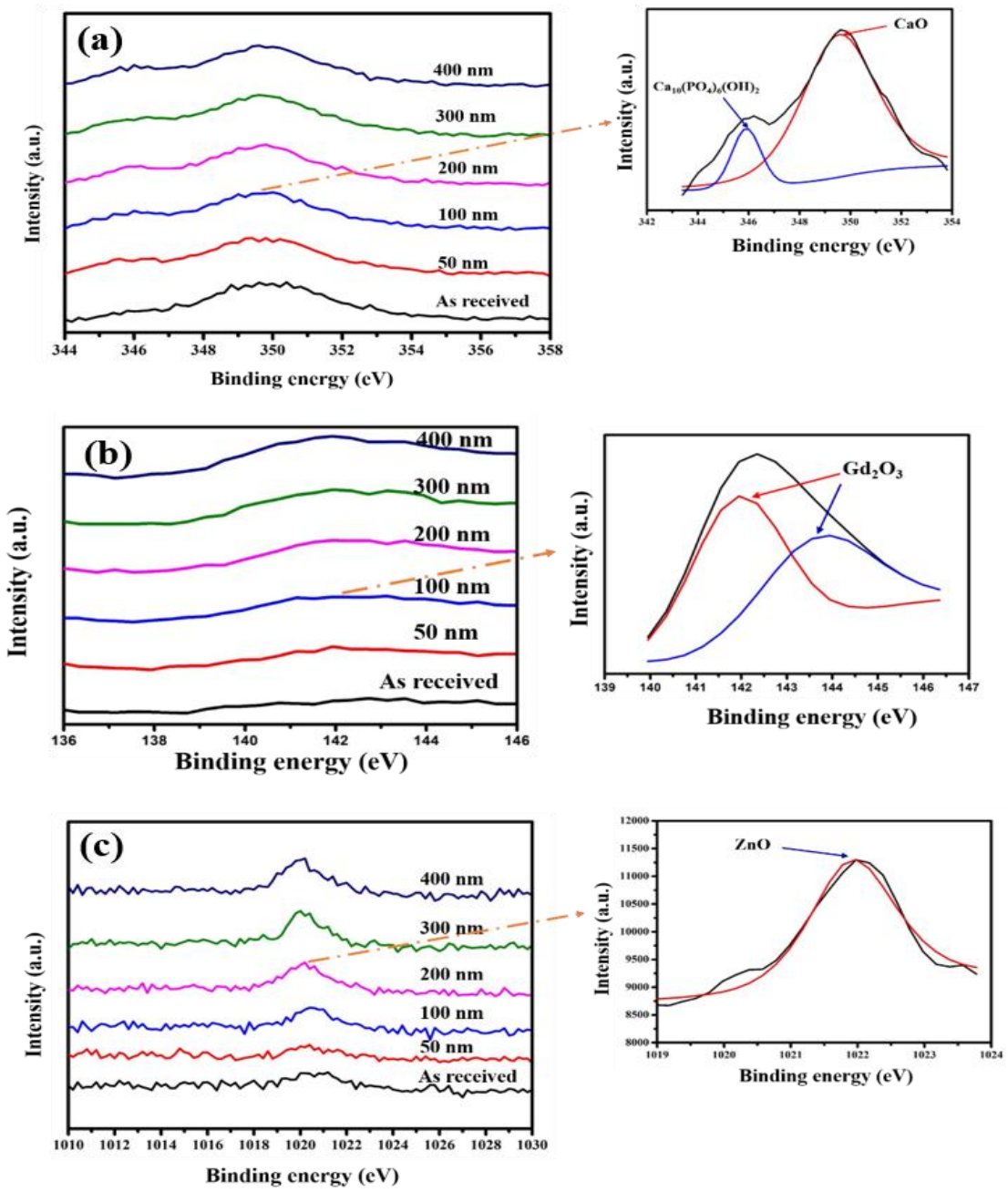

Figure 5.9. DP-XPS spectra of different elements on the degradation layers on samples immersed in cell culture medium for 24h (a) Ca2p of GZ26 (b) Gd4d of GZ101 (c) Zn2p3 of GZ26.

5.3.4. Indirect cell viability tests

5.3.4.1 MTT Assay

The MTT assay results [**Figure 5.10**] showed that the GZ26 alloy had severe toxicity with only a 30% viability in the 1-day test in 100% extract, while GZ22 and GZ101 alloy had excellent viability with 100% and 110% respectively. However, all the alloys showed viability greater than 75% with diluted extract concentrations (50% and 25%). The 3 day MTT assay [**Figure 5.10**] showed that at 100% extract conditions except for GZ101 alloy the other alloys showed a decrease in viability. However, as observed during 1 day period, the viability of all the alloys increased with diluted extracts.

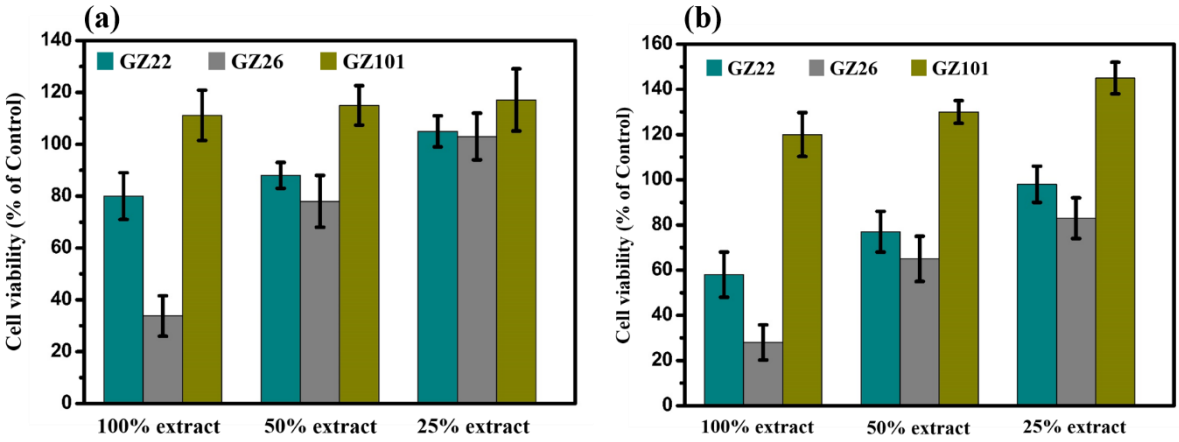

Figure 5.10. MTT assay results of MG63 cells cultured in sample extracts for (a)1 day (b) 3 days.

5.3.4.2 Influence of metal ions on cell viability

The cell viability of the indirect cell culture tests is affected by the release of metal ions into the extract solution. While Mg alloys degrade too fast, due to the release of OH^- ions, the pH of the solution increases beyond 8 and can reach even up to 14. The tolerable limit of pH for cell proliferation requires to be under 8 [31,32]. The pH of the extract medium used for the indirect cell culture experiments was 9.3, 11.2, and 7.95 for GZ22, GZ26, and GZ101 alloys, respectively. Concomitantly, the rise in pH value due to the high degradation rate ensured poor viability of the cells in GZ22 and GZ26.

The cytotoxicity study of different metal ions, Mg^{2+}, Zn^{2+} and Gd^{3+} using MTT assay revealed that the 25000 µM, 120 µM, and 1100 µM concentrations of $MgCl_2$, $ZnCl_2$, and $GdCl_3$ respectively had viability above 75% after 1-day culture. The respective elemental concentrations above the safe limit (Mg - 25000 µM, Zn – 120 µM, and Gd - 1100 µM) led to a severe decline in viability (**Figure 5.11**). To understand the cytotoxicity of studied alloys, the elemental concentrations of 100% extract solutions of different alloys and cell culture medium were analyzed using ICP-MS (**Table 5.4**) and compared with the cytotoxicity of individual metal ions. The analysis revealed that though Zn^{2+} concentration in GZ26 alloy extracts was close to the safe limit and the concentration of Mg^{2+} was almost 2.5 times higher than the safe limit, leading to poor viability at 100% extract conditions. Although a relatively lower amount of Mg and Zn concentrations were observed in the GZ22 alloy, Mg concentration was still high compared to the safe limit. The 100% extract of GZ101 alloy had higher amounts of Mg and Zn than the cell culture medium, nevertheless they were within the safe limits. In general, the Gd concentrations were much lower than the limit for all the alloys. Interestingly, the Ca concentrations were depleted in the extracts of GZ26 and GZ22 alloys compared to that of the cell culture medium. Although the concentration of Ca in the GZ101 extract was also lower than that found in the cell culture medium, the decrease was only marginal. Ca from the cell culture medium gets deposited on the metal surface in the form of CaO and hydroxyapatite [$Ca_{10}(PO_4)_6OH_2$] [confirmed using XPS analysis **Figure 5.8 (c) & 5.9 (a)**], thus resulting in its depletion in the cell culture medium. However, Ca being an essential element for cell proliferation, the depletion of Ca in cell culture medium also leads to poor viability. The alloy with the highest degradation rate (GZ26) had the lowest Ca, and the alloy with the lowest degradation rate (GZ101) had the highest Ca in the extract solution. Due to severe and continuous degradations in GZ22 and GZ26 alloys, the degradation layers in these alloys were not stable, hence more Ca from the cell culture medium was consumed continuously. Thus, the increased amount of Mg and Zn concentrations and the depletion of Ca in the extracts of GZ22 and GZ26 alloys resulted in poor viability.

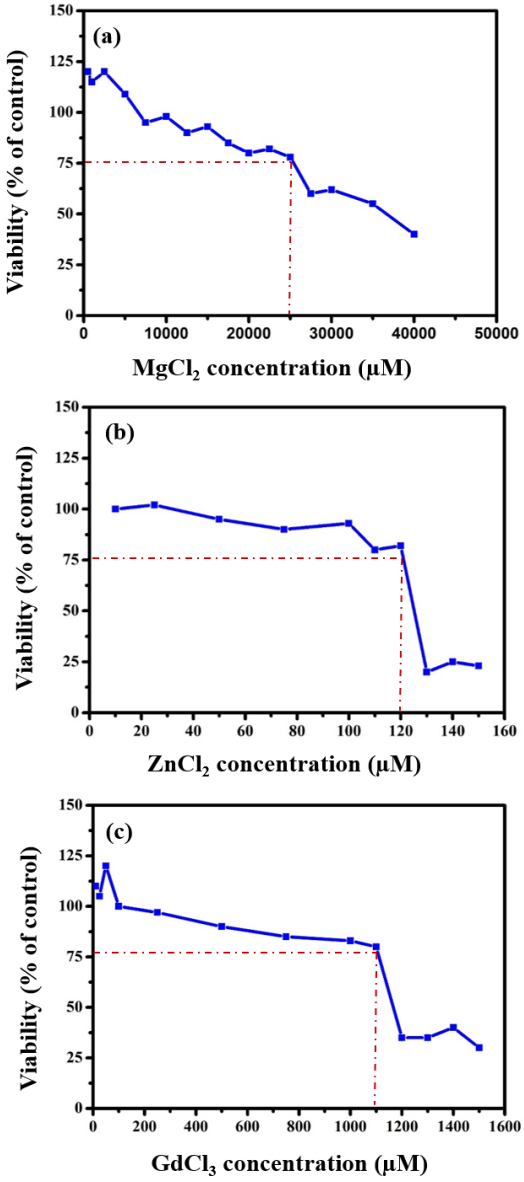

Figure 5.11. MTT assay results of MG63 cells cultured for 1 day in different concentrations of (a) $MgCl_2$ (b) $ZnCl_2$ (c) $GdCl_3$.

Table 5.4. Concentrations of different elements in the 100% extract of alloys immersed in α-MEM with 10% FBS and 1% penicillin.

	Elemental concentration (μM)			
	Mg	**Zn**	**Gd**	**Ca**
GZ22	46743.77	38.55656	3.683088	115.3307
GZ26	66114.84	103.1389	0.230037	69.08158
GZ101	17571.71	10.10976	0.14129	153.2266
Cell culture medium	1131.346	7.925599	0	165.6037

5.3.5 Direct cell culture tests: DAPI staining

The analysis of fluorescent images of cell nucleus on the surface of GZ22 and GZ101 alloys stained using DAPI (**Figure 5.12**) and the cell number count [**Figure 5.12 (e)**] were in agreement with the indirect cell viability assays. Due to the high degradation rate in GZ26 alloy, after 3-day immersion in the culture medium, the metal surface was rough as well as the culture medium was highly alkaline, and hence analysis could not be done for GZ26. The cell count was almost similar for both GZ22 and GZ101 alloys, after 1-day culture. However, the number of cells on GZ22 surface reduced marginally after 3-day culture, while it increased significantly on GZ101 alloy indicating that the cells proliferated on the surface of GZ101 alloy whereas cells were subjected to toxicity in case of GZ22 alloy. This is attributed to the higher degradation rate of the GZ22 alloy compared to the GZ101 alloy, indicating that the surface of GZ22 was less stable. This instability hindered cell proliferation on GZ22. Additionally, the severe degradation of GZ22 led to an increased pH in the surrounding cell culture medium, creating a toxic environment that further inhibited cell growth. Thus, both the instability of the alloy surface and the altered conditions of the surrounding cell culture medium adversely affected cell viability in the case of GZ22.

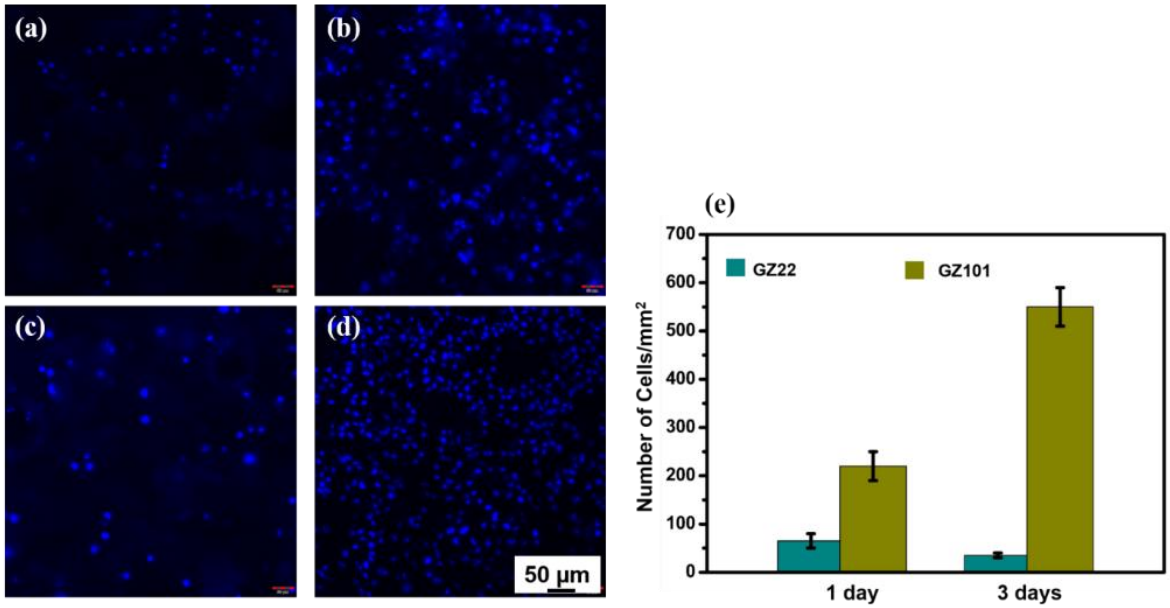

Figure 5.12. Fluorescence microscopy images of DAPI stained MG63 cells cultured on the sample surface (a) GZ22 (b) GZ101 after 1 day; (c) GZ22 (d) GZ101 after 3 days; (e) Quantitative cell count corresponding to the samples.

5.4. Conclusion

In this chapter, three Mg-Zn-Gd alloys with varying Zn/Gd ratios were developed to study the influence of ternary phase formation on microstructure, mechanical, and biological properties. The key findings are summarized below:

- The Mg-2Gd-2Zn-0.5Zr alloy with a Zn/Gd ratio of 1 predominantly exhibited the W phase ($Mg_3Zn_3Gd_2$), a Zn/Gd ratio of 3, the Mg-2Gd-6Zn-0.5Zr alloy consisted primarily of the I phase (Icosahedral phase, Mg_3Zn_6Gd) along with the W phase and for a Zn/Gd ratio of 0.1, the microstructure of Mg-10Gd-1Zn-0.5Zr contained the $(Mg,Zn)_3Gd$ phase and a long period stacking ordered (LPSO) phase distributed in the matrix.
- The Mg-10Gd-1Zn-0.5Zr alloy, containing the LPSO phase, exhibited the highest yield strength due to the strong adherence of the LPSO phase with the α-Mg matrix. However, this alloy also showed the lowest ductility, attributed to the limited deformation ability induced by the LPSO phase.
- Mg-10Gd-1Zn-0.5Zr alloy had better degradation resistance compared to other alloys owing to the formation of Gd_2O_3 containing protective degradation layer.
- Diluted extracts (25 and 50%) of all the alloys showed viability (MG63 cell line) above 75% during in-vitro analysis at all culture conditions (1 or 3 days). However, Mg-10Gd-1Zn-0.5Zr showed excellent (above 95%) viability even with 100 % extracts.

References

[1] Effect of Zn/Gd Ratio on Phase Constitutions in Mg-Zn-Gd Alloys | SpringerLink, (n.d.). https://link.springer.com/chapter/10.1007/978-3-319-48223-1_30 (accessed January 12, 2025).

[2] M. Yamasaki, T. Anan, S. Yoshimoto, Y. Kawamura, Mechanical properties of warm-extruded Mg–Zn–Gd alloy with coherent 14H long periodic stacking ordered structure precipitate, Scr. Mater. 53 (2005) 799–803. https://doi.org/10.1016/j.scriptamat.2005.06.006.

[3] J. Xie, Z. Zhang, H. Dong, J. Zhang, X.-S. Yang, Z. Yu, R. Wu, Insights into corrosion behavior of Mg alloys containing long-period stacking ordered structure in chloride

and sulfate media, Corros. Sci. 243 (2025) 112592. https://doi.org/10.1016/j.corsci.2024.112592.

[4] J. Liu, L. Yang, C. Zhang, B. Zhang, T. Zhang, Y. Li, K. Wu, F. Wang, Role of the LPSO structure in the improvement of corrosion resistance of Mg-Gd-Zn-Zr alloys, J. Alloys Compd. 782 (2019) 648–658. https://doi.org/10.1016/j.jallcom.2018.12.233.

[5] J. Zhang, M. Li, Y. Lai, L. Wen, Y. Ai, X. Ren, W. Zhang, Study on the Microstructure and Properties of Mg-Gd-Ni-Y Alloy Containing LPSO Phase, Metals 13 (2023) 1989. https://doi.org/10.3390/met13121989.

[6] Y. Zhang, Y. Liu, R. Zheng, Y. Zheng, L. Chen, Research progress on corrosion behaviors and biocompatibility of rare-earth magnesium alloys in vivo and in vitro, J. Rare Earths 41 (2023) 1827–1842. https://doi.org/10.1016/j.jre.2023.03.005.

[7] F. Feyerabend, J. Fischer, J. Holtz, F. Witte, R. Willumeit, H. Drücker, C. Vogt, N. Hort, Evaluation of short-term effects of rare earth and other elements used in magnesium alloys on primary cells and cell lines, Acta Biomater. 6 (2010) 1834–1842. https://doi.org/10.1016/j.actbio.2009.09.024.

[8] J. Liu, D. Bian, Y. Zheng, X. Chu, Y. Lin, M. Wang, Z. Lin, M. Li, Y. Zhang, S. Guan, Comparative in vitro study on binary Mg-RE (Sc, Y, La, Ce, Pr, Nd, Sm, Eu, Gd, Tb, Dy, Ho, Er, Tm, Yb and Lu) alloy systems, Acta Biomater. 102 (2020) 508–528. https://doi.org/10.1016/j.actbio.2019.11.013.

[9] N.A. Agha, R. Willumeit-Römer, D. Laipple, B. Luthringer, F. Feyerabend, The Degradation Interface of Magnesium Based Alloys in Direct Contact with Human Primary Osteoblast Cells, PLOS ONE 11 (2016) e0157874. https://doi.org/10.1371/journal.pone.0157874.

[10] F. Cecchinato, N.A. Agha, A.H. Martinez-Sanchez, B.J.C. Luthringer, F. Feyerabend, R. Jimbo, R. Willumeit-Römer, A. Wennerberg, Influence of Magnesium Alloy Degradation on Undifferentiated Human Cells, PLOS ONE 10 (2015) e0142117. https://doi.org/10.1371/journal.pone.0142117.

[11] D. Krüger, B. Zeller-Plumhoff, B. Wiese, S. Yi, M. Zuber, D.C.F. Wieland, J. Moosmann, R. Willumeit-Römer, Assessing the microstructure and *in vitro* degradation behavior of Mg-xGd screw implants using µCT, J. Magnes. Alloys 9 (2021) 2207–2222. https://doi.org/10.1016/j.jma.2021.07.029.

[12] W. Rong, Y. Zhang, Y. Wu, M. Sun, J. Chen, Y. Wang, J. Han, L. Peng, H. Ding, Effects of Zr and Mn additions on formation of LPSO structure and dynamic

recrystallization behavior of Mg-15Gd-1Zn alloy, J. Alloys Compd. 692 (2017) 805–816. https://doi.org/10.1016/j.jallcom.2016.09.068.

[13] H.E. Friedrich, B.L. Mordike, eds., Technology of Magnesium and Magnesium Alloys, in: Magnes. Technol. Metall. Des. Data Appl., Springer, Berlin, Heidelberg, 2006: pp. 219–430. https://doi.org/10.1007/3-540-30812-1_6.

[14] M. Li, K. Zhang, Z.W. Du, X.G. Li, Y.J. Li, M.L. Ma, G.L. Shi, J.W. Yuan, T. Li, J.B. Liu, The effect of homogenization on microstructures and mechanical properties of Mg–7Gd–3Y–1Nd–xZn–0.5Zr (x=0.5, 1 and 2wt.%) alloys, Mater. Charact. 109 (2015) 66–72. https://doi.org/10.1016/j.matchar.2015.08.013.

[15] W. Luo, Y. Guo, Z. Xue, X. Han, Q. Kong, M. Mu, G. Zhang, W. Mao, Y. Ren, Microstructure and mechanical properties of the Mg–Gd–Zn alloy prepared by sintering of rapidly-solidified ribbons, Sci. Rep. 12 (2022) 11003. https://doi.org/10.1038/s41598-022-14753-2.

[16] J.S. Chen, C.J. Ji, Q.Y. Huang, Y.Z. Zeng, H.B. Xie, P. Chen, B.Z. Sun, Formation mechanism of W phase and its effects on the mechanical properties of Mg−Dy−Zn alloys, J. Magnes. Alloys (2024). https://doi.org/10.1016/j.jma.2024.05.009.

[17] L. Luo, Y. Liu, M. Duan, Phase Formation of Mg-Zn-Gd Alloys on the Mg-rich Corner, Materials 11 (2018) 1351. https://doi.org/10.3390/ma11081351.

[18] J. Yang, L. Wang, L. Wang, H. Zhang, Microstructures and mechanical properties of the Mg–4.5Zn–*x*Gd (x = 0, 2, 3 and 5) alloys, J. Alloys Compd. 459 (2008) 274–280. https://doi.org/10.1016/j.jallcom.2007.05.044.

[19] D.K. Xu, L. Liu, Y.B. Xu, E.H. Han, Effect of microstructure and texture on the mechanical properties of the as-extruded Mg–Zn–Y–Zr alloys, Mater. Sci. Eng. A 443 (2007) 248–256. https://doi.org/10.1016/j.msea.2006.08.037.

[20] H. Huang, H. Kato, C. Chen, Z. Wang, G. Yuan, The effect of nanoquasicrystals on mechanical properties of as-extruded Mg–Zn–Gd alloy, Mater. Lett. 79 (2012) 281–283. https://doi.org/10.1016/j.matlet.2012.04.018.

[21] Y. Liu, G. Yuan, W. Ding, C. Lu, Deformation behavior of Mg–Zn–Gd-based alloys reinforced with quasicrystal and Laves phases at elevated temperatures, J. Alloys Compd. 427 (2007) 160–165. https://doi.org/10.1016/j.jallcom.2006.03.027.

[22] S. Yoshimoto, M. Yamasaki, Y. Kawamura, Microstructure and Mechanical Properties of Extruded Mg-Zn-Y Alloys with 14H Long Period Ordered Structure, Mater. Trans. 47 (2006) 959–965. https://doi.org/10.2320/matertrans.47.959.

[23] Y. Wu, L. Peng, F. Zheng, X. Li, D. Li, W. Ding, Microstructure modification and performance improvement of Mg-RE alloys by friction stir processing, in: N. Hort, S.N. Mathaudhu, N.R. Neelameggham, M. Alderman (Eds.), Magnes. Technol. 2013, Springer International Publishing, Cham, 2016: pp. 191–196. https://doi.org/10.1007/978-3-319-48150-0_31.

[24] G.-L. Song, 1 - Corrosion electrochemistry of magnesium (Mg) and its alloys, in: G. Song (Ed.), Corros. Magnes. Alloys, Woodhead Publishing, 2011: pp. 3–65. https://doi.org/10.1533/9780857091413.1.3.

[25] J. Kim, K.C. Wong, P.C. Wong, S.A. Kulinich, J.B. Metson, K.A.R. Mitchell, Characterization of AZ91 magnesium alloy and organosilane adsorption on its surface, Appl. Surf. Sci. 253 (2007) 4197–4207. https://doi.org/10.1016/j.apsusc.2006.09.030.

[26] M.I. Sosulnikov, Yu.A. Teterin, X-ray photoelectron studies of Ca, Sr and Ba and their oxides and carbonates, J. Electron Spectrosc. Relat. Phenom. 59 (1992) 111–126. https://doi.org/10.1016/0368-2048(92)85002-O.

[27] Y. Tanizawa, H. Tsuchikane, K. Sawamura, T. Suzuki, Reaction characteristics of hydroxyapatite with F– and PO3F2– ions. Chemical states of fluorine in hydroxyapatite, J. Chem. Soc. Faraday Trans. 87 (1991) 2235–2240. https://doi.org/10.1039/FT9918702235.

[28] B.R. Strohmeier, D.M. Hercules, Surface spectroscopic characterization of the interaction between zinc ions and γ-alumina, J. Catal. 86 (1984) 266–279. https://doi.org/10.1016/0021-9517(84)90372-5.

[29] Y. Xu, J. Li, M. Qi, W. Guo, Y. Deng, A newly developed Mg-Zn-Gd-Mn-Sr alloy for degradable implant applications: Influence of extrusion temperature on microstructure, mechanical properties and in vitro corrosion behavior, Mater. Charact. 188 (2022) 111867. https://doi.org/10.1016/j.matchar.2022.111867.

[30] W. Li, S. Guan, J. Chen, J. Hu, S. Chen, L. Wang, S. Zhu, Preparation and in vitro degradation of the composite coating with high adhesion strength on biodegradable Mg–Zn–Ca alloy, Mater. Charact. 62 (2011) 1158–1165. https://doi.org/10.1016/j.matchar.2011.07.005.

[31] J. Fischer, D. Pröfrock, N. Hort, R. Willumeit, F. Feyerabend, Reprint of: Improved cytotoxicity testing of magnesium materials, Mater. Sci. Eng. B 176 (2011) 1773–1777. https://doi.org/10.1016/j.mseb.2011.06.002.

[32] A.-M. Galow, A. Rebl, D. Koczan, S.M. Bonk, W. Baumann, J. Gimsa, Increased osteoblast viability at alkaline pH in vitro provides a new perspective on bone regeneration, Biochem. Biophys. Rep. 10 (2017) 17–25. https://doi.org/10.1016/j.bbrep.2017.02.001.

Chapter 6

Effect of Extrusion in Mg-Zn-Gd-Zr Alloys

6.1 Introduction

The findings from Chapter 5 indicated that the as-cast Mg-Zn-Gd-Zr alloys did not meet the desired properties for biodegradable implants, such as a yield strength (YS) greater than 200 MPa, % elongation above 10, and a biodegradation rate of less than 0.5 mm/y. Consequently, secondary processing is necessary to enhance the properties of these alloys. Various secondary processing techniques are employed by researchers to improve the performance of Mg-based biodegradable implants. Conventional methods such as extrusion, rolling, and forging, heat treatment as well as severe plastic deformation techniques like friction stir processing (FSP), equal channel angular pressing (ECAP), and high-pressure torsion (HPT), are widely explored. Among these methods, extrusion stands out due to its scalability, efficiency, and long-established industrial viability, making it a preferred choice for optimizing the microstructure and mechanical properties of Mg alloys for biomedical applications.

Chen et al. [1] demonstrated that increasing the number of extrusion passes significantly improved the mechanical properties of Mg–2Zn–xGd–0.5Zr (x = 0, 0.5, 1, 2 wt%) alloys. For instance, the ultimate tensile strength (UTS), yield strength (YS), and elongation of the 1Gd alloy increased by approximately 17%, 30%, and 60%, respectively, after four passes of extrusion compared to two passes. This enhancement was primarily attributed to grain refinement, which played a more dominant role than second-phase strengthening during severe plastic deformation. However, the mechanical properties of the 0.5Gd, 1Gd, and 2Gd alloys subjected to the same number of extrusion passes (four passes) showed no significant differences, further emphasizing the critical influence of extrusion passes over alloy composition in this context. Du et al. [2] reported that increasing the number of extrusion passes refined grains and secondary phases while strengthening the basal texture, thereby improving both strength and ductility. It was observed that higher dislocation density caused by extensive grain refinement could improve strength at the expense of ductility. However, adopting advanced extrusion processes can enhance both

strength and ductility simultaneously. For example, Zhang et al. [3] found that double extrusion of Mg-Nd-Zn-Zr alloys produced a significantly finer and more uniform microstructure compared to single extrusion. This improvement was attributed to dynamic recrystallization (DRX), initiated by the stored plastic energy from double extrusion, leading to finer and more homogeneous grains. The yield strength, ultimate tensile strength, and elongation of double-extruded alloys were superior due to a combination of grain refinement and the formation of fine precipitated phases such as $Mg_{12}Nd$ during hot extrusion. Furthermore, the activation of both basal and non-basal slip systems in double-extruded fine-grain magnesium alloys improved ductility significantly. For instance, a double-extruded and aged Mg–2Nd–0.1Zn–0.4Zr alloy exhibited a 27% increase in yield strength, a 16% increase in UTS, and a remarkable 121% improvement in elongation compared to single-pass extrusion [4]. Extrusion has also been shown to impact biodegradation behaviour. Du et al. [2] noted that increasing the extrusion ratio from 7:1 to 14:1 in Mg-4Zn-1.2Y-0.8Nd alloy resulted in complete dynamic recrystallization, producing a homogeneous fine-grain structure and improved biodegradation resistance due to uniform grain distribution. While reducing the biodegradation rate is often desired, achieving uniform biodegradation is equally important for maintaining the mechanical integrity of biodegradable implants over their service life. Zhang et al. [5] observed that extruded GZ61K (Mg-6Gd-1Zn-0.5Zr) alloy exhibited a lower biodegradation rate compared to GZ60K (Mg-6Gd-0.6Zn-0.5Zr) alloy due to its finer grain size. However, GZ60K alloy displayed more uniform biodegradation, resulting in longer retention of mechanical integrity, which is a crucial factor in implant design. These findings highlight that extrusion not only improves mechanical properties by refining grains and optimizing textures but also enhances biodegradation behavior, offering tailored solutions for biodegradable implant applications.

Thus, in this chapter, the alloys Mg-2Gd-2Zn-0.5Zr, Mg-2Gd-6Zn-0.5Zr, and Mg-10Gd-1Zn-0.5Zr were subjected to extrusion, and their microstructural, mechanical, and biological properties were systematically evaluated.

6.2. Materials and Methods

The alloys Mg-2Gd-2Zn-0.5Zr (GZ22), Mg-2Gd-6Zn-0.5Zr (GZ26) and Mg-10Gd-1Zn-0.5Zr (GZ101) were prepared as described in Chapter 3. Ingots of 35 mm diameter and 40 mm length were machined from the cast blocks and extruded into 10 mm rods. The

ingots were preheated at 400 °C for 1 h and were extruded at 350^0C with an extrusion ratio of approximately 12:1 (**Figure 6.1**). The morphology and composition analysis of different phases were carried out with a scanning electron microscope (SEM, Carl Zeiss EVO18) with energy-dispersive X-ray spectroscopy (EDS) and the TEM analysis was done in JEOL JEM F 200 with STEM EDA EELS HRTEM. Tensile tests methods and various in-vitro and in-vivo characterization techniques used to analyze the properties of the prepared alloys are already mentioned in Chapter 3. Tensile tests were conducted on threaded samples (6 mm × 25 mm) per ASTM B557M-10 at 2 mm/min, with mechanical integrity evaluated after 14-day immersion in MEM + 10% FBS under cell culture conditions, followed by tensile testing at 0.1 mm/min. In-vitro biodegradation was assessed by immersing samples in MEM + 10% FBS + 1% penicillin for 14 days (ISO 10993), with electrochemical tests performed at 37 ± 1°C using MEM as the electrolyte. MTT assays (ISO 10993:2009) evaluated cytotoxicity on MG-63 cells, exposed to extracts (100%, 50%, 25%) after 1 and 3 days of culture, followed by MTT incubation and absorbance measurement at 570 nm. Live/dead staining was performed using acridine orange/ethidium bromide and analyzed via fluorescence microscopy. For direct cell viability, DAPI staining was done on 50,000 cells seeded on Mg alloy samples (10 mm × 2 mm) after 3 days of immersion, followed by imaging. Cell adhesion was examined via SEM after fixation and ethanol dehydration. For in-vivo studies, Sprague-Dawley rats (180–220 g) were implanted subcutaneously with Mg alloy samples (5 mm × 2 mm) and monitored for 30 days. Afterward, tissues and organs were harvested, formalin-fixed, H&E-stained, and analyzed. Statistical analysis was performed using one-way ANOVA (GraphPad Prism 8), with $p < 0.05$ considered significant.

Figure 6.1 Photograph of Mg alloy samples before and after extrusion.

6.3 Results and Discussion

6.3.1 Microstructure

In general, the secondary phases in all the alloys seemed to have fragmented during the extrusion process, and the distribution seemed almost uniform (**Figure 6.2**). The network-shaped W phase observed in the as-cast GZ22 alloy was broken into discrete particles. In the case of GZ26 alloys, the skeleton-shaped W phases were not entirely broken down, as there were still a few phases that retained their cast morphology in the extruded state. The secondary phases in GZ101 alloy were distributed uniformly throughout and had the highest volume fraction of secondary phases.

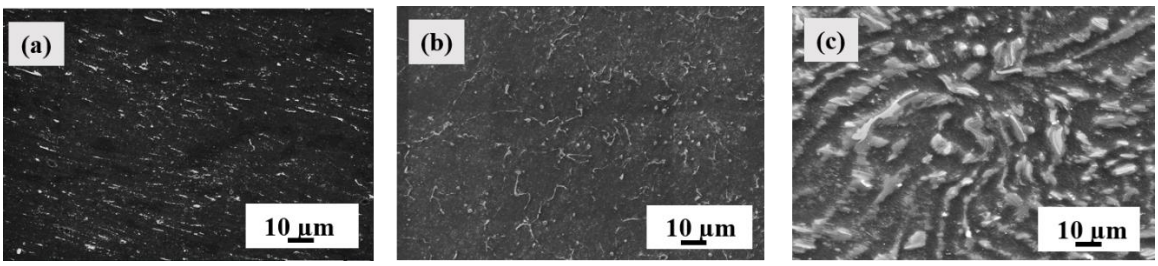

Figure 6.2. SEM micrographs of extruded alloys (a) GZ22 (b) GZ26 (c) GZ101.

The grain boundary overlaid inverse pole figure (IPF) maps [**Figure 6.3 (a-c)**] of the alloys showed a bimodal microstructure for all the alloys with fine equiaxed grains and elongated deformed grains. The above observation might be due to an insufficient extrusion ratio (12:1) or due to the segregation of rare earth elements at grain boundaries that could hinder the dynamic recrystallization (DRX) by arresting the grain boundary mobility, leading to a non-uniform grain size distribution [6–8]. Kernel average misorientation (KAM) maps were used to identify the localized lattice distortions, and localized deformations and to calculate the geometrically necessary dislocations [9,10]. Severe dislocation accumulation could be seen in GZ22 [green region in **Figure 6.3 (d)**] and GZ101 [**Figure 6.3 (f)**] indicating higher strain energy accumulated in these alloys during extrusion. Similarly, the grain orientation spread (GOS) value for the alloys were calculated as 1.67, 2.56, and 5.28 for GZ22, GZ26, and GZ101, respectively. GOS is the ratio of the average deviation of orientations of each point in grain to the average orientation of grains and it is an indicator of the energy stored in the grains [11,12]. Thus the strain energy stored

in the GZ101 alloy [**Figure 6.3 (i)**] was the highest, and it had a higher dislocation density. The highest dynamic recrystallization of 65.8% was observed in GZ26 alloy, and a lowest fraction of dynamic recrystallization of 29.7% was observed in GZ101 alloy. The low dynamic recrystallization fraction observed in GZ101 might be due to the presence of the LSPO phase, which had a highly stable and ordered structure that could resist deformation and delayed the DRX. The average grain size of the dynamically recrystallized grains in all three alloys was similar, 1.85 (±0.12) µm, 3.5 (±0.83) µm and 1.2 µm (±0.12) for GZ22, GZ26, and GZ101 alloys, respectively (ref. **Figure 6.4**).

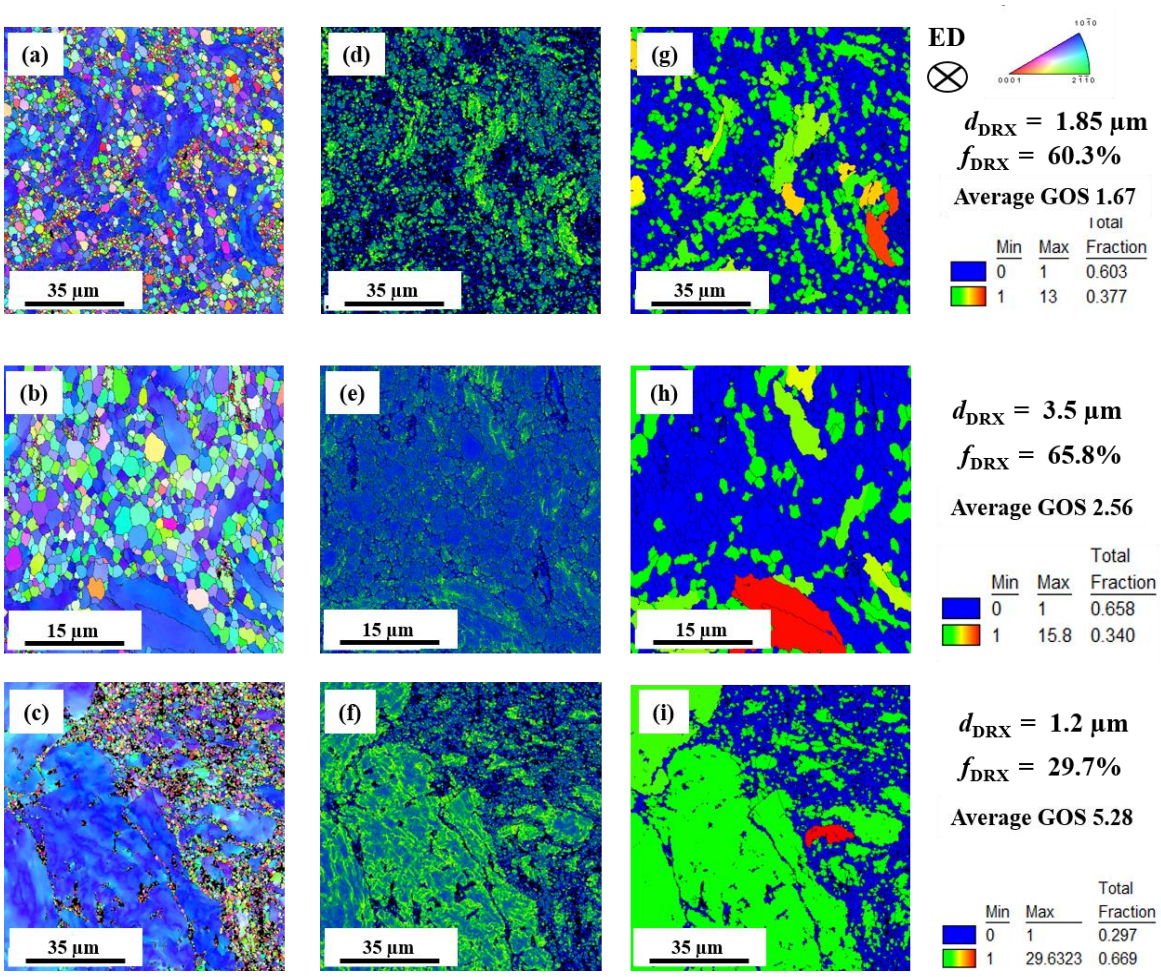

Figure 6.3. IPF of (a) GZ22, (b) GZ26, (c) GZ101, KAM maps of (d) GZ22, (e) GZ26, (f) GZ101, GOS maps of (g) GZ22, (h) GZ26, (i) GZ101.

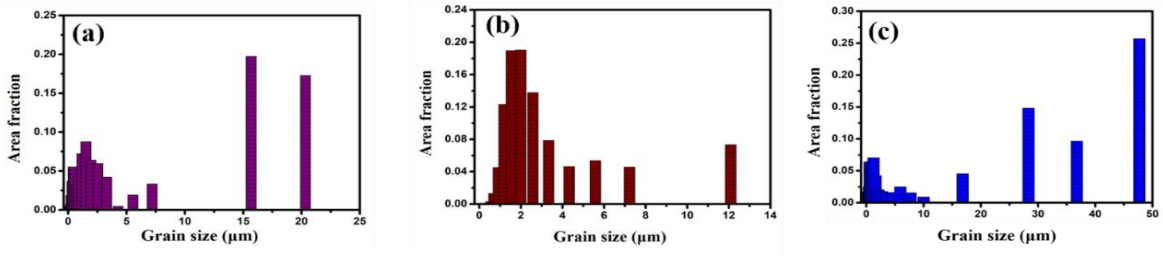

Figure 6.4 Grain size distribution of alloys (a) GZ22 (b) GZ26 (c) GZ101.

6.3.2 Tensile properties

The tensile properties of the alloys (YS, UTS, and % elongation) are summarized in **Table 6.1**, and the corresponding stress-strain curves are shown in **Figure 6.5**. The GZ26 alloy had the lowest YS of 210 (±14.10) MPa, but it had the highest elongation of 18.5% (±1.45). On the other hand, the GZ101 alloy showed the highest YS and UTS of 260 (±9.29) MPa and 328 (±15.8) MPa, respectively. The tensile properties of the alloys can be influenced by the factors such as grain size, dislocation density, secondary phases present, and texture development during extrusion. Since the DRXed grain size was almost similar for all the alloys, the influence of grain size on strength enhancement might be marginal. The dislocation density in the extruded alloys was significantly different, which had a significant impact on the mechanical properties. The increase in dislocation density induces a higher strain-hardening effect, as the flow stress is proportional to the dislocation density [13]. This is in agreement with the fact that the GZ101 alloy, with the highest dislocation density, showed the highest tensile strength, while the GZ26 alloy, with the lowest dislocation density, showed the lowest yield strength.

Even though the dislocation density and grain size of the GZ22 and GZ101 alloys were almost similar, the yield strength was significantly lower for the GZ22 alloy with respect to GZ101. According to Schmid law, the decrease in the Schmid factor increases the yield strength of the material [14], as $\sigma = \frac{\tau}{m}$; σ is the yield strength of the material, τ is the critically resolved shear stress and m is the Schmid factor of the material. In the present study, the average Schmid factor calculated using TSL OIM software was 0.33, 0.34, and 0.24 for alloys GZ22, GZ26, and GZ101, respectively. Thus the low Schmid factor also contributed to the better yield strength of the GZ101 alloy.

Table 6.1. Yield strength (YS), Ultimate tensile strength (UTS) and Elongation (%) of extruded alloys.

Alloy	Y.S (MPa)	UTS (MPa)	% Elongation
GZ22	240 (±6.37)	260 (±7.86)	16.2 (±2.23)
GZ26	210 (±14.10)	255 (±13.64)	18.5 (±1.45)
GZ101	260 (±9.29)	328 (±15.8)	12.76 (±2.36)

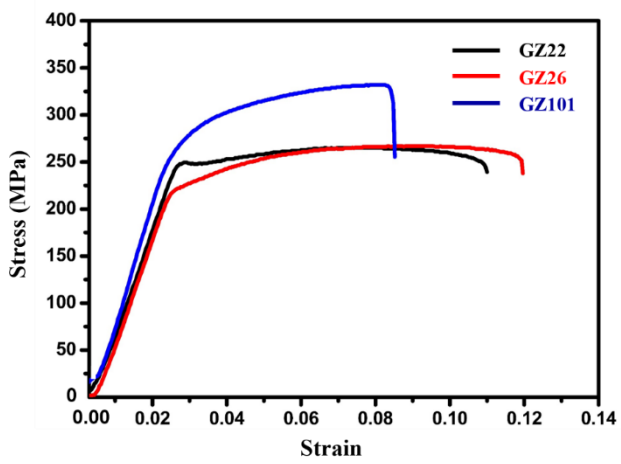

Figure 6.5. Tensile stress-strain curves of the extruded alloys.

The results also showed that the increase in the yield strength of the alloys was accompanied by a reduction in ductility (as seen in **Table 6.1**). It is a well-known phenomenon in Mg alloys that the poor ductility is due to the difficulty in activating <c+a> pyramidal dislocations. The deformation mechanism of Mg alloys is dominated by the basal slip of {0001} <11-20> which has a low critically resolved shear stress. However, basal slip alone cannot accommodate strain along the c-axis and as a result, the alloys are at risk of failure at even low strain. Thus, activating slip in other directions through alloying or secondary processing can improve ductility [10,11].

The addition of REEs can result in a weakening of the basal texture of the material as they can inhibit or suppress the growth of the basal texture [15–17]. The basal texture in magnesium alloys is caused by the preferred orientation of the material's hexagonal close-packed (HCP) crystal structure. The addition of REEs can disrupt the formation of the preferred orientation by altering the nucleation and growth behaviour of the grains in the

material that can result in a more random distribution of crystal orientations and weakening of the basal texture [18,19]. The REEs can also form complex intermetallic compounds with magnesium, further disrupting the basal texture's growth. These compounds can act as nucleation sites for new grains, leading to a more uniform distribution of crystal orientations in the material [20,21]. In the present study, inverse pole figure analysis indicated that the GZ22 and GZ26 alloys had weak basal component (000) [**Figure 6.6 (a) & (b)**] but exhibited strong prismatic (1010) component [**Figure 6.6 (a) & (b)**] contributed in their better ductility. Similarly, the weak prismatic texture in the GZ101 alloy [**Figure 6.6 (c)**], might be the reason for its lowest ductility.

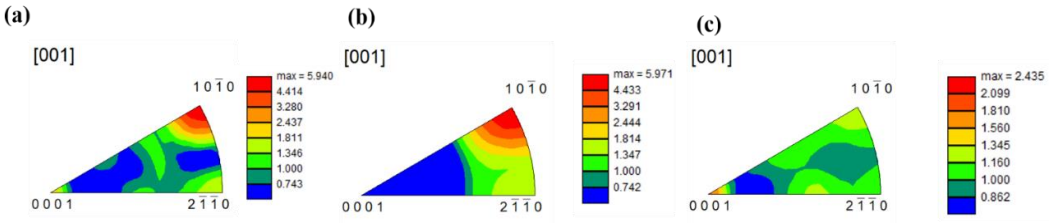

Figure 6.6. Inverse pole figures of (a) GZ22 (b) GZ26 (c) GZ101 alloy.

6.3.3 Electrochemical corrosion measurement

The potentiodynamic polarization curves and the Tafel fitting values of the alloys immersed in α-MEM for 30 min. are presented in **Figure 6.7** and **Table 6.2**, respectively. The most negative E_{corr} and lowest i_{corr} values were obtained for the GZ101 alloy, while the most positive E_{corr} and highest i_{corr} values were obtained for the GZ26 alloy. Immediately after Mg alloys are immersed in MEM, electrochemical cells form and in most cases α-Mg matrix serves as anode and second phases serve as cathode. The standard electrode potentials of Mg, Gd, Zn, and Zr are -2.372, -2.279, -0.7618, and -1.45 V, respectively. The alloy (GZ26) having the highest amount of Zn had the highest positive E_{corr} value, and the alloy (GZ101) with the lowest amount of Zn and the highest amount of Gd had the E_{corr} shift towards a more negative value. In addition, the highest i_{corr} (64.98 μA/cm^2) observed for GZ26, and the lowest i_{corr} (25.12 μA/cm^2) observed for GZ101 alloy indicated that GZ101 had the highest degradation resistance compared to GZ26. The above observations suggested that the presence of Gd in the alloy improved the degradation resistance, while the presence of Zn increased the corrosion susceptibility.

Table 6.2. E_{corr} and i_{corr} values of extruded alloys [calculated from Tafel plots: polarization measurements done in α- MEM solution at 37˚C].

Alloy	E_{corr} (mV vs SCE)	i_{corr} (μA/cm^2)
GZ22	-1680 (±85)	58.23 (±3.5)
GZ26	-1590 (±75)	64.98 (±6.7)
GZ101	-1820 (±50)	25.12 (±2.8)

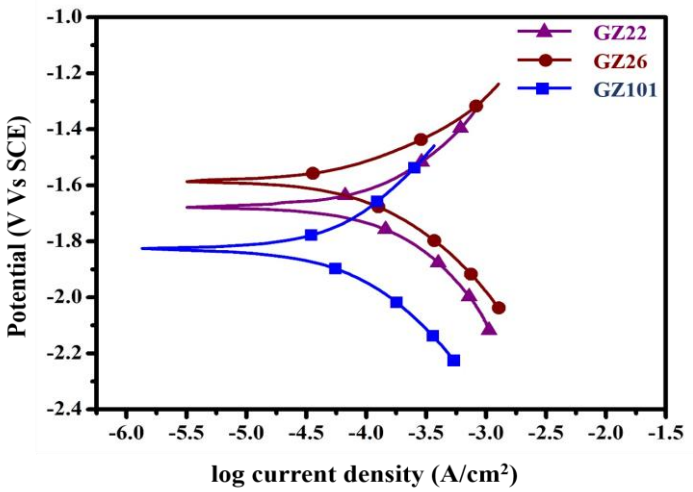

Figure 6.7. Polarization curves of extruded alloys in α- MEM solution at 37˚C.

The EIS analysis of the alloys was performed using Nyquist and Bode plots (**Figure 6.8**). The Nyquist plots [**Figure 6.8 (a)**] of the GZ22 and GZ26 alloys were almost similar, suggesting that the corrosion rates and mechanisms were similar. The diameter of the Nyquist plot of the GZ101 alloy [**Figure 6.8 (a)**] was almost double compared to the other alloys, indicating its better corrosion resistance. In addition, the inductive loop was absent in all the alloys, suggesting that pitting corrosion was not initiated [22] [23]. The results were also plotted in Bode plots [log Zmod vs log *f*, and phase angle vs log *f* [**Figure 6.8 (b & c)**]. The Z_{mod} of the alloys [**Figure 6.8 (b)**] increased in the following order: GZ26 (600 Ω.cm^2) < GZ22 (605 Ω.cm^2) < GZ101 (1200 Ω.cm^2). The Bode plots also revealed that there were no sudden dips indicating no pitting corrosion associated with any of the alloys.

The EIS spectra of the alloys were fitted using the ZSimpWin 3.20 software with the electrochemical circuit as shown in **Figure 6.10 (d)** for GZ22 and GZ26 alloys and

Figure 6.10 (e) for the GZ101 alloy. The fitting values are presented in Table 6.3. The R_s indicate the solution resistance, R_0 represents the charge transfer resistance, CPE_0 represents the double layer capacitance, R_1 represents the resistance to mass transport and CPE_1 indicates the corresponding capacitance, and R_2 and CPE_2 indicate the film resistance. The GZ22 and GZ26 alloys had two-time constants, while the GZ101 alloy had three-time constants. The first-time constant representing the capacitive loop in the is attributed to the charge transfer resistance. The second time constant representing the capacitive loop is due to the diffusion of ions from the electrolyte to the metal surface. The third time constant observed in GZ101 represents the resistance offered by the protective film formed on the surface. GZ101 showed highest polarization resistance, R_p (R_0+R_1 or R_0+R_1+R_2), (1195.2 Ω.cm^2) compared to that of GZ22 (548.9 Ω.cm^2) and GZ26 (540.5 Ω.cm^2), and exhibited low CPE_0 value (2.8 x 10^{-9} Sn/ Ω.cm^2) compared to that of the GZ22 (6.6 x10^{-6} Sn/ Ω.cm^2) and GZ26 (4 x 10^{-6} Sn/ Ω.cm^2) alloys (**Table 6.3**). The low CPE_0 value indicated that corrosion was restricted to minimum area in GZ101.

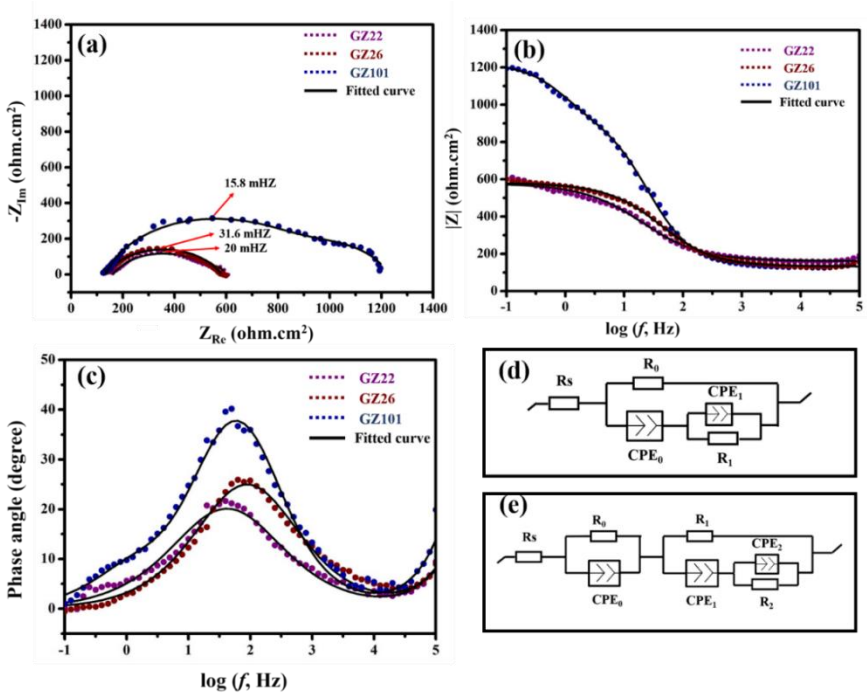

Figure 6.8. (a) Nyquist plots (b) Bode plots of log Zmod *vs.* log *f*, (c) Bode plot of Phase angle *vs.* log *f*, of alloys measured in α- MEM solution at 37 ˚C (d) Equivalent electrochemical circuits of GZ22 & GZ26, (e) Equivalent electrochemical circuits of GZ101 alloy.

Table 6.3. The fitted values of EIS measurements of alloys using equivalent circuits shown in **Figure 6.10**.

Alloy	R_s ($\Omega.cm^2$)	R_0 ($\Omega.cm^2$)	CPE_0 ($S^n/\Omega.cm^2$)	n	R_1 ($\Omega.cm^2$)	CPE_1 x 10^{-5} ($S^n/\Omega.cm^2$)	n_1	R_2 ($\Omega.cm^2$)	CPE_2 x 10^{-5} ($S^n/\Omega.cm^2$)	n_2	Rp = ($R_0+R_1+R_2$) ($\Omega.cm^2$)
GZ22	48.73 (±3.15)	386.8 (±25.06)	6.6 x10^{-6} (±0.3 x 10^{-6})	0.95 (±0.05)	162.1 (±10.5)	9.02 (±0.5)	0.69 (±0.04)	N.A	N.A	N.A	548.9 (±35.56)
GZ26	39.6 (±2.58)	370.5 (±20.2)	4 x 10^{-6} (±0.24 x 10^{-6})	0.98 (±0.02)	170 (±12.2)	4.98 (±0.25)	0.72 (±0.05)	N.A	N.A	N.A	540.5 (±32.4)
GZ101	21.09 (±1.5)	273.5 (±15.8)	2.8 x 10^{-9} (±0.1 x 10^{-9})	0.97 (±0.06)	114.5 (±6.2)	2.5 (±0.22)	0.8 (±0.045)	807.2 (±67.98)	87.47 (±4.5)	0.83 (±0.12)	1195.2 (±89.9)

6.3.4 Biodegradation test

The electrochemical experiments are short-term experiments that give an idea about the initial behaviour of the alloys in the degradation medium. For long-term analysis of the degradation behaviour, the alloys were immersed in cell culture medium for 14 days by maintaining the pH between 7.4 to 8. The results [**Figure 6.9 (a)**] showed that the degradation rate was lowest for the GZ101 alloy (0.21 mm/y), similar to the electrochemical results. Though, the electrochemical corrosion analysis revealed that the initial corrosion resistance of the alloys was almost similar for GZ22 and GZ26 alloys, 14 days of immersion test in the cell culture medium suggested that the degradation rate of the GZ26 alloy [0.75 (±0.08) mm/y] was almost double that of the GZ22 alloy [0.38 (±0.11) mm/y]. The degradation surface of the alloys after 14 days of immersion [**Figure 6.9(b)**] showed that the GZ26 alloy suffered severe pitting corrosion while the GZ22 had a shallow corroded area. However, the GZ101 alloy showed no signs of pits, and the surface exhibited a uniformly corroded region indicating its superior resistance to degradation in cell culture medium. The cross-section morphology of the degraded surface of the alloys was observed using SEM (**Figure 6.10**), and it was found that the GZ101 alloy had no signs of degradation spreading into the interior. In contrast, the GZ22 and GZ26 alloys had

indications of pitting corrosion, with severe pitting observed in the GZ26 alloy. The pit formation in the alloys was spreading into the grain interior adjacent to the secondary phases [shown in the inset of **Figure 6.10(b)**], indicating that these phases were cathodic to the surrounding matrix.

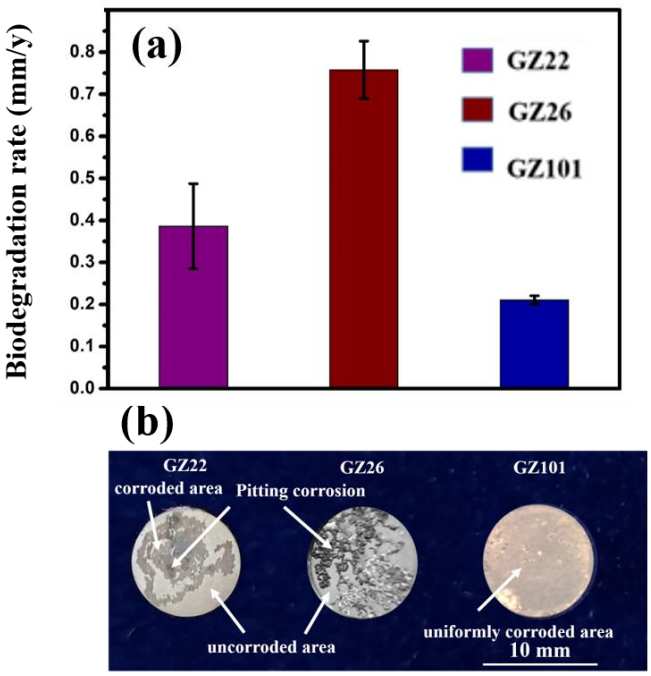

Figure 6.9. (a) Degradation rate of alloys immersed in cell culture medium for 14 days, (b) Photographs of degraded samples after immersed in cell culture medium for 14 days. Values are the mean ± SD, n=4, **p < 0.01, ****p <0.0001.

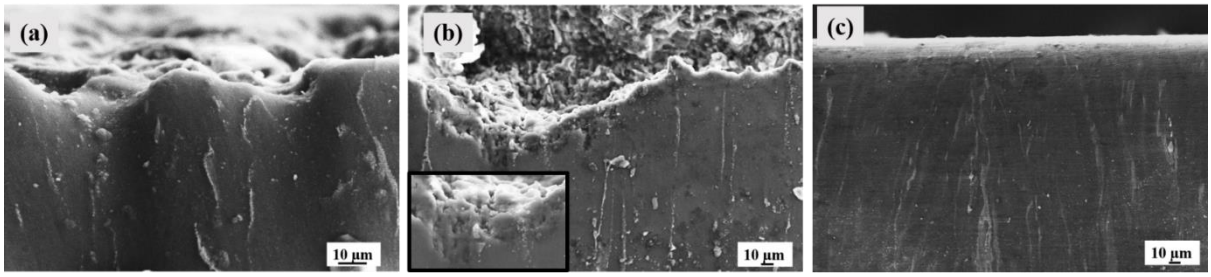

Figure 6.10. Degradation morphology of the samples (cross section) immersed in cell culture medium for 14 days (after the degradation product removal) (a) GZ22 (b) GZ26 (c) GZ101.

Factors such as secondary phases, grain size, texture, and the degradation layer can influence the degradation of Mg alloys [24,25]. In general, the degradation rate increases with an increase in the number of secondary phases in a Mg alloy due to the generation of more micro-galvanic sites [26]. However, in the present study, the lowest degradation rate was observed for the GZ101 alloy, which had the highest volume fraction of secondary phases, indicating that the ill effect of volume fraction of secondary phases was nullified by other factors. Likewise, the grain size also seemed to have a marginal effect on the degradation rate of the alloys as the measured grain size of the extruded alloys was almost similar. However, the EBSD analysis indicated that the amount of strain stored in the alloys was significantly differed alloy to alloy after extrusion. Although few reports suggested that the accumulation of dislocation in the grains increase the degradation rate of the alloys, in the present study, GZ101 with the highest dislocation density showed the lowest degradation rate, and GZ26 with the lowest dislocation density showed the highest degradation rate (**Figure 6.9)** [24,26]. On the other hand, the texture of the alloys also plays a crucial role in determining their degradation resistance [14,27]. The basal plane {0001} in Mg alloys has a lower surface energy compared to the prism planes {1010} and {1120}. This results in the basal plane being more resistant to degradation than the prism planes. The reported theoretical corrosion rate of the prism planes is also much higher than that of the basal planes, further highlighting the importance of texture in determining corrosion resistance [28,29]. For instance, Song et al. [30] found that the presence of a dominant basal plane in AZ31 alloy contributed to its better resistance. Similarly, Xin et al. [27] reported that the high intensity of {1010} and {1120} planes in rolled AZ31 alloy leads to its poor corrosion resistance in 3.5 wt.% NaCl. The pole figures that showed the texture of the alloys studied in the present study in terms of the orientation of the crystals are presented in **Figure 6.11**. A very weak basal component was observed with GZ26 alloy, indicating that it had a high proportion of prismatic planes, which are normally more susceptible to corrosion. On the other hand, GZ22 and GZ101 showed a high intensity of the basal component and a similar texture intensity in the prismatic planes. Still, their degradation resistance was found to be significantly different from each other. The above observed discrepancies might be due to the characteristics of degradation layers formed during degradation. The XPS analysis of the degradation layer formed on the as-cast alloys after immersion in cell culture medium, as discussed in Chapter 5 (**Figure 5.8-5.10**) for GZ22, GZ26, and GZ101 alloys, provided valuable insights into their composition. Since the alloy composition remains

unchanged in the as-extruded condition, the degradation layer was expected to retain the same characteristics. The degradation layers of GZ22 and GZ26 primarily consisted of $Mg(OH)_2$, MgO, $MgCO_3$, $Ca_{10}(PO_4)_6(OH)_2$, CaO, and ZnO. In contrast, the GZ101 alloy exhibited the presence of Gd_2O_3 in addition to these compounds. The incorporation of Gd_2O_3, along with $MgCO_3$, $Ca_{10}(PO_4)_6(OH)_2$, and CaO, made the typically porous $Mg(OH)_2$ and MgO layer more compact, significantly enhancing the corrosion resistance of the GZ101 alloy.

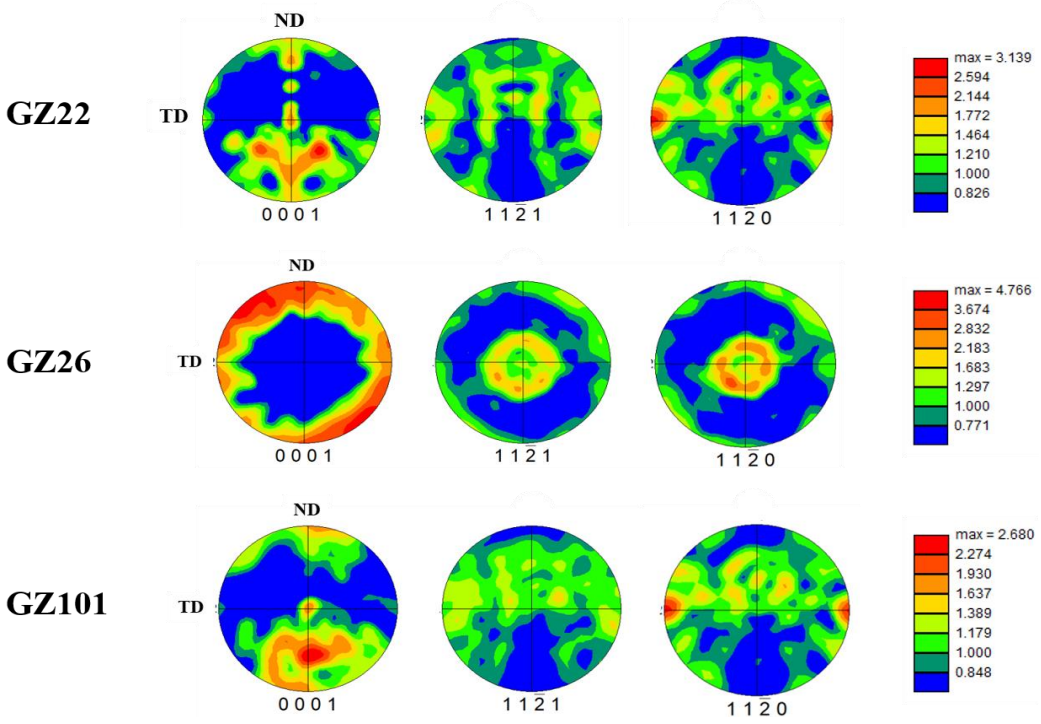

Figure 6.11. Basal pole figures of alloys obtained from EBSD analysis.

6.3.5 Mechanical Integrity after degradation

Typically, the mechanical support provided by degradable implants also weakens as they degrade; the load-bearing capacity of the sample decreases due to the reduction in the cross-sectional area caused by degradation. Premature loss of mechanical integrity could lead to structural failure, compromising the healing process. Moreover, the test helps identify uniformity in degradation, as uneven degradation can cause localized stress concentrations, potentially leading to implant failure. By correlating the changes in mechanical properties with degradation rates, this evaluation ensures that the implant

degrades at a controlled rate, maintaining mechanical support while promoting tissue regeneration. This is critical for optimizing implant design and ensuring both safety and efficacy in clinical applications [31].

To evaluate the mechanical integrity of these alloys, tensile samples were immersed in CCM for 14 days to allow degradation to occur under simulated physiological conditions. After the immersion period, tensile tests were conducted to assess the extent of degradation-induced weakening. **Figure 6.12** shows the tensile samples after immersion in CCM for 14 days. Prominent localized pitting corrosion was observed in the GZ22 and GZ26 alloys. Additionally, a large crack was visible at the centre of the GZ22 alloy, whereas smaller cracks were dispersed across the tensile surface of the GZ26 alloy. In contrast, while signs of pitting corrosion initiation were present in the GZ101 alloy, they were significantly smaller compared to the other alloys, indicating its superior degradation resistance. The presence of severe pitting and crack formation in the GZ22 and GZ26 alloys suggested a more pronounced reduction in mechanical integrity, likely leading to a greater decline in tensile strength and ductility. Conversely, the minimal pitting observed in the GZ101 alloy indicated that it retained better mechanical properties after immersion, with a lesser reduction in tensile strength and elongation compared to GZ22 and GZ26.

The results of the tensile properties of the alloys after 14 days of immersion in a cell culture medium under physiological conditions indicated that the GZ101 alloy maintained its mechanical integrity even after a 14-day immersion period [**Figure 6.13 and Table 6.4**] due to its lower degradation rate. Both GZ22 and GZ26 alloys showed a significant loss in tensile properties, with an approximately 42% to 84% decrease in yield strength, ultimate tensile strength, or elongation. GZ101 alloy with highest mechanical properties as well as lowest degradation rate showed the highest mechanical integrity. Thus optimum combination of superior mechanical properties and degradation resistance is required for the design of a degradable implant material.

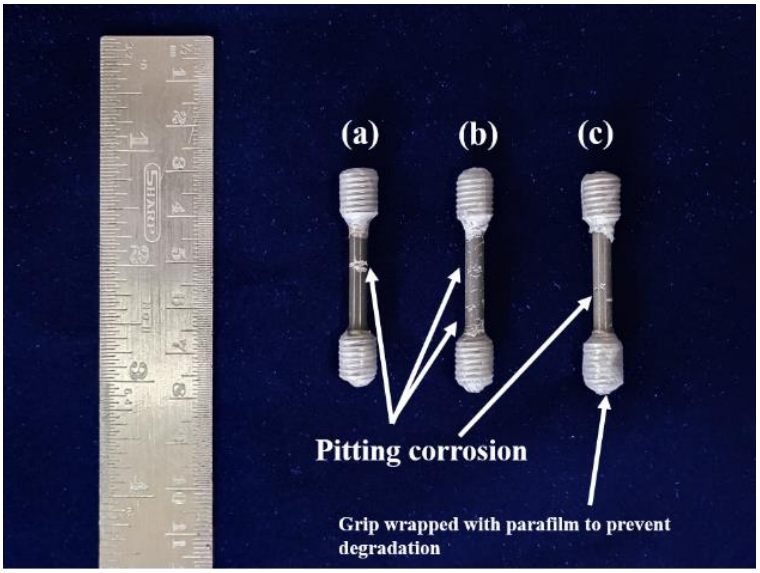

Figure 6.12. Tensile samples immersed in CCM for 14 days (a) GZ22 (b) GZ26 (c) GZ101.

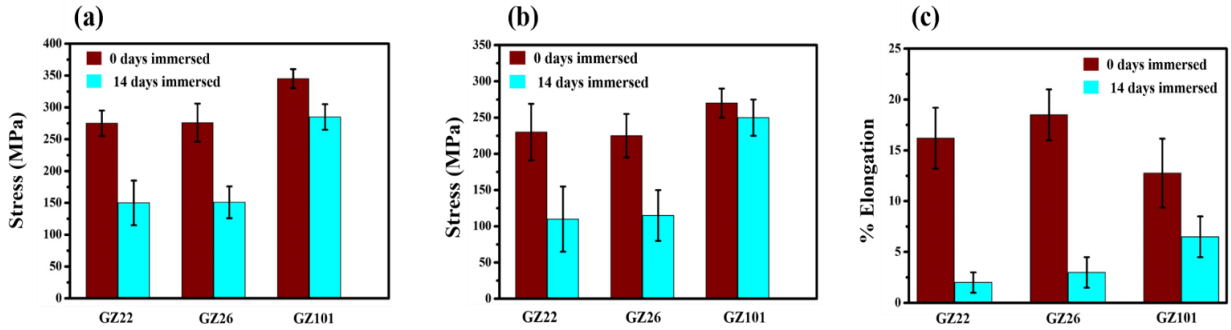

Figure 6.13. Tensile properties of alloys immersed in cell culture medium for 14 days (a) Ultimate tensile strength (b) Yield strength (c) % elongation.

Table 6.4. % decrease in tensile properties of alloys after 14-day immersion in cell culture medium

Alloy code	% decrease in UTS	% decrease in YS	% decrease in elongation
GZ22	45.58	56.71	84.33
GZ26	42.08	50.38	77.42
GZ101	16.17	7.41	45

6.3.6 Indirect cell viability tests

6.3.6.1 MTT assay

The MTT assay results [**Figure 6.14 (a)**] showed that the GZ26 alloy had severe toxicity with only a 20% viability in the 1-day test in 100% extract, while GZ22 and GZ101 alloy had excellent viability with 90% and 98% respectively. However, all the alloys showed viability greater than 75% with diluted extract concentrations (50% and 25%). MTT assay after 3-day culture [**Figure 6.14 (b)**] showed that at 100% extract conditions, GZ26 and GZ22 alloys had poor viability while GZ101 alloy showed still excellent viability (120%). In general, all the alloys showed an increase in viability when diluted extract concentrations were used for culturing.

6.3.6.2 Live dead staining

The acridine orange-ethidium bromide dual staining images (**Figure 6.15 & 6.16**) show the characteristics of cells cultured with extract solutions of different concentrations of GZ22, GZ26, and GZ101 alloys. Three different cell types were noticed: live cells (green nuclei with an organized structure), apoptotic cells (condensed or fragmented cells with green or orange stain), and necrotic cells (nuclei stained red) [32,33]. After 1 day of culture in 100% extract [**Figure 6.15**], GZ22 and GZ101 alloys had no apoptotic cells, while GZ26 extract solution showed signs of early apoptosis. All alloys showed good proliferation with diluted extract concentrations (50% and 25%). After 3 days of culture [**Figure 6.16**], cells cultured with 100% extracts of GZ22 and GZ26 alloy showed severe apoptosis and necrosis. Diluting the culture medium to 50% and 25%, improved cell proliferation, however, still necrotic cells in certain areas were seen. In contrast, cells cultured with all extract concentrations of GZ101 alloy showed similar morphology to that of cultured with the control, and no apoptosis or necrosis was observed. The cell viability calculated from the live-dead analysis [**Figure 6.17**] indicated that all alloys had a viability greater than 75% at all culture times when 50% and 25% extracts were used. However, 100% extracts of GZ26 alloy and GZ22 alloy after 3 days had poor viability.

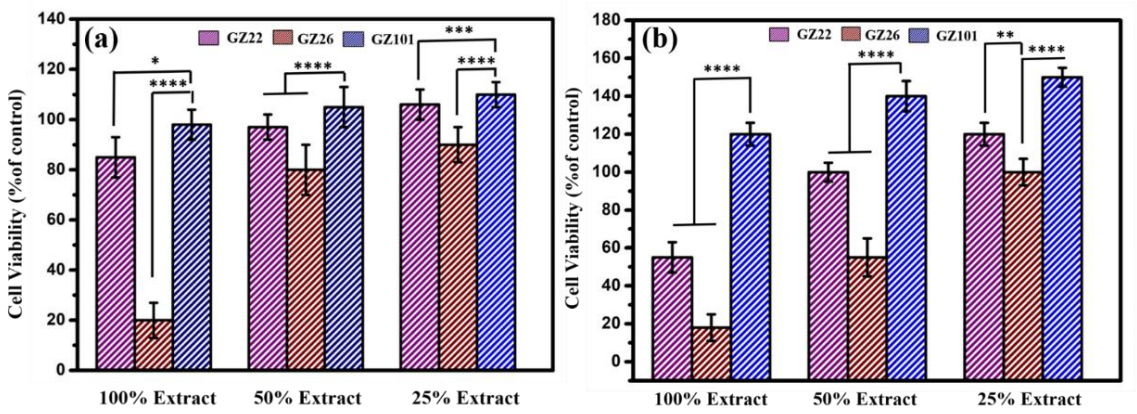

Figure 6.14. MTT assay results of MG63 cells cultured in sample extracts for (a) 1 day, (b) 3 days. Values are the mean ± SD, n=4, *p < 0.05, **p < 0.01, ***p < 0.001, ****p < 0.0001.

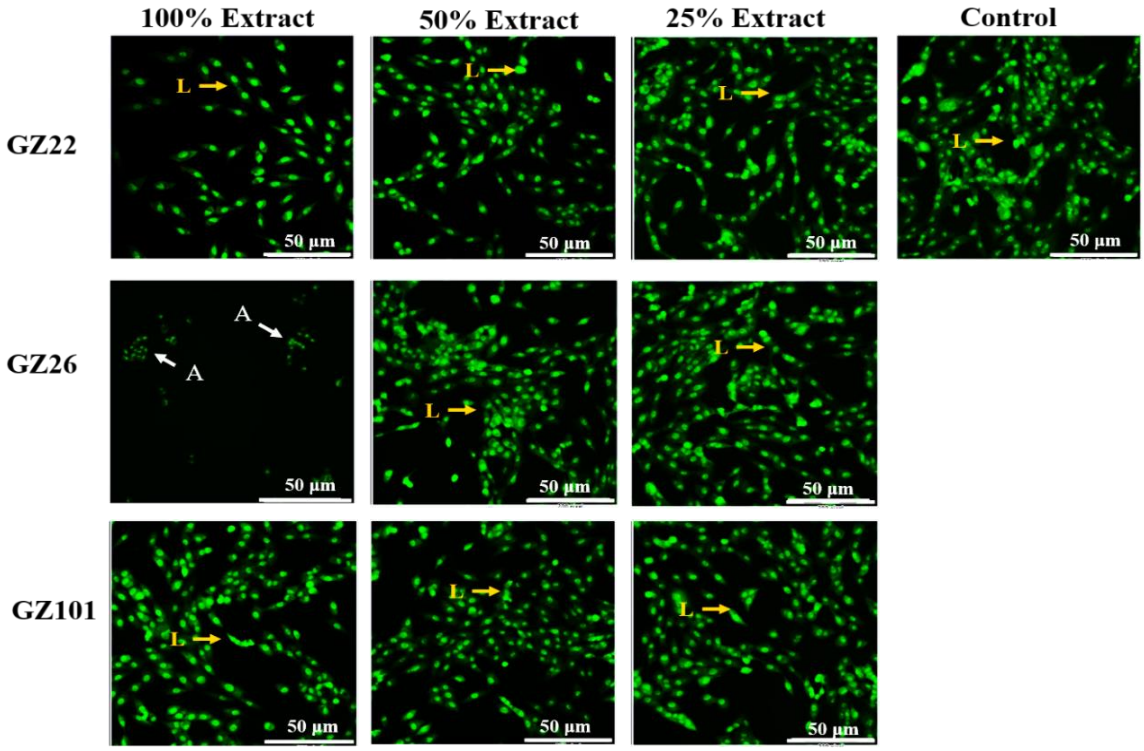

Figure 6.15. Live dead staining images of MG63 cells cultured in sample extracts for 1 day (L- Live cells, A- Apoptotic cells).

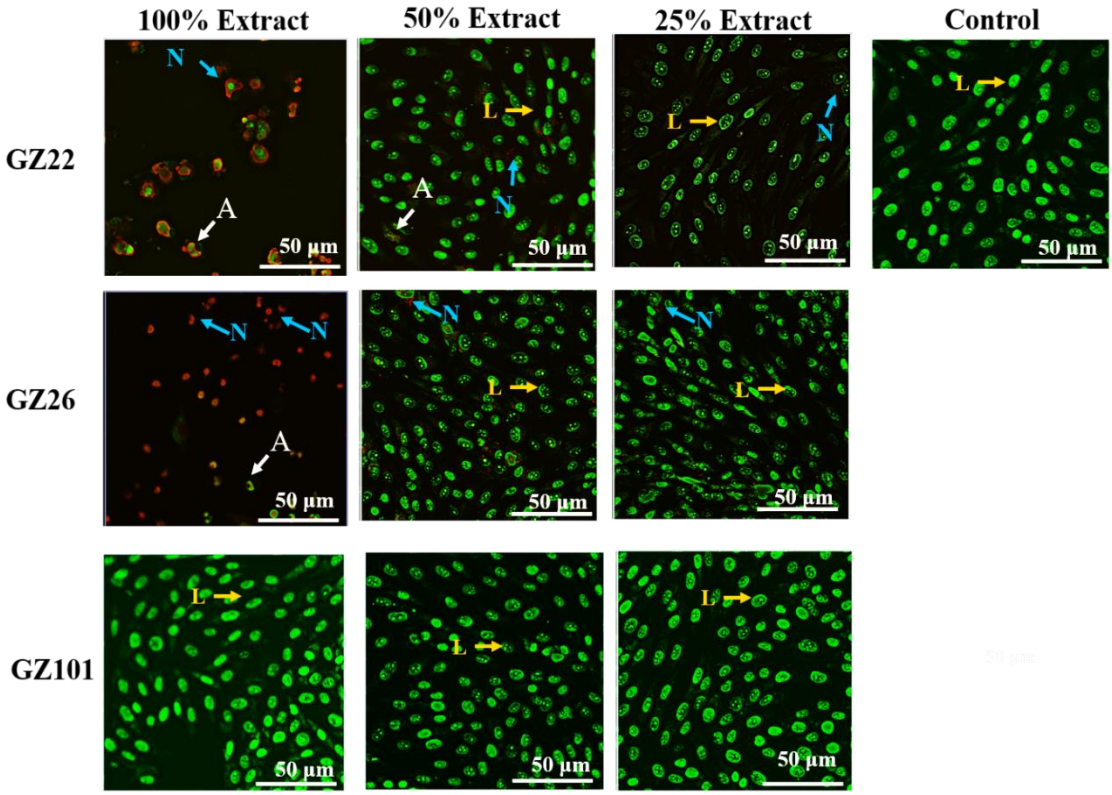

Figure 6.16. Live dead staining images of MG63 cells cultured in sample extracts for 3 days (L- Live cells, A- Apoptotic cells, N- Necrotic cells).

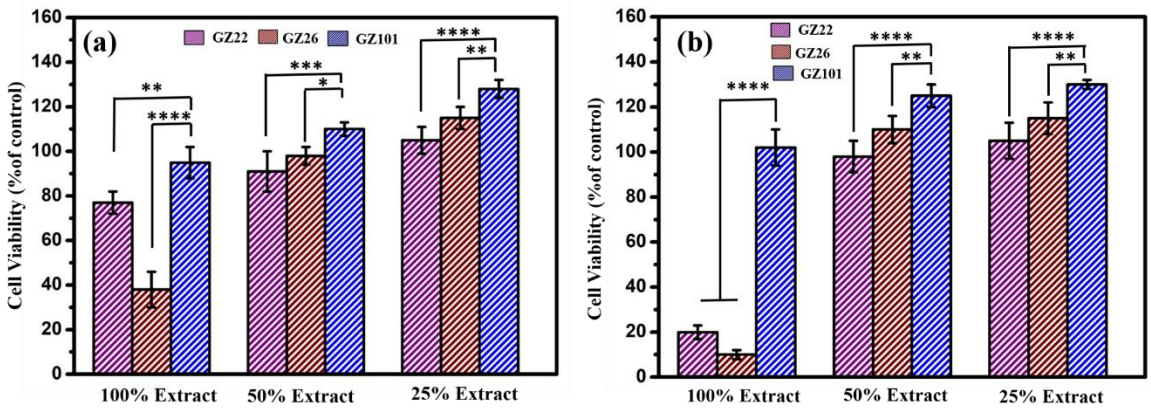

Figure 6.17. Cell viability calculated from live dead staining images of MG63 cells cultured in sample extracts for (a) 1 day (b) 3 days. Values are the mean ± SD, n=4, *p < 0.05, **p < 0.01, ***p < 0.001, ****p < 0.0001.

6.3.7 Direct cell culture tests

6.3.7.1 DAPI staining

The analysis of fluorescent images of cell nucleus on the surface of GZ22 and GZ101 alloys stained using DAPI [**Figure 6.18 (a-d)**] and the cell number count [**Figure 6.18 (e)**] were in agreement with the indirect cell viability assays. Due to the high degradation rate in GZ26 alloy, after 3-day immersion in the culture medium, the metal surface was rough as well as the culture medium was highly alkaline, and hence direct cell culture analysis could not be done for GZ26. The cell count was almost similar for both GZ22 and GZ101 alloys, after 1-day culture. However, the number of cells on GZ22 surface reduced marginally after 3-day culture, while it increased significantly (almost a fivefold increase) on GZ101 alloy indicating that the cells proliferated on the surface of GZ101 alloy whereas cells subjected to toxicity in case of GZ22 alloy.

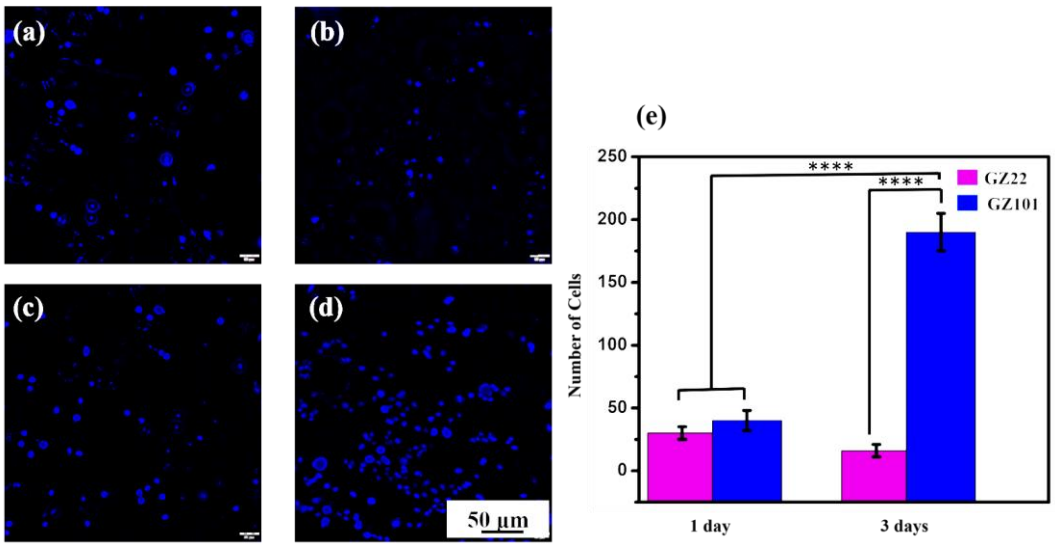

Figure 6.18. Fluorescence microscopy images of DAPI stained MG63 cells cultured on the sample surface for 1 day (a) GZ22, (c) GZ101 and for 3 days (b) GZ22, (d) GZ101, (e) cell count.

6.3.7.2 Cell attachment and proliferation

The interaction of cells with GZ22 and GZ101 metal surface after 1-day and 3-day culture was inspected using SEM [**Figure 6.19 & 6.20**]. Initially, after 1day cell culture, the cells on the metal surface of both the alloys [shown by yellow arrows in **Figure 6.19 (a) & 6.20 (a)**] were seen to have a round morphology. Higher magnification SEM image in both [**Figure 6.19 (b) and 6.20 (b)**] of a selected area shows that the cells were beginning to merge and indicates the beginning of proliferation. After 3-day culture, the surface of GZ22 alloys was covered with degradation products and the cells on the surface were not visible [**Figure 6.19 (c)**]. However, at higher magnification cells (marked in yellow arrows) are visible beneath the degradation layer suggesting that although the surface of GZ22 alloy was not stable due to the severe degradation, the proliferation of cells also occurred.

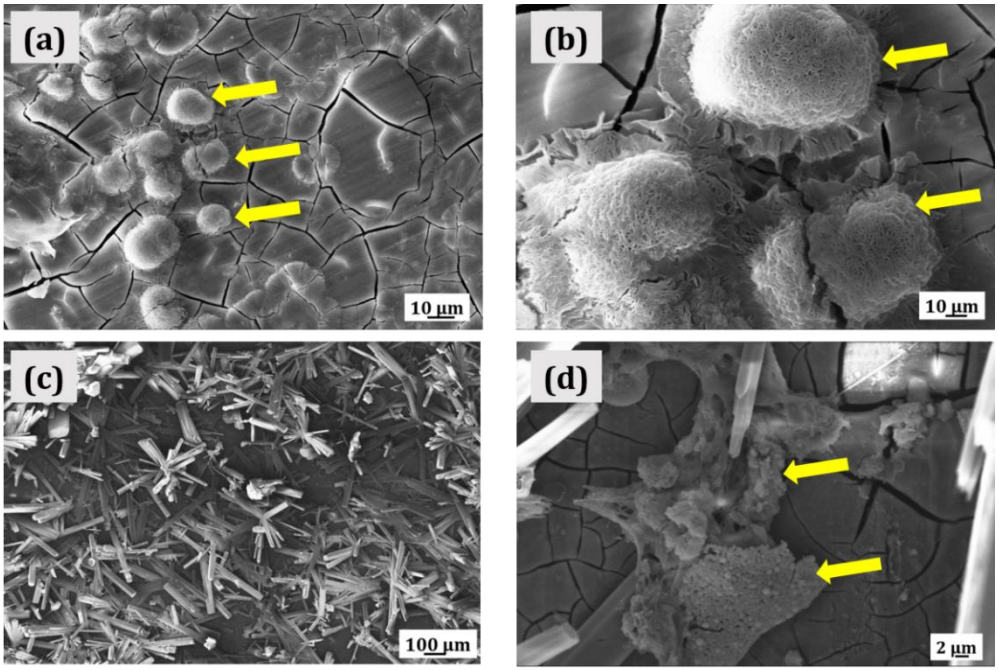

Figure 6.19. SEM images of adherent cells on the surface of GZ22 alloy (a & b) 1-day culture, (c & d) 3-day culture.

Whereas, after 3-day culture cells on GZ101 surface [shown in yellow arrows in **Figure 6.20 (c)**] were seen to have spread all over the metal surface and covered the cracks of the degradation layer on the metal surface. Also the higher magnification SEM micrograph of GZ101 alloy [**Figure 6.20 (d)**] revealed that the cells with pseudopods were

spreading in all directions. The excellent proliferation of the cells on the GZ101 surface was due to the presence of a protective degradation film which was confirmed using XPS analysis [**Figure 5.7-5.9**]. The formation of a stable surface film consisting of Gd_2O_3, $MgCO_3$, $Ca_{10}(PO_4)_6(OH)_2$, CaO, MgO, and $Mg(OH)_2$ on the surface of GZ101 resulted in better cell attachment and proliferation. The proliferation of cells on the GZ101 alloys surface could also be due to the enhanced formation of hydroxyapatite ($Ca_{10}(PO_4)_6(OH)_2$) in the GZ101 alloy compared to other alloys [as observed in the XPS analysis, **Figure 5.8 (c)**].

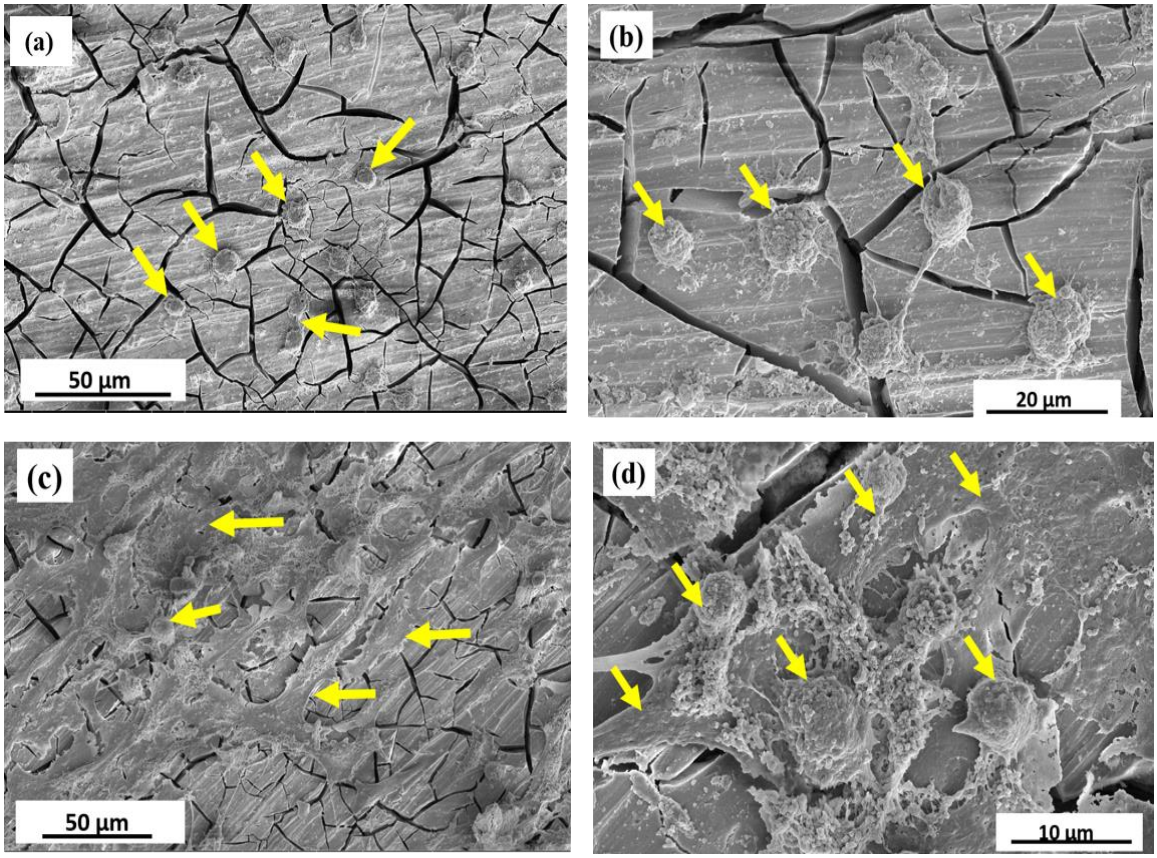

Figure 6.20. SEM images of adherent cells on the surface of GZ101 alloy (a &b) 1-day culture, (c & d) 3-day culture.

6.3.8 In-vivo evaluation

The GZ101 alloy which showed better viability, degradation resistance, and mechanical integrity during in-vitro analysis was considered for short term in-vivo evaluation by subcutaneous implantation in rats. A rat subcutaneously implanted with GZ101 sample is shown in **Figure 6.21 (a & b)**. The subcutaneous implantation sites after 14 and 30 days [**Figure 6.21 (c) & (d)**] showed minor H_2 bubbles near the tissue surrounding the metal (shown by yellow arrows). The biodegradation rates of the alloy after 14 and 30 days of implantation were 0.28 (±0.07) and 0.35 (±0.04) mm/y respectively. The surface topographies of the samples after 14 and 30 days of implantation [**Figure 6.21 (f) & (g)**] showed degradation pits (black arrows) only at the edge of the samples indicating non-uniform degradation. The 14-day sample [**Figure 6.21 (f)**] exhibited moderate surface roughness with localized corrosion patches, indicating early-stage degradation. The 30-day sample [**Figure 6.21 (g)**] displayed a more pronounced degradation pattern, with increased roughness and visible corrosion zones, indicating advanced material dissolution. The progression in surface deterioration suggests a continuous biodegradation process, influenced by body fluid interactions and pH fluctuations.

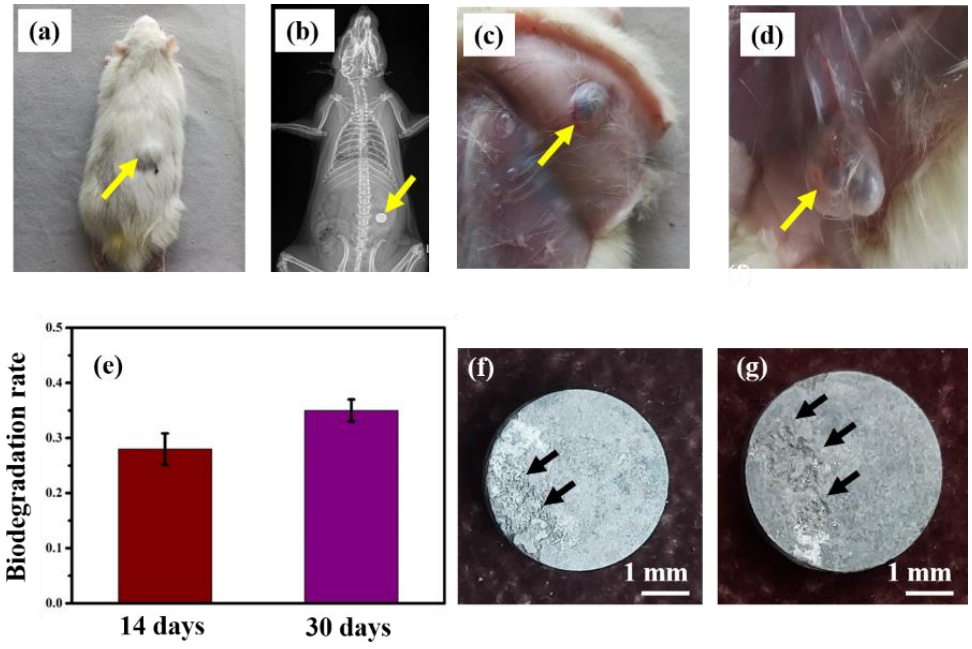

Figure 6.21. (a) Photograph of GZ101 subcutaneously implanted rat (b) X-ray image after 14 days' implantation, (c) & (d) a photographs of implants post-surgery after 14 days and 30 days respectively, (e) biodegradation rate of GZ101 alloy, (f) & (g) the photographs of implanted samples after 14 days and 30 days respectively.

The histological examination of organs evaluates the effects of biodegradable materials during their digestion and excretion in vivo. The H&E staining of various organs from the metal-implanted rats is shown in **Figure 6.22**. After 30 days of implantation, there were no significant pathological changes observed in any of the organ tissues. The section from the heart showed normal architecture with myocardial fibres, and myocytes having no significant pathology. There was no indication of architectural destruction, edema, inflammatory infiltrates, or necrosis. The section from the liver showed lobular architecture with mild interface hepatitis. Individual hepatocytes showed focal mild cytoplasmic vacuolation. The portal triad showed no significant pathology, while the central vein showed mild dilation and congestion. The section of skin showed a normal epidermis, and the subcutaneous tissue showed no considerable pathology. There was no indication of inflammation, edema, or necrosis. These results suggested that the extruded GZ101 alloy had excellent biocompatibility as well as in-vivo degradation resistance. Mg alloy usually has higher degradation rate during subcutaneous implantation than when it is implanted near a bone. Hence still much lower degradation rate is expected for GZ101 alloy when it is considered for orthopaedic scaffold applications.

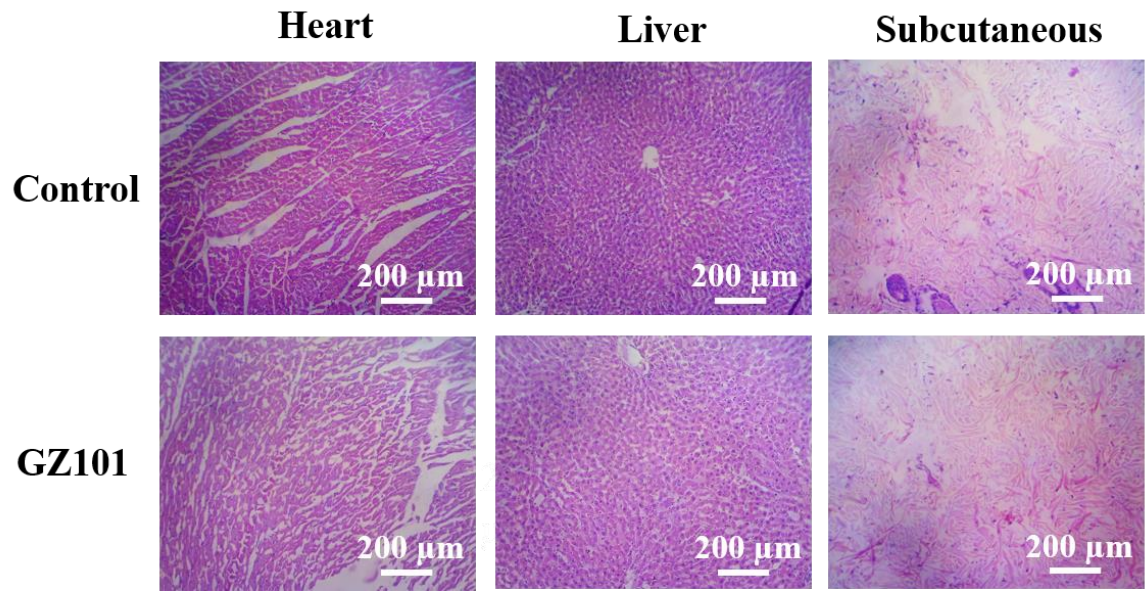

Figure 6.22. H & E staining of heart, liver and subcutaneous tissue samples after implantation of GZ101 alloy for 30 days.

6.4 Conclusion

The evaluation of extruded Mg-Zn-Gd-Zr alloys for biodegradable implant applications involved assessing their tensile properties, biodegradation behavior, and biocompatibility through in-vitro and in-vivo studies. The key findings were as follows:

1. After extrusion, all Mg-Zn-Gd-Zr alloys exhibited YS > 200 MPa and elongation > 10%, demonstrating a significant improvement in strength and ductility compared to their as-cast counterparts. The increase in tensile properties was primarily attributed to grain refinement, and the formation of a strong basal texture induced by the extrusion process.
2. Mg-10Gd-1Zn-0.5Zr alloy showed superior YS and UTS with reasonable good ductility among the studied alloys due to the combined effect of higher dislocation density, low Schmid factor, and strong basal texture.
3. Diluted extracts (25 and 50%) of all the alloys showed viability (MG63 cell line) above 75% during in-vitro analysis at all culture conditions (1 or 3 days). However, Mg-10Gd-1Zn-0.5Zr showed excellent (above 95%) viability even with 100% extracts.
4. In-vivo analysis of subcutaneously implanted Mg-10Gd-1Zn-0.5Zr alloy on rats revealed that the degradation rate was 0.35 mm/y after 30 days of implantation and exhibited good in-vivo biocompatibility.

References

[1] J.-X. Chen, X.-Y. Zhu, L.-L. Tan, K. Yang, X.-P. Su, Effects of ECAP Extrusion on the Microstructure, Mechanical Properties and Biodegradability of Mg–2Zn–xGd–0.5Zr Alloys, Acta Metall. Sin. Engl. Lett. 34 (2021) 205–216. https://doi.org/10.1007/s40195-020-01136-7.

[2] B. Du, Z. Hu, J. Wang, L. Sheng, H. Zhao, Y. Zheng, T. Xi, Effect of extrusion process on the mechanical and in vitro degradation performance of a biomedical Mg-Zn-Y-Nd alloy, Bioact. Mater. 5 (2020) 219–227. https://doi.org/10.1016/j.bioactmat.2020.02.002.

[3] X. Zhang, Z. Wang, G. Yuan, Y. Xue, Improvement of mechanical properties and corrosion resistance of biodegradable Mg–Nd–Zn–Zr alloys by double extrusion,

Mater. Sci. Eng. B 177 (2012) 1113–1119. https://doi.org/10.1016/j.mseb.2012.05.020.

[4] K. Chen, X.B. Zhang, J.W. Dai, Y. Fei, Z.Z. Wang, Enhanced mechanical and corrosion properties of NZ20K alloy by double extrusion and aging processes for biomedical applications, Mater. Technol. 31 (2016) 210–215. https://doi.org/10.1179/1753555715Y.0000000043.

[5] X. Zhang, J. Dai, Q. Dong, Z. Ba, Y. Wu, Corrosion behavior and mechanical degradation of as-extruded Mg–Gd–Zn–Zr alloys for orthopedic application, J. Biomed. Mater. Res. B Appl. Biomater. 108 (2020) 698–708. https://doi.org/10.1002/jbm.b.34424.

[6] J.P. Hadorn, K. Hantzsche, S. Yi, J. Bohlen, D. Letzig, J.A. Wollmershauser, S.R. Agnew, Role of Solute in the Texture Modification During Hot Deformation of Mg-Rare Earth Alloys, Metall. Mater. Trans. A 43 (2012) 1347–1362. https://doi.org/10.1007/s11661-011-0923-5.

[7] W. Tang, G. Zhou, Y. Shao, D. Li, Y. Peng, H. Wang, On the role of yttrium in microstructure evolution and texture modification during magnesium alloy extrusion, Mater. Charact. 162 (2020) 110189. https://doi.org/10.1016/j.matchar.2020.110189.

[8] C. Tang, J. Chen, X. Ma, W. Liu, H. Xie, M. Li, X. Liu, Effects of extrusion speed on the formation of bimodal-grained structure and mechanical properties of a Mg-Gd-based alloy, Mater. Charact. 189 (2022) 111952. https://doi.org/10.1016/j.matchar.2022.111952.

[9] Y. Jin, C. Blawert, H. Yang, B. Wiese, F. Feyerabend, J. Bohlen, D. Mei, M. Deng, M. del R. Silva Campos, N. Scharnagl, K. Strecker, J. Bode, C. Vogt, R. Willumeit, Microstructure-corrosion behaviour relationship of micro-alloyed Mg-0.5Zn alloy with the addition of Ca, Sr, Ag, In and Cu, Mater. Des. 195 (2020) 108980. https://doi.org/10.1016/j.matdes.2020.108980.

[10] S. Sanyal, S. Kanodia, R. Saha, T.K. Bandyopadhyay, S. Mandal, Influence of hard plate hot forging temperature on the microstructure, texture and mechanical properties in a lean Mg–Zn–Al alloy, J. Alloys Compd. 800 (2019) 343–354. https://doi.org/10.1016/j.jallcom.2019.06.026.

[11] S.-C. Jin, J.U. Lee, J. Go, H. Yu, S.H. Park, Effects of Sn addition on the microstructure and mechanical properties of extruded Mg–Bi binary alloy, J. Magnes. Alloys 10 (2022) 850–861. https://doi.org/10.1016/j.jma.2021.04.015.

[12] S.I. Wright, M.M. Nowell, D.P. Field, A Review of Strain Analysis Using Electron Backscatter Diffraction, Microsc. Microanal. 17 (2011) 316–329. https://doi.org/10.1017/S1431927611000055.

[13] M.-S. Chen, W.-Q. Yuan, H.-B. Li, Z.-H. Zou, New insights on the relationship between flow stress softening and dynamic recrystallization behavior of magnesium alloy AZ31B, Mater. Charact. 147 (2019) 173–183. https://doi.org/10.1016/j.matchar.2018.10.031.

[14] D. Liu, Z. Liu, E. Wang, Effect of rolling reduction on microstructure, texture, mechanical properties and mechanical anisotropy of AZ31 magnesium alloys, Mater. Sci. Eng. A 612 (2014) 208–213. https://doi.org/10.1016/j.msea.2014.06.034.

[15] J. Bohlen, S. Yi, D. Letzig, K.U. Kainer, Effect of rare earth elements on the microstructure and texture development in magnesium–manganese alloys during extrusion, Mater. Sci. Eng. A 527 (2010) 7092–7098. https://doi.org/10.1016/j.msea.2010.07.081.

[16] U.M. Chaudry, K. Hamad, J.-G. Kim, On the ductility of magnesium based materials: A mini review, J. Alloys Compd. 792 (2019) 652–664. https://doi.org/10.1016/j.jallcom.2019.04.031.

[17] The texture and its optimization in magnesium alloy, J. Mater. Sci. Technol. 42 (2020) 175–189. https://doi.org/10.1016/j.jmst.2019.10.010.

[18] L.W.F. Mackenzie, B. Davis, F.J. Humphreys, G.W. Lorimer, The deformation, recrystallisation and texture of three magnesium alloy extrusions, Mater. Sci. Technol. 23 (2007) 1173–1180. https://doi.org/10.1179/174328407X226509.

[19] G. Wu, J. Yu, L. Jia, W. Xu, B. Dong, Z. Zhang, B. Hao, Microstructure and Texture Evolution of Mg-Gd-Y-Zr Alloy during Reciprocating Upsetting-Extrusion, Materials 13 (2020) 4932. https://doi.org/10.3390/ma13214932.

[20] J. Zhao, B. Jiang, J. Xu, W. He, G. Huang, F. Pan, The influence of Gd on the recrystallisation, texture and mechanical properties of Mg alloy, Mater. Sci. Eng. A 839 (2022) 142867. https://doi.org/10.1016/j.msea.2022.142867.

[21] H. Yu, Y. Hongge, C. Jihua, S. Bin, Z. Yi, S. Yanjin, M. Zhaojie, Effects of minor Gd addition on microstructures and mechanical properties of the high strain-rate rolled Mg–Zn–Zr alloys, J. Alloys Compd. 586 (2014) 757–765. https://doi.org/10.1016/j.jallcom.2013.10.005.

[22] A.K. S, R.K. R, J. Jayaraj, K.G. Raghu, A. Srinivasan, Corrosion Behavior of Mg-Zn-RE Alloys (RE = Gd, Y, Nd), J. Mater. Eng. Perform. 32 (2023) 2840–2852. https://doi.org/10.1007/s11665-022-07213-5.

[23] Electrochemical noise analysis on the pit corrosion susceptibility of biodegradable AZ31 magnesium alloy in four types of simulated body solutions, J. Mater. Sci. Technol. 34 (2018) 1876–1884. https://doi.org/10.1016/j.jmst.2018.01.015.

[24] A. Bahmani, M. Lotfpour, M. Taghizadeh, W.-J. Kim, Corrosion behavior of severely plastically deformed Mg and Mg alloys, J. Magnes. Alloys 10 (2022) 2607–2648. https://doi.org/10.1016/j.jma.2022.09.007.

[25] N. Birbilis, M.A. Easton, A.D. Sudholz, S.M. Zhu, M.A. Gibson, On the corrosion of binary magnesium-rare earth alloys, Corros. Sci. 51 (2009) 683–689. https://doi.org/10.1016/j.corsci.2008.12.012.

[26] A. Bahmani, S. Arthanari, K.S. Shin, Formulation of corrosion rate of magnesium alloys using microstructural parameters, J. Magnes. Alloys 8 (2020) 134–149. https://doi.org/10.1016/j.jma.2019.12.001.

[27] R. Xin, Y. Luo, A. Zuo, J. Gao, Q. Liu, Texture effect on corrosion behavior of AZ31 Mg alloy in simulated physiological environment, Mater. Lett. 72 (2012) 1–4. https://doi.org/10.1016/j.matlet.2011.11.032.

[28] Y. Liu, J. Wen, H. Li, J. He, Effects of extrusion parameters on the microstructure, corrosion resistance, and mechanical properties of biodegradable Mg–Zn–Gd–Y–Zr alloy, J. Alloys Compd. 891 (2022) 161964. https://doi.org/10.1016/j.jallcom.2021.161964.

[29] X. Liu, G. Chen, X. Zhong, T. Wang, X. He, W. Yuan, P. Zhang, Y. Liu, D. Cao, S. Chen, K. Manabe, Z. Jiang, T. Furushima, D. Kent, Y. Chen, G. Ni, M. Gao, H. Li, Degradation of differently processed Mg-based implants leads to distinct foreign body reactions (FBRs) through dissimilar signaling pathways, J. Magnes. Alloys (2022). https://doi.org/10.1016/j.jma.2022.03.017.

[30] G.-L. Song, R. Mishra, Z. Xu, Crystallographic orientation and electrochemical activity of AZ31 Mg alloy, Electrochem. Commun. 12 (2010) 1009–1012. https://doi.org/10.1016/j.elecom.2010.05.011.

[31] R. Hou, J. Victoria-Hernandez, P. Jiang, R. Willumeit-Römer, B. Luthringer-Feyerabend, S. Yi, D. Letzig, F. Feyerabend, In vitro evaluation of the ZX11 magnesium alloy as potential bone plate: Degradability and mechanical integrity, Acta Biomater. 97 (2019) 608–622. https://doi.org/10.1016/j.actbio.2019.07.053.

[32] L.M. Gabriel, E.F. Sanchez, S.G. Silva, R.G. Santos, Tumor cytotoxicity of leucurolysin-B, a P-III snake venom metalloproteinase from Bothrops leucurus, J. Venom. Anim. Toxins Trop. Dis. 18 (2012) 24–33. https://doi.org/10.1590/S1678-91992012000100004.

[33] K. Ho, L.S. Yazan, N. Ismail, M. Ismail, Apoptosis and cell cycle arrest of human colorectal cancer cell line HT-29 induced by vanillin, Cancer Epidemiol. 33 (2009) 155–160. https://doi.org/10.1016/j.canep.2009.06.003.

Chapter 7

Summary and Future Perspectives

7.1 Summary

The thesis presents a systematic investigation into the microstructural, mechanical, and biological performance of Mg-Zn-RE alloys, with a focus on their potential as biodegradable orthopaedic implant materials. The present research work aimed to develop and optimize Mg-Zn-RE alloys by varying rare-earth (RE) content, Zn/RE ratios, and incorporating secondary processing (extrusion) to achieve the desired combination of high strength, controlled biodegradation rate, and biocompatibility. The work systematically examined the effects of Nd and Gd additions, grain refinement through Zr, Zn/Gd ratio optimization, and extrusion processing on the microstructure, mechanical integrity, corrosion resistance, and biocompatibility of alloys. The findings contribute significantly to the development of next-generation biodegradable Mg-based alloys for biomedical applications. The present chapter will provide an overview of the various findings of the research works reported in Chapters 4-6.

Chapter 4 explored the role of RE and Grain refiner in Mg-4Zn-1RE alloys. The first stage of the study focused on understanding the individual effects of rare-earth elements (Nd and Gd) on the corrosion behaviour of Mg-Zn-RE alloys in 1wt.% NaCl. Although assessing the biodegradation resistance of metallic alloys in simulated body fluids is crucial for biomedical applications, researchers often use 1 wt.% NaCl solution for preliminary corrosion screening due to its simplicity and reproducibility. Therefore, in the present study, 1 wt.% NaCl solution was initially utilized to gain a fundamental understanding of the corrosion behavior of Mg-Zn-RE alloys before conducting more physiologically relevant tests. The study revealed that Nd addition resulted in significant grain refinement (grain size of Mg-4Zn-1Nd : 203 μm) compared to Gd addition (grain size of Mg-4Zn-1Gd : 524 μm) in Mg-Zn-RE alloys. The corrosion results indicated that Mg-4Zn-1Nd alloy exhibited superior corrosion resistance across electrochemical, hydrogen evolution, and weight loss measurements. The enhanced corrosion performance was attributed to the network-like distribution of secondary phases,

which effectively acted as a barrier against corrosion progression, as well as the rapid formation of a protective Nd_2O_3 incorporated corrosion film. Additionally, the fine-grained microstructure of Mg-4Zn-1Nd facilitated the development of a compact and uniform surface film, further improving its resistance to the aggressive chloride-containing environment. The addition of Zr significantly altered the behavior of Mg-Zn-RE alloys, particularly Mg-4Zn-1Gd, by inducing a substantial grain size reduction [from 524 (±171) to 144 (±50) μm], whereas Mg-4Zn-1Nd exhibited only a marginal refinement (from 203 to 166 μm). The grain refinement in Mg-4Zn-1Gd-0.5Zr led to a significant reduction in its corrosion rate compared to its Zr-free counterpart, bringing it closer to the corrosion resistance of Mg-4Zn-1Nd. Additionally, both Mg-4Zn-1Gd and Mg-4Zn-1Nd alloys exhibited enhanced mechanical properties after Zr addition due to grain refinement, with Mg-4Zn-1Gd-0.5Zr demonstrating superior tensile strength**.**

Following the promising results of Mg-Zn-Gd-Zr alloys, **Chapter 5** focused on the influence of Zn/Gd ratio on phase formation, mechanical performance, and biodegradation properties. The study revealed that varying the Zn/Gd ratio led to the formation of different secondary phases, significantly influencing alloy properties. The Mg-2Gd-2Zn-0.5Zr (Zn/Gd = 1) alloy contained W phase ($Mg_3Zn_3Gd_2$), Mg-2Gd-6Zn-0.5Zr (Zn/Gd = 3) contained both W phase and I phase (Mg_3Zn_6Gd) and Mg-10Gd-1Zn-0.5Zr (Zn/Gd = 0.1) exhibited LPSO (Long-Period Stacking Ordered) structures and $(Mg,Zn)_3Gd$ phase. The LPSO phase in Mg-10Gd-1Zn-0.5Zr resulted in exceptional yield strength, making it ideal for load-bearing orthopedic applications. However, the alloy exhibited reduced ductility, suggesting that further optimization is needed for applications requiring higher elongation. In vitro biodegradation studies confirmed that Mg-10Gd-1Zn-0.5Zr had the lowest degradation rate, attributed to the formation of a protective Gd_2O_3 layer, which significantly enhanced corrosion resistance. Biocompatibility analysis (MTT assay and MG63 cell line) showed that all alloys exhibited cell viability above 75%, with Mg-10Gd-1Zn-0.5Zr demonstrating the highest viability (>95%) even in 100% extract concentration, further confirming its potential as a biocompatible implant material.

Despite the promising properties observed in the as-cast Mg-Zn-Gd-Zr alloys, they did not fully meet the mechanical property requirements for biodegradable implants, particularly in yield strength (>200 MPa), elongation (>10%), and biodegradation rate (<0.5 mm/y). Therefore, **Chapter 6** focused on the effect of extrusion as a secondary processing method to

enhance alloy performance. The extruded (extrusion ratio: 12:1) Mg-Zn-Gd-Zr alloys demonstrated significant improvements in tensile strength and ductility, with all compositions achieving YS > 200 MPa and % elongation > 10, making them suitable for orthopedic applications. Among the studied alloys, Mg-10Gd-1Zn-0.5Zr exhibited optimum tensile properties [YS: 260 (±9.29) MPa, UTS: 328 (±15.8) MPa and %Elongation: 12.76 (±2.36)], due to higher dislocation density, lower Schmid factor, and strong basal texture development during extrusion. Biodegradation and biocompatibility studies further reinforced the suitability of the alloy, as Mg-10Gd-1Zn-0.5Zr exhibited over 95% cell viability in 100% extract. Additionally, the alloy maintained mechanical integrity even after immersion in cell culture medium for 14 days, as it showed only a moderate reduction in UTS (16.17%), YS (7.41%), and elongation (45%). Given its outstanding performance, Mg-10Gd-1Zn-0.5Zr was selected for in vivo testing, where subcutaneous implantation in rats confirmed a degradation rate of 0.35 (±0.04) mm/y after 30 days, aligning with clinical requirements (<0.5 mm/y). Histological analysis of vital organs further revealed no adverse effects**,** indicating that the degradation products were biocompatible**.**

Overall Conclusions

The present study established that Mg-Zn-Gd-Zr alloys have a strong potential as biodegradable orthopedic implants, provided they undergo careful alloy design and secondary processing. The key findings of the research work are:

1. Zr addition significantly improves grain refinement, enhancing corrosion resistance and tensile properties.
2. The Zn/Gd ratio plays a crucial role in tailoring the microstructure that allowing fine-tuning of tensile and degradation properties.
3. Extrusion processing effectively enhances mechanical integrity and biodegradation behavior, making Mg-Zn-Gd-Zr alloys more viable for biomedical applications.
4. Among all compositions, Mg-10Gd-1Zn-0.5Zr demonstrated the best overall performance, with superior strength, high cytocompatibility, and controlled biodegradation in vivo, making it a strong candidate for next-generation biodegradable orthopedic implants.

These findings provide a solid foundation for further development of Mg-based biomaterials, potential alternative to WE43. Future research should focus on long-term in vivo studies and clinical validation to fully establish Mg-Zn-Gd-Zr alloys as viable implant materials.

7.2 Future Perspectives

Although Mg-10Gd-1Zn-0.5Zr showed strong potential as a biodegradable implant, further validation is required through longer-term in vivo studies in different animal models. Further improvement in strength properties and degradation resistance ensure the suitability of the alloy for the said applications. Improvements in alloy purity, further microstructural optimization through extrusion and surface treatment, mainly biocompatible coatings could further enhance performance of the alloy. Thus some of the key aspects that can be focused on the future work are:

- Alloy purity: Impurities play a vital role in deciding the corrosion or degradation behavior of Mg alloys. Threshold of impurity elements in commercial Mg alloys: Fe < 50 ppm, Ni < 50 ppm and Cu < 300 ppm. However, even the Mg-10Gd-1Zn-0.5Zr alloy which showed better degradation resistance had 180 ppm of Fe, 51 ppm Cu and 44 ppm of Ni. Thus strategies such as using high pure elements, or by using Ni free stainless crucibles (to reduce Fe and Ni contamination from crucible) and by adding Mn (to reduce Fe contamination), the degradation resistance can be enhanced even further.
- Optimization of extrusion process: All the alloys were extruded under identical conditions however, not with the optimum conditions as none of the studied alloys achieved complete recrystallization after extrusion. Optimizing the extrusion parameters, such as extrusion ratio and extrusion temperature, to achieve a fully recrystallized microstructure can ensure uniform and better tensile and degradation properties.
- Biocompatible coating: Biocompatible coatings play a crucial role in delaying the initial degradation and enhancing biocompatibility of Mg-RE alloys for biodegradable implants. coatings such as calcium phosphate (CaP), hydroxyapatite (HA), biodegradable polymers (e.g., PLGA, PLLA, chitosan) etc., can act as protective barriers, reducing early corrosion and controlling ion release.
- Detailed in-vivo studies: Extended in vivo studies need to be conducted, at least for 3–6 months in rat or rabbit models to understand long-term implant behaviour. Similarly,

implantation in different locations (subcutaneous, femoral bone etc.,) and under different conditions (fracture and non-fracture model, etc.) are also provide more insights about the alloy behaviours.

ABSTRACT OF THE THESIS

Name of the Student: **Arunkumar S** Registration No.: **20EE20J39023**

Faculty of Study: **Engineering Sciences** Year of Submission: **2025**

AcSIR academic centre/CSIR Lab: **CSIR-NIIST, Trivandrum Kerala**

Name of Supervisors: **Dr. A. Srinivasan (Supervisor)** & **Dr. K.G Raghu (Co-Supervisor)**

Title of the thesis: **Evaluation of Microstructure, Mechanical and Biological properties of Mg-Zn-RE alloys for Biocompatible and Biodegradable Implant Applications**

Magnesium (Mg) and its alloys have emerged as promising biodegradable materials for orthopaedic implants due to their ability to mitigate stress shielding effect and naturally degrade in the human body. However, their clinical application is hindered by challenges such as rapid degradation and lower tensile strength. This research presents a systematic investigation into the microstructural, mechanical, and biological properties of Mg-Zn-RE (rare-earth) alloys, with a focus on optimizing alloy composition and processing routes to enhance their performance as biodegradable implants. The study explored the effects of rare-earth elements (Gd and Nd), grain refinement through zirconium (Zr), and Zn/RE ratio variations on the microstructure, corrosion resistance, and mechanical properties of Mg-Zn-RE alloys. Initial corrosion studies in 1 wt.% NaCl revealed that Mg-4Zn-1Nd exhibited superior corrosion resistance due to grain refinement and the formation of a protective Nd_2O_3 layer. Although the Mg-4Zn-1Gd alloy had lower corrosion resistance, the introduction of Zr significantly refined the grain structure, improving its tensile properties and corrosion resistance. Further investigations into Zn/Gd ratio variations led to the development of Mg-10Gd-1Zn-0.5Zr, which exhibited the best combination of tensile strength and degradation resistance. The presence of long-period stacking order (LPSO) phases contributed to superior yield strength, while the formation of a protective Gd_2O_3 layer reduced degradation rates, making it a strong candidate for load-bearing orthopaedic applications. However, as-cast alloys did not meet the required tensile properties for biomedical use, necessitating secondary processing. To address this, extrusion processing was employed, resulting in a significant enhancement in mechanical properties and biodegradation behaviour. The extruded Mg-Zn-Gd-Zr alloys demonstrated yield strength (YS) > 200 MPa and elongation > 10%, with Mg-10Gd-1Zn-0.5Zr exhibiting the highest mechanical performance (YS: 260 MPa, UTS: 328 MPa, %Elongation: 12.76). Biocompatibility assessments using MG63 cell lines confirmed excellent cytocompatibility, with Mg-10Gd-1Zn-0.5Zr achieving >95% cell viability in 100% extract concentration. Given its superior properties, Mg-10Gd-1Zn-0.5Zr was selected for in vivo testing via subcutaneous implantation in *Sprague Dawley* rats for one month. The alloy exhibited a degradation rate of 0.35 mm/year, well within clinically acceptable limits (<0.5 mm/year), with no observed toxicity to surrounding tissues. Histological analysis confirmed excellent biocompatibility, further validating its potential as a biodegradable implant material.

List of Publications

List of Publication Emanating from the thesis work

1. **Arun Kumar S**, Rajesh K. R, Jithu Jayaraj, K.G. Raghu, and A. Srinivasan, "Corrosion Behavior of Mg-Zn-RE Alloys (RE=Gd, Y, Nd)", Journal of Materials Engineering and Performance (2022), Volume 3, pages 2840-2852, https://doi.org/10.1007/s11665-022-07213-5.
2. **Arun Kumar S**, Jithu Jayaraj, V Rajinikanth, Manoj Gupta, A Srinivasan, K G Raghu, Gd added Mg alloy for biodegradable implant applications, Journal of Biomedical Materials Research – Part B 112 (2024), e35474, https://doi.org/10.1002/jbm.b.35474.
3. **Arun Kumar S**, Jithu Jayaraj, A Srinivasan, K G Raghu, "Mg-Rare earth based alloys for biodegradable implant applications: A review on the current status and future perspectives", (Manuscript under preparation).
4. **Arun Kumar S**, Jithu Jayaraj, A Srinivasan, K G Raghu, "The influence of different biological fluids on the degradation behaviour of Mg-Zn-Gd/Y alloys", (Manuscript under preparation).

List of Publications not related to thesis work

1. Jithu Jayaraj, **Arun Kumar S**, A. Srinivasan, K. G. Raghu, C. Arunchandran, Rajinikanth V, "Corrosion and In vitro Characteristics of Cerium-Based Chemical Conversion Coating on AZ31 Magnesium Alloy" Applied Surface Science 644 (2024) 158797, https://doi.org/10.1016/j.apsusc.2023.158797.

List of conference presentations

1. **Arun Kumar S**, Jithu Jayaraj, and A. Srinivasan, K.G. Raghu, Magnesium alloys for Bio-implant applications, MRSI – 2022, IIST, Trivandrum
2. **Arun Kumar S**, Jithu Jayaraj, and A. Srinivasan, K.G. Raghu, "Effect of Zn/Gd ratio and Extrusion on the microstructure, mechanical and biological characteristics of Mg-Zn-Gd alloys", AMMT – 2023, NIIST, Trivandrum.

Contributions to Academic Conferences

Magnesium alloys for Bio-implant applications

Arun Kumar S[1,2], Jithu Jayaraj[1,2], K G Raghu[1,2], A Srinivasan[1,2*]
[1]CSIR-National Institute for Interdisciplinary Science and Technology, Thiruvananthapuram-695019, India
[2]Academy of Scientific and Innovative Research (AcSIR), Ghaziabad-201002, India
asrinivasan@niist.res.in

Abstract

Magnesium alloys have emerged as promising candidates for biodegradable bio-implant applications due to their inherent biocompatibility, favorable mechanical properties, and natural ability to degrade in vivo. In this presentation, we focus on the development and characterization of Mg-RE (rare earth) based alloys tailored for orthopedic implant applications. Our research explores the influence of rare earth additions on the microstructure, corrosion behavior, and mechanical performance of these alloys, aiming to achieve an optimal balance between strength, controlled biodegradation, and biocompatibility.

Key investigations include the evaluation of processing routes ranging from conventional casting to advanced extrusion techniques to refine grain structures and enhance corrosion resistance. Electrochemical assessments, hydrogen evolution tests, and in vitro cytocompatibility assays collectively indicate that select Mg-RE compositions exhibit a controlled degradation rate, superior tensile properties, and excellent cell viability under simulated physiological conditions. These findings underscore the potential of Mg-RE based alloys as next-generation biodegradable implants, offering a viable alternative to conventional permanent metallic implants while mitigating the risks associated with stress shielding and premature failure. The presentation will address both the current challenges and future prospects in the application of magnesium alloys for bio-implant applications, providing insights into their clinical translation.

Influence of Zn/Gd ratio on the mechanical and biological characteristics of Mg-Zn-Gd-Zr alloys

Arun Kumar S[1,2], Jithu Jayaraj[1,2], K G Raghu[1,2], A Srinivasan[1,2*]
[1]CSIR-National Institute for Interdisciplinary Science and Technology, Thiruvananthapuram-695019, India
[2]Academy of Scientific and Innovative Research (AcSIR), Ghaziabad-201002, India
asrinivasan@niist.res.in

Abstract

Being a biocompatible metal with similar mechanical properties as bones, magnesium bears both biodegradability suitable for bone substitution and chemical reactivity detrimental in bio-ambiences. Hence, extensive research is focused on the development of Mg based alloys with superior mechanical and degradation performance. Among the different alloy systems being pursued, combination of rare earth and zinc with magnesium shows promising properties as a potential bio degradable implant. To benefit biomaterial applications of Mg, different alloys with varying Zn/Gd ratios ranging from 0.1 to 3 were extruded at an extrusion ratio of 12.25:1 and a die temperature of 350^0C. As the Zn/Gd ratio of alloys varies the major secondary phases changes from W ($Mg_3Zn_3Gd_2$), X ($Mg_{12}GdZn$) and I (Mg_3Zn_6Gd) which influences the mechanical as well as biological characteristics of the alloys. X phase containing Mg-10Gd-1Zn-0.5Zr alloy showed highest yield strength and ultimate tensile strength of 270 and 330 MPa respectively and its elongation is 12%. The biodegradation rate was the lowest for Mg-10Gd-1Zn-0.5Zr as well as it showed the highest viability and cell proliferation. The optimum combination of mechanical strength as well as biological characteristics of Mg-10Gd-1Zn-0.5Zr alloy is really promising and needs further validation using in vivo analysis.

SCI PUBLICATION

JMEPEG
https://doi.org/10.1007/s11665-022-07213-5

©ASM International
1059-9495/$19.00

TECHNICAL ARTICLE

Corrosion Behavior of Mg-Zn-RE Alloys (RE=Gd, Y, Nd)

Arun Kumar S, Rajesh K. R, Jithu Jayaraj, K.G. Raghu, and A. Srinivasan

Submitted: 6 January 2022 / Revised: 19 May 2022 / Accepted: 31 July 2022

The effect of different rare earth elements (Gd, Y, Nd) with similar atomic percentage on the corrosion behavior of Mg-1.52Zn (at.%) was investigated. The secondary phases and corrosion film formed on the surface of the alloys during immersion in aqueous NaCl solution affects the corrosion behavior of the alloy. The electrochemical, weight loss and hydrogen evolution tests revealed that corrosion rate of Mg-1.52Zn-0.15Gd was the highest and the corrosion rate of other three alloys were almost similar. The discrete second phases in Mg-1.52Zn-0.15Gd acted as severe cathodes to the matrix and accelerated the micro-galvanic corrosion whereas network shaped and uniformly distributed phases in Mg-1.52Zn-0.15Nd alloy effectively retarded corrosion. The immediate formation of Nd_2O_3 in the corrosion film of Mg-1.52Zn-0.15Nd alloy also contributed in improved corrosion resistance. Dominant presence of Y_2O_3 in Mg-1.52Zn-0.16Yalloy contributed to its better corrosion resistance.

Keywords B. magnesium, C. rare earths, corrosion

1. Introduction

The high strength to weight ratio, low density, high specific strength, specific stiffness and appreciable biocompatibility of magnesium and its alloys makes them suitable for applications in aerospace, automobile and biomedical industries (Ref 1, 2). Further wide spread use of Mg alloys is possible by improving the corrosion resistance (Ref 3, 4). Researchers are constantly working to enhance the corrosion resistance of Mg alloys by analyzing the role of different alloying elements in corrosion behavior (Ref 5, 6). Among the alloying elements, rare earth (RE) improve the corrosion resistance of Mg based alloys significantly (Ref 7–9). The enhancement of corrosion resistance of Mg-RE based alloys is attributed to (1) the presence of RE elements in the surface film which enhances the protective nature of the surface film thereby reducing the dissolution of the alloy (2) scavenger effect, i.e., RE elements form intermetallic phases with the common impurity elements found in Mg alloys such as Fe, Cu and Ni and thus the micro-galvanic corrosion associated with these impurities is reduced (Ref 9, 10). In addition, the Mg-RE based alloys invites special attention as they find application in biomedical industries due to their optimum combination of mechanical strength and biodegradation.

This invited article is part of a special topical focus in the *Journal of Materials Engineering and Performance* on Magnesium. The issue was organized by Prof. C. (Ravi) Ravindran, Dr. Raja Roy, Mr. Payam Emadi, and Mr. Bernoulli Andilab, Ryerson University.

Arun Kumar S, Rajesh K. R, Jithu Jayaraj, K.G. Raghu, and **A. Srinivasan**, CSIR-National Institute for Interdisciplinary Science and Technology, Thiruvananthapuram 695019, India; and Academy of Scientific and Innovative Research (AcSIR), Ghaziabad 201002, India. Contact e-mail: asrinivasan@niist.res.in.

The effect of different REs on the corrosion behavior of Mg-RE binary alloys were investigated earlier (Ref 11, 12). Birbilis et al. (Ref 11) reported that Mg-Ce alloy exhibited highest corrosion rate compared with Mg-Nd or Mg-La alloys, and also found that an increase in the volume fraction of secondary phases in all these alloys resulted in an increase in corrosion rate. Moreover, the micro capillary electrochemical test revealed that $Mg_{12}Ce$ was the most inert and $Mg_{12}La$ was the least inert, thus Mg-Ce alloys suffered severe micro-galvanic corrosion due to the presence of secondary phases (Ref 11). In contrast, Azzedine et al. (Ref 12) reported that Mg-Ce binary alloy showed better corrosion resistance than that of Mg-La and Mg-Nd. With different RE elements studied, they found that corrosion rate of alloys increased in the following order: Mg-0.41Dy<Mg- 0.3Ce<Mg-0.63Gd<Mg- 1.44Nd<Mg-1.43La (wt.%). The presence of complete protective oxide film formed in Mg- 0.41Dy, and partially protective oxide film formed on Mg- 0.3Ce, Mg- 1.44Nd and Mg-0.63Gd were reported to contribute in corrosion resistance of these alloys. Although the corrosion mechanism of Mg- 0.3Ce, Mg- 1.44Nd and Mg-0.63Gd were similar, the small grain size (70 μm) observed in Mg-0.3Ce alloy enhanced the corrosion resistance whereas the presence of diverse secondary phases ($Mg_{12}Nd$, $Mg_{41}Nd_5$ and $Mg_{24}Nd$) in Mg- 1.44Nd resulted in its poor corrosion resistance compared to Mg- 0.3Ce and Mg-0.63Gd. The poor corrosion resistance of Mg-1.43La alloy was attributed to the presence of $Mg_{12}La$ secondary phase along the grain boundaries. It should be noted that the weight percent of RE elements were not uniform in these alloys and the effect of volume fraction of secondary phases on the corrosion behavior was not discussed.

Recently, combination of RE and Zn in Mg alloys draw a special attention due to the enhanced mechanical properties as well as corrosion resistance (Ref 13, 14). Moreover, ZE41 (Mg-4Zn-1RE, wt.%) alloy already find potential applications ranging from aerospace to biomedical industries (Ref 15, 16). In early stage of development, La based misch metal (MM) were added to Mg-Zn to prepare ZE alloys. Later MM was

Published online: 15 August 2022

replaced by Nd for the better mechanical properties. As observed in Mg-RE binary alloys, corrosion rate of Mg-Zn-RE alloys is influenced by RE elements as different elements introduce different secondary phases with different electrochemical behaviors. However, a study devoted to establish the influence of different REs on the corrosion behavior of Mg-Zn-RE alloys is not reported elsewhere. Given this background, four different Mg-Zn-RE alloys (RE=Gd, Y and Nd) were prepared (having same at.% of RE and Zn, to replicate ZE41 alloys) and the effects of these REs on the microstructure and corrosion behavior of Mg-Zn-RE alloys were investigated.

2. Materials and Methods

2.1 Materials Preparation

The magnesium alloys with compositions of Mg-1.52Zn-0.15Gd, Mg-1.52Zn-0.16Y and Mg-1.52Zn-0.15Nd (at.%, hereinafter referred to as GZ, YZ and NZ, respectively) were prepared in a steel crucible protected by a gas mixture of Ar +0.02% SF_6. The alloys were prepared using Pure Mg, Zn, Y, Gd and Mg-30Nd master alloy. The required amount of Mg ingots was melted and at 740 °C RE and Zn was added. The chemical composition the alloys analyzed using ICP-AES is shown in Table 1. After the complete addition of different elements, the melt was stirred manually for 2 min. to achieve a homogeneous composition as well as to ensure the complete dissolution of these elements. The superheated melt was then poured into a preheated (300 °C) steel mold to obtain a casting block of size 200 mm × 120 mm × 25 mm.

2.2 Microstructure Characterization

The microstructure of the alloys was observed using Leica DMRX optical microscope and the grain size and volume fraction of the secondary phases were measured using imageJ software (free software). The grain size measurement was done using linear intercept method. The microstructure and corrosion morphology of the alloys were observed using a scanning electron microscope (SEM, Zeiss EVO 18 cryo-SEM) equipped with energy dispersive X-ray spectroscopy (EDS). The specimens prior to microstructural observations were ground with different grades of SiC abrasive papers followed by cloth polishing with 1 µm alumina suspension. Subsequently, the specimens were etched in a solution of 6 g picric acid, 5 mL glacial acetic acid, 10 mL distilled water and 100 mL ethanol for 5 s.

2.3 Corrosion Studies

2.3.1 Electrochemical Measurements. The electrochemical tests were performed using AMETEK VersaStat 4, with reference electrode of saturated calomel electrode (SCE), counter electrode of platinum mesh, and the working electrode as sample. The tests were performed under ambient conditions (room temperature 25±1 °C) and in electrolyte of 1 wt.% NaCl. A sample surface area of 1 cm^2 was exposed to 200 mL electrolyte solution throughout the testing period. The samples were immersed in the electrolyte for 30–40 min. prior to open circuit potential (OCP) measurements. The samples were scanned at a rate of 1 mV/s from−250 to+350 mV with respect to their OCP values. The corrosion potential (E_{corr} vs. SCE) and corrosion current density (i_{corr}) were obtained from the Tafel plot. The impedance of the alloys was measured at their OCP with a peak-to-peak amplitude of 10 mV in the frequency range from 10^4 to 10^{-1} Hz. The impedance values of all the alloys were fitted using equivalent circuit and the corresponding circuit element values were obtained from ZSimpWin 3.21 software. The electrochemical tests were performed three times for repeatability. Electrochemical experiments were done according to ASTM G3-89 (Ref 17).

2.3.2 Weight Loss Measurement. Weight loss measurement was performed on samples having dimension of 15 mm × 15 mm × 3 mm maintaining solution volume to surface area as 50 mL/cm^2. Each cleaned and weighed samples were immersed separately in 1 wt.% NaCl solution for a period of 1, 3, 7 and 14 days at room temperature (25±1 °C). Distilled water followed by ethanol was used to clean the samples after weight loss measurement. The corrosion products were removed using chromic acid (180 g/l) at room temperature for 10 min according to ASM handbook on Magnesium and Magnesium alloys (Ref 18). The following formula was used for calculating the corrosion rate of samples in millimeter per year (mm/y):

$$\text{Corrosion rate} = \frac{8.76\text{X}10^4\text{X}\Delta}{\rho\text{X}A\text{X}t} \quad \text{(Eq 1)}$$

where Δ is weight loss in g, A is total surface area in cm^2, ρ is density of the alloy in g/cm^3, t is immersion time in h. The weight loss measurements were done in accordance with ASTM G31-72 (Ref 19).

2.3.3 Hydrogen Evolution Test. Reduction in hydrogen ions is the main cathodic reaction during the corrosion of magnesium alloys. Hence, volume of hydrogen evolved during corrosion can be related to the corrosion rate of magnesium alloys. Hydrogen evolution tests were done using samples having dimension of 15 mm × 15 mm × 3 mm. Similar to weight loss measurement test, solution volume to surface area of 50 mL/cm^2 was maintained. The hydrogen evolution tests were carried out for 14 days and the evolved hydrogen was collected using a setup similar to eudiometer (Ref 20).

2.4 Corrosion Surface and Corrosion Product Analysis

2.4.1 X-ray Photoelectron Spectroscopy (XPS). The composition of the oxide layers formed on the surface of the alloys immersed in 1 wt.% NaCl solution for 30 min. were

Table 1 Chemical composition of the developed alloys (at.%)

	Analyzed chemical composition (at.%)					
Nominal composition	**RE**	**Zn**	**Fe**	**Cu**	**Ni**	**Mg**
Mg-1.52Zn-0.15Gd (GZ)	0.146	1.42	0.0068	0.0036	0.0012	Bal
Mg-1.52Zn-0.16Y (YZ)	0.157	1.45	0.0072	0.0046	0.0020	Bal
Mg-1.52Zn-0.15Nd (NZ)	0.148	1.44	0.0087	0.0041	0.0033	Bal

studied using XPS (PHI 5000 VersaProbe II, ULVAC-PHI Inc., USA) equipped with micro-focused (200 µm, 15 KV) monochromatic Al-Kα X-Ray source (hν = 1486.6 eV). XPS data were analyzed using multipak software in the instrument.

2.4.2 2.4.2. X-ray Diffraction (XRD). XRD studies were carried out on the corrosion product collected from the samples immersed in 1 wt.% NaCl for 14 days. Cu-Kα radiation (wavelength λ=0.15406 nm, voltage=40 kV and current=40 mA) was used to carry out the analysis with a scanning range of 10–90° (step interval=0.033°, scan rate=0.05/s). XRD data analysis was done using X'Pert highscore Plus 2.1 software.

3. Results

3.1 Microstructure

The grain size of the alloys was different owing to the different RE elements (Fig. 1). Lowest grain size was seen in Nd containing alloy whereas highest grain size in Y containing alloy. The average grain size of the alloys GZ, YZ and NZ were 260 (±43.96), 522 (±17.24) and 164 (±11.06) µm, respectively. The measured volume fraction of secondary phases in GZ, YZ and NZ were 12, 10 and 15%, respectively. Although a significant change in volume fraction of secondary phases was not observed, the alloy with slightly higher volume fraction of secondary phases (NZ) exhibited relatively finer grain size.

Figure 2 shows the SEM micrographs of the developed alloys and Table 2 shows EDS analysis of various phases observed in these alloys. The GZ and YZ alloys had bulk secondary particles distributed along the grain boundaries [Fig. 2(a and b)] whereas NZ alloy had network of secondary phases distributed more evenly throughout the grain/dendritic boundaries [Fig. 2(c)]. GZ alloy consisted of secondary phases with different morphologies as seen in Fig. 2(a). Elongated phases and large spherical particles [shown as A & B in Fig. 2 (d)] had stoichiometric composition of Zn/Gd ratio equal to 3.21 and 4.17, respectively, which are close to the ideal ratio 2 reported for W ($Mg_3Zn_3Gd_2$) phase (Ref 20). The cuboid phase, marked as C in Fig. 2(d), was identified as Mg_5Gd. EDS analysis of small spherical particles, [marked as D in Fig. 2(d)], revealed that these were Mg-Zn binary phases. EDS analysis of bulk phases in YZ alloy [marked as A and B in Fig. 2(e)] suggested that the Zn/Gd ratio was 5.28 and 4.97, respectively, which is close to the ideal Zn/Gd ratio of 6 for I phase (Mg_3Zn_6Y) (Ref 21). Small spherical particles marked as C and D in Fig. 2(e) were Mg-Zn binary phases. Unlike GZ and YZ alloys, a semi network of secondary phases along with small sized particles were observed in NZ alloy. From the EDS analysis, both these phases [marked as A, B and C in Fig. 2(f)] were identified as T (Mg_7Zn_3Nd) phases as the measured composition of Mg, Zn and RE were approximately 7:3:1 (Ref 22, 23). Though few binary phases were (Mg-Zn, Mg-RE) observed in all alloys, ternary phases such as W phase in GZ, I phase in YZ, and T phases in NZ alloy were dominant.

3.2 Electrochemical Measurement

The cathodic and anodic branches of a polarization curve represents the hydrogen evolution and Mg matrix dissolution, respectively, during the polarization measurement. The polarization curves (Fig. 3) and Table 3 show that the YZ Alloy had a more negative E_{corr} compared to that of GZ alloy. However, i_{corr} value of YZ alloy was lower than that of GZ indicating that YZ had better corrosion resistance. The lower corrosion potential of YZ alloy indicated that the corrosion potential difference between Y containing secondary phases and Mg matrix was lower and hence resulted in lesser cathodic activity as evident from the cathodic branch of polarization curve. Though NZ alloy showed higher cathodic activity (relatively high cathodic current density at all cathodic potentials), it exhibited a more positive corrosion potential due to the lesser anodic dissolution behavior. However, the i_{corr} of alloys NZ were the lowest.

Electrochemical Impedance behavior of alloys after immersion in 1 wt.% NaCl for 30 min., and 1, 3, 7 and 14 days (Fig. 4) show that initially all the alloys had a similar behavior (although the dimensions of the loops seem to be different indicating marginal differences in corrosion rates). The Nyquist plots of alloys measured after 30 min. immersion in electrolyte [Fig. 4(a)] showed two capacitive loops: well defined at high-medium frequencies and depressed at low frequencies. However, all the alloys showed inductive loop [Fig. 4(b)] after 1 day immersion indicating the initiation of pits. Also the capacitive loops became single with reduced diameters suggesting that the dissolution of corrosion layers occurred. Similarly, the continuous decrease in size of the capacitive loops after 3, 7 and 14

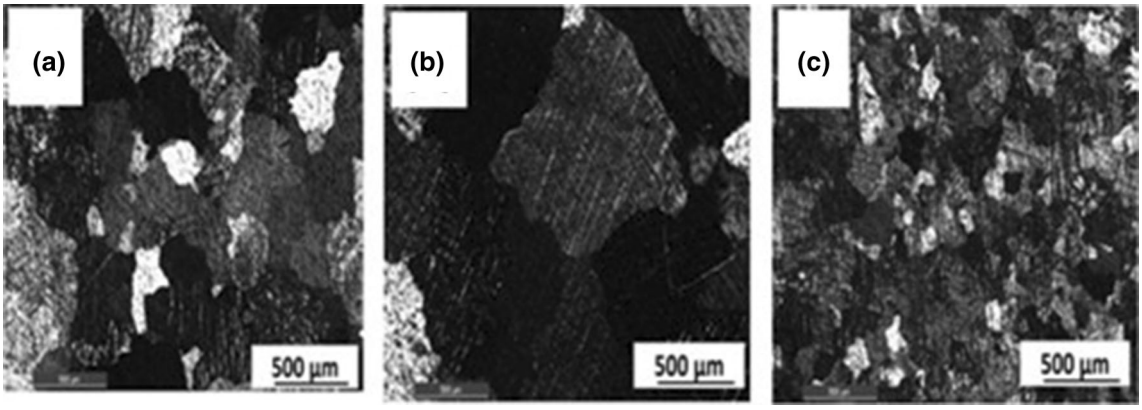

Fig. 1 Optical micrographs of the developed alloys (a) GZ, (b) YZ, (c) NZ

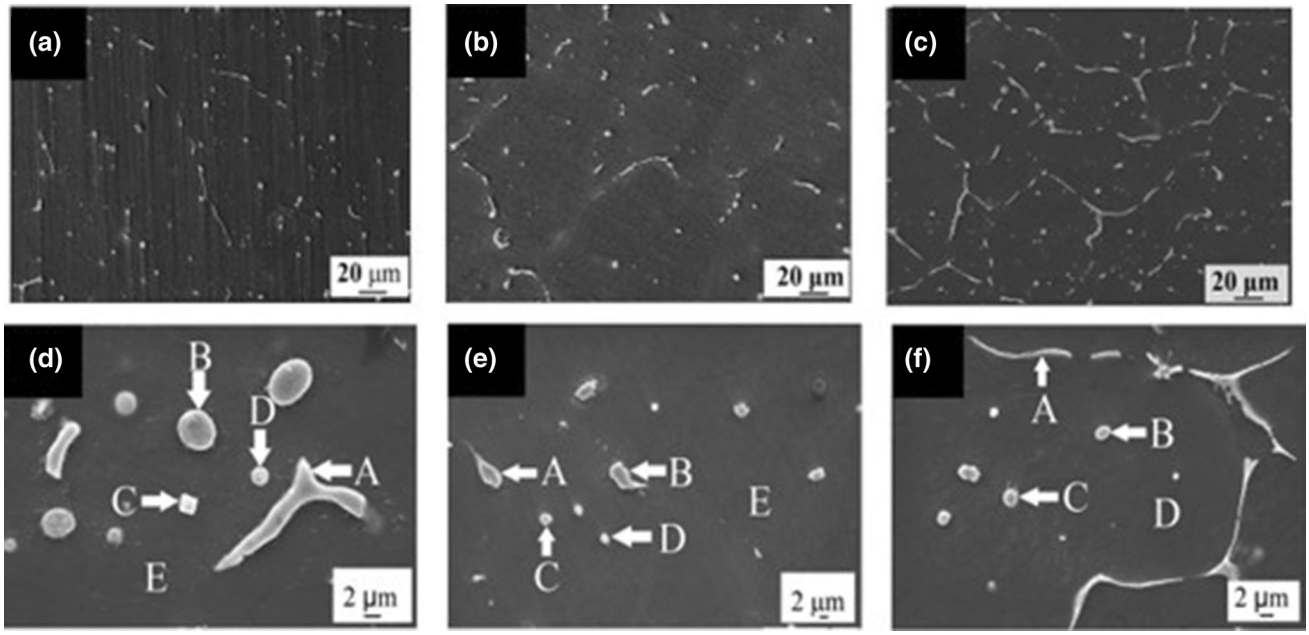

Fig. 2 SEM micrographs of alloys (a&d) GZ, (b&e) YZ, (c&f) NZ

Table 2 EDS analysis of different secondary phases in the alloys

Alloy	Position	Elements (at.%)			Phase
		Mg	Zn	RE	
GZ	Figure 2 (d)-A	61.9	28.83	8.97	W ($Mg_3Zn_3Gd_2$)
	Figure 2 (d)-B	69.35	24.73	5.92	W ($Mg_3Zn_3Gd_2$)
	Figure 2 (d)-C	76.53	1.37	22.09	Mg_5Gd
	Figure 2 (d)-D	87.34	10.94	1.73	Mg-Zn binary
	Figure 2 (d)-E	98.5	1.05	0.45	Matrix
YZ	Figure 2 (e)-A	71.07	24.33	4.6	I (Mg_3Zn_6Y)
	Figure 2 (e)-B	50.98	40.91	8.11	I (Mg_3Zn_6Y)
	Figure 2 (e)-C	91.33	7.59	1.07	Mg-Zn binary
	Figure 2 (e)-D	78.75	18.72	2.53	Mg-Zn binary
	Figure 2 (e)-E	98.79	1.21	0.01	Matrix
NZ	Figure 2 (f)-A	71.9	22.11	6	T (Mg_7Zn_3Nd)
	Figure 2 (f)-B	72.03	22.58	5.38	T (Mg_7Zn_3Nd)
	Figure 2 (f)-C	69.52	24.17	6.31	T (Mg_7Zn_3Nd)
	Figure 2 (f)-D	98.82	1.11	0.07	Matrix

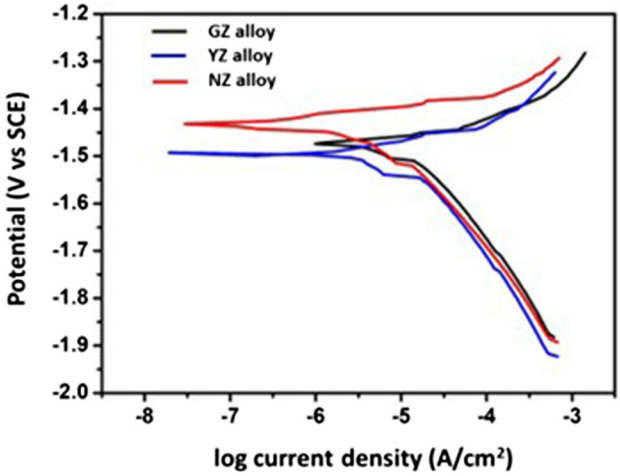

Fig. 3 Polarization curves of alloys in 1 wt.% NaCl solution at 25 °C

days of immersion indicated that the corrosion layer was unstable and leading to continuous dissolution of alloys. However, initially the alloys showed strong inductive loops after 1 day immersion but as immersion time increased this behavior was suppressed. It seems that the formation of pits during initial stage of corrosion leads to a strong inductive loop whereas spreading of pits further into the matrix leads to weakened inductive loops (Ref 20, 24, 25).

For more details on the corrosion characteristics of the alloys, the EIS spectra were fitted using the equivalent circuits as shown in Fig. 5. The data were fitted using ZSimpWin 3.20 software where, R_s refers to solution resistance, R_{ct} represents charge transfer resistance, CPE_{dl} represents electric double layer capacitance at the interface of substrate and solution, R_f represents film resistance, CPE_f represents film capacitance,

Table 3 OCP, E_{corr} and i_{corr} values of alloys obtained from polarization measurements in 1 wt.% NaCl

Alloy	OCP, mV vs SCE	E_{corr}, mV vs SCE	i_{corr}, μA/cm^2
GZ	−1571	−1486	12.58
YZ	−1554	−1500	10
NZ	−1423	−1430	5.16

and R_L and L represents resistance and inductance of the low frequency inductive loop, respectively. The capacitive loop at high frequencies represents double layer capacitance and charge transfer resistance. The resistance offered by the

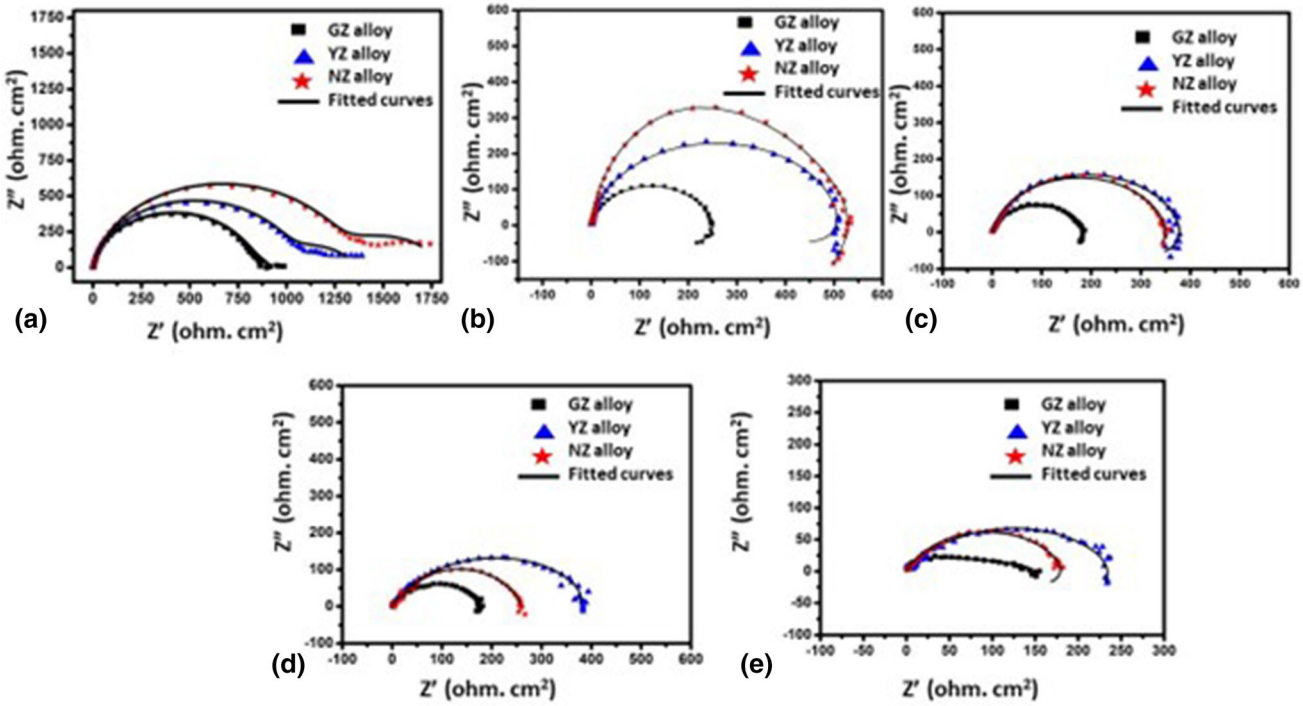

Fig. 4 Nyquist plots of alloys measured in 1 wt.% NaCl at different times (a) 30 min.; (b) 1 day; (c) 3 days; (d) 7 days; (e) 14 days

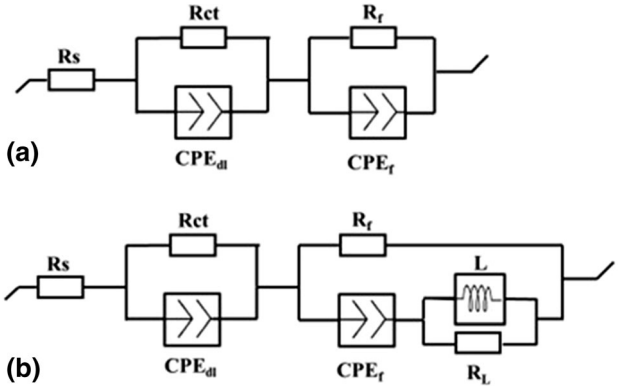

Fig. 5 Equivalent circuits used to fit Nyquist plots of the alloys obtained at different immersion times in 1 wt.% NaCl (a) 30 min.; (b) 1–14 days

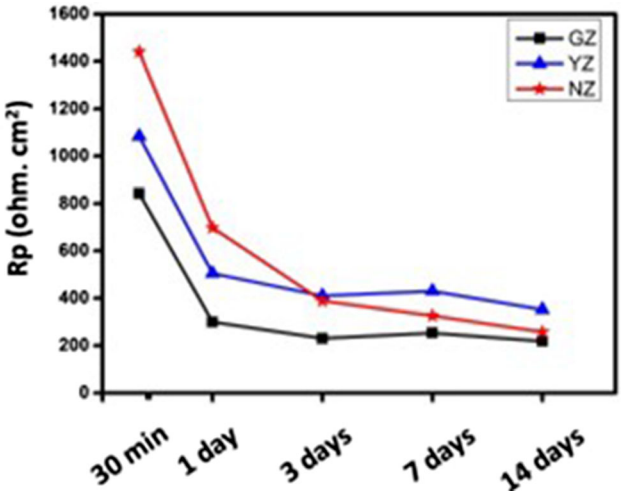

Fig. 6 (a) R_p (R_{ct}+R_f or R_{ct}+R_f+R_L) of alloys obtained from impedance measurement in 1 wt.% NaCl at different immersion time

corrosion film on the surface was indicated by the capacitive loop at medium or lower frequencies. Inductive loop is an indication of the failure of the surface film and initiation of pits (Ref 20, 26). The polarization resistance R_p ($R_{ct} + R_f$ or $R_{ct} + R_f + R_L$) (Ref 27–29) calculated for all the alloys (Fig. 6) after 30 min. immersion indicated that NZ alloys had the highest whereas GZ alloys had the lowest resistance which was in agreement with the i_{corr} values obtained from Tafel plots. After 1 day of immersion, due to inductive loops at lower frequencies the R_p values of all the alloys dropped. However, beyond 3 days the resistance of the alloys had only a marginal change till the 14 days immersion. GZ alloys exhibited lowest resistance at all immersion times indicating that it was most susceptible to corrosion among the studied alloys.

3.3 XPS Analysis of Corrosion Layer

To analyze the composition of corrosion layer, XPS measurements were done on the samples immersed in 1wt.% NaCl for 30 min. Depth profiling measurement was carried out for 1800 seconds of sputtering and the sputtered depth was calculated from a related removal rate of 20 nm/min. for SiO_2 which was found to be approximately 600 nm (The sputtering was not carried out beyond 600 nm due to the limitations of the instrument and machine safety concerns). The depth profiles of the corrosion films on the samples (Fig. 7) indicated that the atomic concentration of Mg at a depth of 600 nm increased in

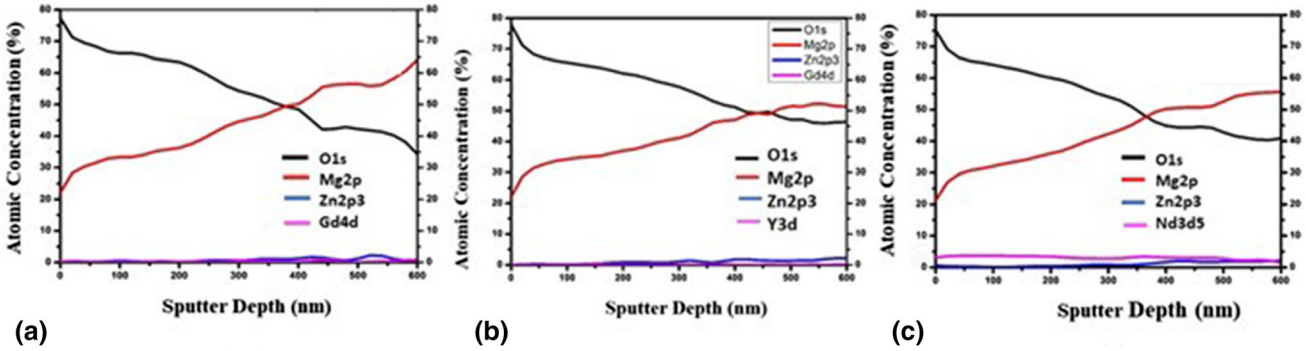

Fig. 7 Depth profile analysis of the corrosion layers on the samples immersed in 1 wt.% NaCl for 30 min. (a) GZ, (b) YZ, (c) NZ

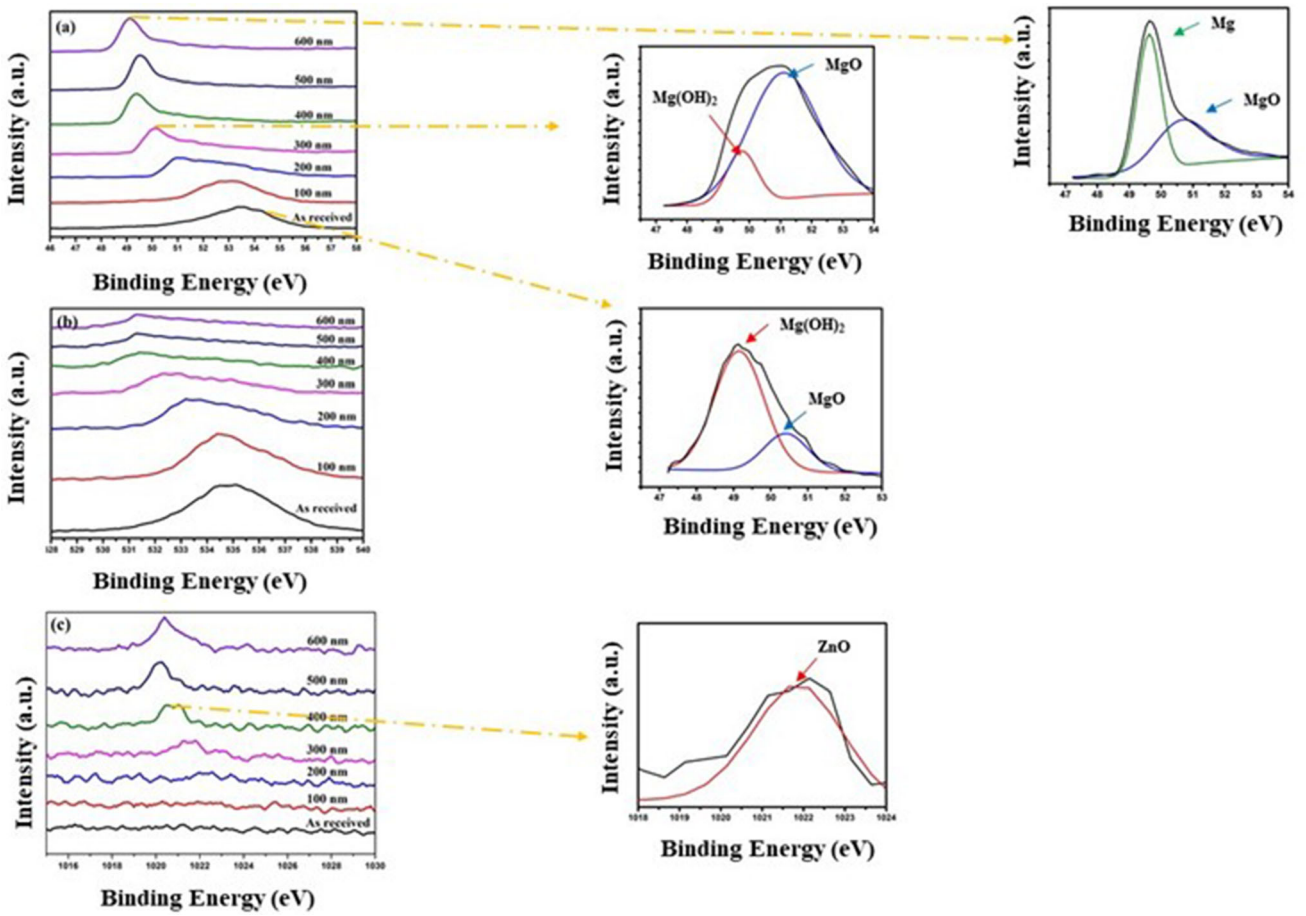

Fig. 8 DP-XPS spectra of the corrosion layers on GZ alloy sample immersed in 1 wt.% NaCl for 30 min. (a) Mg2p (b) O1s (c) Zn2p3

the order YZ< NZ< GZ. The above result revealed that after 30 min. immersion, corrosion layer thickness was lowest for GZ and highest for YZ. Moreover, all the alloys showed the presence of Zn and relatively minimum or negligible atomic concentration of rare earths in the corrosion layers. In contrast, an appreciable amount of Nd was present in the oxide layer on NZ alloy from the surface to the end of sputter depth up to 600 nm.

The DP-XPS spectra of O1s, Mg2p and Zn2p3 of the alloys were similar. Therefore, for analysis, XPS depth profiling (DP-XPS) spectra of O1s, Mg2p and Zn2p3 of the corrosion film on the GZ alloy is shown in Fig. 8. The higher bond energy (BE) peak centered at 533.5 eV in O1s spectra [Fig. 8(b)] and the broader low BE peak at 300 nm depth centered at 531 eV confirmed the presence of hydroxide and oxide state of oxygen, respectively (Ref 14). Mg2p spectra [Fig. 8(a)] were in good agreement with the O1s spectra [Fig. 8(b)]. The Mg2p spectra of the surface of GZ alloy shows the BE peak is centered between 49.5 eV ($Mg(OH)_2$) and 50.25 eV (MgO). The energy peak at 49.6 eV and 51 eV at 400 nm corresponded to magnesium hydroxide and magnesium oxide (Ref 30). Energy peak of Mg2p spectra at 600 nm shows the presence of Mg

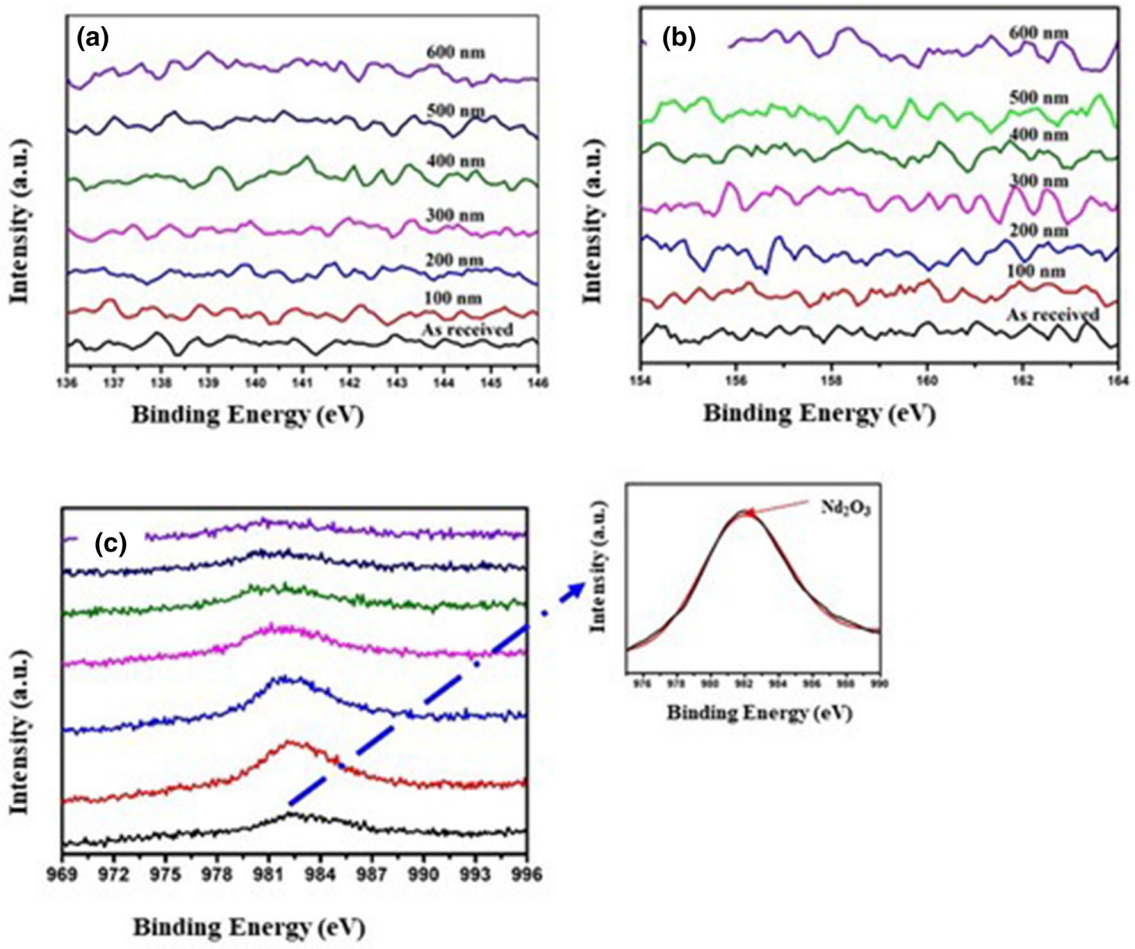

Fig. 9 DP-XPS spectra of the rare earth elements on the corrosion layers on the alloys immersed in 1 wt.% NaCl for 30 min. (a) Gd4d (b) Y3d (c) Nd3d5

(49.4 eV) and MgO (50.8 eV). However, the area fraction of the $Mg(OH)_2$ decreased where as that of MgO and Mg increased as the sputtering depth increased. This also explains why the atomic percentage of oxygen decreases as the sputtering depth increases. Zn2p3 profile [Fig. 8(c)] showed a distinguishable peak after 400 nm at 1021.2 eV that corresponds to ZnO (Ref 31). However, no such distinguishable peaks were seen in the DP-XPS spectra of Gd and Y [Fig. 9(a and b)], indicating that the presence of Gd and Y were minimal in the corrosion film till 600 nm of depth. However, in the NZ alloy presence of broader BE peaks at 983.2 eV [Fig. 9(c and d)] in Nd3d5 spectra indicating the presence of Nd_2O_3 in the corrosion layer.

Thus, the XPS analysis of corrosion layer after 30 min. immersion revealed that all the alloys consisted of $Mg(OH)_2$ in the outer layer and MgO and ZnO in the inner layer (Fig. 7). In addition, NZ alloy had the presence of Nd_2O_3 in the corrosion layer. Although the presence of rare earths in GZ and YZ were minimal in corrosion layer, the surface films were reasonably protective in nature initially as it was evident from EIS analysis of the alloys after 30 min. immersion [Fig. 4(a)] that there were no inductive loops in any of the alloys. The R_p values obtained using electrochemical impedance measurement (Fig. 6) show that NZ alloy had the highest resistance at 30 min. immersion owing to the presence of Nd_2O_3 on the surface [Fig. 7(d) and Fig. 11(d)]. Though, YZ alloy had similar surface film characteristics to that of GZ, yet the R_p value of the YZ alloy was slightly higher (Fig. 6). This might be due to the thicker oxide film found in YZ alloy.

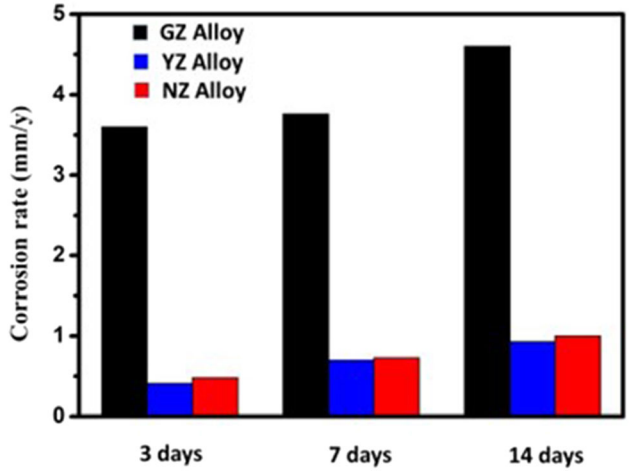

Fig. 10 Corrosion rate of the alloys calculated from weight loss measurement of samples immersed in 1 wt.% NaCl at different immersion times

3.4 Weight Loss Measurement

The results of weight loss measurement in 1 wt.% NaCl for 3, 7 and 14 days (Fig. 10) show that GZ alloy exhibited highest corrosion rate at all immersion time intervals. However, corrosion rates of other two alloys (YZ and NZ) were similar and much lower than that of GZ alloy at all-time intervals. Slight increase in corrosion rate beyond 3 days of immersion was observed for all these alloys and the corrosion rate was more or less same till 14 days of immersion. This is in agreement with the EIS results as the R_p value (Fig. 6) decreases as immersion time increases but the changes in R_p values is marginal beyond 3 days immersion.

3.5 Hydrogen Evolution

Figure 11 shows the hydrogen volume measured during immersion of samples in 1 wt.% NaCl for 336 h (14 days). Among all the alloys, GZ alloy had the highest slope of hydrogen volume curve which indicated that it had undergone severe corrosion compared to rest of the alloys. The measurement for GZ alloy was stopped at 120 h since the maximum measurable amount of H_2 was reached (the maximum limit of the apparatus was 330 mL). The result of hydrogen evolution of the alloys was in good agreement with the weight loss measurements as the total hydrogen evolution volume was lowest for alloy YZ and highest for alloy GZ.

3.6 Corrosion Product Analysis

The XRD analysis (Fig. 12(a–c)) of the corrosion product obtained by immersing the samples in 1 wt.% NaCl for 14 days suggested that they mainly composed of $Mg(OH)_2$ (JCPDS: 019–0771) and traces of ZnO (JCPDS: 001–1136). Other than these elements the diffraction patterns suggested the presence of Gd_2O_3 (JCPDS: 01–088-2165) in GZ alloy, Y_2O_3 (JCPDS: 039-1063) in YZ alloy and Nd_2O_3 (JCPDS: 040-1283) in NZ alloy. As expected, the number of peaks corresponding to Gd_2O_3 in GZ alloy was minimal. Interestingly, predominant peaks corresponding to Y_2O_3 observed in YZ alloys indicated the presence of reasonable amount of Y_2O_3 in the corrosion product after 14 days of immersion. The above observation was in contrast to the XPS analysis of 30 min. immersed samples, where negligible amount of Y_2O_3 was present in the corrosion layer in YZ alloy in the beginning of corrosion. Thus the corrosion layer in the YZ alloy became rich in Y_2O_3 after long time immersion which made the otherwise porous oxide layer more compact and offered better protection to the alloy surface. No diffraction peaks corresponding to any of the second phases in the alloys were seen and might be due to the restriction in the detecting limit of XRD.

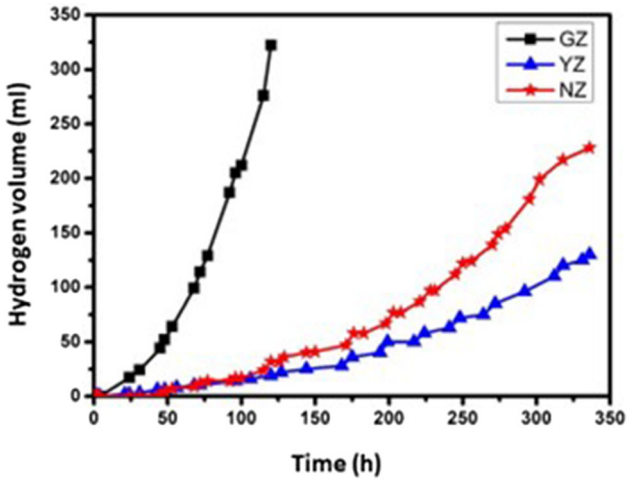

Fig. 11 Volume of evolved hydrogen from the alloys immersed in 1 wt.% NaCl for 14 days

3.7 Corrosion Morphology

SEM analysis of the corroded samples at different immersion times were carried out to understand the corrosion initiation and propagation in the alloys. The second phases in Mg alloys are usually more inert than α-Mg matrix and they act as cathodic sites resulting in initiation of corrosion in the matrix next to the second phase (Ref 4). The corrosion then spreads and gets accelerated as immersion time increases. The SEM micrograph of the alloys (Fig. 13(a–c)) immersed in 1 wt.% NaCl for 30 min. and without removing the corrosion products revealed that the corrosion was initiated next to the secondary phases as corrosion products (marked in white arrows) could be seen in the close proximity of secondary phases. More corrosion products were seen around the secondary phases in GZ alloy unlike other alloys, suggesting that secondary phases found in GZ alloys were more cathodic in nature and susceptible to severe micro-galvanic corrosion. As the immersion time increased to 12 h, the SEM micrographs of all the alloys taken after cleaning the corrosion products exhibited a filament type propagation [Fig. 14(a-c)] of corrosion indicating the occurrence of filiform corrosion. Filiform corrosion occurs due to the movement of an active corrosion cell across the metal surface. Filament head acts as the anode and the tail acts as cathode. It is usually observed in anodized or protective coated surfaces. However, the filiform corrosion in uncoated Mg alloys are also reported due to breakage of protective corrosion film on the alloy surfaces (Ref 32, 33). The filaments propagated through the matrix adjacent to the secondary phases. Pitting corrosion occurred in all the alloys but was least in YZ alloy. Few secondary phases still intact in the alloys are shown in Fig. 14(d-f) by white arrows. The cross section of the alloys after 12 h immersion shows that severe pitting has occurred in GZ alloy and that the secondary phases are in fact accelerating the corrosion [Fig. 15(a)]. No such pits were observed in YZ alloy, and the corrosion product formation [marked in white arrows, Fig. 15(b)] is also not seen in the vicinity of I phase [marked in blue arrows Fig. 15(b)]. Similar to GZ alloy, the cross section of the NZ alloy also showed small pits; however, the propagation of pits further seemed to be impeded by the dendritic T phase [marked in blue arrows, Fig. 15(c)]. Similarly, the cross-sectional SEM images of the alloys immersed after 3 days showed that GZ alloy exhibited severe pitting corrosion [Fig. 16(a)]. However, careful examination revealed that the elongated dendritic shaped W phase [marked in white arrows, Fig. 16(b)] was still intact, although the corrosion pits were spreading into the grain interior. This suggests that the dendritic W phase was not accelerating the corrosion unlike other discrete secondary phases found in GZ alloy and was able to retard it to an extent. YZ alloy also showed pits after 3 days immersion [Fig. 16(c)]; however, the corrosion propagation was not initiated near the I phase. The cross sectional morphology of the 3 days immersed NZ alloy showed that T phase [marked in white arrows, Fig. 16(d)] was able to impede the corrosion propagation.

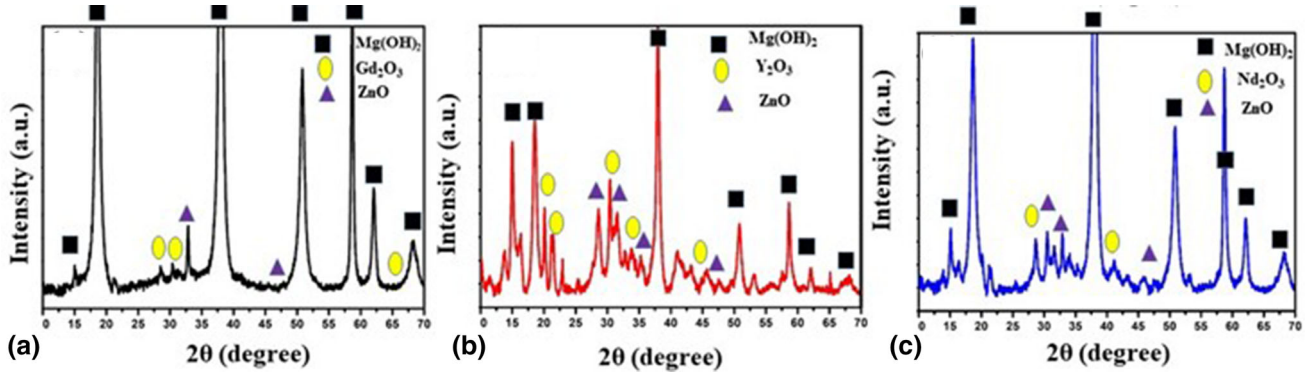

Fig. 12 XRD analysis of the corrosion products obtained from samples immersed in 1 wt.% NaCl for 14 days (a) GZ (b) YZ (c) NZ alloys

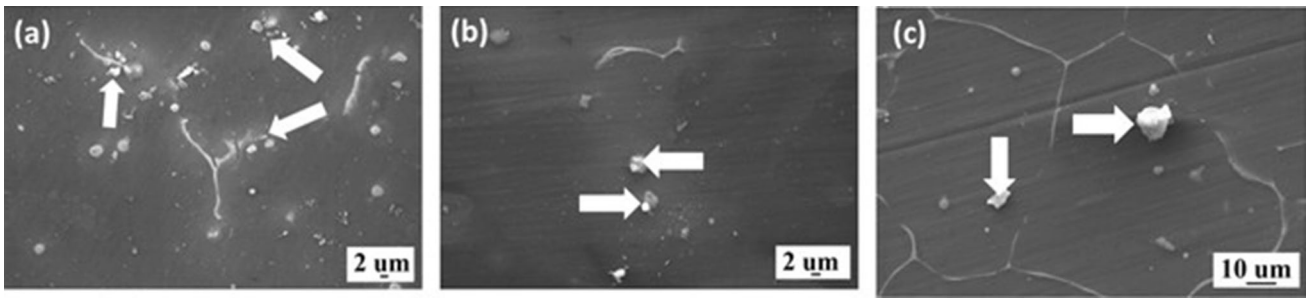

Fig. 13 Corrosion morphology of alloys immersed in 1 wt.% NaCl for 30 min. without the removal of corrosion products (a) GZ (b) YZ (c) NZ alloy (corrosion products are marked in white arrows)

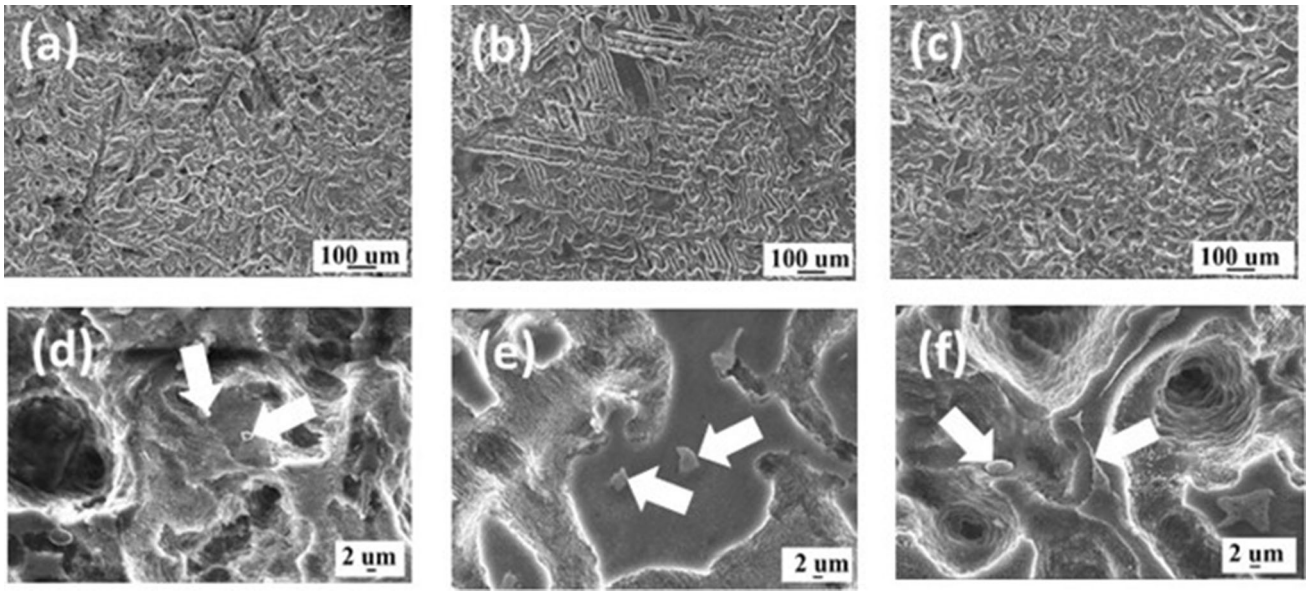

Fig. 14 Corrosion morphology of samples immersed in 1 wt.% NaCl after the removal of corrosion product for 12 h (a& d) GZ, (b & e) YZ, (c & f) NZ (secondary phases are marked in white arrows)

4. Discussion

4.1 Effect of Microstructure

Mg is highly active due to the negative standard potential of about−2.4 V, which is more negative than any other standard engineering metal. In addition, the non-uniform microstructure, composition and crystalline orientation in a Mg alloy can generate micro-galvanic couples. The activity of anodic and cathodic processes in a Mg alloy vary from area to area, grain to grain and phase to phase. The Mg matrix with lower alloying element always acts as a micro anode and gets corroded. On the

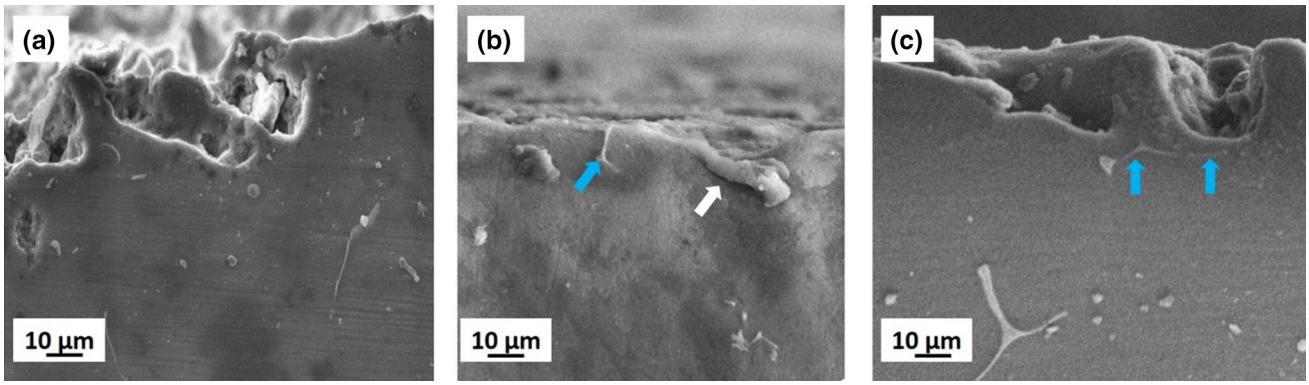

Fig. 15 Corrosion morphology of the cross section of samples immersed in 1 wt.% NaCl after the removal of corrosion product for 12 h (a) GZ, (b) YZ and (c) NZ

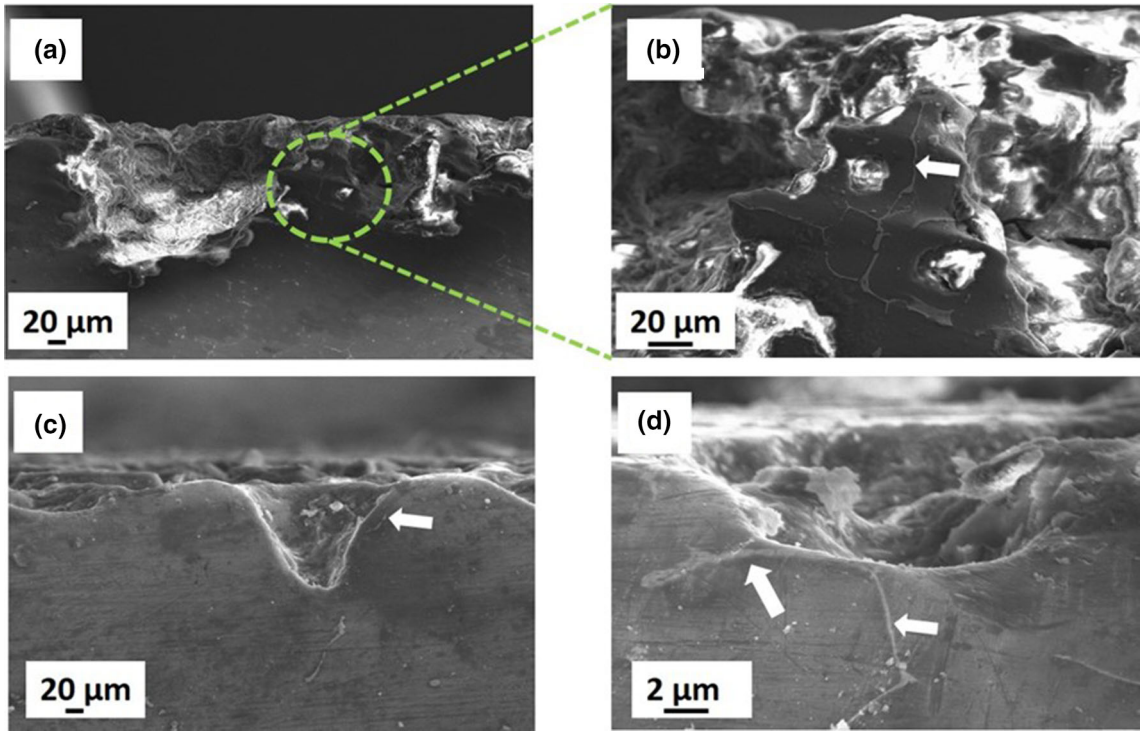

Fig. 16 Corrosion morphology of the cross section of samples immersed in 1 wt.% NaCl after the removal of corrosion product for 3 days (a &b) GZ, (c) YZ and (d) NZ

other hand, the impurity elements, intermetallic particles, secondary phases and matrix with higher amount of alloying elements act as micro cathodes (Ref 32, 34). Moreover, the grain size, volume fraction and distribution of secondary phases play a decisive role in the corrosion behavior of alloys. Grain refinement usually decreases the corrosion rate owing to the formation of a uniform oxide layer over the surface (Ref 35). The grain size of the studied alloys increase in the order of NZ, GZ and YZ. However, NZ alloys had only a marginal difference in grain size. Though the poor corrosion resistance of GZ alloy could be attributed to the coarse grain structure and better performance of NZ alloy could be related to the fine grains, the enhanced corrosion resistance of YZ need further explanation. In general, the various studies reported on the microstructure and corrosion behavior of alloys suggests that the influence of grain size on corrosion resistance is still ambiguous. In addition, most of the studies have discussed the effect of change in grain size on corrosion performance of the same material under varying conditions (Ref 36, 37). The above observation suggested that grain size is not the deciding factor in corrosion performance and the influence of secondary phases must be considered to understand the corrosion behavior of these alloys.

The secondary phase in Mg alloys can either act as micro cathode to accelerate corrosion or to retard corrosion by acting as an effective barrier depending up on the volume fraction and distribution. This dual role of secondary phase is more obvious in AZ alloys where continuously distributed β phase (second phase) effectively retards the corrosion whereas corrosion is accelerated by the presence of discontinuously distributed *β*

phase (Ref 14, 38). Although almost all secondary phases found in Mg alloys are cathodic in nature, the secondary phases in certain Mg alloys are reported to be relatively anodic, and corrodes preferentially (Ref 4, 32). In the present study, micro-galvanic corrosion initiated around the secondary phases in all the alloys (Fig. 13) and it gradually spread into grain interior (Fig. 14), indicating that secondary phases present in these alloys were cathodes to α Mg matrix. It was also evident from the SEM analysis of YZ alloy after 30 min. immersion [Fig. 13 (b)] that the corrosion products nucleated near the secondary phases were relatively less. On the other hand, the secondary phases in GZ alloys were more cathodic [Fig. 3] and more cluster of corrosion products near the phases in GZ alloy after 30 min. immersion [Fig. 13(a)]. In addition, severe pits in the corrosion morphology after 12 h immersion [Fig. 14(d)] suggesting that severe micro-galvanic corrosion occurred in GZ alloy. Similarly, Tafel analysis (Fig. 3) showed higher cathodic activity in NZ alloy due to second phase, and the corrosion pits evident from the SEM analysis of corrosion morphology after 12 h immersion [Fig. 14(f)] suggesting that the secondary phase in NZ acted as cathodic and accelerated micro-galvanic corrosion. In spite of that, the uniformly distributed network shaped secondary phases in NZ alloys inhibited the corrosion and improved the overall corrosion resistance of the alloy. The corrosion barrier effect of network secondary phases was also evident from the SEM analysis of corrosion morphology after 12 h immersion [Fig. 14(f)] that showed a severely corroded matrix surrounded by a network of secondary phases. Since, only a marginal change was observed in the volume fraction of secondary phases in the studied alloys (within a range of 10 to 15%), the effect of volume fraction on the corrosion behavior of these alloys was minimal. However, the distribution of secondary phases was different from alloy to alloy, and continuous network of phases retarded the corrosion spreading as evident from NZ alloy.

4.2 Effect of Surface Films

The electrochemical reactions when magnesium is exposed to an aqueous medium are (Ref 14):

$$Mg \rightarrow Mg^{2+} + 2e^{-} (\text{Anodic reaction}); \quad \text{(Eq 2)}$$

$$2H_2O + 2e^{-} \rightarrow H_2 + 2OH^{-} (\text{Cathodic reaction}); \quad \text{(Eq 3)}$$

$$Mg^{2+} + 2\,OH^{-} \rightarrow Mg(OH)_2 (\text{Product formation}); \quad \text{(Eq 4)}$$

$$Mg + 2H_2O \rightarrow Mg(OH)_2 + H_2 (\text{Overall corrosion reaction}) \quad \text{(Eq 5)}$$

The $Mg(OH)_2$ thus formed has a hexagonal crystalline structure and makes way for an easy basal cleavage. The hydrogen evolution accompanied with the cathodic reaction further weaken the surface film. The equilibrium pH of $Mg(OH)_2$ is around 11 which suggests that the film is non protective in normal aqueous environments where the pH is usually less than 11. Moreover, anions such as chloride, sulfate, and nitrate tends to destroy the passivity of Mg as they are capable of breaking down the surface film on Mg (Ref 39). However, the incorporation of alloying elements in the surface film influences the stability as well as dissolution kinetics of the film. For example, the presence of Al_2O_3 in the surface film of Mg-Al alloy offers better protection to the surface compared to $Mg(OH)_2$ or MgO (Ref 40, 41). The XPS analysis (Fig. 7-9) of the corrosion film formed on alloys (after 30 min. immersion in 1 wt.% NaCl solution) and the XRD analysis (Fig. 12) of the corrosion product after 14 days immersion established that the corrosion film was dominated by $Mg(OH)_2$, MgO and ZnO followed by the corresponding rare earth oxides in the alloys. However, the presence of rare earths oxides was found to be minimal in GZ alloy. On the other hand, the presence of Nd_2O_3 in the surface film immediately after 30 min. [Fig. 7(d) and Fig. 9(c)] immersion, and the dominant presence of Y_2O_3 in the corrosion product after 14 days immersion in the YZ alloy [Fig. 12(b)] indicated that the presence of RE oxides in the surface film played a major role in the better corrosion resistance of these alloys. It was reported that the reason for the enhanced corrosion resistance of WE43 alloy was due to the enrichment of Y_2O_3 in the corrosion products (Ref 42). Similarly, Zhang et al. reported that the spontaneous formation of Nd_2O_3 on the corrosion layer enhanced the compactness of the surface film in Mg-2Zn-0.2Mn-xNd (Ref 43). Incorporation of the Nd_2O_3 on the corrosion film found to improve the corrosion resistance of AZ91 alloy (Ref 44) as well as in Mg-8Li-3Al-2Zn alloy containing Nd (Ref 45).

5. Conclusion

- Among the studied RE elements (Gd, Y and Nd) with similar atomic percentage, corrosion rate of Gd containing alloy was the highest and Y and Nd containing alloys were the lowest.
- Although the volume fraction of secondary phases were similar, secondary phases observed in Mg-1.52Zn-0.15Gd and Mg-1.52Zn-0.16Y alloys were discrete whereas they were distributed as network shape in Mg-1.52Zn-0.15Nd alloys.
- The discontinuously distributed secondary phases accelerated corrosion in Mg-1.52Zn-0.15Gd alloy. On the other hand, low corrosion potential of second phases and the presence of Y_2O_3 in the corrosion layer were attributed to the better corrosion resistance in Mg-1.52Zn-0.16Y alloy.
- In spite of higher cathodic activity of second phases, the network morphology as well as the presence of Nd_2O_3 in the corrosion layer significantly improve the corrosion resistance of Mg-1.52Zn-0.15Nd alloy.

Acknowledgments

This research was financially supported by the Science and Engineering Research Board (SERB, Award number: EMR/2017/001286) and Council of Scientific and Industrial Research (CSIR, Award number: MLP0043). The authors also thank the Director, CSIR-NIIST, Trivandrum for providing an opportunity to conduct the study.

Declarations

Conflict of interest The authors declare that they have no conflict of interest.

References

1. S.Z. Khalajabadi, M.R. Abdul Kadir, S. Izman and M. Marvibaigi, The Effect of MgO on the Biodegradation, Physical Properties and Biocompatibility of a Mg/HA/MgO Nanocomposite Manufactured by Powder Metallurgy Method, *J. Alloys Compd.*, 2016, **655**, p 266
2. W.J. Joost and P.E. Krajewski, Towards Magnesium Alloys for High-Volume Automotive Applications, *Scripta Mater.*, 2017, **128**, p 107–112. https://doi.org/10.1016/j.scriptamat.2016.07.035
3. R.G. Hu, S. Zhang, J.-F. Bu, C.-J. Lin and G.-L. Song, Recent Progress in Corrosion Protection of Magnesium Alloys by Organic Coatings, *Prog. Org. Coat.*, 2012, **73**, p 129–141. https://doi.org/10.1016/j.porgcoat.2011.10.011
4. G. Song and A. Atrens, Understanding Magnesium Corrosion—A Framework for Improved Alloy Performance, *Adv. Eng. Mater.*, 2003, **5**, p 837–858. https://doi.org/10.1002/adem.200310405
5. Y. Ding, C. Wen, P. Hodgson and Y. Li, Effects of Alloying Elements on the Corrosion Behavior and Biocompatibility of Biodegradable Magnesium Alloys: A Review, *J. Mater. Chem. B.*, 2014, **2**, p 1912–1933. https://doi.org/10.1039/C3TB21746A
6. M. Esmaily, J.E. Svensson, S. Fajardo, N. Birbilis, G.S. Frankel, S. Virtanen, R. Arrabal, S. Thomas and L.G. Johansson, Fundamentals and Advances in Magnesium Alloy Corrosion, *Prog. Mater Sci.*, 2017, **89**, p 92–193. https://doi.org/10.1016/j.pmatsci.2017.04.011
7. J. Meng, W. Sun, Z. Tian, X. Qiu, D. Zhang, 2-Corrosion Performance of Magnesium (Mg) Alloys Containing Rare-Earth (RE) Elements, in G.-L. Song (Ed.), *Corrosion Prevention of Magnesium Alloys*, (Woodhead Publishing, 2013) p. 38–60. https://doi.org/10.1533/9780857098962.1.38
8. Y. Huang, A. Srinivasan, K.U. Kainer, L. Mendis, C. Blawert, K.U. Hort, Corrosion Behavior of Mg-Gd-Zn Based Alloys in Aqueous NaCl Solution (2014), http://ir.niist.res.in:8080/jspui/handle/123456789/2263 Accessed 11 Aug 2020
9. A. Boby, A. Srinivasan, U.T.S. Pillai and B.C. Pai, Mechanical Characterization and Corrosion Behavior of Newly Designed Sn and Y Added AZ91 Alloy, *Mater. Des.*, 2015, **88**, p 871–879. https://doi.org/10.1016/j.matdes.2015.09.010
10. F. Rosalbino, E. Angelini, S. De Negri, A. Saccone and S. Delfino, Electrochemical Behaviour Assessment of Novel Mg-rich Mg-Al-RE Alloys (RE=Ce, Er), *Intermetallics*, 2006, **14**, p 1487–1492. https://doi.org/10.1016/j.intermet.2006.01.056
11. N. Birbilis, M.A. Easton, A.D. Sudholz, S.M. Zhu and M.A. Gibson, On the Corrosion of Binary Magnesium-Rare Earth Alloys, *Corros. Sci.*, 2009, **51**, p 683–689. https://doi.org/10.1016/j.corsci.2008.12.012
12. H. Azzeddine, A. Hanna, A. Dakhouche, L. Rabahi, N. Scharnagl, M. Dopita, F. Brisset, A.-L. Helbert and T. Baudin, Impact of Rare-Earth Elements on the Corrosion Performance of Binary Magnesium Alloys, *J. Alloy. Compd.*, 2020, **829**, 154569. https://doi.org/10.1016/j.jallcom.2020.154569
13. S. Tekumalla, S. Seetharaman, A. Almajid and M. Gupta, Mechanical Properties of Magnesium-Rare Earth Alloy Systems: A Review, *Metals*, 2015, **5**, p 1–39. https://doi.org/10.3390/met5010001
14. G.-L. Song, 1-Corrosion Electrochemistry of Magnesium (Mg) and Its Alloys, in: G. Song (Ed.), *Corrosion of Magnesium Alloys*, (Woodhead Publishing, 2011) p. 3–65. https://doi.org/10.1533/9780857091413.1.3
15. S. Verdier, N. van der Laak, S. Delalande, J. Metson and F. Dalard, The surface reactivity of a magnesium–aluminium alloy in acidic fluoride solutions studied by electrochemical techniques and XPS, *Appl. Surf. Sci.*, 2004, **235**, p 513–524. https://doi.org/10.1016/j.apsusc.2004.03.250
16. I. Polmear, *Light Alloys: From Traditional Alloys to Nanocrystals*, (Elsevier, 2005)
17. Standard Practice for Conventions Applicable to Electrochemical Measurements in Corrosion Testing, (n.d.). https://www.astm.org/g0003-89r10.html Accessed 12 May 2022
18. M.M. Avedesian, H. Baker, *ASM Specialty Handbook: Magnesium and Magnesium Alloys*, (ASM International, 1999)
19. ASTM G31–72_Laboratory Immersion Corrosion Testing of Metals - Free Download PDF, (n.d.). https://kupdf.net/download/astm-g31-72laboratory-immersion-corrosion-testing-of-metals_59966135dc0d607665300d1d_pdf Accessed 12 May 2022
20. A. Srinivasan, C. Blawert, Y. Huang, C.L. Mendis, K.U. Kainer and N. Hort, Corrosion Behavior of Mg-Gd-Zn Based Alloys in Aqueous NaCl Solution, *J. Magnes. Alloy.*, 2014, **2**, p 245–256. https://doi.org/10.1016/j.jma.2014.08.002
21. D.H. Bae, S.H. Kim, D.H. Kim and W.T. Kim, Deformation Behavior of Mg-Zn-Y Alloys Reinforced by Icosahedral Quasicrystalline Particles, *Acta Mater.*, 2002, **50**, p 2343–2356. https://doi.org/10.1016/S1359-6454(02)00067-8
22. W.C. Neil, M. Forsyth, P.C. Howlett, C.R. Hutchinson and B.R.W. Hinton, Corrosion of Magnesium alloy ZE41–The Role of Microstructural Features, *Corros. Sci.*, 2009, **51**, p 387–394. https://doi.org/10.1016/j.corsci.2008.11.005
23. A.E. Coy, F. Viejo, P. Skeldon and G.E. Thompson, Susceptibility of Rare-Earth-Magnesium Alloys to Micro-Galvanic Corrosion, *Corros. Sci.*, 2010, **52**, p 3896–3906. https://doi.org/10.1016/j.corsci.2010.08.006
24. R. Arrabal, A. Pardo, M.C. Merino, M. Mohedano, P. Casajús, K. Paucar and G. Garcés, Effect of Nd on the Corrosion Behaviour of AM50 and AZ91D Magnesium Alloys in 3.5wt.% NaCl Solution, *Corros. Sci.*, 2012, **55**, p 301–312. https://doi.org/10.1016/j.corsci.2011.10.033
25. R. Pinto, M.G.S. Ferreira, M.J. Carmezim and M.F. Montemor, The Corrosion Behaviour of Rare-Earth Containing Magnesium Alloys in Borate Buffer Solution, *Electrochim. Acta*, 2011, **56**, p 1535–1545. https://doi.org/10.1016/j.electacta.2010.09.081
26. L. Bao, Z. Zhang, Q. Le, S. Zhang and J. Cui, Corrosion Behavior and Mechanism of Mg-Y-Zn-Zr Alloys with Various Y/Zn Mole Ratios, *J. Alloy. Compd.*, 2017, **712**, p 15–23. https://doi.org/10.1016/j.jallcom.2017.04.053
27. M. Jamesh, S. Kumar and T.S.N. Sankara Narayanan, Corrosion Behavior of Commercially Pure Mg and ZM21 Mg Alloy in Ringer's Solution–Long Term Evaluation by EIS, *Corros. Sci.*, 2011, **53**, p 645–654. https://doi.org/10.1016/j.corsci.2010.10.011
28. M.I. Jamesh, G. Wu, Y. Zhao, D.R. McKenzie, M.M.M. Bilek and P.K. Chu, Electrochemical Corrosion Behavior of Biodegradable Mg-Y-RE and Mg-Zn-Zr Alloys in Ringer's Solution and Simulated Body Fluid, *Corros. Sci.*, 2015, **91**, p 160–184. https://doi.org/10.1016/j.corsci.2014.11.015
29. M.I. Jamesh, G. Wu, Y. Zhao, D.R. McKenzie, M.M.M. Bilek and P.K. Chu, Effects of Zirconium and Oxygen Plasma Ion Implantation on the Corrosion Behavior of ZK60 Mg Alloy in Simulated Body Fluids, *Corros. Sci.*, 2014, **82**, p 7–26. https://doi.org/10.1016/j.corsci.2013.11.044
30. J. Kim, K.C. Wong, P.C. Wong, S.A. Kulinich, J.B. Metson and K.A.R. Mitchell, Characterization of AZ91 Magnesium Alloy and Organosilane Adsorption on its Surface, *Appl. Surf. Sci.*, 2007, **253**, p 4197–4207. https://doi.org/10.1016/j.apsusc.2006.09.030
31. B.R. Strohmeier and D.M. Hercules, Surface Spectroscopic Characterization of the Interaction Between Zinc Ions and γ-Alumina, *J. Catal.*, 1984, **86**, p 266–279. https://doi.org/10.1016/0021-9517(84)90372-5
32. G.L. Song and A. Atrens, Corrosion Mechanisms of Magnesium Alloys, *Adv. Eng. Mater.*, 1999, **1**, p 11–33. https://doi.org/10.1002/(SICI)1527-2648(199909)1:1%3c11::AID-ADEM11%3e3.0.CO;2-N
33. O. Lunder, K. Nisancioglu, R.S. Hansen, in *Corrosion of Die Cast Magnesium-Aluminum Alloys*, (SAE International, Warrendale, PA, 1993). https://doi.org/10.4271/930755
34. M. Ali, M.A. Hussein and N. Al-Aqeeli, Magnesium-Based Composites and Alloys for Medical Applications: A Review of Mechanical and Corrosion Properties, *J. Alloy. Compd.*, 2019, **792**, p 1162–1190. https://doi.org/10.1016/j.jallcom.2019.04.080
35. A. Bahmani, S. Arthanari and K.S. Shin, Formulation of Corrosion Rate of Magnesium Alloys Using Microstructural Parameters, *J. Magnesium and Alloys.*, 2020, **8**, p 134–149. https://doi.org/10.1016/j.jma.2019.12.001
36. K.D. Ralston and N. Birbilis, Effect of Grain Size on Corrosion: A Review, *Corrosion*, 2010, **66**, p 075005-075005–075013. https://doi.org/10.5006/1.3462912
37. S. Zhang, J. Li, Y. Song, C. Zhao, C. Xie and X. Zhang, Influence of Heat Treatments on In Vitro Degradation Behavior of Mg-6Zn Alloy Studied by Electrochemical Measurements, *Adv. Eng. Mater.*, 2010, **12**, p B170–B174. https://doi.org/10.1002/adem.200980052
38. Y.-C. Zhao, M.-C. Zhao, R. Xu, L. Liu, J.-X. Tao, C. Gao, C. Shuai and A. Atrens, Formation and Characteristic Corrosion Behavior of Alternately Lamellar Arranged α and β in as-Cast AZ91 Mg Alloy,

J. Alloy. Compd., 2019, **770**, p 549–558. https://doi.org/10.1016/j.jallcom.2018.08.103

39. J.-W. Chang, X.-W. Guo, P.-H. Fu, L.-M. Peng and W.-J. Ding, Effect of Heat Treatment on Corrosion and Electrochemical Behaviour of Mg-3Nd-0.2Zn-0.4Zr (wt.%) Alloy, *Electrochim. Acta.*, 2007, **52**, p 3160–3167. https://doi.org/10.1016/j.electacta.2006.09.069
40. J.H. Nordlien, S. Ono, N. Masuko and K. Nisancioglu, A TEM Investigation of Naturally Formed Oxide Films on Pure Magnesium, *Corros. Sci.*, 1997, **39**, p 1397–1414. https://doi.org/10.1016/S0010-938X(97)00037-1
41. J.H. Nordlien, K. NişancioĞu, S. Ono and N. Masuko, Morphology and Structure of Oxide Films Formed on MgAl Alloys by Exposure to Air and Water, *J. Electrochem. Soc.*, 1996, **143**, p 2564. https://doi.org/10.1149/1.1837048
42. S. Leleu, B. Rives, J. Bour, N. Causse and N. Pébère, On the Stability of the Oxides Film Formed on a Magnesium Alloy Containing Rare-Earth Elements, *Electrochim. Acta*, 2018, **290**, p 586–594. https://doi.org/10.1016/j.electacta.2018.08.093
43. Y. Zhang, J.-Y. Li, P.K. Liaw, Xu. Yu-zhao and H.-Y. Lai, Effects of Heat Treatment on the Mechanical Properties and Corrosion Behaviour of the Mg-2Zn-0.2Mn-xNd Alloys, *J. Alloy. Compd.*, 2018, **769**, p 552–565. https://doi.org/10.1016/j.jallcom.2018.07.359
44. Y.L. Song, Y.H. Liu, S.R. Yu, X.Y. Zhu and S.H. Wang, Effect of Neodymium on Microstructure and Corrosion Resistance of AZ91 Magnesium Alloy, *J Mater Sci.*, 2007, **42**, p 4435–4440. https://doi.org/10.1007/s10853-006-0661-z
45. M.Y. Gu, G.L. Wei, W.C. Liu and G.H. Wu, Influence of Neodymium on Microstructure and Corrosion Behavior of Mg-8Li-3Al-2Zn Alloy, *Mater. Corros.*, 2017, **68**, p 436–443. https://doi.org/10.1002/maco.201609141

Publisher's Note Springer Nature remains neutral with regard to jurisdictional claims in published maps and institutional affiliations.

Check for updates

Journal of Biomedical Materials Research Part B: Applied Biomaterials

WILEY

Society For Biomaterials

RESEARCH ARTICLE

Gd Added Mg Alloy for Biodegradable Implant Applications

Arun Kumar Surendran[1,2] | Jithu Jayaraj[1,2] | Rajinikanth Veerappan[2,3] | Manoj Gupta[4] | Srinivasan Amirthalingam[1,2] | Raghu K Gopalan[1,2]

[1]Material Science and Technology Division, CSIR-National Institute for Interdisciplinary Science and Technology, Thiruvananthapuram, India | [2]Academy of Scientific and Innovative Research (AcSIR), Ghaziabad, India | [3]Materials Engineering Department, CSIR-National Metallurgical Laboratory, Jamshedpur, India | [4]Department of Mechanical Engineering, The National University of Singapore, Singapore, Singapore

Correspondence: Srinivasan Amirthalingam (asrinivasan@niist.res.in)

Received: 9 November 2023 | **Revised:** 17 April 2024 | **Accepted:** 9 August 2024

Funding: This work was supported by the Science and Engineering Research Board (SERB, Project numbers: IMRC/AISTDF/CRD/2019/000144 and EMR/2017/001286) and Council of Scientific and Industrial Research, India (CSIR, Project number: MLP0043).

Keywords: cytocompatibility | extrusion | magnesium alloy | subcutaneous implantation

ABSTRACT

Microstructure, mechanical, in vitro and in vivo behavior of extruded Mg alloys with varying Zn/Gd ratios, Mg-2Gd-2Zn-0.5Zr (Zn/Gd = 1), Mg-2Gd-6Zn-0.5Zr (Zn/Gd = 3), and Mg-10Gd-1Zn-0.5Zr (Zn/Gd = 0.1) were investigated. The results revealed that the major secondary phases such as W ($Mg_3Zn_3Gd_2$), $(Mg,Zn)_3Gd$, LPSO (Long period stacking order) and I (Mg_3Zn_6Gd) phase in alloys depended on Zn/Gd ratio. These second phases influenced the mechanical as well as biological characteristics of the alloys. Among studied alloys, Mg-10Gd-1Zn-0.5Zr alloy showed the highest yield strength and tensile strength of 270 (±9.29) and 330 MPa (±15.8), respectively, with a reasonably good elongation of 12% (±2.36). The presence of Gd_2O_3 in the degradation film of Mg-10Gd-1Zn-0.5Zr enhanced the resistance offered by the film, which resulted in its lowest biodegradation, better viability, and cell proliferation under in vitro condition. The short term (subcutaneous implantation in rats for 1 month) in vivo studies showed that the alloy Mg-10Gd-1Zn-0.5Zr degraded at a rate of 0.35 mm/y (±0.02) and did not induce any toxicity to the vital organs.

1 | Introduction

Magnesium and its alloys have been widely researched as a potential biodegradable implant material in recent decades. Magnesium is a vital element in the human body, with an adult requiring a daily intake of 240–420 mg. Use of magnesium alloys can avoid the stress shielding effect observed with permanent metallic implants as the Young's modulus and density of magnesium ($E = 45$ GPa, $\rho = 1.7$ g/cc) are similar to those of human bone ($E = 15$–25 GPa, $\rho = 1.8$–2.1 g/cc). Furthermore, magnesium has been shown to stimulate bone regeneration when used as a bone-regenerative material. The biodegradable nature of magnesium in the body makes it a suitable replacement for permanent implants, eliminating the need for a second surgery to remove the implant. In case of magnesium alloys as implants, the degradation products are typically bio-absorbable and can be excreted through the kidneys. However, the highly active magnesium (−2.37 V vs. SHE) tends to severely degrade in the presence of chloride ions in bodily fluids that may results in the dissolution of the alloy into the body before bone healing is completed. Rapid degradation can also lead to the formation of gas pockets in adjacent tissues, delaying bone healing. Therefore, researchers focus on developing magnesium alloys with high degradation resistance and mechanical strength that can maintain their integrity until bone healing is completed [1–5].

RE added Mg alloys are familiar as addition of RE provide many advantages such as enhancing melt purification and improving the properties. Rare earth elements acts as nucleation sites for various non-metallic inclusions like oxides, sulfide, and nitrides. Rare earth elements forms compounds with these inclusions which are heavier than the surrounding Mg matrix and thus

© 2024 Wiley Periodicals LLC.

they settle readily thus enhancing their removal from the melt by gravitational forces. This purification process concomitantly increases the corrosion resistance, mechanical properties, and overall performance of Mg alloys in various industrial applications. Moreover, the presence of rare earth elements refines the microstructure of Mg alloys, resulting in enhanced mechanical strength, creep resistance, and ductility. Additionally, the incorporation of rare earth elements can also improve the high temperature stability and corrosion resistance of Mg alloys, making them suitable for a wide range of applications [6–10]. Though, certain RE elements such as cerium, praseodymium, and holmium have been reported to be toxic to the body, elements such as gadolinium and neodymium are acceptable up to a specific limits [11, 12]. It's worth mentioning that the Mg-RE based Magnezix screws developed by Syntellix and drug eluting stents (Magmaris) developed by Biotronik, Germany had received CE (Conformité Européene) approval for commercial use in 2013 [13, 14].

Additionally, gadolinium-based particles are used as contrast agents for magnetic resonance imaging. Also, Gd has been shown to possess anti-inflammatory and immunomodulatory properties, which can be beneficial in minimizing adverse tissue reactions and promoting the healing process. While challenges like controlling the degradation rate and managing the release of alloy constituents remain, Gd containing alloys hold potential in the development of safer and more effective biodegradable implants [15–18]. Studies show that the release of Gd from Mg-xGd alloys has been demonstrated to remain below toxicity thresholds in cell culture [12, 19]. Furthermore, Mg-10Gd alloy has exhibited enhanced osteoblast-induced mineralization in cell culture conditions [20]. Cells cultured on Mg-10Gd alloy have demonstrated healthy cellular structures, promoting strong adhesion to the surface [21]. Krüger et al. [22], studied the degradation behavior of Mg-5Gd and Mg-10Gd screw implants and reported that Mg-10Gd exhibited lower degradation rate, and less pronounced texture compared to Mg-5Gd. The weaker texture, characterized by a more random orientation of crystallographic poles within grains, results in favorable mechanical properties [22]. Furthermore, Harmuth et al. [23] demonstrated that it is possible to tailor the mechanical properties of Mg-Gd alloys to meet medical requirements by adjusting the extrusion process and Gd content, without affecting the degradation rate.

Moreover, Mg alloys with the combined Gd and zinc have shown to enhance both strength and corrosion resistance in magnesium alloys. Mg-Zn-Y based alloys are already familiar and subjected to in depth investigations. Gadolinium is also one such RE elements having high solubility (22.8%) in Mg, recently considered as more effective alloying element to Mg. The properties of Mg-Zn-Gd alloy can be tailored with different combination of Zn and Gd additions as Zn/Gd ratio leads to different ternary phases, such as W phase ($Mg_3Zn_3Gd_2$) with a cubic structure, I phase (Mg_3Zn_6Gd) with an icosahedral quasicrystalline structure, and X phase ($Mg_{12}ZnGd$) with a long period stacking order (LPSO) structure [18, 24]. As far as medical applications are concerned, the daily allowable limits of zinc and RE in the human body are around 15 and 4.2 mg, respectively [11, 25].

In spite of these, Gd added Mg alloys are not explored much as like conventional WE43 and Mg-Zn-Ca alloys for biomedical applications. In the present work, three different Mg-Zn-Gd-Zr alloys with different Zn/Gd ratios were prepared to have different ternary phases and studied their mechanical and biological properties in extruded condition.

2 | Materials and Methods

2.1 | Preparation of Mg-Zn-Gd-Zr Alloys

The alloys Mg-2Gd-2Zn-0.5Zr (GZ22), Mg-2Gd-6Zn-0.5Zr (GZ26), and Mg-10Gd-1Zn-0.5Zr (GZ101) were prepared in a resistance furnace under a protective gas mixture of argon and 0.1% sulfur hexafluoride (SF_6). Pure magnesium, gadolinium, zinc granules, and Mg-30 Zirconium master alloy were used for preparation. Magnesium was melted and superheated to 740°C, and then gadolinium was added to the melt. After 20 min, zinc granules were added, followed by the Mg-30Zr master alloy, and the melt was hand-stirred for 2 min to obtain a homogenous composition throughout the melt. The melt was poured into a preheated (350°C) rectangular-shaped cast iron mold. The chemical composition the alloys were determined using ICP-AES (Table 1). Ingots of 35 mm diameter and 40 mm length were machined from the cast blocks and extruded into 10 mm rods. The ingots were preheated at 400°C for 1 h and were extruded at 350°C with an extrusion ratio of approximately 12.25:1.

2.2 | Microstructure Characterization

The morphology and composition analysis of different phases were carried out with a scanning electron microscope (SEM, Carl Zeiss EVO18) with energy-dispersive X-ray spectroscopy (EDS). The samples for microstructural characterization underwent grinding using different grades of SiC papers and by cloth polishing using 1 μm size alumina suspension. The samples were then etched using a solution containing 10 mL distilled water, 100 mL ethanol, 6 g picric acid, and 5 mL glacial acetic acid. The TEM analysis was done in JEOL JEM F 200 with STEM EDA EELS

TABLE 1 | Chemical composition of the developed alloys (wt.%).

	Analyzed chemical composition						
Nominal composition	**Gd**	**Zn**	**Zr**	**Fe**	**Cu**	**Ni**	**Mg**
Mg-2Gd-2Zn-0.5Zr (GZ22)	1.92	2.05	0.42	0.0089	0.0045	0.0020	Bal.
Mg-2Gd-6Zn-0.5Zr (GZ26)	2.08	6.43	0.48	0.0075	0.0034	0.0032	Bal.
Mg-10Gd-1Zn-0.5Zr (GZ101)	10.24	1.40	0.45	0.0110	0.0051	0.0044	Bal.

15524981, 2024, 9, Downloaded from https://onlinelibrary.wiley.com/doi/10.1002/jbm.b.35474 by Srinivasan Amirthalingam - Nti Institute For Interdis. Sci. And Tech , Wiley Online Library on [01/09/2024]. See the Terms and Conditions (https://onlinelibrary.wiley.com/terms-and-conditions) on Wiley Online Library for rules of use; OA articles are governed by the applicable Creative Commons License

HRTEM. The specimens for TEM observations were initially ground to a thickness of 100 μm, then 3 mm discs were punched out and thinned down using ion milling (Gatan precision ion-polishing system). Electron backscatter diffraction (EBSD) analysis was carried out using a Nova Nano SEM 450 with velocity pro EBSD detector at a scan step size of 0.08 μm. The specimens for EBSD analysis was electro polished using a solution having 10% perichloric acid in methanol at 20 V and −15°C. The EBSD data was analyzed using TSL OIM software.

2.3 | Tensile Test

Threaded tensile samples of 6 mm gauge diameter and a gauge length of 25 mm were made from extruded rods according to ASTM standard B557M-10. The tensile testing was carried out at a crosshead speed of 2 mm/min (strain rate: 1.66×10^{-3}) and at room temperature. Minimum four to five samples from each alloy were tested and average values were reported.

2.4 | In Vitro Biodegradation Behavior

2.4.1 | Electrochemical Test

The electrochemical experiments were carried out using an AMETEK Versastat4 instrument. A saturated calomel electrode (SCE), a platinum mesh, and the specimen were used as reference, counter, and working electrodes, respectively. The electrochemical experiments were conducted at 37 ± 1°C with minimum essential medium (MEM) as the electrolyte. The specimen was exposed to α-MEM for around 30 min before open circuit potential (OCP) measurement. A scan rate of 1 mV/s and a scan range of −400 mV to +400 mV concerning OCP value was followed for the Tafel experiment. The impedance values of the alloys were measured in the frequency range from 10^5 to 10^{-1} Hz at open potential with a scanning rate of 2 mV/s, and impedance values were fitted using the corresponding equivalent circuit using ZSimpWin 3.21 software. The experiments were performed in triplicates.

2.4.2 | Immersion Test

The samples were immersed in cell culture medium containing MEM supplemented with 10% fetal bovine serum (BSA) and 1% penicillin for 14 days, maintaining a medium volume to the surface area of sample ratio of 1.25 cm^2/mL according to ISO 10993 under cell culture conditions (37°C, 5% CO_2, 20% O_2, 95% relative humidity). The medium was changed every 2 days to maintain the pH and semi-static conditions. After 14 days of immersion, the specimens were cleaned using distilled water and 100% ethanol. After immersion, the degradation products of the samples were removed by immersing them in a chromic acid solution (180 g/L) for 15 min at room temperature. The weight loss measurement was taken after the 14 days immersion in cell culture medium. The formula used for calculating the degradation rate in millimeters per year (mm/year) is as follows:

$$\text{Degradation rate} = \frac{8.76 \times 10^4 \times \Delta g}{\rho \times A \times t} \quad (1)$$

Where, Δg = weight loss (g), ρ = density of the alloy (g/cm^3), A = exposed area (cm^2), and t = exposure time (h) [26].

2.4.3 | X-ray Photoelectron Spectroscopy (XPS)

The composition of the degradation layer developed on the sample surface after being immersed in cell culture medium for 24 h was analyzed with PHI 5000 VersaProbe II, ULVAC-PHI Inc., USA equipped with a micro-focused monochromatic Al-Kα X-Ray source ($h\nu = 1486.6$ eV) with a spot size of 200 μm and an acceleration voltage of 15 kV. The X-ray Photoelectron Spectroscopy (XPS) data were analyzed using multipak software integrated into the instrument.

2.4.4 | Mechanical Integrity

The tensile samples were immersed in MEM + 10% FBS under cell culture conditions (37°C, 5% CO_2, 20% O_2, 95% relative humidity) for 14 days before testing. To restrict the degradation on the gauge length, the samples were covered using parafilm in such a way that the gauge length of the samples were only exposed to the culture medium. The volume of culture medium to sample surface area of 1.25 cm^2/mL was maintained. The medium was refreshed every 2 to 3 days. After 14 days' immersion period, samples were taken out and cleaned with distilled water. Then the samples were tensile tested at a cross head speed of 0.1 mm/min.

2.5 | In Vitro Cell Culture Tests

2.5.1 | Extract Preparation

The metallic samples (diameter: 10 mm, height: 2 mm) were immersed in cell culture medium (CCM) containing MEM, 10% FBS and 1% penicillin for 3 days by maintaining a medium volume to the surface area of sample ratio of 1.25 cm^2/mL. The supernatant solution was then centrifuged at 3000 rpm for 15 min and filtered using a 0.22 μm filter, and the extract was then used for indirect cell culture studies.

2.5.2 | Indirect Cell Viability Tests

2.5.2.1 | MTT (3-(4,5-Dimethylthiazol-2-Yl) −2,5 Diphenyltetrazolium Bromide) Assay. MTT assays were performed according to ISO 10993:2009 to evaluate the toxicity of the alloys. MG-63 cells (from National Centre for Cell Science [NCCS] Pune) were cultured with CCM and incubated in a CO_2 incubator at 37°C. A cell suspension (100 μL) with CCM containing 1×10^4 cells was seeded in the 96-well cell culture plate. After 24 h, the culture medium was replaced with extracts (100%, 50%, or 25%) and was incubated for 1 and 3 days. After the specified incubation time, the extracts were discarded, and MTT was added to each well (1 μL MTT in 100 μL MEM) and was incubated for 2–4 h in the cell culture conditions. After incubation, 100 μL of dimethyl sulfoxide (DMSO) was added to each well. Viability of cells was determined by measuring the absorbance at 570 nm using a TECAN microplate reader

15524981, 2024, 9, Downloaded from https://onlinelibrary.wiley.com/doi/10.1002/jbm.b.35474 by Srinivasan Amirthalingam - Nil Institute For Interdis. Sci. And Tech. , Wiley Online Library on [01/09/2024]. See the Terms and Conditions (https://onlinelibrary.wiley.com/terms-and-conditions) on Wiley Online Library for rules of use; OA articles are governed by the applicable Creative Commons License

(USA). The assay was performed in triplicates, and the percentage of cell viability was calculated as follows:

$$\text{Cell viability} = \frac{\text{Absorbance of sample}}{\text{Absorbance of control}} \times 100 \quad (2)$$

2.5.2.2 | Elemental Toxicity Evaluation. The chlorides of Mg, Zn, and Gd obtained from Sigma–Aldrich was used for elemental toxicity studies. The chlorides were dissolved in sterile water at a concentration of 50,000 μM. Cell culture medium was used to dilute the chloride solutions to different concentrations. The toxicity study was done using MT assay as explained above.

2.5.2.3 | Live/Dead Staining. A cell suspension (100 μL) with MEM containing 1×10^4 cells was seeded in the 96 well black cell culture plate. After 24 h, the culture medium was replaced with extracts (100%, 50%, or 25%) and was incubated for 1 and 3 days. After the specified incubation time, the extracts were discarded, and wells were washed with 1×-phosphate buffer saline (PBS). The cells were stained using acridine orange and ethidium bromide solution for 10 min. Finally, wells were rinsed with PBS and observed under fluorescence microscope (Olympus IX–83). At least five images were taken and analyzed to quantify the fluorescence using free software ImageJ.

2.5.3 | Inductively Coupled Plasma Mass Spectroscopy (ICP-MS) Analysis

The extract solutions used for viability studies analyzed using ICP-MS to find out the concentration of different elements in the solution. Inductively coupled plasma spectrometer iCAP RQ (Make:Thermo Scientific) equipped with quadrupole mass analyzer and an auto-sampler ASX-280 (Teledyne, CETAC Technologies, USA) was used for the multi-elemental analysis.

2.5.4 | Cell Attachment and Proliferation

2.5.4.1 | DAPI Staining. The metallic samples (diameter: 10 mm, height: 2 mm) were immersed in CCM for 3 days by maintaining a medium volume to the surface area of sample ratio of 1.25 cm^2/mL. After discarding the CCM, 50,000 cells were seeded on top of the samples and incubated for 1 h, followed by adding 3 mL of CCM to the wells containing metallic samples. After 1 and 3 days of culturing, the samples were washed using PBS, then stained using DAPI (1:1000 in MEM) for 15 min. Finally, samples were rinsed with PBS and observed using fluorescence microscope (Olympus IX–83). At least six images were taken and analyzed to quantify the cells using the free software ImageJ.

2.5.4.2 | Cell Observation Using SEM. The cells were seeded on top of the metallic samples as in DAPI staining analysis. After the respective incubation, the cells were fixed in 2.5% glutaraldehyde for 30 min. Then the samples were washed with PBS and subjected to gradual ethanol dehydration with various concentrations of 10%, 20%, 40%, 60%, 80%, or 100% for 10 min each. The samples were air-dried and were images were taken using SEM Carl Zeiss EVO18.

2.6 | In Vivo Studies

2.6.1 | Animal Model and Experimental Design

The animal experiments conducted in this study were approved by the institutional animal ethical committee at KMCH College of Pharmacy, Coimbatore, India (Approval Number: KMCRET/ReRc/Ph.D/33/2021). Sprague dawley rats, aged four to 8 weeks and weighing between 180 and 220 g, were obtained and housed in a controlled, pathogen-free environment throughout the duration of the experiment. The rats were divided into three groups ($n = 3$) and underwent anesthesia using Ketamine hydrochloride injection. Following anesthesia, the rats were shaved, and a subcutaneous injection of buprenorphine (0.6 mg/kg) was administered. After sterilizing the area with betadine, a 20 mm dorsal midline incision was made over the thoracolumbar region. Two tissue scaffolds were inserted on both sides, and the adjacent fascia was released. Segments of cellular porcine pericardium, measuring 20 mm × 20 mm, were placed over the muscle beneath the skin. The samples (5 mm in diameter and 2 mm in height) were subcutaneously implanted without the need for suturing or fixation. The subcutaneous implantation sites were closed using Vicryl 4-0, and topical tetracycline was applied. The rats were then monitored for a period of 30 days post-implantation.

2.6.2 | Histological Evaluation After Surgery

Subcutaneous tissues and vital organs (heart and liver) were harvested after 30 days. The subcutaneous tissues and vital organs were fixed in 10% formalin and embedded in paraffin. The tissue sections were deparaffined by xylol for 5 to 10 min, and xylol was removed by 100% ethanol. The tissue sections were stained using hematoxylin, counter-stained with 0.5% eosin, and observed under microscope for any ultrastructural changes.

2.7 | Statistical Analysis

The data are reported as mean ± standard deviation, and the statistical significance of difference between groups was evaluated using one-way analysis of variance (ANOVA). A significance level of $p < 0.05$ was considered significant. The statistical analyses were conducted using GraphPad Prism 8 software (GraphPad Software Inc., San Diego, CA).

3 | Results and Discussion

3.1 | Microstructures of As-Cast and Extruded Mg-Zn-Gd-Zr Alloys

The SEM micrographs and the EDS analysis of the as-cast alloys are shown in Figure 1 and Table 2, respectively. As the Zn/Gd ratio varied, the microstructures of alloys also showed significant changes. Network-like secondary phases were dominant in GZ22 alloy (Zn/Gd ratio of 1) whereas, skeleton-shaped secondary phases and discrete particles were uniformly distributed in GZ26 alloy (Zn/Gd ratio of

15524981, 2024, 9, Downloaded from https://onlinelibrary.wiley.com/doi/10.1002/jbm.b.35474 by Srinivasan Amirthalingam - Nil Institute For Interdis. Sci. And Tech , Wiley Online Library on [01/09/2024]. See the Terms and Conditions (https://onlinelibrary.wiley.com/terms-and-conditions) on Wiley Online Library for rules of use; OA articles are governed by the applicable Creative Commons License

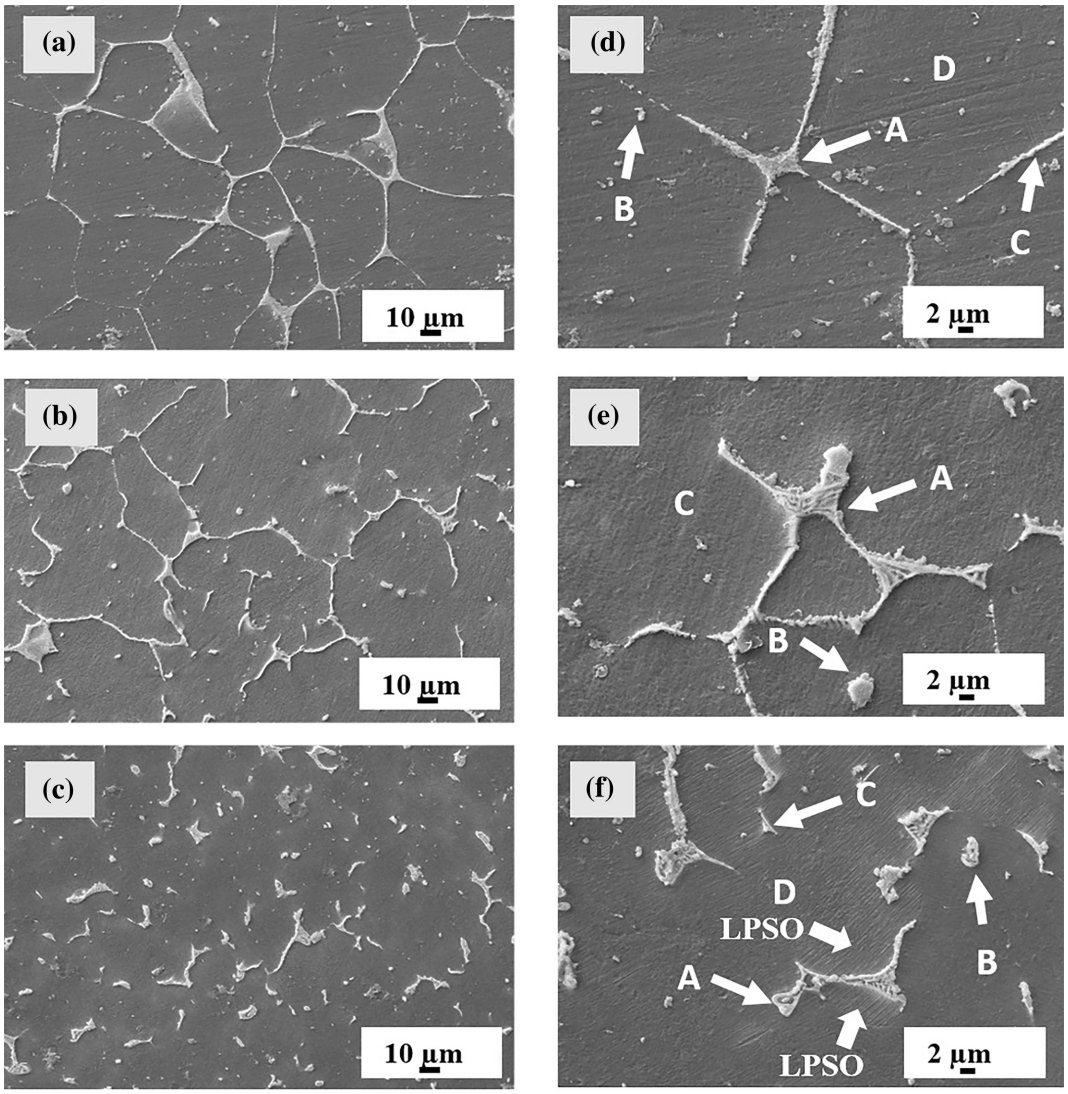

FIGURE 1 | SEM micrographs of as-cast alloys (a, d) GZ22, (b, e) GZ26, and (c, f) GZ101.

3). GZ101 alloy (Zn/Gd ratio of 0.1) exhibited mainly flake-like secondary phases. The EDS analysis revealed that the network-shaped phase (marked as A in Figure 1d) and discrete particle (marked as B in Figure 1d) in GZ22 had a Zn to Gd atomic ratio of 1.92 and 1.79, respectively, which is close to the ideal atomic ratio of 1.5 for $Mg_3Zn_3Gd_2$ phase (W phase). Similarly, the skeleton-shaped phase (marked as A in Figure 1e) in GZ26 had a Zn/Gd atom ratio of 2.23 which is similar to the W phase, and small discrete particles (marked as B in Figure 1e) had a Zn/Gd atom ratio of 7.08 which is close to the ideal Zn/Gd ratio of 6 for Mg_3Zn_6Gd phase (I phase). The flake-like phases (marked as A in Figure 1f) and other discrete phases (marked as B and C in Figure 1f) in GZ101 had a Zn/Gd ratio close to 0.6. However, the stoichiometric composition of this particular phase was not similar to the well-reported $(Mg,Zn)_3Gd$ phase found in high Gd containing Mg-Gd-Zn alloys in the literature [27, 28]. Hence TEM analysis was carried out to identify the phase (Figure 2a) and confirmed that the phase was $(Mg,Zn)_3Gd$ phase with face-center-cubic structure with a lattice constant of 0.73 nm. Also, the TEM micrograph showed the presence of LPSO phase in α-Mg matrix of GZ101 (Figure 2b).

The number of different secondary phases in the alloys was analyzed using SEM analysis by considering at least 800 particles in each alloy (Figure 3). For making the analysis simple, Zn/Gd ratio between 0 and 0.5 was considered as the Mg-Gd binary phase, 0.5 to 1 as $(Mg,Zn)_3Gd$, 1 to 3.5 was considered as the W phase, 3.5 to 8.5 was I phase and greater than 8.5 was considered as Mg-Zn binary phase. The analysis revealed that GZ22 had 75% of the W phase, GZ26 had 43.7% I phase and 29.5% W phase, and GZ101 had 72.7% $(Mg,Zn)_3Gd$ phase. Thus the major ternary phases were found to be the W phase in GZ22, a mixture of W and I phase in GZ26, and $(Mg,Zn)_3Gd$ phase in GZ101 alloy.

In general, the secondary phases in all the alloys seemed to have fragmented during the extrusion process, and the distribution seems almost uniform (Figure 4). The network-shaped W phase observed in the as-cast GZ22 alloy was broken into discrete particles. In the case of GZ26 alloys, the skeleton-shaped W phases were not entirely broken down, as there were still a few phases that retained their cast morphology in the extruded state. The secondary phases in GZ101 alloy were distributed uniformly throughout and had the highest volume fraction of secondary phases.

15524981, 2024, 9, Downloaded from https://onlinelibrary.wiley.com/doi/10.1002/jbm.b.35474 by Srinivasan Amirthalingam - Nti Institute For Interdis. Sci. And Tech. , Wiley Online Library on [01/09/2024]. See the Terms and Conditions (https://onlinelibrary.wiley.com/terms-and-conditions) on Wiley Online Library for rules of use; OA articles are governed by the applicable Creative Commons License

TABLE 2 | EDS analysis of different phases in the alloys.

Position	Elements (atm.%)			Zn/Gd	Phase
	Mg	Zn	Gd		
Figure 1d (A)	85.98	9.22	4.80	1.92	W phase
Figure 1d (B)	94.16	3.75	2.09	1.79	W phase
Figure 1d (C)	84.36	10.48	5.16	2.03	W phase
Figure 1d (D)	99.02	0.7	0.28	—	Matrix
Figure 1e (A)	67.93	22.15	9.92	2.23	W phase
Figure 1e (B)	62.83	32.57	4.60	7.08	I phase
Figure 1e (C)	98.67	1.08	0.25	—	Matrix
Figure 1f (A)	89.88	4	6.12	0.65	$(Mg,Zn)_3Gd$
Figure 1f (B)	91.53	3.27	5.20	0.62	$(Mg,Zn)_3Gd$
Figure 1f (C)	91.68	3.19	5.13	0.62	$(Mg,Zn)_3Gd$
Figure 1f (D)	98.52	0.10	1.38	—	Matrix

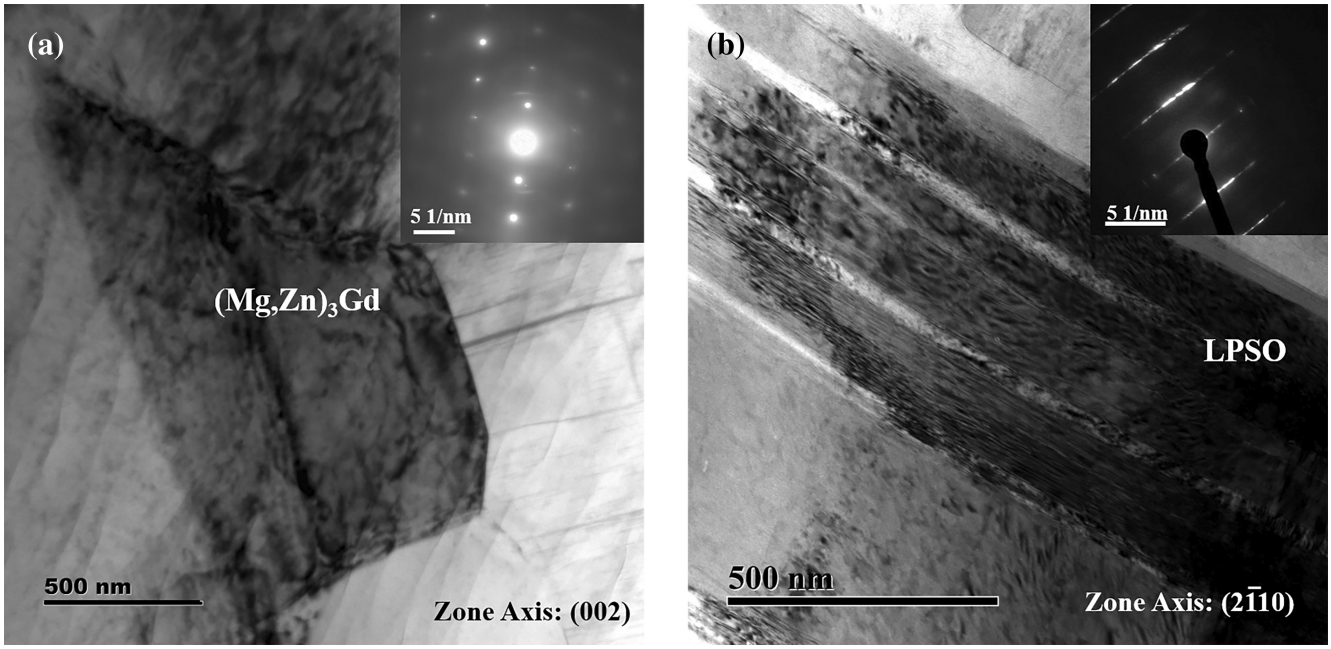

FIGURE 2 | Bright-field TEM micrographs and corresponding diffraction patterns of (a) $(Mg,Zn)_3Gd$ phase and (b) LPSO phase in GZ101 alloy.

The grain boundary overlaid inverse pole figure (IPF) maps (Figure 5a–c) of the alloys showed a bimodal microstructure for all the alloys with fine equiaxed grains and elongated deformed grains. The above observation might be due to an insufficient extrusion ratio (12.25:1) or due to the segregation of rare earth elements at grain boundaries that could hinder the dynamic recrystallization (DRX) by arresting the grain boundary mobility, leading to a non-uniform grain size distribution [29–31]. Kernel average misorientation (KAM) maps were used to identify the localized lattice distortions, and localized deformations and to calculate the geometrically necessary dislocations [32, 33]. Severe dislocation accumulation could be seen in GZ22 (green region in Figure 5d) and GZ101 (Figure 5f) indicating higher strain energy accumulated in these alloys during extrusion. Similarly, the grain orientation spread (GOS) value for the alloys are calculated as 1.67, 2.56, and 5.28 for GZ22, GZ26, and GZ101, respectively. GOS is the ratio of the average deviation of orientations of each point in grain to the average orientation of grains and it is an indicator of the energy stored in the grains [34, 35]. Thus the strain energy stored in the GZ101 alloy (Figure 5i) was the highest, and it had a higher dislocation density. The highest dynamic recrystallization of 65.8% was observed in GZ26 alloy, and a lowest fraction of dynamic recrystallization of 29.7% was observed in GZ101 alloy. The low dynamic recrystallization fraction observed in GZ101 might be due to the presence of the LSPO phase, which has a highly stable and ordered structure that could resist deformation and delayed the DRX. The

15524981, 2024, 9, Downloaded from https://onlinelibrary.wiley.com/doi/10.1002/jbm.b.35474 by Srinivasan Amirthalingam - Nil Institute For Interdis. Sci. And Tech , Wiley Online Library on [01/09/2024]. See the Terms and Conditions (https://onlinelibrary.wiley.com/terms-and-conditions) on Wiley Online Library for rules of use; OA articles are governed by the applicable Creative Commons License

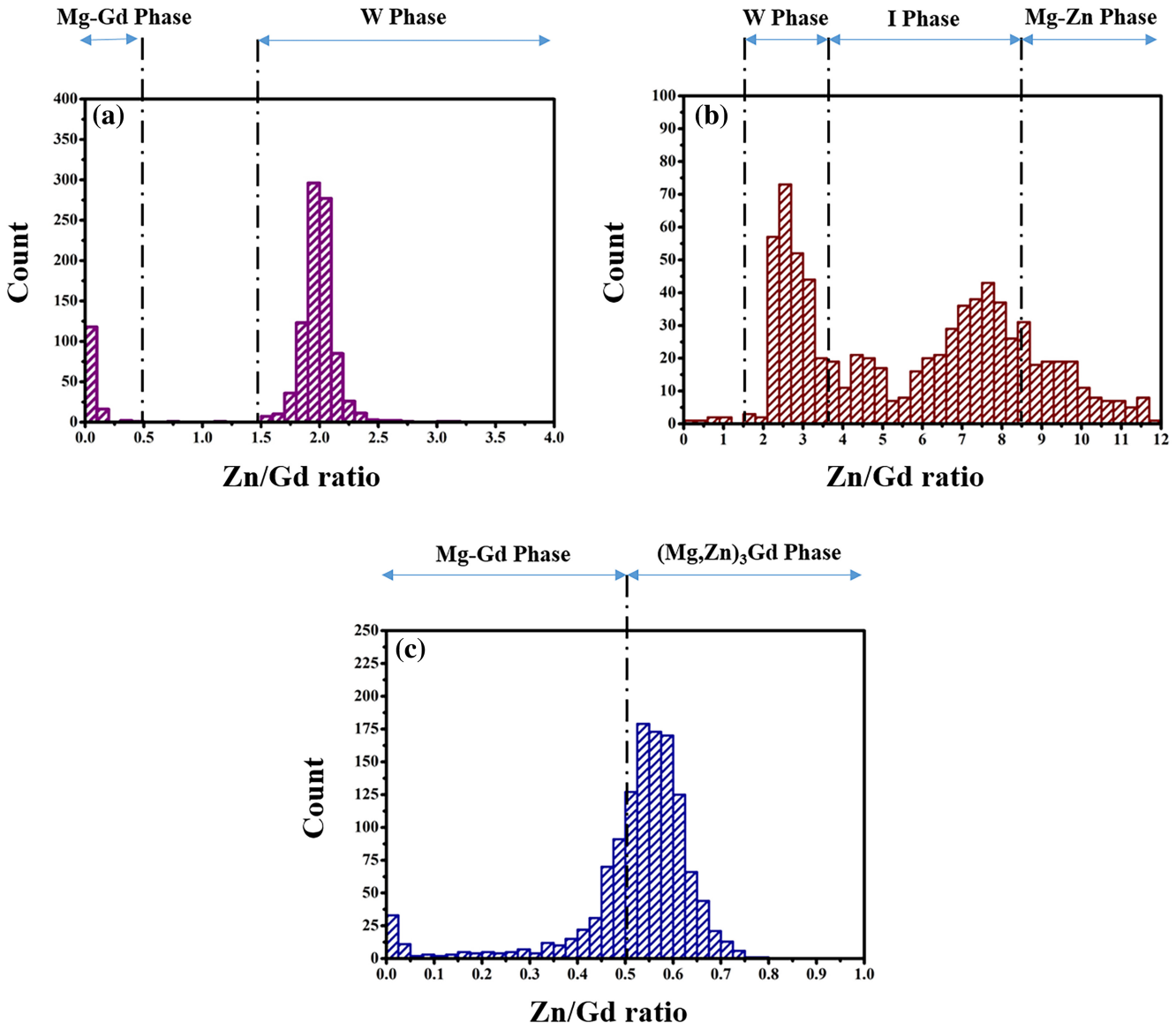

FIGURE 3 | The number of different ternary phases in as-cast alloys (a) GZ22, (b) GZ26, and (c) GZ101.

average grain size of the dynamically recrystallized grains in all three alloys was similar, 1.85, 3.5, and 1.2 μm for GZ22, GZ26, and GZ101 alloys, respectively (refer Figure 6).

3.2 | Tensile Properties

The tensile properties of the alloys (YS, UTS, and % elongation) are summarized in Table 3, and the corresponding stress–strain curves are shown in Figure 7. The GZ26 alloy had the lowest YS of 210 MPa, but it had the highest elongation of 18.5%. On the other hand, the GZ101 alloy showed the highest YS and UTS of 270 and 328 MPa, respectively. The tensile properties of the alloys can be influenced by the factors such as grain size, dislocation density, secondary phases present, and texture development during extrusion. Since the DRXed grain size was almost similar for all the alloys, the influence of grain size on strength enhancement might be marginal. The bimodal microstructure of fine and coarse grains observed in the alloys led to an excellent combination to improve both strength and ductility. The coarse grains can accommodate more dislocations and improve ductility through enhanced slip activities, while the refined grains result in more grain boundaries, leading to enhancement of strength through the pile-up of dislocations [33, 36]. The dislocation density in the extruded alloys was significantly different, which had a significant impact on the mechanical properties. The increase in dislocation density induces a higher strain-hardening effect, as the flow stress is proportional to the dislocation density [37]. This is in agreement with the fact that the GZ101 alloy, with the highest dislocation density, showed the highest tensile strength, while the GZ26 alloy, with the lowest dislocation density, showed the lowest yield strength.

Even though the dislocation density and grain size of the GZ22 and GZ101 alloys were almost similar, the yield strength was significantly lower for the GZ22 alloy with respect to GZ101. According to Schmid law, the decrease in the Schmid factor will increase the yield strength of the material [38], as $\sigma = \frac{\tau}{m}$; σ is the yield strength of the material, τ is the critically resolved shear

15524981, 2024, 9, Downloaded from https://onlinelibrary.wiley.com/doi/10.1002/jbm.b.35474 by Srinivasan Amirthalingam - Nti Institute For Inerdis. Sci. And Tech. , Wiley Online Library on [01/09/2024]. See the Terms and Conditions (https://onlinelibrary.wiley.com/terms-and-conditions) on Wiley Online Library for rules of use; OA articles are governed by the applicable Creative Commons License

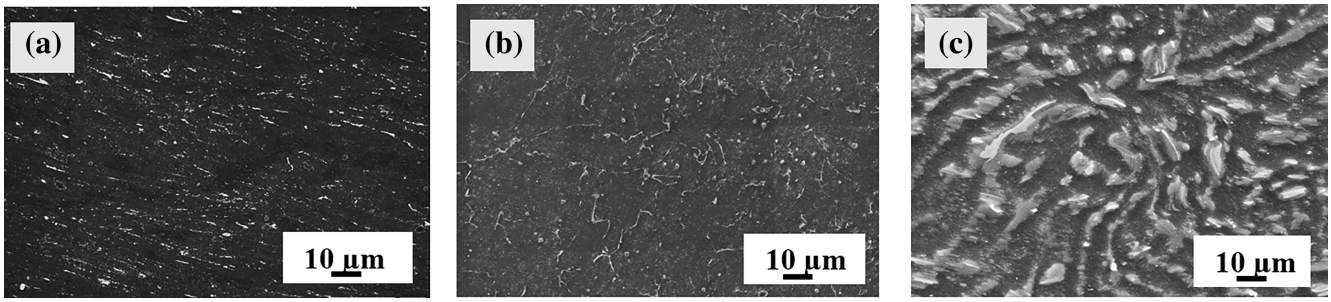

FIGURE 4 | SEM micrographs of extruded alloys (a) GZ22, (b) GZ26, and (c) GZ101.

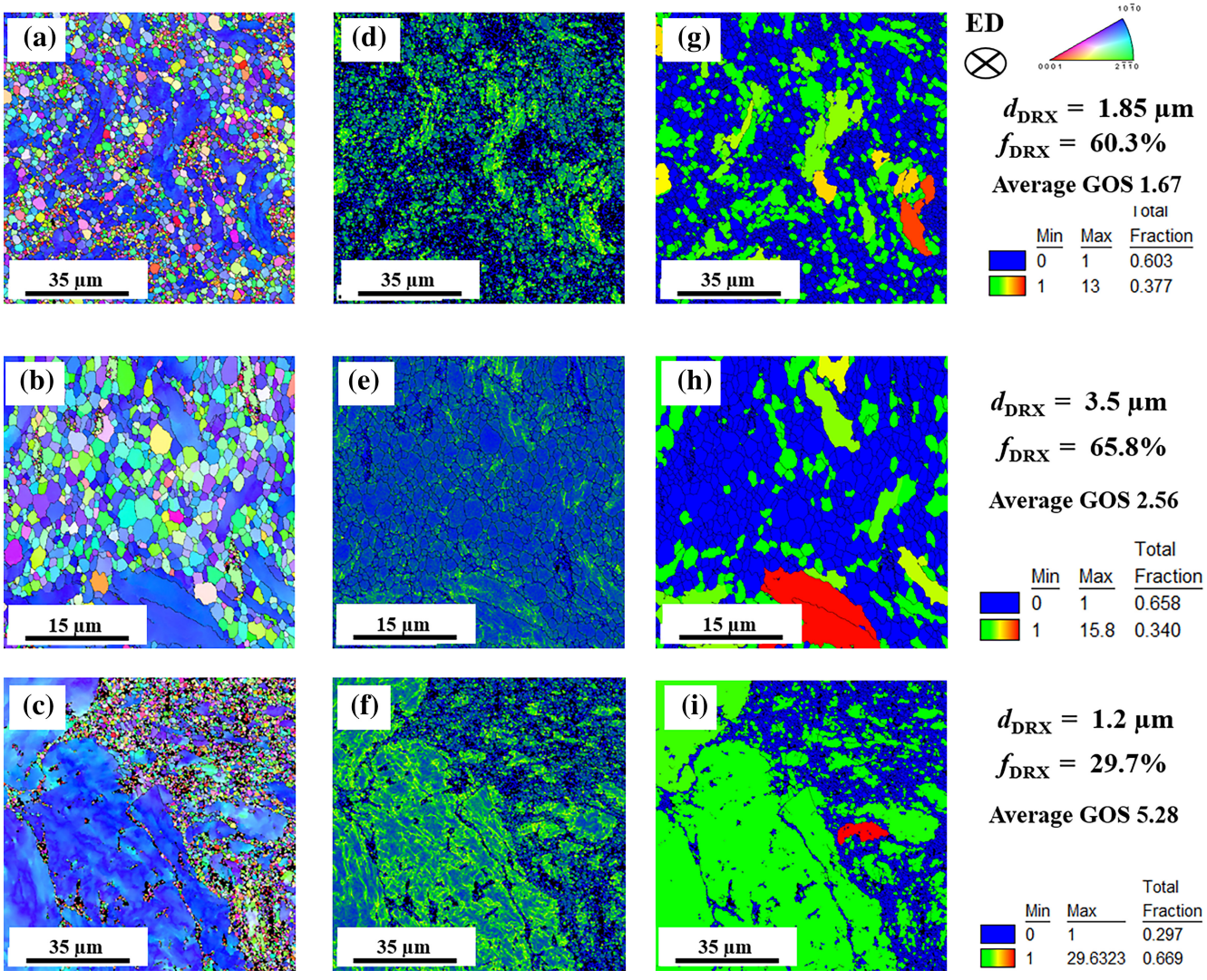

FIGURE 5 | IPF (a–c), KAM maps (d–f), and GOS maps (g–i) of GZ alloys: (a), (d), and (g) GZ22, (b), (e), and (h) GZ26, and (c), (f), and (i) GZ101.

stress and m is the Schmid factor of the material. In the present study, the average Schmid factor calculated using TSL OIM software was 0.33, 0.34, and 0.24 for alloys GZ22, GZ26, and GZ101, respectively. Thus, the low Schmid factor also contributed to the better yield strength of the GZ101 alloy.

The influence of secondary phases also needs to be carefully investigated, as the ternary phases present in the alloys were different. The SEM micrographs of the fracture surfaces of the tensile test samples are shown in Figure 8. The fracture surface of the GZ22 (Figure 8a) alloy primarily consisted of dimples and micro-voids (marked by dotted black circles), indicating ductile fracture. The higher magnification image (Figure 8d) shows that the cracks originated near the secondary phase and the crack spread through the matrix. The EDS analysis revealed that the second phase was the W phase and the crack initiating near the phase-matrix interface that reinforced the fact that the W phase is incoherent with the Mg matrix. The fracture surface of GZ26 (Figure 8b) alloy also had microvoids and dimples (marked by dotted black circles) as well as cleavages (red arrows in Figure 8b). However, the dominant presence of dimples suggested that the alloy also

15524981, 2024, 9, Downloaded from https://onlinelibrary.wiley.com/doi/10.1002/jbm.b.35474 by Srinivasan Amirthalingam - Nti Institute For Inerdis. Sci. And Tech. , Wiley Online Library on [01/09/2024]. See the Terms and Conditions (https://onlinelibrary.wiley.com/terms-and-conditions) on Wiley Online Library for rules of use; OA articles are governed by the applicable Creative Commons License

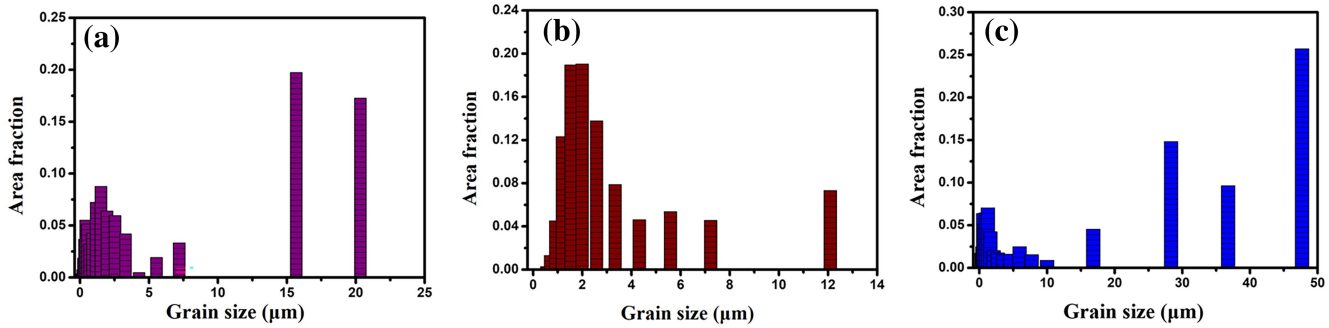

FIGURE 6 | Grain size distribution of alloys (a) GZ22, (b) GZ26, and (c) GZ101.

TABLE 3 | Yield strength (YS), ultimate tensile strength (UTS), and elongation (%) of extruded alloys.

Alloy	YS (MPa)	UTS (MPa)	% Elongation
GZ22	220 (±6.37)	260 (±7.86)	16.2 (±2.23)
GZ26	210 (±14.10)	255 (±13.64)	18.5 (±1.45)
GZ101	270 (±9.29)	328 (±15.8)	12.76 (±2.36)

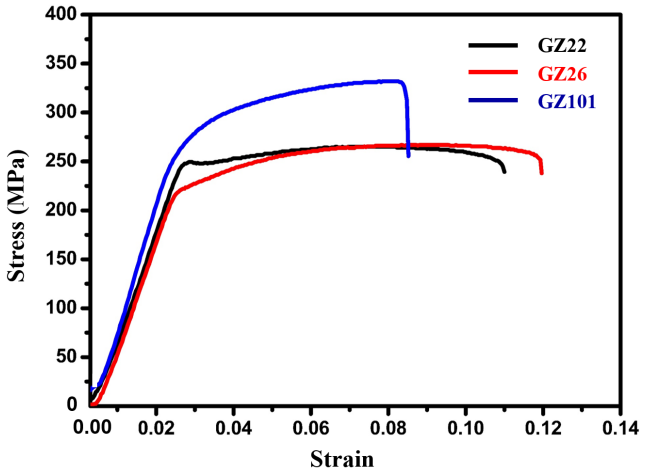

FIGURE 7 | Tensile stress–strain curves of the extruded alloys.

exhibited ductile fracture. The higher magnification SEM micrographs show that the crack spread through the W phase (marked in white arrows Figure 8e), whereas the I phase (marked in yellow arrows Figure 8e) seemed to be intact suggesting that the phase was coherent. The fracture surface of GZ101 alloy showed a mixed fracture mode as it had dimples and microvoids at certain locations, (marked in black dotted circles Figure 8c) and the facets and cleavages (marked in red arrows Figure 8c) in most of the regions. High-magnification SEM images also revealed the presence of few Mg-Gd binary particles (confirmed by EDS) (Figure 8f).

The results also showed that the increase in the yield strength of the alloys was accompanied by a reduction in ductility (as seen in Table 3). It is a well-known phenomenon in Mg alloys that the poor ductility is due to the difficulty in activating <c+a> pyramidal dislocations. The deformation mechanism of Mg alloys is dominated by the basal slip of {0001} <11–20> which has a low critically resolved shear stress. However, basal slip cannot accommodate strain along the c-axis and as a result; the alloys are at risk of failure at even low strain. Thus, activating slip in other directions through alloying or secondary processing can improve ductility [33, 34].

The addition of REEs can result in a weakening of the basal texture of the material as they can inhibit or suppress the growth of the basal texture [39–41]. The basal texture in magnesium alloys is caused by the preferred orientation of the material's hexagonal close-packed (HCP) crystal structure. The addition of REEs can disrupt the formation of the preferred orientation by altering the nucleation and growth behavior of the grains in the material that can result in a more random distribution of crystal orientations and weakening of the basal texture [42, 43]. The REEs can also form complex intermetallic compounds with magnesium, further disrupting the basal texture's growth. These compounds can act as nucleation sites for new grains, leading to a more uniform distribution of crystal orientations in the material [44, 45]. In the present study, inverse pole figure analysis indicated that the GZ22 and GZ26 alloys had weak basal component (000) (Figure 9a,b) but exhibited strong prismatic (1010) component (Figure 9a,b) contributed in their better ductility. Similarly, the weak prismatic texture in the GZ101 alloy (Figure 9c), might be the reason for its lowest ductility.

3.3 | Electrochemical Corrosion Measurement

The potentiodynamic polarization curves and the Tafel fitting values of the alloys immersed in α-MEM for 30 min are presented in Figure 10 and Table 4, respectively. The most negative E_{corr} and lowest i_{corr} values were obtained for the GZ101 alloy, while the most positive E_{corr} and highest i_{corr} values were obtained for the GZ26 alloy. Immediately after Mg alloys are immersed in MEM, electrochemical cells are formed and in most cases α-Mg matrix serve as the anode and the second phases serve as the cathode. The standard electrode potentials of Mg, Gd, Zn, and Zr are −2.372, −2.279, −0.7618, and −1.45 V, respectively. The alloy (GZ26) having the highest amount of Zn had the highest positive E_{corr} value, and the alloy (GZ101) with the lowest amount of Zn and the highest amount of Gd had the E_{corr} shift towards a more negative value. In addition, the highest i_{corr} (64.98 μA/cm^2) observed for GZ26, and the lowest i_{corr} (25.12 μA/cm^2) observed for GZ101 alloy indicated

15524981, 2024, 9, Downloaded from https://onlinelibrary.wiley.com/doi/10.1002/jbm.b.35474 by Srinivasan Amirthalingam - Nti Institute For Interdis. Sci. And Tech , Wiley Online Library on [01/09/2024]. See the Terms and Conditions (https://onlinelibrary.wiley.com/terms-and-conditions) on Wiley Online Library for rules of use; OA articles are governed by the applicable Creative Commons License

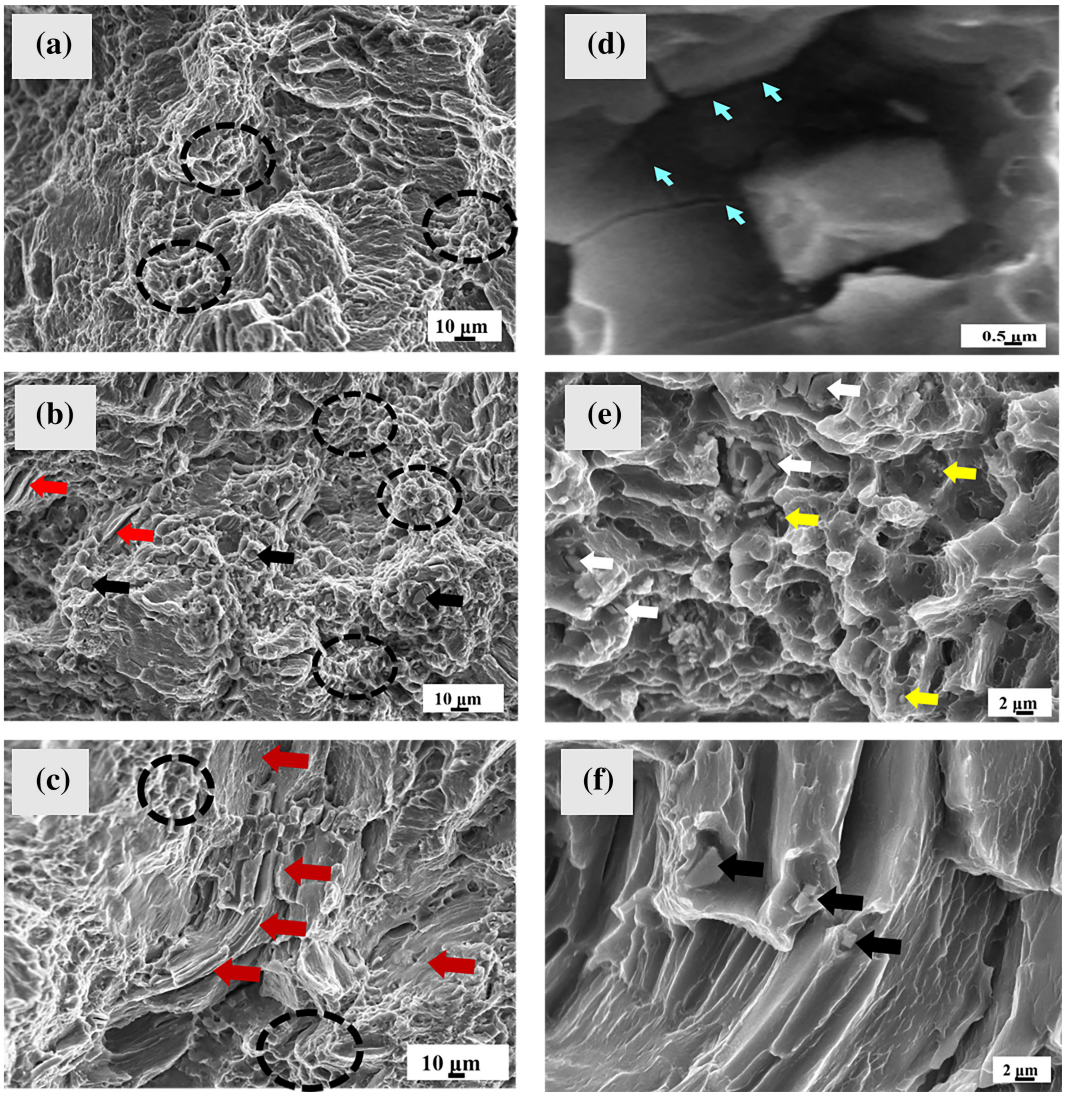

FIGURE 8 | SEM micrographs of fractured tensile samples of (a, d) GZ22, (b, e) GZ26, and (c, f) GZ101.

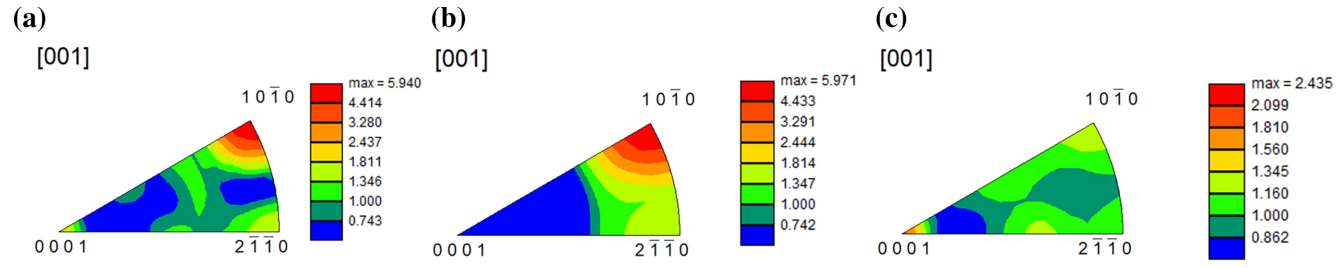

FIGURE 9 | Inverse pole figures of (a) GZ22, (b) GZ26, and (c) GZ101 alloy.

that GZ26 had the lowest degradation resistance and GZ101 had the highest degradation resistance. The above observations suggested that the presence of Gd in the alloy improves the degradation resistance, while the presence of Zn increases the corrosion susceptibility.

The EIS analysis of the alloys was performed using Nyquist and Bode plots (Figure 11). The Nyquist plots (Figure 11a) of the GZ22 and GZ26 alloys were almost similar, suggesting that the corrosion rates and mechanisms were similar. The diameter of the Nyquist plot (Figure 11a) of the GZ101 alloy was almost double compared to the other alloys, indicating its better corrosion resistance. In addition, the inductive loop was absent in all the alloys, suggesting that pitting corrosion was not initiated [46, 47]. The results were also plotted in Bode plots (log Z_{mod} vs. log f, and phase angle vs. log f [Figure 11b,c]). The Z_{mod} of the alloys (Figure 11b) increased in the following order: GZ26 ($600\,\Omega\,cm^2$) < GZ22 ($605\,\Omega\,cm^2$) < GZ101

15524981, 2024, 9, Downloaded from https://onlinelibrary.wiley.com/doi/10.1002/jbm.b.35474 by Srinivasan Amirthalingam - Nti Institute For Inerdis. Sci. And Tech , Wiley Online Library on [01/09/2024]. See the Terms and Conditions (https://onlinelibrary.wiley.com/terms-and-conditions) on Wiley Online Library for rules of use; OA articles are governed by the applicable Creative Commons License

(1200 Ω cm^2). The Bode plots also revealed that there were no sudden dips indicating no pitting corrosion associated with any of the alloys.

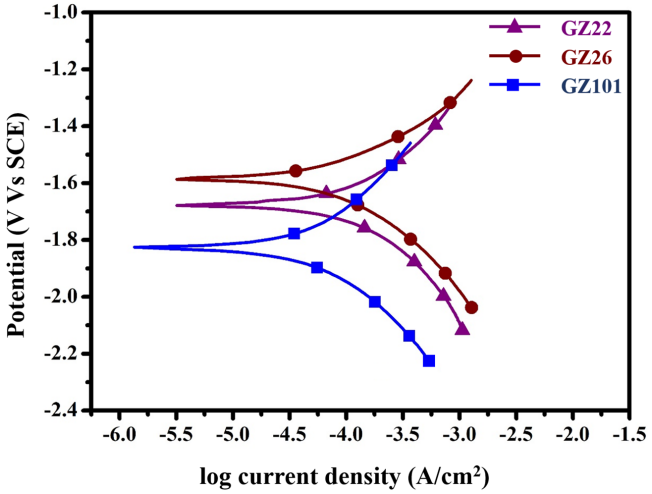

FIGURE 10 | Polarization curves of extruded alloys in α-MEM solution at 37°C.

The EIS spectra of the alloys were fitted using the ZSimpWin 3.20 software with the electrochemical circuit as shown in Figure 11d for GZ22 and GZ26 alloys and Figure 11e for the GZ101 alloy. The fitting values are presented in Table 5. The R_s indicate the solution resistance, R_0 represents the charge transfer resistance, CPE_0 represents the double layer capacitance, R_1 represents the resistance to mass transport and CPE_1 indicates the corresponding capacitance, and R_2 and CPE_2 indicate the film resistance. The GZ22 and GZ26 alloys had two-time constants, while the GZ101 alloy had three-time constants. The first time constant representing the capacitive loop in the higher frequency region is attributed to the charge transfer resistance.

TABLE 4 | E_{corr} and i_{corr} values of extruded alloys (calculated from Tafel plots: Polarization measurements done in α-MEM solution at 37°C).

Alloy	E_{corr} (mV vs. SCE)	i_{corr} (μA/cm^2)
GZ22	−1680 (±85)	58.23 (±3.5)
GZ26	−1590 (±75)	64.98 (±6.7)
GZ101	−1820 (±50)	25.12 (±2.8)

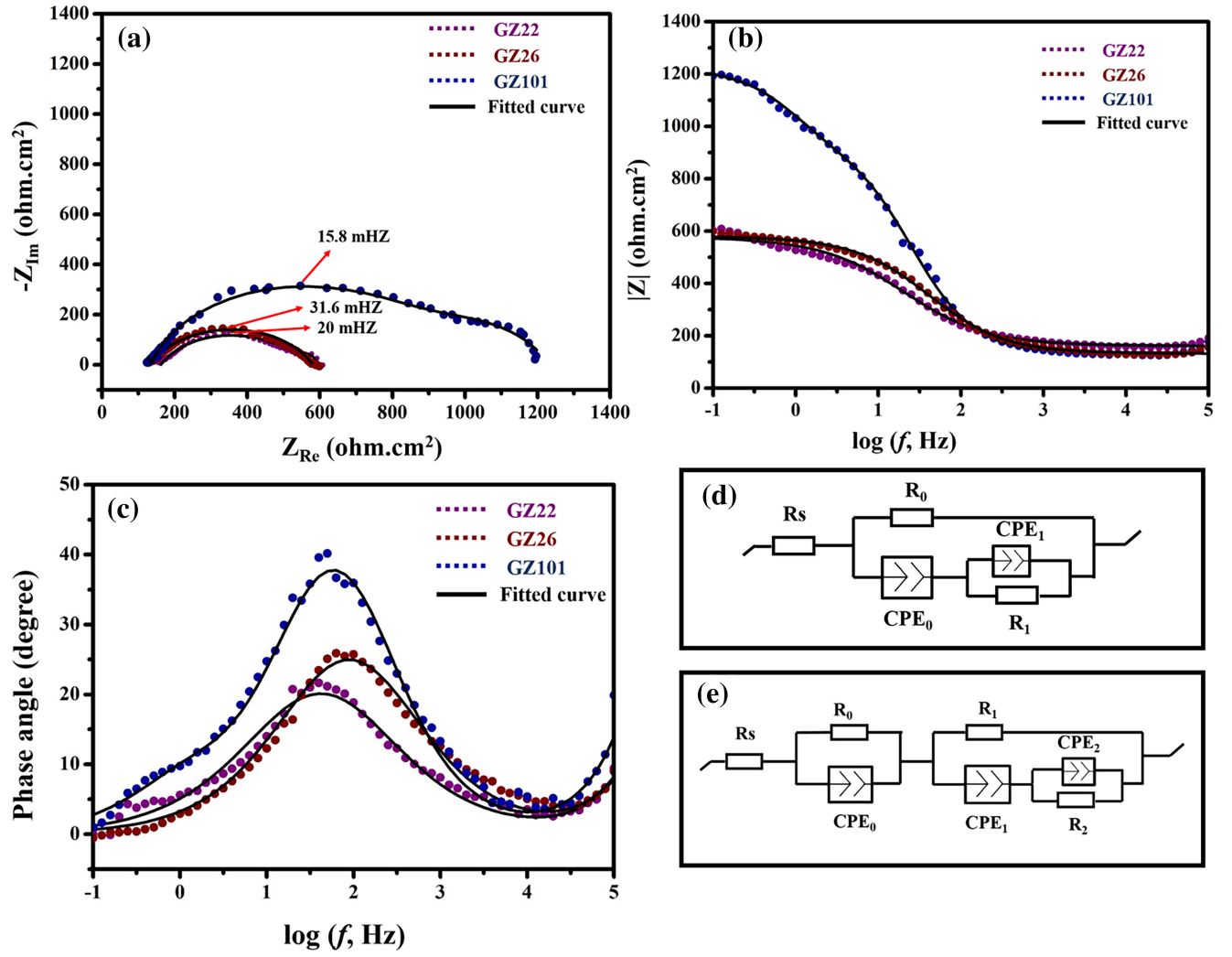

FIGURE 11 | (a) Nyquist plots, (b) Bode plots of log Z_{mod} versus log *f*, (c) Bode plot of Phase angle versus log *f*, of alloys measured in α- MEM solution at 37°C; equivalent circuits used to fit Nyquist and Bode plots of the alloys (d) GZ22 and GZ26 (e) GZ101.

15524981, 2024, 9, Downloaded from https://onlinelibrary.wiley.com/doi/10.1002/jbm.b.35474 by Srinivasan Amirthalingam - Nti Institute For Interdis. Sci. And Tech , Wiley Online Library on [01/09/2024]. See the Terms and Conditions (https://onlinelibrary.wiley.com/terms-and-conditions) on Wiley Online Library for rules of use; OA articles are governed by the applicable Creative Commons License

TABLE 5 | The fitted values of EIS measurements of alloys using equivalent circuits shown in Figure 9.

Alloy	R_s (Ωcm^2)	R_0 (Ωcm^2)	CPE_0 ($S^n/\Omega cm^2$)	n	R_1 (Ωcm^2)	$CPE_1 \times 10^{-5}$ ($S^n/\Omega cm^2$)	n_1	R_2 (Ωcm^2)	$CPE_2 \times 10^{-5}$ ($S^n/\Omega cm^2$)	n_2	$Rp = (R_0 + R_1 + R_2)$ (Ωcm^2)
GZ22	48.73 (±3.15)	386.8 (±25.06)	6.6×10^{-6} ($\pm 0.3 \times 10^{-6}$)	0.95 (±0.05)	162.1 (±10.5)	9.02 (±0.5)	0.69 (±0.04)	NA	NA	NA	548.9 (±35.56)
GZ26	39.6 (±2.58)	370.5 (±20.2)	4×10^{-6} ($\pm 0.24 \times 10^{-6}$)	0.98 (±0.02)	170 (±12.2)	4.98 (±0.25)	0.72 (±0.05)	NA	NA	NA	540.5 (±32.4)
GZ101	21.09 (±1.5)	273.5 (±15.8)	2.8×10^{-9} ($\pm 0.1 \times 10^{-9}$)	0.97 (±0.06)	114.5 (±6.2)	2.5 (±0.22)	0.8 (±0.045)	807.2 (±67.98)	87.47 (±4.5)	0.83 (±0.12)	1195.2 (±89.9)

The second time constant representing the capacitive loop in the medium frequency region is due to the diffusion of ions from the electrolyte to the metal surface. The third time constant observed in GZ101 represents the resistance offered by the protective film formed on the surface. GZ101 showed highest polarization resistance, R_p ($R_0 + R_1$ or $R_0 + R_1 + R_2$), (1195.2 Ωcm^2), and exhibited low CPE_0 value (2.8×10^{-9} $Sn/\Omega cm^2$) compared to that of the GZ22 (6.6×10^{-6} $Sn/\Omega cm^2$) and GZ26 (4×10^{-6} $Sn/\Omega cm^2$) alloys (Table 5). The low CPE_0 value indicated that corrosion was restricted to minimum area in GZ101.

3.4 | Immersion Test

The electrochemical experiments are short-term experiments that give an idea about the initial behavior of the alloys in the degradation medium. For long-term analysis of the degradation behavior, the alloys were immersed in cell culture medium for 14 days by maintaining the pH between 7.4 and 8. The results (Figure 12a) showed that the degradation rate was lowest for the GZ101 alloy (0.21 mm/year), similar to the electrochemical results. Though, the electrochemical corrosion analysis revealed that the initial corrosion resistance of the alloys was almost similar for GZ22 and GZ26 alloys, 14 days of immersion test in the cell culture medium suggested that the degradation rate of the GZ26 alloy (0.75 mm/year) was almost double that of the GZ22 alloy (0.38 mm/year). The degradation surface of the alloys after 14 days of immersion (Figure 12b) showed that the GZ26 alloy suffered severe pitting corrosion while the GZ22 had a shallow corroded area. However, the GZ101 alloy showed no signs of pits, and the surface exhibited a uniformly corroded region indicating its superior resistance to degradation in cell culture medium. The cross-section morphology of the degraded surface of the alloys was observed using SEM (Figure 13), and it was found that the GZ101 alloy had no signs of degradation spreading into the interior. In contrast, the GZ22 and GZ26 alloys had indications of pitting corrosion, with severe pitting observed in the GZ26 alloy. The pit formation in the alloys was spreading into the grain interior adjacent to the secondary phases (shown in the inset of Figure 13b), indicating that these phases were cathodic to the surrounding matrix.

Factors such as secondary phases, grain size, texture, and the degradation layer can influence the degradation of Mg alloys [48, 49]. In general, the degradation rate increases with an increase in the number of secondary phases in a Mg alloy due to the generation of more micro-galvanic sites [50]. However, in the present study, the lowest degradation rate was observed for the GZ101 alloy, which had the highest volume fraction of secondary phases, indicating that the ill effect of volume fraction of secondary phases was nullified by other factors. Likewise, the grain size also seemed to have a marginal effect on the degradation rate of the alloys, as the measured grain size of the extruded alloys was almost similar. However, the EBSD analysis indicated that the amount of strain stored in the alloys was significantly different after extrusion. Although few reports suggested that the accumulation of dislocation in the grains increase the degradation rate of the alloys, in the present study, GZ101 with the highest dislocation density showed the lowest degradation rate, and GZ26 with the lowest dislocation density showed the highest degradation rate (Figure 5) [48, 50]. On the other hand, the texture of the alloys also plays a crucial role in determining their degradation

15524981, 2024, 9, Downloaded from https://onlinelibrary.wiley.com/doi/10.1002/jbm.b.35474 by Srinivasan Amirthalingam - Nil Institute For Interdis. Sci. And Tech , Wiley Online Library on [01/09/2024]. See the Terms and Conditions (https://onlinelibrary.wiley.com/terms-and-conditions) on Wiley Online Library for rules of use; OA articles are governed by the applicable Creative Commons License

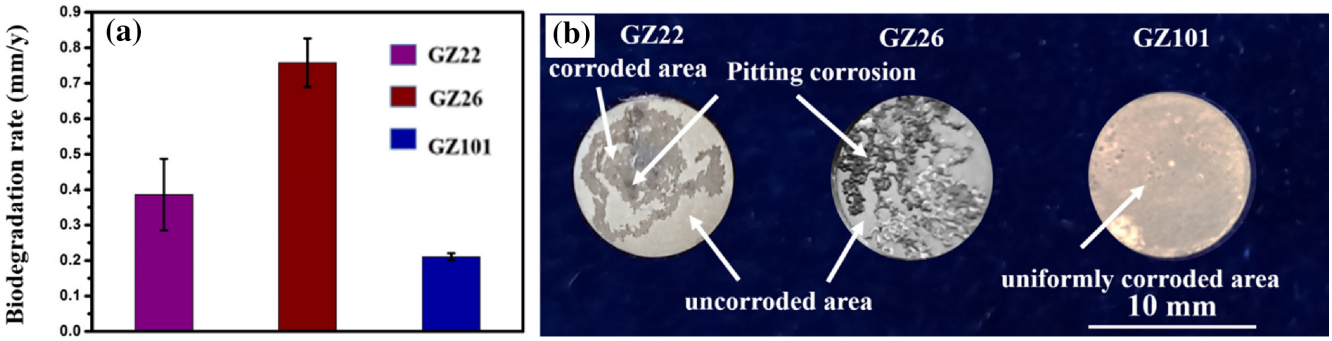

FIGURE 12 | (a) Degradation rate of alloys immersed in cell culture medium for 14 days, (b) Photographs of degraded samples after immersed in cell culture medium for 14 days. Values are the mean ± SD, $n = 4$, $^{**}p < 0.01$, $^{****}p < 0.0001$.

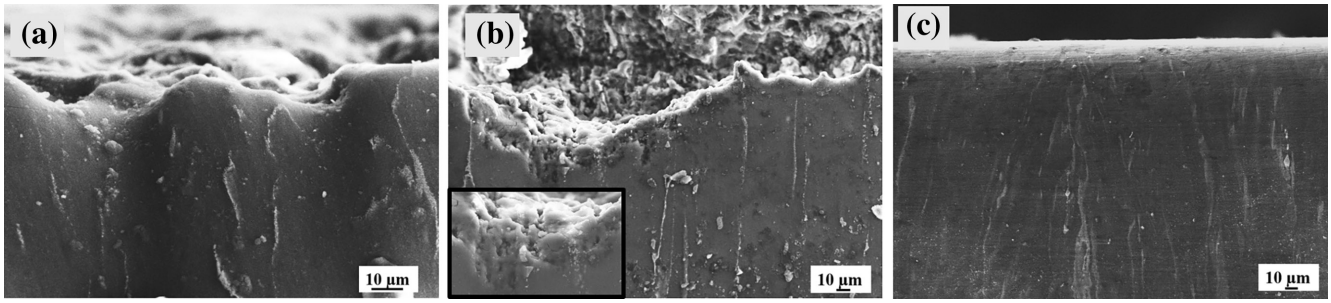

FIGURE 13 | Degradation morphology of the samples (cross section) immersed in cell culture medium for 14 days (after the degradation product removal) (a) GZ22, (b) GZ26, and (c) GZ101.

resistance [38, 51]. The basal plane {0001} in Mg alloys has a lower surface energy compared to the prism planes {1010} and {1120}. This results in the basal plane being more resistant to degradation than the prism planes. The reported theoretical corrosion rate of the prism planes is also much higher than that of the basal planes, further highlighting the importance of texture in determining corrosion resistance [52, 53]. For instance, Song et al. [54] found that the presence of a dominant basal plane in AZ31 alloy contributed to its better resistance. Similarly, Xin et al. [51] reported that the high intensity of {1010} and {1120} planes in rolled AZ31 alloy leads to its poor corrosion resistance in 3.5 wt.% NaCl. The pole figures that showed the texture of the alloys studied in the present study in terms of the orientation of the crystals are presented in Figure 14. A very weak basal component was observed with GZ26 alloy, indicating that it had a high proportion of prismatic planes, which are normally more susceptible to corrosion. On the other hand, GZ22 and GZ101 showed a high intensity of the basal component and a similar texture intensity in the prismatic planes. Still, their degradation resistance was found to be significantly different from each other. The above observed discrepancies might be due to the characteristics of degradation layers formed during degradation.

The XPS analysis of the degradation layer formed on the alloys immersed in cell culture medium for 24 h was done, and the depth profiling measurement was also carried out till 400 nm (Sputtering was limited to 400 nm due to the safety concerns and limitation of the machine). Depth profile (DP) analysis showed that throughout the thickness of the degradation layer, the elements such as O, Ca, and Mg did not have significant changes in the atomic concentrations indicating that the distribution of these elements was almost uniform throughout the degradation layers in all the alloys (Figure 15). Moreover, the presence of Gd was not detected in GZ22, and GZ26 alloys, and Zn was absent in the degradation layer of GZ101 alloy. The DP-XPS spectra of O1s and Mg2p of all the alloys were almost similar, and hence for representation, only DP-XPS spectra of GZ101 alloy are shown in Figure 16. The binding energy (BE) peaks of O1s (Figure 16a) centered at 530.5, 532.3, and 533.5 eV were attributed to the presence of oxide, phosphate, and hydroxide states of oxygen, respectively [55]. The Mg2p spectra (Figure 16b) of the surface of the alloy showed the presence of $MgCO_3$ (50.81 eV) as well as $Mg(OH)_2$ (49.7 eV). At 200 nm depth, the presence of MgO (51.1 eV) along with $MgCO_3$ and $Mg(OH)_2$ was observed [56]. The Ca2p spectra of GZ101 (Figure 16c) confirmed the presence of CaO (350.5 eV) and hydroxyapatite ($Ca_{10}(PO_4)_6(OH)_2$ [347.7 eV]) in the degradation layer [57, 58]. Though the presence of CaO (350.5 eV) and hydroxyapatite ($Ca_{10}(PO_4)_6(OH)_2$ [347.7 eV]) was observed from the Ca2P spectra of GZ26 (Figure 17a), unlike in case of GZ101, intensity of $Ca_{10}(PO_4)_6(OH)_2$ was lower compared to that of CaO suggesting that more hydroxyapatite deposition occurred on the surface of GZ101 alloy. The Gd4d spectra (Figure 17b) from GZ101 alloy confirmed the presence of Gd_2O_3 (143.5 and 141.4 eV), and Zn2p3 spectra (Figure 17c) from GZ26 alloy showed that the degradation layer comprised ZnO (1021.9 eV) [59].

Thus the degradation layer of GZ22 and GZ26 alloys consisted of $Mg(OH)_2$, MgO, $MgCO_3$, $Ca_{10}(PO_4)_6(OH)_2$, CaO, and ZnO, whereas GZ101 alloy had Gd_2O_3 in the layer in addition to other said compounds above. The presence of Gd_2O_3 along with $MgCO_3$, $Ca_{10}(PO_4)_6(OH)_2$, and CaO made the otherwise porous oxide layer of $Mg(OH)_2$ and MgO more compact in GZ101 alloy, and contributed greatly to the observed superior resistance of GZ101 alloys [60, 61].

15524981, 2024, 9, Downloaded from https://onlinelibrary.wiley.com/doi/10.1002/jbm.b.35474 by Srinivasan Amirthalingam - Nil Institute For Interdis. Sci. And Tech , Wiley Online Library on [01/09/2024]. See the Terms and Conditions (https://onlinelibrary.wiley.com/terms-and-conditions) on Wiley Online Library for rules of use; OA articles are governed by the applicable Creative Commons License

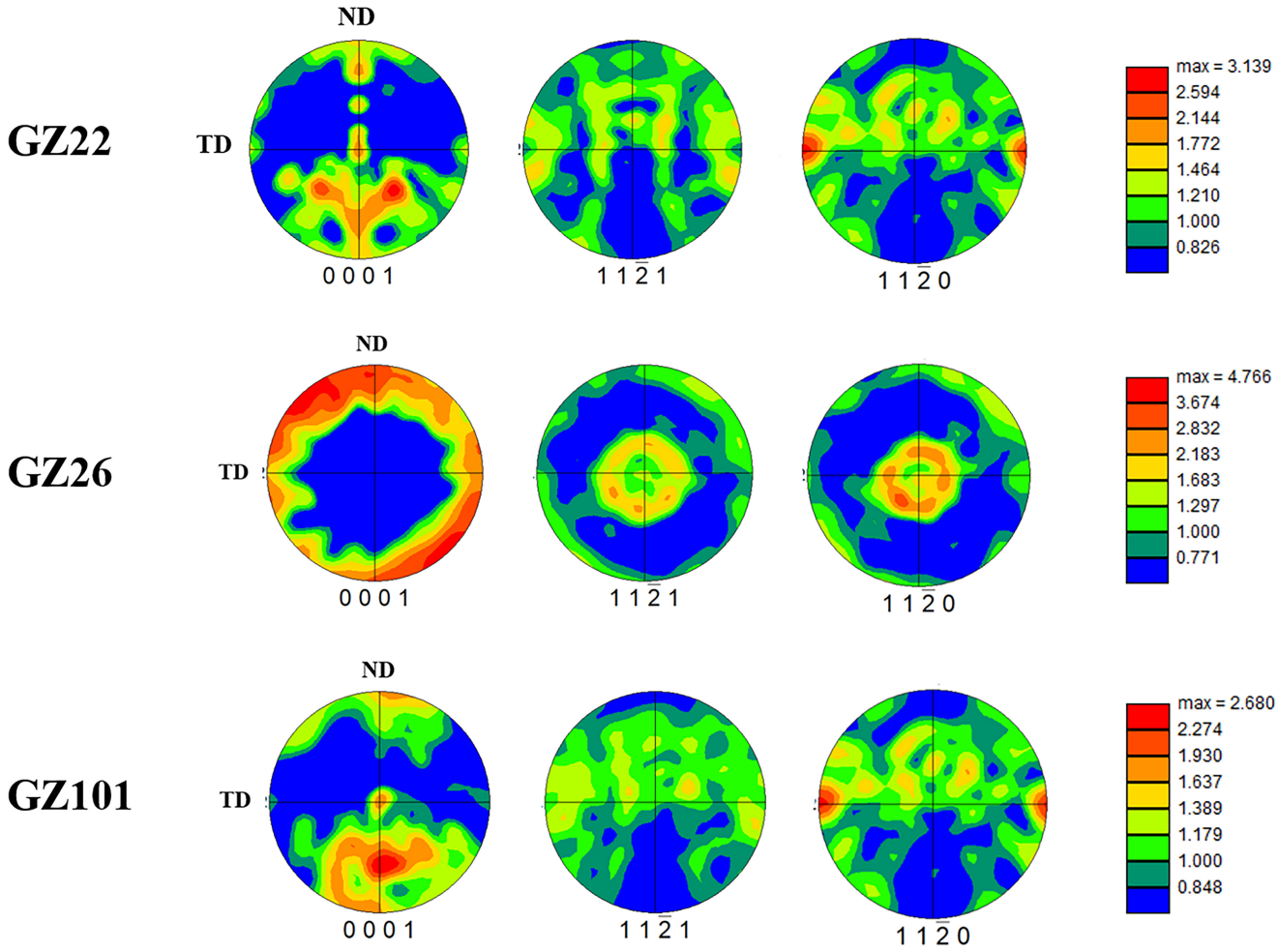

FIGURE 14 | Basal pole figures of alloys obtained from EBSD analysis.

3.5 | Mechanical Integrity after Degradation

Typically, the mechanical support provided by degradable implants also weakens as they degrade; the load-bearing capacity of the sample decreases due to the reduction in the cross-sectional area caused by degradation [62]. The results of the tensile properties of the alloys after 14 days of immersion in a cell culture medium under physiological conditions indicated that the GZ101 alloy maintained its mechanical integrity even after a 14-day immersion period (Figure 18 and Table 6) due to its lower degradation rate. Both GZ22 and GZ26 alloys showed a significant loss in tensile properties, with an approximately 42% to 84% decrease in yield strength, ultimate tensile strength, or elongation.

3.6 | Indirect Cell Viability Tests

3.6.1 | MTT Assay

The MTT assay results (Figure 19a) showed that the GZ26 alloy had severe toxicity with only a 20% viability in the 1 day test in 100% extract, while GZ22 and GZ101 alloy had excellent viability with 90% and 98% respectively. However, all the alloys showed viability greater than 75% with diluted extract concentrations (50% and 25%). The 3 day MTT assay (Figure 19b) showed that at 100% extract conditions, GZ26 and GZ22 alloys had poor viability while GZ101 alloy showed still excellent viability (120%). In general, all the alloys showed an increase in viability when diluted extract concentrations were used for culturing.

3.6.2 | Live Dead Staining

The acridine orange-ethidium bromide dual staining images (Figures 20 and 21) show the characteristics of cells cultured with extract solutions of different concentrations of GZ22, GZ26, and GZ101 alloys. Three different cell types were noticed: live cells (green nuclei with an organized structure), apoptotic cells (condensed or fragmented cells with green or orange stain), and necrotic cells (nuclei stained red) [63, 64]. After 1 day of culture in 100% extract (Figure 19), GZ22 and GZ101 alloys had no apoptotic cells, while GZ26 extract solution showed signs of early apoptosis. All alloys showed good proliferation with diluted extract concentrations (50% and 25%). After 3 days of culture (Figure 21), cells cultured with 100% extracts of GZ22 and GZ26 alloy showed severe apoptosis and necrosis. Diluting the culture medium to 50% and 25%, improved cell proliferation, however, still necrotic cells in certain areas were seen. In contrast, cells cultured with all

15524981, 2024, 9, Downloaded from https://onlinelibrary.wiley.com/doi/10.1002/jbm.b.35474 by Srinivasan Amirthalingam - Nil Institute For Interdis. Sci. And Tech , Wiley Online Library on [01/09/2024]. See the Terms and Conditions (https://onlinelibrary.wiley.com/terms-and-conditions) on Wiley Online Library for rules of use; OA articles are governed by the applicable Creative Commons License

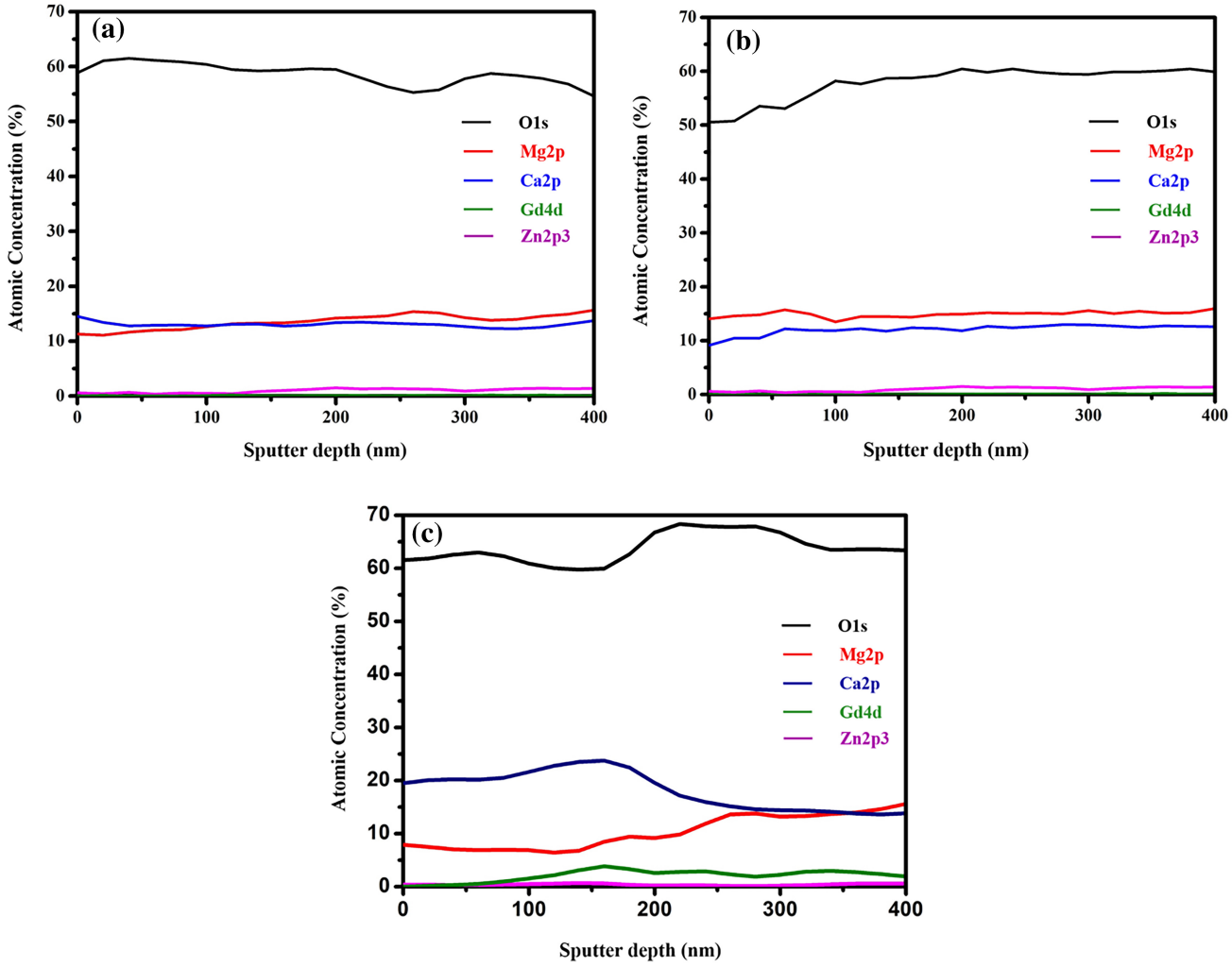

FIGURE 15 | Depth profile analysis of the degradation layers on the sample immersed in cell culture medium for 24 h (a) GZ22, (b) GZ26, and (c) in GZ101.

extract concentrations of GZ101 alloy showed similar morphology to that of cultured with the control, and no apoptosis or necrosis was observed. The cell viability calculated from the live-dead analysis (Figure 22) indicated that all alloys had a viability greater than 75% at all culture times when 50% and 25% extracts were used. However, 100% extracts of GZ26 alloy and GZ22 alloy after 3 days had poor viability.

3.6.3 | Influence of Metal Ions on Cell Viability

The cell viability of the indirect cell culture tests is affected by the release of metal ions into the extract solution. While Mg alloys degrade too fast, due to the release of OH^- ions, the pH of the solution increases beyond 8 and can reach even up to 14. The tolerable limit of pH for cell proliferation requires to be under 8 [65, 66]. The pH of the extract medium used for the indirect cell culture experiments was 9.3, 11.2, and 7.95 for GZ22, GZ26, and GZ101 alloys, respectively. Concomitantly, the rise in pH value due to the high degradation rate ensured poor viability of the cells in GZ26.

The cytotoxicity study of different metal ions, Mg^{2+}, Zn^{2+}, and Gd^{3+} using MTT assay revealed that the 25,000, 120, and 1100 μM concentrations of $MgCl_2$, $ZnCl_2$, and $GdCl_3$, respectively had viability above 75% after 1-day culture. The respective elemental concentrations above the safe limit (Mg—25,000 μM, Zn—120 μM, and Gd—1100 μM) led to a severe decline in viability (Figure 23). To understand the cytotoxicity of studied alloys, the elemental concentrations of 100% extract solutions of different alloys and cell culture medium were analyzed using ICP-MS (Table 7) and compared with the cytotoxicity of individual metal ions. The analysis revealed that though Zn^{2+} concentration in GZ26 alloy extracts was close to the safe limit and the concentration of Mg^{2+} was almost 2.5× higher than the safe limit, leading to poor viability at 100% extract conditions. Although a relatively lower amount of Mg and Zn concentrations were observed in the GZ22 alloy, Mg concentration was still high compared to the safe limit. The 100% extract of GZ101 alloy had higher amounts of Mg and Zn than the cell culture medium; nevertheless, they were within the safe limits. In general, the Gd concentrations were much lower than the limit for all the alloys. Interestingly, the Ca concentrations were depleted in the extracts of GZ26 and GZ22 alloys compared to that of the cell culture medium. Although the concentration of Ca in the GZ101 extract was also lower than that found in the cell culture medium, the decrease was only marginal. Ca from the cell

15524981, 2024, 9, Downloaded from https://onlinelibrary.wiley.com/doi/10.1002/jbm.b.35474 by Srinivasan Amirthalingam - Nil Institute For Interdis. Sci. And Tech , Wiley Online Library on [01/09/2024]. See the Terms and Conditions (https://onlinelibrary.wiley.com/terms-and-conditions) on Wiley Online Library for rules of use; OA articles are governed by the applicable Creative Commons License

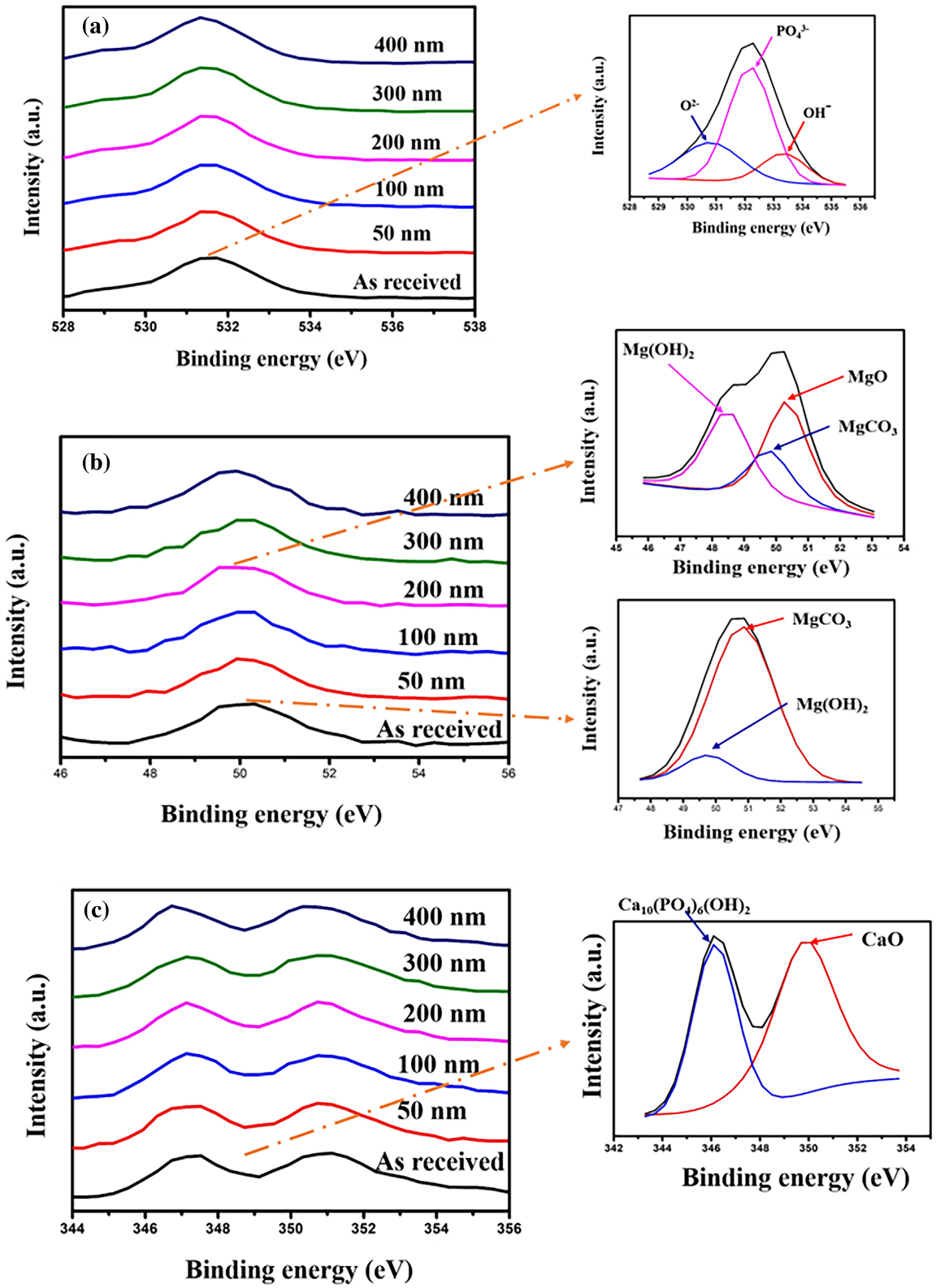

FIGURE 16 | DP-XPS spectra of the corrosion layers on GZ101 alloy sample immersed in cell culture medium for 24 h (a) O1s, (b) Mg2p, and (c) Ca2p.

culture medium gets deposited on the metal surface in the form of CaO and hydroxyapatite ($Ca_{10}(PO_4)_6OH_2$) (confirmed using XPS analysis Figures 16c and 17a), thus resulting in its depletion in the cell culture medium. However, Ca being an essential element for cell proliferation, the depletion of Ca in cell culture medium also leads to poor viability. The alloy with the highest degradation rate (GZ26) had the lowest Ca, and the alloy with the lowest degradation rate (GZ101) had the highest Ca in the extract solution. Due to severe and continuous degradations in GZ22 and GZ26 alloys, the degradation layers in these alloys

15524981, 2024, 9, Downloaded from https://onlinelibrary.wiley.com/doi/10.1002/jbm.b.35474 by Srinivasan Amirthalingam - Nil Institute For Interdis. Sci. And Tech. , Wiley Online Library on [01/09/2024]. See the Terms and Conditions (https://onlinelibrary.wiley.com/terms-and-conditions) on Wiley Online Library for rules of use; OA articles are governed by the applicable Creative Commons License

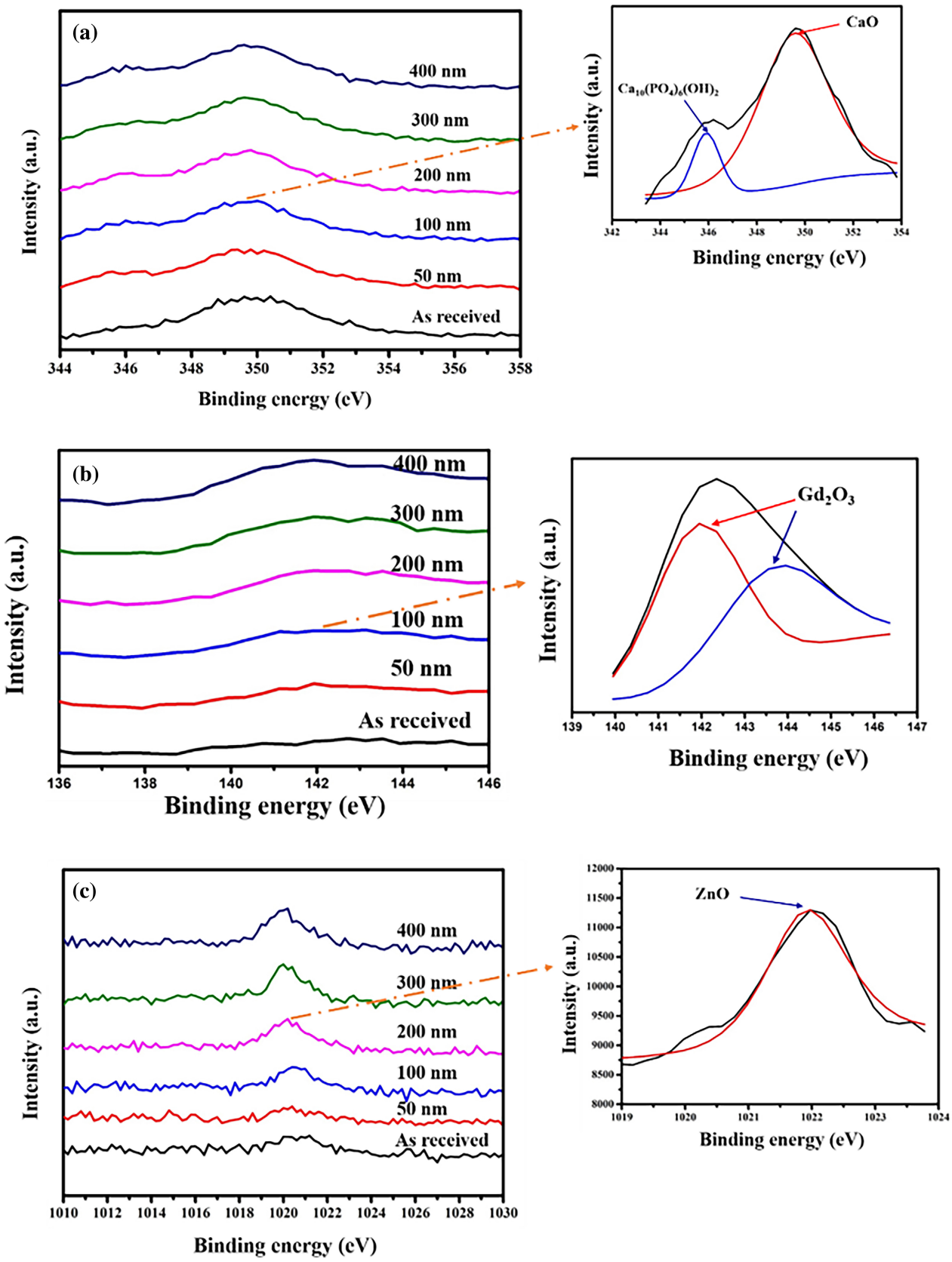

FIGURE 17 | DP-XPS spectra of the degradation layers on samples immersed in cell culture medium for 24 h (a) Ca2p of GZ26, (b) Gd4d of GZ101, and (c) Zn2p3 of GZ26.

15524981, 2024, 9, Downloaded from https://onlinelibrary.wiley.com/doi/10.1002/jbm.b.35474 by Srinivasan Amirthalingam - Nti Institute For Interdis. Sci. And Tech. , Wiley Online Library on [01/09/2024]. See the Terms and Conditions (https://onlinelibrary.wiley.com/terms-and-conditions) on Wiley Online Library for rules of use; OA articles are governed by the applicable Creative Commons License

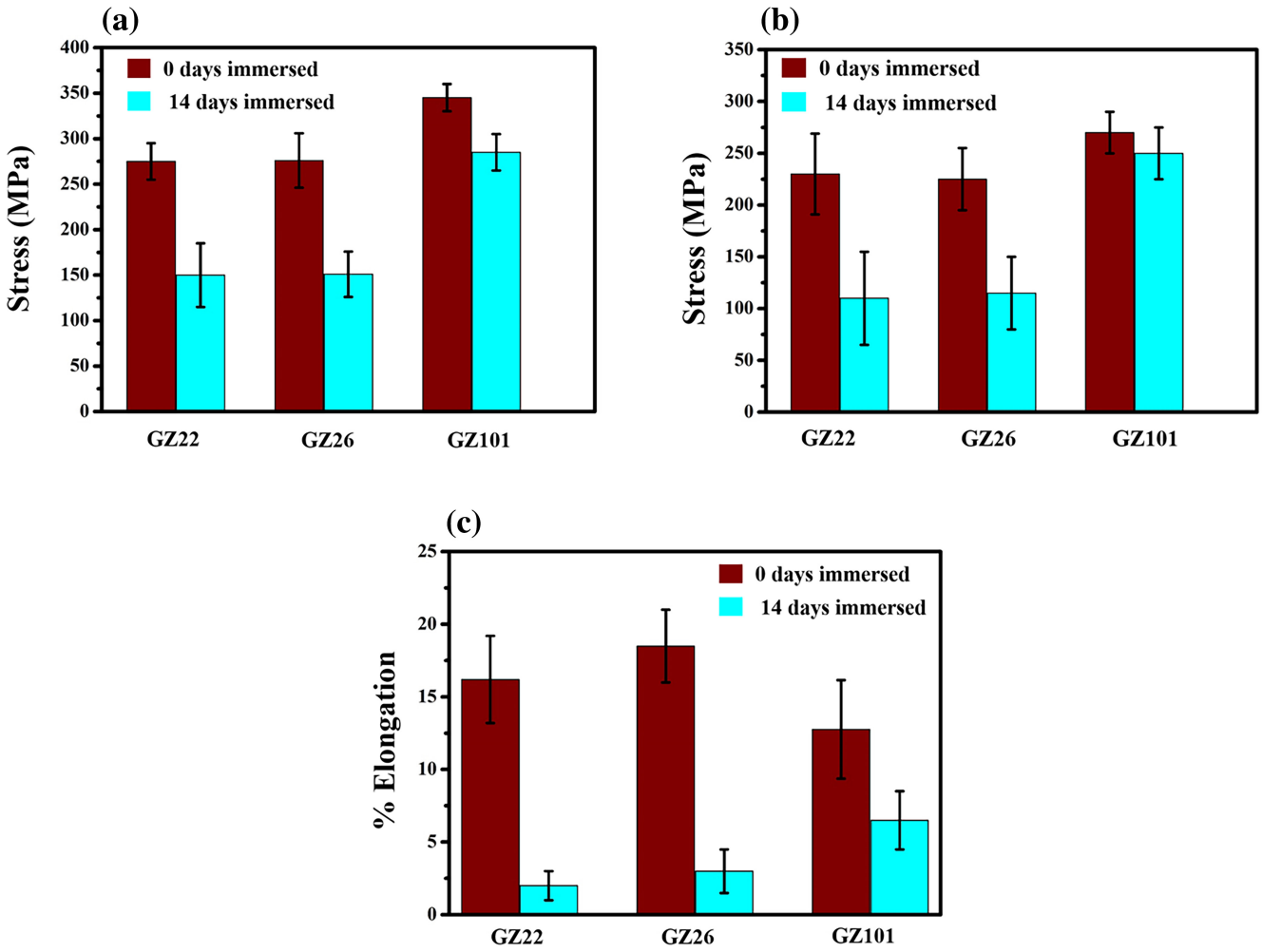

FIGURE 18 | Tensile properties of alloys immersed in cell culture medium for 14 days (a) Ultimate tensile strength, (b) Yield strength, and (c) % elongation.

were not stable, hence more Ca from the cell culture medium was consumed continuously. Thus, the increased amount of Mg and Zn concentrations and the depletion of Ca in the extracts of GZ22 and GZ26 alloys resulted in poor viability.

3.7 | Direct Cell Culture Tests

3.7.1 | DAPI Staining

The analysis of fluorescent images of cell nucleus on the surface of GZ22 and GZ101 alloys stained using DAPI (Figure 24a–d) and the cell number count (Figure 24e) were in agreement with the indirect cell viability assays. Due to the high degradation rate in GZ26 alloy, after 3-day immersion in the culture medium, the metal surface was rough as well as the culture medium was highly alkaline, and hence analysis could not be done for GZ26. The cell count was almost similar for both GZ22 and GZ101 alloys, after 1-day culture. However, the number of cells on GZ22 surface reduced marginally after 3-day culture, while it increased significantly (almost a five-fold increase) on GZ101 alloy indicating that the cells proliferated on the surface of GZ101 alloy whereas cells subjected to toxicity in case of GZ22 alloy.

3.7.2 | Cell Attachment and Proliferation

The interaction of cells with GZ101 metal surface after 1- and 3-day culture was inspected using SEM (Figure 25). Initially, after 1 day cell culture, the cells on the metal surface (shown by yellow arrows in Figure 25a,b) were seen to have a round morphology. Higher magnification SEM image (Figure 25b) of a selected area shows that the cells were beginning to merge and indicates the beginning of proliferation. After 3-day culture, the cells (shown in yellow arrows in Figure 25c) were seen to have spread all over the metal surface and covered the cracks of the degradation layer on the metal surface. Also the higher magnification SEM image (Figure 25d) revealed that the cells with pseudopods were spreading in all directions. The excellent proliferation of the cells on the metal surface was due to the presence of a protective degradation film which was confirmed using XPS analysis (Figures 15–17). The formation of a stable surface film consisting of Gd_2O_3, $MgCO_3$, $Ca_{10}(PO_4)_6(OH)_2$, CaO, MgO, and $Mg(OH)_2$ on the surface of GZ101 resulted in better cell attachment and proliferation. The proliferation of cells on the GZ101 alloys surface could also be due to the enhanced formation of hydroxyapatite ($Ca_{10}(PO_4)_6(OH)_2$) in the GZ101 alloy compared to other alloys (as observed in the XPS analysis, Figure 16c).

15524981, 2024, 9, Downloaded from https://onlinelibrary.wiley.com/doi/10.1002/jbm.b.35474 by Srinivasan Amirthalingam - Nil Institute For Interdis. Sci. And Tech , Wiley Online Library on [01/09/2024]. See the Terms and Conditions (https://onlinelibrary.wiley.com/terms-and-conditions) on Wiley Online Library for rules of use; OA articles are governed by the applicable Creative Commons License

TABLE 6 | Percentage decrease in tensile properties of alloys after 14-day immersion in cell culture medium.

Alloy code	Percentage decrease in UTS	Percentage decrease in YS	Percentage decrease in elongation
GZ22	45.58	56.71	84.33
GZ26	42.08	50.38	77.42
GZ101	16.17	7.41	45

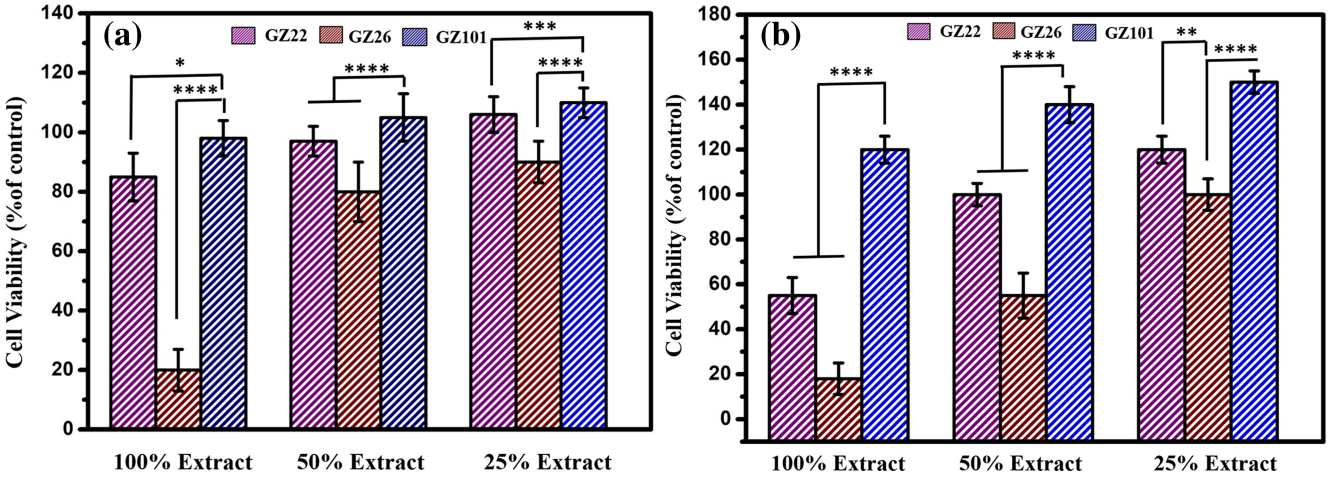

FIGURE 19 | MTT assay results of MG63 cells cultured in sample extracts for (a) 1 day and (b) 3 days. Values are the mean ± SD, $n = 4$, $^{*}p < 0.05$, $^{**}p < 0.01$, $^{***}p < 0.001$, $^{****}p < 0.0001$.

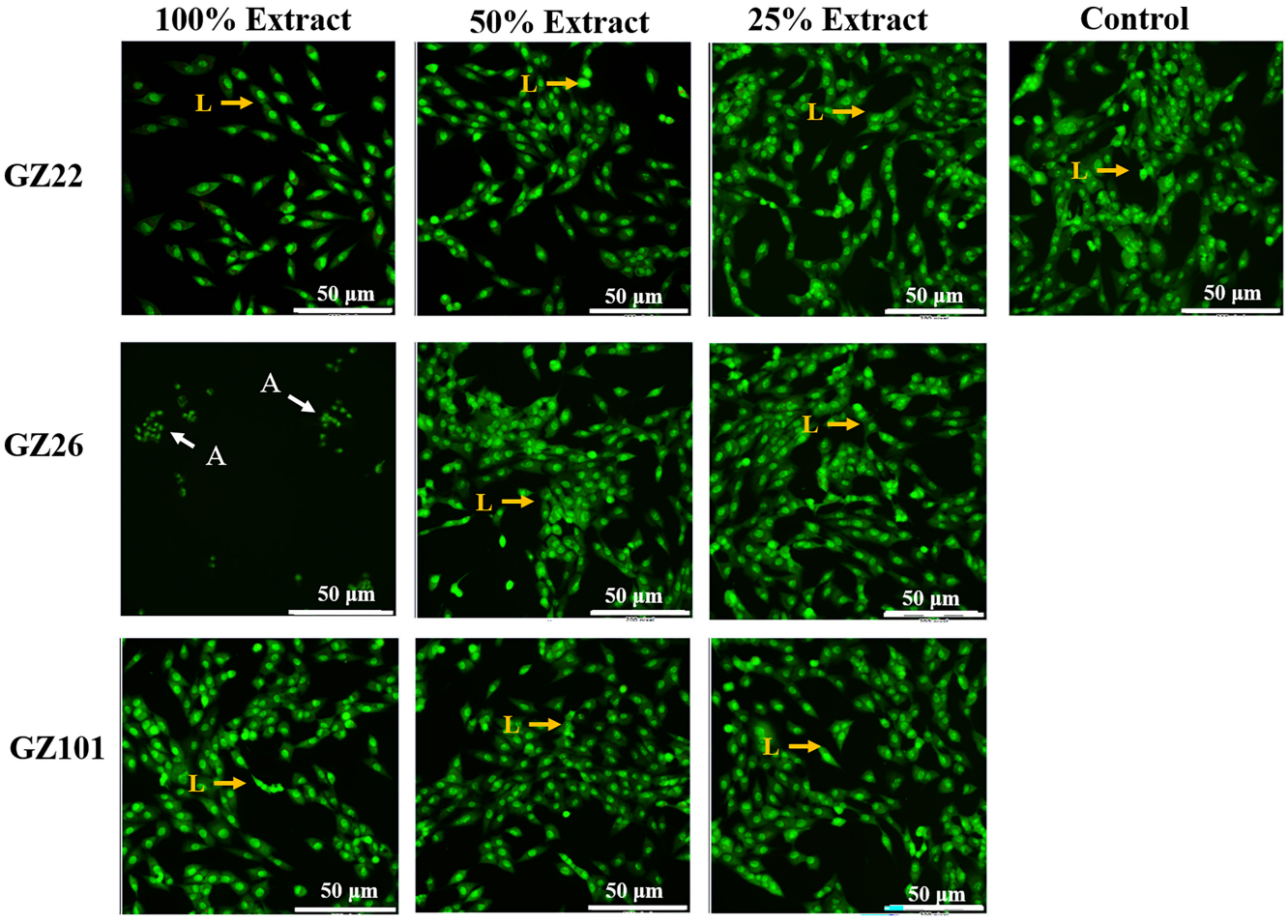

FIGURE 20 | Live dead staining images of MG63 cells cultured in sample extracts for 1 day (L—Live cells, A—Apoptotic cells).

15524981, 2024, 9, Downloaded from https://onlinelibrary.wiley.com/doi/10.1002/jbm.b.35474 by Srinivasan Amirthalingam - Nhl Institute For Interdis. Sci. And Tech , Wiley Online Library on [01/09/2024]. See the Terms and Conditions (https://onlinelibrary.wiley.com/terms-and-conditions) on Wiley Online Library for rules of use; OA articles are governed by the applicable Creative Commons License

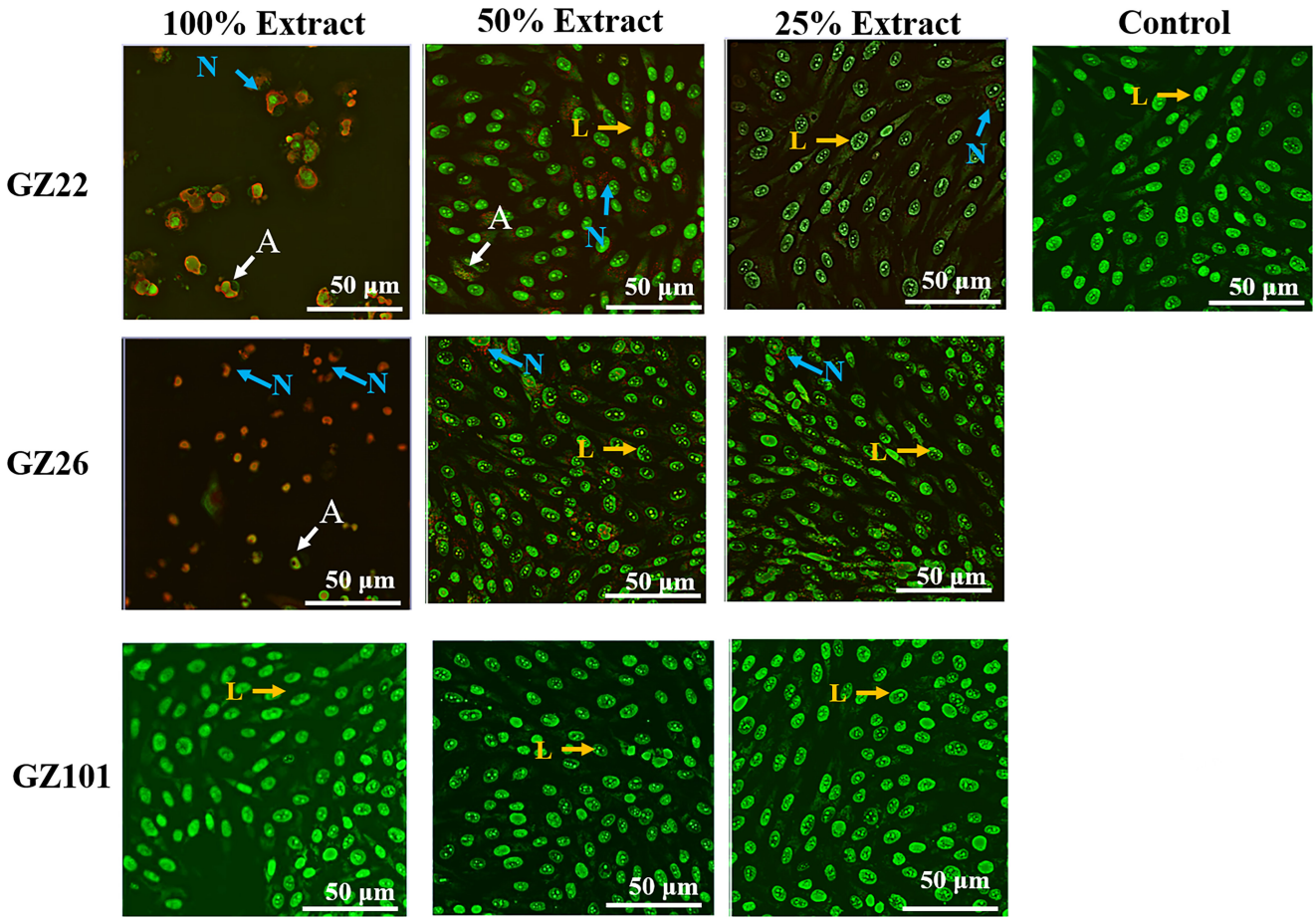

FIGURE 21 | Live dead staining images of MG63 cells cultured in sample extracts for 3 days (L—Live cells, A—Apoptotic cells, N—Necrotic cells).

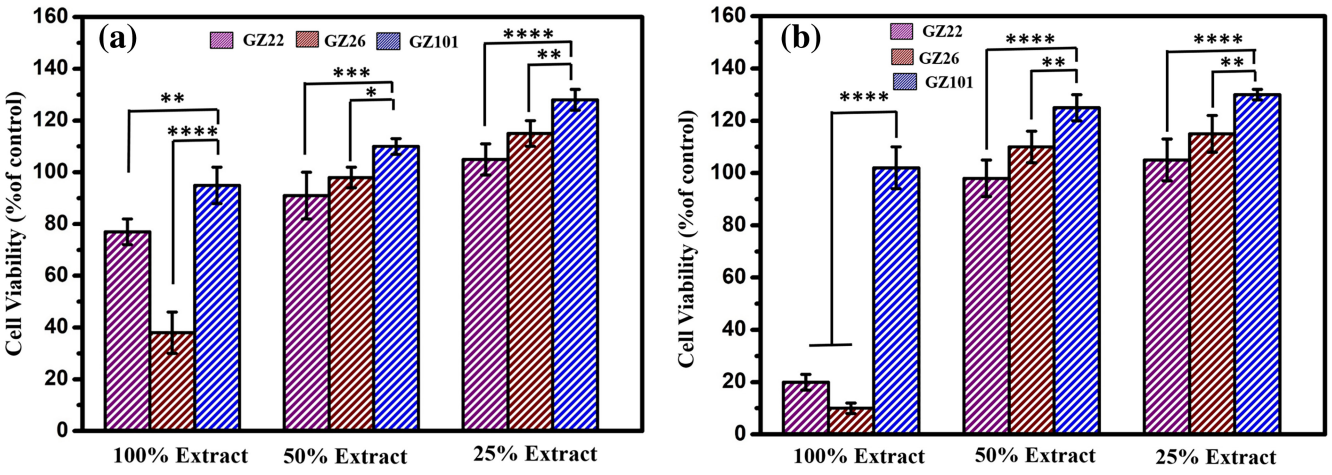

FIGURE 22 | Cell viability calculated from live dead staining images of MG63 cells cultured in sample extracts for (a) 1 day and (b) 3 days. Values are the mean ± SD, $n = 4$, $^{*}p < 0.05$, $^{**}p < 0.01$, $^{***}p < 0.001$, $^{****}p < 0.0001$.

3.8 | In Vivo Evaluation

The GZ101 alloy which showed better viability, degradation resistance, and mechanical integrity during in vitro analysis was considered for in vivo evaluation by subcutaneous implantation in rats. A rat subcutaneously implanted with GZ101 sample is shown in Figure 26a,b. The subcutaneous implantation sites after 14 and 30 days (Figure 26c,d) shows minor H_2 bubbles near the tissue surrounding the metal (shown by yellow arrows). The biodegradation rates of the alloy after 14 and 30 days implantation period were 0.28 (±0.028) and 0.35 (±0.02) mm/year. respectively. The surface topographies of the samples after 14 and 30 days implantation period (Figure 26c,d) showed degradation pits (black arrows) only at the edge of the samples indicating non-uniform degradation.

15524981, 2024, 9, Downloaded from https://onlinelibrary.wiley.com/doi/10.1002/jbm.b.35474 by Srinivasan Amirthalingam - Nti Institute For Interdis. Sci. And Tech , Wiley Online Library on [01/09/2024]. See the Terms and Conditions (https://onlinelibrary.wiley.com/terms-and-conditions) on Wiley Online Library for rules of use; OA articles are governed by the applicable Creative Commons License

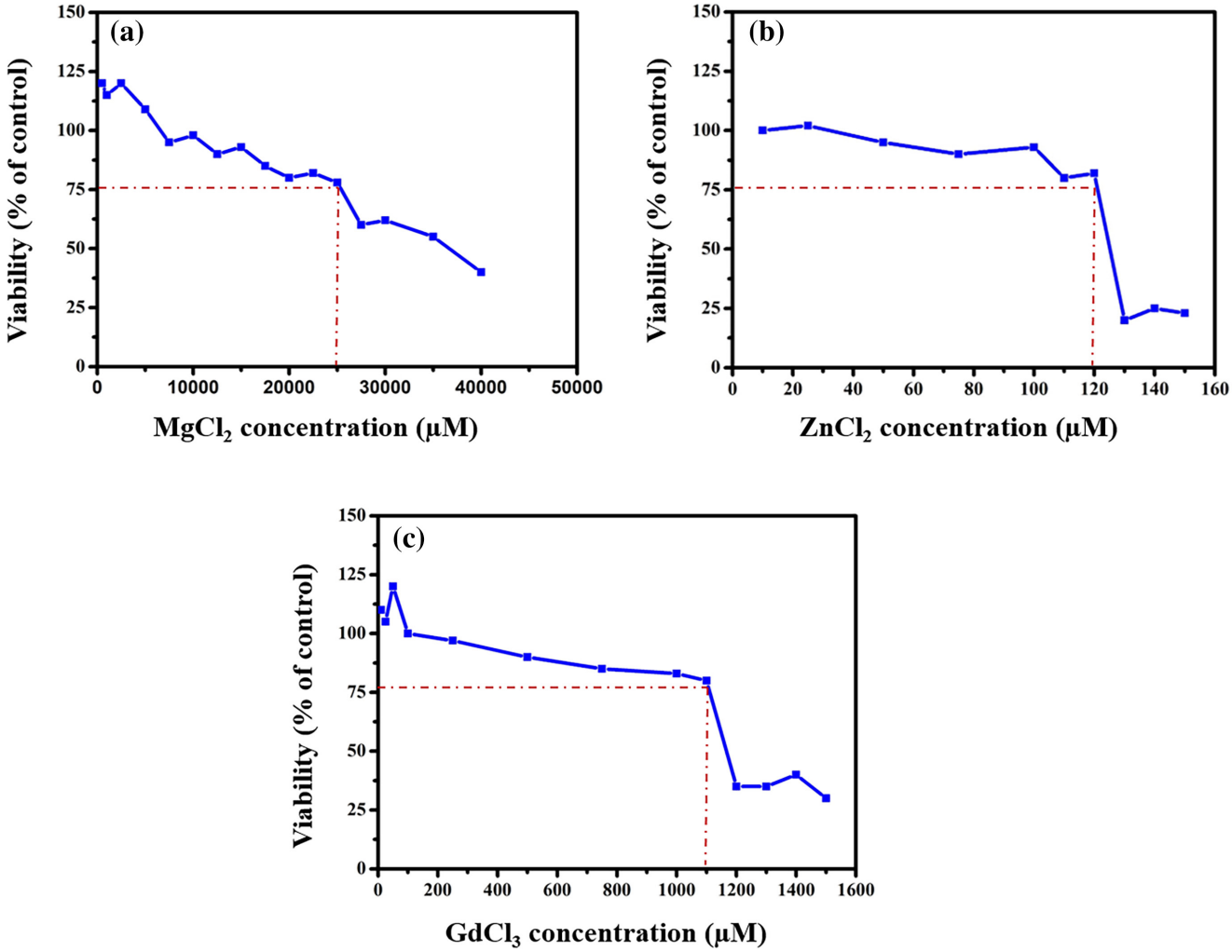

FIGURE 23 | MTT assay results of MG63 cells cultured in different elemental concentrations for 1 day (a) $MgCl_2$, (b) $ZnCl_2$, and (c) $GdCl_3$.

TABLE 7 | Concentrations of different elements in the 100% extract of alloys immersed in α-MEM with 10% FBS and 1% penicillin.

	Elemental concentration (μM)			
	Mg	Zn	Gd	Ca
GZ22	46743.77	38.55656	3.683088	115.2307
GZ26	66114.84	103.1389	0.230037	69.08158
GZ101	17571.71	10.10976	0.14129	153.2266
Cell culture medium	1131.346	7.925599	0	165.5037

The histological examination of organs evaluates the effects of biodegradable materials during their digestion and excretion in vivo. The H&E staining of various organs from the metal-implanted rats is shown in Figure 27. After 30 days of implantation, there were no significant pathological changes observed in any of the organ tissues. The section from the heart showed normal architecture with myocardial fibers, and myocytes having no significant pathology. There was no indication of architectural destruction, edema, inflammatory infiltrates, or necrosis. The section from the liver showed lobular architecture with mild interface hepatitis. Individual hepatocytes showed focal mild cytoplasmic vacuolation. The portal triad showed no significant pathology, while the central vein showed mild dilation and congestion. The section of skin showed a normal epidermis, and the subcutaneous tissue showed no considerable pathology. There was no indication of inflammation, edema, or necrosis. These results suggested that the extruded GZ101 alloy had excellent biocompatibility

15524981, 2024, 9, Downloaded from https://onlinelibrary.wiley.com/doi/10.1002/jbm.b.35474 by Srinivasan Amirthalingam - Nti Institute For Interdis. Sci. And Tech. , Wiley Online Library on [01/09/2024]. See the Terms and Conditions (https://onlinelibrary.wiley.com/terms-and-conditions) on Wiley Online Library for rules of use; OA articles are governed by the applicable Creative Commons License

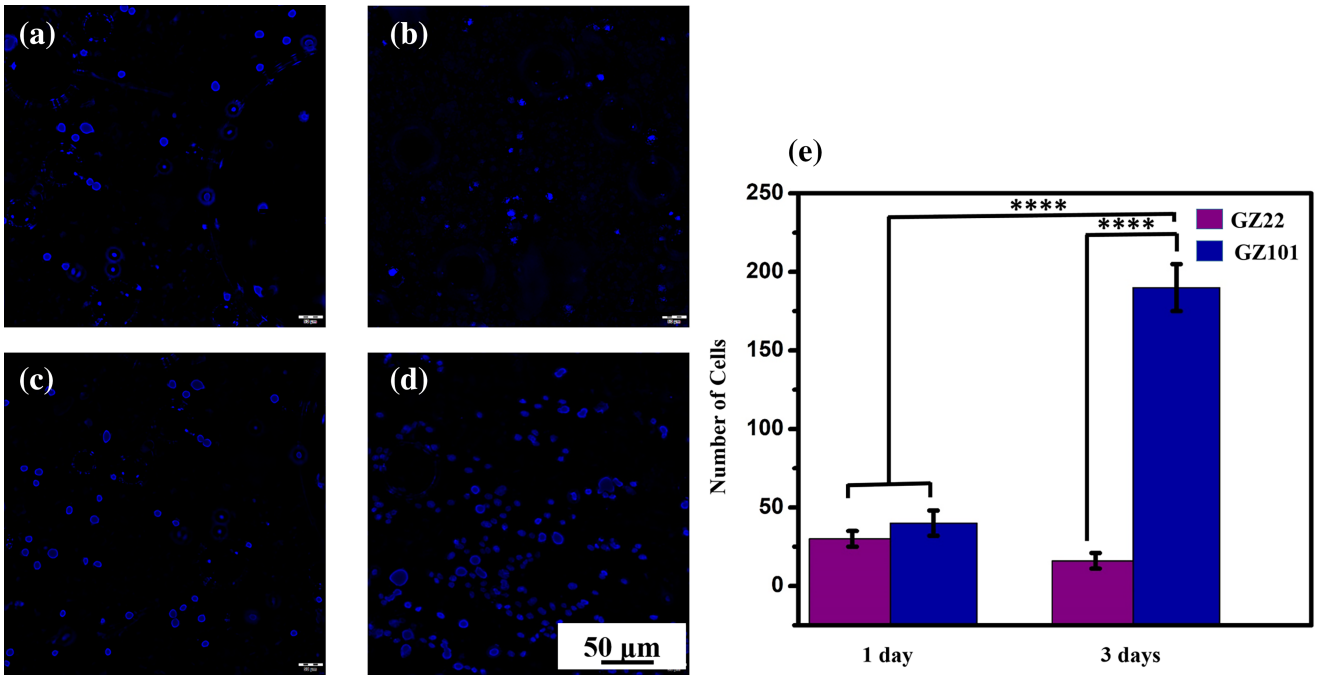

FIGURE 24 | Fluorescence microscopy images of DAPI stained MG63 cells cultured on the sample surface for 1 day (a) GZ22 and (c) GZ101 and for 3 days (b) GZ22, (d) GZ101, and (e) cell count. Values are the mean ± SD, $n = 4$, ****$p < 0.0001$.

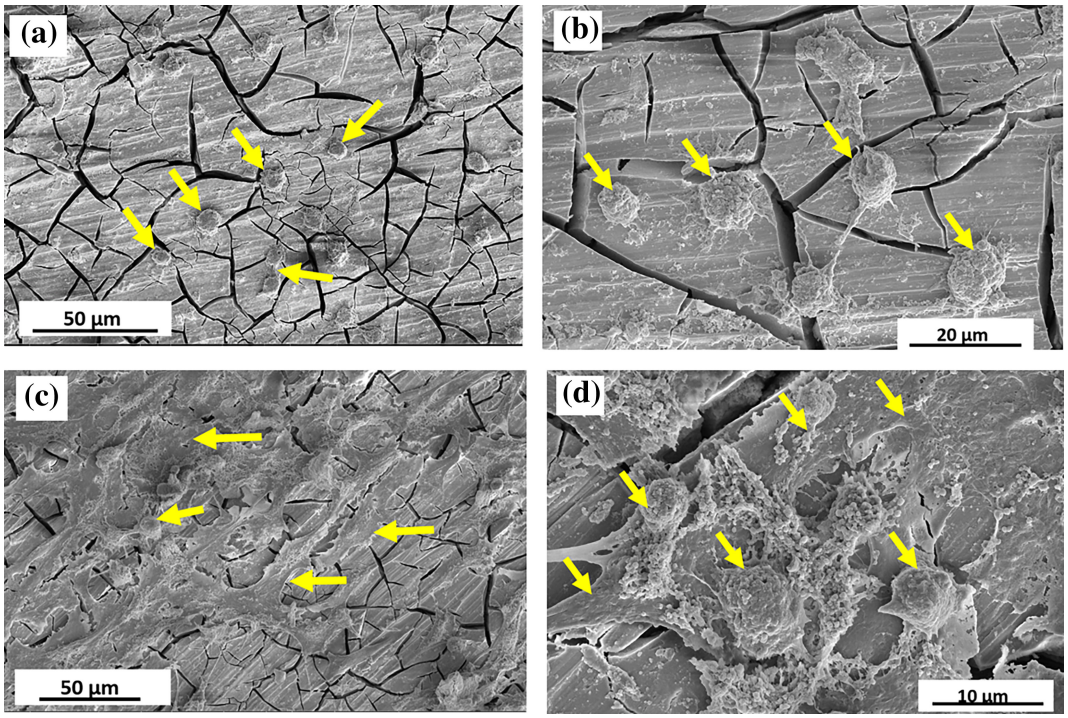

FIGURE 25 | SEM images of adherent cells on the surface of GZ101 alloy (a, b) 1 day culture and (c, d) 3 day culture.

as well as in vivo degradation resistance. Mg alloy usually has higher degradation rate during subcutaneous implantation than when it is implanted near a bone. Hence, still much lower degradation rate is expected for GZ101 alloy when it is considered for orthopedic scaffold applications. The further in vivo analysis are planned to evaluate the performance of the GZ101 alloy in the bone healing process.

4 | Summary

The study was conducted to explore the feasibility of extruded Mg-Zn-Gd-Zr alloys with varying Zn/Gd ratios as potential biodegradable implant material by assessing their tensile properties, degradation resistance, and viability in vitro and in vivo conditions. The key findings were as follows: Major

15524981, 2024, 9, Downloaded from https://onlinelibrary.wiley.com/doi/10.1002/jbm.b.35474 by Srinivasan Amirthalingam - Nti Institute For Interdis. Sci. And Tech. , Wiley Online Library on [01/09/2024]. See the Terms and Conditions (https://onlinelibrary.wiley.com/terms-and-conditions) on Wiley Online Library for rules of use; OA articles are governed by the applicable Creative Commons License

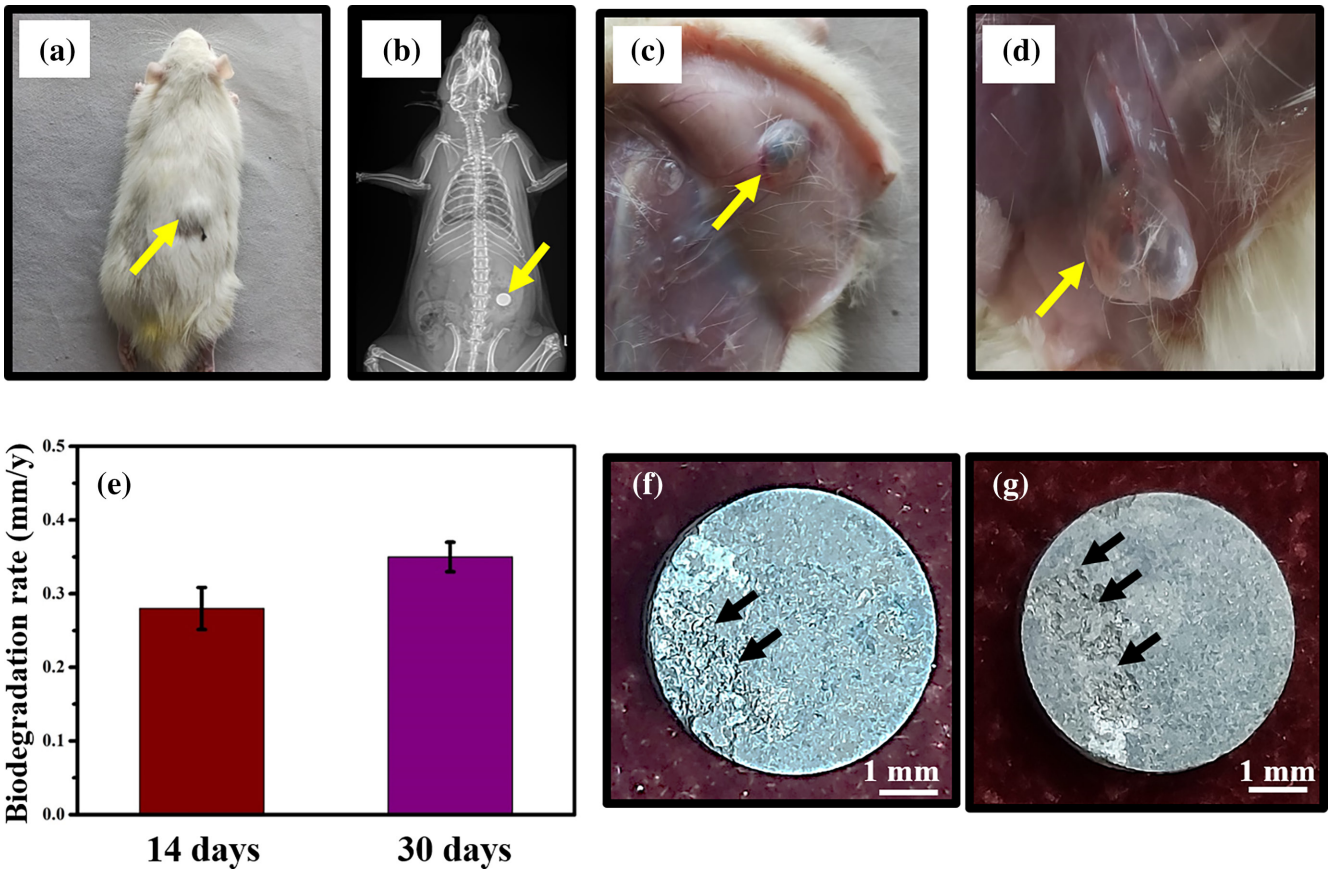

FIGURE 26 | (a) Photograph of GZ101 subcutaneously implanted rat, (b) X-ray image after 14 days' implantation, (c and d) a photographs of implants post-surgery after 14 and 30 days, respectively, (e) biodegradation rate of GZ101 alloy, (f and g) the photographs of implanted samples after 14 and 30 days, respectively.

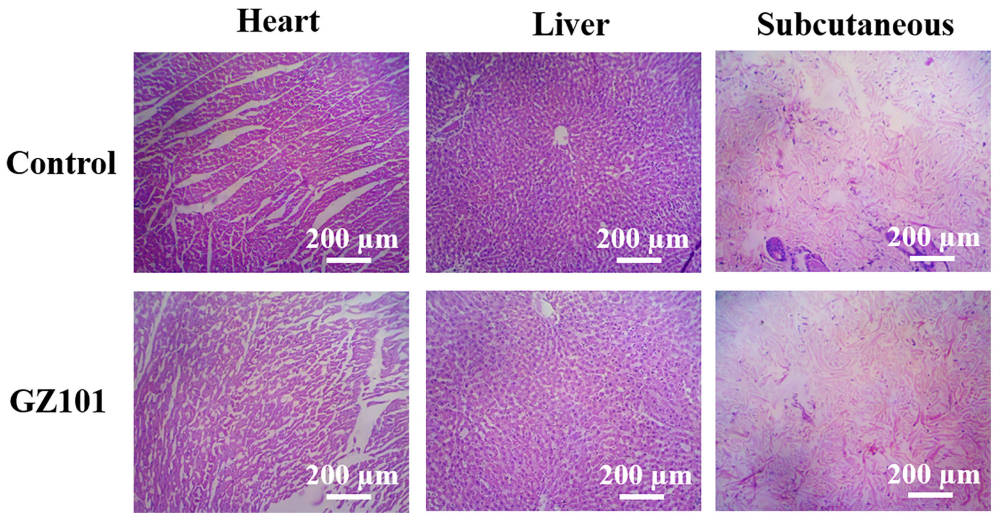

FIGURE 27 | H&E staining of heart liver and subcutaneous tissue samples after implantation of GZ101 alloy for 30 days.

ternary phase observed in the Mg-Gd-Zn-Zr alloys varied with change in Zn/Gd ratios. Mg-2Gd-2Zn-0.5Zr alloy with a Zn/Gd = 1 showed a dominant presence of W phase ($Mg_3Zn_3Gd_2$). Mg-2Gd-6Zn-0.5Zr with Zn/Gd = 3 consisted of W phase and I phase (Mg_3Zn_6Gd). Mg-10Gd-1Zn-0.5Zr with Zn/Gd = 0.1 had $(Mg,Zn)_3Gd$ phase as well as long period stacking order phase (LPSO) in the matrix.

1. Mg-10Gd-1Zn-0.5Zr alloy showed superior YS and UTS with reasonable good ductility due to the combined effect

15524981, 2024, 9, Downloaded from https://onlinelibrary.wiley.com/doi/10.1002/jbm.b.35474 by Srinivasan Amirthalingam - Nti Institute For Interdis. Sci. And Tech. , Wiley Online Library on [01/09/2024]. See the Terms and Conditions (https://onlinelibrary.wiley.com/terms-and-conditions) on Wiley Online Library for rules of use; OA articles are governed by the applicable Creative Commons License

of higher dislocation density, low Schmid factor, and strong basal texture.

2. Mg-10Gd-1Zn-0.5Zr alloy had better degradation resistance compared to other alloys owing to the presence of strong basal texture as well as the formation of Gd_2O_3 containing protective degradation layer.
3. Diluted extracts (25% and 50%) of all the alloys showed viability (MG63 cell line) above 75% during in vitro analysis at all culture conditions (1 or 3 days). However, Mg-10Gd-1Zn-0.5Zr showed excellent (above 95%) viability even with 100% extracts.
4. In vivo analysis of subcutaneously implanted Mg-10Gd-1Zn-0.5Zr alloy on rats revealed that the degradation rate was 0.35 mm/year after 30 days' implantation and exhibited good in vivo biocompatibility.

Acknowledgments

This research was financially supported by the Science and Engineering Research Board (SERB, Project numbers: IMRC/AISTDF/CRD/2019/000144 and EMR/2017/001286) and Council of Scientific and Industrial Research, India (CSIR, Project number: MLP0043). The authors also thank the Director, CSIR-NIIST, Trivandrum for providing an opportunity to conduct the study.

Conflicts of Interest

The authors declare no conflicts of interest.

Data Availability Statement

The raw/processed data required to reproduce these findings cannot be shared at this time as the data also forms part of an ongoing study.

References

1. D. Bairagi and S. Mandal, "A Comprehensive Review on Biocompatible Mg-Based Alloys as Temporary Orthopaedic Implants: Current Status, Challenges, and Future Prospects," *Journal of Magnesium and Alloys* 10 (2022): 627–669, https://doi.org/10.1016/j.jma.2021.09.005.

2. W. Greatbatch and C. F. Holmes, "History of Implantable Devices," *IEEE Engineering in Medicine and Biology Magazine* 10 (1991): 38–41, https://doi.org/10.1109/51.84185.

3. S. K. Jaganathan, E. Supriyanto, S. Murugesan, A. Balaji, and M. K. Asokan, "Biomaterials in Cardiovascular Research: Applications and Clinical Implications," *BioMed Research International* 2014 (2014): 459465, https://doi.org/10.1155/2014/459465.

4. M. Peron, J. Torgersen, and F. Berto, "Mg and Its Alloys for Biomedical Applications: Exploring Corrosion and Its Interplay With Mechanical Failure," *Metals* 7 (2017): 252, https://doi.org/10.3390/met7070252.

5. N. Li and Y. Zheng, "Novel Magnesium Alloys Developed for Biomedical Application: A Review," *Journal of Materials Science and Technology* 29 (2013): 489–502, https://doi.org/10.1016/j.jmst.2013.02.005.

6. X.-B. Chen, M. A. Easton, N. Birbilis, H.-Y. Yang, and T. B. Abbott, "10 – Corrosion-Resistant Coatings for Magnesium (Mg) Alloys," in *Corrosion Prevention of Magnesium Alloys*, Woodhead Publishing Series in Metals and Surface Engineering (Woodhead Publishing, 2013), 282–312, https://doi.org/10.1533/9780857098962.2.282.

7. F. Pan, M. Yang, and X. Chen, "A Review on Casting Magnesium Alloys: Modification of Commercial Alloys and Development of New Alloys," *Journal of Materials Science and Technology* 32 (2016): 1211–1221, https://doi.org/10.1016/j.jmst.2016.07.001.

8. P. Wan, L. Tan, and K. Yang, "Surface Modification on Biodegradable Magnesium Alloys as Orthopedic Implant Materials to Improve the Bio-Adaptability: A Review," *Journal of Materials Science and Technology* 32 (2016): 827–834, https://doi.org/10.1016/j.jmst.2016.05.003.

9. S. F. Chen, H. W. Song, M. Cheng, C. Zheng, S. H. Zhang, and M. G. Lee, "Texture Modification and Mechanical Properties of AZ31 Magnesium Alloy Sheet Subjected to Equal Channel Angular Bending," *Journal of Materials Science and Technology* 67 (2021): 211–225, https://doi.org/10.1016/j.jmst.2020.06.034.

10. J. Wang, L. Cui, Y. Ren, et al., "In Vitro and in Vivo Biodegradation and Biocompatibility of an MMT/BSA Composite Coating Upon Magnesium Alloy AZ31," *Journal of Materials Science and Technology* 47 (2020): 52–67, https://doi.org/10.1016/j.jmst.2020.02.006.

11. H. Miao, D. Zhang, C. Chen, et al., "Research on Biodegradable Mg–Zn–Gd Alloys for Potential Orthopedic Implants: In Vitro and in Vivo Evaluations," *ACS Biomaterials Science & Engineering* 5 (2019): 1623–1634, https://doi.org/10.1021/acsbiomaterials.8b01563.

12. F. Feyerabend, J. Fischer, J. Holtz, et al., "Evaluation of Short-Term Effects of Rare Earth and Other Elements Used in Magnesium Alloys on Primary Cells and Cell Lines," *Acta Biomaterialia* 6 (2010): 1834–1842, https://doi.org/10.1016/j.actbio.2009.09.024.

13. J. Bennett, Q. De Hemptinne, and K. McCutcheon, "Magmaris Resorbable Magnesium Scaffold for the Treatment of Coronary Heart Disease: Overview of Its Safety and Efficacy," *Expert Review of Medical Devices* 16 (2019): 757–769, https://doi.org/10.1080/17434440.2019.1649133.

14. Y. Zhang, Y. Liu, R. Zheng, Y. Zheng, and L. Chen, "Research Progress on Corrosion Behaviors and Biocompatibility of Rare-Earth Magnesium Alloys in Vivo and in Vitro," *Journal of Rare Earths* 41 (2023): 1827–1842, https://doi.org/10.1016/j.jre.2023.03.005.

15. Z. G. Huan, M. A. Leeflang, J. Zhou, L. E. Fratila-Apachitei, and J. Duszczyk, "In Vitro Degradation Behavior and Cytocompatibility of Mg-Zn-Zr Alloys," *Journal of Materials Science. Materials in Medicine* 21 (2010): 2623–2635, https://doi.org/10.1007/s10856-010-4111-8.

16. S. D. Cramer and B. S. Covino, "Methods of Corrosion Protection," Accessed January 27, 2023, https://dl.asminternational.org/handbooks/edited-volume/46/chapter/531345/Methods-of-Corrosion-Protection.

17. M. H. Tsai, M. S. Chen, L. H. Lin, et al., "Effect of Heat Treatment on the Microstructures and Damping Properties of Biomedical Mg-Zr Alloy," *Journal of the Less-Common Metals* 509 (2011): 813–819, https://doi.org/10.1016/j.jallcom.2010.09.098.

18. A. Srinivasan, C. Blawert, Y. Huang, C. L. Mendis, K. U. Kainer, and N. Hort, "Corrosion Behavior of Mg–Gd–Zn Based Alloys in Aqueous NaCl Solution," *Journal of Magnesium and Alloys* 2 (2014): 245–256, https://doi.org/10.1016/j.jma.2014.08.002.

19. J. Liu, D. Bian, Y. Zheng, et al., "Comparative in Vitro Study on Binary Mg-RE (Sc, Y, La, Ce, Pr, Nd, Sm, Eu, Gd, Tb, Dy, Ho, Er, Tm, Yb and Lu) Alloy Systems," *Acta Biomaterialia* 102 (2020): 508–528, https://doi.org/10.1016/j.actbio.2019.11.013.

20. N. A. Agha, R. Willumeit-Römer, D. Laipple, B. Luthringer, and F. Feyerabend, "The Degradation Interface of Magnesium Based Alloys in Direct Contact With Human Primary Osteoblast Cells," *PLoS One* 11 (2016): e0157874, https://doi.org/10.1371/journal.pone.0157874.

21. F. Cecchinato, N. A. Agha, A. H. Martinez-Sanchez, et al., "Influence of Magnesium Alloy Degradation on Undifferentiated Human Cells," *PLoS One* 10 (2015): e0142117, https://doi.org/10.1371/journal.pone.0142117.

22. D. Krüger, B. Zeller-Plumhoff, B. Wiese, et al., "Assessing the Microstructure and In Vitro Degradation Behavior of Mg-xGd Screw Implants Using μCT," *Journal of Magnesium and Alloys* 9 (2021): 2207–2222, https://doi.org/10.1016/j.jma.2021.07.029.

15524981, 2024, 9, Downloaded from https://onlinelibrary.wiley.com/doi/10.1002/jbm.b.35474 by Srinivasan Amirthalingam - Nil Institute For Interdis. Sci. And Tech , Wiley Online Library on [01/09/2024]. See the Terms and Conditions (https://onlinelibrary.wiley.com/terms-and-conditions) on Wiley Online Library for rules of use; OA articles are governed by the applicable Creative Commons License

23. J. Harmuth, B. Wiese, J. Bohlen, T. Ebel, and R. Willumeit-Römer, "Wide Range Mechanical Customization of Mg-Gd Alloys With Low Degradation Rates by Extrusion," *Frontiers in Materials* 6 (2019): 201 Accessed January 10, 2024, https://www.frontiersin.org/articles/10.3389/fmats.2019.00201.

24. J. Wang, P. Song, S. Gao, Y. Wei, and F. Pan, "Influence of Y on the Phase Composition and Mechanical Properties of as-Extruded Mg–Zn–Y–Zr Magnesium Alloys," *Journal of Materials Science* 47 (2012): 2005–2010, https://doi.org/10.1007/s10853-011-5998-2.

25. S. Zhang, J. Li, Y. Song, C. Zhao, C. Xie, and X. Zhang, "Influence of Heat Treatments on In Vitro Degradation Behavior of Mg-6Zn Alloy Studied by Electrochemical Measurements," *Advanced Engineering Materials* 12 (2010): B170–B174, https://doi.org/10.1002/adem.200980052.

26. ASTM G31-72, "Standard for Laboratory Immersion Corrosion Testing of Metals," (2017), https://kupdf.net/download/astm-g31-72laboratory-immersion-corrosion-testing-of-metals_59966135dc0d607665300d1d_pdf.

27. W. Rong, Y. Zhang, Y. Wu, et al., "Effects of Zr and Mn Additions on Formation of LPSO Structure and Dynamic Recrystallization Behavior of Mg-15Gd-1Zn Alloy," *Journal of Alloys and Compounds* 692 (2017): 805–816, https://doi.org/10.1016/j.jallcom.2016.09.068.

28. H. E. Friedrich and B. L. Mordike, eds., "Technology of Magnesium and Magnesium Alloys," in *Magnesium Technology: Metallurgy, Design Data, Applications* (Berlin, Heidelberg: Springer, 2006), 219–430, https://doi.org/10.1007/3-540-30812-1_6.

29. J. P. Hadorn, K. Hantzsche, S. Yi, et al., "Role of Solute in the Texture Modification During Hot Deformation of Mg-Rare Earth Alloys," *Metallurgical and Materials Transactions A: Physical Metallurgy and Materials Science* 43 (2012): 1347–1362, https://doi.org/10.1007/s11661-011-0923-5.

30. W. Tang, G. Zhou, Y. Shao, D. Li, Y. Peng, and H. Wang, "On the Role of Yttrium in Microstructure Evolution and Texture Modification During Magnesium Alloy Extrusion," *Materials Characterization* 162 (2020): 110189, https://doi.org/10.1016/j.matchar.2020.110189.

31. C. Tang, J. Chen, X. Ma, et al., "Effects of Extrusion Speed on the Formation of Bimodal-Grained Structure and Mechanical Properties of a Mg-Gd-Based Alloy," *Materials Characterization* 189 (2022): 111952, https://doi.org/10.1016/j.matchar.2022.111952.

32. Y. Jin, C. Blawert, H. Yang, et al., "Microstructure-Corrosion Behaviour Relationship of Micro-Alloyed Mg-0.5Zn Alloy With the Addition of Ca, Sr, Ag, In and Cu," *Materials & Design* 195 (2020): 108980, https://doi.org/10.1016/j.matdes.2020.108980.

33. S. Sanyal, S. Kanodia, R. Saha, T. K. Bandyopadhyay, and S. Mandal, "Influence of Hard Plate hot Forging Temperature on the Microstructure, Texture and Mechanical Properties in a Lean Mg–Zn–Al Alloy," *Journal of Alloys and Compounds* 800 (2019): 343–354, https://doi.org/10.1016/j.jallcom.2019.06.026.

34. S.-C. Jin, J. U. Lee, J. Go, H. Yu, and S. H. Park, "Effects of Sn Addition on the Microstructure and Mechanical Properties of Extruded Mg–Bi Binary Alloy," *Journal of Magnesium and Alloys* 10 (2022): 850–861, https://doi.org/10.1016/j.jma.2021.04.015.

35. S. I. Wright, M. M. Nowell, and D. P. Field, "A Review of Strain Analysis Using Electron Backscatter Diffraction," *Microscopy and Microanalysis* 17 (2011): 316–329, https://doi.org/10.1017/S1431927611000055.

36. P. Minárik, R. Král, J. Pešička, S. Daniš, and M. Janeček, "Microstructure Characterization of LAE442 Magnesium Alloy Processed by Extrusion and ECAP," *Materials Characterization* 112 (2016): 1–10, https://doi.org/10.1016/j.matchar.2015.12.002.

37. M.-S. Chen, W.-Q. Yuan, H.-B. Li, and Z.-H. Zou, "New Insights on the Relationship Between Flow Stress Softening and Dynamic Recrystallization Behavior of Magnesium Alloy AZ31B," *Materials Characterization* 147 (2019): 173–183, https://doi.org/10.1016/j.matchar.2018.10.031.

38. D. Liu, Z. Liu, and E. Wang, "Effect of Rolling Reduction on Microstructure, Texture, Mechanical Properties and Mechanical Anisotropy of AZ31 Magnesium Alloys," *Materials Science and Engineering A* 612 (2014): 208–213, https://doi.org/10.1016/j.msea.2014.06.034.

39. J. Bohlen, S. Yi, D. Letzig, and K. U. Kainer, "Effect of Rare Earth Elements on the Microstructure and Texture Development in Magnesium–Manganese Alloys During Extrusion," *Materials Science and Engineering A* 527 (2010): 7092–7098, https://doi.org/10.1016/j.msea.2010.07.081.

40. U. M. Chaudry, K. Hamad, and J.-G. Kim, "On the Ductility of Magnesium Based Materials: A Mini Review," *Journal of Alloys and Compounds* 792 (2019): 652–664, https://doi.org/10.1016/j.jallcom.2019.04.031.

41. J. Wu, L. Jin, J. Dong, F. Wang, and S. Dong, "The Texture and Its Optimization in Magnesium Alloy," *Journal of Materials Science and Technology* 42 (2020): 175–189, https://doi.org/10.1016/j.jmst.2019.10.010.

42. L. W. F. Mackenzie, B. Davis, F. J. Humphreys, and G. W. Lorimer, "The Deformation, Recrystallisation and Texture of Three Magnesium Alloy Extrusions," *Materials Science and Technology* 23 (2007): 1173–1180, https://doi.org/10.1179/174328407X226509.

43. G. Wu, J. Yu, L. Jia, et al., "Microstructure and Texture Evolution of Mg-Gd-Y-Zr Alloy During Reciprocating Upsetting-Extrusion," *Materials (Basel)* 13 (2020): 4932, https://doi.org/10.3390/ma13214932.

44. J. Zhao, B. Jiang, J. Xu, W. He, G. Huang, and F. Pan, "The Influence of Gd on the Recrystallisation, Texture and Mechanical Properties of Mg Alloy," *Materials Science and Engineering A* 839 (2022): 142867, https://doi.org/10.1016/j.msea.2022.142867.

45. H. Yu, Y. Hongge, C. Jihua, et al., "Effects of Minor Gd Addition on Microstructures and Mechanical Properties of the High Strain-Rate Rolled Mg–Zn–Zr Alloys," *Journal of Alloys and Compounds* 586 (2014): 757–765, https://doi.org/10.1016/j.jallcom.2013.10.005.

46. J. Jayaraj, K. G. Raghu, and A. Srinivasan, "Corrosion Behavior of Mg-Zn-RE Alloys (RE = Gd, Y, Nd)," *Journal of Materials Engineering and Performance* 32 (2023): 2840–2852, https://doi.org/10.1007/s11665-022-07213-5.

47. C. Wang, L. Wu, F. Xue, et al., "Electrochemical Noise Analysis on the Pit Corrosion Susceptibility of Biodegradable AZ31 Magnesium Alloy in Four Types of Simulated Body Solutions," *Journal of Materials Science and Technology* 34 (2018): 1876–1884, https://doi.org/10.1016/j.jmst.2018.01.015.

48. A. Bahmani, M. Lotfpour, M. Taghizadeh, and W.-J. Kim, "Corrosion Behavior of Severely Plastically Deformed Mg and Mg Alloys," *Journal of Magnesium and Alloys* 10 (2022): 2607–2648, https://doi.org/10.1016/j.jma.2022.09.007.

49. N. Birbilis, M. A. Easton, A. D. Sudholz, S. M. Zhu, and M. A. Gibson, "On the Corrosion of Binary Magnesium-Rare Earth Alloys," *Corrosion Science* 51 (2009): 683–689, https://doi.org/10.1016/j.corsci.2008.12.012.

50. A. Bahmani, S. Arthanari, and K. S. Shin, "Formulation of Corrosion Rate of Magnesium Alloys Using Microstructural Parameters," *Journal of Magnesium and Alloys* 8 (2020): 134–149, https://doi.org/10.1016/j.jma.2019.12.001.

51. R. Xin, Y. Luo, A. Zuo, J. Gao, and Q. Liu, "Texture Effect on Corrosion Behavior of AZ31 Mg Alloy in Simulated Physiological Environment," *Materials Letters* 72 (2012): 1–4, https://doi.org/10.1016/j.matlet.2011.11.032.

52. Y. Liu, J. Wen, H. Li, and J. He, "Effects of Extrusion Parameters on the Microstructure, Corrosion Resistance, and Mechanical

15524981, 2024, 9, Downloaded from https://onlinelibrary.wiley.com/doi/10.1002/jbm.b.35474 by Srinivasan Amirthalingam - Nti Institute For Interdis. Sci. And Tech , Wiley Online Library on [01/09/2024]. See the Terms and Conditions (https://onlinelibrary.wiley.com/terms-and-conditions) on Wiley Online Library for rules of use; OA articles are governed by the applicable Creative Commons License

Properties of Biodegradable Mg–Zn–Gd–Y–Zr Alloy," *Journal of Alloys and Compounds* 891 (2022): 161964, https://doi.org/10.1016/j.jallcom.2021.161964.

53. X. Liu, G. Chen, X. Zhong, et al., "Degradation of Differently Processed Mg-Based Implants Leads to Distinct Foreign Body Reactions (FBRs) Through Dissimilar Signaling Pathways," *Journal of Magnesium and Alloys* 11 (2022): 2106–2124, https://doi.org/10.1016/j.jma.2022.03.017.

54. G.-L. Song, R. Mishra, and Z. Xu, "Crystallographic Orientation and Electrochemical Activity of AZ31 Mg Alloy," *Electrochemistry Communications* 12 (2010): 1009–1012, https://doi.org/10.1016/j.elecom.2010.05.011.

55. G.-L. Song, "1 – Corrosion Electrochemistry of Magnesium (Mg) and Its Alloys," *Corrosion of Magnesium Alloys*, Woodhead Publishing Series in Metals and Surface Engineering (Woodhead Publishing, 2011), 3–65, https://doi.org/10.1533/9780857091413.1.3.

56. J. Kim, K. C. Wong, P. C. Wong, S. A. Kulinich, J. B. Metson, and K. A. R. Mitchell, "Characterization of AZ91 Magnesium Alloy and Organosilane Adsorption on Its Surface," *Applied Surface Science* 253 (2007): 4197–4207, https://doi.org/10.1016/j.apsusc.2006.09.030.

57. M. I. Sosulnikov and Y. A. Teterin, "X-Ray Photoelectron Studies of Ca, Sr and Ba and Their Oxides and Carbonates," *Journal of Electron Spectroscopy and Related Phenomena* 59 (1992): 111–126, https://doi.org/10.1016/0368-2048(92)85002-O.

58. Y. Tanizawa, H. Tsuchikane, K. Sawamura, and T. Suzuki, "Reaction Characteristics of Hydroxyapatite With F– and PO3F2– Ions. Chemical States of Fluorine in Hydroxyapatite," *Journal of the Chemical Society, Faraday Transactions* 87 (1991): 2235–2240, https://doi.org/10.1039/FT9918702235.

59. B. R. Strohmeier and D. M. Hercules, "Surface Spectroscopic Characterization of the Interaction Between Zinc Ions and γ-Alumina," *Journal of Catalysis* 86 (1984): 266–279, https://doi.org/10.1016/0021-9517(84)90372-5.

60. Y. Xu, J. Li, M. Qi, W. Guo, and Y. Deng, "A Newly Developed Mg-Zn-Gd-Mn-Sr Alloy for Degradable Implant Applications: Influence of Extrusion Temperature on Microstructure, Mechanical Properties and in Vitro Corrosion Behavior," *Materials Characterization* 188 (2022): 111867, https://doi.org/10.1016/j.matchar.2022.111867.

61. W. Li, S. Guan, J. Chen, et al., "Preparation and in Vitro Degradation of the Composite Coating With High Adhesion Strength on Biodegradable Mg–Zn–Ca Alloy," *Materials Characterization* 62 (2011): 1158–1165, https://doi.org/10.1016/j.matchar.2011.07.005.

62. R. Hou, J. Victoria-Hernandez, P. Jiang, et al., "In Vitro Evaluation of the ZX11 Magnesium Alloy as Potential Bone Plate: Degradability and Mechanical Integrity," *Acta Biomaterialia* 97 (2019): 608–622, https://doi.org/10.1016/j.actbio.2019.07.053.

63. L. M. Gabriel, E. F. Sanchez, S. G. Silva, and R. G. Santos, "Tumor Cytotoxicity of Leucurolysin-B, a P-III Snake Venom Metalloproteinase From *Bothrops leucurus*," *Journal of Venomous Animals and Toxins Including Tropical Diseases* 18 (2012): 24–33, https://doi.org/10.1590/S1678-91992012000100004.

64. K. Ho, L. S. Yazan, N. Ismail, and M. Ismail, "Apoptosis and Cell Cycle Arrest of Human Colorectal Cancer Cell Line HT-29 Induced by Vanillin," *Cancer Epidemiology* 33 (2009): 155–160, https://doi.org/10.1016/j.canep.2009.06.003.

65. J. Fischer, D. Pröfrock, N. Hort, R. Willumeit, and F. Feyerabend, "Reprint of: Improved Cytotoxicity Testing of Magnesium Materials," *Materials Science and Engineering B* 176 (2011): 1773–1777, https://doi.org/10.1016/j.mseb.2011.06.002.

66. A.-M. Galow, A. Rebl, D. Koczan, S. M. Bonk, W. Baumann, and J. Gimsa, "Increased Osteoblast Viability at Alkaline pH in Vitro Provides a New Perspective on Bone Regeneration," *Biochemistry and Biophysics Reports* 10 (2017): 17–25, https://doi.org/10.1016/j.bbrep.2017.02.001.

15524981, 2024, 9, Downloaded from https://onlinelibrary.wiley.com/doi/10.1002/jbm.b.35474 by Srinivasan Amirthalingam - Nti Institute For Inerdis. Sci. And Tech , Wiley Online Library on [01/09/2024]. See the Terms and Conditions (https://onlinelibrary.wiley.com/terms-and-conditions) on Wiley Online Library for rules of use; OA articles are governed by the applicable Creative Commons License